SAND 75-0174

PREDICTIONS OF PROJECTILE PENETRATION PHENOMENA AND COMPARISON WITH EXPERIMENTS IN A SOIL MEDIUM

Sandia Laboratories

P.O. Box 5800

Albuquerque, New Mexico 87115

8 October 1975

Final Report for Period February 1974—January 1975

DNA CONTRACT ORDER No.
IACRO No. DNA 74-835

APPROVED FOR PUBLIC RELEASE;
DISTRIBUTION UNLIMITED.

THIS WORK SPONSORED BY THE DEFENSE NUCLEAR AGENCY
UNDER SUBTASK L35IAXSX338-06.

Prepared for

Director

DEFENSE NUCLEAR AGENCY

Washington, D. C. 20305

Destroy this report when it is no longer
needed. Do not return to sender.

SECURITY CLASSIFICATION OF THIS PAGE (When Data Entered)

REPORT DOCUMENTATION PAGE		READ INSTRUCTIONS BEFORE COMPLETING FORM
1. REPORT NUMBER SAND-75-0174	2. GOVT ACCESSION NO.	3. RECIPIENT'S CATALOG NUMBER
4. TITLE (and Subtitle) PREDICTIONS OF PROJECTILE PENETRATION PHENOMENA AND COMPARISON WITH EXPERIMENTS IN A SOIL MEDIUM		5. TYPE OF REPORT & PERIOD COVERED Final Report for Period February 1974–January 1975
		6. PERFORMING ORG. REPORT NUMBER
7. AUTHOR(s) R. K. Byers A. J. Chabai R. T. Walsh		8. CONTRACT OR GRANT NUMBER(s) DNA Contract Order No. IACRO No. DNA 74-835
9. PERFORMING ORGANIZATION NAME AND ADDRESS Sandia Laboratories P.O. Box 5800 Albuquerque, New Mexico 87115		10. PROGRAM ELEMENT, PROJECT, TASK AREA & WORK UNIT NUMBERS RMSS/Subtask L35IAXSX338-06
11. CONTROLLING OFFICE NAME AND ADDRESS Director Defense Nuclear Agency Washington, D.C. 20305		12. REPORT DATE 8 October 1975
		13. NUMBER OF PAGES 364
14. MONITORING AGENCY NAME & ADDRESS(if different from Controlling Office)		15. SECURITY CLASS (of this report) UNCLASSIFIED
		15a. DECLASSIFICATION/DOWNGRADING SCHEDULE

16. DISTRIBUTION STATEMENT (of this Report)

Approved for public release; distribution unlimited.

17. DISTRIBUTION STATEMENT (of the abstract entered in Block 20, if different from Report)

DNA-NWET-L35IAXS

18. SUPPLEMENTARY NOTES

This work sponsored by the Defense Nuclear Agency under Subtask L35IAXSX338-06.

19. KEY WORDS (Continue on reverse side if necessary and identify by block number)

Earth Penetration	Terradynamics
Soil Mechanics	Projectile Decelerations
Finite Difference Solutions	Soil Stress Measurements
Two-dimensional Calculations	TOODY

20. ABSTRACT (Continue on reverse side if necessary and identify by block number)

Results of calculations are presented to predict effects of earth penetration experiments conducted in mid-July 1974 at the Watching Hill site of the Defense Research Establishment, in Alberta, Canada. Calculations were performed with the TOODY Lagrangian code for both a rigid and deformable projectile. Soil cap models describing four layers of the glacial silt target were employed in the calculations. All calculations are for a projectile 0.1651 m in diameter (6.5 inches), of mass 181.44 kg (400 pounds) with tangent

DD FORM 1473 1 JAN 73 EDITION OF 1 NOV 65 IS OBSOLETE

20.   ABSTRACT (Continued)

ogive nose shape impacting the earth target at a velocity of 152.4 m/s
(500 ft/sec). A zero friction boundary condition is employed at the
projectile-soil interface. Stress, strain, and velocity distributions,
produced in the medium by the penetrating projectile, are computed.
Axial retarding forces exerted by the medium on the projectile and
normal stress distributions on the projectile surface are also calcu-
lated. Comparisons of predictions with experimental measurements of
rigid body projectile deceleration and soil stress histories indicate
that computer simulations should be able to provide a detailed and
reasonably accurate description of soil response and projectile motion
during penetration.

PREFACE

1

TABLE OF CONTENTS

List of Illustrations

SECTION I

INTRODUCTION

The immediate purpose of calculations presented here is to provide predictions of effects associated with earth pe. etration experiments conducted at the Watching Hill site in Alberta, Canada, in mid-July 1974. In particular, predictions of deceleration history and medium stre s histories at specific locations were desired for comparison with experimental measurements of these quantities. Such comparisons permit evaluation of current theoretical prediction capabilities and, in addition, provide insights into the primary mechanisms and relevant phenomena governing projectile penetration into earth media. Ultimate objectives of the computational effort are (1) to develop methods for confidently predicting loads on earth penetrating projectiles in order to facilitate rational design of penetrators with a minimum reliance on empirical testing, (2) to develop an understanding of the detailed mechanisms involved in earth penetration to the extent that the empirical soil factor of Young's penetration equations[1,2] may be correlated with appropriate target medium properties, and (3) to establish the degree of complexity in description of target medium properties necessary for accurate calculation of projectile decelerations, loads, and depths of penetration.

Two finite difference code calculations were made to estimate results of the Watching Hill experiments. The TOODY Lagrangian code[3,4] was employed to predict penetration performance of both a rigid and a deformable projectile. In both cases, the target medium properties were described by using identical soil cap models. With the projectile considered as a
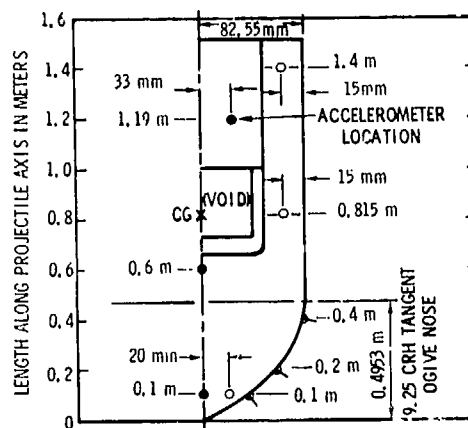
7

rigid body, the finite difference code is capable of more efficient operations than when the projectile is taken to be a deformable body. Rigid body calculations then permit examination of penetration to deeper projectile depths in reasonable amounts of computer time. To verify the validity of the rigid body assumption, a deformable body calculation was performed until the nose of the projectile was fully embedded. From the deformable body calculation, stress and strain histories and distributions within the projectile are obtained.

Projectile penetration experiments[5] at the Watching Hill site included one for direct comparison with calculations in which the projectile impacted the target medium at a velocity of 152.4 m/s (500 ft/sec). The projectile,[6] fabricated from D6AC steel, had a diameter of 0.165 m (6.5 inches), a length of 1.524 m (60 inches), and a mass of 181.44 kg (400 pounds). Nose shape was 9.25 CRH tangent ogive with a slight blunting of the tip. Accelerometers mounted within the projectile provided deceleration histories during penetration. Integrations of deceleration histories result in projectile velocity and position information including depth of penetration. Projectile deceleration and penetration depth were felt to be insufficient information for critically evaluating results of computer code calculations, particularly the material property models employed in the codes.[7] A much more severe test of target medium constitutive models is provided by measurements of the medium response. For these reasons, lithium niobate pressure or stress transducers[8,9] were incorporated into the Watching Hill experiments. Six stress-history transducers, four of which were to measure mean stress and two radial stress, were emplaced in the target medium in two vertical holes near the vicinity of the projectile penetration locations. Positions of the stress

transducers are indicated in Figure I-1. At the position (range/depth relative to the projectile impact point) of 0.45 m/1.8 m, a mean stress transducer is located. A mean stress and a radial stress transducer are located at 0.45 m/3.6 m, and at 0.45 m/5.4 m, two mean stress gauges are placed. A single radial stress gauge is located at 0.9 m/3.6 m. Gauges shown in Figure I-1 at a range of 1.5 m were used for another projectile penetration experiment but are physically the same set of gauges shown at a range of 0.45 m   ie experiment of primary interest. Measurements of target response a..   .jectile penetration apparently have never before been made; the successful recording of medium stress histories[10] during the Watching Hill penetration experiments has provided valuable information for more direct verification of computer code calculations.

Output desired from computer code calculations has been specified in detail[11] and is briefly summarized in Figures I-1 and I-2 for the rigid body calculations. Similarly, for the deformable projectile calculations, desired output is indicated in Figures I-3 and I-4.

9

RIGID BODY CALCULATIONS

RANGE IN METERS

Figure I-1. Rigid Body Calculation. Medium
field points for history displays
of displacements, velocities and
stresses.

RIGID BODY CALCULATIONS

Figure I-2. Rigid Body Calculation. Projectile
positions at which times contour plots
are required.

DEFORMABLE BODY CALCULATION

- REQUIRED HISTORY CALCULATION FOR VERTICAL ACCELERATION, VELOCITY AND DISPLACEMENT

- REQUIRED HISTORY CALCULATION FOR p AND $\sqrt{J'_2}$ (OR σ_r, σ_θ, σ_z, σ_{rz})

- REQUIRED HISTORY CALCULATION FOR NORMAL STRESS AND SHEAR STRESS ON PROJECTILE SURFACE

Figure 1-3. Deformable Body Calculation. Positions in projectile at which displacements, velocities, accelerations and stress are displayed.

DEFORMABLE BODY CALCULATION
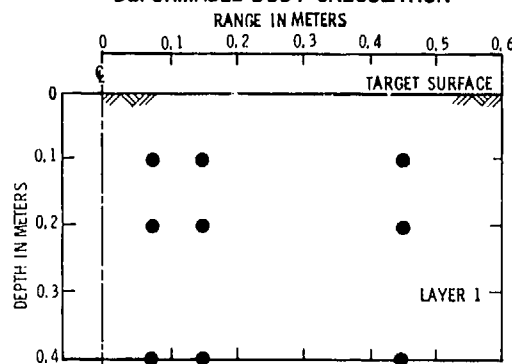
- REQUIRED HISTORY FOR $\dot{u}$, $\dot{w}$, u, w, p AND $\sqrt{J'_2}$

FIELD PLOTS AT PROJECTILE PENETRATION
DEPTHS OF 10, 20 AND 40 cm
 DEFORMED GRID
 VELOCITY VECTOR OR CONTOUR
 STRESS VECTOR OR CONTOUR
 MEAN STRESS CONTOUR
 VOLUMETRIC STRAIN CONTOUR
 GRID SHOWING ZONES OF FAILURE

Figure 1-4. Deformable Body Calculation. Medium field points for history displays of displacements, velocities and stresses.

11

SECTION II

MATERIAL MODELS FOR TARGET MEDIUM

The Watching Hill Blast Range of the Canadian Defense Research Estab-
lishment, on which site the earth penetrator experiments[5] were conducted,
is located about 30 miles north of Medicine Hat near Suffield, Alberta.
The target medium at Watching Hill consists of a thick succession of
glacial lake deposits, outwash materials, and glacial tills; the near
surface deposit is composed of thin interbedded layers of lacustrine silt,
sand, and clay sediments.[12] The medium is porous and contains varying
amounts of water, increasing with depth.[14] For purposes of modeling the
target medium in computer calculations of projectile penetration, the
medium has been represented by four uniform, homogeneous isotropic layers.
The three uppermost layers were each taken to be 2.4 m (7.87 feet) thick.
The fourth layer, beginning at 7.2 m (23.6 feet), is below the water table.
Material properties derived from uniaxial strain and triaxial stress
experiments[12] have been specified[13,14] for each of the four layers.*

---

*Of course, many more, and much thinner layers actually exist in the region
of interest. It was felt that the short time available for material
modeling made it necessary to average properties into the sturcture chosen,
using overall similarities of adjacent materials as guides. It was also
necessary in some cases to estimate the effects of loading rates on
material response. Therefore, the term "data" appearing in this section
should be taken to mean what is commonly referred to as "recommended
properties."

For the calculations of projectile penetration with both a rigid and deformable projectile, a soil cap model is used to describe each of the four layers of the Watching Hill medium. The cap models[15] employ a failure envelope or fixed plastic yield surface represented by a function of the form $f_1(\tau, p) = 0$ in which p is the mean stress or pressure and τ is the octahedral shear stress (see Figure II-1). Octahedral shear stress is defined by $\tau = (\sigma'_{ij}\sigma'_{ij}/3)^{\frac{1}{2}}$, where the deviator stress, $\sigma'_{ij} = \sigma_{ij} - p\delta_{ij}$. The "cap" on this surface is given by $f_2(p, \tau, \epsilon_p) = 0$, where ϵ_p is the plastic volumetric strain. Position of the cap on the failure envel- is determined by ϵ_p, and the cap expands or contracts as ϵ_p increases or decreases. Plastic strain increments are determined from f_1 and f_2 by means of the associated flow rule. Figure II-2 illustrates an example
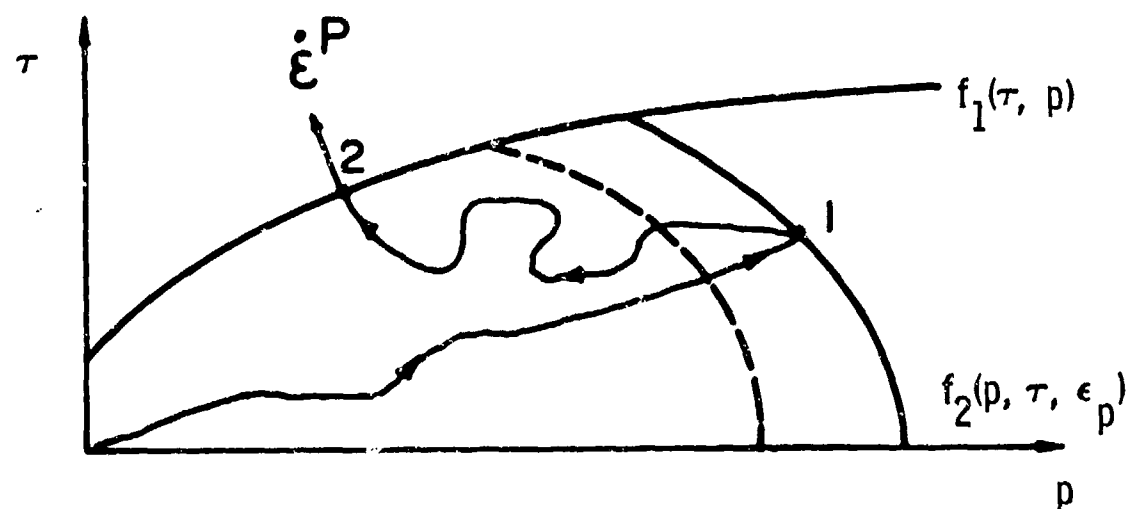
Figure II-1. Cap Model Illustrating Failure Envelope, Cap, a Stress Path, and Cap Contraction

of the hysteresis produced by a cap model description in a series of load-unload cycles of a uniaxial strain test and the corresponding path in $\tau - p$ space. Information supplied[12] for the Watching Hill target medium consis-

ted of a single uniaxial strain, load-unload path and a failure envelope considered to be representative of each of four layers of the medium. From the data available for each of the idealized four layers, parameters were determined for the functions f_1 and f_2 . For Layers 1, 2, and 3, the failure envelope is given by

$$\tau = A - C \exp(-Bp)$$

and for Layer 4 by

$$\tau = A[1 - 3p/B)^2] + C, p < B/3$$

$$\tau = A + C, \qquad p \geq B/3$$

where p is pressure. The yield surface ellipse for Layers 1, 2 and 3 is described by

$$\tau = [(X - L)^2 - (\sqrt{3}p - L)^2]^{\frac{1}{2}}/R \ ,$$

where X represents the intersection of the cap with the p axis and is given by

$$X = -[\ell n(1 - \epsilon_p/w)]/D$$

L represents the value of p at which the cap and failure envelope intersect, and at which the cap has a horizontal tangent and is given by

$$L(\epsilon_p) = \begin{cases} \ell \text{ for } \ell \geq 0 \\ 0 \text{ for } \ell < 0 \end{cases}$$

where ℓ is the solution of the transcendental equation

$$\ell + R\{A - C \exp(-B\ell/\sqrt{3})\} = X(\epsilon_p)$$

14
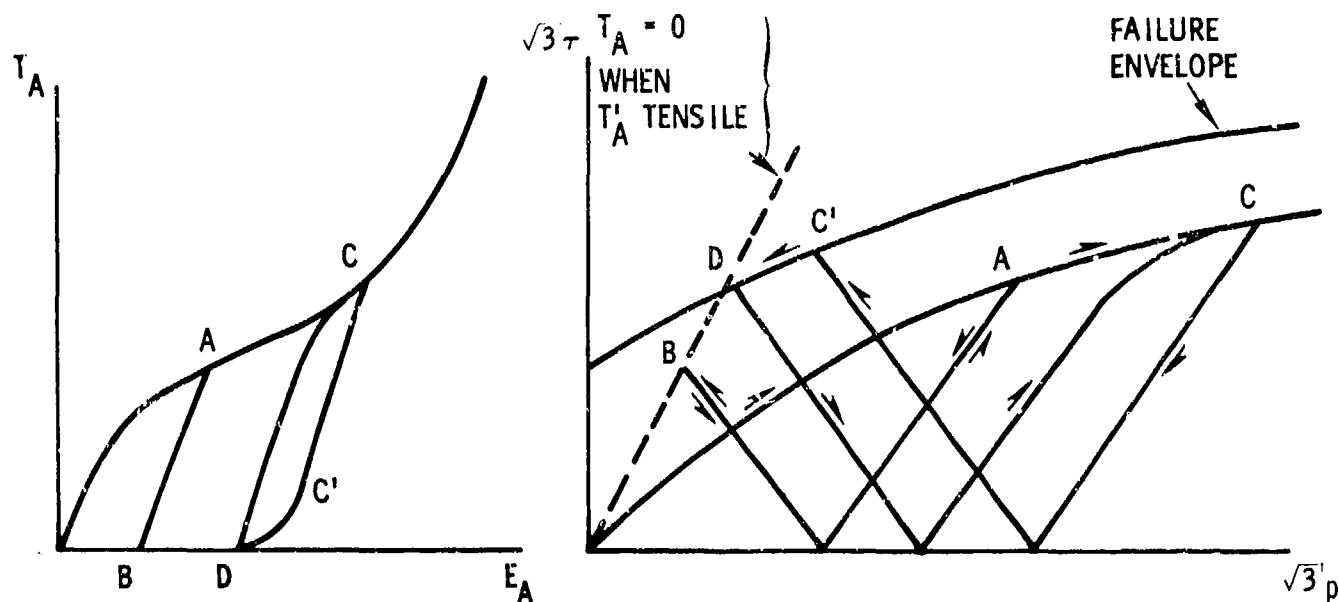
Figure II-2. Loading and Unloading Cycles for Cap Model
Material in Stress-Strain and Shear Stress-
Pressure Space

For Layer 4, the yield surface is taken as

$$\tau = X/\sqrt{6} - p/\sqrt{2} .$$

In the calculation, the cap determines the plastic strain increment whenever $p \geq L/\sqrt{3}$. This, coupled with the fact that the normal to the cap never has a negative spherical component, precludes bulking, or dilatancy, when the loading state is on the cap.

The initial value of the quantity X for each material was taken to be one percent of the value necessary for the cap-envelope intersection point to be at $p = 0$. This results in a very small initial elastic range. As plastic deformation occurs, the growing cap remains centered on the origin, until X exceeds 100 times its initial value.

Elastic bulk moduli are given by

$$K = B_0\{1 - B_1 \exp(-B_2 p)\}$$

for Layers 1, 2, and 3, and by

$$K = \mathrm{Min}\{B_0 \exp(B_2 p/B_1); \quad B_0 \exp(B_2/\sqrt{3})\}$$

for Layer 4. The elastic shear moduli are

$$\frac{3(1 - 2\nu)}{2(1 + \nu)} \frac{\{1 + S_1 \exp(-S_2 p)\}}{(1 + S_1)} K ,$$

in which ν is Poisson's ratio. Constants for the various expressions are listed in Table II-1. Figures II-3 through II-6 compare data obtained from the cap models (which are used in code calculations of projectile penetration) with laboratory data from uniaxial strain and triaxial stress experiments. Figures II-7 through II-10 show data for uniaxial strain paths in τ - p space and corresponding cap model results. The cap model for Layer 4 fits the data well; however, for Layers 1, 2, and 3, less satisfactory agreement between model predictions and experiment is obtained with the model response being less stiff in shear than indicated by data. This suggests the need, in matching static laboratory data, for a more elaborate model than the 12-parameter model used. One such model has been suggested[16] in which the strain hardening cap is described by an ellipse of variable eccentricity. Cap model formulations with 29 parameters available for fitting data have been described[17,18]; these formulations undoubtedly can better fit the available laboratory data and could be employed in future calculations to assess sensitivity of calculated projectile penetration results to cap model expressions and parameters.

16

TABLE II-1

Cap Model Constants for the Four Layers of the Watching Hill Medium

Constant	Units	Layer 1	Layer 2	Layer 3	Layer 4
ρ_0	(Mg/m^3)	1.490	1.426	1.859	1.971
B_0	(GPa)	0.6237	0.8889	1.214	1.103
ν		0.31	0.14	0.257	0.48
B_1		0	0.7622	0.8622	---
B_1	(MPa)	---	---	---	2.382
B_2	$(MPa)^{-1}$	0	0.2087	0.3965	---
B_2		---	---	---	2.139
S_1		0	0.35	-0.8	0.51
S_2	$(MPa)^{-1}$	0	0.3859	0.3464	0.6603
A	(MPa)	1.966	7.604	0.7084	8.123×10^{-2}
B	$(GPa)^{-1}$	346.4	91.42	468.5	---
B	(MPa)	---	---	---	3.102
C	(MPa)	1.902	7.546	0.6368	8.123×10^{-2}
D	$(GPa)^{-1}$	38.61	131.2	150.0	800.0
W		0.37	0.16	0.12	1.0×10^{-4}
R		2.252	2.179	2.785	---

17
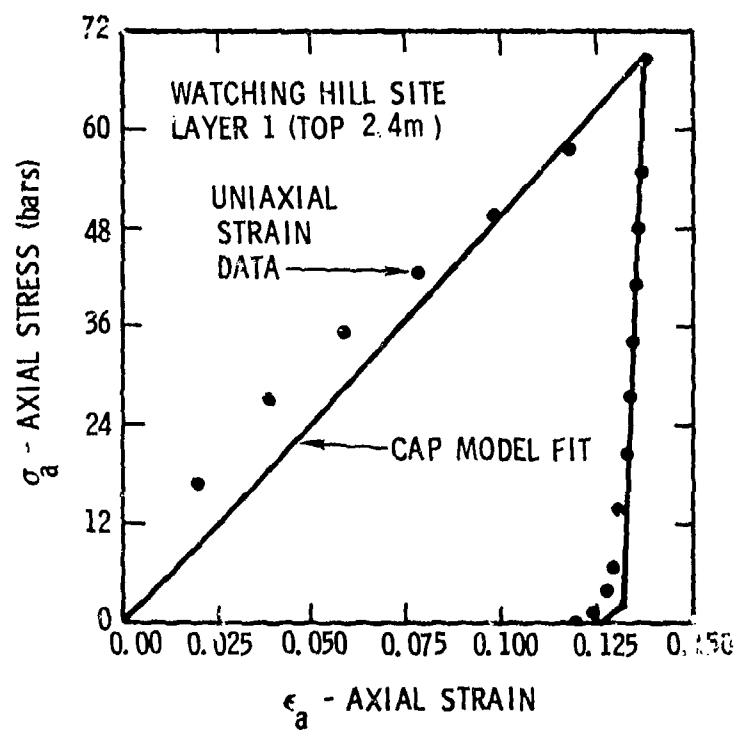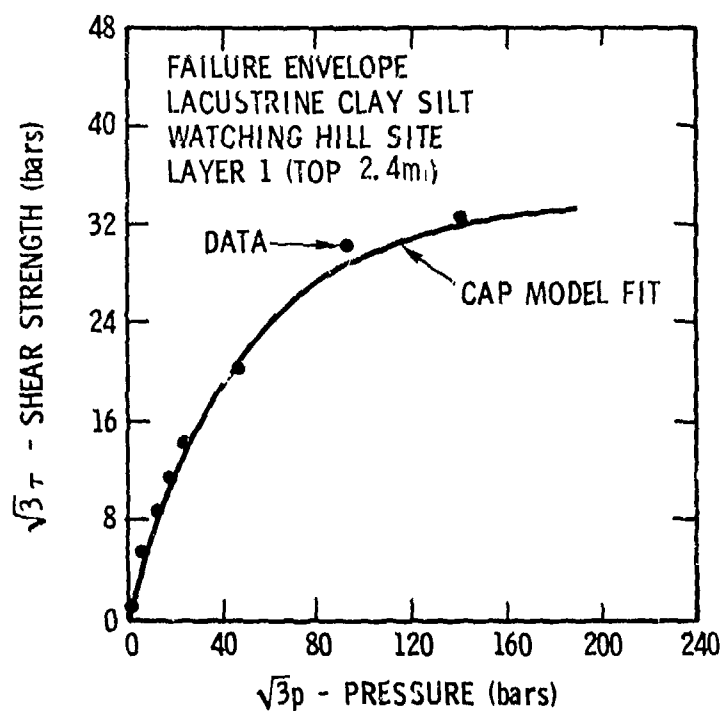
Figure II-3. Cap Model Fit to Uniaxial Strain and Triaxial Failure
Envelope Data for Layer 1 at Watching Hill

FAILURE ENVELOPE
LACUSTRINE CLAY SILT
WATCHING HILL SITE
LAYER 2 (2.4 to 4.8m)

DATA

CAP MODEL FIT

$\sqrt{3}\,\tau$ - SHEAR STRENGTH (bars)

$\sqrt{3}p$ - PRESSURE (bars)

WATCHING HILL SITE
LAYER 2 (2.4 to 4.8m)

UNIAXIAL
STRAIN
DATA

CAP MODEL
FIT

σ_a - AXIAL STRESS (bars)
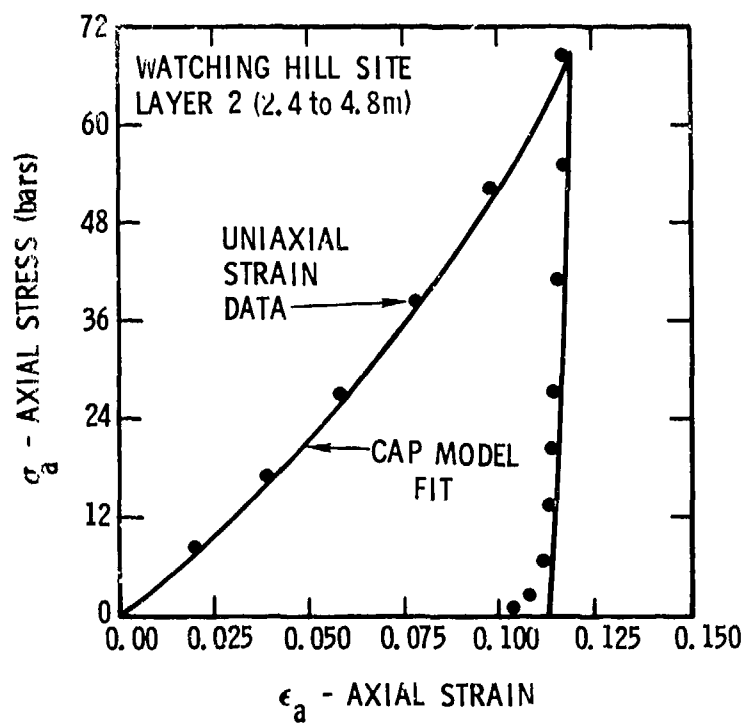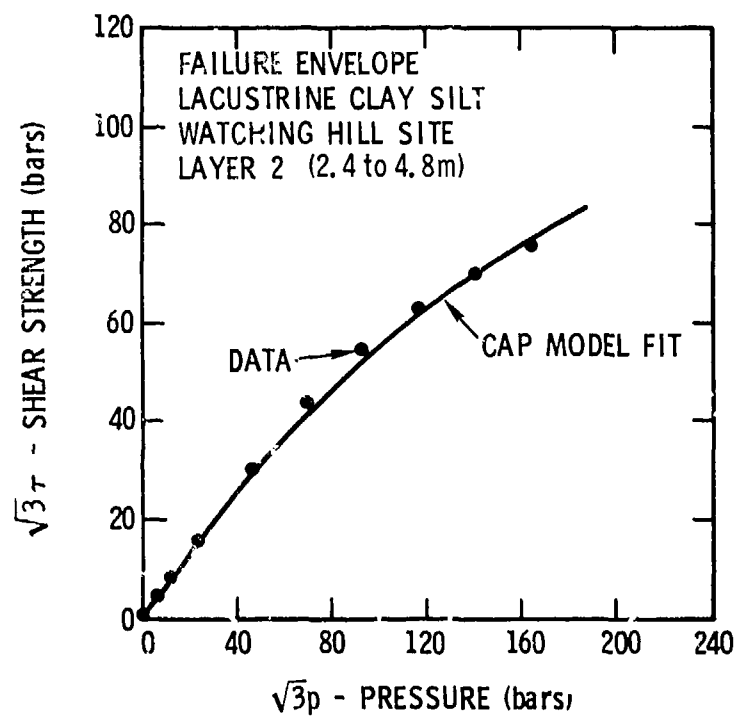
ϵ_a - AXIAL STRAIN

Figure II-4. Cap Model Fit to Uniaxial Strain and Triaxial Failure
Envelope Data for Layer 2 at Watching Hill
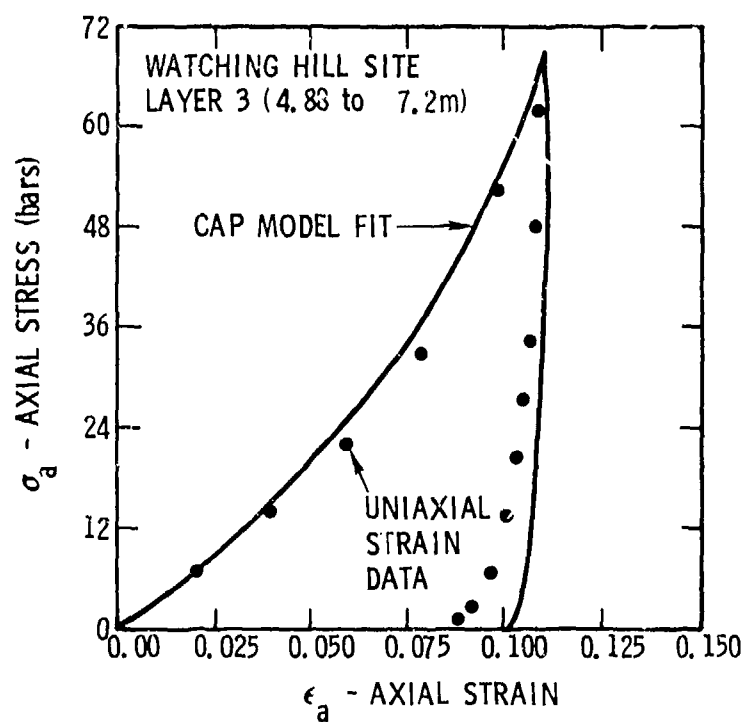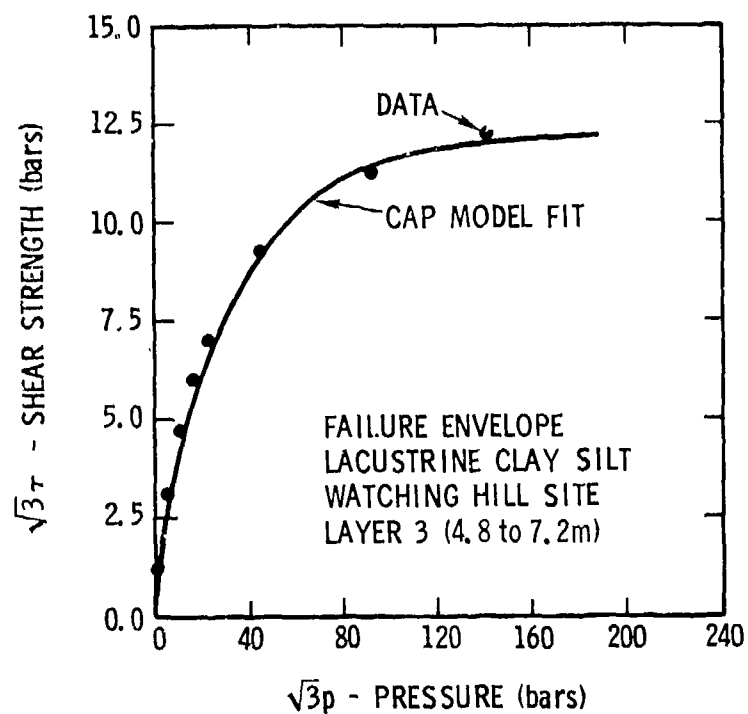
Figure II-5. Cap Model Fit to Uniaxial Strain and Triaxial Failure
Envelope Data for Layer 3 at Watching Hill
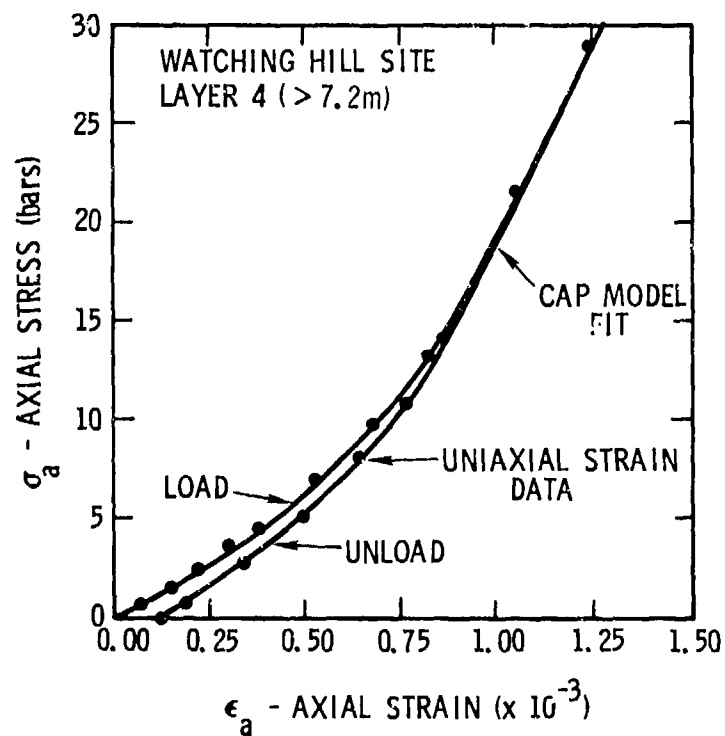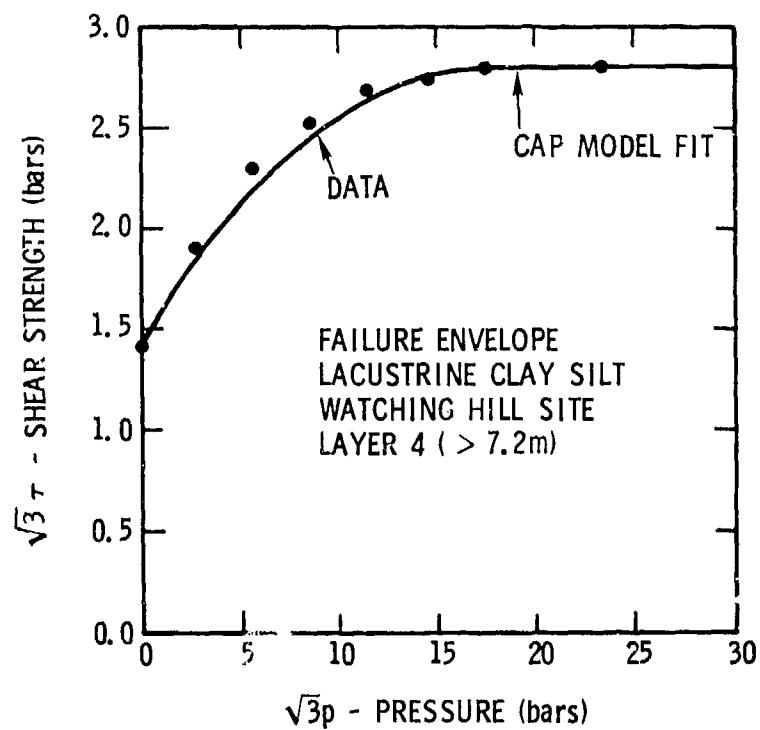
Figure II-6. Cap Model Fit to Uniaxial Strain and Triaxial Failure Envelope Data for Layer 4 at Watching Hill
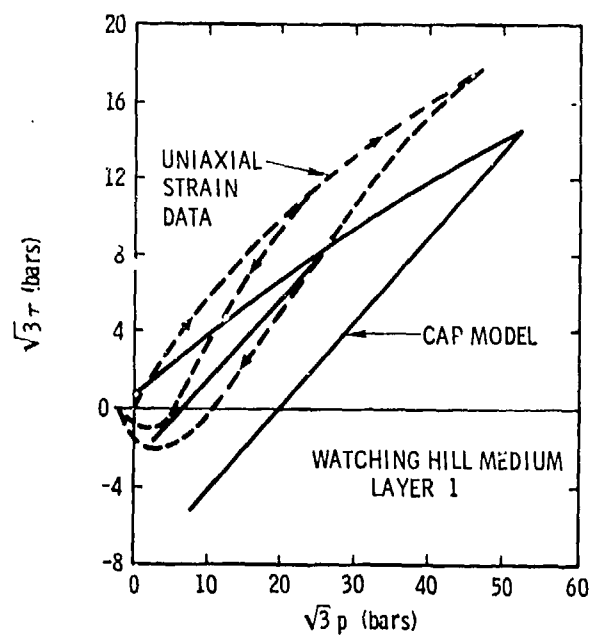
Figure II-7. Uniaxial Strain Path in τ-p Space for Layer 1
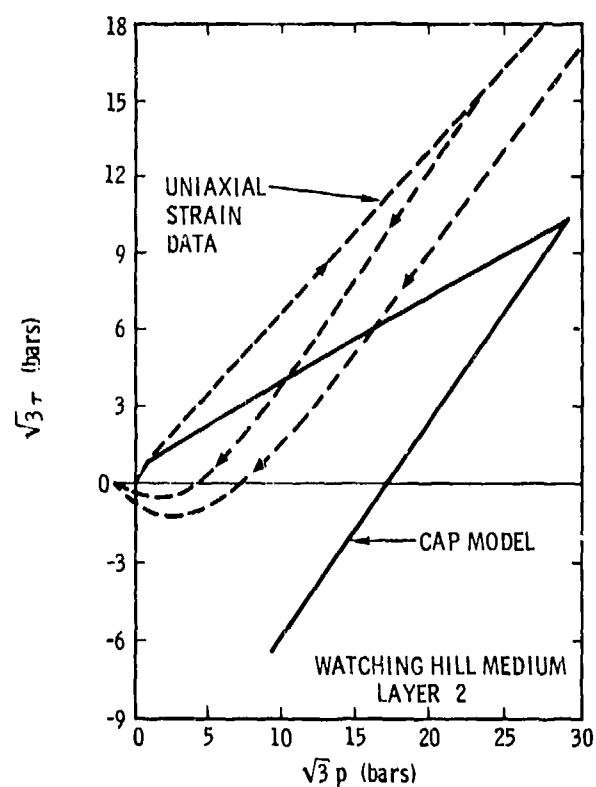
Figure II-8. Uniaxial Strain Path in τ-p Space for Layer 2
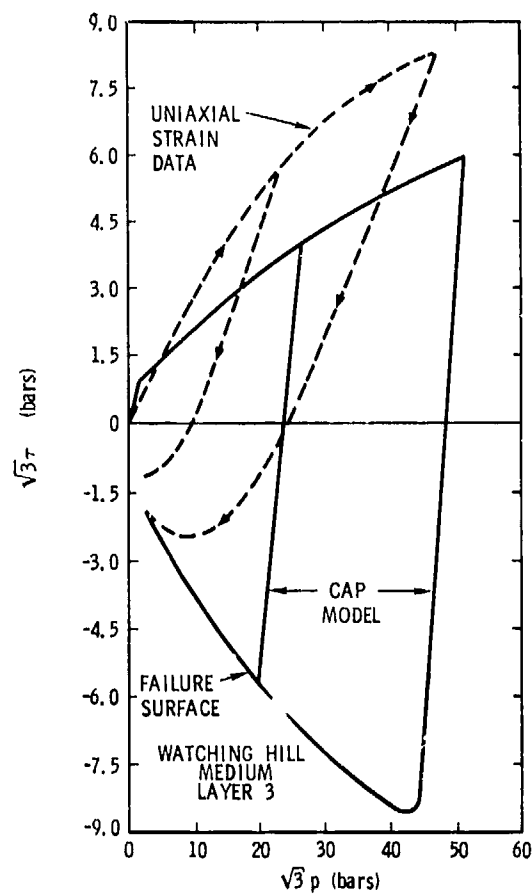
Figure II-9.   Uniaxial Strain Path in τ-p Space
for Layer 3
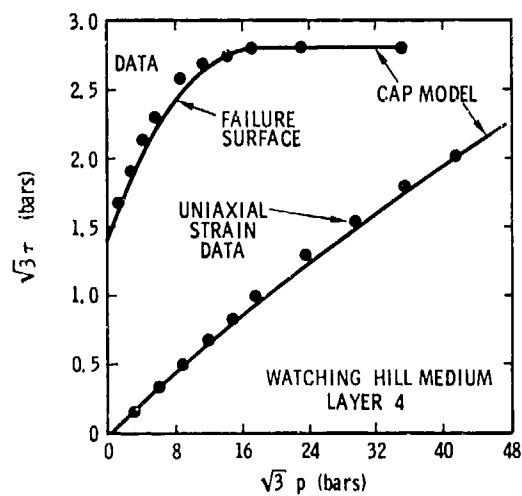
Figure II-10.   Uniaxial Strain Path in τ-p Space
for Layer 4

23

It should be pointed out that the cap model, as implemented in TOODY for the calculations reported here, differs in some details from the cap model described by Nelson et al.[15] In particular, the relations for the variation of bulk and shear moduli with p and τ do not satisfy the compatibility requirements which arise from the assumption of the existence of an elastic strain energy function. Also, the particular function chosen to model the cap for Layer 4 exhibits a "corner" on the pressure axis, reminiscent of those appearing in the Tresca yield condition, for example. The effect of these variations on the particular calculations reported here is difficult to assess, particularly as no purely spherical stress states were encountered in the calculation.

SECTION III

RIGID PROJECTILE CALCULATIONS

The TOODY[3] Lagrangian wave propagation code was used to predict target and penetrator motions and stresses during the experiments planned for the Watching Hill test site. The code is termed Lagrangian because the nodes of the calculational grid move in response to the local stress gradients. The basic process the code performs is to solve difference analogs to the partial differential equations describing the balance of momentum, mass, and energy, and the constitutive relations. This procedure is executed at each node of the grid, the time is then advanced, and the whole process repeated until the desired final time of the calculation is reached.

Since the time-step with which the calculation advances is controlled by the minimum distance on a mesh over the entire grid, large distortions can result in an inefficient calculation. Large distortions can also degrade the accuracy of the numerical methods used in the code, which then yield unrealistic results. For these reasons, the TOOREZ[4] code was developed to permit carrying Lagrangian code calculations past the point where they would otherwise have to be abandoned. TOOREZ allows the user to redistribute the nodes of the calculational grid (i.e. rezone the problem), then repartitions the mass, momentum, and energy in such a way that all these quantities are conserved. Using the output from the rezoning code, the calculation can then be resumed.

The positions of nodes in the calculational grid which originally lie on the axis of rotational symmetry are prevented from occupying the

space occupied by the penetrator. The motion of each of these nodes is first calculated in the standard way from the stress divergence, including the effects of soil-penetrator friction, if any. In this calculation, a condition of perfect slip was assumed for the soil-penetrator interface. If the standard motion calculation for the node yields a position on the surface of, or outside, the projectile, no adjustments are necessary. When a node is calculated to lie inside the penetrator, adjustments to the velocity and position are made so that the normal velocity relative to the penetrator is zero, the tangential velocity has that value already calculated, and the position is on the penetrator surface. In resolving the velocity into normal and tangential components on the ogival nose, the position of the node at the previous time step is used to evaluate the local normal direction. The areas and volumes for material and momentum zones adjacent to the penetrator are adjusted, where necessary, to include the effect of the penetrator surface.

At the beginning of each time step of the calculation, surface tractions for all soil zones in contact with the penetrator are integrated to give the total axial force acting to decelerate the penetrator. For a zone in contact with the penetrator surface the stress is assumed constant, and the axial contributions of the normal stress and frictional stress, if any, are expressed as functions of position on the penetrator surface. These are integrated over the range covered by the zone, so that, on the nose, changes in the local normal direction and surface area are accounted for.

For this calculation, it was desired to model the target to a large depth. Therefore, the initial zoning of the target region utilized expon-

tially increasing zone sizes to allow good resolution near the surface
and maintain a reasonable number of zones in the problem. Table III-1
and Figure III-1 describe the initial zoning. As penetration depth
increases to the regions where the zone sizes become too large for good
resolution, the rezoning code is used to adjust the zoning, providing
smaller zones in front of and on the nose of the penetrator. It was
determined early in the calculation that no significant changes occur in
the soil once the nose of the penetrator has passed by, so nothing is
lost by decreasing the resolution behind the penetrator.

TABLE III-1

Initial Zoning for Rigid Projectile Calculation

FOR ALL REGIONS: $z = z_{j_0} + \frac{\Delta z}{\lambda_z} (\exp((j_0 - j) \ln(1 + \lambda_z)) - 1)$

$x = x_{i_0} + \frac{\Delta x}{\lambda_x} (\exp((i - i_0) \ln(1 + \lambda_x)) - 1)$

REGION:	z_{j_0} (m)	x_{i_0} (m)	Δz (m)	Δx (m)	λ_z	λ_x	j_0	i_0
1 ($1 \le i \le 25$; $67 \le j \le 91$)	0.	0.	.03	.03	0.02	0.02	91	1
2 ($1 \le i \le 25$; $1 \le j \le 67$)	0.9127	0.	0.0483	.03	.05	.02	67	1
3 ($26 \le i \le 46$; $1 \le j \le 68$)	0.	0.9127	0.0483	0.0483	0.05	0.05	68	26
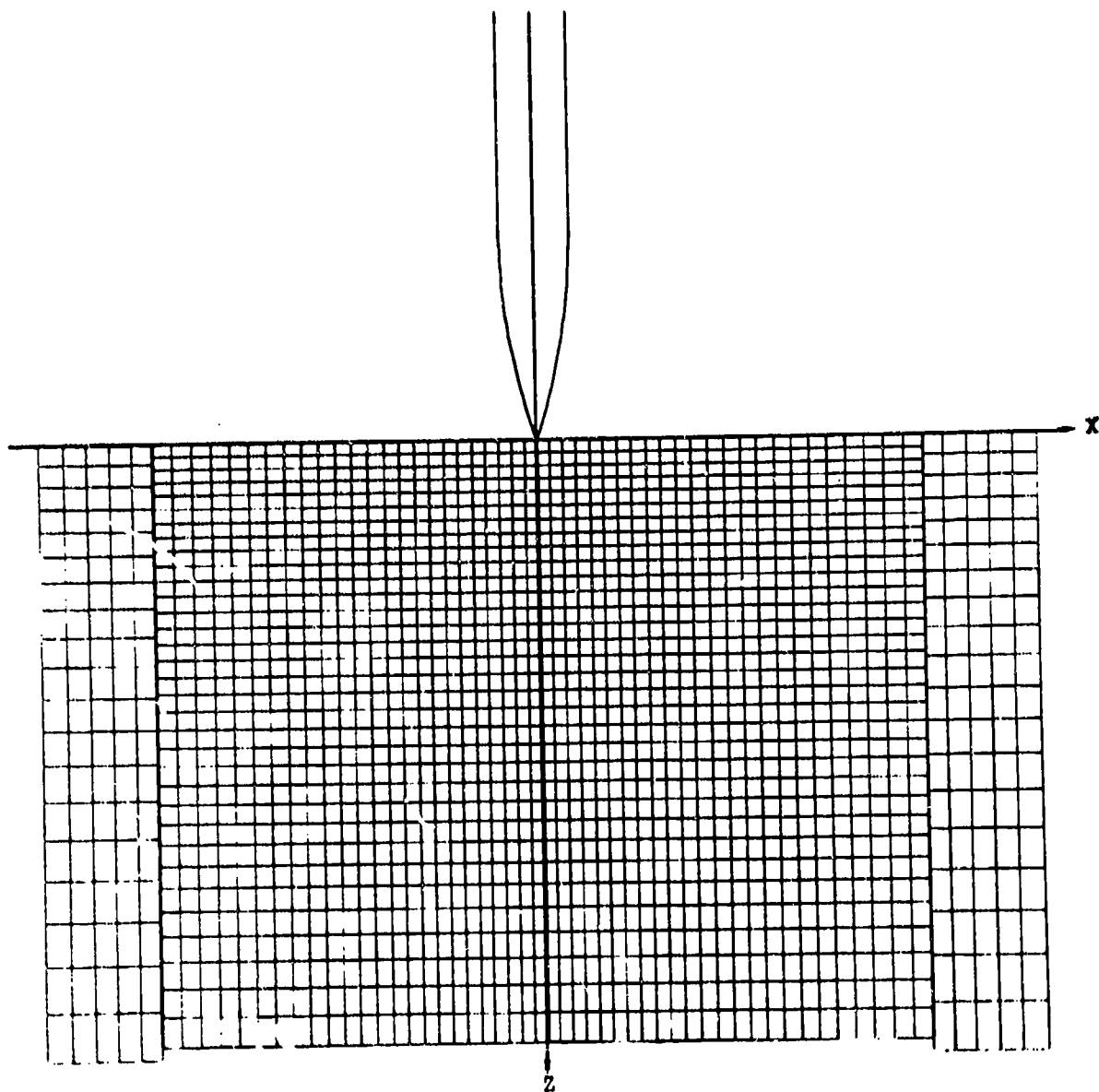
Figure III-1

PARTIAL INITIAL GRID

The calculation was carried out to a time of approximately 52.5 ms, at which time the penetrator had reached a depth of 7.3 m, and retained a velocity of 129 m/sec. The peak deceleration encountered by the penetrator was approximately 55 g's, and at the end of the calculation the deceleration appeared to be decreasing, as the nose begins to enter layer 4, to a value less than 20 g's.

Taking a constant deceleration of 20 g's in the assumed uniform material of layer 4 below 7.2 m leads to a value of about 0.7 sec for total time to penetration depth and a value of 50 m for final depth of penetration. These are the results expected, based on calculated projectile motion through the first three layers, had the calculation been carried out until the penetrator comes to rest. The duration of projectile penetration and final depth thus predicted are much larger than observed in experiment, suggesting a shortcoming in the calculation due possibly to friction effects or to use of a material response model for Layer 4 which is not an accurate representation of the actual medium encountered by the penetrator (see Section V for further discussion).

The calculations indicated that the value of deceleration achieved was somewhat sensitive to zone size, although the precise degree of this sensitivity was not known. For this reason, an analysis of the effect of zone size was undertaken. Three calculations were run with a projectile penetrating 0.6 m of Layer 1, with initially square zones of 0.015, 0.03, and 0.06 m. Initial conditions were identical to those of the main problem. Figures III-2 and III-3 show deceleration-depth curves and normal stress distribution along the nose at a penetrator depth of 0.4 m, respectively. It may be noted from these graphs that while alterations in initial zone

29

Figure III-2

DECELERATION vs DEPTH FOR ZONE SIZE TEST PROBLEMS
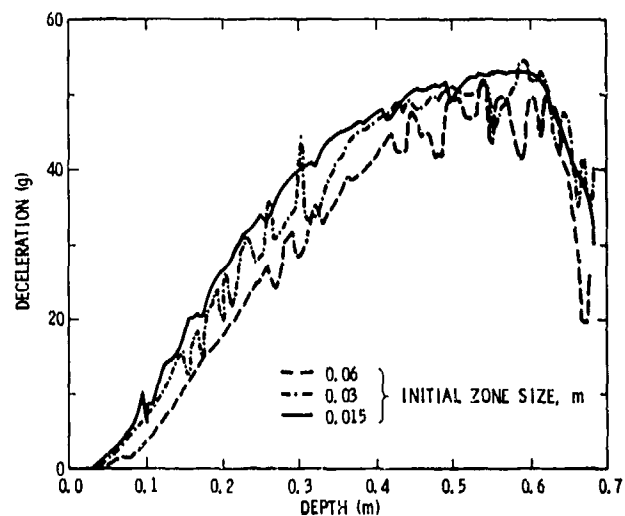
Figure III-3

NORMAL STRESS DISTRIBUTION ON PROJECTILE
NOSE FOR ZONE SIZE TEST PROBLEMS
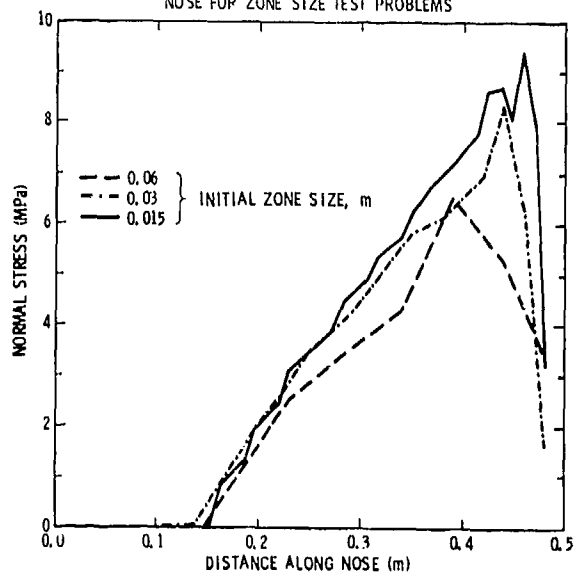
Figure III-4

PRESSURE vs RADIAL POSITION FOR ZONE SIZE TEST PROBLEMS
AT VERTICAL POSITION ON NOSE WHERE PRESSURE IS MAXIMUM
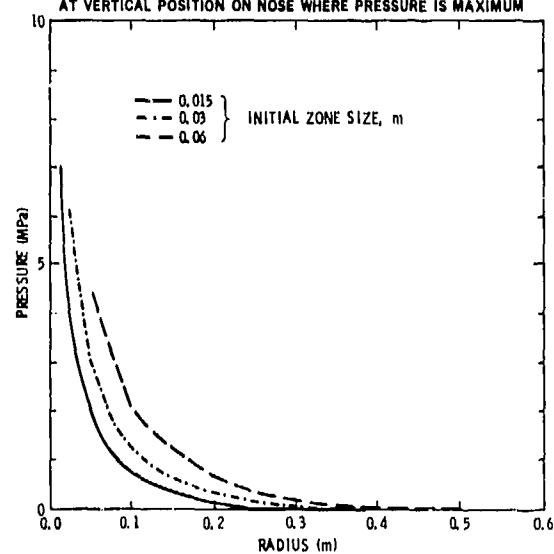
size have a marked effect on the normal stress distribution, the deceleration is much less affected for the range of zone sizes considered. This is evidently due to the fact that where disparities in the normal stress distributions are largest, the area over which the normal stress acts is relatively small. That is to say that for the smaller mesh calculations the normal stress distribution along the projectile nose has its maximum shifted toward the nose tip (see Figure III-3). Figure III-4 shows pressure vs radial position at the depth of peak normal stress, at a penetrator depth of 0.4 m. As expected, the finer zoning allows resolution of steeper gradients. Some sort of extrapolation to obtain the stress at the soil-projectile interface, rather than one half-zone away, would have yielded somewhat higher decelerations, but pr bably not enough higher, taken by itself to cause a large change in duration of the calculation or to influence significantly the values of projectile deceleration calculated. A combination of considerably finer zoning than was used in the main calculation, and extrapolation to find stress at the soil-projectile interface would provide a slightly more realistic calculation, but would also be quite expensive in terms of computer time. Increases in calculated normal stress and projectile decelerations due to finer zoning and extrapolation are estimated to amount to at most 20% using the techniques employed in the rigid body calculation.

It was hoped that the rezones of the problem could be accomplished with no significant effects on the histories being accumulated at the selected points in the soil. This goal is really only a reasonable one for those quantities and their integrals which are conserved during the rezoning process. The higher degree of smoothness of the velocity histories as compared to the stress measure histories reflects this fact.

31

Rezones of the problem were performed at

TIME (ms)	DEPTH (m)
1.38	.21
3.05	.46
8.0	1.2
11.9	1.78
14.6	2.18
23.4	3.45
33.8	4.88
41.6	5.91

Due to tape handling problems, history information for the period from 11.9 ms to 14.6 ms was lost.

Appendix A presents results of the calculation in graphical form. Figures A-1 through A-5 show deceleration, velocity and depth vs. time, and deceleration velocity vs. depth. Figures A-6 through A-9 show projectile kinetic energy, soil kinetic energy due to radial velocity, soil kinetic energy due to vertical velocity, and total kinetic energy of the soil, all per radian, and all vs. time. Table A-1 and Figure A-10 provide keys to figures A-11 through A-78, which show histories of various quantities at selected points in the soil. (Where they appear, radial and axial stress components are plotted positive in compression). Figures A-79 through A-141 show the calculational grid near the projectile, normal and shear stress distributions along the projectile, and contours of selected quantities in the soil. Due to the rezoning method used, only the grid lines with depths near that of the nose region are representative of target deformation. Also, for projectile depths greater than 0.4 m, the spatial scaling is distorted, so that radial distances appear twice as large as their actual value. The grid plots contain "x" in the

center of a zone calculated as failing in tension, and "c" where the stress state is on the failure envelope. When a mesh is calculated to fail in hydrostatic tension, its pressure is set to zero, and its stress deviator is limited by the smaller of the deviator stress on the cap and the failure envelope at zero pressure. Therefore, a zone may, in some cases, contain both x and c. It should also be noted that the normal and shear stresses plotted are actually those at zone centers; i.e., one-half zone away from the projectile. For these plots, a positive normal stress and a negative shear stress would retard the projectile.

Table A-2 provides a key to Figures A-79 through A-141. It should be noted that the sign convention for stress components is opposite that used for the history plots; i.e. consistent with a positive normal stress being one of extension.

33

SECTION IV

DEFORMABLE PROJECTILE CALCULATION

To test the assumption of a rigid body and to calculate the response
of the vehicle to the imposed loads, a second TOODY calculation was per-
formed. The vehicle was zoned as shown in Figure IV-1, and the ground
was defined by 30-mm squares to a radius of 0.6 m and a depth of 0.9 m.
For this calculation the 45° conical tip was included, as on the actual
vehicle, rather than the idealized perfect ogive used in the rigid body
calculation. Figure IV-1 also shows points in the projectile at which
the progress of the calculation was recorded and plotted. Plots were
also made for points in the soil corresponding to depths of 0.1 m, 0.2 m,
and 0.4 m, with distances from the central axis of 75 mm, 0.14 m, 0.28 m,
0.44 m, and 0.58 m.

The spacer was treated as an aluminum shell containing a vacuum.
The electronics package was modeled with a hydrodynamic "foam" equation
of state. The rest of the vehicle was treated as steel. The ground was
represented by the cap model for Layer 1. The input parameters for the
vehicle materials were

FIGURE IV-1

ZONING OF THE DEFORMABLE PENETRATOR,
• POINTS AT WHICH HISTORY WAS RECORDED
RADIAL DIMENSIONS QUADRUPLED TO SHOW DETAIL
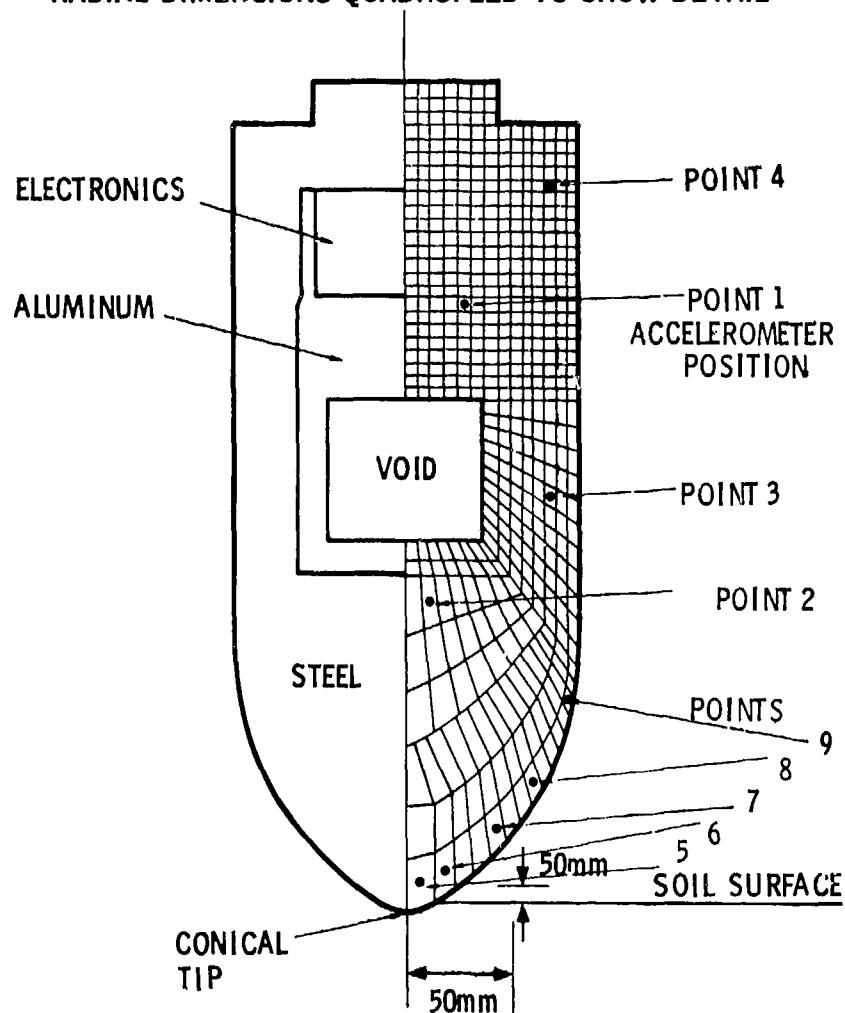
• Points Used for Plotting Histories

ID	R(m)	Z(m)	Figs. (App. A)
1	.022	-1.155	22, 23, 24
2	.010	- .580	25, 26, 27
3	.069	- .785	31, 32
4	.069	-1.388	33, 34
5	.006	- .028	28, 29, 30
6	.017	- .048	35, 36
7	.041	- .136	37
8	.060	- .225	38
9	.077	- .376	39
Nose tip		+ .003	

35

	Steel	Aluminum	Electronics
$\rho_0 (Mg/m^3)$	7.850	2.700	1.400
$c_0 (km/s)$	4.610	5.390	2.000
ν	.296	.333	--
$K = \rho_0 c^2 (GPa)$	166.8	78.4	5.6
$Y_0 (GPa)$	1.324	0.02	--
$c_e (m/s)$	--	--	500
α_0	--	--	2
$p_e (MPa)$	--	--	1
$p_s (MPa)$	--	--	10

The last four parameters pertain to the p-α foam model[19]; c_e is the ambient value of the sound speed in the virgin foam at the initial distention α_0, p_e is the elastic limit, and p_s is the compaction pressure for which all voids are assumed to be closed. Therefore, c_0 is the bulk sound speed of the fully compacted solid.

Friction at the vehicle-soil interface was neglected, and separation of soil from projectile surface was not permitted. The calculation was run to a time of 2.40 msec, at which time the nose tip had reached a depth of 0.398 m. This calculation consumed 2.94 hours of CDC-6600 central processor time. The problem was not rezoned.

Figures B-1 through B-7 in Appendix B describe the configuration, velocities and stresses 0.40 msec after impact, with the nose tip 0.094 m below the ground surface. The situation at 1.10 msec is shown in Figures B-8 through B-14, corresponding to a penetration depth of 0.20 m. Figures B-15 through B-21 give the final configuration. Velocity and

stress contours are not shown for the projectile material because the high-frequency ringing of the vehicle renders contours there incomprehensible. A few contours are shown as passing through the projectile region; these are intended to clarify the relationship of the contours and are unrelated to actual values in the projectile material.

Figures B-22 through B-30 display motion history for three points in the projectile. The motion of points away from the tip is dominated by ringing that masks the rigid body deceleration of the vehicle. Point 5, 40.5 mm back from the tip and 6.35 mm from the axis, experienced an initial acceleration associated with deformation of the nose on impact, followed by a deceleration as the nose absorbed the initial ground resistance (Figure B-28).

Stress histories at selected points within the vehicle are shown in Figures B-31 through B-36. In these and subsequent plots, "J2" is the label for the quantity $\sqrt{\sigma'_{ij}\sigma'_{ij}/2}$, which was the requested output quantity, where σ' is the deviator stress tensor. This quantity is proportional to octahedral shear stress, $\sqrt{\sigma'_{ij}\sigma'_{ij}/3}$. At a point in the projectile 61 mm from the tip and 12 mm from the axis, the peak mean stress exceeded 0.14 GPa and $\sqrt{\frac{1}{2}\sigma'_{ij}\sigma'_{ij}}$ exceeded 0.28 GPa (Figures B-35 and B-36). At the tip of the vehicle (not plotted), mean stresses in excess of 0.5 GPa and axial stresses in excess of 1.3 GPa were noted both in compression and tension, and plastic yielding occurred.

Figures B-37 through B-39 contain normal stress histories at three points along the nose of the projectile (see Figure IV-1); the shear stresses were assumed to be zero. Because stresses were not calculated at the interface, the values given were calculated within the vehicle,

37

one-half mesh width from the surface. The largest stress in these figures is 43 MPa, which occurred at the point closest to the nose tip (Figure B-37).

The total kinetic energy calculated for the soil followed the history shown in Figure B-40. The saw-tooth pattern is caused by numerical noise, a peak occurring each time the nose tip encounters a new grid point in the soil. The noise is accentuated because the total kinetic energy in the soil is small, because it is concentrated in a few zones near the axis of symmetry, and because the approximation used to sum the kinetic energy has undesirable characteristics when applied near the axis of symmetry. This effect was not seen in the rigid body calculation (Fig. A-9) because the time interval chosen for recording the energy happened to be almost exactly one period for this oscillation, and because the omission of the conical tip allowed a smoother solution in the rigid case.

The history of motion and stresses at the selected points in the soil are shown in Figures B-41 through B-112. Histories were also recorded at three points with range 0.6 m from the impact line, but the mean stress never exceeded 10 kPa, the level required to activate calculation of motion. Before comparing these results to the rigid projectile calculation, the times shown must be increased by 0.4 msec to account for the nose tip being 26 mm shorter and for the tip being buried 33 mm at the beginning of this calculation. With this adjustment, the soil histories are in excellent agreement. The peak mean stress observed at the closest point (range .105 m, depth 75 mm) was 2 MPa, and the largest radial velocity was 16 m/s (Figures B-41 through B-46).

38

The total momentum in the vehicle was summed at 0.2-ms intervals and then differenced to obtain the deceleration history shown in Figure IV-2. The deceleration is up to thirty six percent larger than the results for the rigid body calculation (Figure III-2). This difference is related, in part, to the use of an ideal ogive in the rigid body calculation, compared with the 45° tip appearing on the actual vehicle and included in the deformable body calculation. The soil velocity reaches 180 m/s on the 45° nose tip, whereas in the rigid body calculation the soil velocity does not exceed 60 m/s. In the case of the perfect ogive, the soil must reach a velocity of at least 50 m/s to get out of the path of the oncoming vehicle. The higher velocity produces larger stresses in the soil; with the deformable body stress components larger than 12 MPa were calculated, whereas no stress in excess of 8.5 MPa was noted for the rigid body calculation.

Unfortunately, there are no hard experimental data with which to compare the calculated transient vehicle response. However, the experience with this deformable body calculation demonstrates that calculation of the early-time vehicle loads and response is a reasonable and straight-forward application of existing numerical methods, in sharp contrast to the difficulties in calculating penetration depth or to the impossibility of obtaining this information from force law or cavity expansion theories.

FIGURE IV-2
DECELERATION HISTORY FOR DEFORMABLE PROJECTILE

40
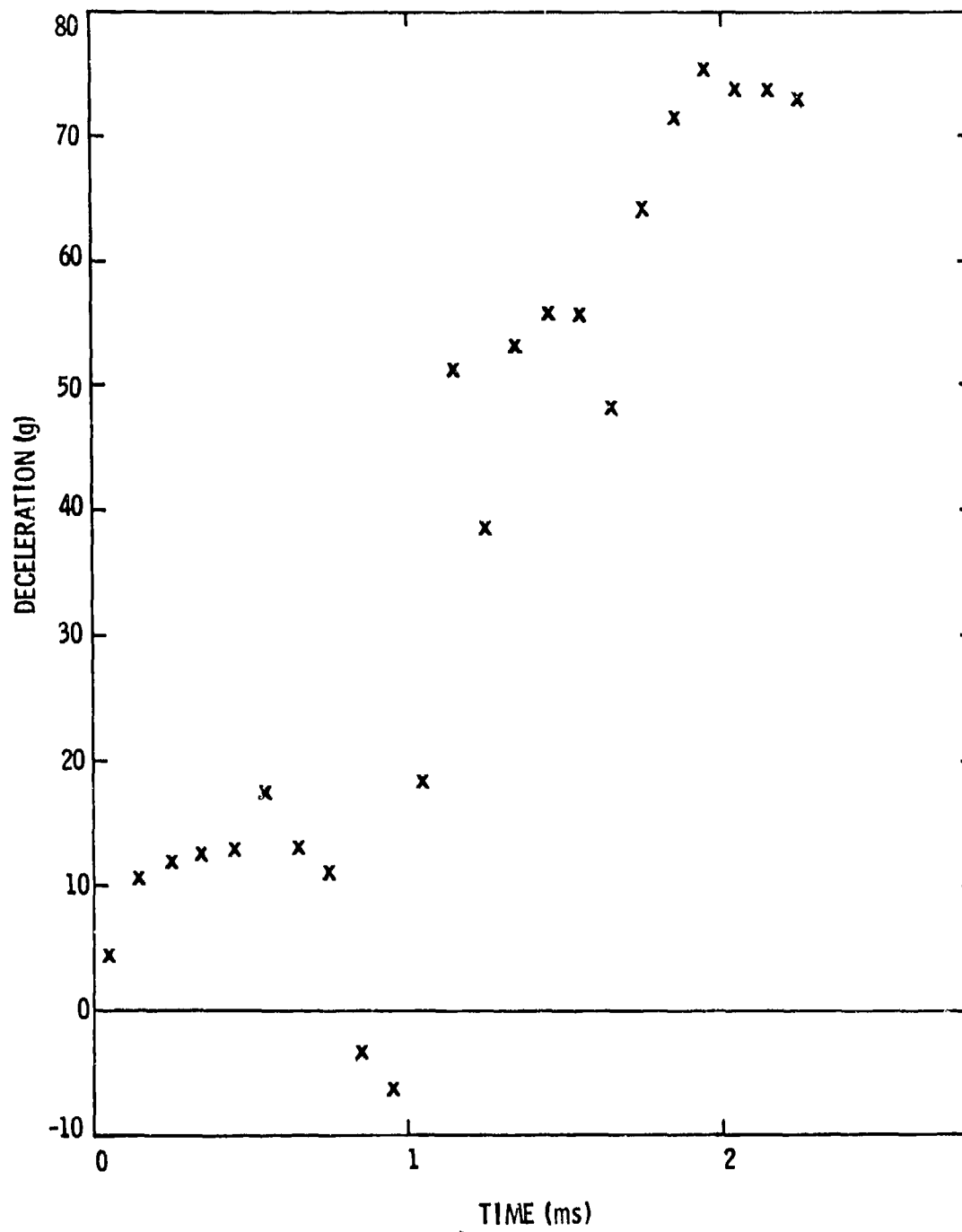
SECTION V

COMPARISON OF PREDICTIONS WITH EXPERIMENTS

More than a dozen projectile penetration experiments were conducted[5] at the Watching Hill site with projectiles of various diameters, weights, lengths and nose shapes and with projectile impact velocities ranging from 93 to 202 m/s (305 to 660 ft/sec). Test number 6 had an impact velocity of 150 m/s (493 ft/sec), a 0.1651 m(6.5 in) diameter projectile of mass 181.44 kg (400 lb) with 9.25 CRH tangent ogive nose. This test closely matches conditions employed in calculations and provided projectile motion data for comparison with predictions. Test number 4 was performed[5] with a 0.1524 m (6 in) diameter projectile of mass 127.12 kg (280 lb), 6.25 CRH tangent ogive nose and impacted at a velocity of 158.5 m/s (520 ft/sec). From this test, medium stress histories were obtained with which calculated results can be approximately compared.

Projectile Motion

Projectile motion measurements[5] were obtained from accelerometers mounted within the projectile and consist of deceleration versus time during penetration, together with projectile velocity and position histories derived from integrations of deceleration data.[5] Medium response measurements[10] were made with six lithium niobate stress transducers[9] at four locations within the top three designated layers of the target medium. From projectile deceleration data, information is obtained regarding the nature of the resistive forces offered by the soil medium in retarding the projectile's motion. Also, together with calculations, inferences regarding frictional forces acting on the projectile may be made.

Further, from the deceleration history indications are obtained of the gross layering structure within the target medium. From dynamic stress data amplitudes, durations and arrival times are obtained of the pressure disturbance produced in the medium by projectile penetration. The comparison of this information with calculated results provides one measure of how accurately the medium response is modeled in calculations.

Figures V-1 and V-2 illustrate projectile decelerations, calculated and measured (Test No. 6, real time, 200 Hz LPF).[5] The rigid body calculation with zero friction predicts a deceleration of about 55 g's which remains roughly constant during projectile penetration through layers 1 and 2 (each 2.4 m thick). After projectile entry into layer 3 (also 2.4 m thick) calculated deceleration falls to about 35 g's and in layer 4 deceleration again drops to 20 g's or less. This stair-step result is related to the material properties assigned to each of the four idealized layers (Section II). Layers 1 and 2 have shear strengths which differ at most by a factor of 2 at pressures below 10 MPa (see Figures II-3 and II-4). Layers 3 and 4 both have shear strengths much less than layers 1 and 2 and the strength of layer 4 material is considerably less than that of layer 3 over the pressure range of interest (see Figures II-5 and II-6). Assuming that the soil medium's resistance to shear deformation is the primary mechanism influencing projectile deceleration level then the shear strength properties attributed to the four layers, and utilized in calculations, account for the stair-step deceleration history calculated as the projectile penetrates layers 3 and 4. Measured deceleration levels in layers 1 and 2, as indicated by the data trace, the smoothed (by $\bar{a} = \int_0^t a(t)dt / \int_0^t dt$) data curve, and the effective constant deceleration over each designated layer are greater than calculated.

42
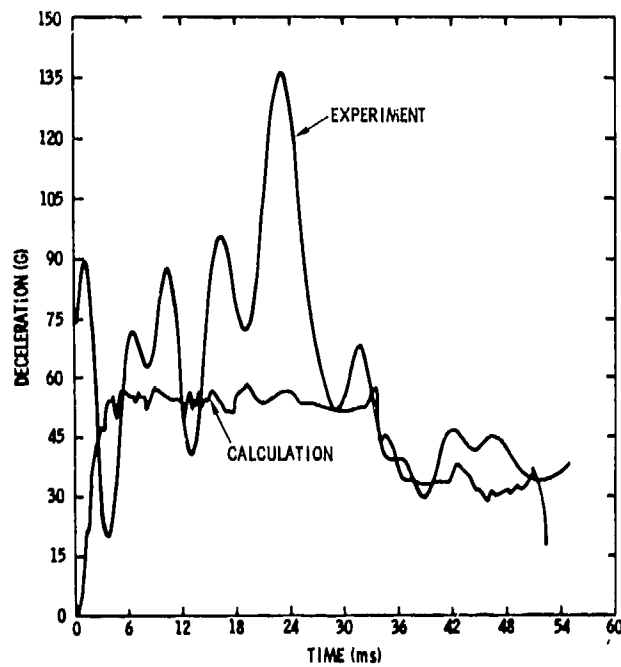
Figure V-1a
Comparisons of Predicted and Measured Projectile Deceleration History.
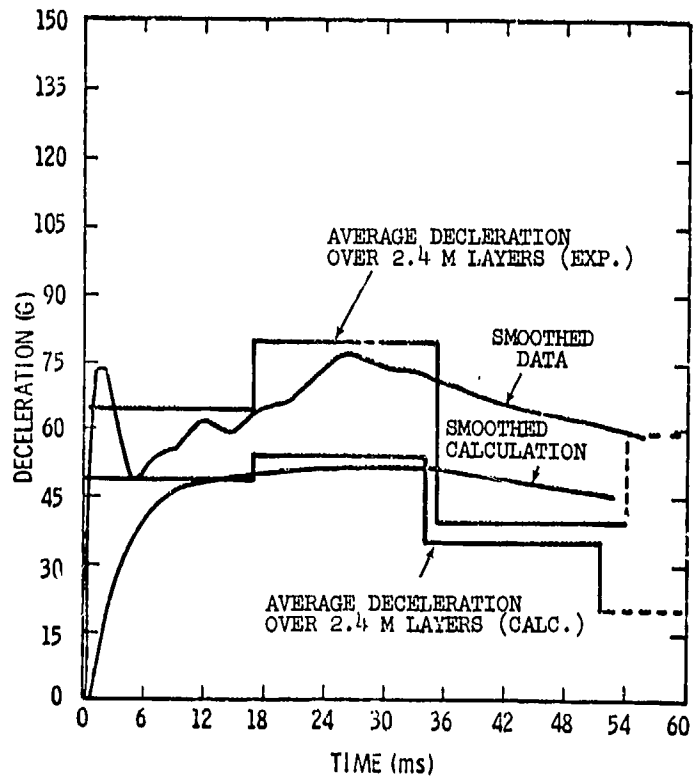
Figure V-1b
Comparisons of Predicted and Measured Projectile Deceleration History.
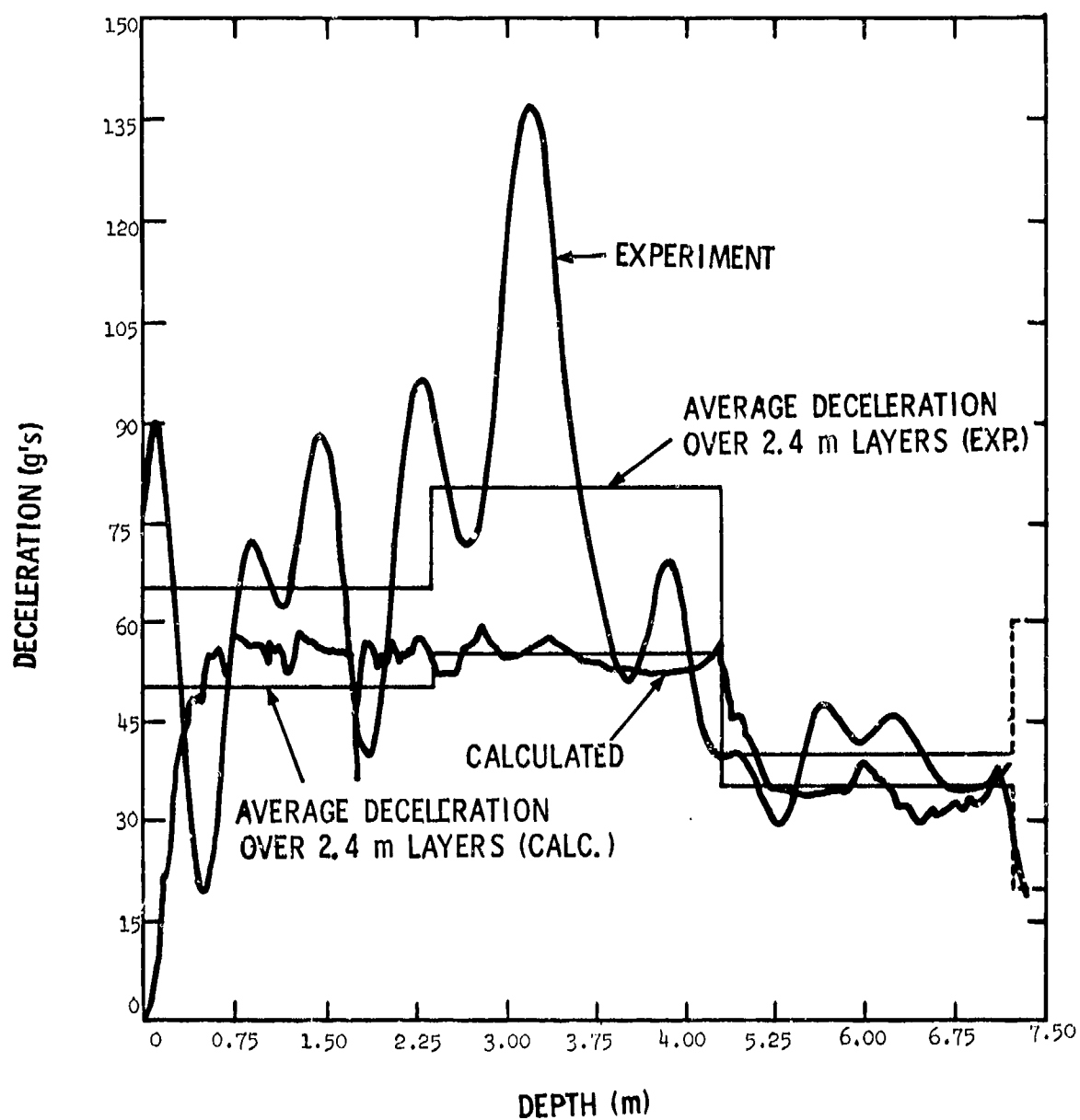
Figure V-2

Comparison of Predicted and Measured Projectile Deceleration versus Depth.

Comparing calculated and measured average deceleration levels (Table V-1) for each of the first 3 layers it is seen that predicted values are 23, 31 and 13% lower, respectively than observed. For layer 4 the difference is considerably greater and the reasons for this are discussed further below.

Since the average decelerations, predicted by the no friction calculation, are less than those observed one may speculate whether or not the differences are a measure of the friction forces operative. For layers 1, 2 and 3, it is seen (Table V-1) that the difference is greatest for the layer 2 of highest shear strength and least for the layer 3 of lowest shear strength. It is apparent that the differences between experimental and predicted average decelerations are in monotonic correspondence to shear strengths of the materials at the normal stress experienced on the projectile nose (Figures A-98, A-116 and A-134). This suggests that a form of the friction law involving the second invariant of the deviator stresses, such as $\tau_f \propto \tau$ (τ_f = frictional stress along soil projectile interface, τ = octahedral shear stress), is not inconsistent with data. Similarly, the data of Table V-1 suggests that a friction law related to projectile velocity is probably not correct.

It is of interest to explore the possible sources of discrepancy between calculations and experiment to determine whether or not more definitive information regarding friction forces may be obtained

45

Table V-1

Difference Between Predicted and Measured Average Projectile
Decelerations in the Four Layers Assumed for the
Watching Hill Medium

Average Deceleration (g's)

Layer	Calculated*	Observed	Difference (%)
1	50	65	23
2	55	80	31
3	35	40	13
4	< 20	> 60	> 67

* No Friction

in order to refine or perfect the prediction technique. Sources of
discrepancy include errors in the deceleration measurement, errors in
laboratory measurements of material properties, approximations or assum-
ptions made in calculation of the penetration problem and possible in-
accuracies associated with the computational method. Approximations and
assumptions made in calculation of the penetration problem include neg-
lect of variations in lithostatic pressure with depth, neglect of friction
forces, layering in target and use of the soil cap material response model
to represent the target medium   Inaccuracies in the computational method
involve size of mesh and the closeness with which the cap model is made
to represent laboratory data on material properties of the medium.

While the uncertainty associated with each of these sources of
error is not known, it is expected that taken in combination all the
sources of error from both experiment and calculation are great enough
to account for the 13 to 31% discrepancies noted between predictions and

observations. As a result, no definitive conclusions can be drawn regarding the absolute magnitude of friction forces contributing to deceleration of the projectile in layers 1, 2 and 3. However, it appears that the friction forces are most likely less than 50% of the total axial force acting on the projectile. California Research and Technology predictions,[20] obtained with friction on the projectile specified by $\tau_f = 0.6 \sqrt{J'_{2max}}$, yielded deceleration amplitudes of 110 g and 125 g for layers 1 and 2 respectively. Here, $\sqrt{J'_{2max}}$ is the function describing the failure envelope, evaluated at the normal stress acting on the projectile. The contribution from friction to the total axial retarding force was about 55% and 56%, respectively. This amount of friction is clearly too great, producing decelerations larger than observed. At most, the amount of friction for layers 1, 2 and 3 is that suggested by differences indicated in Table V-1.

The difference between measured and calculated decelerations in layer 4 material is likely greater than can be accounted for by uncertainties in the experimental data on deceleration and in the computational method. The large discrepancy is felt to be a consequence of material property data and the resultant material response model which is not representative of the actual material of layer 4. Credence to this supposition is given by the full experimental deceleration record[5] shown in Figure V-3. At a depth of 7.2 m, where layer 4 is assumed to begin, projectile deceleration begins to increase and from 7.2 m to 10 m the projectile experiences an increase in retarding force which implies a layer of greater shear strength than that of layer 3. Below a depth of 10 m the projectile enters another layer of lesser strength than the last (but still greater than layer 3 strength) and maintains a nearly
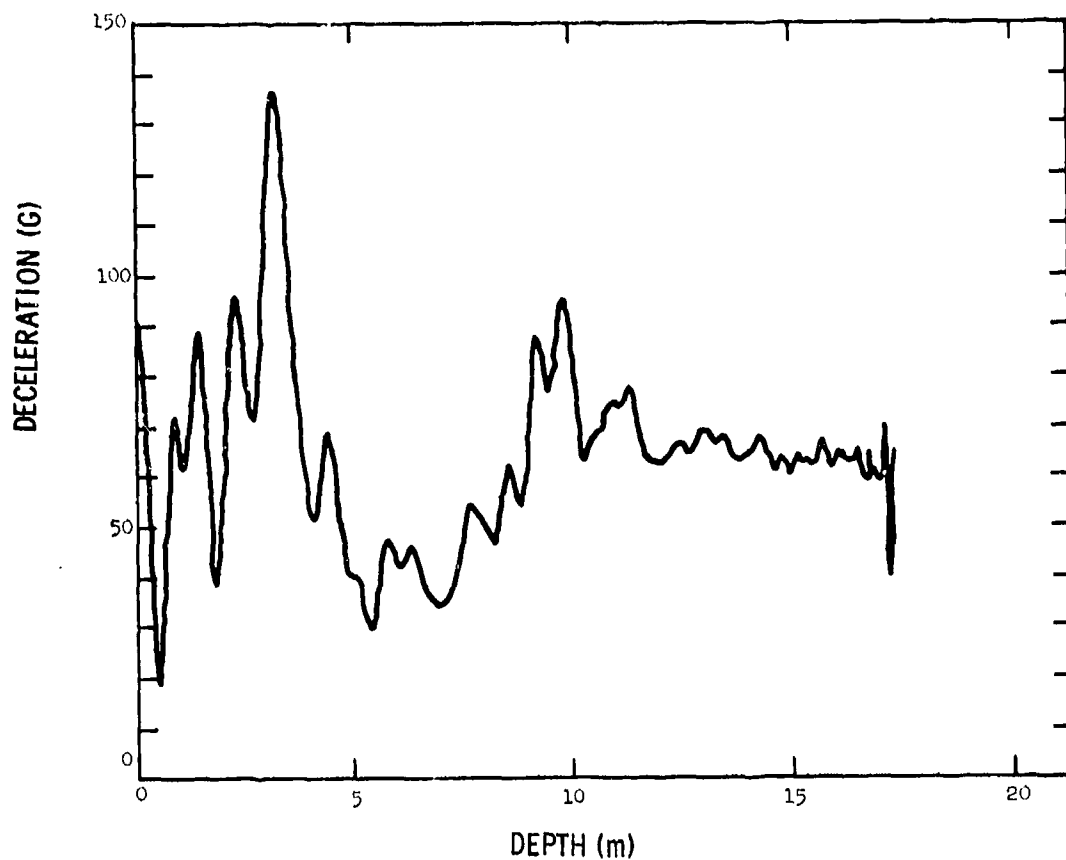
Figure V-3

Measured Projectile Deceleration versus Depth.
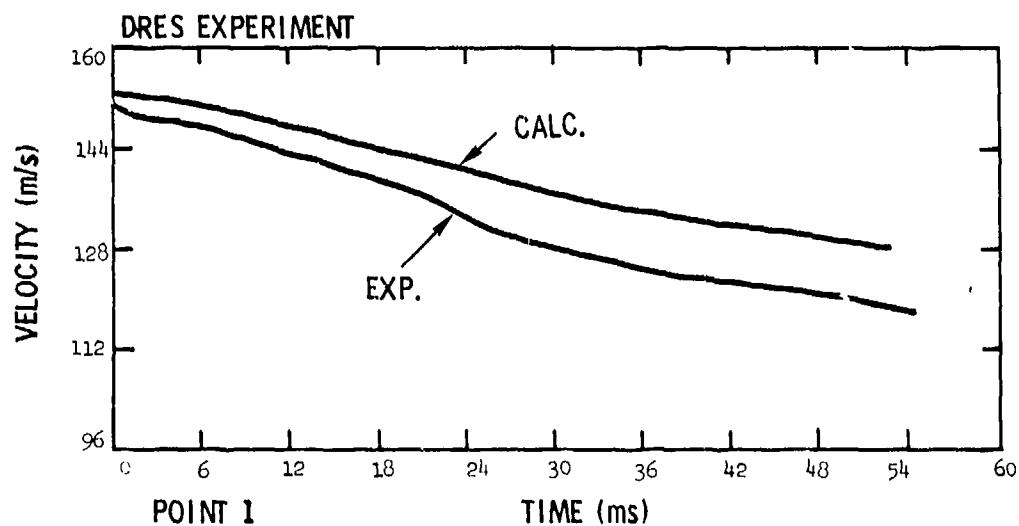
Figure V-4

Comparison of Predicted and Measured Velocity Histories.

constant deceleration of slightly more than 60 g's. These observations indicate that the target medium would have been modeled better with five layers rather than four and also that the material properties used for layer four are not representative of any of the layers assumed for the penetrated area of the Watching Hill medium. In retrospect, it is apparent that a prior choice of four layers for use in calculations was not the best. Considerably improved results for predicted deceleration history would be obtained in a recalculation of the problem by using five layers rather than four, by taking layer four to be much stiffer in shear than that used in the first calculation, and also by employing a small amount of friction.

Further comparisons of calculated projectile motion with information derived from deceleration data are shown in Figures V-4 through V-8. Of particular interest among these is Figure V-7 for deceleration versus velocity. Within a given layer the calculated curve is independent of projectile velocity indicating a constant retarding force within each uniform layer of material. This result for the Watching Hill medium seems to confirm the force law relationship proposed by Robins and Euler[1], as opposed to those, such as Resal's,[1] which require an explicit dependence on projectile velocity.

Target Medium Response

To measure medium response during projectile penetration, six lithium niobate stress gauges were located[10] at positions as indicated in Figure V-9a. Figure V-9b illustrates the orientation of four penetration experiments about the stress transducer locations and Table V-3 lists particulars for those four penetrator experiments.[5]

DRES EXPERIMENT
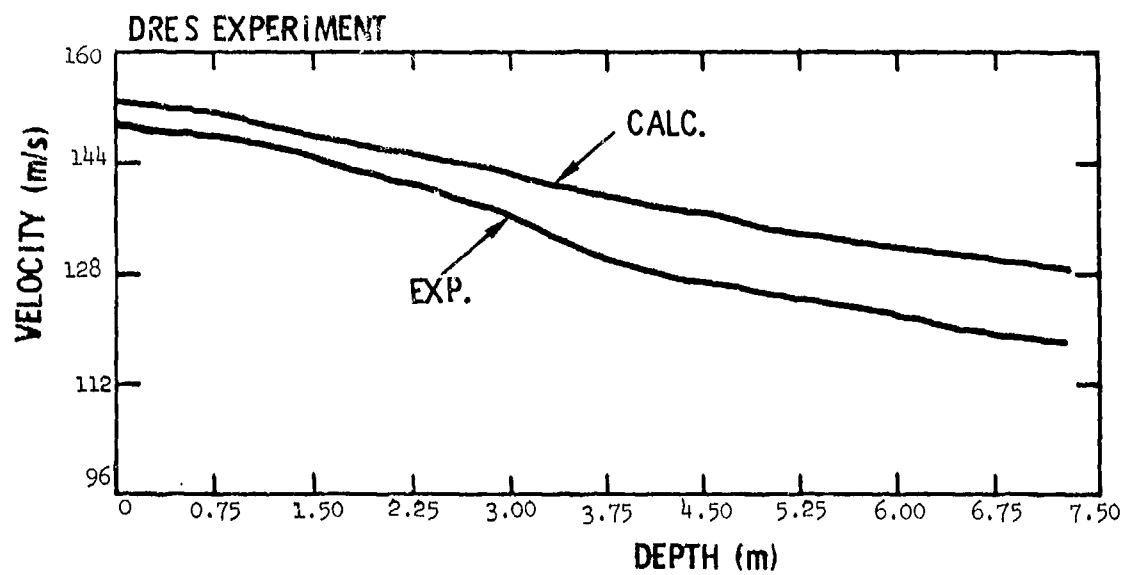
Figure V-5

Comparison of Predicted and Measured Projectile Velocity versus Depth.
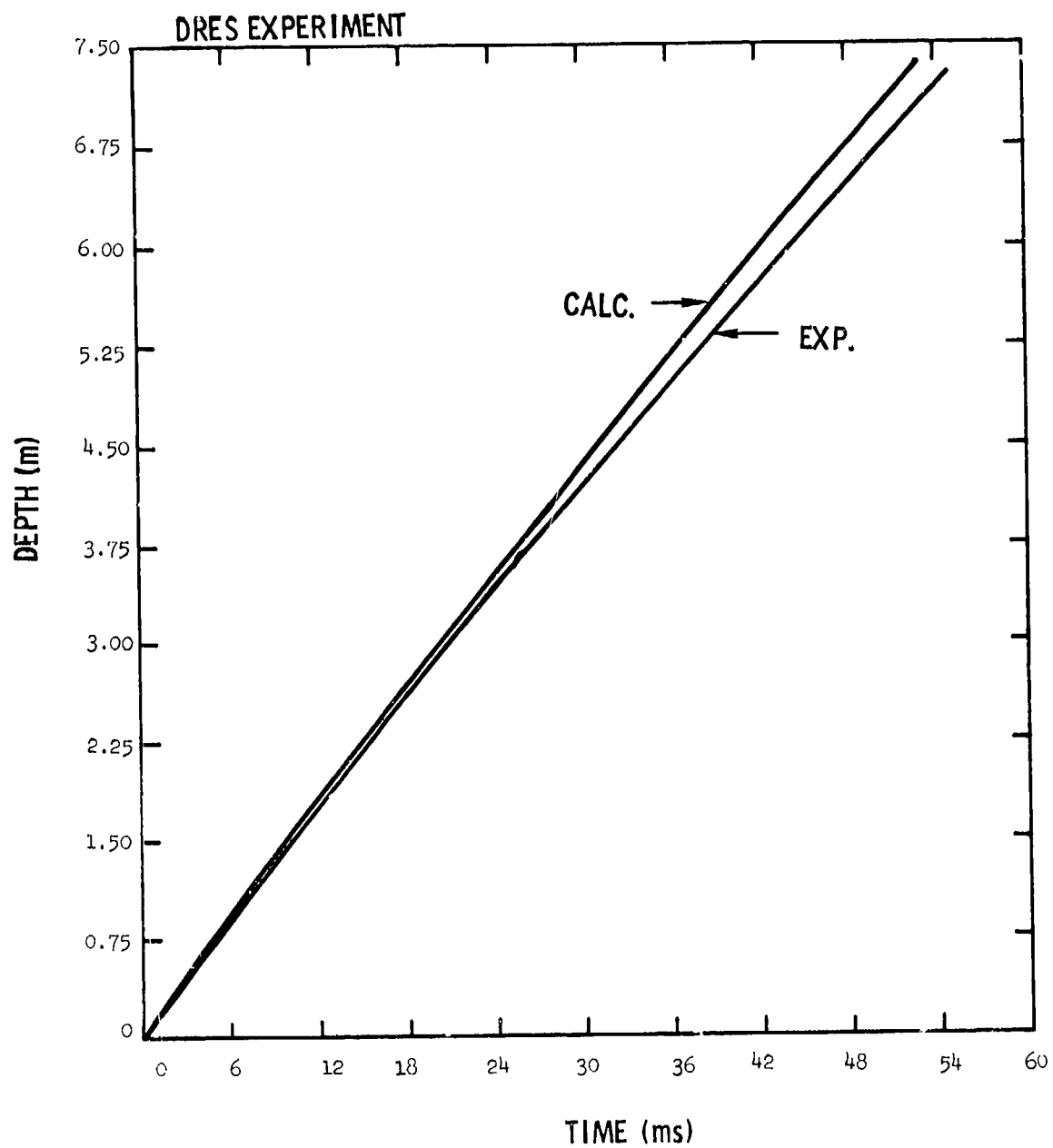
Figure V-6

Comparison of Predicted and Measured Depth versus Time Curves.

51
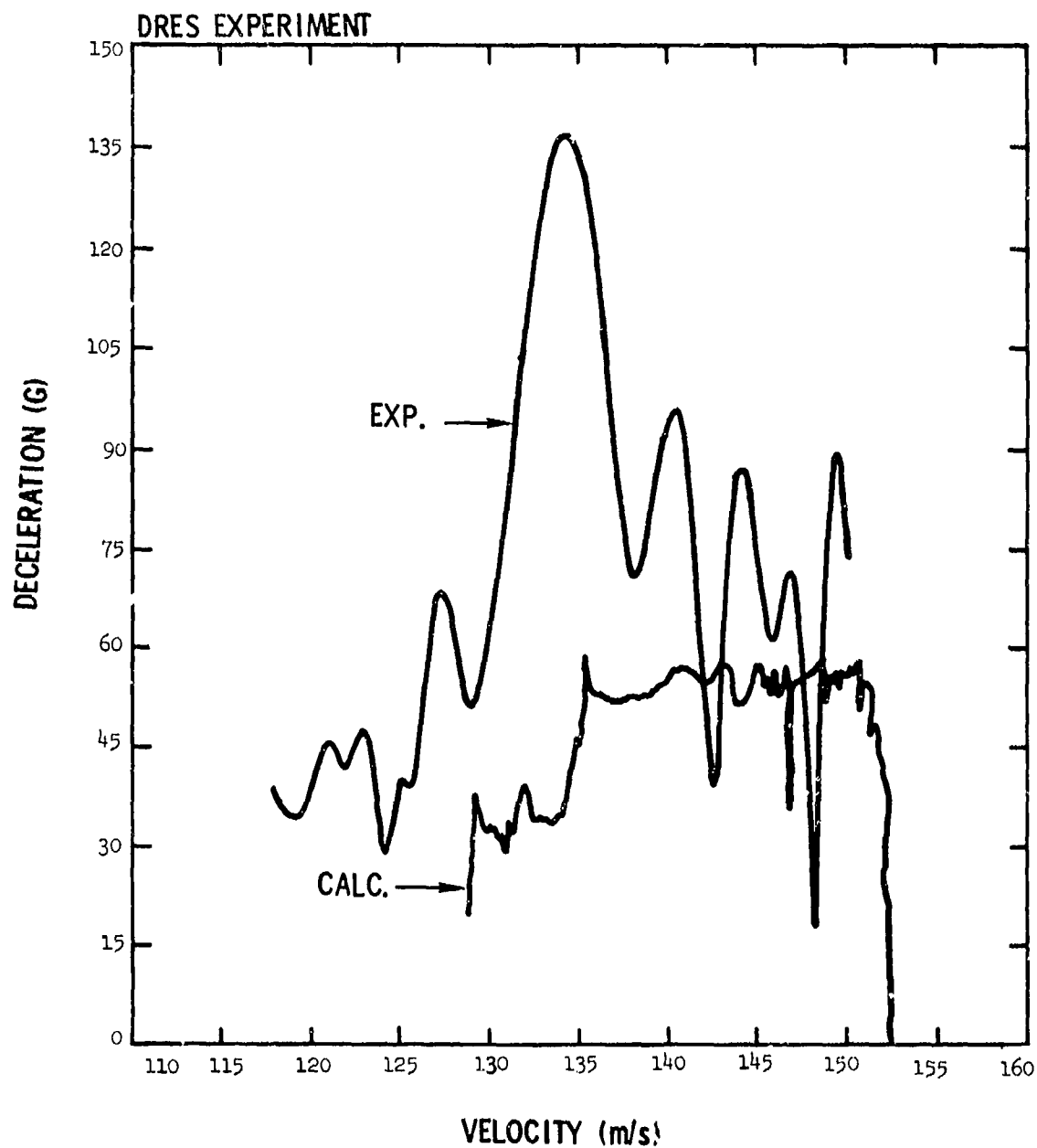
Figure V-7

Projectile Deceleration versus Projectile Velocity, Measured and Predicted.
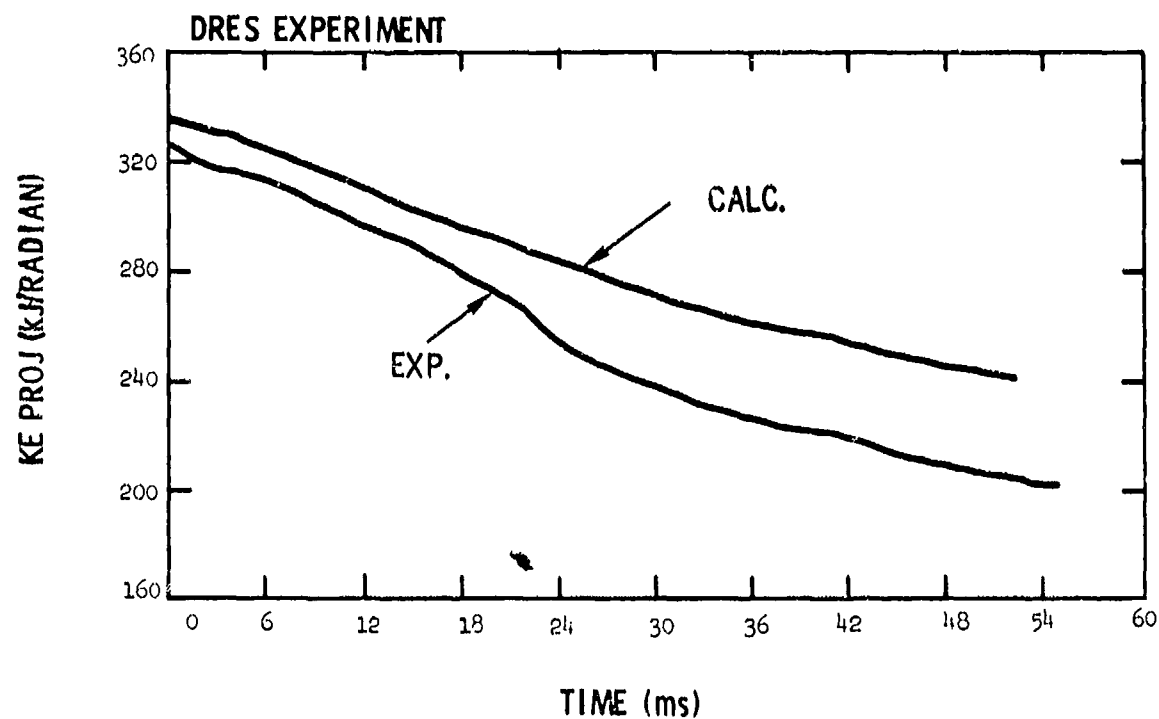
Figure V-8

Projectile Kinetic Energy versus Time, Measured and Predicted.
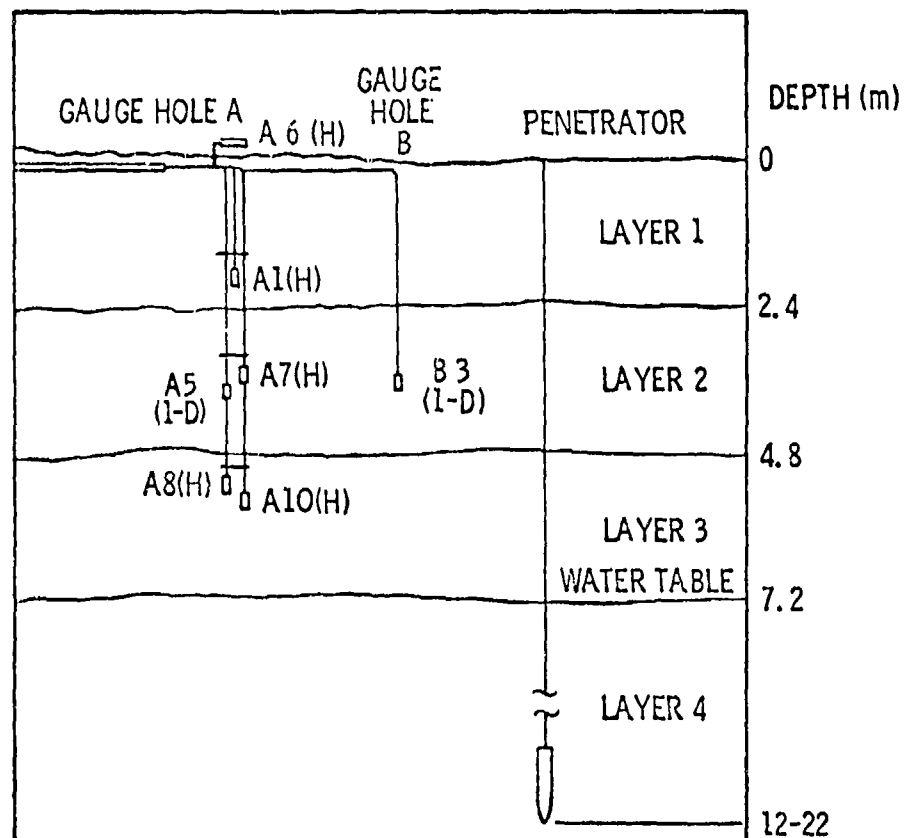
Figure V-9a

Vertical Location of Earth Stress Transducers and Orientation of
Stress Gauge Holes Relative to Penetrator Impact Positions.
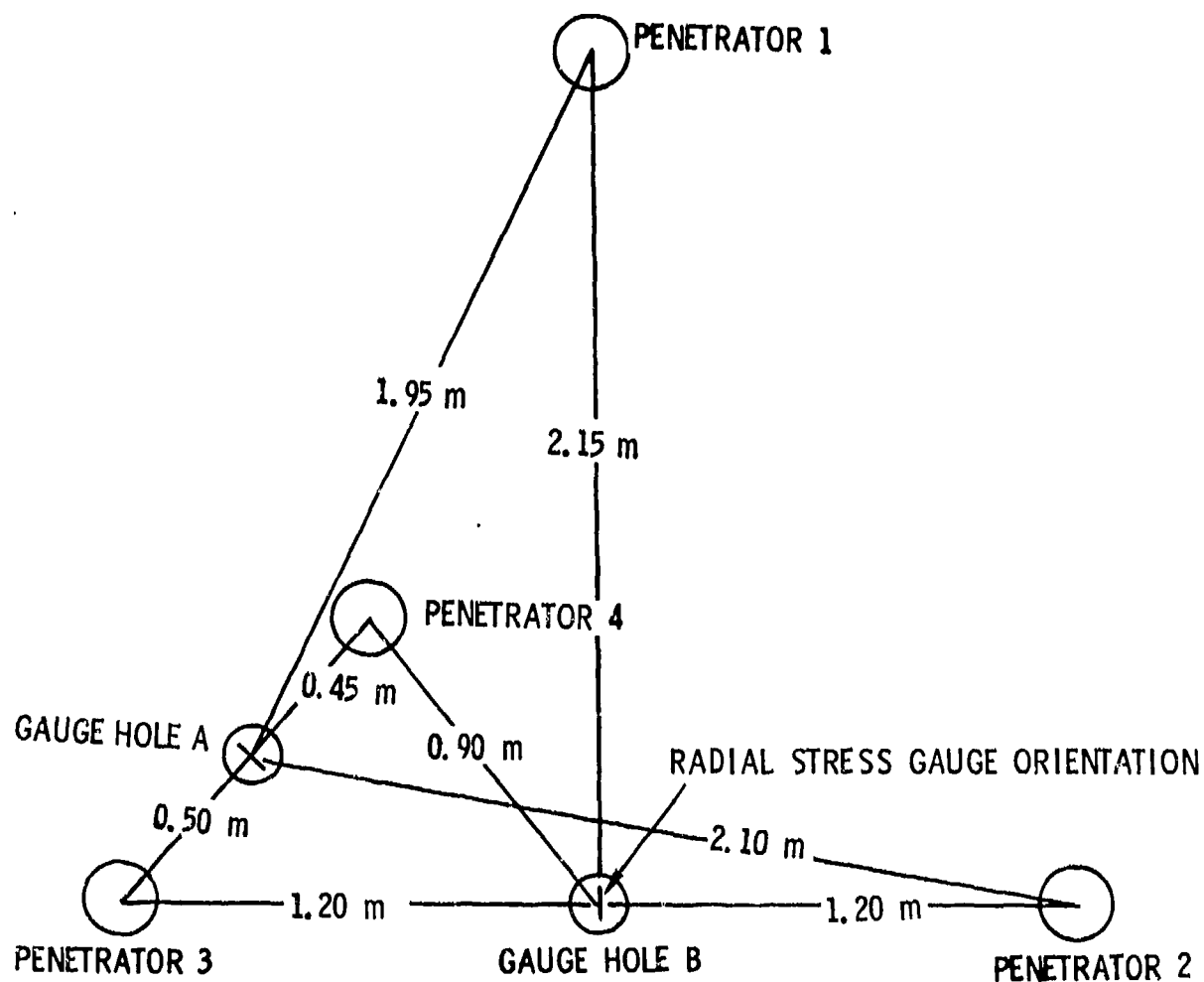
Figure V-9b

Vertical Location of Earth Stress Transducers and Orientation of

Stress Gauge Holes Relative to Penetrator Impact Positions.

Table V-3

Characteristics of Projectiles Penetrating
Medium in Neighborhood of Stress Gauges

Test No.	Projectile Mass (Kg)	Diameter (m)	Velocity (m/s)
1	127	0.152	174
2	181	0.165	125
3	127	0.152	122
4	127	0.152	156

No detectable signals were sensed by any stress transducers which were more than 1.2 m horizontal distance from the projectile path. Excellent stress histories were measured for penetrator test number 4. Also, the gauge in hole B measured a signal from penetrator test number 2. Data were obtained from penetrator test number 3 also, but were unfortunately lost during playback of recording tapes.

Measured stress histories are compared with those calculated in Figures V-10 through V-15, where it is seen that amplitudes, pulse shapes and arrival times are all in generally good agreement with predictions. Zero time in Figures V-10 through V-15 is when the projectile is 0.3 m above target surface.[10] Peak values of stresses are summarized in Table V-4 where uncertainties in measured peak stresses associated with base line shift are also tabulated. Error in peak stresses is 11% or less for stress transducers closest to the impact axis (0.45 m). At greater distances from the impact axis, error due to base line shift increases appreciably as the magnitude of the signal goes down. Errors from other possible sources are difficult to estimate. The extent to

Table V-4

STRESS GAGE Number[a]	Type	Depth (m)	Distance From Impact Axis (m)	Penetrator Test No.	Predicted Peak Stress (MPa)	Measured Peak Stress (MPa)	Maximum Base Line Shift (MPa)	Uncertainty In Peak Stress (%)
A-1	Pressure	1.83	0.45	4	0.25	0.29	~0	~0
A-7	Pressure	3.56	0.45	4	0.23	0.36	0.04	11
A-5	Radial Stress	3.76	0.45	4	0.49[b] (0.23)	0.33	0.02	6
A-8	Pressure	5.39	0.45	4	0.35	0.61	0.04	7
A-10	Pressure	5.59	0.45	4	0.35	0.37	0.02	5
B-3	Radial Stress	3.66	0.90	4	0.16[b] (0.064)	0.059[d]	0.01	17
B-3	Radial Stress	3.66	1.20	2	0.019[b,c] (0.0048)	0.025	0.01	40

a) See reference 10
b) Radial stress value, mean stress given in parenthesis below radial stress
c) Radial and mean stress values for 3.6 m depth and 1.5 u range
d) On penetration test, No. 4 gage B-3 was not oriented normal to radial from impact axis.
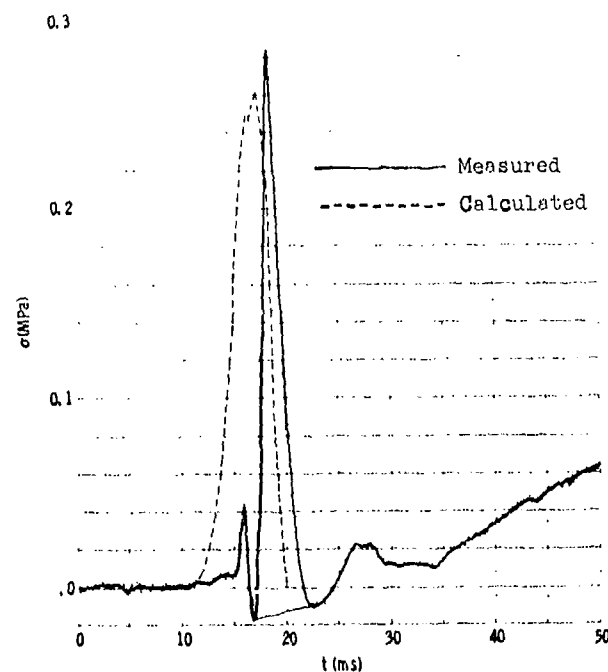
Figure V-10

Mean Stress History Measured at Depth (Z) of 1.83 m and Radius (R) of 0.45 m (Time of Impact = 2 ms).
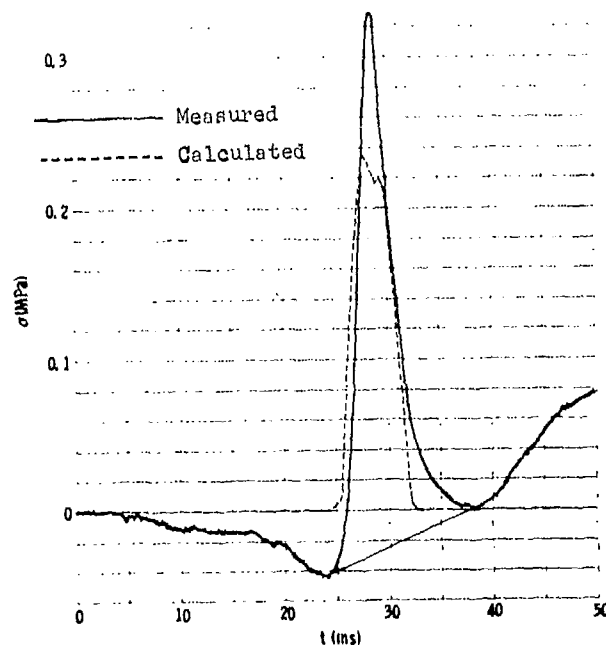
Figure V-11

Mean Stress History Measured at Z = 3.56 m and R = 0.45 m (Time of Impact = 2 ms).
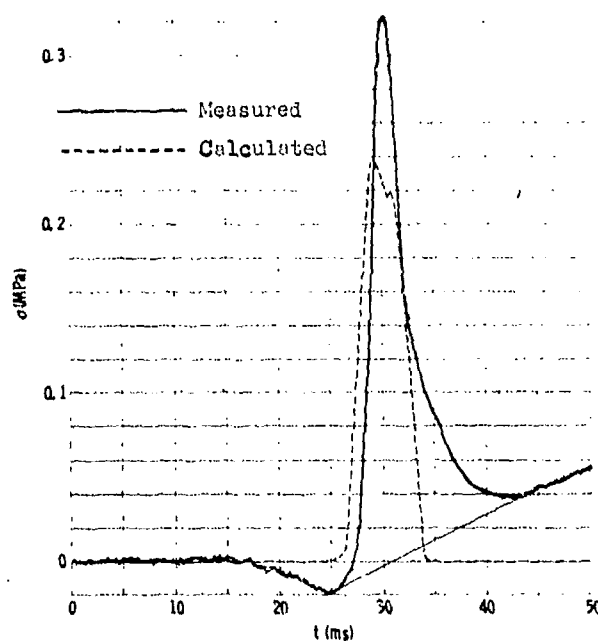
Figure V-12

Radial Stress History Measured at Z = 3.76 m and R = 0.45 m
(Time of Impact = 2 ms).
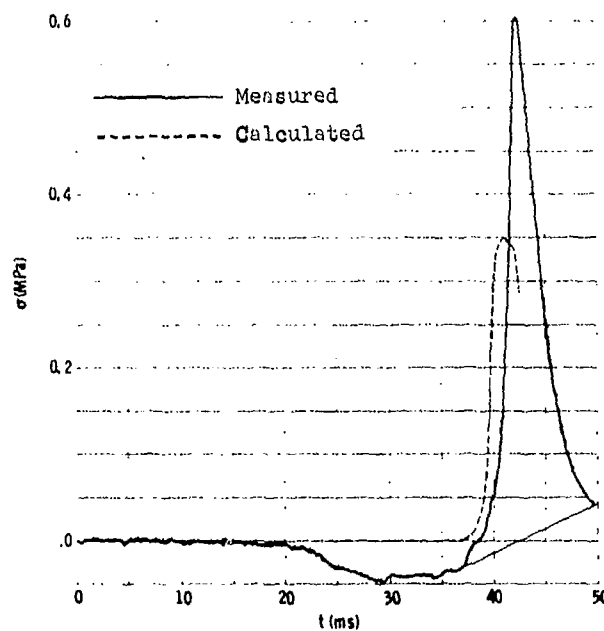
Figure V-13

Mean Stress History Measured at Z = 5.39 m and R = 0.45 m
(Time of Impact = 2 ms).
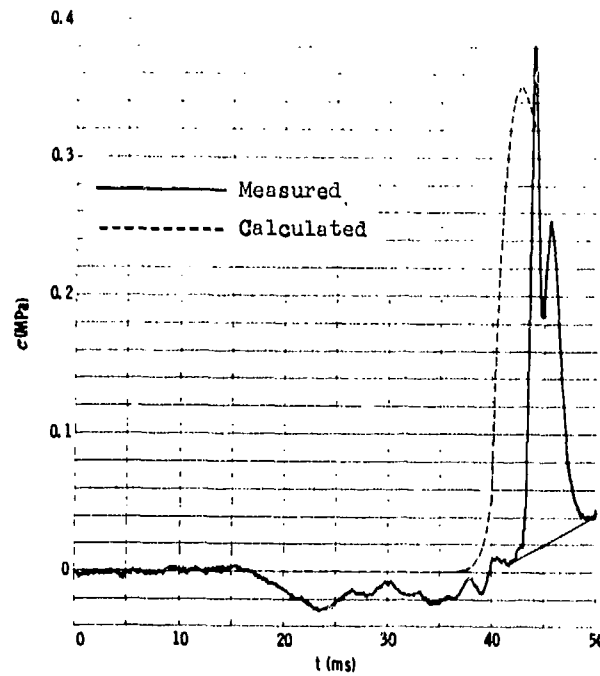
Figure V-14

Mean Stress History Measured at $Z = 5.59$ m and $R = 0.45$ m
(Time of Impact = 2 ms).
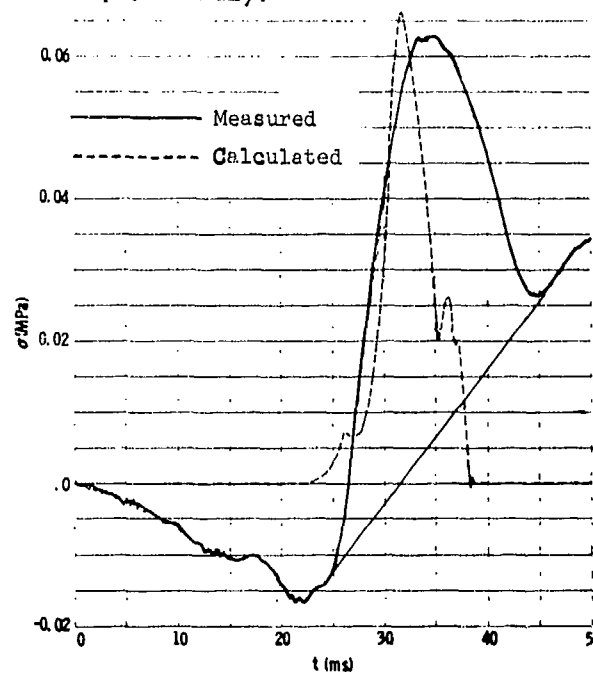
Figure V-15

Radial Stress History Measured at $Z = 3.66$ m and $R = 0.90$ m
(Time of Impact = 2 ms).

60

which earlier penetration experiments disturb the medium and possibly influence the accuracy of stress history measurements on subsequent experiments cannot be ascertained with available data. The disturbance produced by penetrator test number 3 (Figure V-9b) in terms of calculated peak displacement at the gauge positions amounts to about 10 mm. Further experiments are necessary to evaluate whether or not this magnitude disturbance affects the measurements made on penetrator test number 4. It is clear that penetrator tests numbers 1 and 2 produced relatively much smaller disturbances at the gauges.

Shown in Figure V-16 are peak pressure and radial stress data from gauges in hole A plotted as a function of gauge depth. Also shown are the calculated curves for peak pressure and radial stress. Except for the datum from gauge A-8, all the data fall within a band bounded by the calculated curves. Also, all data are closer to the predicted mean stress curve than to the radial stress curve. The datum at 3.76 m from the radial stress gauge (A-5) appears to be essentially identical to the pressure measurement from gauge A-7 suggesting that both gauges are measuring the same quantity. Lithium niobate transducers for measurement of total stress components are still under development. More work is necessary to establish their capability in this mode. Mean stress gauges of lithium niobate, however, have received much more attention[9] and use[21] and should be considered the more reliable transducer in examination of data from the penetration experiments.

Attenuation of peak pressure and peak radial stress with radial position from impact axis is illustrated in Figure V-17. Predicted curves shown are for stress attenuation at a depth of 3.6 m and may be compared with data at that depth (circle and triangles). It is seen

61
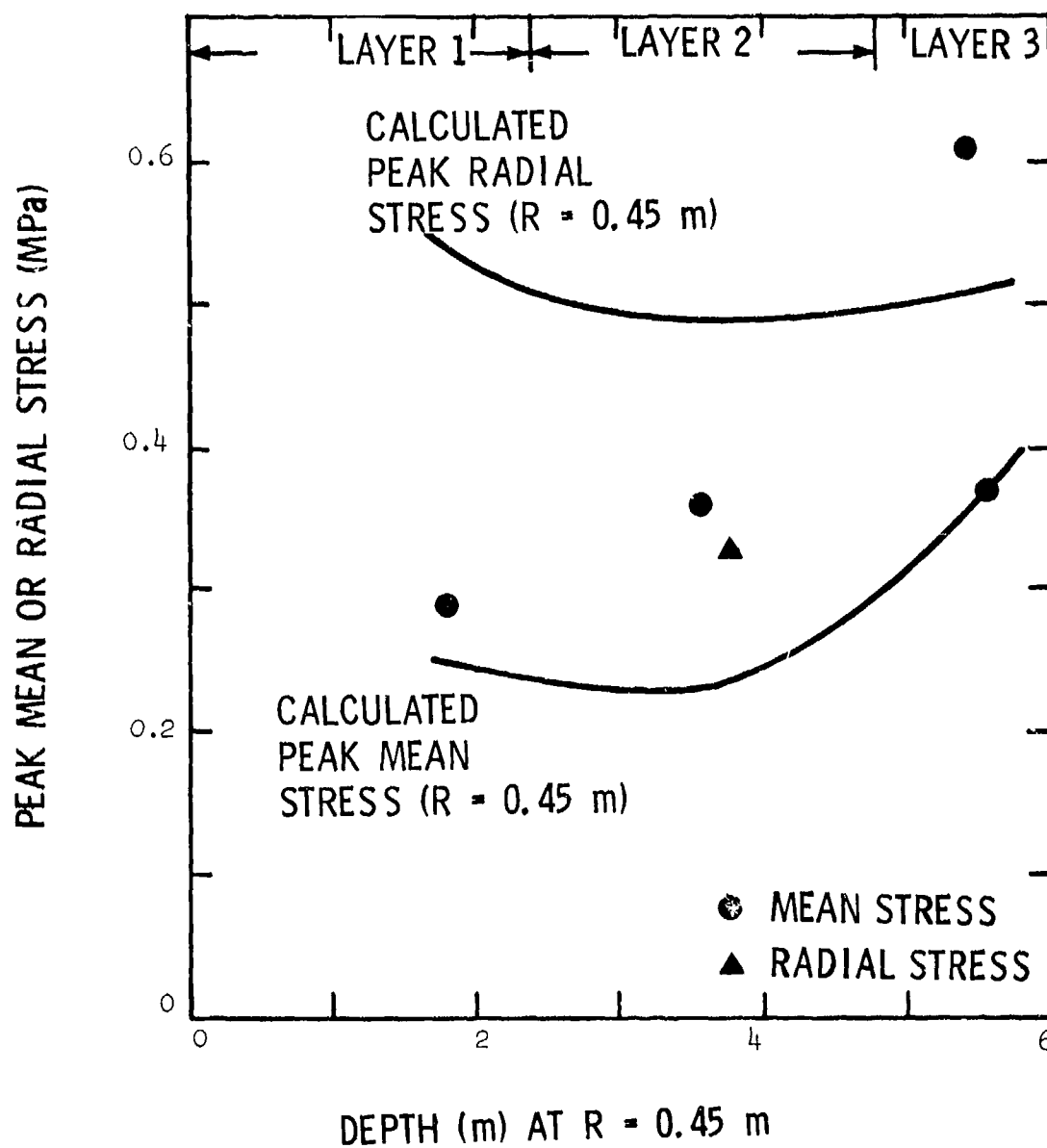
Figure V-16
Predicted Peak Radial and Peak Mean Stress versus Depth at

Constant Radial Position R = 0.45 Compared with Measurements.
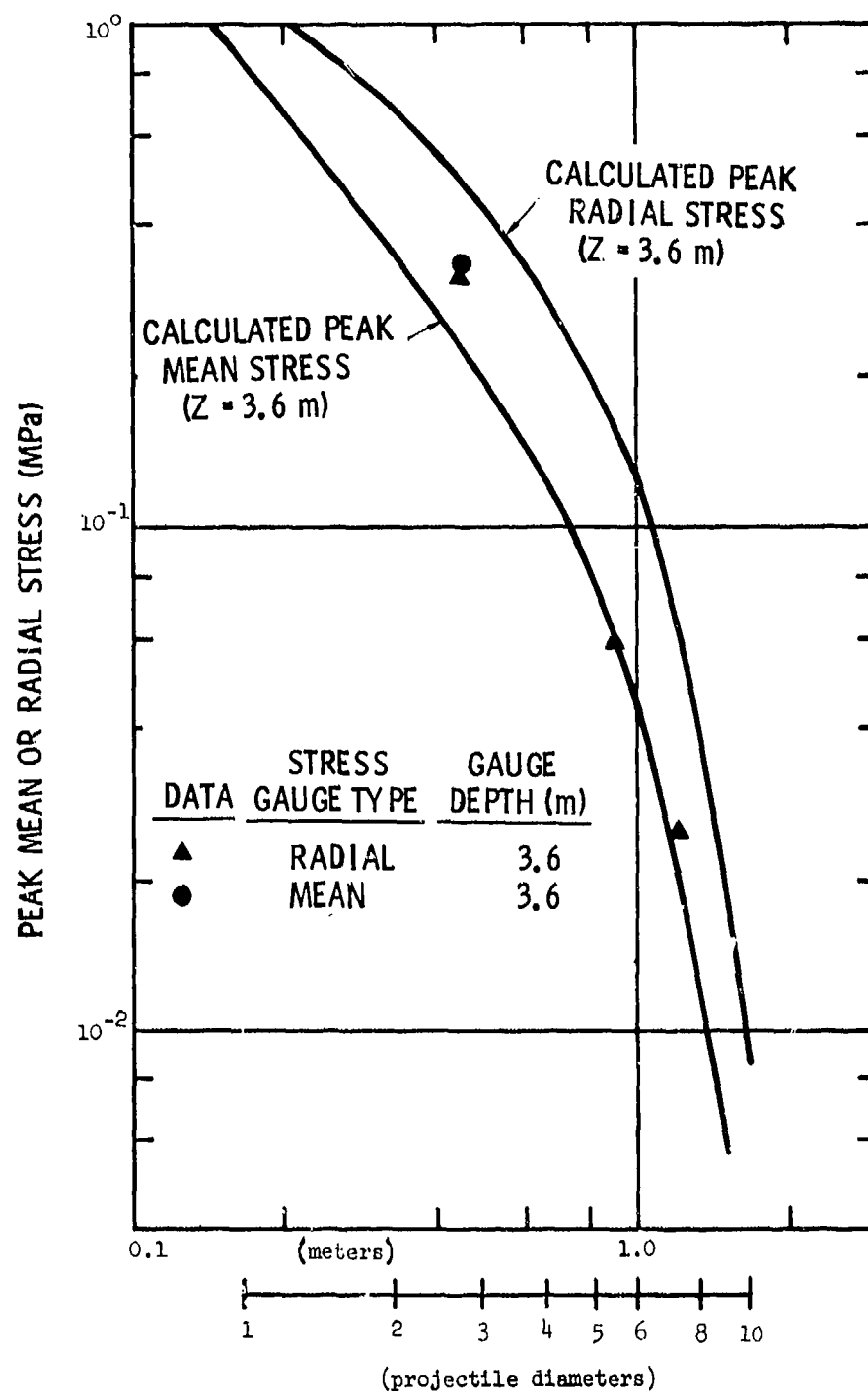
Figure V-17

Predicted Peak Radial and Peak Mean Stress versus Distance from

Impact Axis at Constant Depth Z = 3.6 m Compared with Measurements.

that the 3.6 m data compare reasonably well with the predicted mean stress attenuation curve and that peak stress amplitude falls off rapidly (faster than r^{-2}) with distance away from the projectile path axis.

In general, it is felt that the soil stress measurement technique has been demonstrated and that the information obtained provides confidence regarding validity of the material property data and material response models used in calculations for layers 1, 2 and 3. The satisfactory agreement between measurement and calculation of stress pulse shape and amplitude also verifies methods employed in the computational technique. Without the earth stress data much less credibility might have been attached to results of computations. Penetration tests (numbers 2 and 4), which provided the earth stress history data were conducted with projectiles of 127 kg mass and diameter 0.152 m rather than the 181 kg, 0.165 m diameter projectiles assumed in calculations. While another calculation would be required for the slightly smaller projectile in order to definitely establish differences, it is felt that stress history results for the smaller projectile would be similar to those of the larger projectile within the uncertainties that exist.

SECTION VI

SUMMARY AND CONCLUSIONS

All phenomena connected with producing significant loads on the projectile occur in a relatively small region of the target medium about the projectile nose. Shown in Figure VI-1 are three-dimensional plots of radial and vertical soil velocity as a function of depth in target and distance from projectile path axis at a time when the projectile nose is at 4.4 m depth (see also Figures A-122 and A-123). It is seen that the region of greatest disturbance in the soil is small and confined to the immediate vicinity of the nose. Figure VI-2a also illustrates how rapidly the disturbance in soil vanishes with distance from the projectile. With the projectile nose tip at 4.4 m, at a depth of 4.2 m (0.2 m behind projectile nose) soil pressure is about 3 MPa (30 bars, 450 psi) at a distance of slightly less than one projectile radius from the projectile axis. At a distance 2.5 projectile diameters from the axis, the soil pressure is down an order of magnitude to 0.3 MPa and at 5 projectile diameters another order of magnitude reduction is found. Figure VI-2b indicates in yet another way the highly isolated nature of the projectile generated disturbance in the soil. For the zones of the computational mesh originally on the symmetry axis and later adjacent to the penetrator, mean stress is plotted as a function of vertical position relative to nose tip location. The pressure profile ahead of and along the projectile surface is shown in Figure VI-2b for the penetrator in layer 1 (nose tip at 2 m depth) and in layer 2 (4.4 m depth). For materials similar to those of the Watching Hill target medium, it is
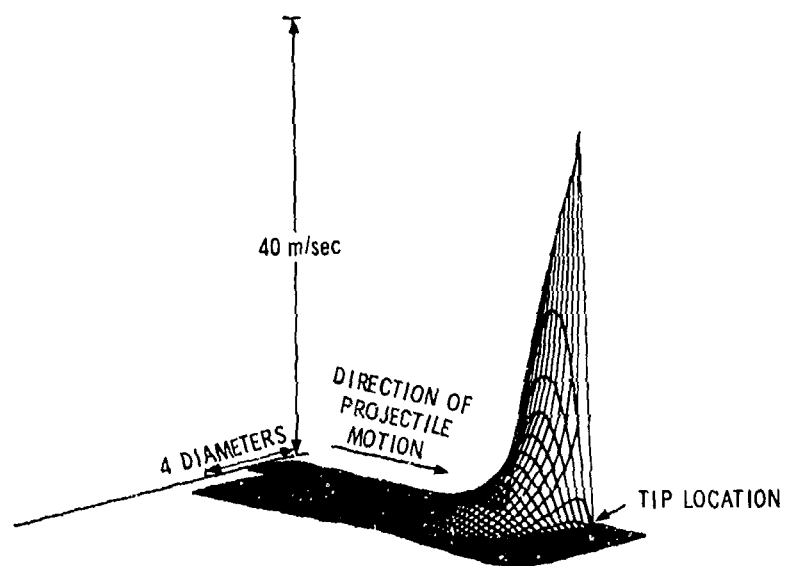
(a) RADIAL VELOCITY
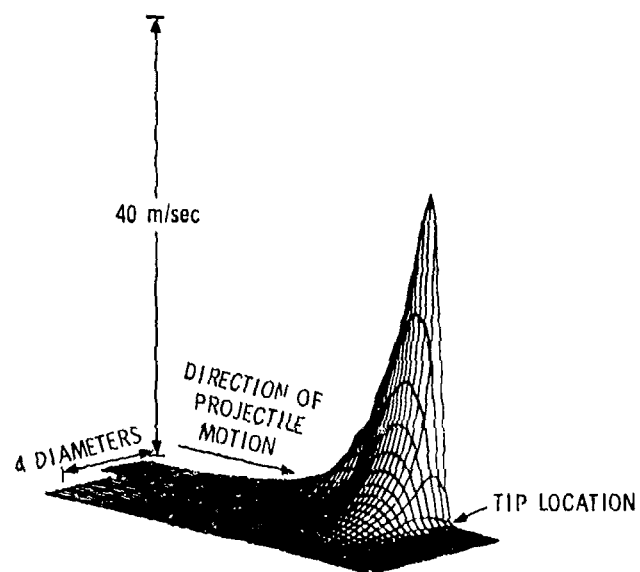
(b) VERTICAL VELOCITY

Figure VI-1

Radial Velocity (a) and Vertical Velocity, (b) in Soil as a Function

of Depth and Distance from Impact Axis when Projectile is at 4.4 m Depth.

66

PROJECTILE DIAMETERS

RADIAL DISTANCE FROM PROJECTILE AXIS
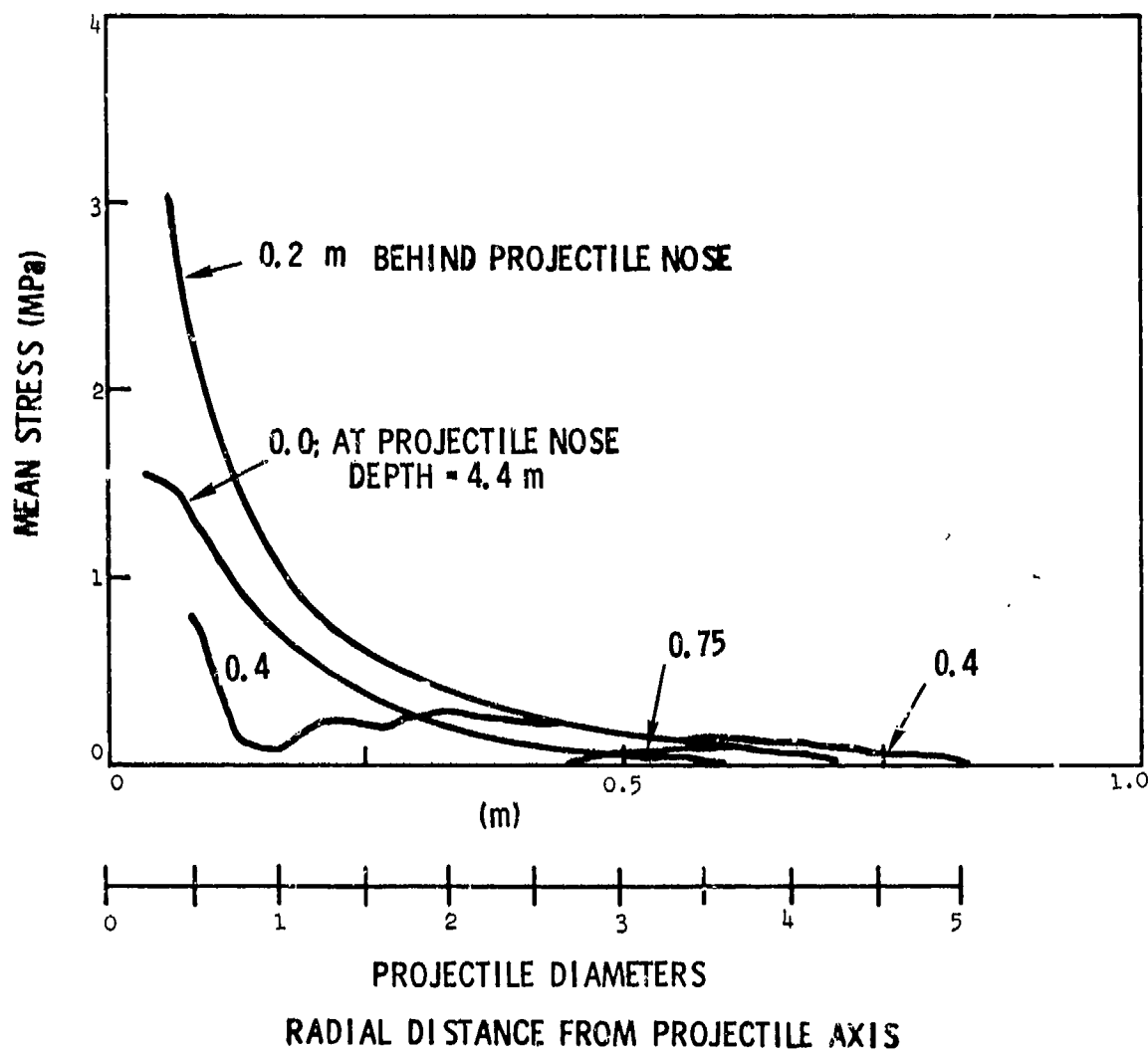
Figure VI-2a

(a) Decay of Mean Stress in ...il with Radial Distance from Projectile at Time when Projectile is at 4.4 m Depth.

p vs. Z NEXT TO PROJECTILE
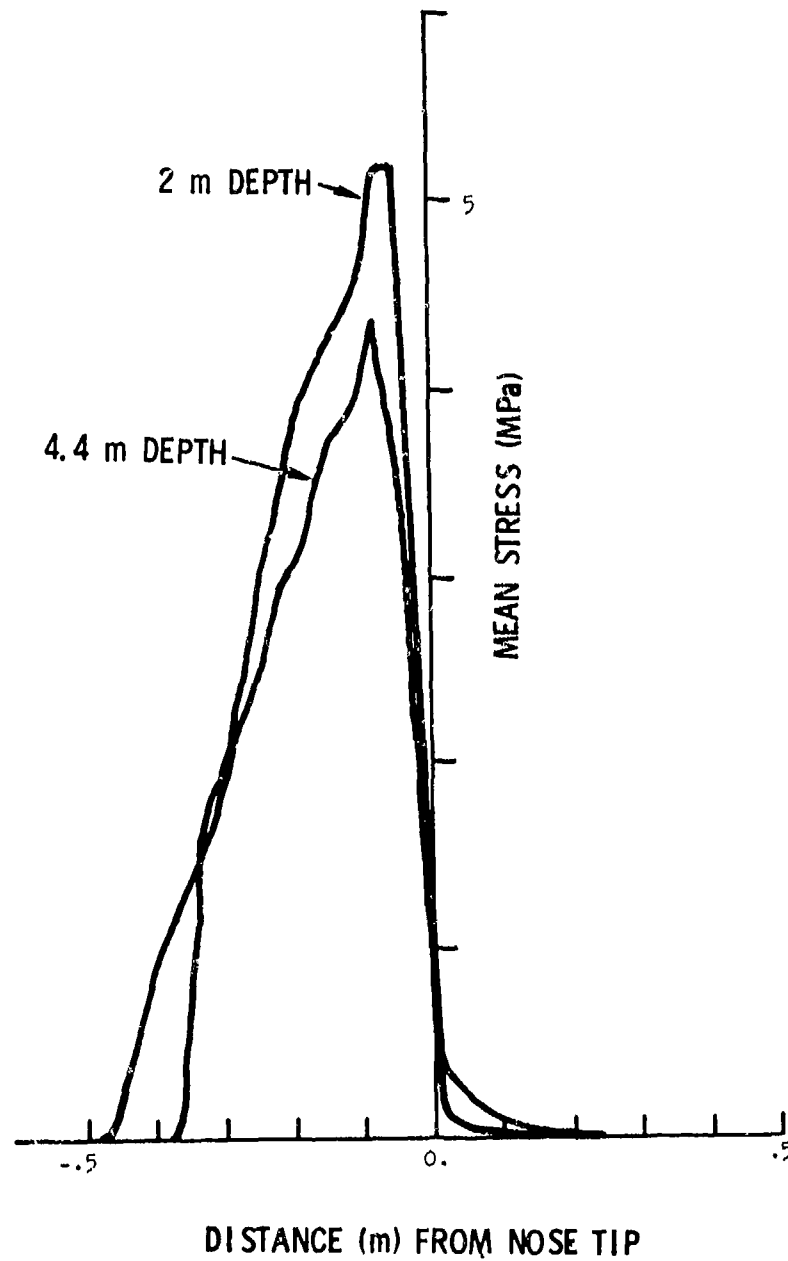
Figure VI-2b

(b) Mean Stress in Soil versus Depth Next to Projectile at Projectile Depths of 2 and 4.4 m.

68

seen that essentially all of the disturbance produced in the soil occurs within a cylindrical volume with radius equal to 3 projectile diameters. For purposes of calculating loads on penetrators, radial extent of the target need not be more than about 5 penetrator diameters in materials like those of this calculation.

Figure VI-3 shows the path a soil particle follows in the stress plane, $\sqrt{\frac{3}{2}} \tau$ vs. p. The particle of Figure VI-3 is identified by its initial coordinates $Z = 3.6$ m, $R = 0.15$ m and so is located in layer 2 material at a distance less than one projectile diameter from the impact axis. During loading the particle follows the path shown. On unloading the particle finds itself very close to the failure envelope and follows it to zero pressure. A close examination of the calculation reveals that the stress state for the particle should actually be at the intersection of the cap and the failure envelope: the fact that it does not quite coincide with this point is a consequence of a slight "over-shrinking" of the cap caused by the finite difference approximation used for the constitutive equations. Figures VI-2b and VI-3 taken together indicate that accurate modeling of the failure envelope and unloading behavior for the material are important parts of the calculation. Similarly, Figure VI-4 illustrates the path of the same soil particle in the strain invariant plane, $\sqrt{I_2}$ vs. η, where I_2 is the second moment of the strain deviators and η is volumetric strain. After unloading, the particle finds itself with a large deviatoric strain and at a density less than its initial density. These paths experienced by soil particles as a result of target penetration by projectiles are considerably different from paths attained in conventional uniaxial strain and triaxial stress experiments. Strain energy density of a particle within the region of

69
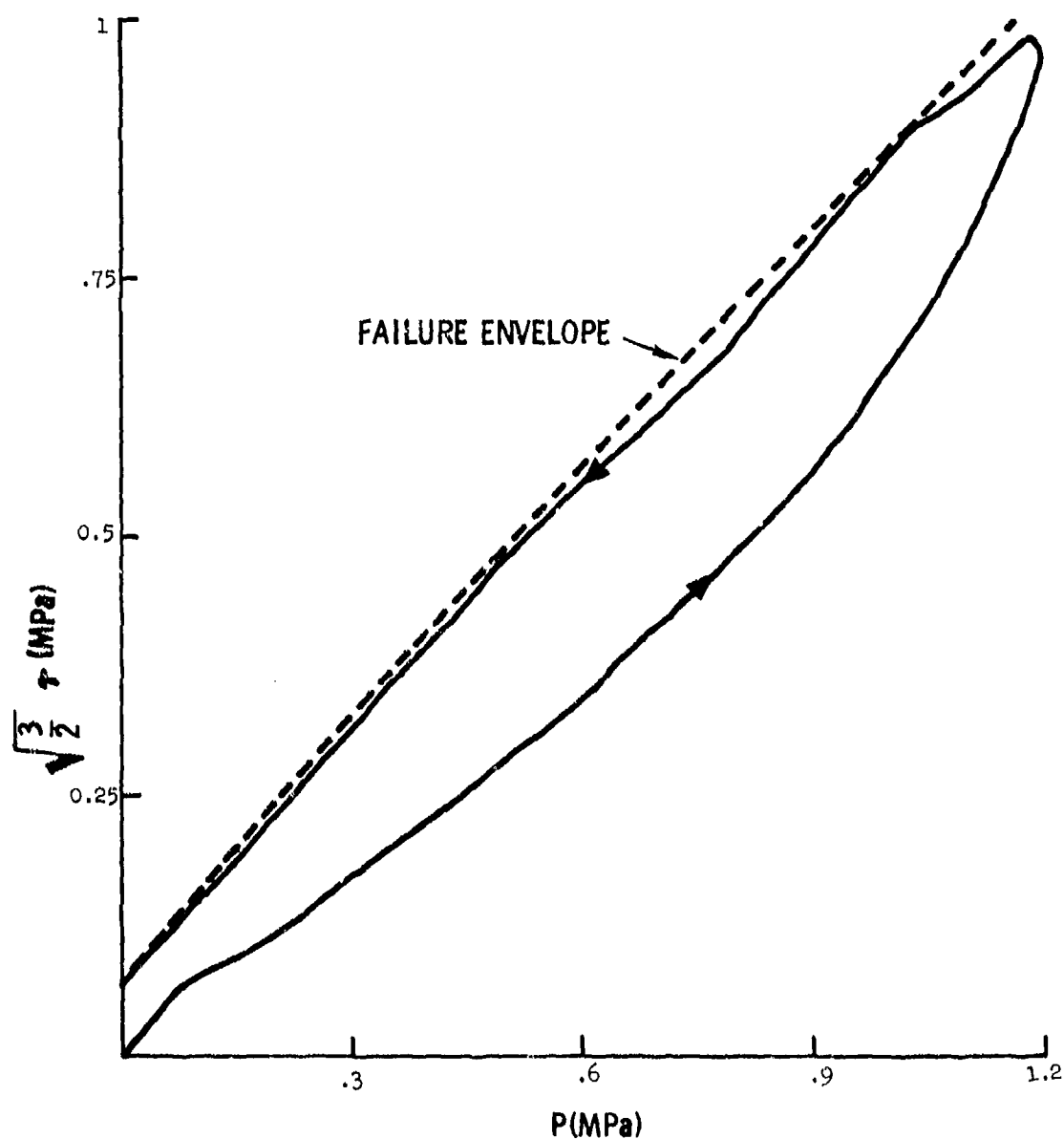
STRESS PATH FOR A PARTICLE AT Z = 3.6 m, R = 0.15 m

Figure VI-3

Stress Path, During Projectile Penetration, for a Soil Particle at

Z = 3.6 m, R = 0.15 m in Shear Stress-Pressure Space.
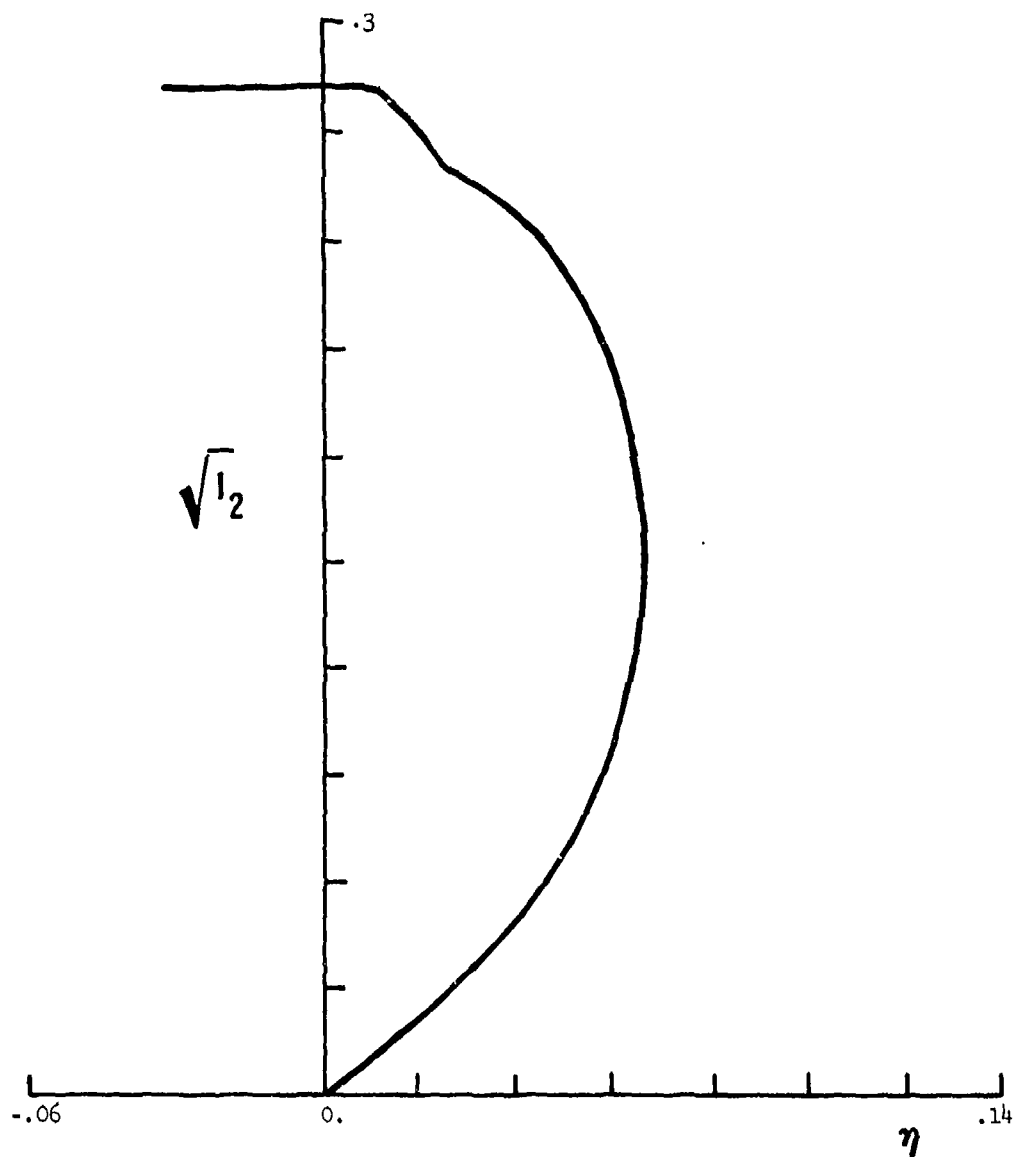
POINT 3: $\sqrt{I_2}$ vs. η

$(I_2 = E'_{ij}E'_{ij})$

Figure VI-4

Strain Path, During Projectile Penetration, for a Soil Particle

at $Z = 3.6$ m, $R = 0.15$ m.

71

soil highly disturbed by the projectile is of the order of 0.1 to 0.5 MJ/ m^3 for the Watching Hill medium. Consequences of the dilatancy inherent in the soil cap model, as indicated in Figure VI-4, appear to be manifested in two ways. These are lack of a definitive soil separation point on the projectile and the size of the projectile-produced borehole. Results of the rigid body calculation indicate that the diameter of the borehole is never greater than the projectile diameter and may in fact be less. Accurate determination of borehole diameter behind the projectile is not possible owing to the continual rezoning to a coarser mesh in this region. It is known, however, that soil rebound occurs and boreholes have been observed[22] whose final diameters are less than the projectile diameter. Unfortunately, no attempt was made to measure borehole sizes for the penetrator experiments at Watching Hill. The rigid body calculations also suggest that the Watching Hill soil does not separate from the projectile but appears to remain attached throughout the entire length of the projectile. This occurs even though the normal stress on the projectile is significantly larger than zero only on the nose. (What appears to be a soil separation position in Figures A-97, A-106, A-115, A-124 and A-133 is interpreted, rather, to be a perturbation in the calculation resulting from the transition from a region of fine to coarser zoning). That soil separation or detachment from the projectile may not occur has been observed[22] experimentally. Those experimental results, however, cannot distinguish between soil detachment on the projectile nose with later reattachment and complete lack of soil separation.

To investigate this point further, additional calculations should be performed which include friction and a response model such as the cap model which demonstrates dilatancy. As appears to be the case here

72

in calculations with no friction, dilatancy in the response model prevents or retards soil detachment from the projectile surface. By the inclusion of friction in such calculations even a small frictional stress, acting over the large area of the projectile afterbody, could contribute a large axial retarding force comparable to or possibly greater than that contributed by the nose area of the projectile. Results from such a calculation, when compared with projectile deceleration data, would imply a smaller friction coefficient than one inferred from calculations with response models having no dilatancy in which soil separation might occur, for example, at the position on the projectile where the nose meets the afterbody.

Figure VI-5 illustrates the partitioning of energy to the penetrated medium at the expense of projectile kinetic energy. From the zero friction calculation, it is apparent that projectile kinetic energy losses manifest themselves primarily in the form of plastic work done in deformation of the penetrated medium. Energies associated with motion of the soil and with recoverable elastic work are very small, each being on the order of 1/10 or less of the plastic work (internal energy = plastic work + elastic work).

The calculated deceleration history indicates that sudden changes in the problem occur only when the nose region of the projectile is entering a new layer of material. Also, Figure VI-5 shows that the dominant mode of the rate of energy transfer from projectile to soil is nearly constant through a layer in which there is little velocity change. Moving pictures made of numerous plots of normal stress distribution and three-dimensional plots of pressure vs. axial and radial position, for example, confirm that the process being calculated is primarily quasi-static. Thus, the

73
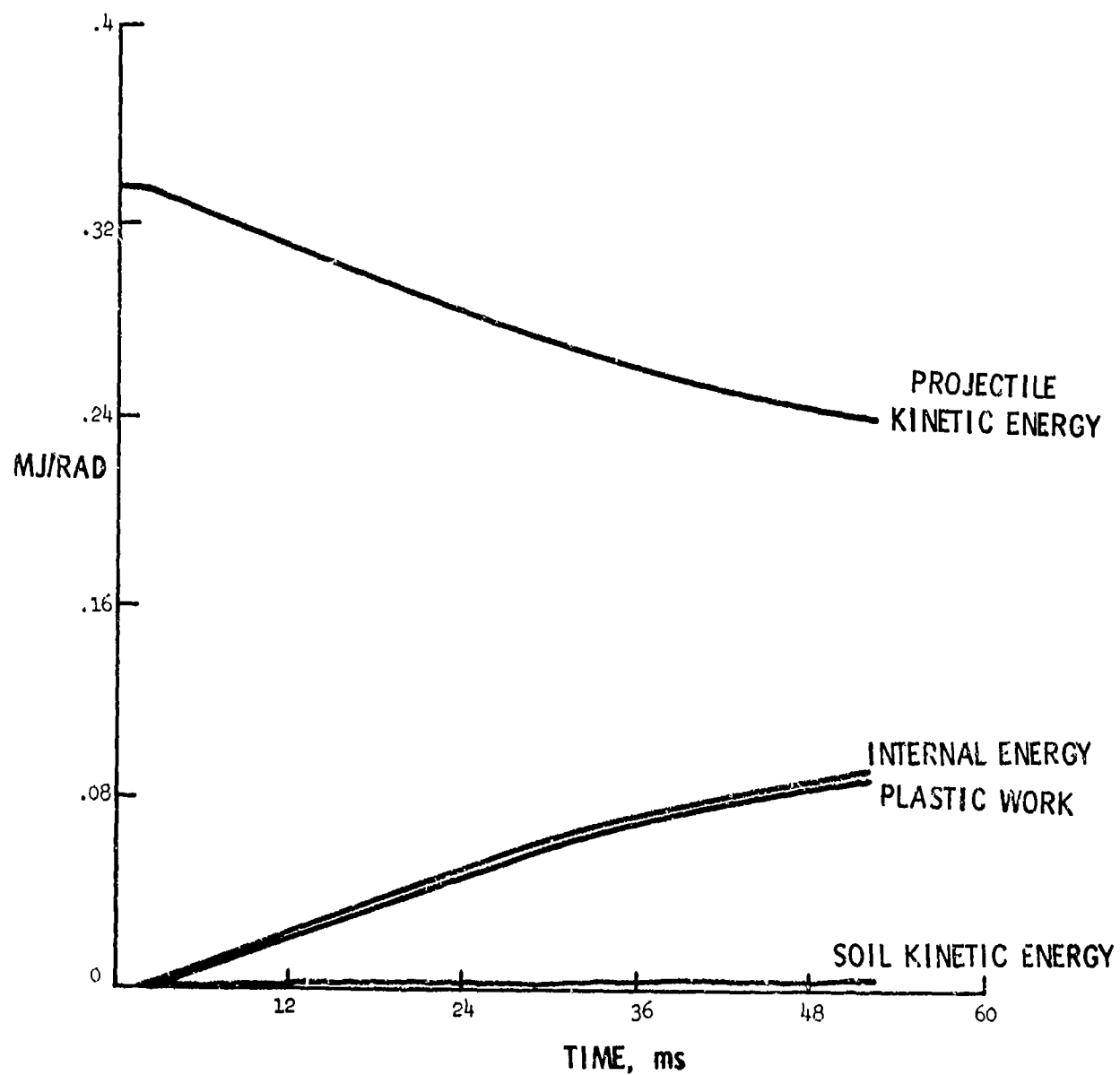
Figure VI-5
Projectile Kinetic Energy, Soil Kinetic Energy, Soil Plastic

Work and Soil Internal Energy versus Time.

method of "skipping" through layers, and calculating only transition periods, as employed by California Research and Technology,[20] appears to be a useful means of performing deep penetration calculations with large-scale wave propagation codes with a reasonable degree of economy although it may be necessary to perform multiple calculations in layers that produce large velocity decreases. It also appears, however, that detailed analysis of the results of this and similar calculations should lead to the development of much less sophisticated methods which would also yield necessary information for depth prediction and projectile design.

During the deformable projectile calculation, the maximum radial displacement that was observed for the projectile surface was 30 μm. Although this displacement was too small to alter the effective shape of the vehicle, fluctuations in displacement were sufficient to produce large charges in normal stress at the vehicle-soil interface, as shown in Figures B-37 through B-39. Thus, the dominant effect of the rigid-body approximation was to eliminate transient variations in the normal stress.

The agreement in predicted soil histories between the two calculations demonstrates that, for the particular material model used, these transients are damped out less than 20 mm from the vehicle and do not affect the predicted wave motion in the soil. However, the deformable body calculation predicts a deceleration about forty percent larger than that calculated for a rigid body. This comparison demonstrates that the deceleration is determined by the soil response in regions much closer to the vehicle than the locations at which stress measurements were made. The motion is similar to aerodynamic behavior, with the drag determined by the response in a narrow region, or boundary layer.

The differences between the results of the two calculations are related to their description of this boundary layer. The inclusion of the 45° nose tip results in a stress increase of less than 5 MPa, effective over a cross-sectional area of about 4×10^{-4} m^2, accounting for a deceleration difference of about 1 g. Of greater significance is the procedure for obtaining the stress at the interface. In the calculations, stress histories are recorded only at zone centers and, therefore, not at the interface. For the rigid body calculation, the stress in the nearest soil zone was used to determine the decelerating force, as discussed in Section III. In the deformable body calculation, no interface stress or force was explicitly obtained; the sliding interface procedure results in an effective normal stress that is between the stress in the soil zone and the (usually higher) stress in the nearest vehicle zone.

While many questions remain to be investigated, this first attempt to predict projectile motion and target material response has been highly successful and most encouraging. Given data describing properties of each layer in the target medium, realistic soil response models were constructed and utilized in the finite difference code computations. Resulting predictions of projectile deceleration and of stress history at several points in the soil generally agreed well with measurements, lending credence to the method of analysis. Consequently greater confidence may now be placed in prediction of nonmeasurable quantities, such as normal stress distribution on projectile surface, which are necessary for design of earth penetrating projectiles.

REFERENCES

1. Young, C. W., "Depth Prediction for Earth Penetrating Projectiles," _J. Soil Mechanics and Foundations Division_, Proceedings ASCE, May 1969, p. 803.

2. Young, C. W., _Empirical Equations for Predicting Penetration Performance in Layered Earth Materials for Complex Penetrator Configurations_, Sandia Laboratories, Albuquerque, New Mexico, SC-DR-72-0523, December 1972.

3. Benzley, S. E., Bertholf, L. D., and Clark, G. E., TOODY II-A, _A Computer Program for Two-Dimensional Wave Propagation_, Sandia Laboratories, Albuquerque, New Mexico, SC-DR-69-516, November 1969.

4. Thorne, B. J., and Holdridge, D. B., _The TOOREZ Lagrangian Rezoning Code_, Sandia Laboratories, Albuquerque, New Mexico, SLA-73-1057, April 1974.

5. Patterson, W. J., _DNA/Sandia Soil Penetration Experiment at DRES Results and Analysis_, Sandia Laboratories, Albuquerque, New Mexico, SAND-75-0001, January 1975.

6. Letter, Patterson, W. J., Terradynamics Division, Sandia Laboratories, to T. D. Stong, DNA, _Projectile and Instrumentation Package Assembly Drawing for DNA Penetrator Experiments_, May 7, 1974.

7. Thigpen, L., _Penetration of Projectiles into Continuous Earth Media_, Sandia Laboratories, Albuquerque, New Mexico, SC-RR-72-0204, May 1972.

8. Graham, R. A., _Pressure Dependence of the Piezoelectric Polarization of Lithium Niobate_, IEEE Transactions on Sonics and Ultrasonics, Vol. SU-21, No. 1, January 1974, p. 63.

9. Reed, R. P., _Lithium Niobate Free-Field Stress Measuring System for_ the _Rock Springs, Wyoming, Oil Shale In Situ Retorting_ Experiment of the U.S. Bureau of Mines, Sandia Laboratories, Albuquerque, New Mexico, SAND74-0396, March 1975.

10. Carlson, G. A., _Stress Wave Measurements in Earth Penetrator Experiments_, Sandia Laboratories, Albuquerque, New Mexico, SAND-74-0257, December 1974.

11. Letter, Jackson, J. G. Jr., Waterways Experiment Station to Distribution, _Output Display Requirements of DNA Earth Penetrator Experiments at DRES_, Canada, May 16, 1974.

12. Jackson, J. G. Jr., _Physical Property and Dynamic Compressibility Analysis of the Watching Hill Blast Range_, U. S. Army Engineer Waterways Experiment Station, Vicksburg, Mississippi, Tech. Rpt. S-72-4, April 1972.

13. Letter, Jackson, J. G. Jr., Waterways Experiment Station to Distribution, _Recommended Soil Profile and Properties for DNA Penetrator Test Site_, DRES, Canada, March 25, 1974.

14. Letter, Jackson, J. G. Jr., Waterways Experiment Station to Distribution, _Soil Classification and Triaxial Shear Test Data for DNA Penetrator Test Site_, DRES, Canada, May 30, 1974.

15. Nelson, I., Baron, M. L., and Sandler, I., "Mathematical Models for Geological Materials for Wave-Propagation Studies," _Shock Waves and the Mechanical Properties of Solids_, Syracuse University Press, Syracuse, New York, Editors: J. J. Burke and V. Weiss, 1971.

16. Baladi, G. Y., Waterways Experiment Station (private communication, June 16, 1974).

17. Baladi, G. Y., _Isotropic Constitutive Model Equations and Fitting Parameter Values Used for Postshot Mixed Company Calculations_, U. S. Army Engineer Waterways Experiment Station, Vicksburg, Mississippi, August 1973.

18. Baladi, G. Y., _Transverse Isotropic Constitutive Model Equations and Fitting Parameter Values for Postshot Mixed Company Calculations_, U. S. Army Engineer Waterways Experiment Station, Vicksburg, Mississippi, February 1974.

19. Lawrence, R. J. and Mason, D. S., _WONDY-IV ---A Computer Program for One-Dimensional Wave Propagation with Rezoning_, Sandia Laboratories, Albuquerque, New Mexico, SC-RR-710284, August 1971.

20. Wagner, M. and Kreyenhagen, K. N., _Numerical Analysis of DNA Earth Penetrator Experiments at DRES_, California Research and Technology, 6269 Variel Avenue, Woodland Hills, California 91364, (DNA report, to be published).

21. Vortman, L. J., and Beyeler, J. A., _Results of Ground Motion and Air Blast Measurements, Project Essex I, Phase 1_, Sandia Laboratories, Albuquerque, New Mexico, SLA-73-0918, November 1974.

22. Patterson, W. J., _Terradynamic Results and Structural Performance of a 650-Pound Penetrator Impacting at 2570 Feet Per Second_, Sandia Laboratories, Albuquerque, New Mexico, SC-DR-69-782, December 1969.

APPENDIX A

81

List of Illustrations Appendix A

TABLE A-1

TABLE OF HISTORY PLOTS

Point	Radius (m)	Depth (m)	Radial Velocity	Axial Velocity	Radial Displacement	Axial Displacement	Pressure	Deviator Stress	Radial Stress	Axial Stress
	X	Z	UX	UZ	DX	DZ	P	J2	TXX	TZZ
3	0.15	3.6	A-11	A-12	A-13	A-14	A-15	A-16	A-17	A-18
4	0.15	0.4	A-19	A-20	A-21	A-22	A-23	A-24		
5	0.15	0.1	A-25	A-26	A-27	A-28	A-29	A-30		
7	0.45	5.4	A-31	A-32	A-33	A-34	A-35	A-36	A-37	
8	0.45	3.6	A-38	A-39	A-40	A-41	A-42	A-43	A-44	A-45
9	0.45	1.8	A-46	A-47	A-48	A-49	A-50	A-51	A-52	
10	0.45	0.4	A-53	A-54	A-55	A-56	A-57	A-58		
11	0.45	0.1	A-59	A-60	A-61	A-62	A-63	A-64		
12	0.9	3.6	A-65	A-66	A-67	A-68	A-69	A-70	A-71	A-72
13	1.5	5.4					A-73		A-74	
14	1.5	3.6					A-75		A-76	
15	1.5	1.8					A-77		A-78	

Table A-2

Table of Figure Numbers for Contour Plots, Lagrangian
Grid Plots and Plots of Normal and Tangential
Stress Along Projectile Surface

Projectile Depth (m) (Layer)	Time After Impact (ms)	Grid	Normal Stress	Tangential Stress	Axial Stress Contours	Radial Stress Contours	Hoop Stress Contours	Shear Stress Contours	Axial Velocity Contours	Radial Velocity Contours
0.1 (1)	0.657	A-79	A-80	A-81	A-82	A-83	A-84	A-85	A-86	A-87
0.4 (1)	2.63	A-88	A-89	A-90	A-91	A-92	A-93	A-94	A-95	A-96
2.0 (1)	13.4	A-97	A-98	A-99	A-100	A-101	A-102	A-103	A-104	A-105
2.8 (2)	18.9	A-106	A-107	A-108	A-109	A-110	A-111	A-112	A-113	A-114
4.4 (2)	30.3	A-115	A-116	A-117	A-118	A-119	A-120	A-121	A-122	A-123
5.2 (3)	36.2	A-124	A-125	A-126	A-127	A-128	A-129	A-130	A-131	A-132
6.8 (3)	48.4	A-133	A-134	A-135	A-136	A-137	A-138	A-139	A-140	A-141

ORES RIGID PROJECTILE CALCULATION
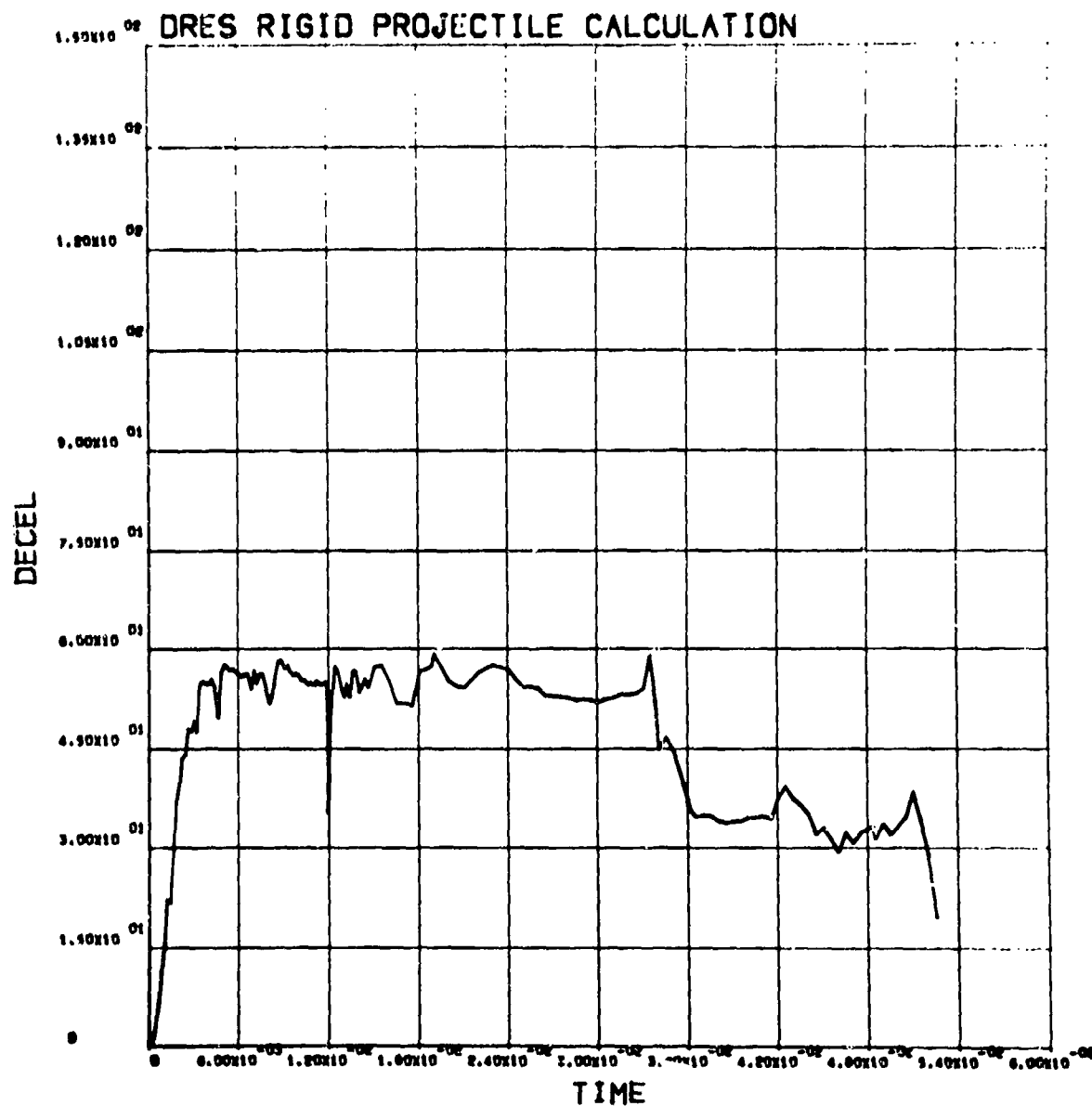
DECEL

TIME

Figure A-1

Projectile Deceleration vs. Time.

94
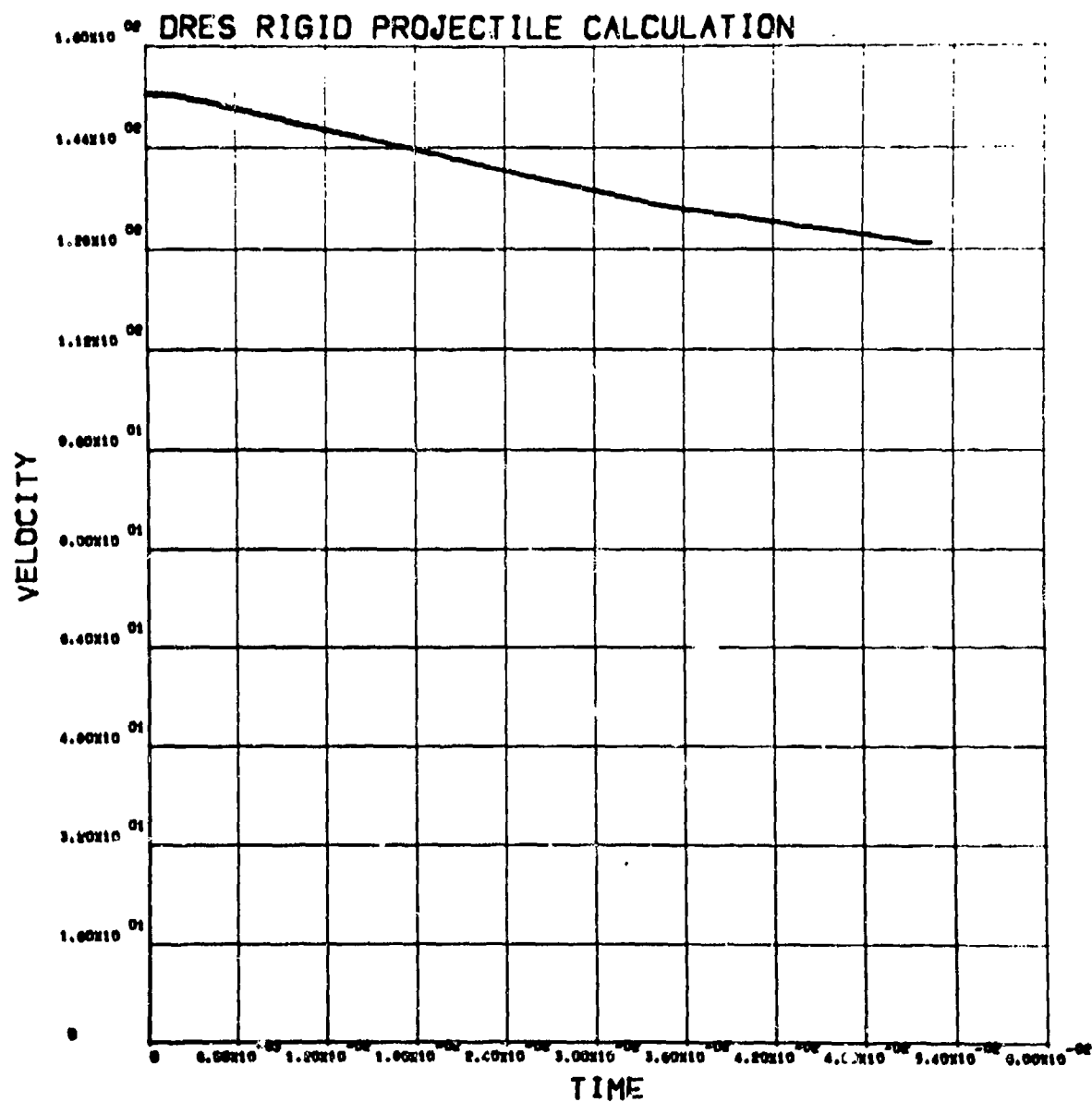
Figure A-2

Projectile Velocity vs. Time.

DRES RIGID PROJECTILE CALCULATION
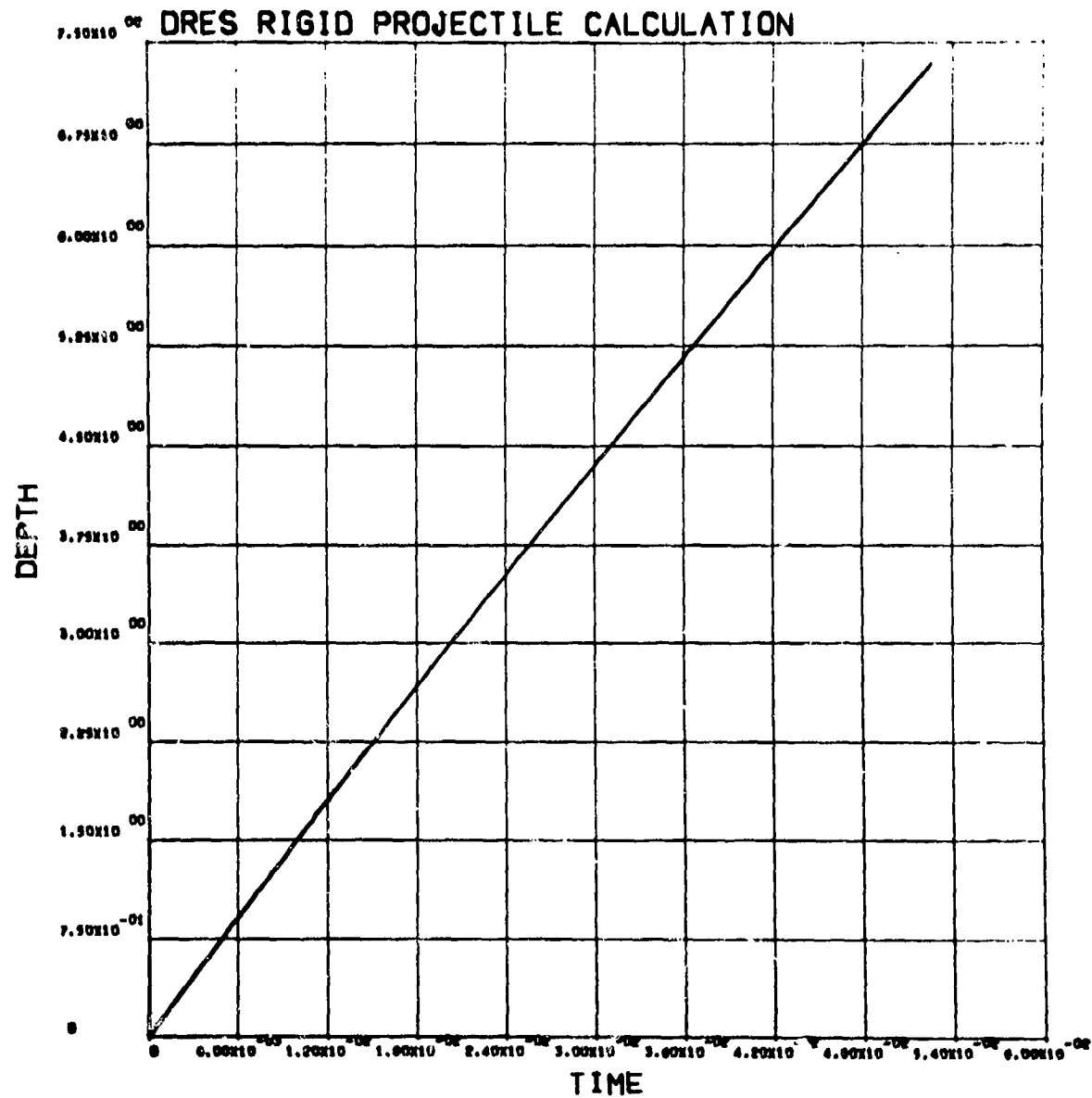
Figure A-3

Projectile Depth vs. Time.

96
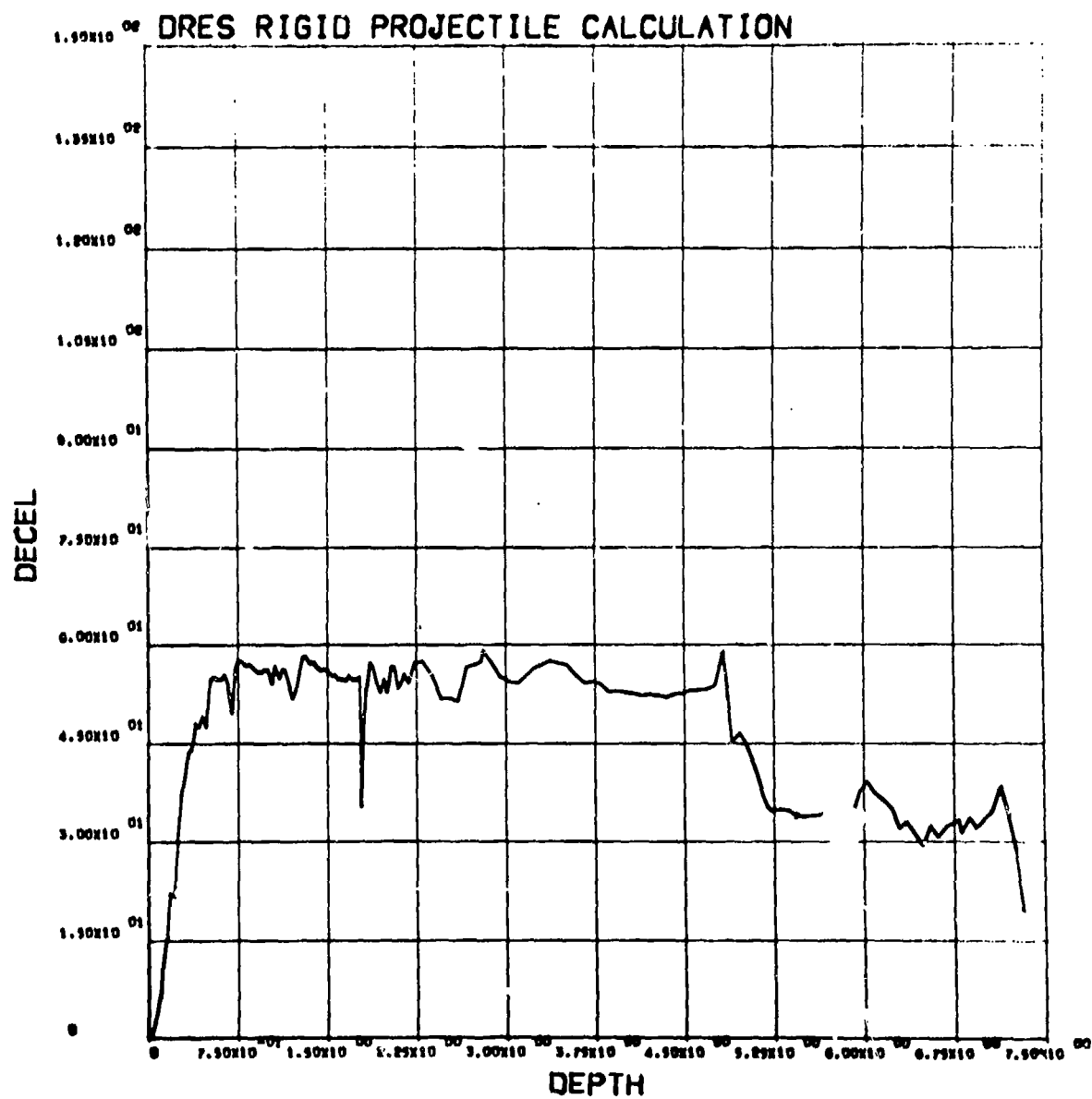
Figure A-4

Projectile Deceleration vs. Depth.

97

DRES RIGID PROJECTILE CALCULATION
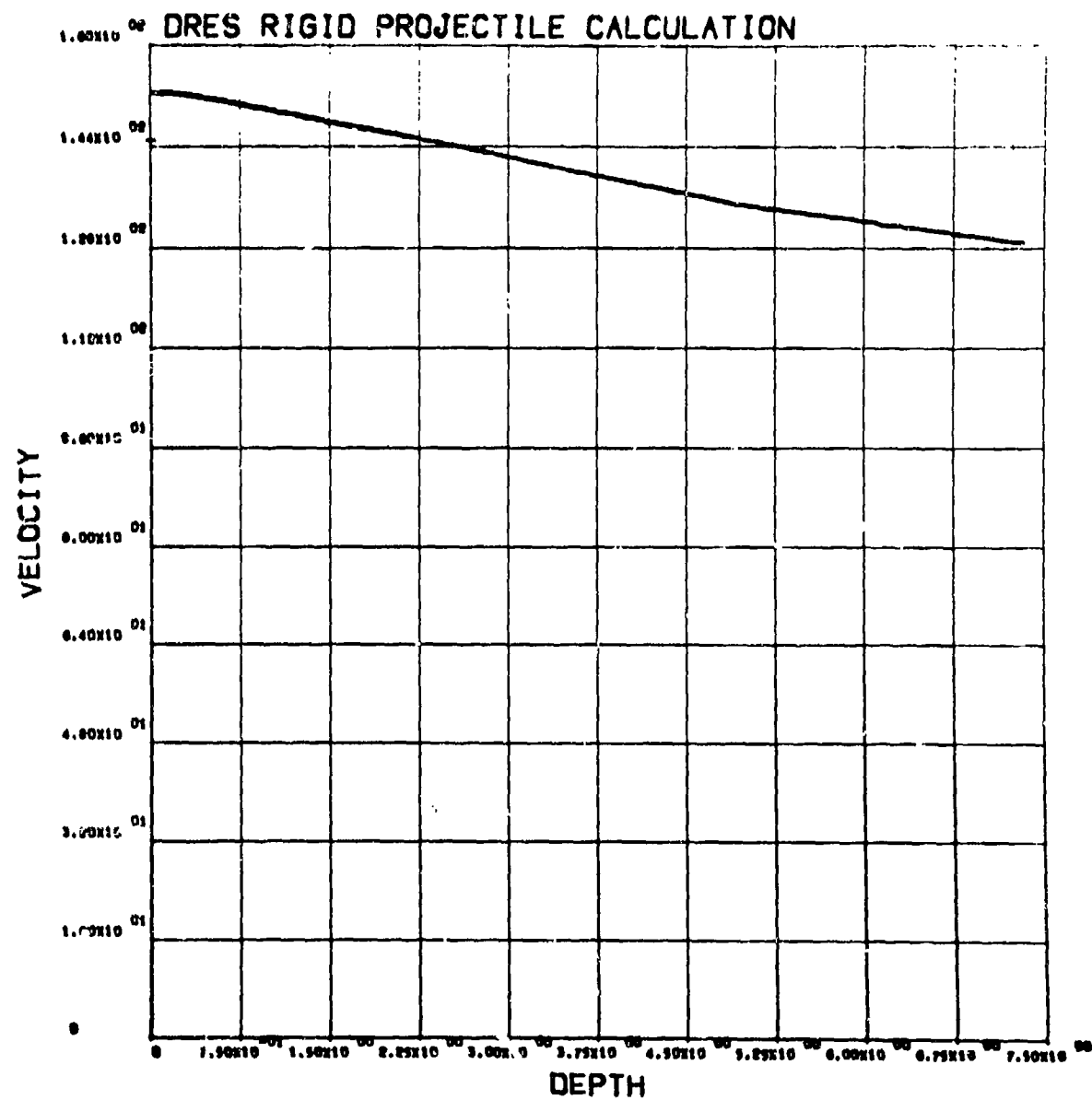
Figure A-5

Projectile Velocity vs. Depth.

98
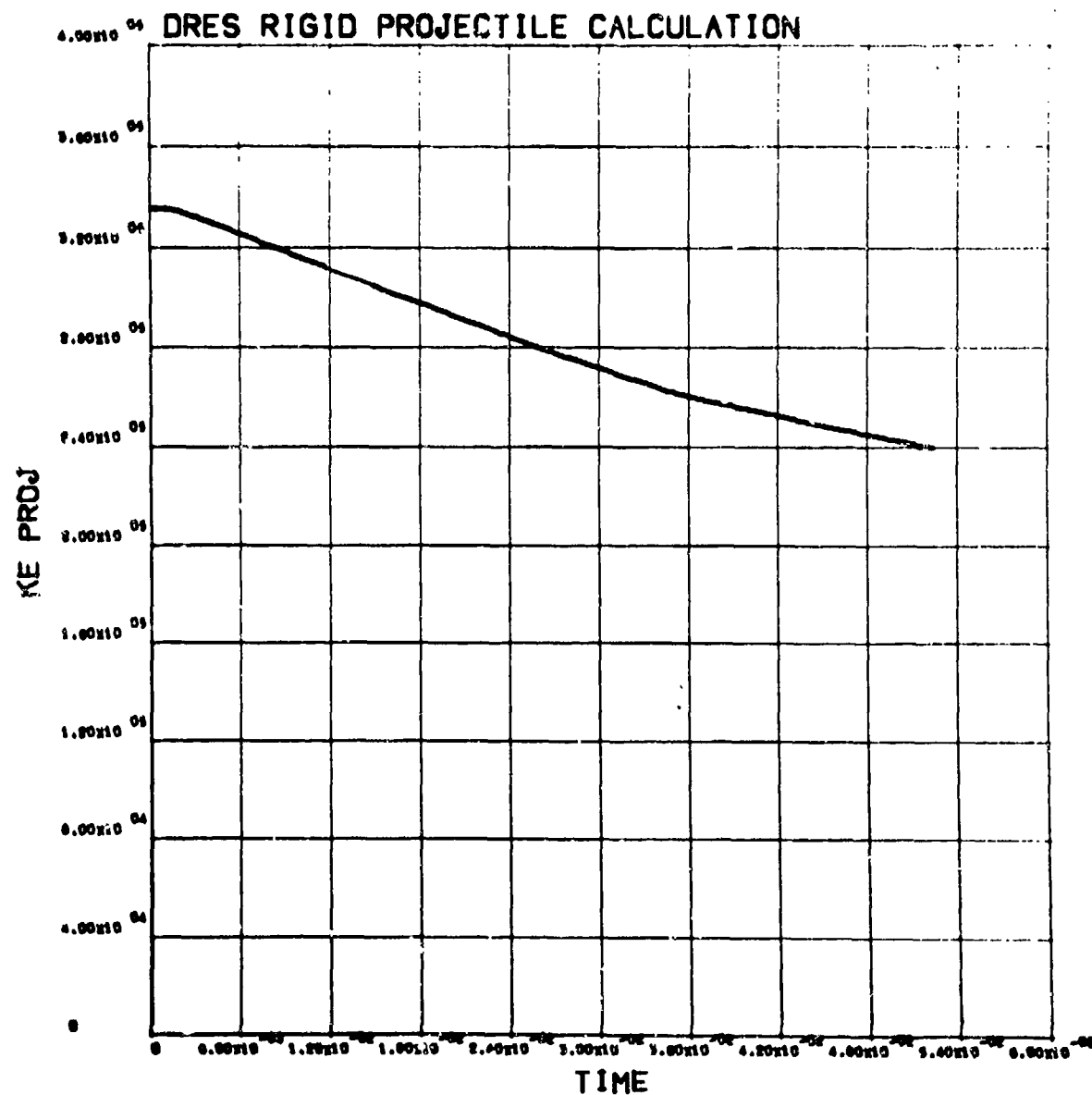
Figure A-6

Projectile Kinetic Energy/Radian vs. Time.
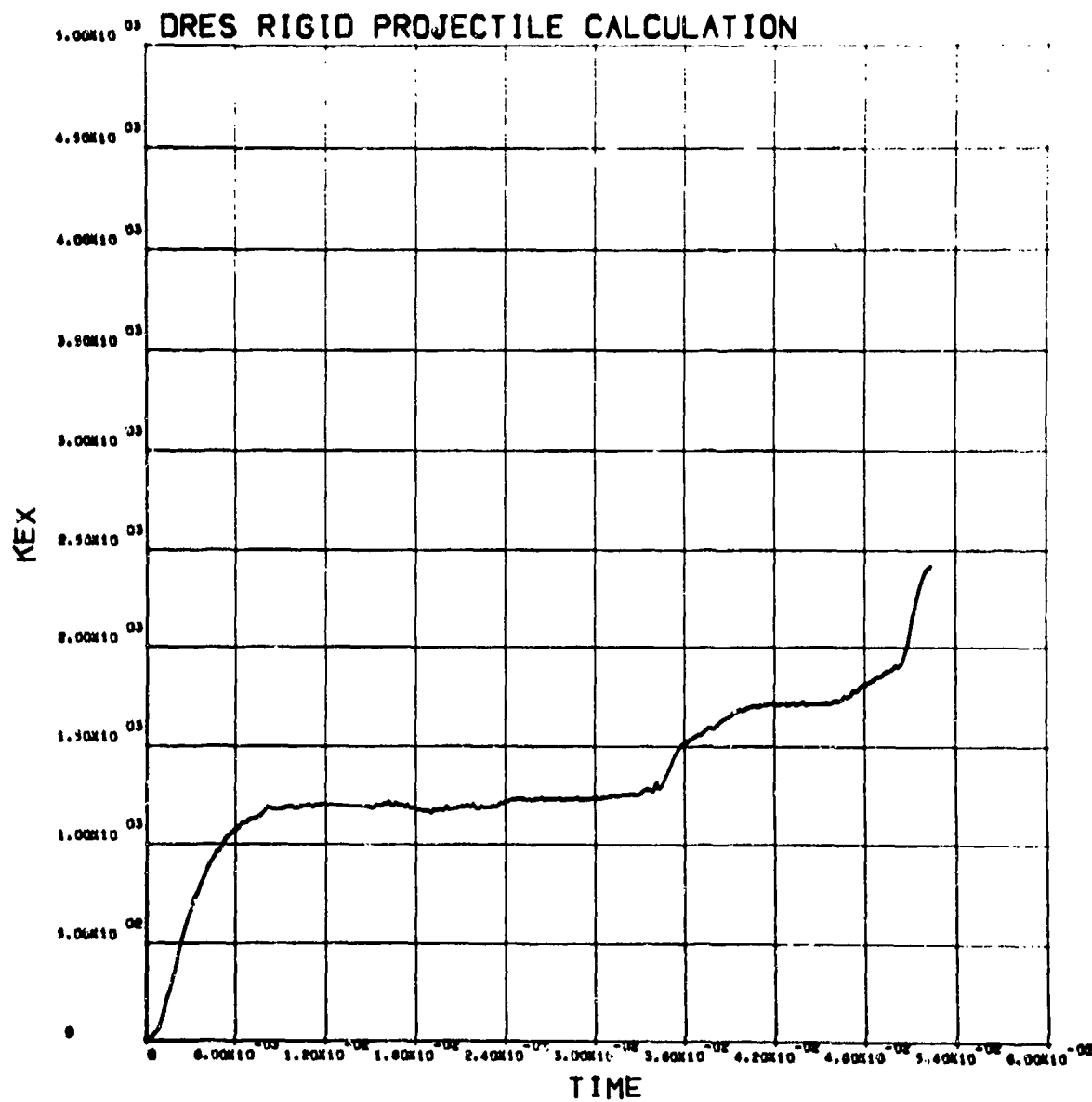
Figure A-7

Soil Kinetic Energy/Radian, Due to Radial Velocity, vs. Time.
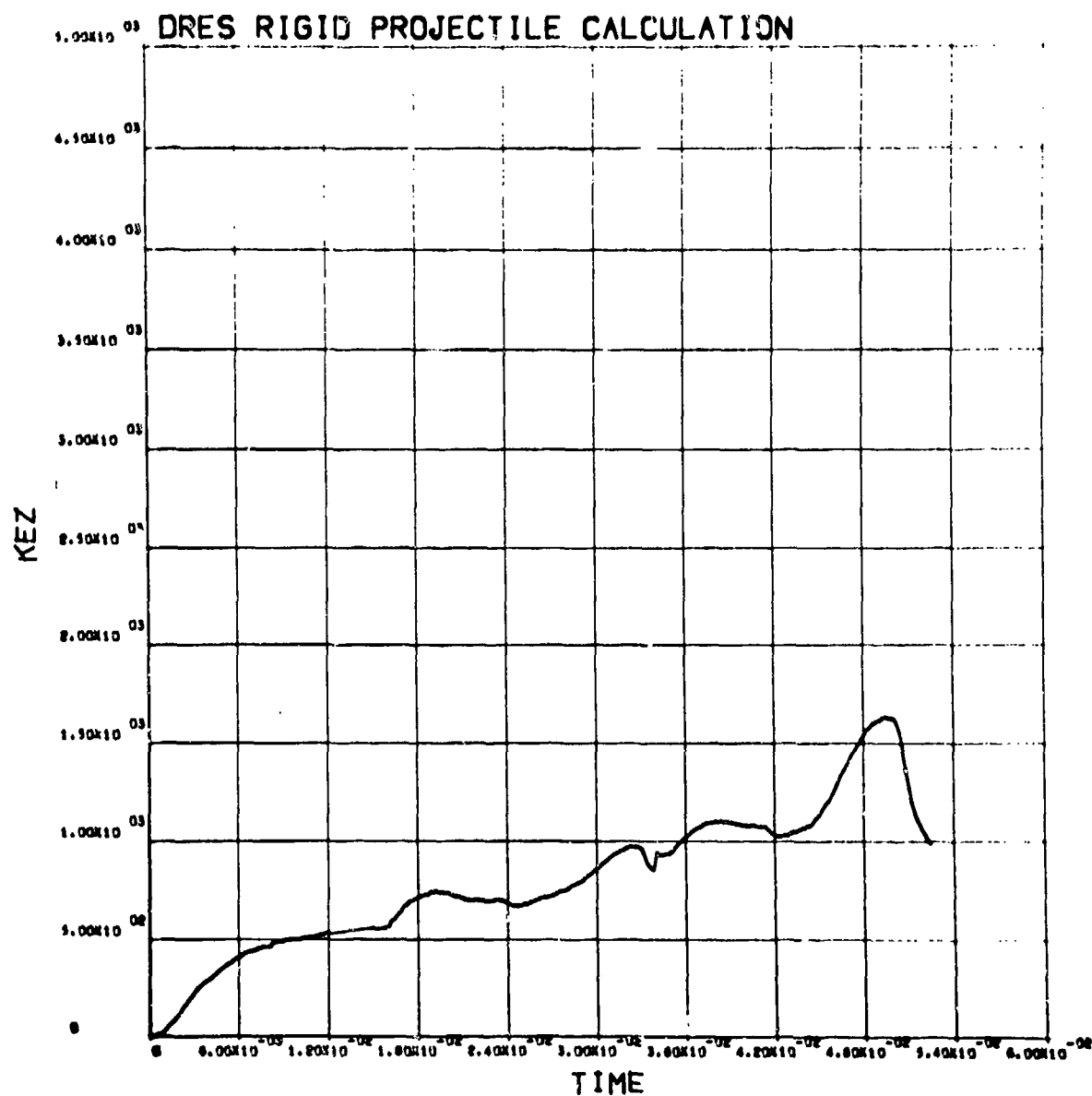
Figure A-8

Soil Kinetic Energy/Radian, Due to Axial Velocity, vs. Time.

101
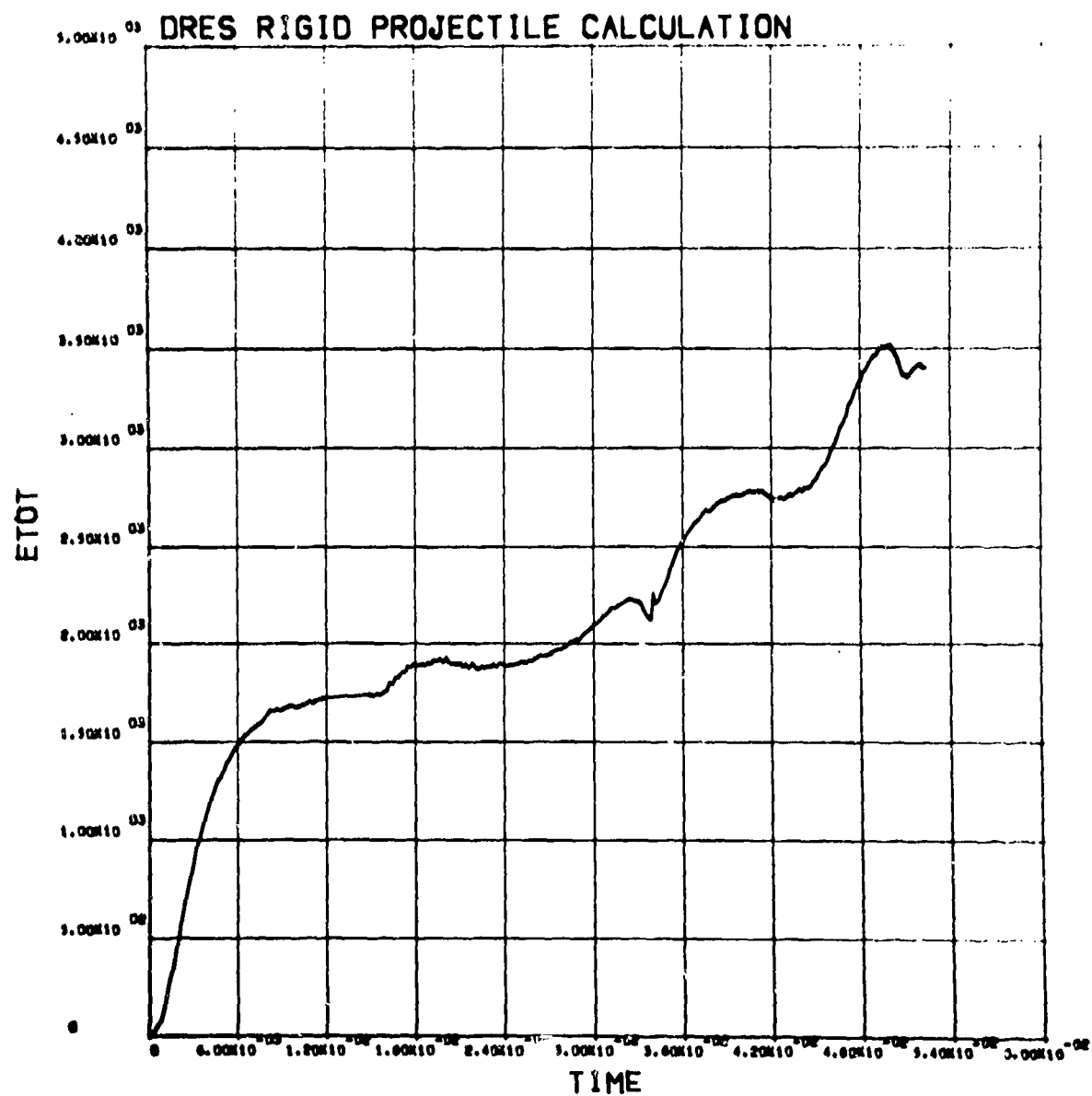
Figure A-9

Total Soil Kinetic Energy/Radian vs. Time.
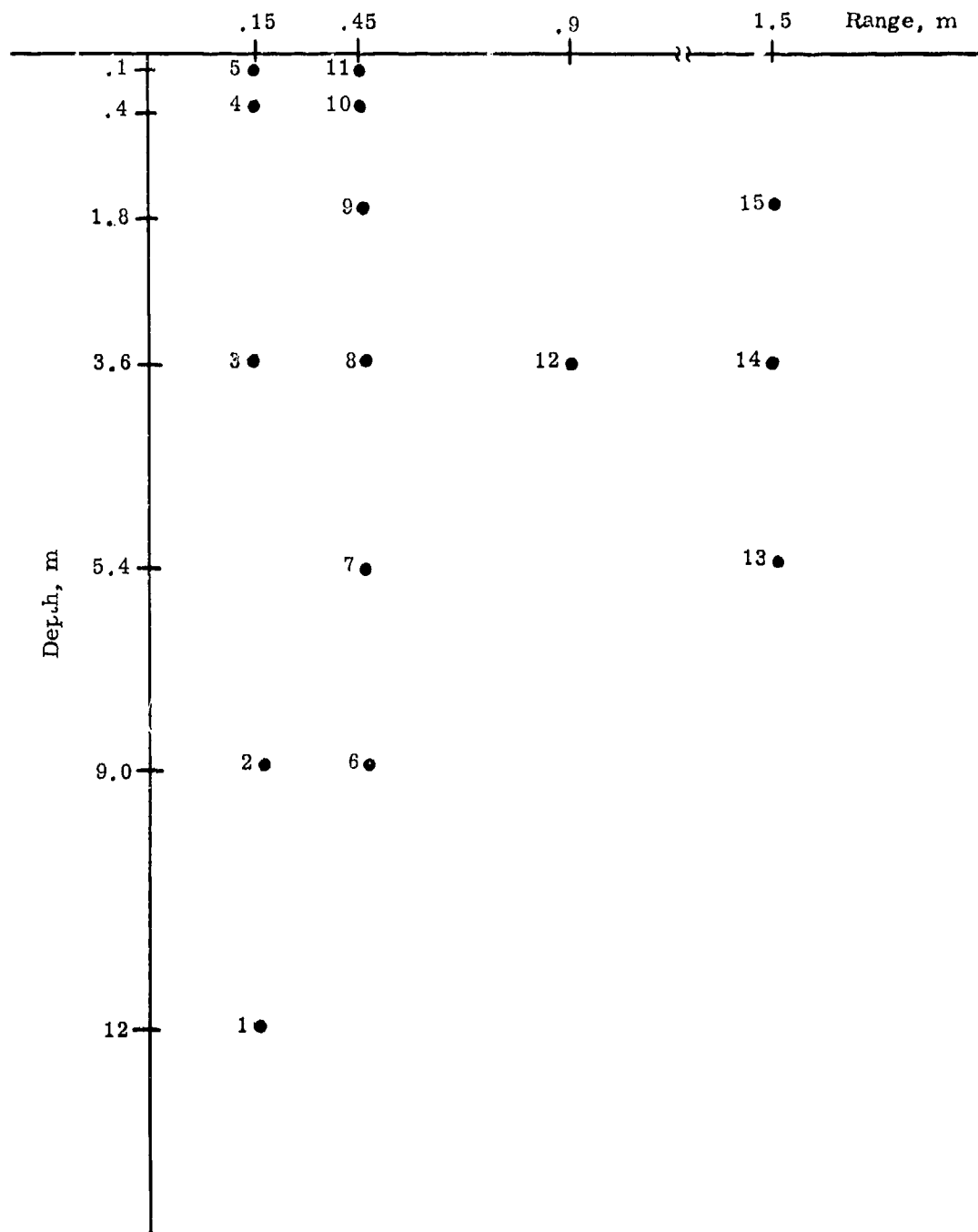
Figure A-10

Legend for Point History Plots from Rigid Projectile Calculation.

103
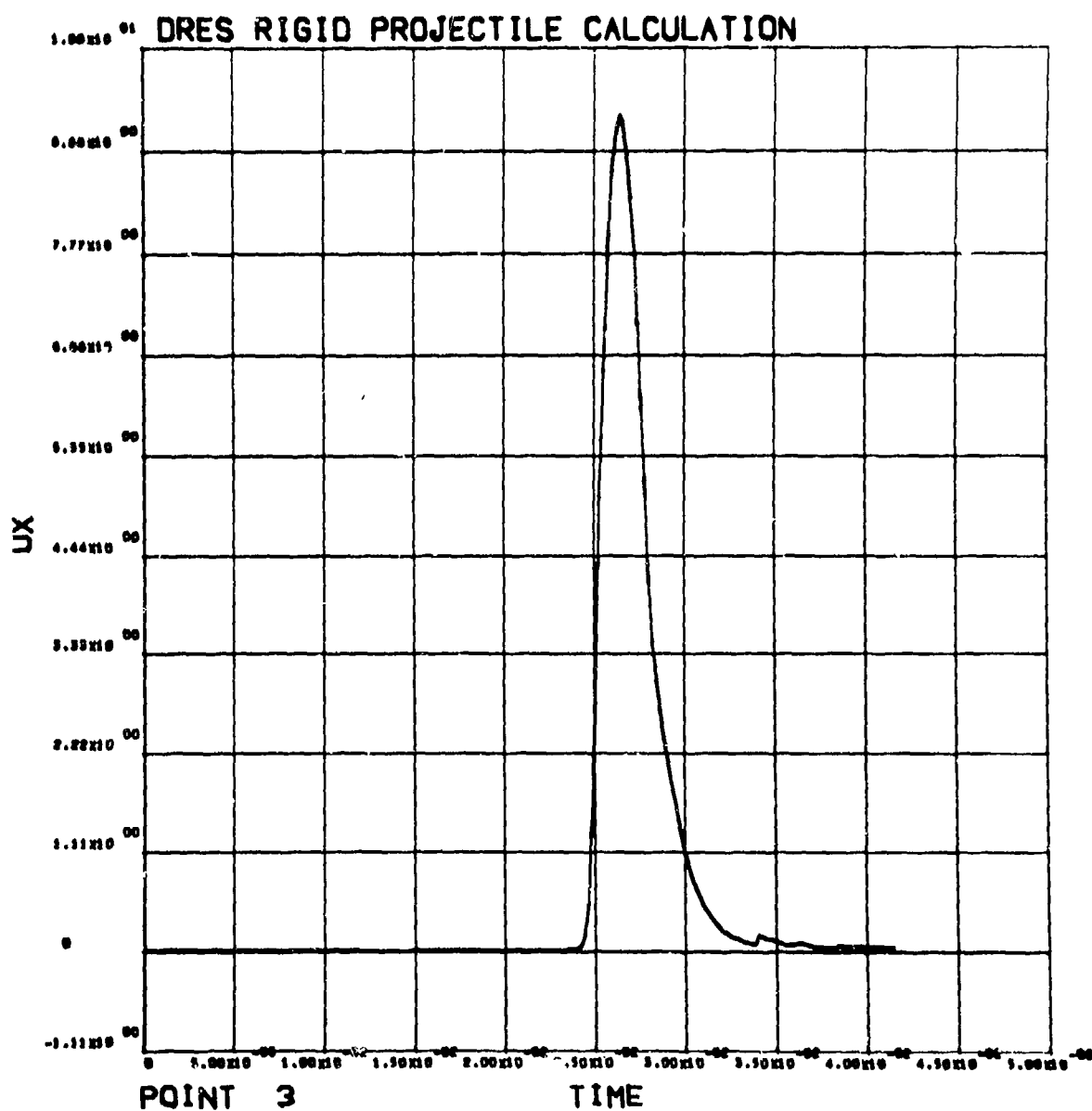
Figure A-11

Radial Velocity (m/s) versus Time (s) for Particle at Point 3,
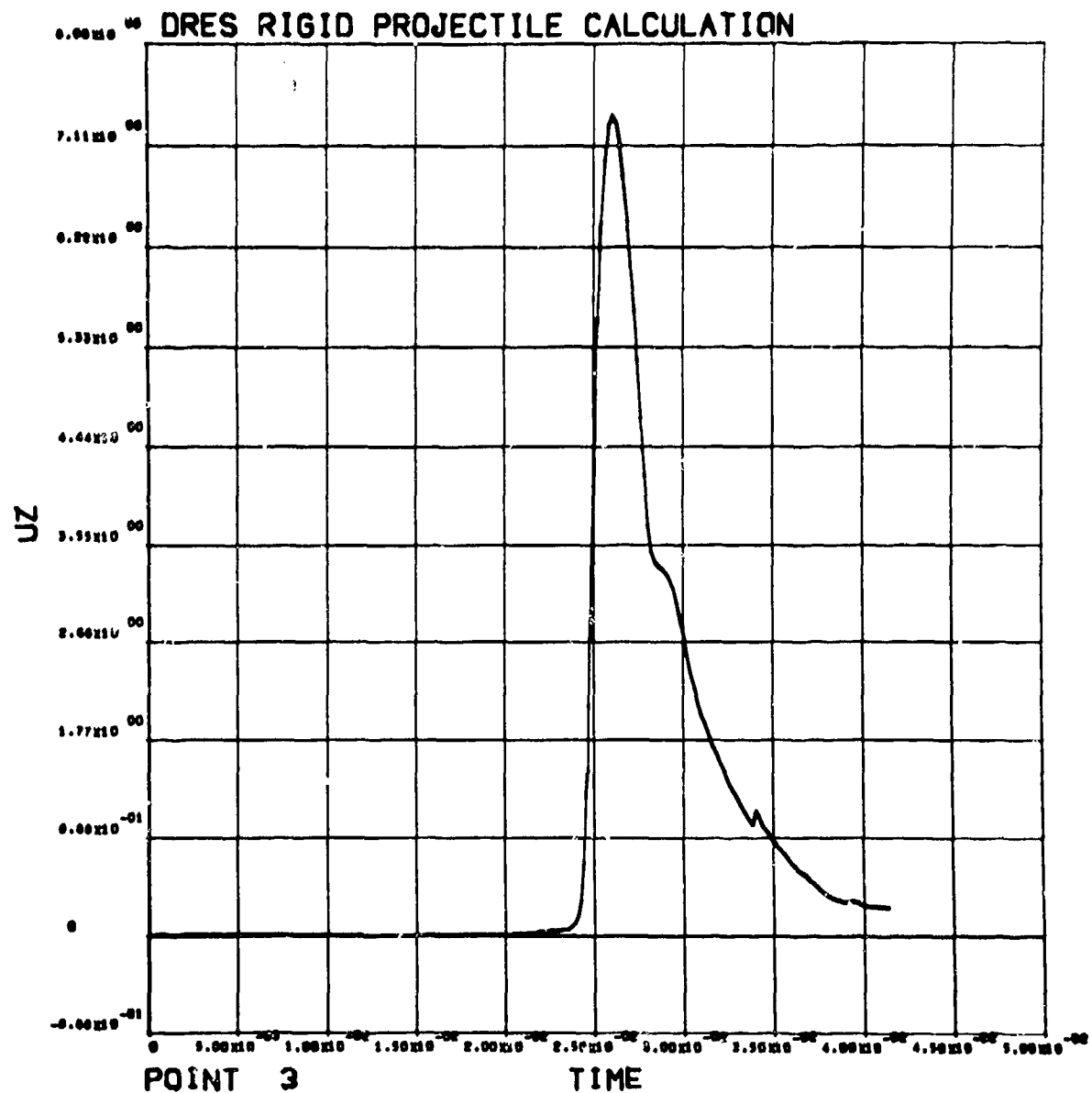
Z = 3.6 m, R = 0.15 m.

Figure A-12

Axial Velocity (m/s) versus Time (s) for Particle at Point 3,
Z = 3.6 m, R = 0.15 m.
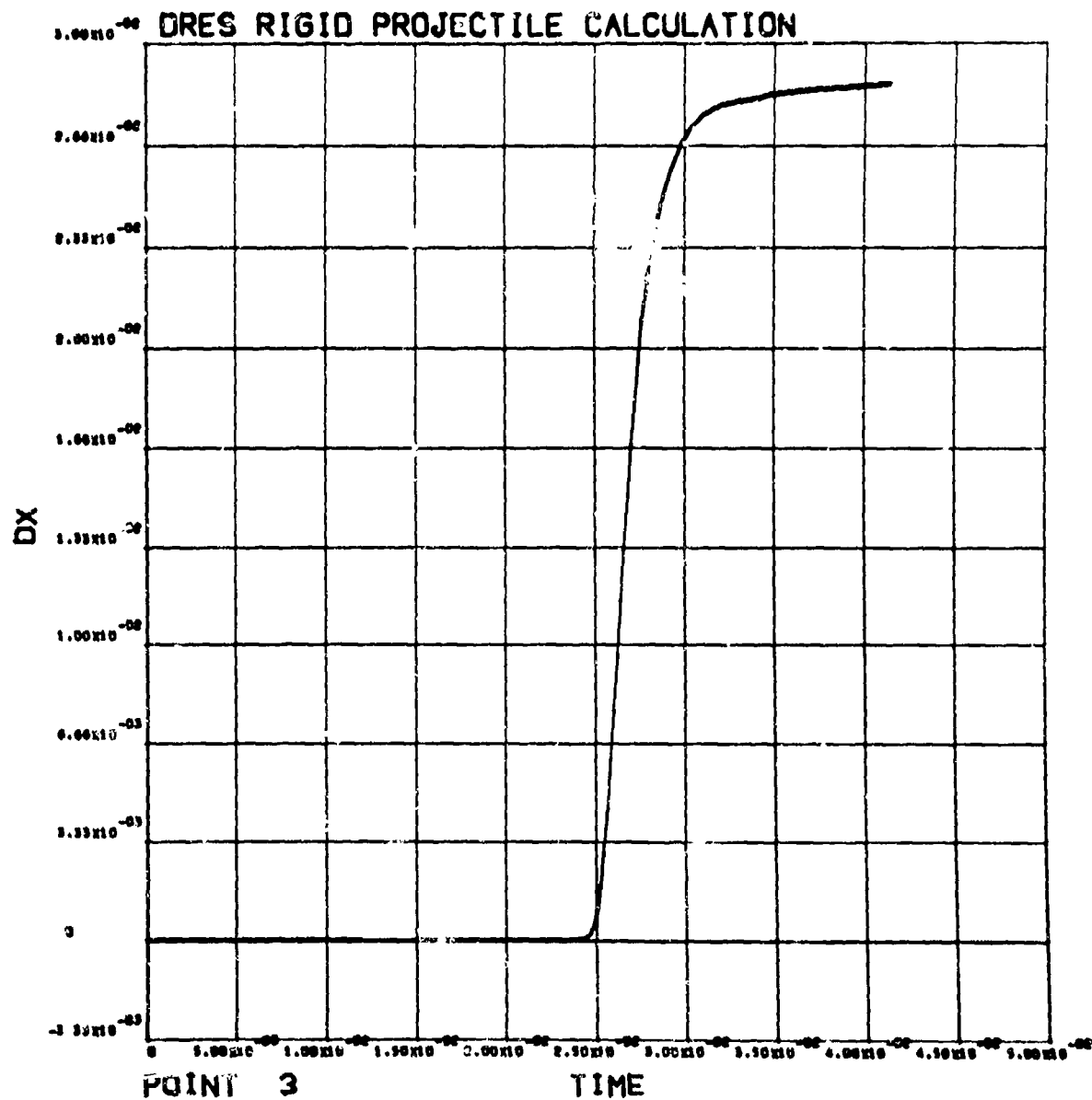
Figure A-13

Radial Displacement (m) versus Time (s) for Particle at Point 3,
Z = 3.6 m, R = 0.15 m.
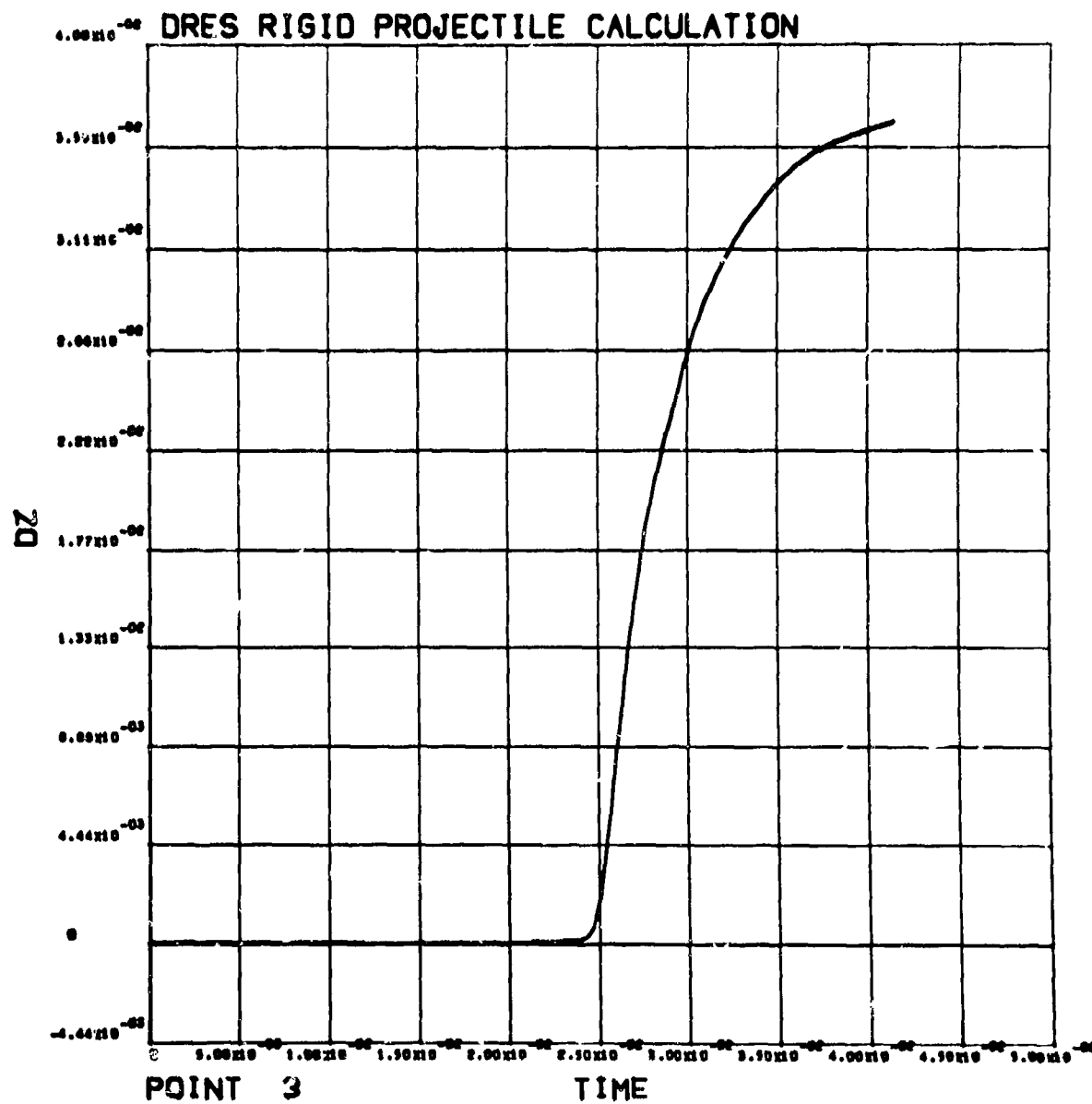
Figure A-14

Axial Displacement (m) versus Time (s) for particle at Point 3,
Z = 3.6 m, R = 0.15 m.
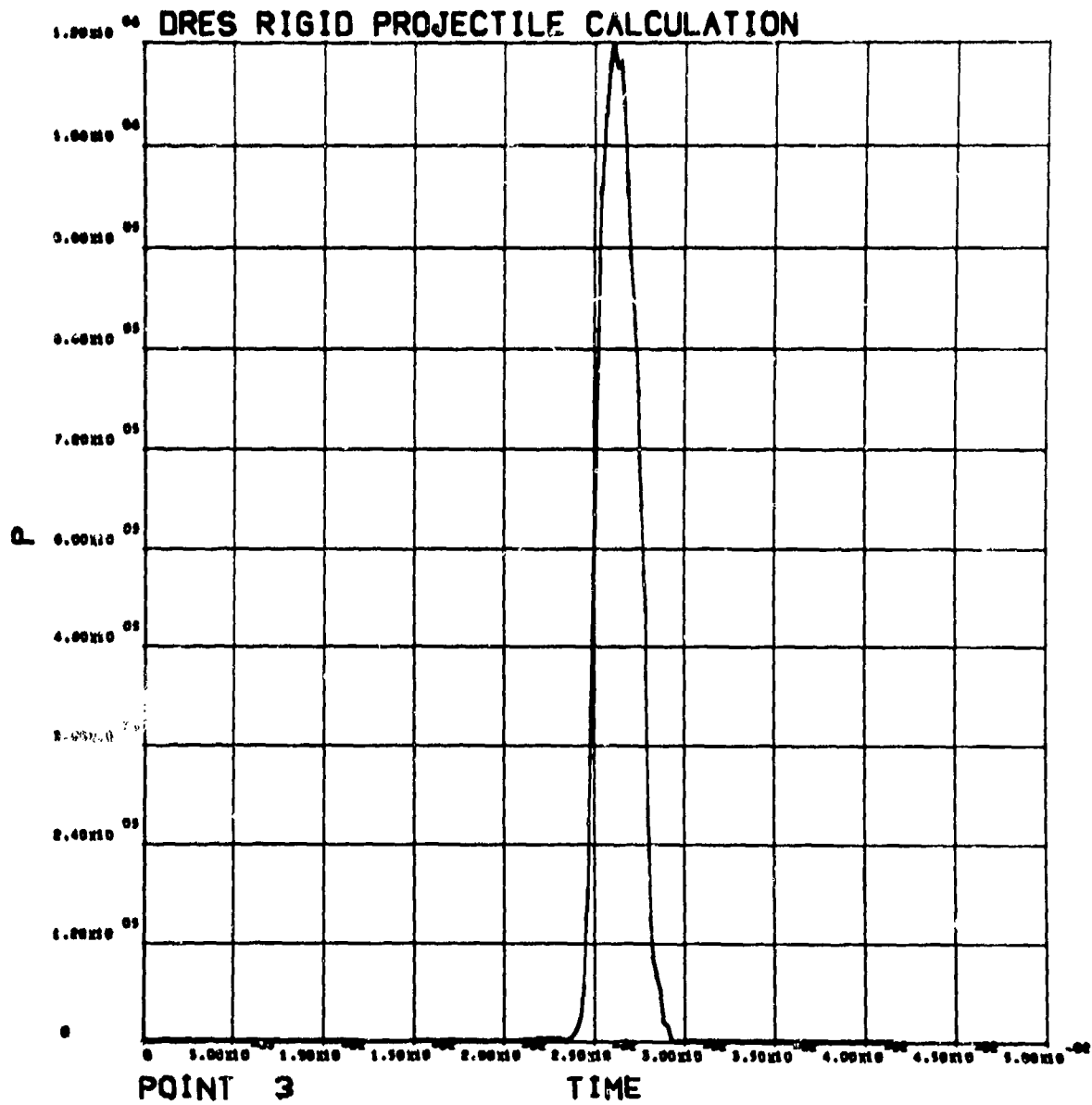
Figure A-15

Pressure (Pa) versus Time (s) for Particle at Point 3, Z = 3.6 m, R = 0.15 m.
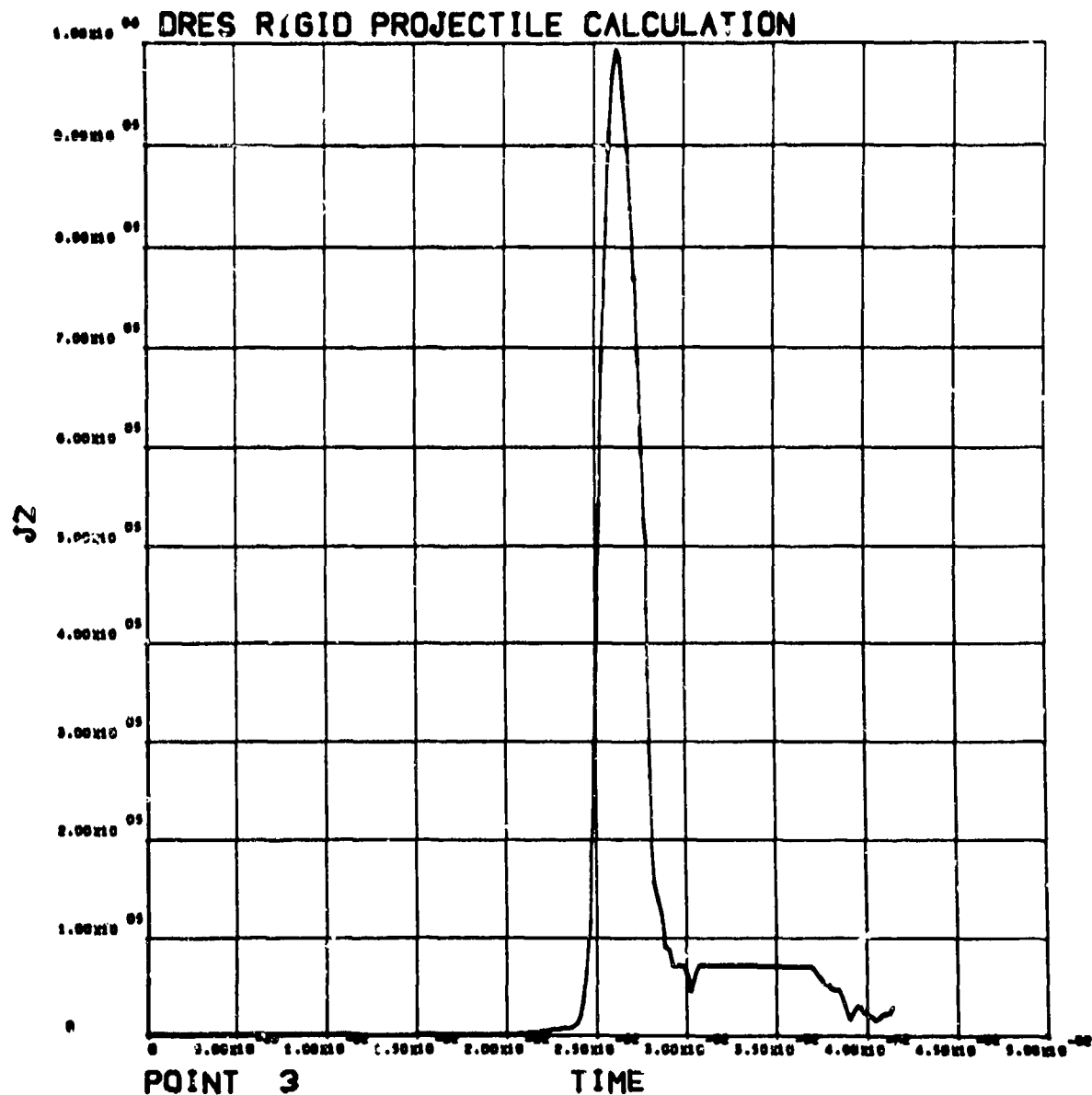
Figure A-16

Deviator Stress J2, History (Pa) for Particle at Point 3, $Z = 3.6$ m, $R = 0.15$ m, (Octahedral Shear Stress $= \sqrt{2/3}(J2)$).

109
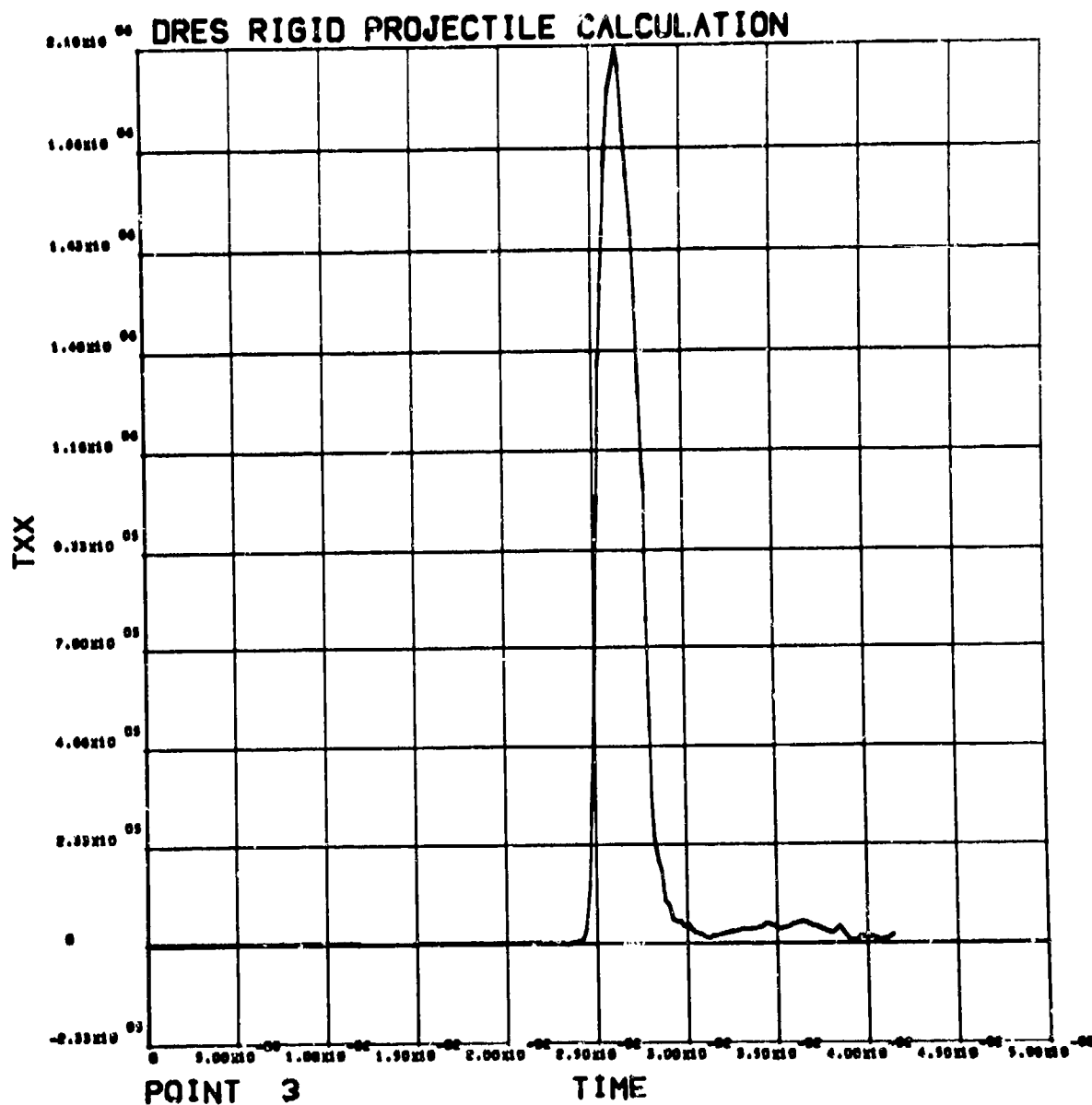
Figure A-17

Radial Stress (Pa) History for Particle at Point 3, Z = 2.6 m, R = 0.15 m.

110
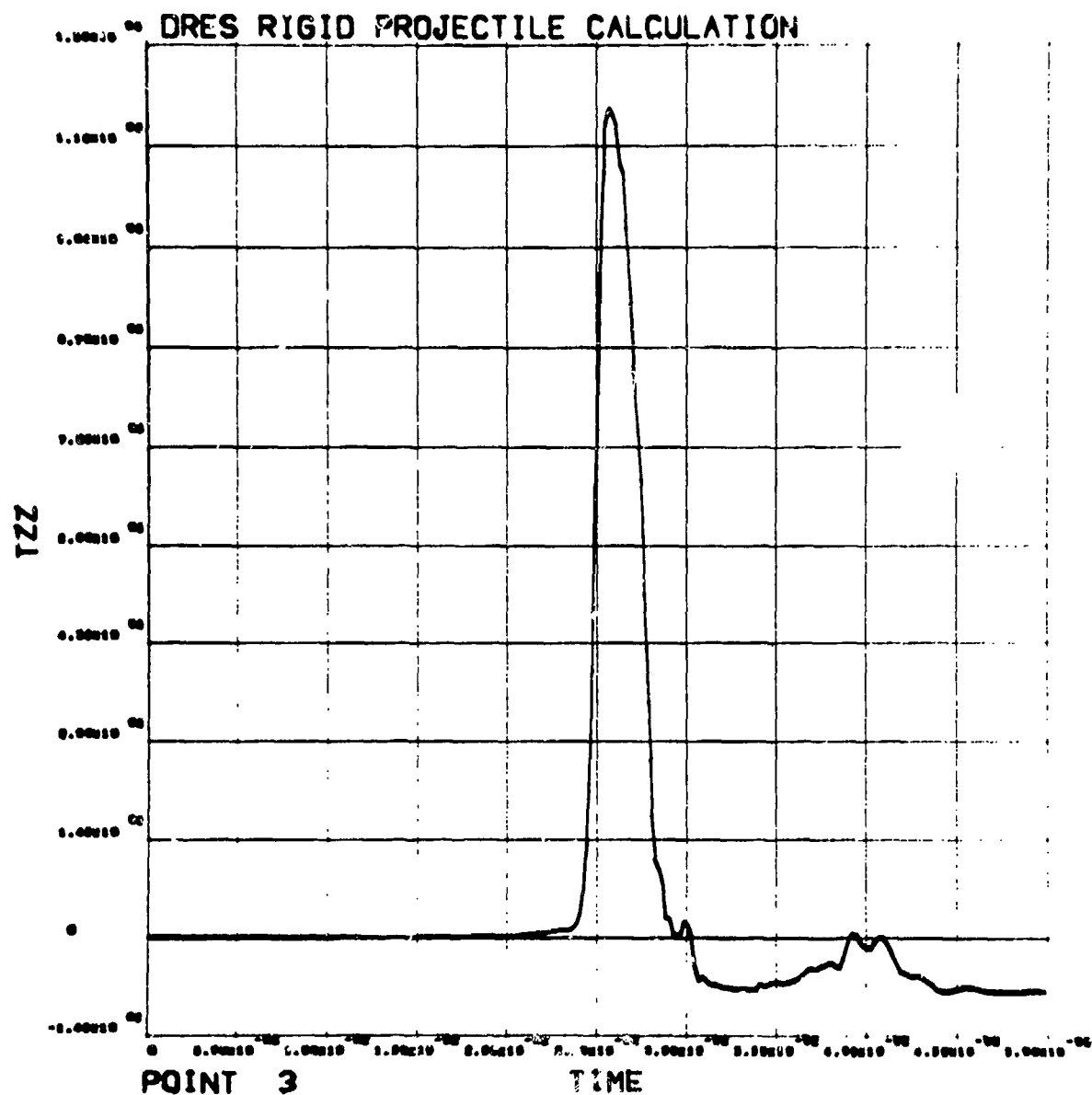
Figure A-18

Axial Stress (Pa) History for Particle at Point 3, Z = 3.6 m, R = 0.15 m.

111

DRES RIGID PROJECTILE CALCULATION

POINT 4   TIME
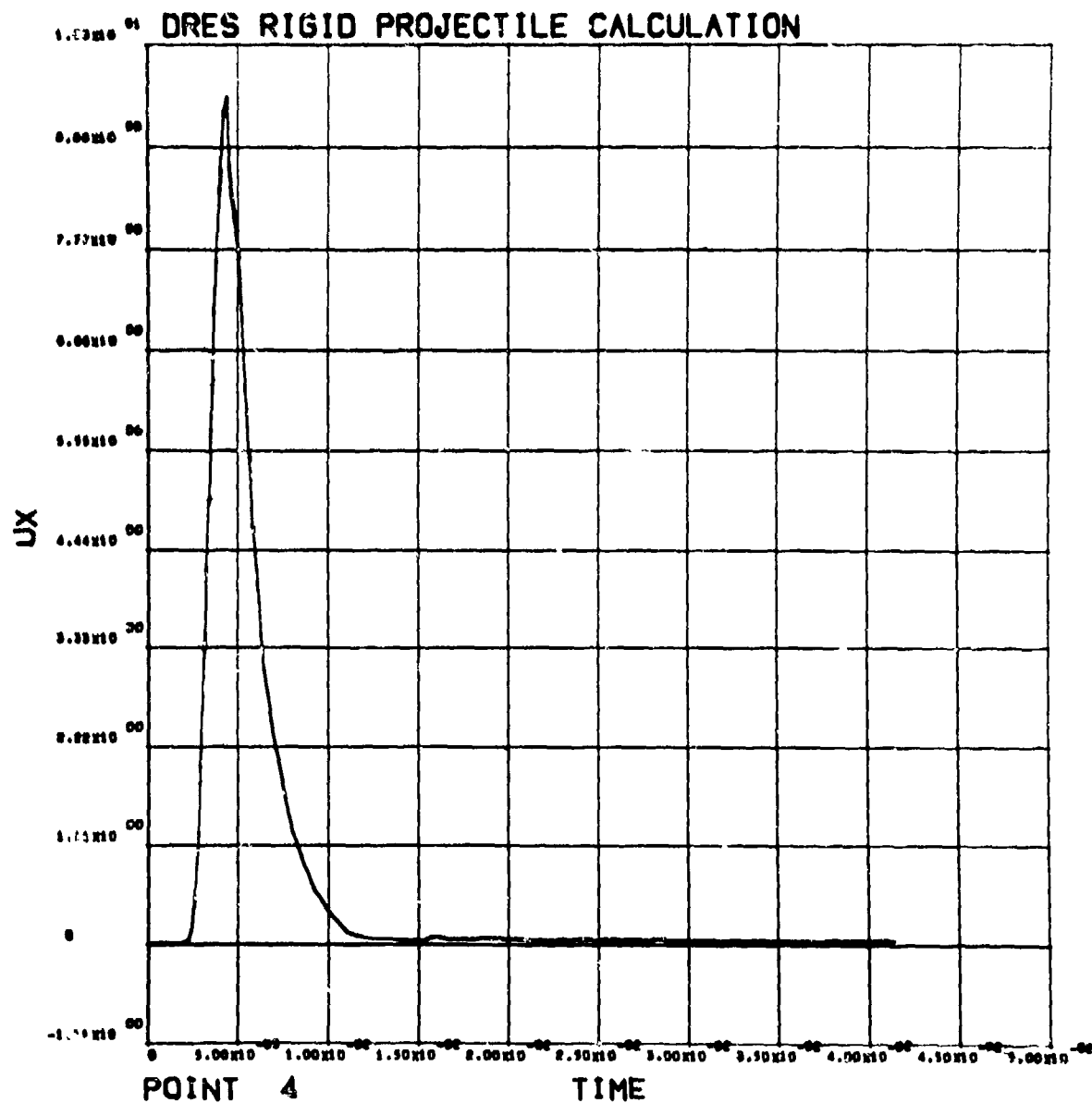
Figure A-19

Radial Velocity (m/s) versus Time (s) for Particle at Point 4,
Z = 0.4 m, R = 0.15 m.

112
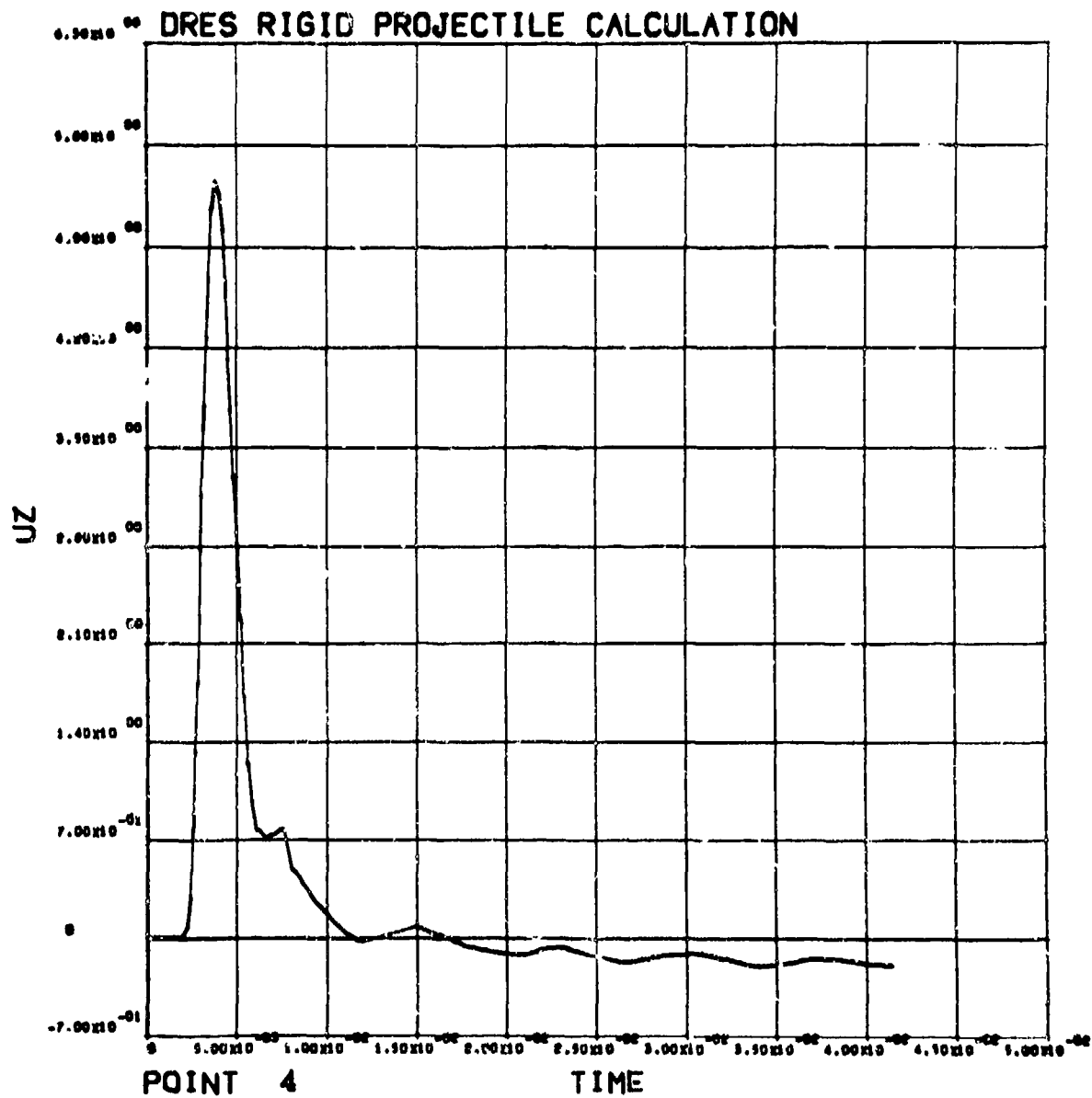
Figure A-20

Axial Velocity (m/s) versus Time (s) for Particle at Point 4,
Z = 0.4 m, R = 0.15 m.

113
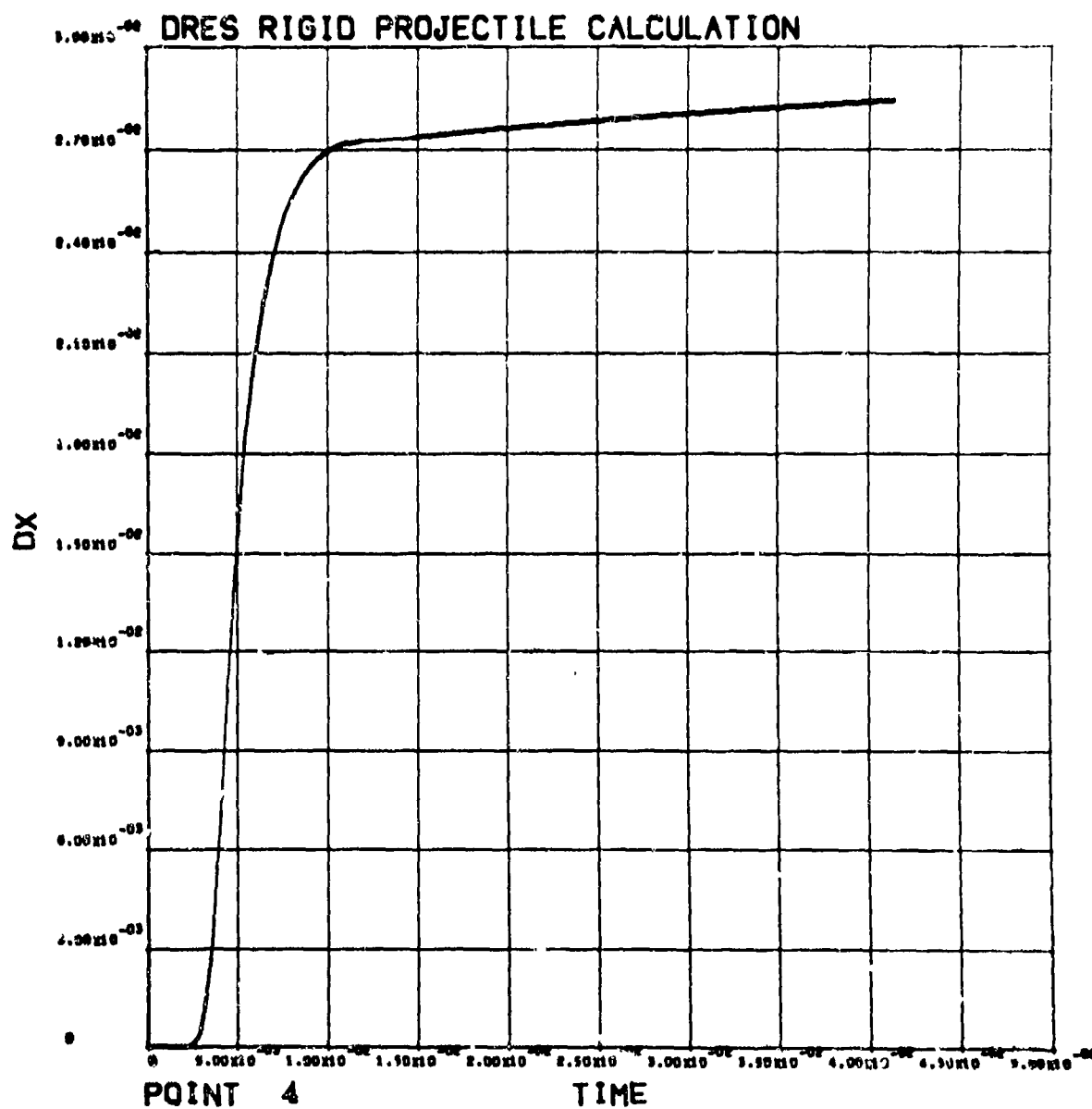
Figure A-21

Radial Displacement (m) versus Time (s) for Particle at Point 4,
Z = 0.4 m, R = 0.15 m.

114

DRES RIGID PROJECTILE CALCULATION
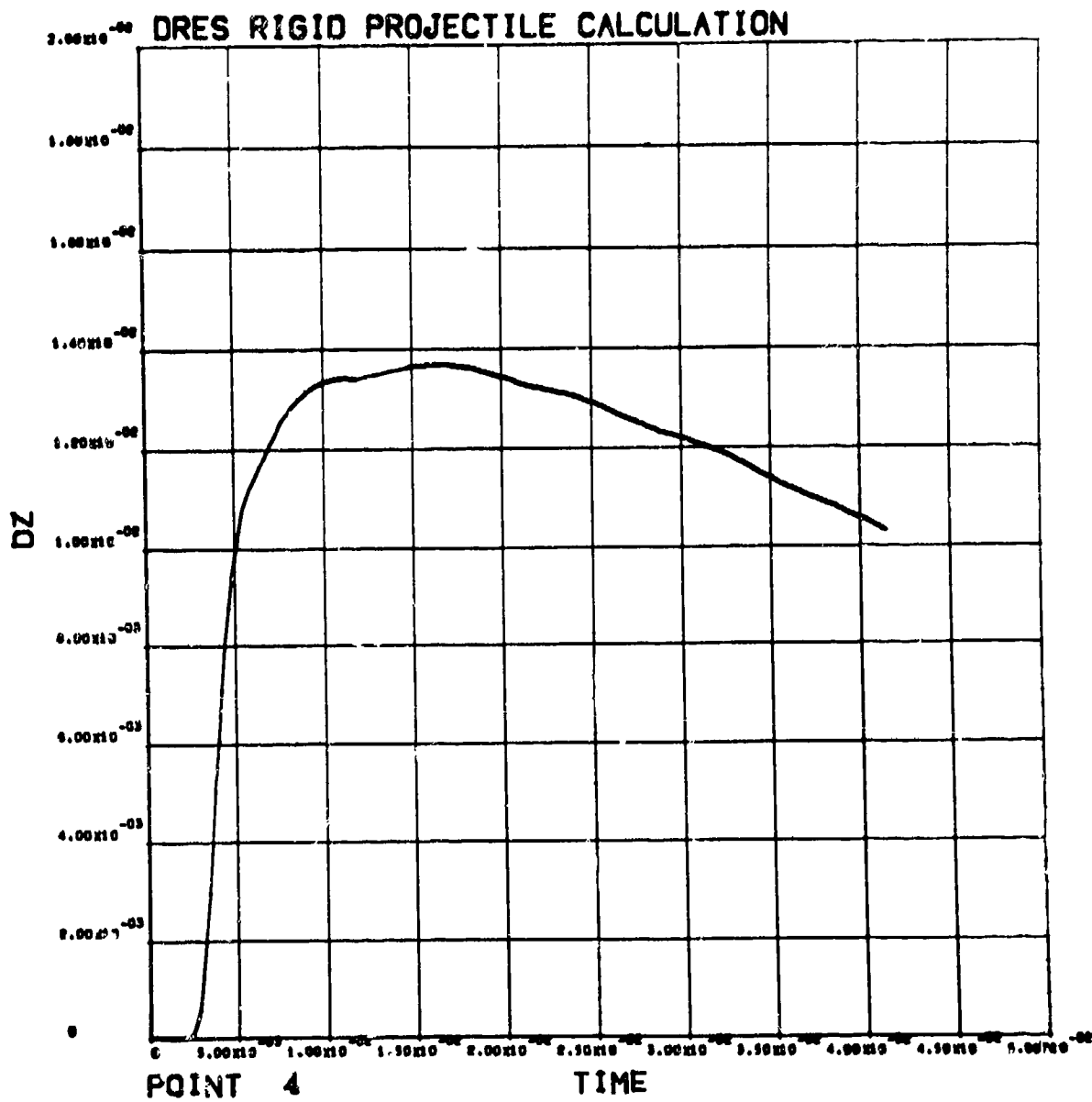
Figure A-22

Axial Displacement (m) versus Time (s) for Particle at Point 4,
Z = 0.4 m, R = 0.15 m.

115
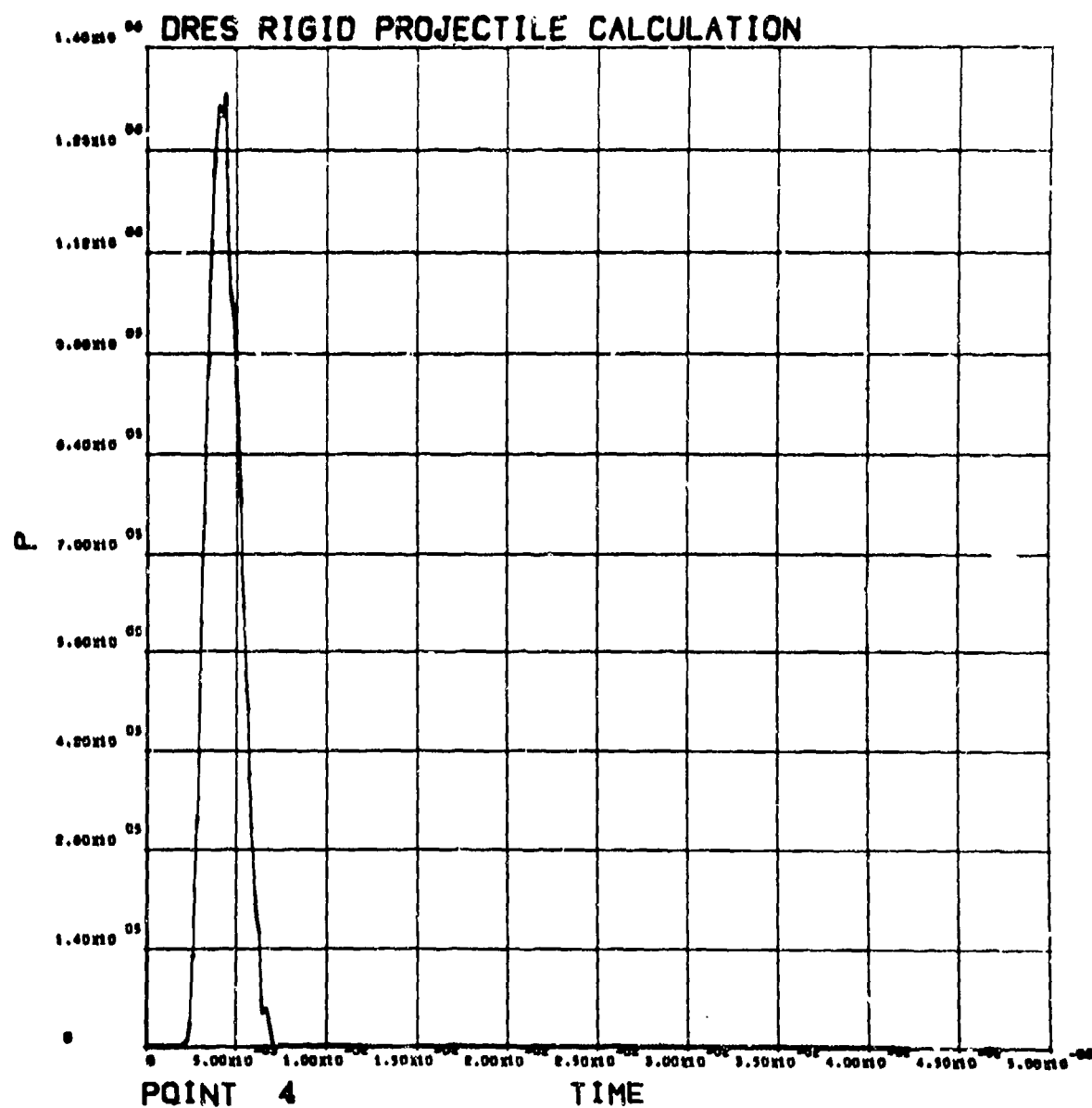
Figure A-23

Pressure (Pa) versus Time (s) for Particle at Point 4, $Z = 0.4$ m, $R = 0.15$ m.
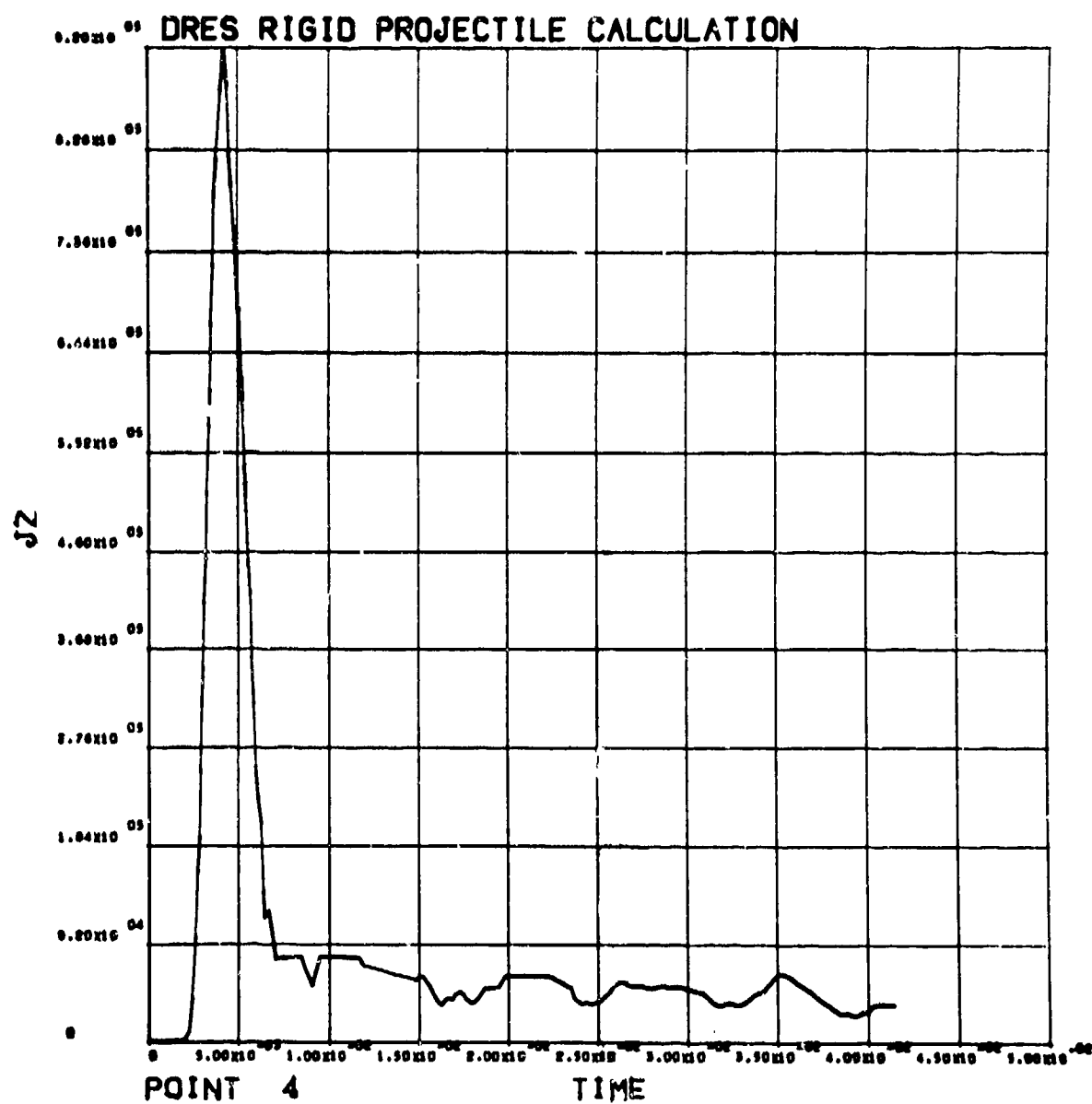
Figure A-24

Deviator Stress J2, History (Pa) for Particle at Point 4, Z = 0.4 m, R = 0.15 m,
(Octahedral Shear Stress = $\sqrt{2/3}(J2)$).
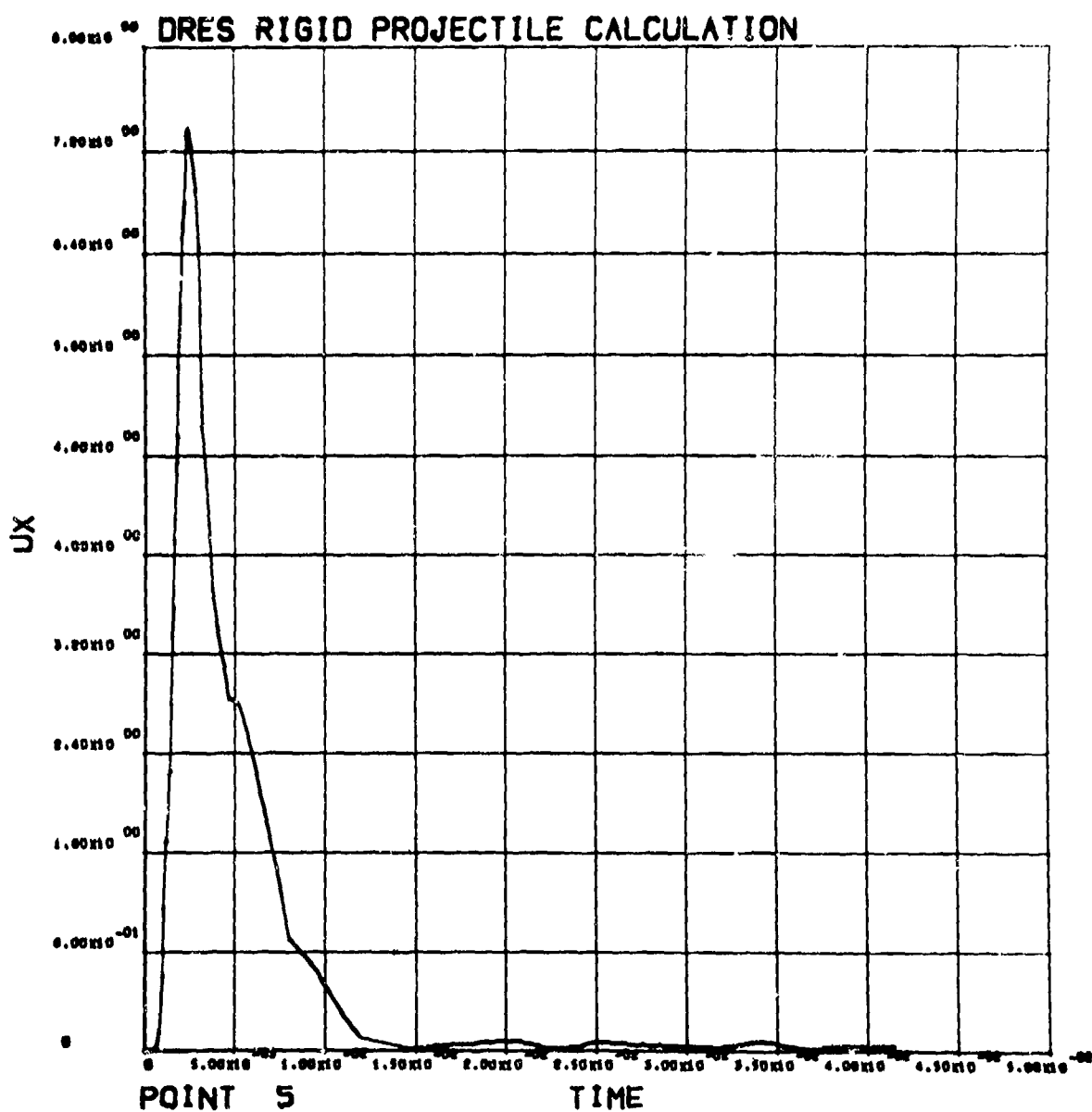
Figure A-25

Radial Velocity (m/s) versus Time (s) for Particle at Point 5, Z = 0.1 m, R = 0.15 m.
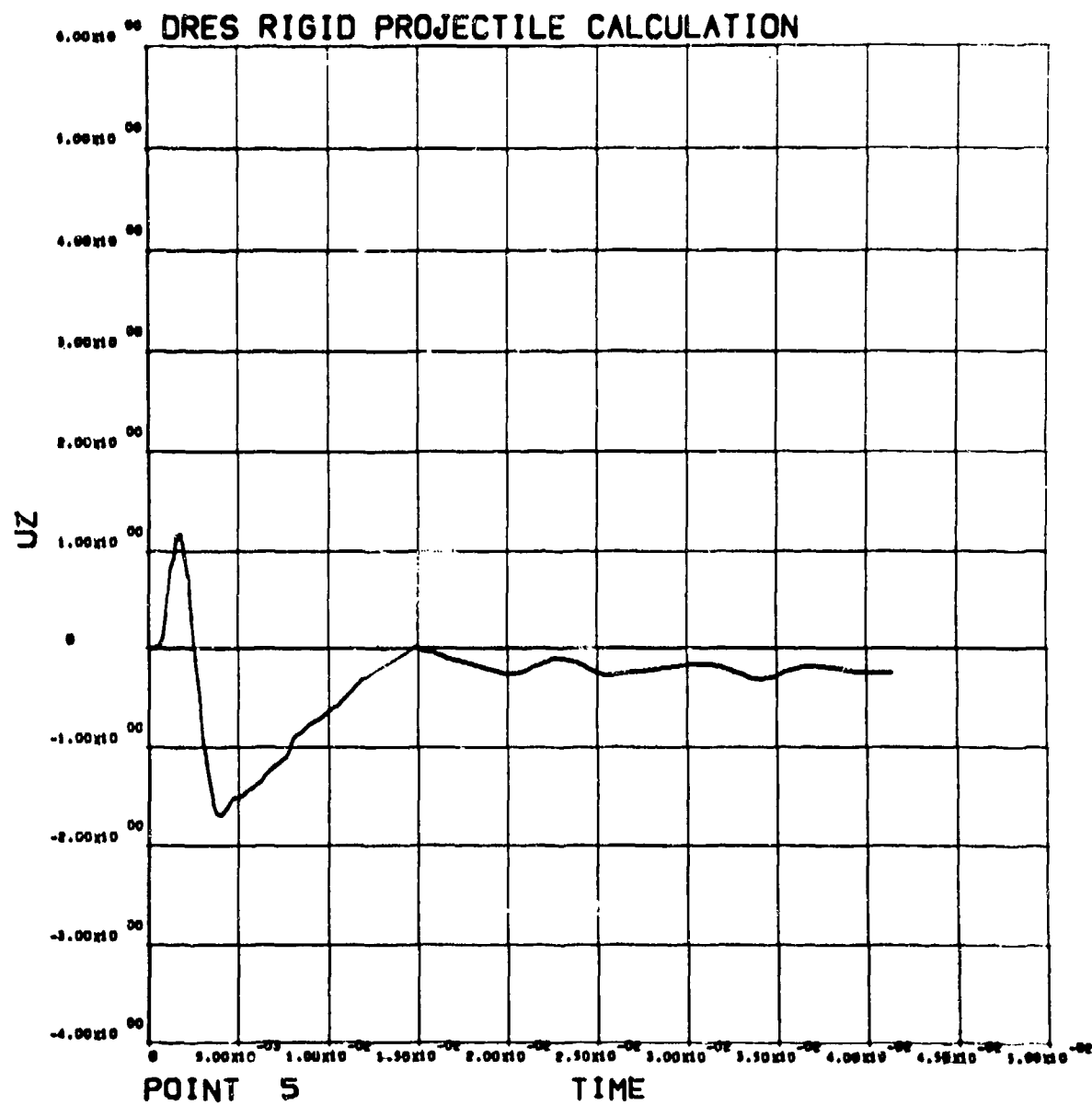
Figure A-26

Axial Velocity (m/s) versus Time (s) for Particle at Point 5, Z = 0.1 m, R = 0.15 m.
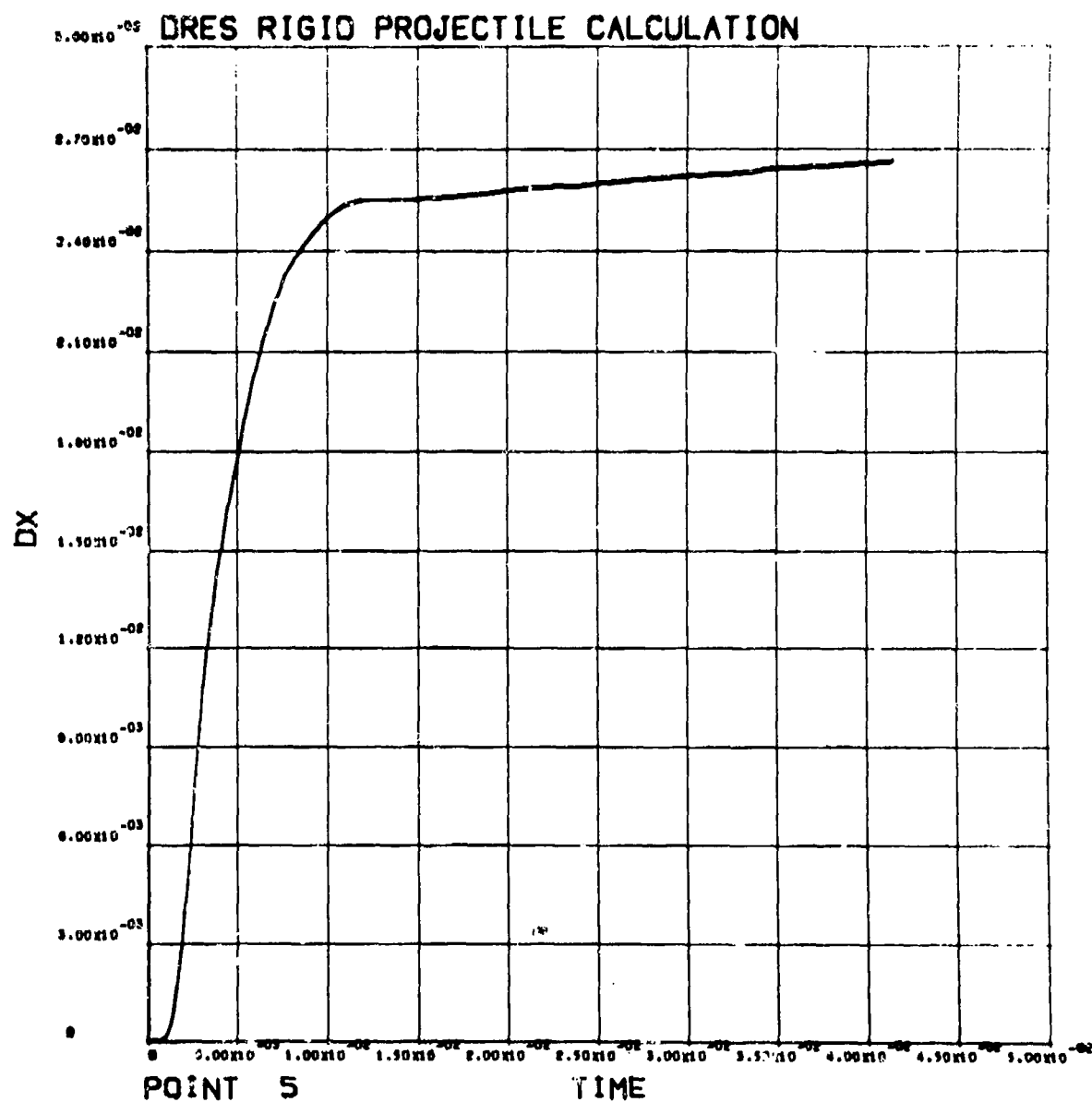
Figure A-27

Radial Displacement (m) versus Time (s) for Particle at Point 5, Z = 0.1 m. R = 0.15 m.

120
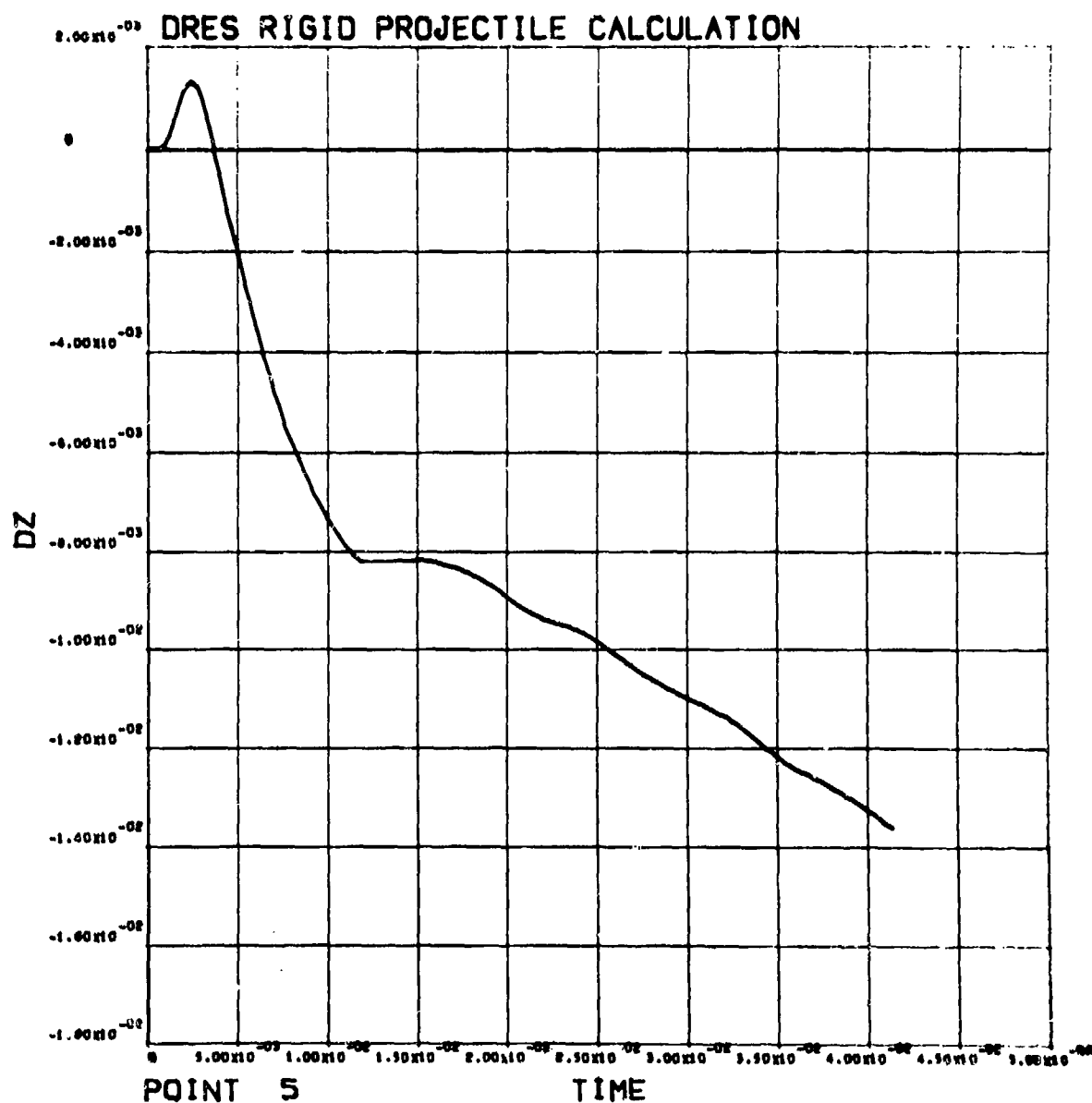
Figure A-28

Axial Displacement (m) versus Time (s) for Particle at Point 5, $Z = 0.1$ m, $R = 0.15$ m.

121

DRES RIGID PROJECTILE CALCULATION
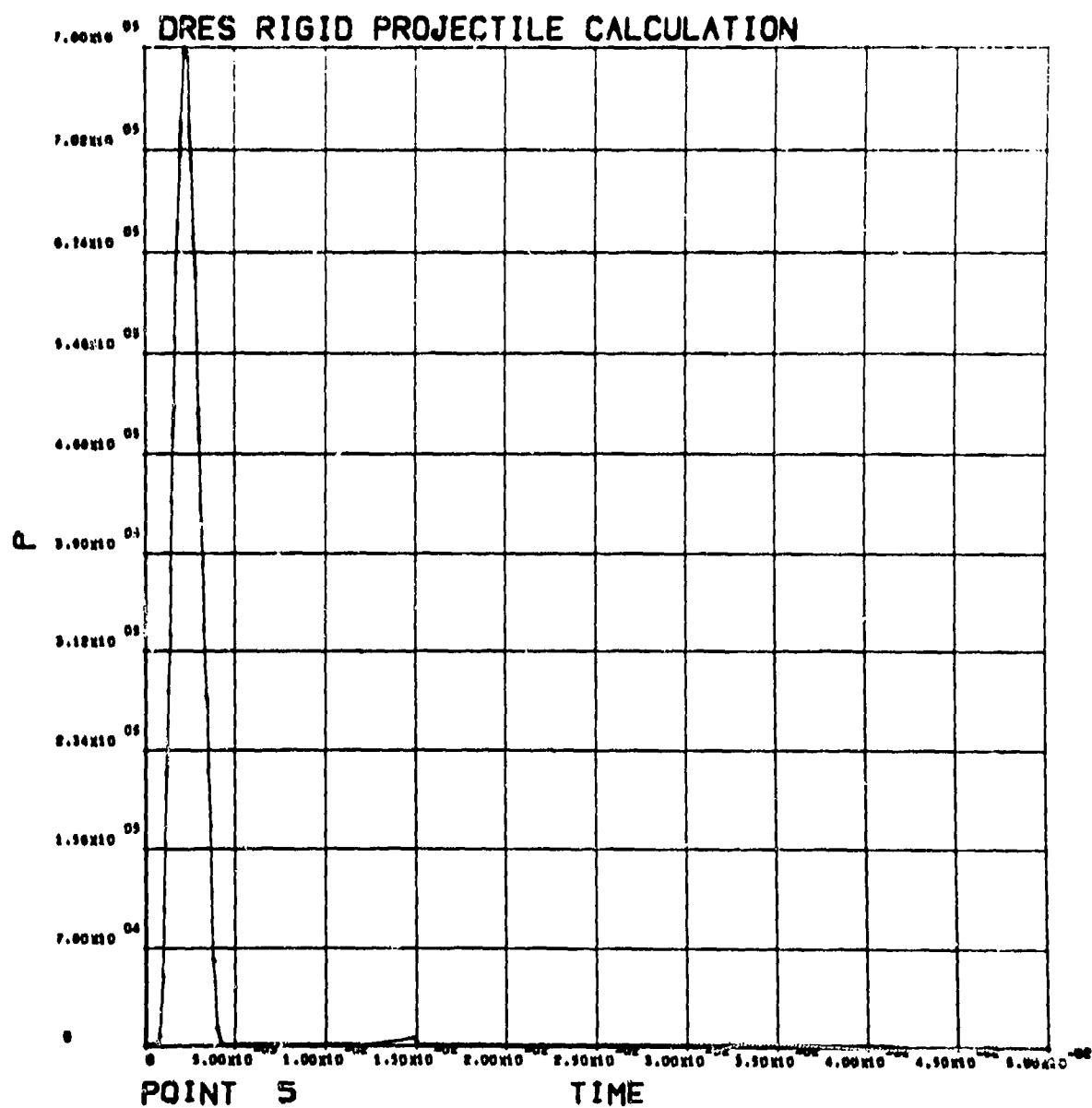
Figure A-29

Pressure (Pa) versus Time (s) for Particle at Point 5, Z = 0.1 m, R = 0.15 m.
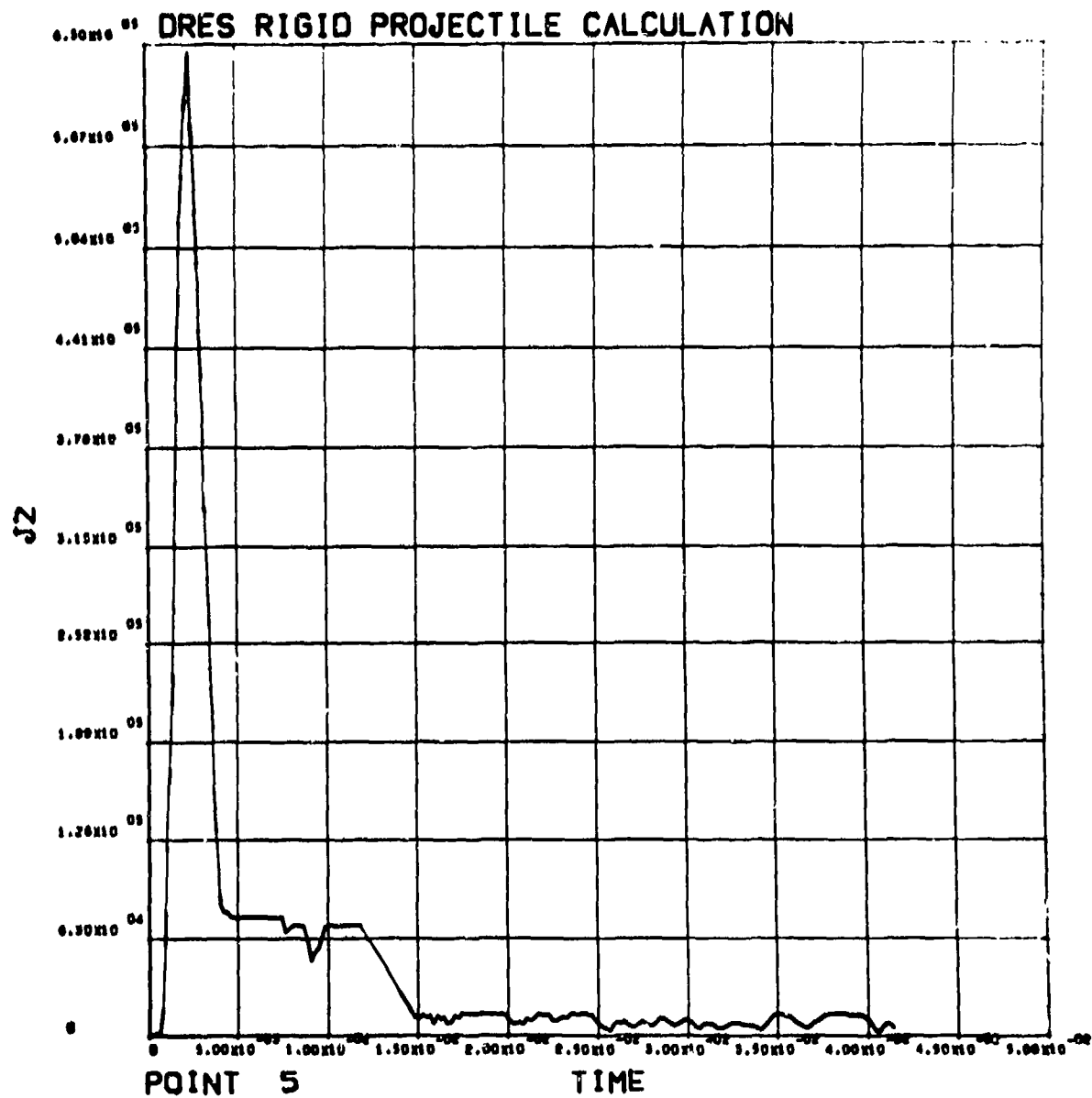
Figure A-30

Deviator Stress J2, History (Pa) for Particle at Point 5, Z = 0.1 m, R = 0.15 m,
(Octanedral Shear Stress = $\sqrt{2/3}(J2)$).
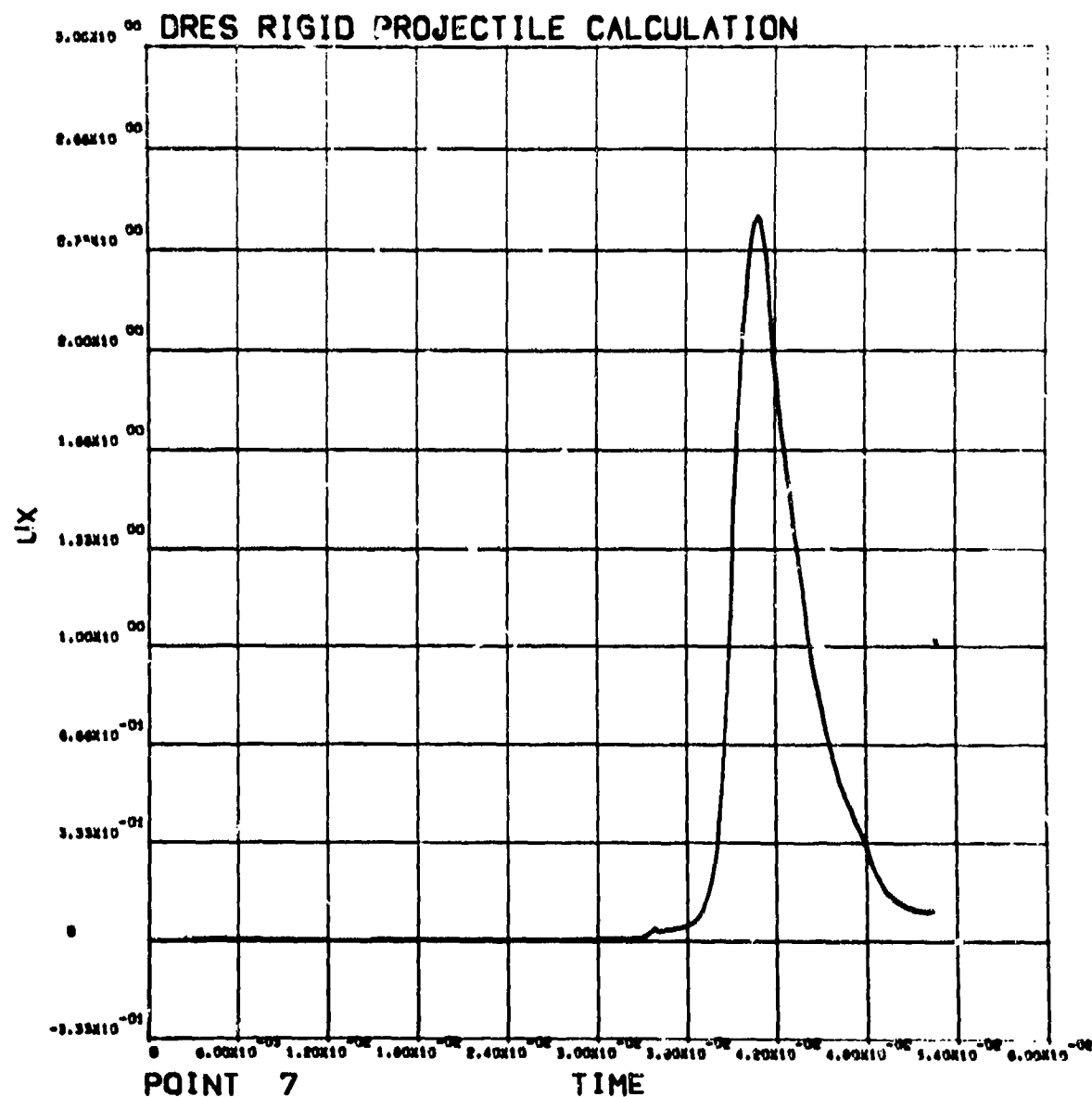
Figure A-31

Radial Velocity (m/s) versus Time (s) for Particle at Point 7, Z = 5.4 m, R = 0.45 m.

124

DRES RIGID PROJECTILE CALCULATION
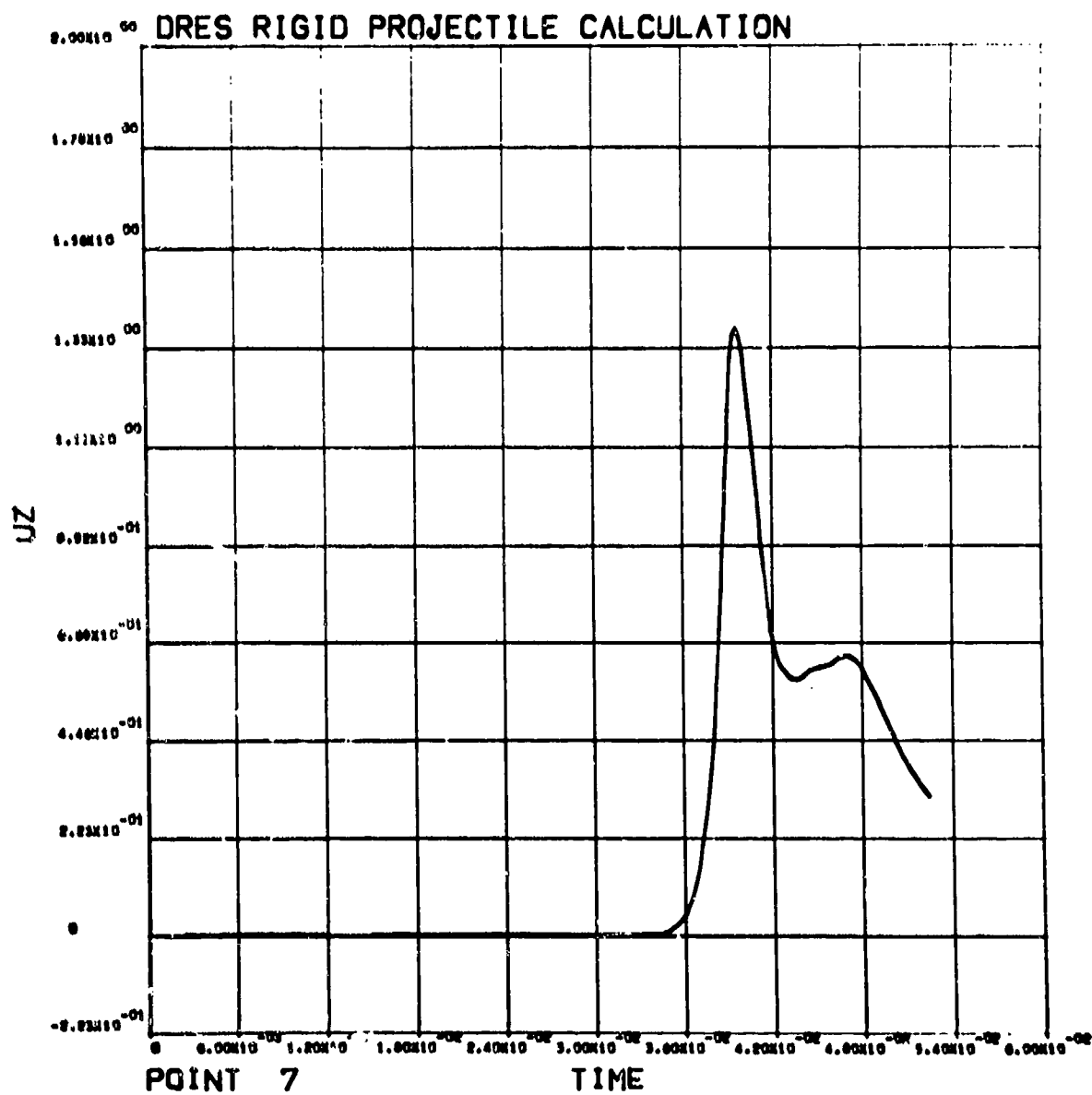
Figure A-32

Axial Velocity (m/s) versus Time (s) for Particle at Point 7, Z = 5.4 m, R = 0.45 m.

125
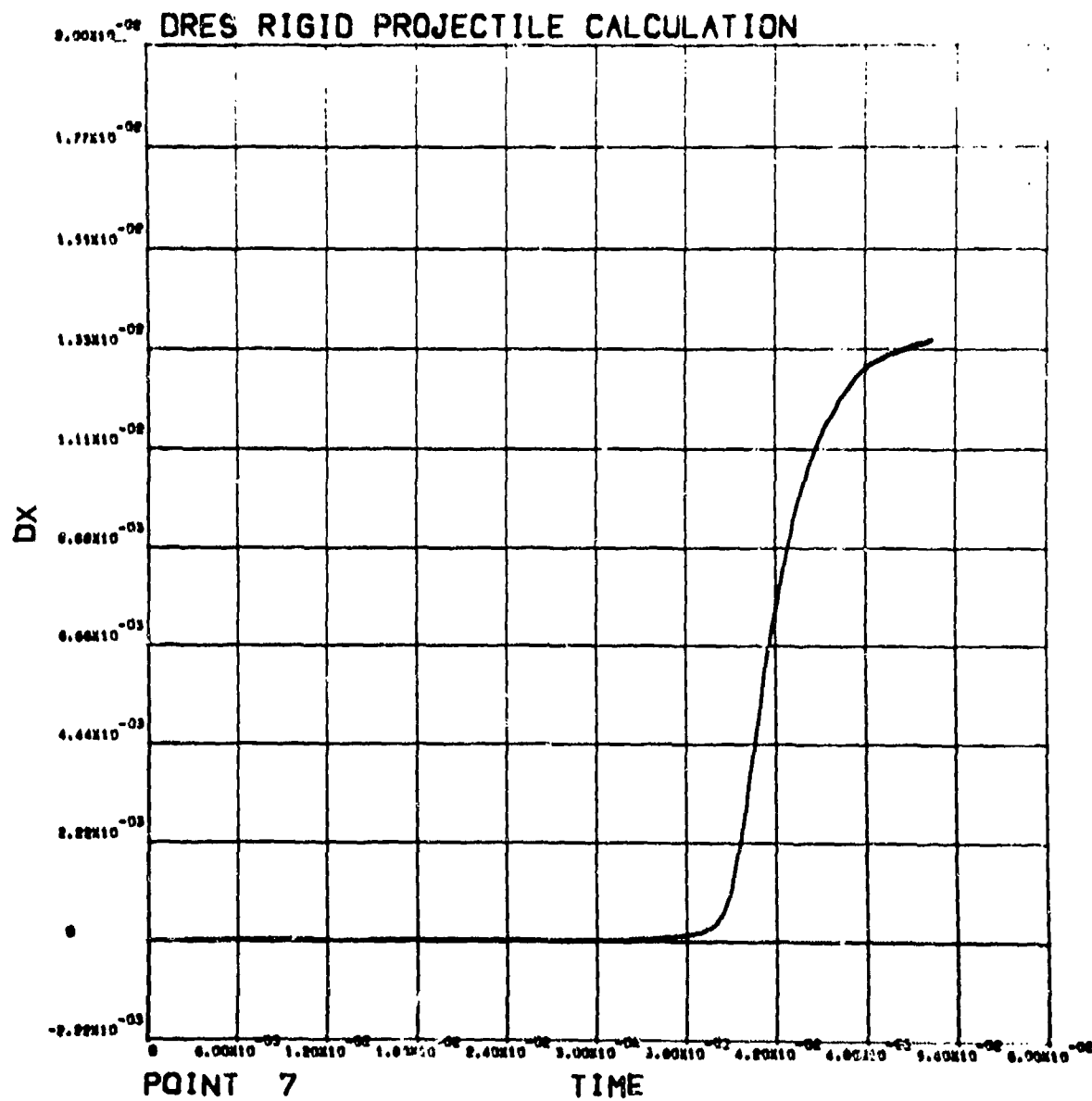
Figure A-33

Radial Displacement (m) versus Time (s) for Particle at Point 7, z = 5.4 m, R = 0.45 m.

126
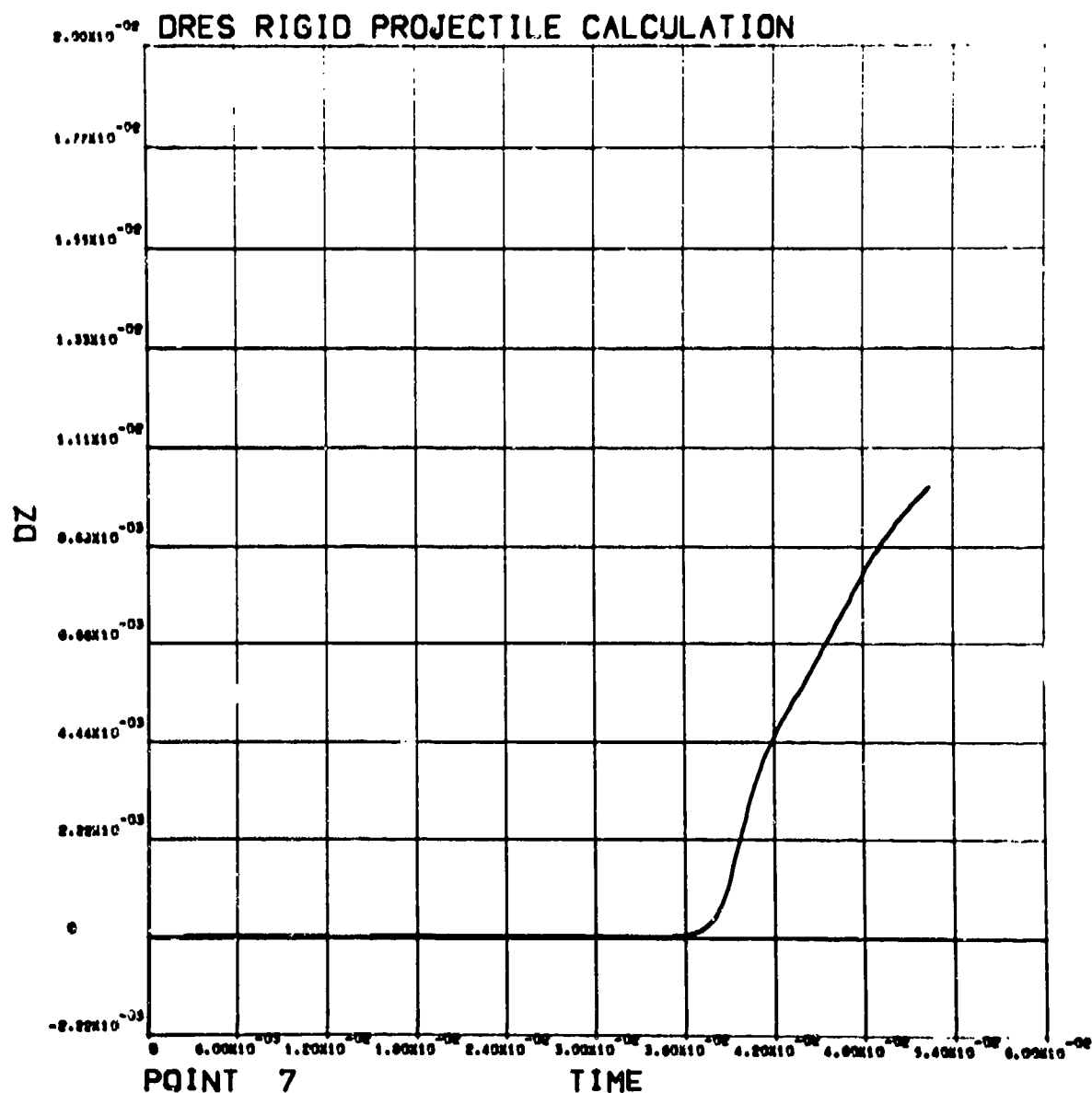
Figure A-34

Axial Displacement (m) versus Time (s) for Particle at Point 7, Z = 5.4 m, R = 0.45 m.

127
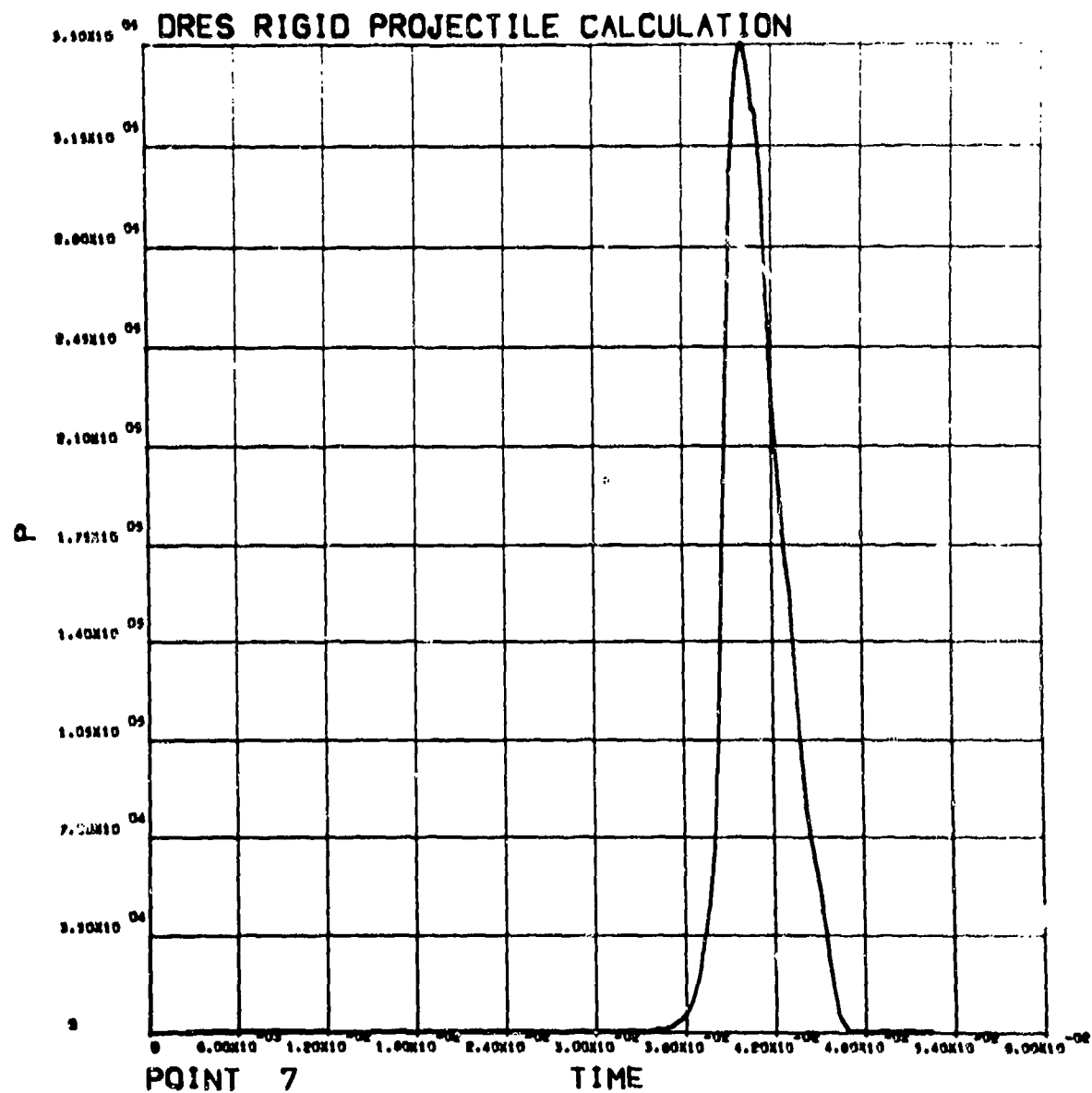
Figure A-35

Pressure (Pa) versus Time (s) for Particle at Point 7, Z = 5.4 m, R = 0.45 m.

128
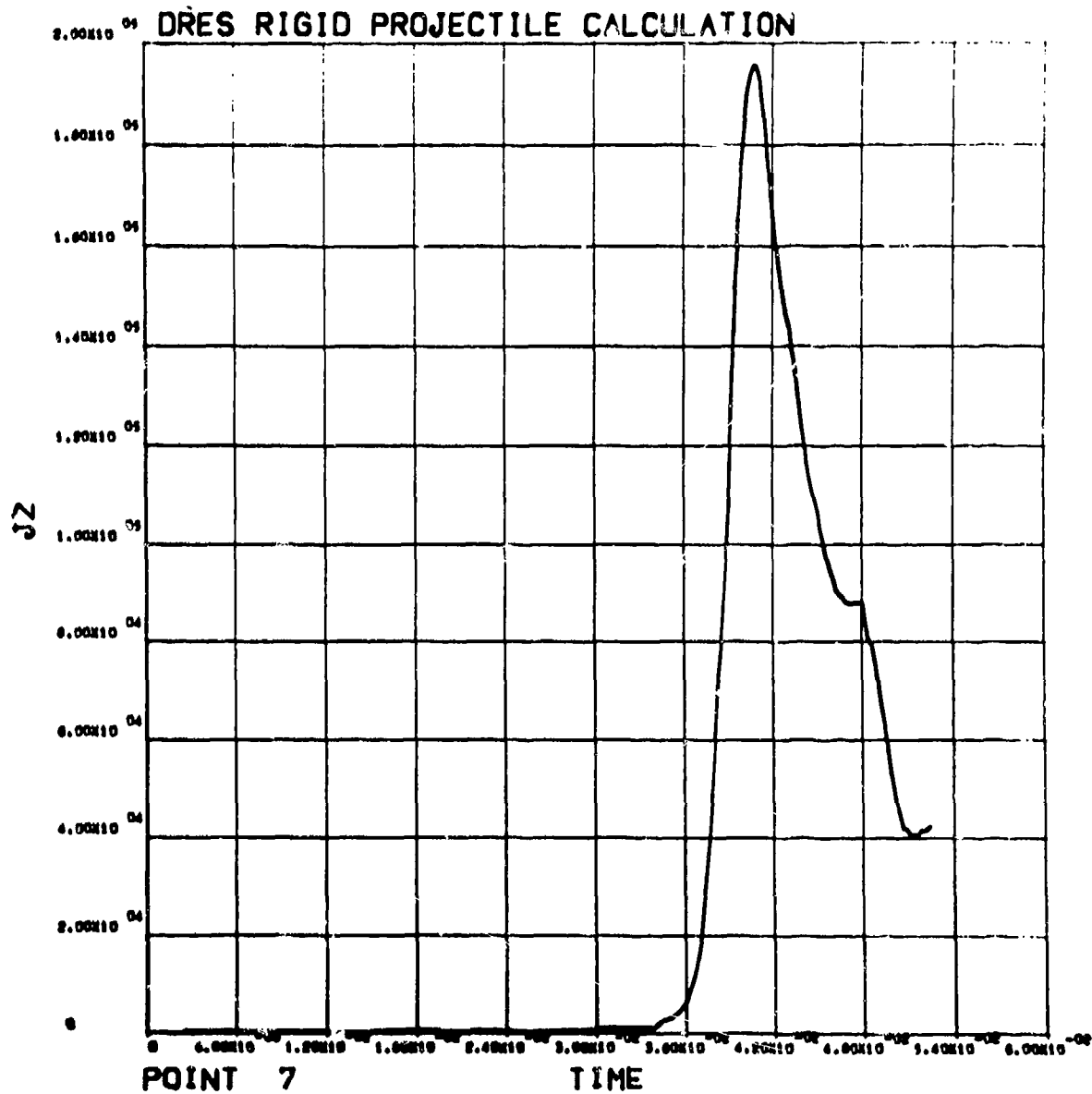
Figure A-36

Deviator Stress, J2, History (Pa) for Particle at Point 7, Z = 5.4 m, R = 0.45 m (Octahedral Shear Stress = $\sqrt{2/3}(J2)$).
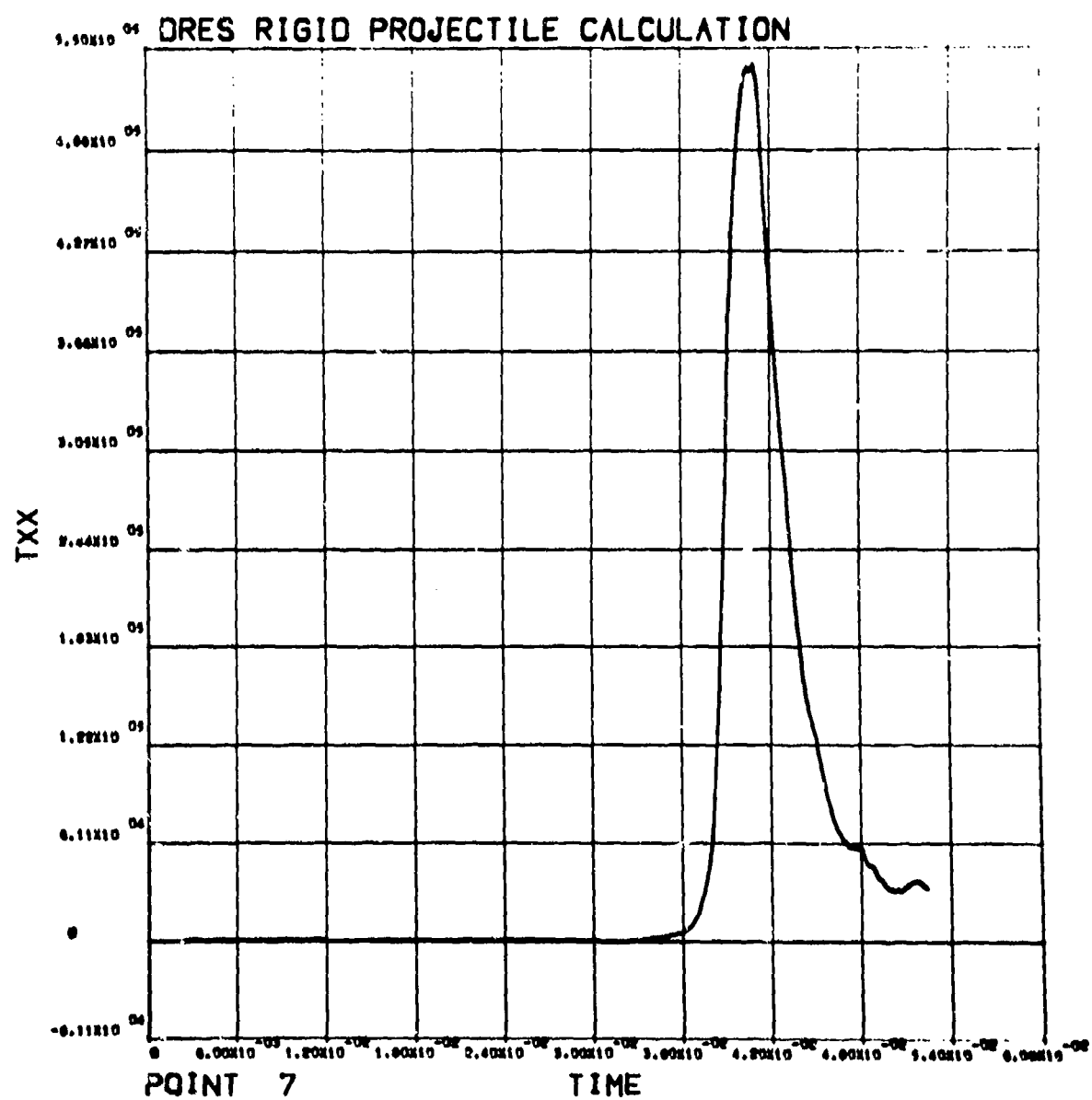
Figure A-37

Radial Stress (Pa) History for Particle at Point 7, Z = 5.4 m, R = 0.45 m.
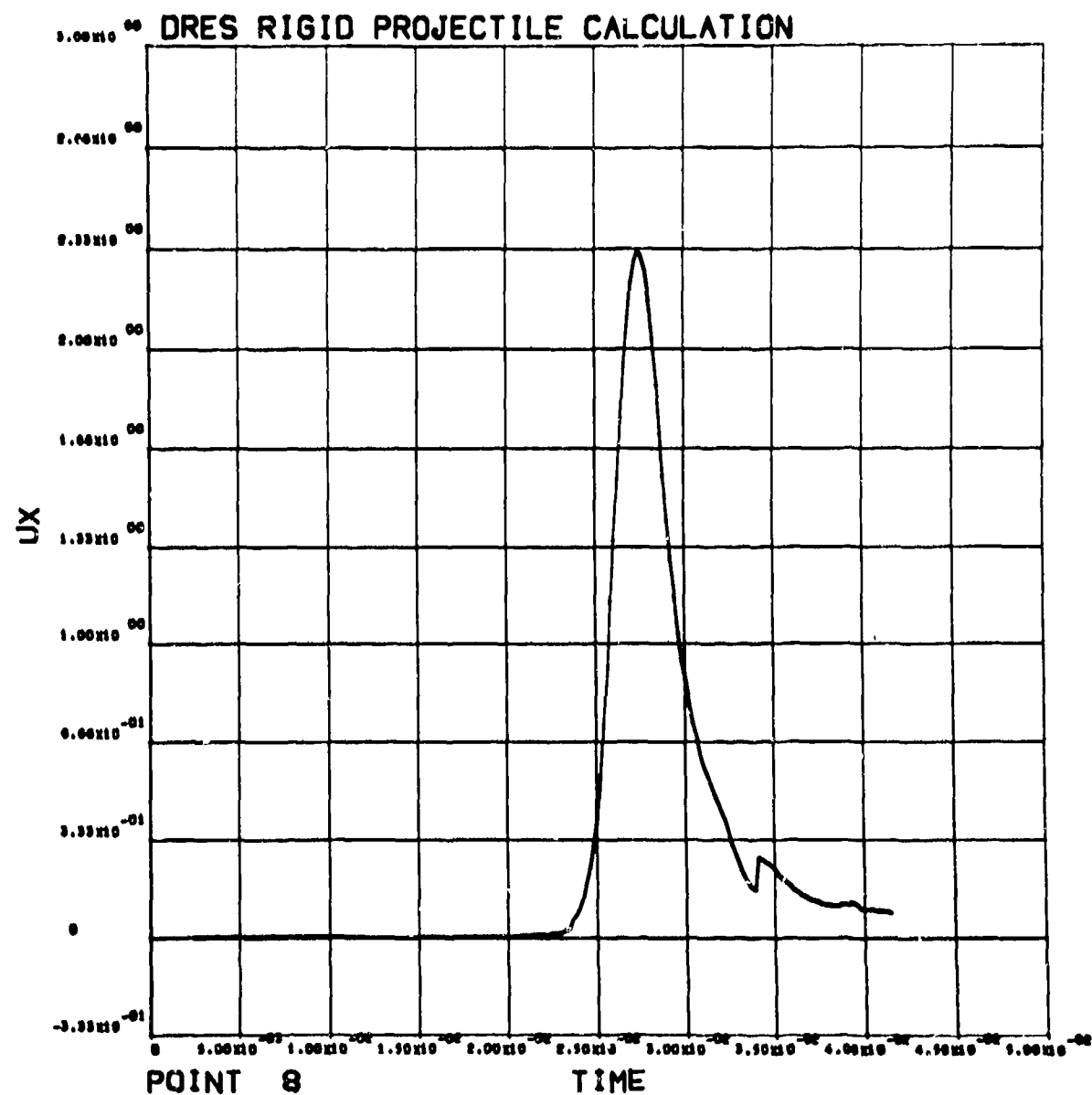
Figure A-38

Radial Velocity (m/s) versus Time (s) for Particle at Point 8, Z = 3.6 m, R = 0.45 m.

DRES RIGID PROJECTILE CALCULATION
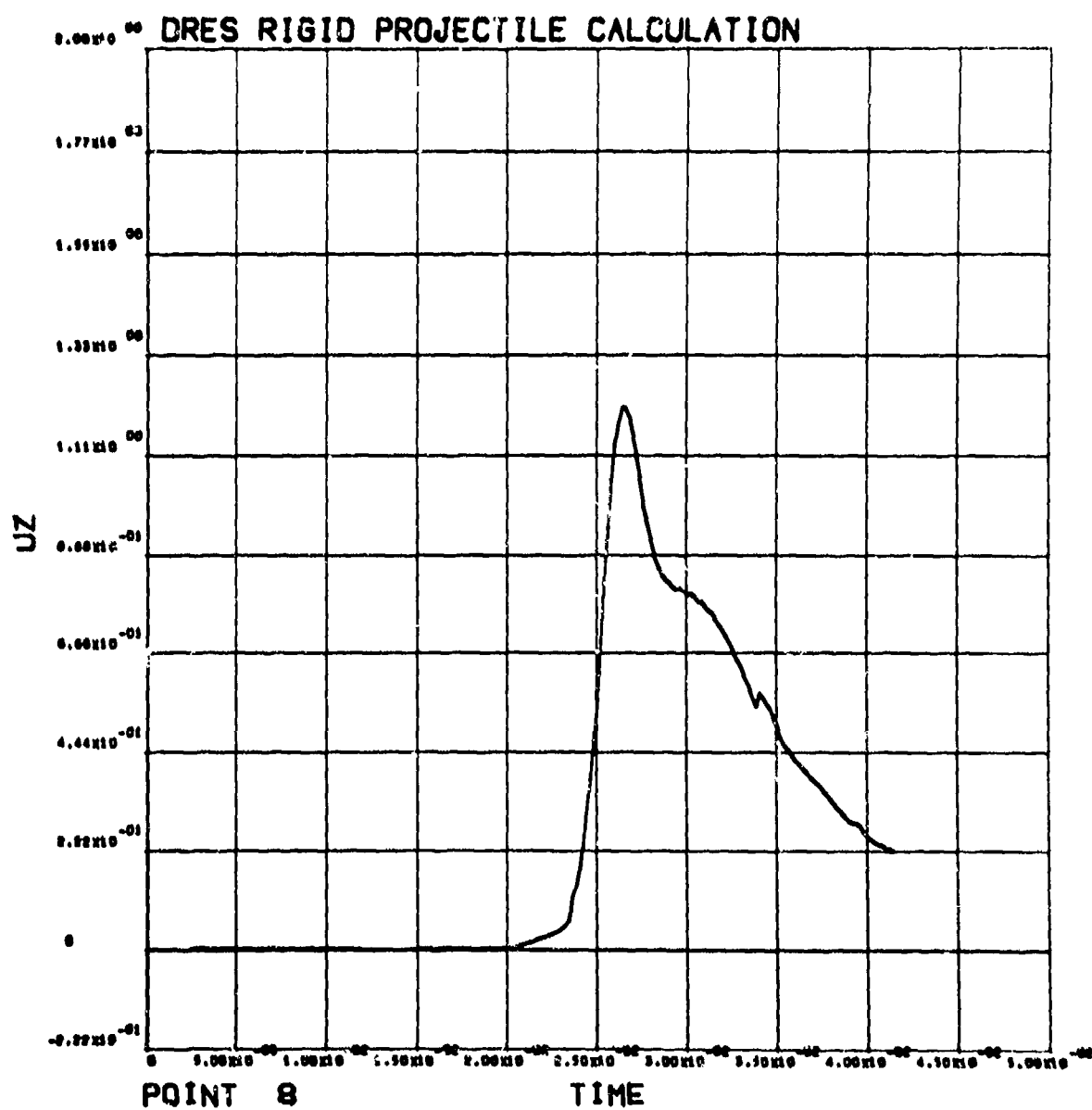
Figure A-39

Axial Velocity (m/s) versus Time (s) for Particle at Point 8, Z = 3.6 m, R = 0.45 m.

132
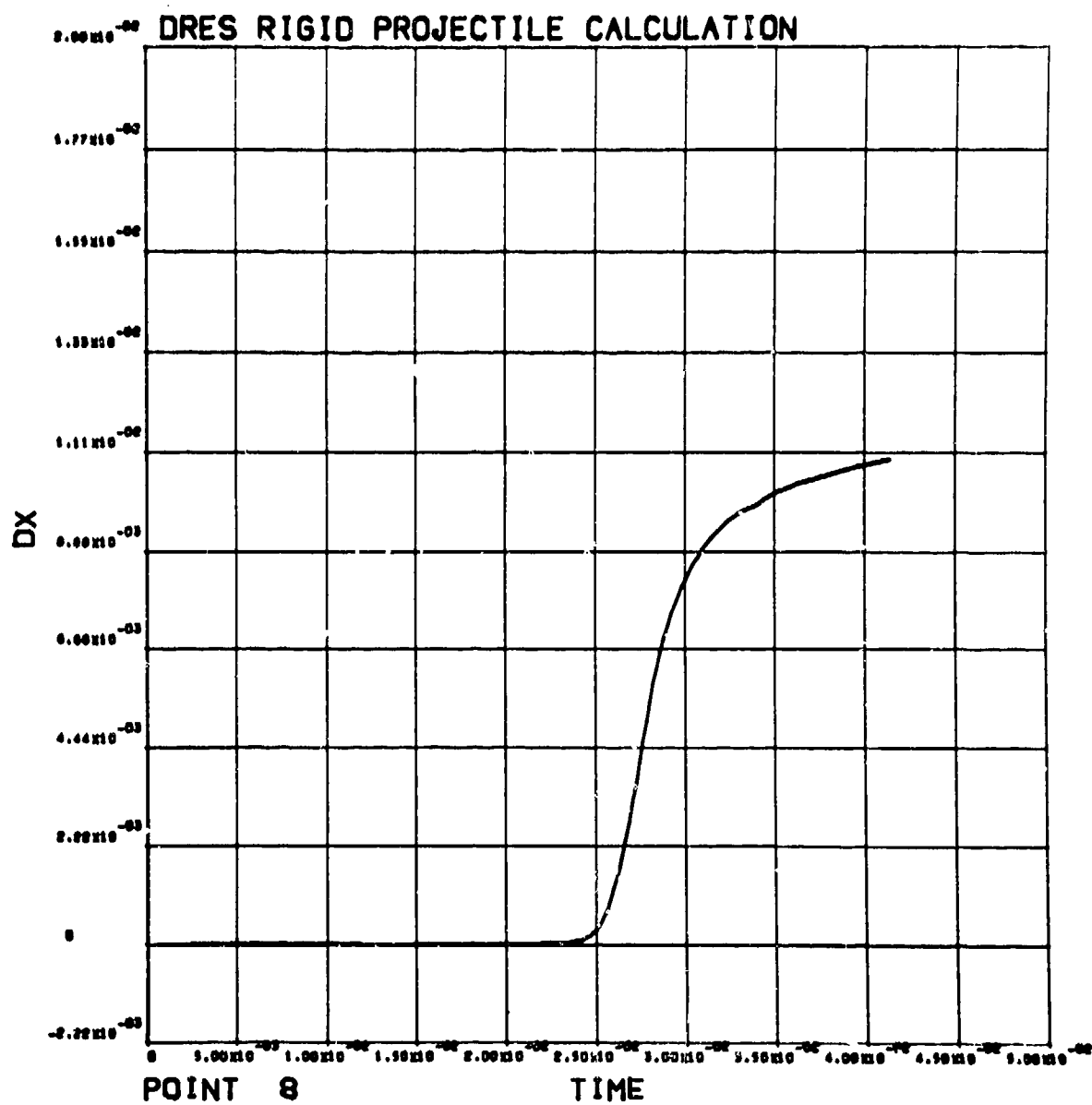
Figure A-40

Radial Displacement (m) versus Time (s) for Particle at Point 8, Z = 3.6 m, R = 0.45 m.
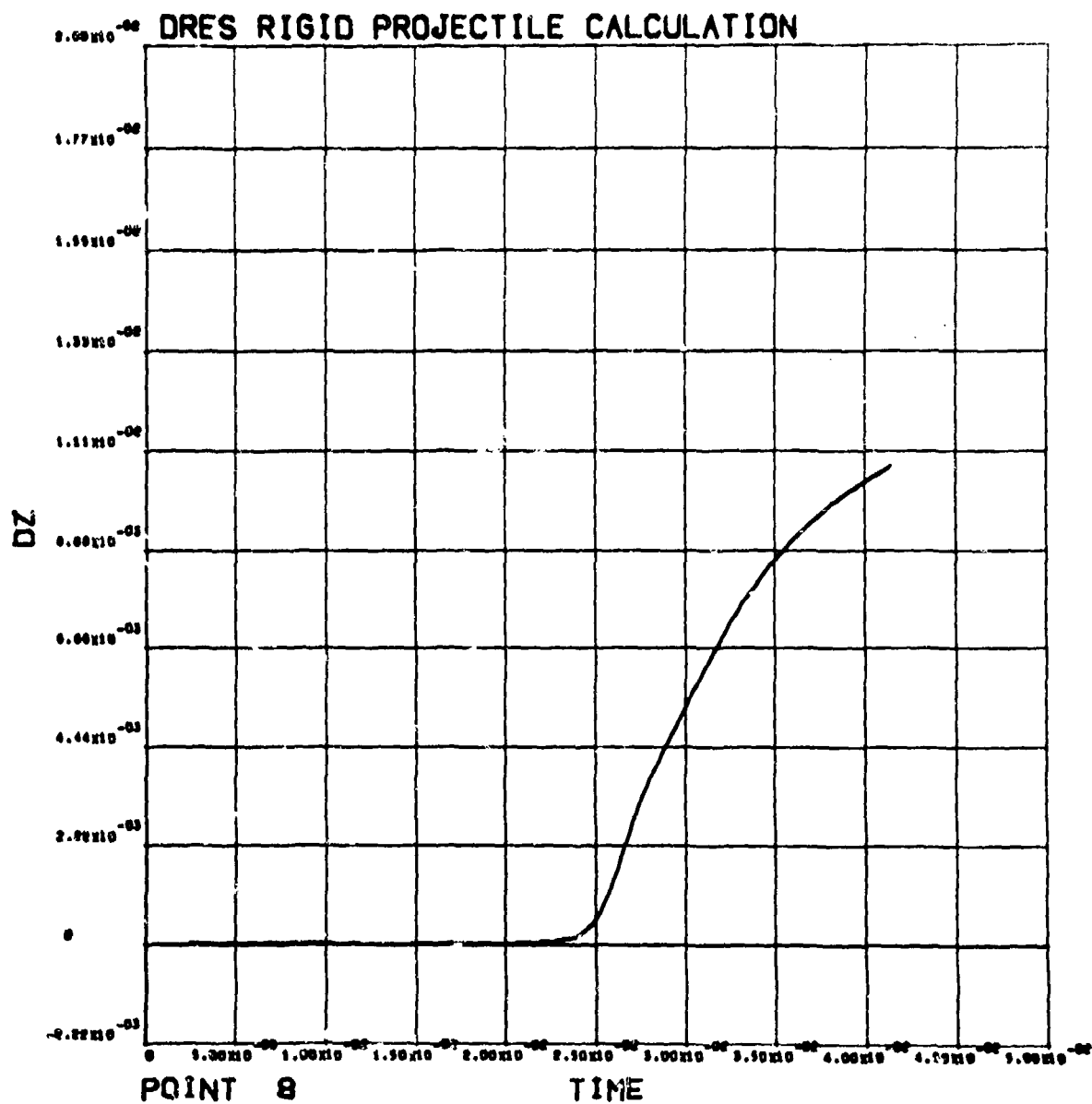
Figure A-41

Axial Displacement (m) versus Time (s) for Particle at Point 8, Z = 3.6 m, R = 0.45 m.

134
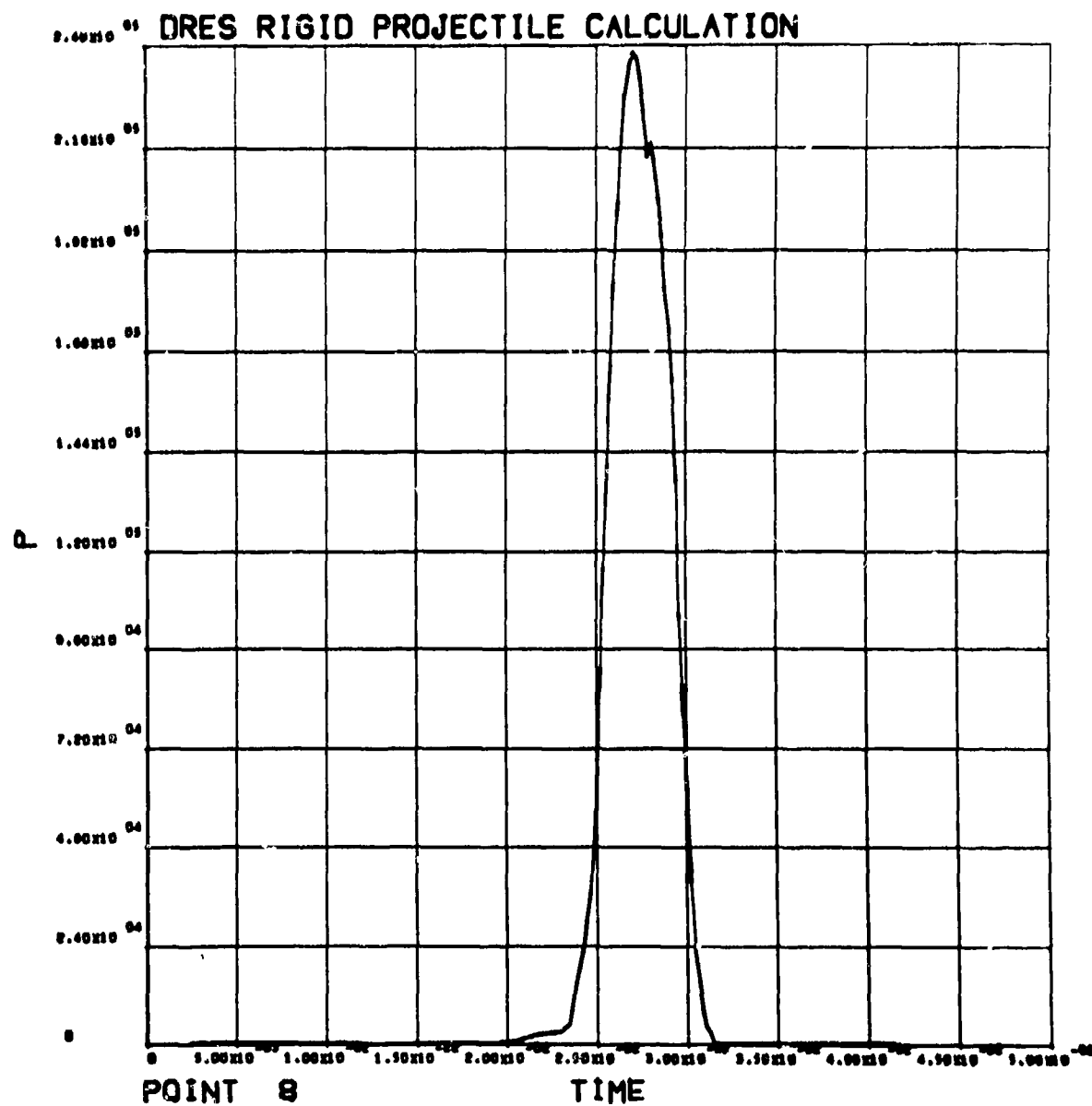
Figure A-42

Pressure (Pa) versus Time (s) for Particle at Point 8, Z = 3.6 m, R = 0.45 m.

135
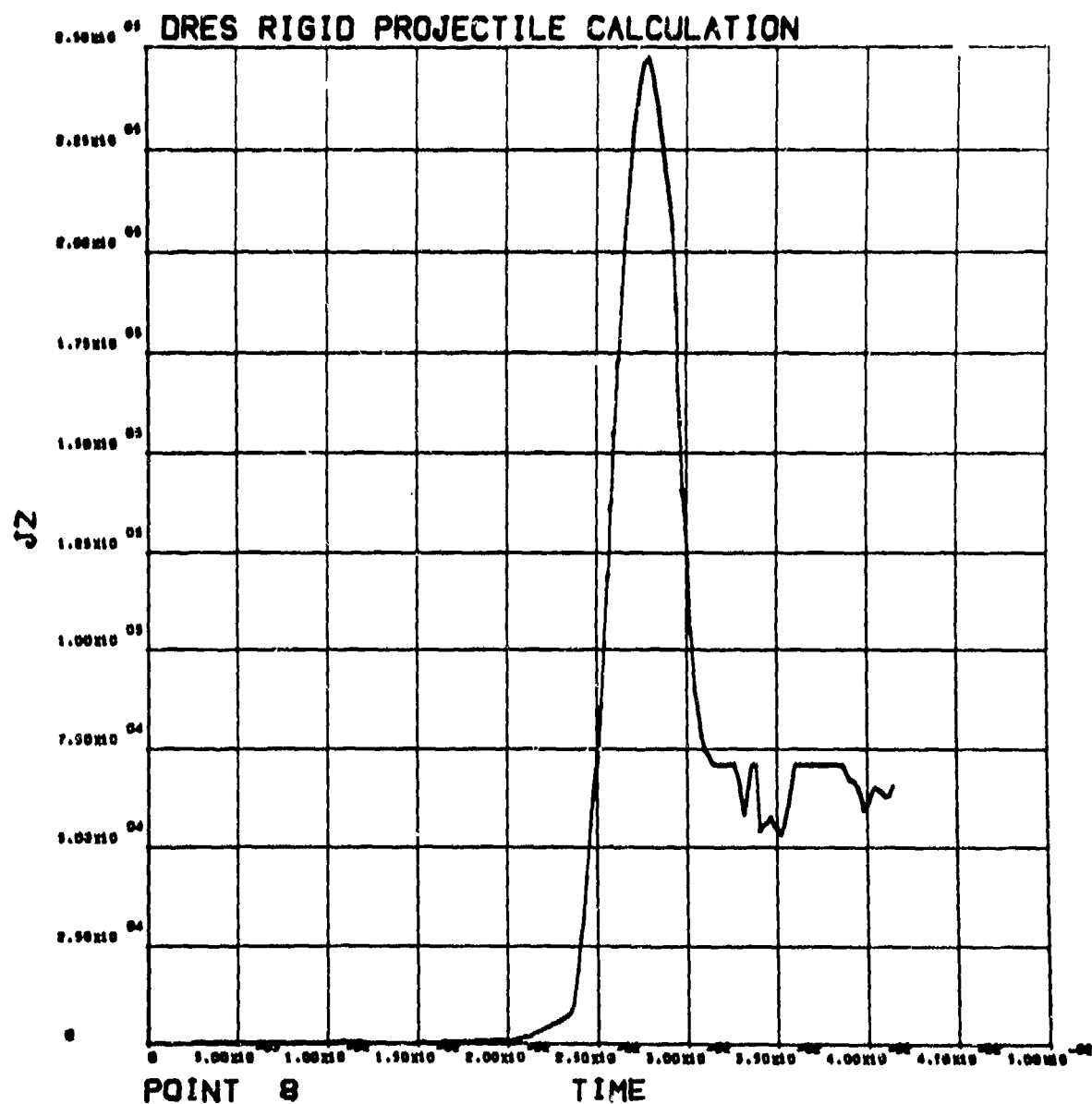
Figure A-43

Deviator Stress, J2, History (Pa) for Particle at Point 8, Z = 3.6 m, R =.0.45 m
(Octahedral Shear Stress = $\sqrt{2/3}(J2)$).
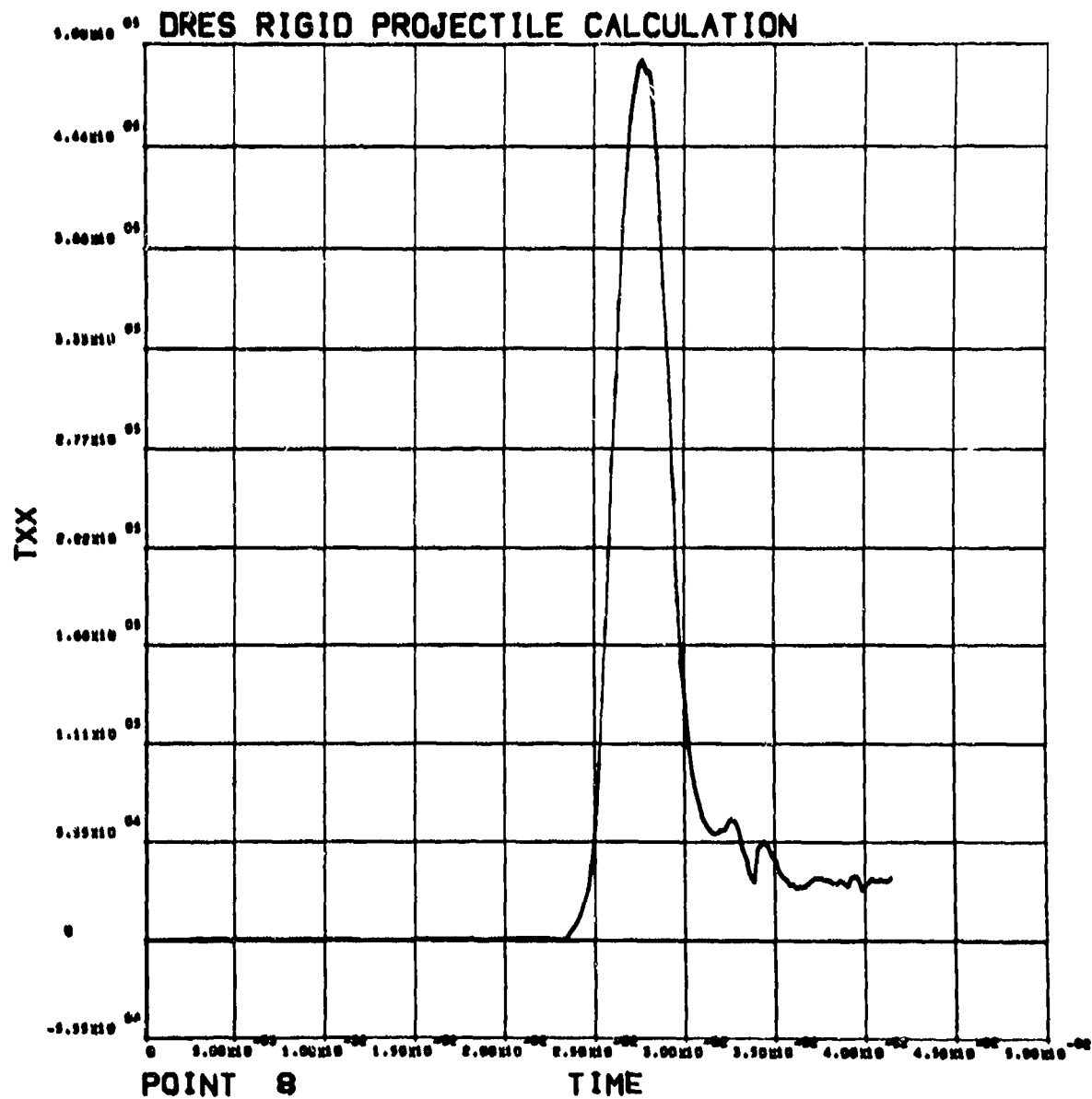
Figure A-44

Radial Stress (Pa) History for Particle at Point 8, Z = 3.6 m, R = 0.45 m.
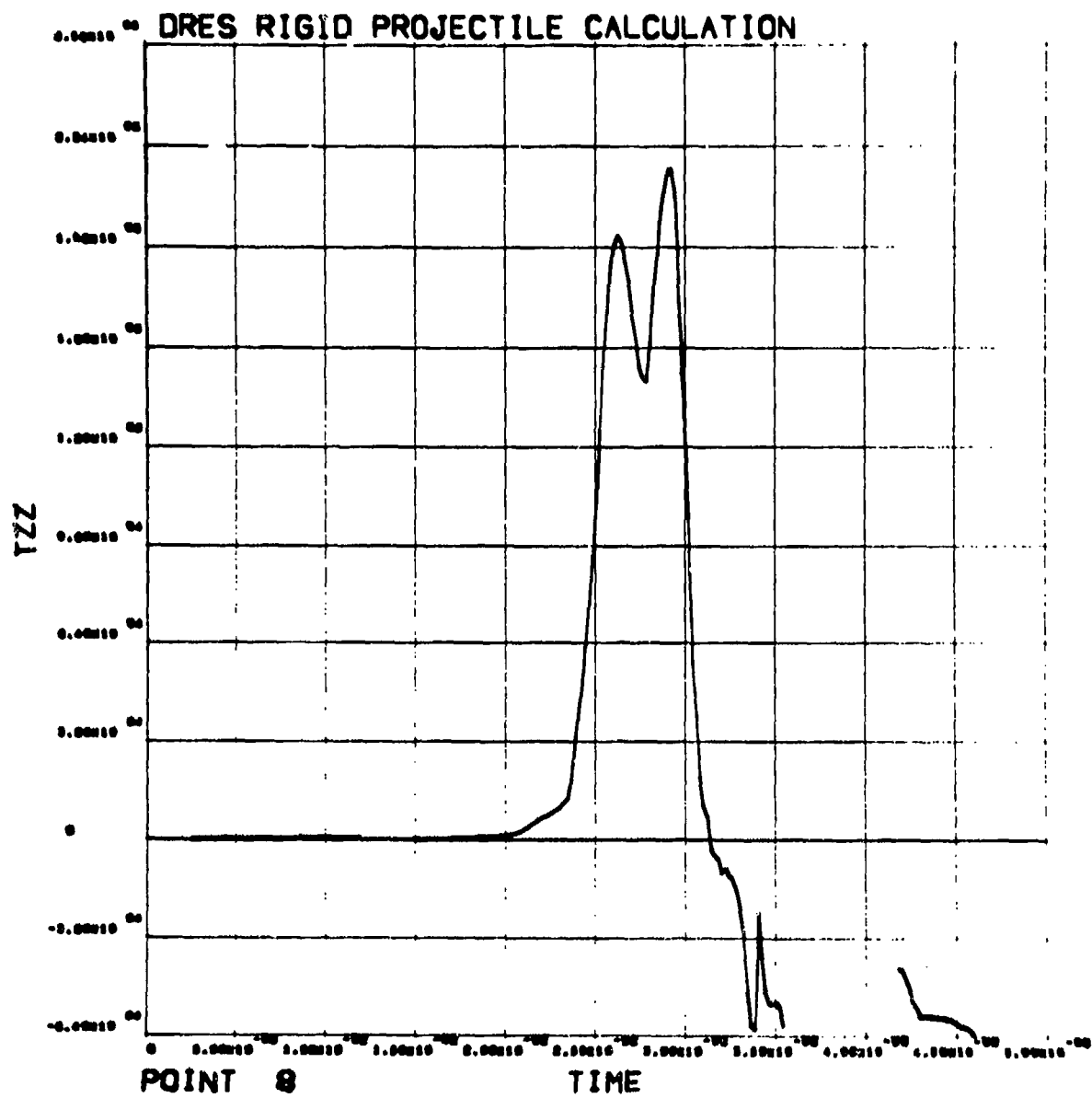
Figure A-45

Axial Stress (Pa) History for Particle at Point 8, Z = 3.6 m, R = 0.45 m.
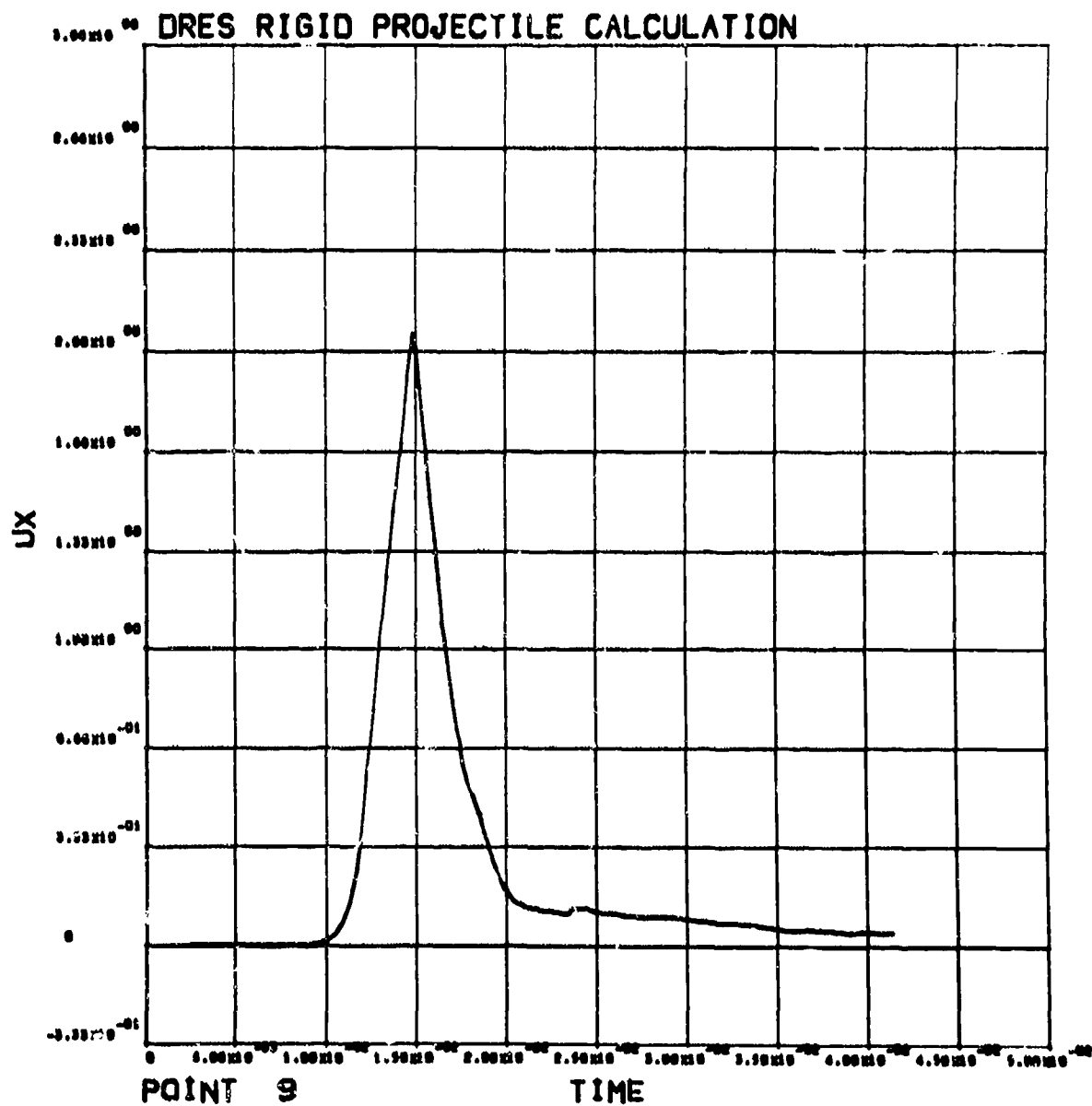
Figure A-46

Radial Velocity (m/s) versus Time (s) for Particle at Point 9, Z = 1.8 m, R = 0.45 m.

139
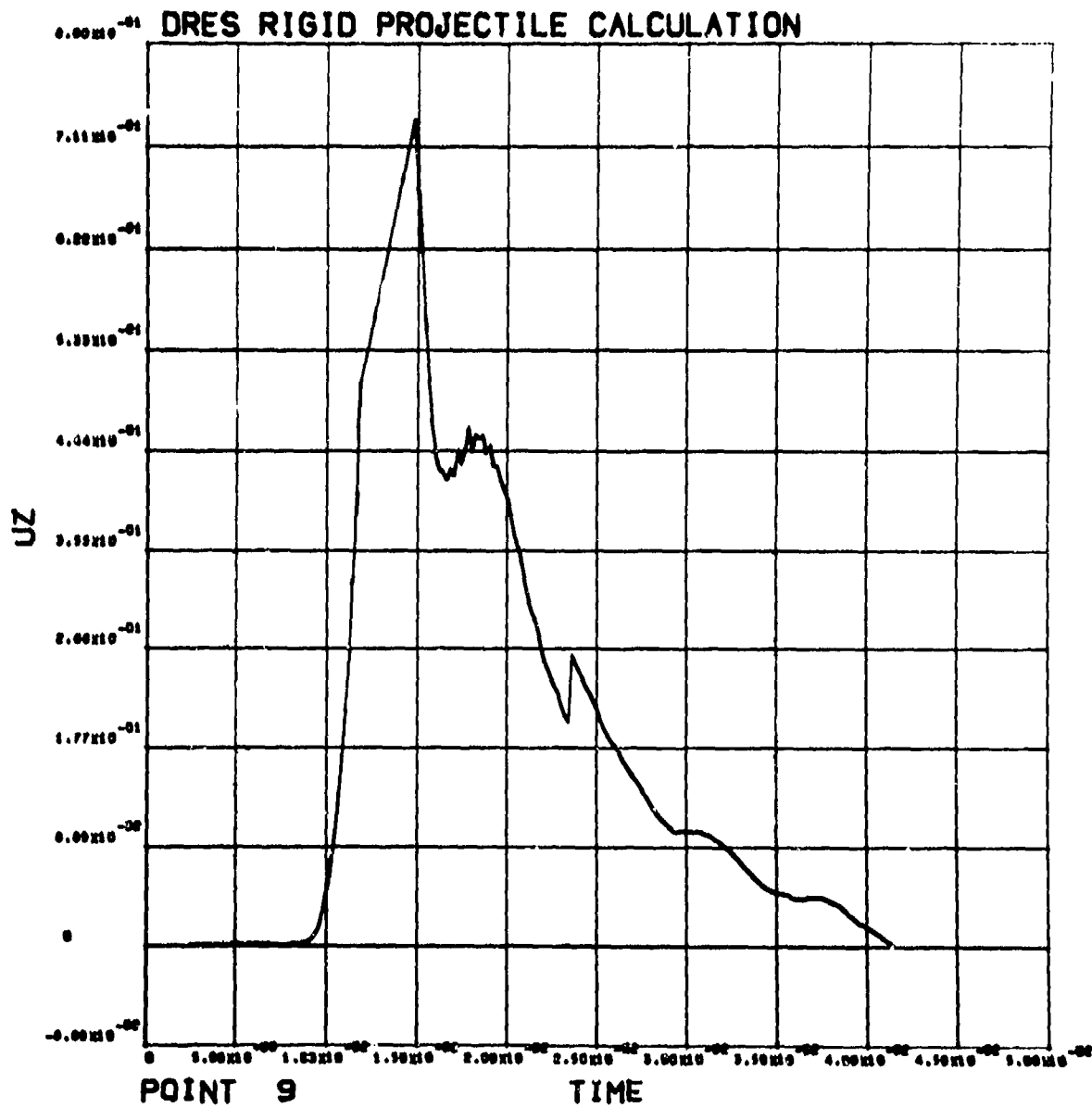
Figure A-47

Axial Velocity (m/s) versus Time (s) for Particle at Point 9, Z = 1.8 m, R = 0.45 m.

DRES RIGID PROJECTILE CALCULATION

POINT 9   TIME
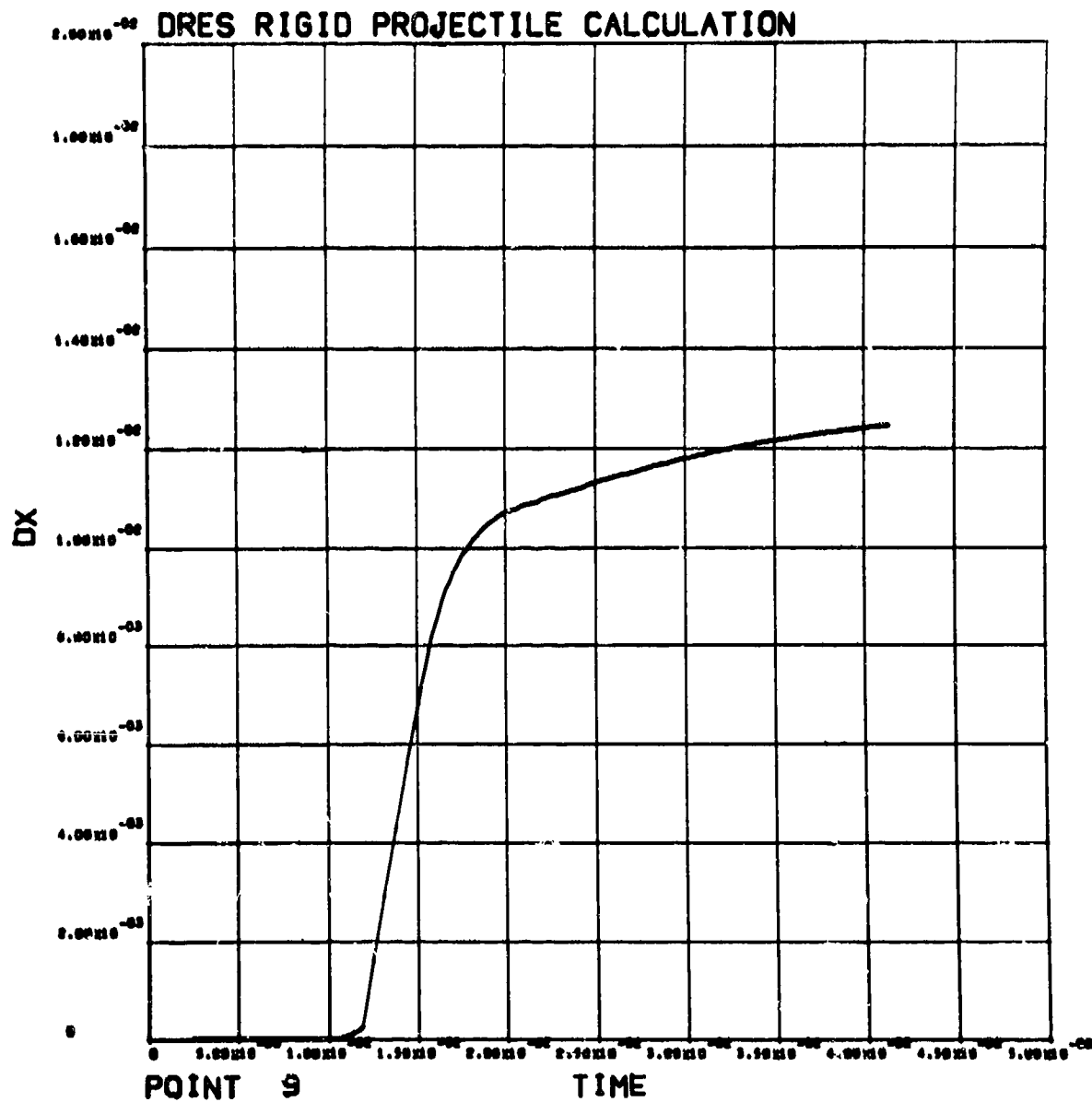
Figure A-48

Radial Displacement (m) versus Time (s) for Particle at Point 9, Z = 1.8 m, R = 0.45 m.
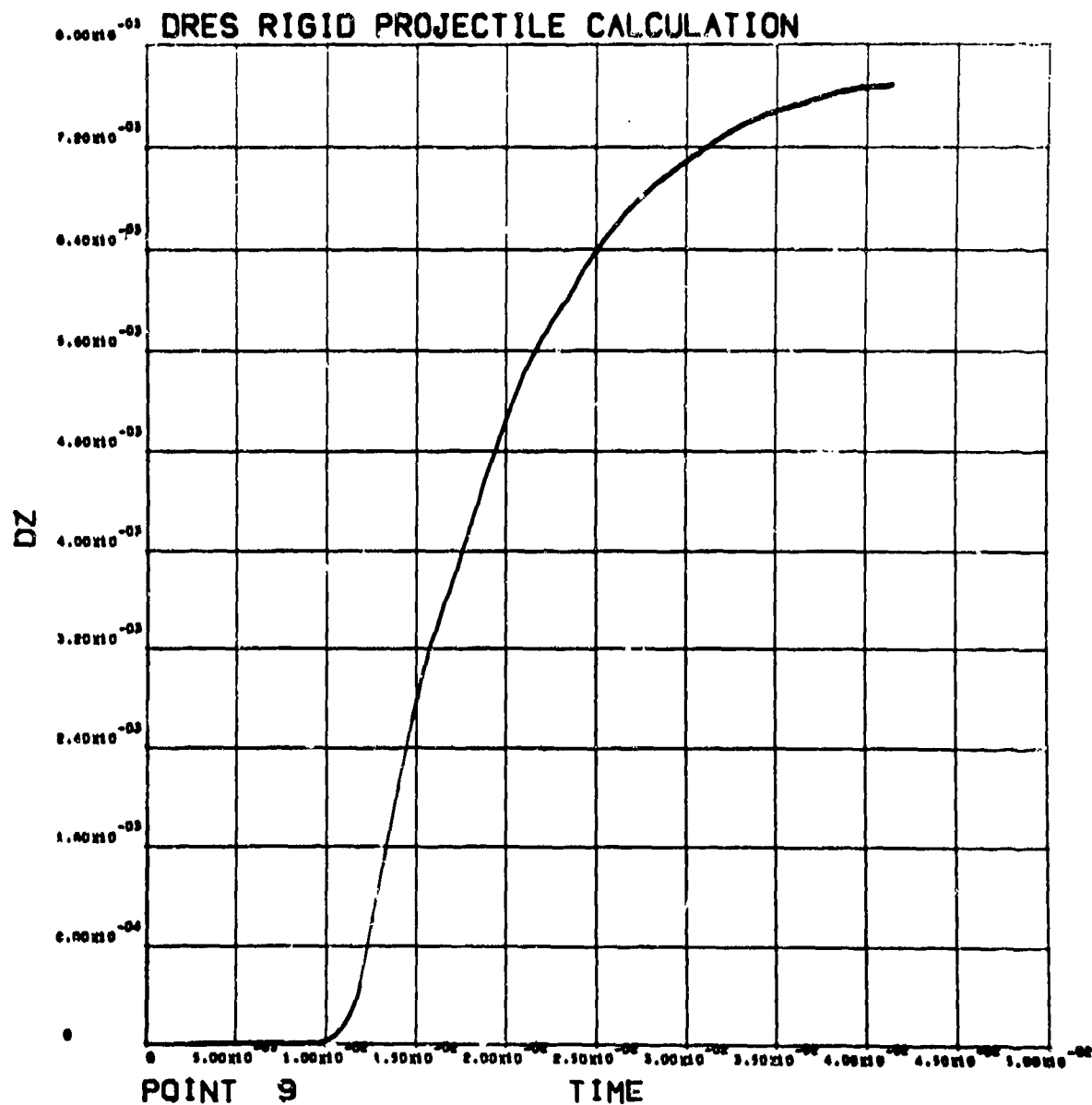
Figure A-49

Axial Displacement (m) versus Time (s) for Particle at Point 9, Z = 1.8 m, R = 0.45 m.
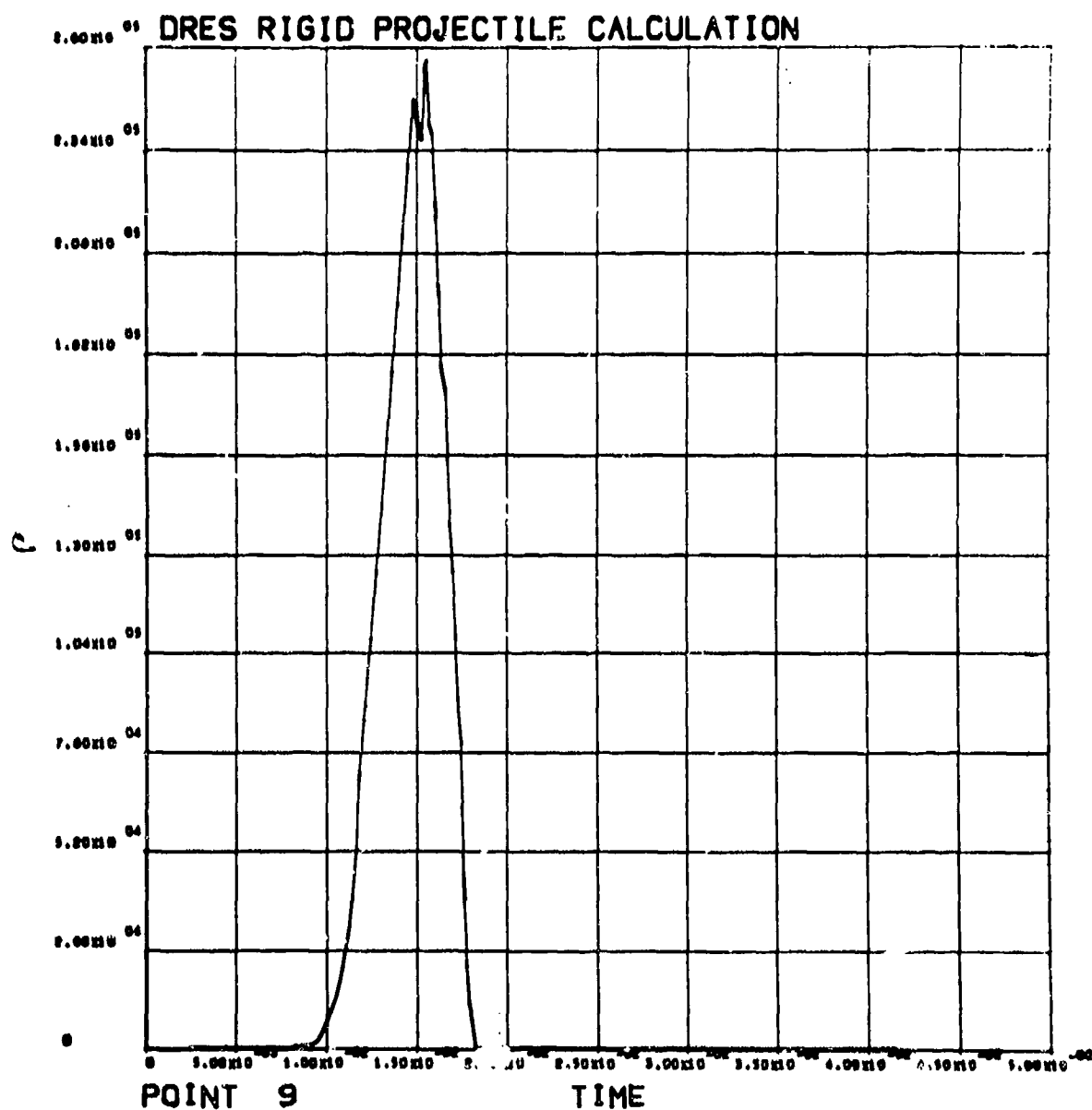
Figure A-50

Pressure (Pa) versus Time (s) for Particle at Point 9, Z = 1.8 m, R = 0.45 m.

143
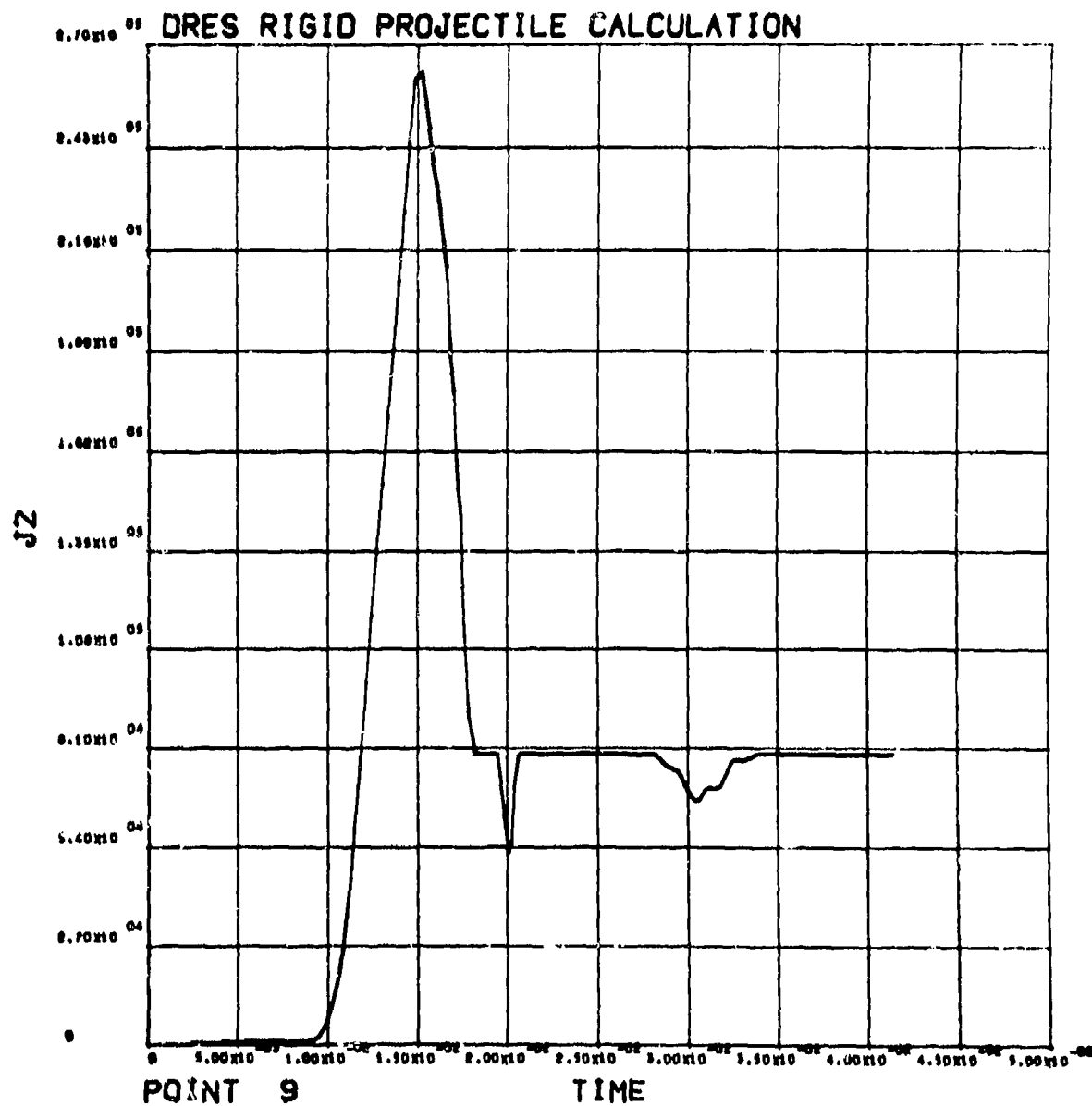
Figure A-51

Deviator Stress, J2, History (Pa) for Particle at Point 9, Z = 1.8 m, R = 0.45 m (Octahedral Shear Stress = $\sqrt{2/3}$(J2)).
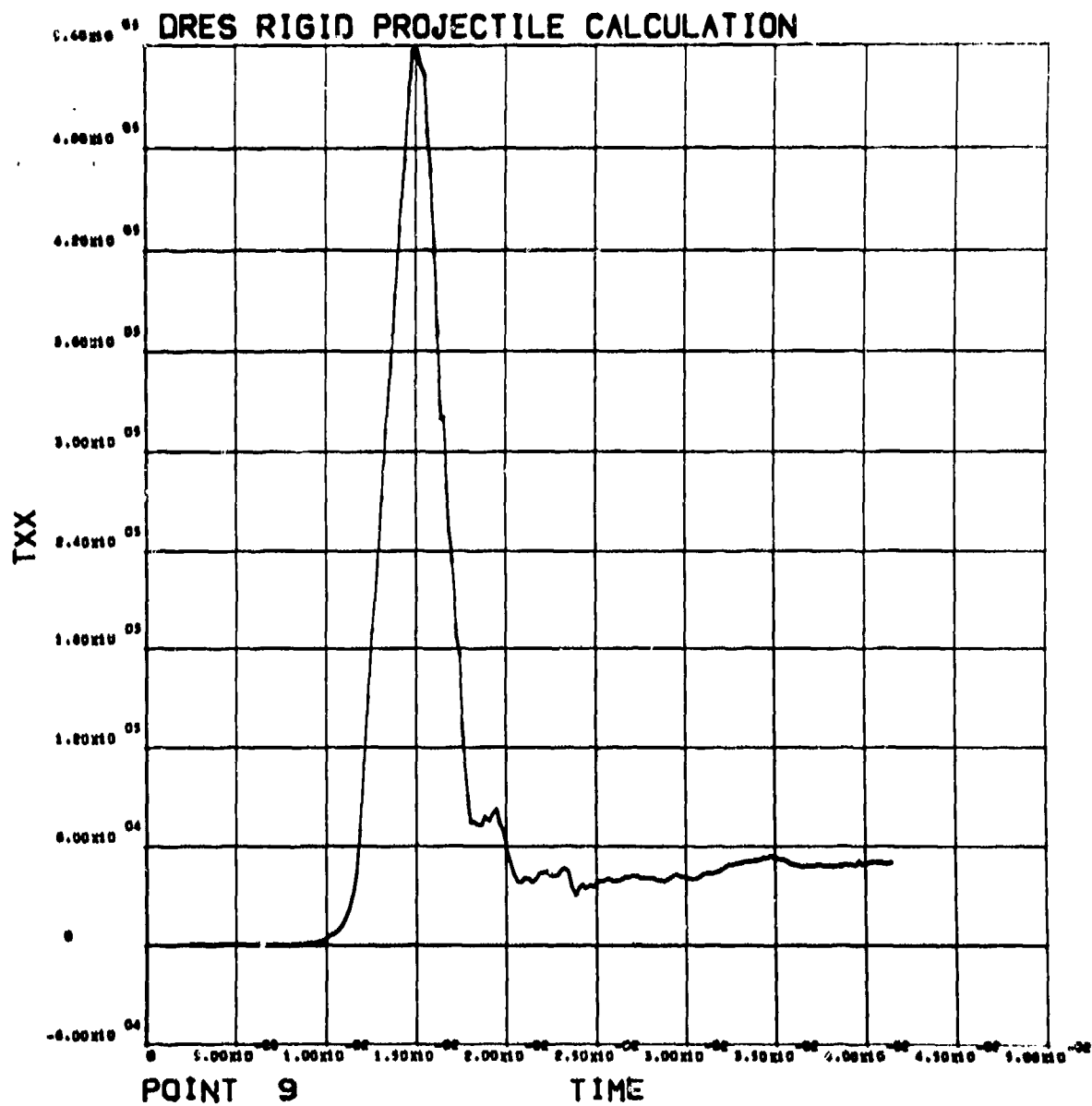
Figure A-52

Radial Stress (Pa) History for Particle at Point 9, $Z = 1.8$ m, $R = 0.45$ m.
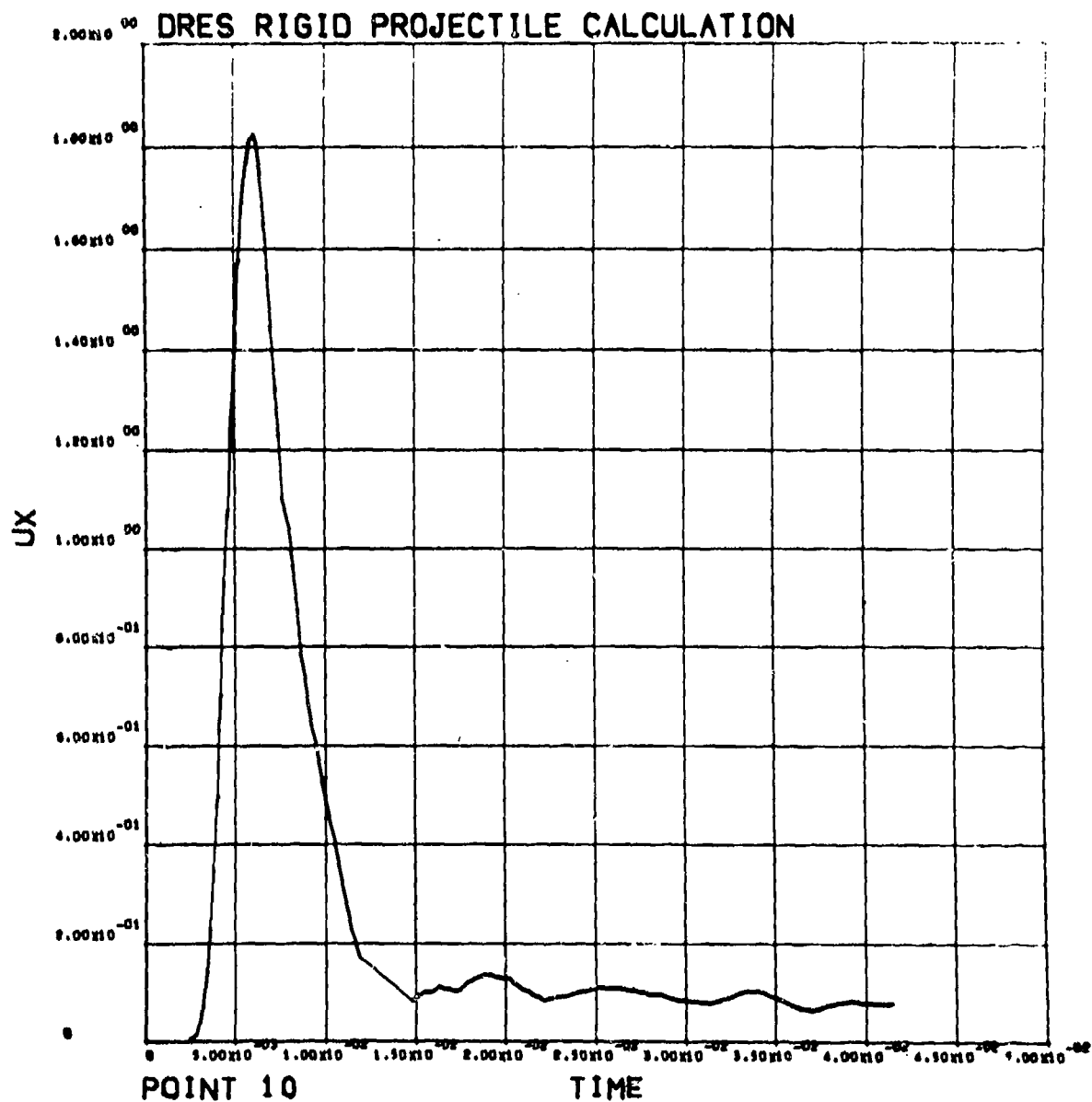
Figure A-53

Radial Velocity (m/s) versus Time (s) for Particle at Point 10, Z = 0.4 m, R = 0.45 m.

146
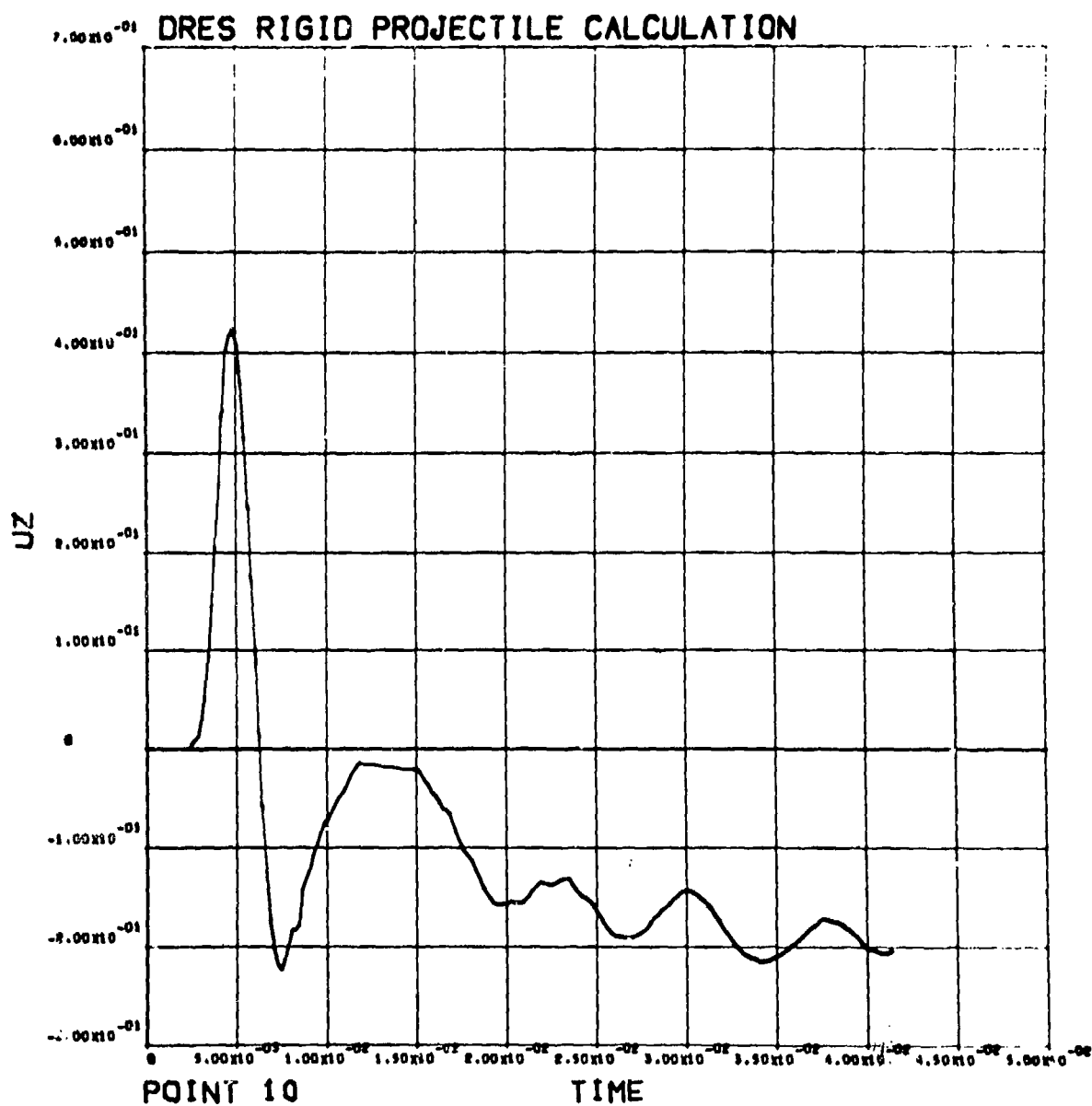
Figure A-54

Axial Velocity (m/s) versus Time (s) for Particle at Point 10, Z = 0.4 m, R = 0.45 m.

147

DRES RIGID PROJECTILE CALCULATION

POINT 10

TIME

DX
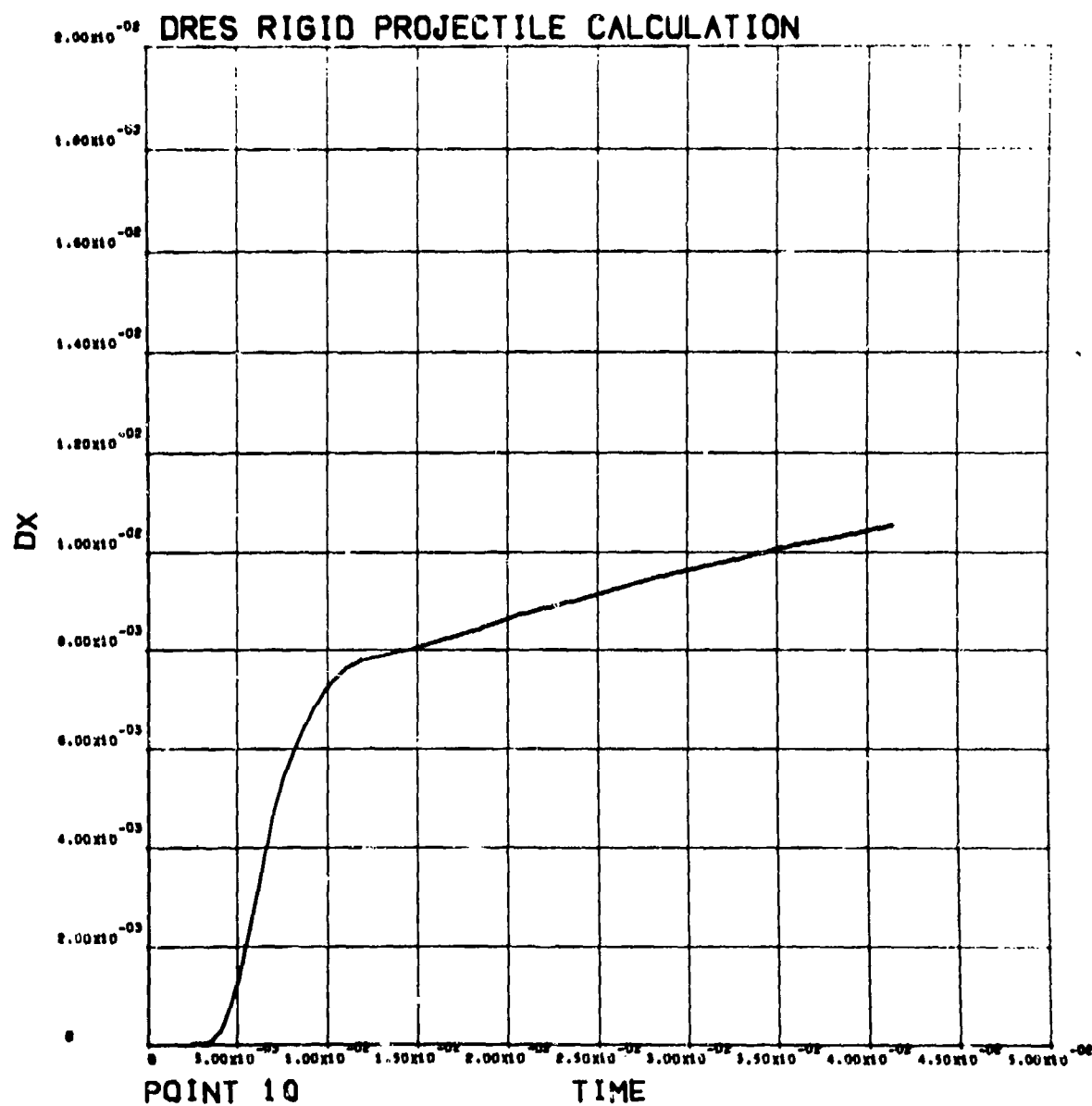
Figure A-55

Radial Displacement (m) versus Time (s) for Particle at Point 10, $Z = 0.4$ m, $R = 0.45$ m.

148
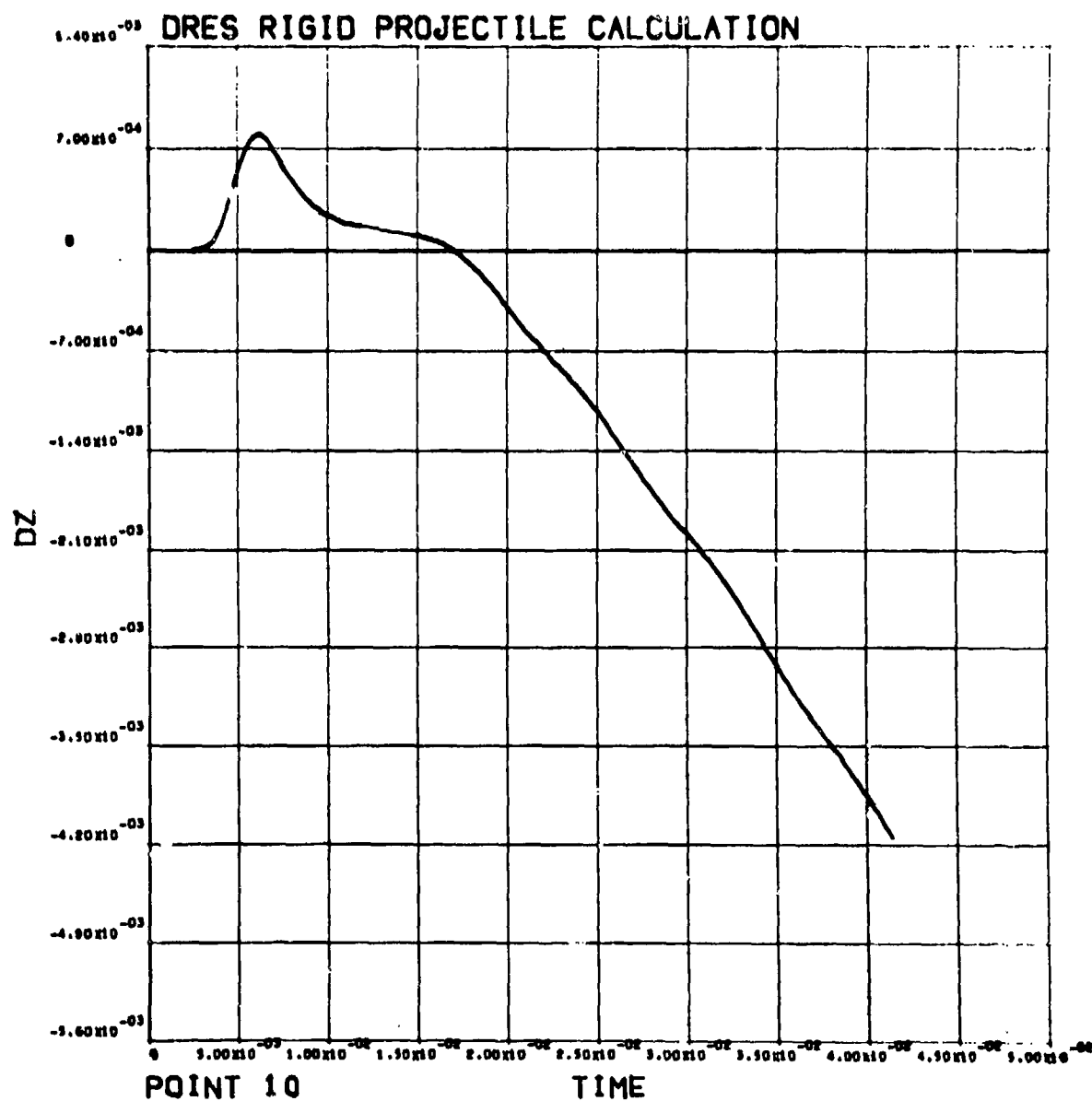
Figure A-56

Axial Displacement (m) versus Time (s) for Particle at Point 10, Z = 0.4 m, R = 0.45 m.

DRES RIGID PROJECTILE CALCULATION
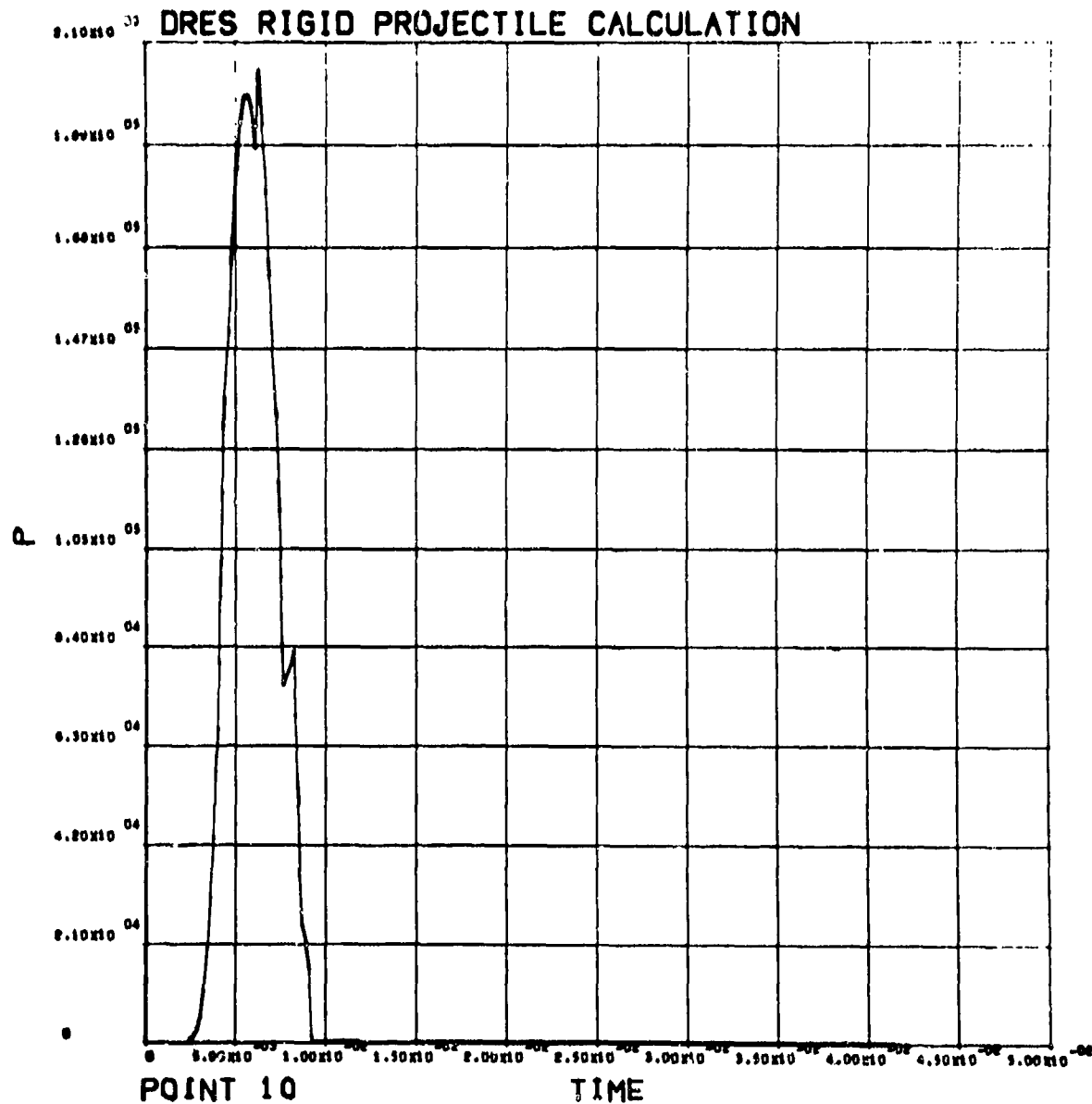
POINT 10

TIME

Figure A-57

Pressure (Pa) versus Time (s) for Particle at Point 10, Z = 0.4 m, R = 0.45 m.

150
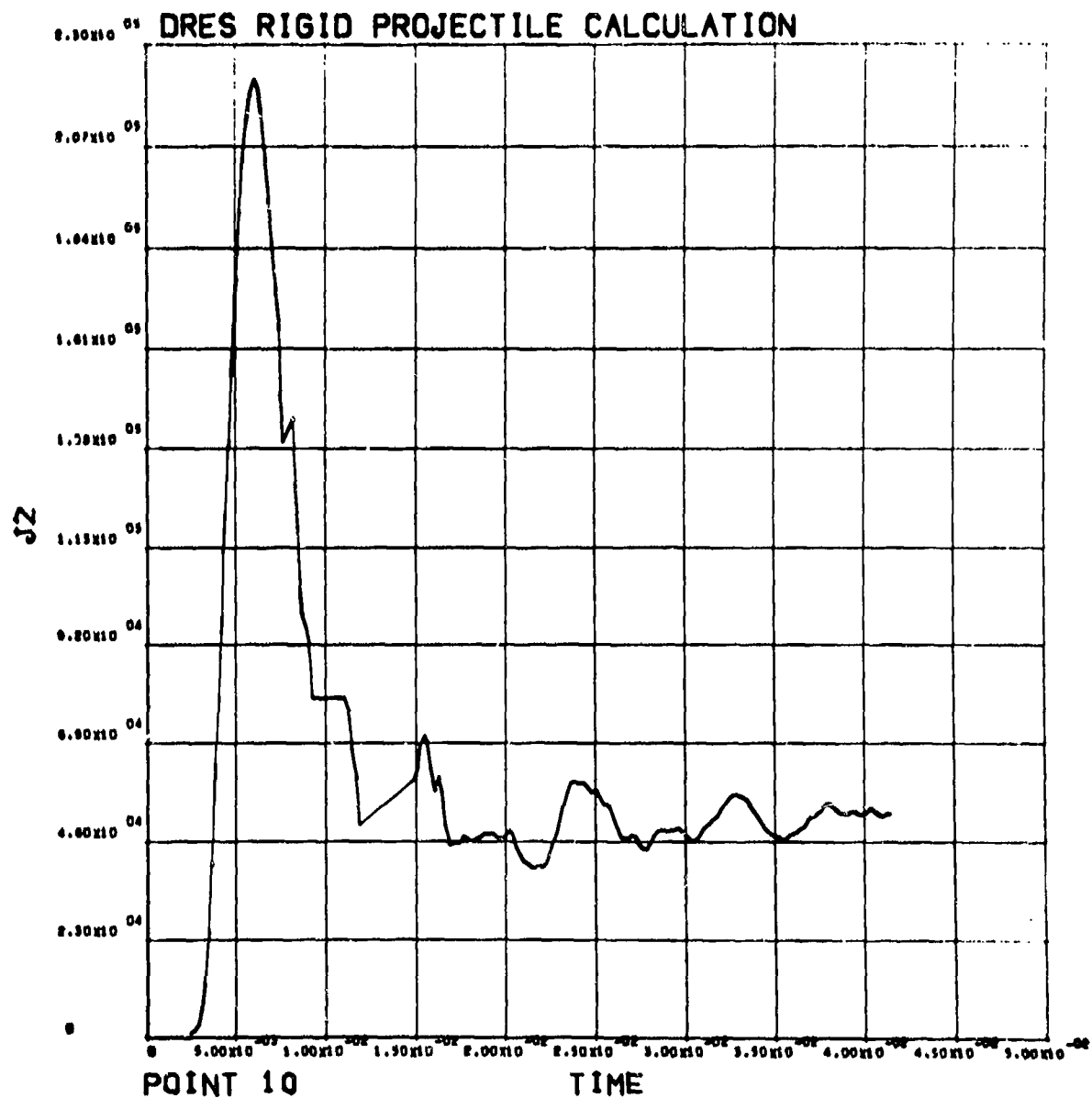
Figure A-58

Deviator Stress, J2, History (Pa) for Particle at Point 10, Z = 0.4 m, R = 0.45 m (Octahedral Shear Stress = $\sqrt{2/3}(J2)$).

DRES RIGID PROJECTILE CALCULATION
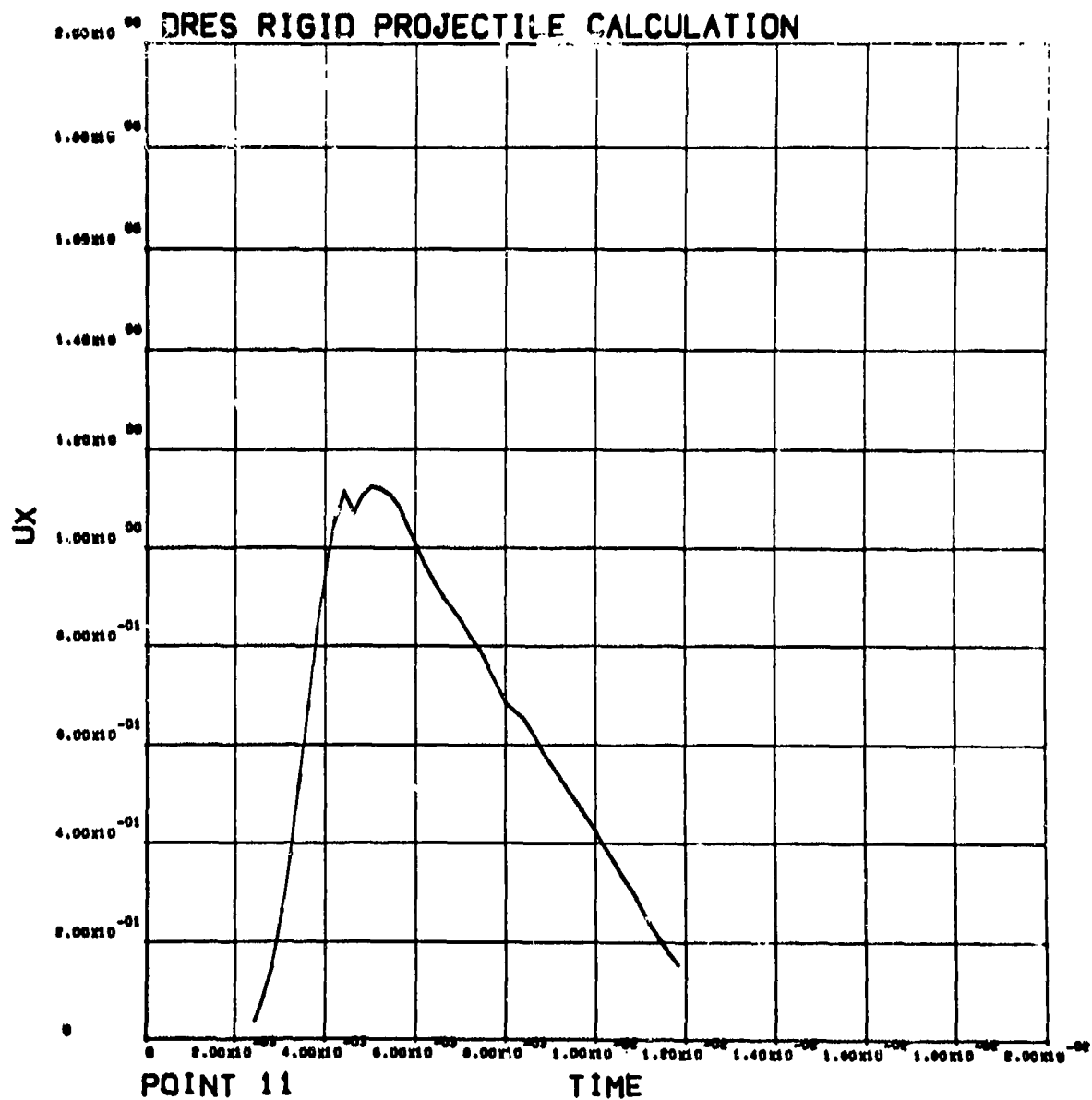
POINT 11   TIME

Figure A-59

Radial Velocity (m/s) versus Time (s) for Particle at Point 11, Z = 0.1 m, R = 0.45 m.

152
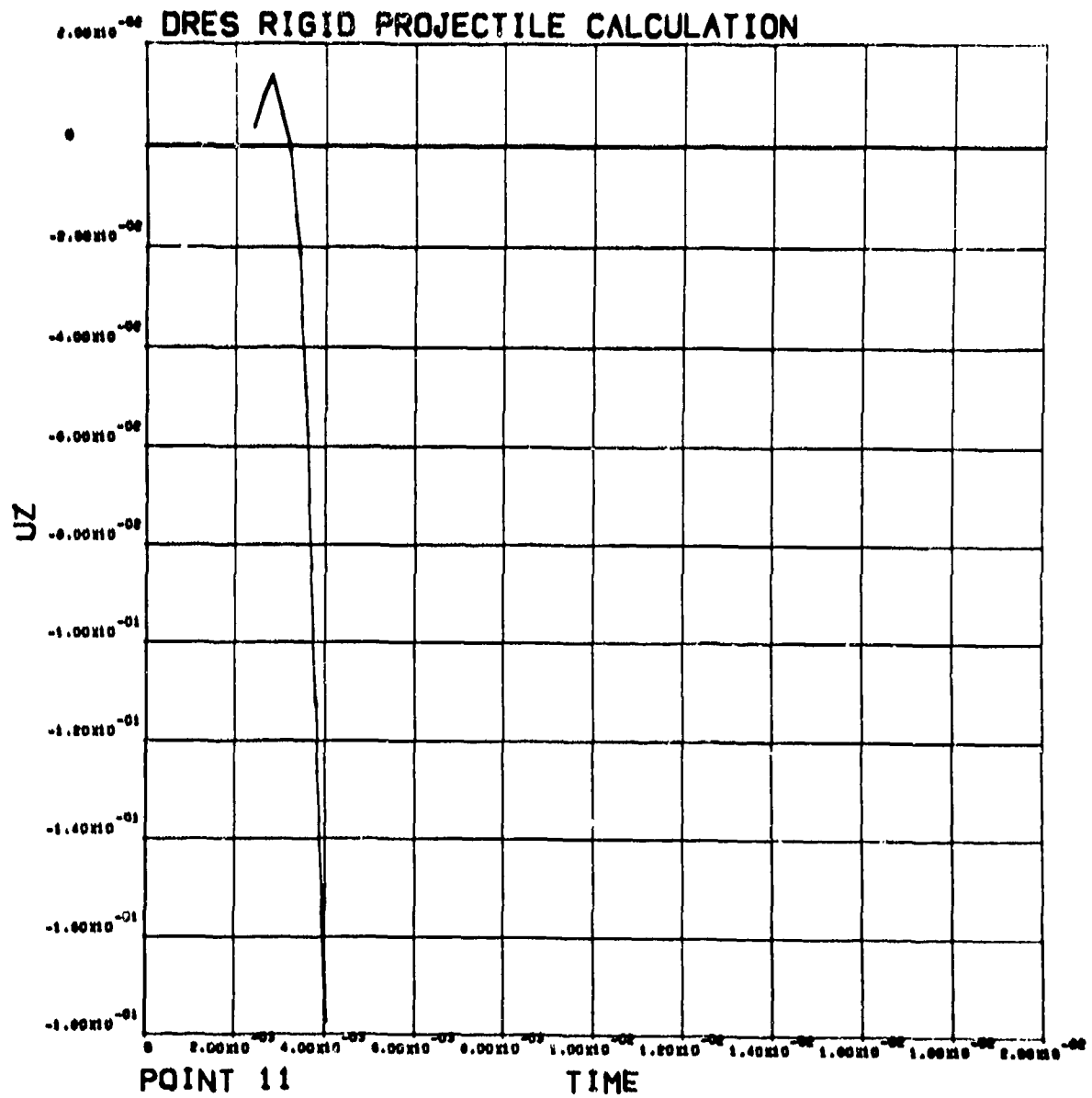
Figure A-60

Axial Velocity (m/s) versus Time (s) for Particle at Point 11, Z = 0.1 m, R = 0.45 m.

153
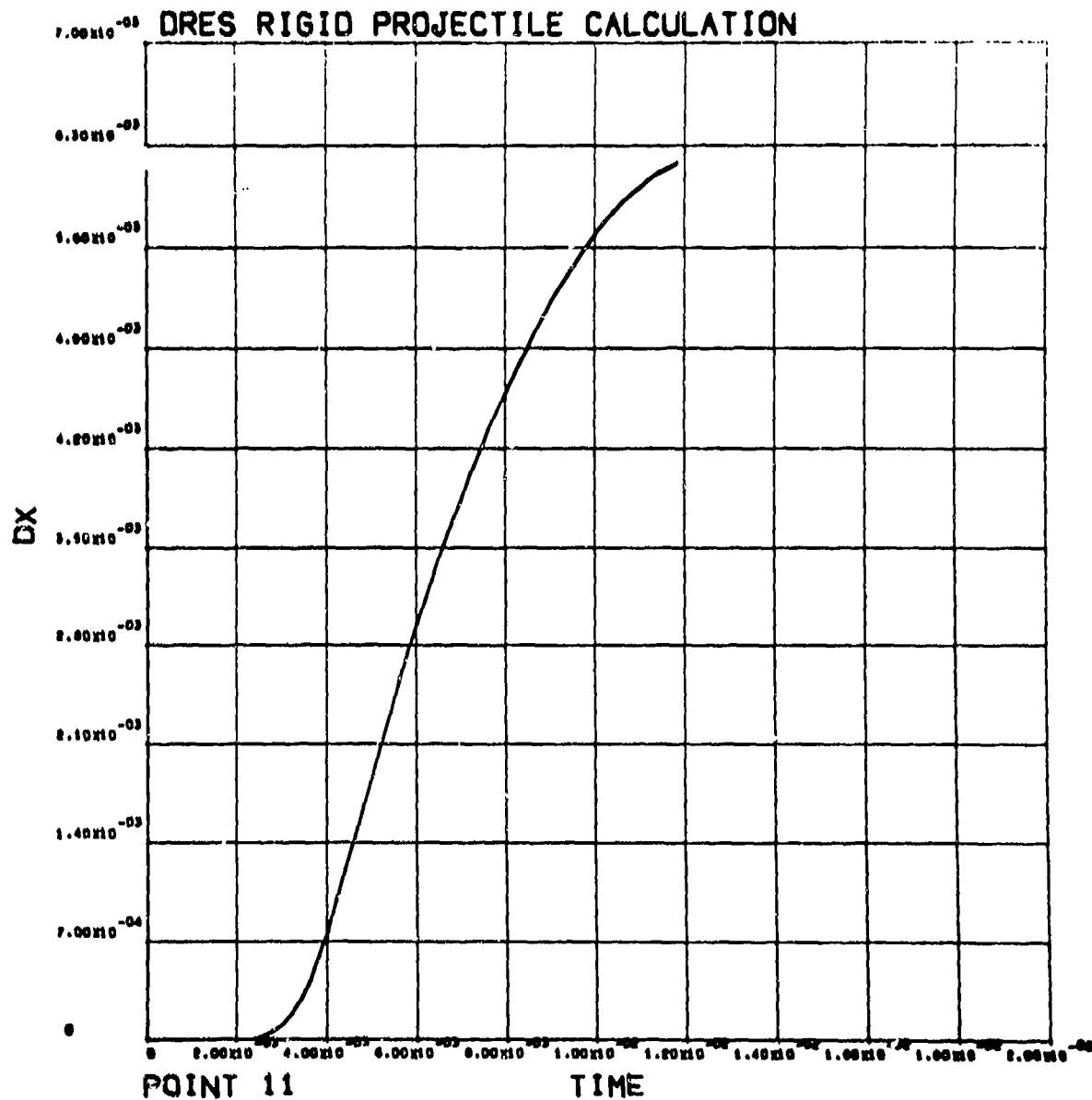
Figure A-61

Radial Displacement (m) versus Time (s) for Particle at Point 11, Z = 0.1 m, R = 0.45 m.
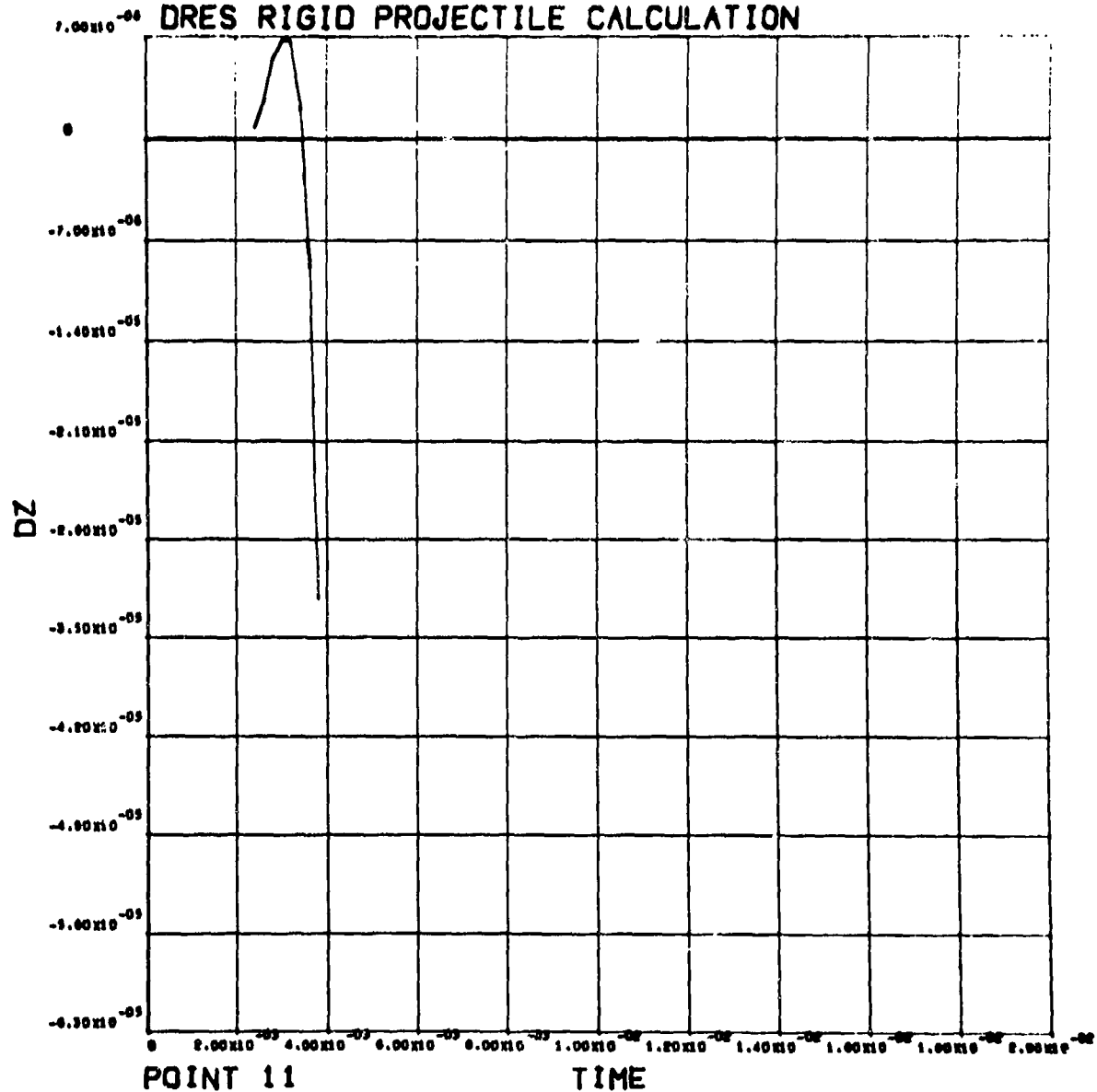
Figure A-62

Axial Displacement (m) versus Time (s) for Particle at Point 11, Z = 0.1 m, R = 0.45 m.
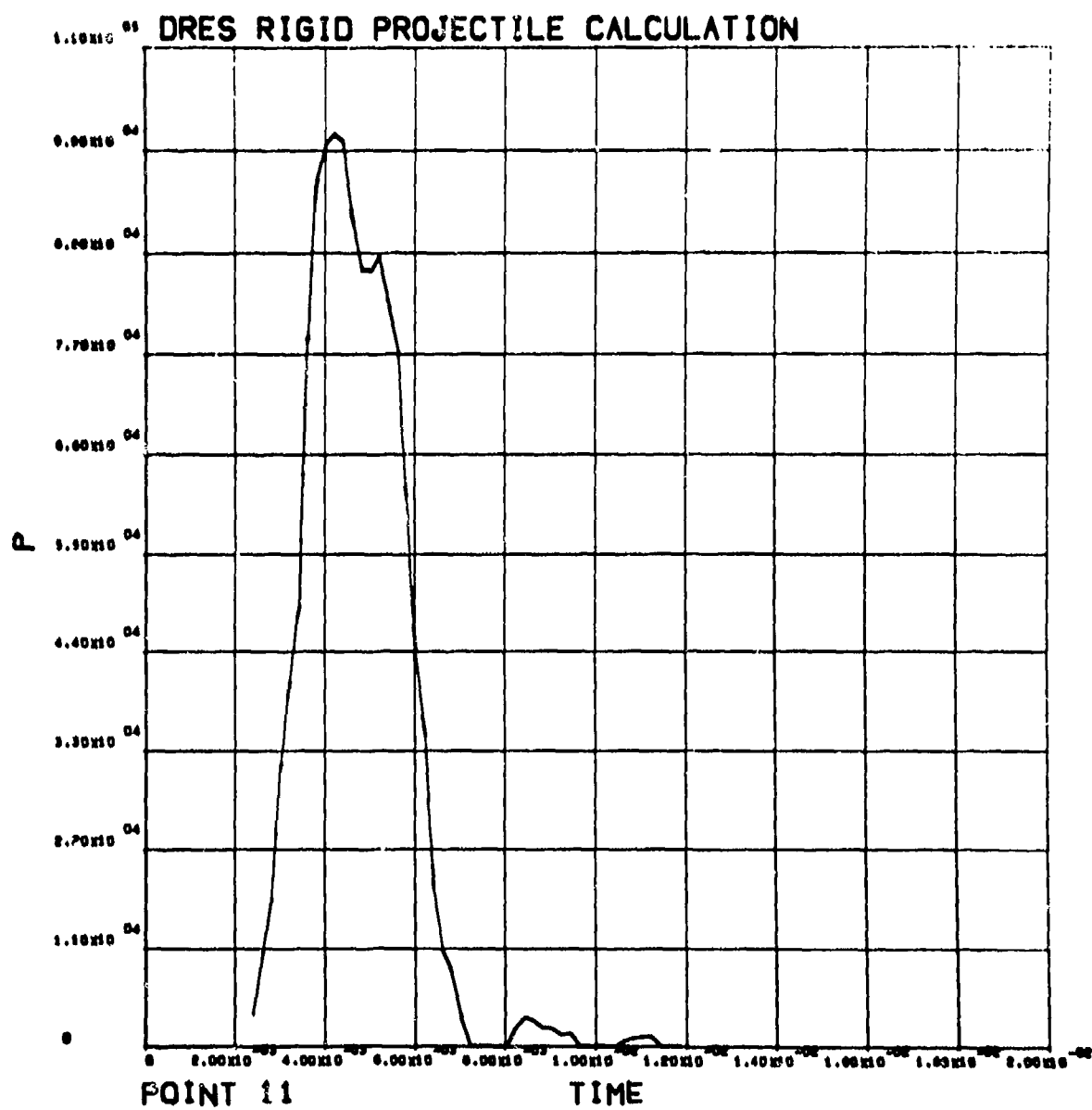
Figure A-63

Pressure (Pa) versus Time (s) for Particle at Point 11, Z = 0.1 m, R = 0.45 m.

156

DRES RIGID PROJECTILE CALCULATION
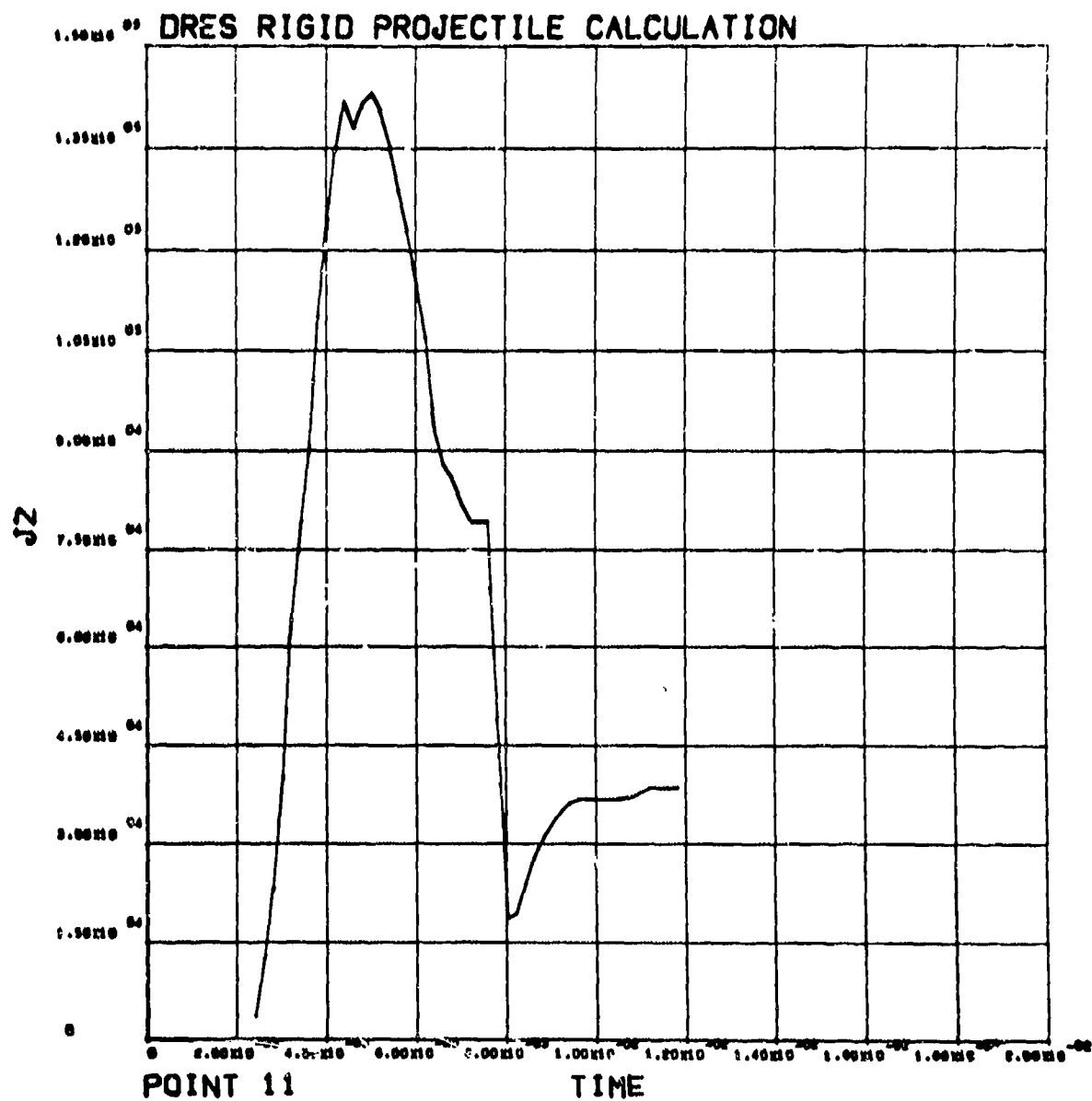
POINT 11

TIME

Figure A-64

Deviator Stress, J2, History (Pa) for Particle at Point 11, $Z = 0.1$ m, $R = 0.45$ m
(Octahedral Shear Stress $= \sqrt{2/3}(J2)$).

157
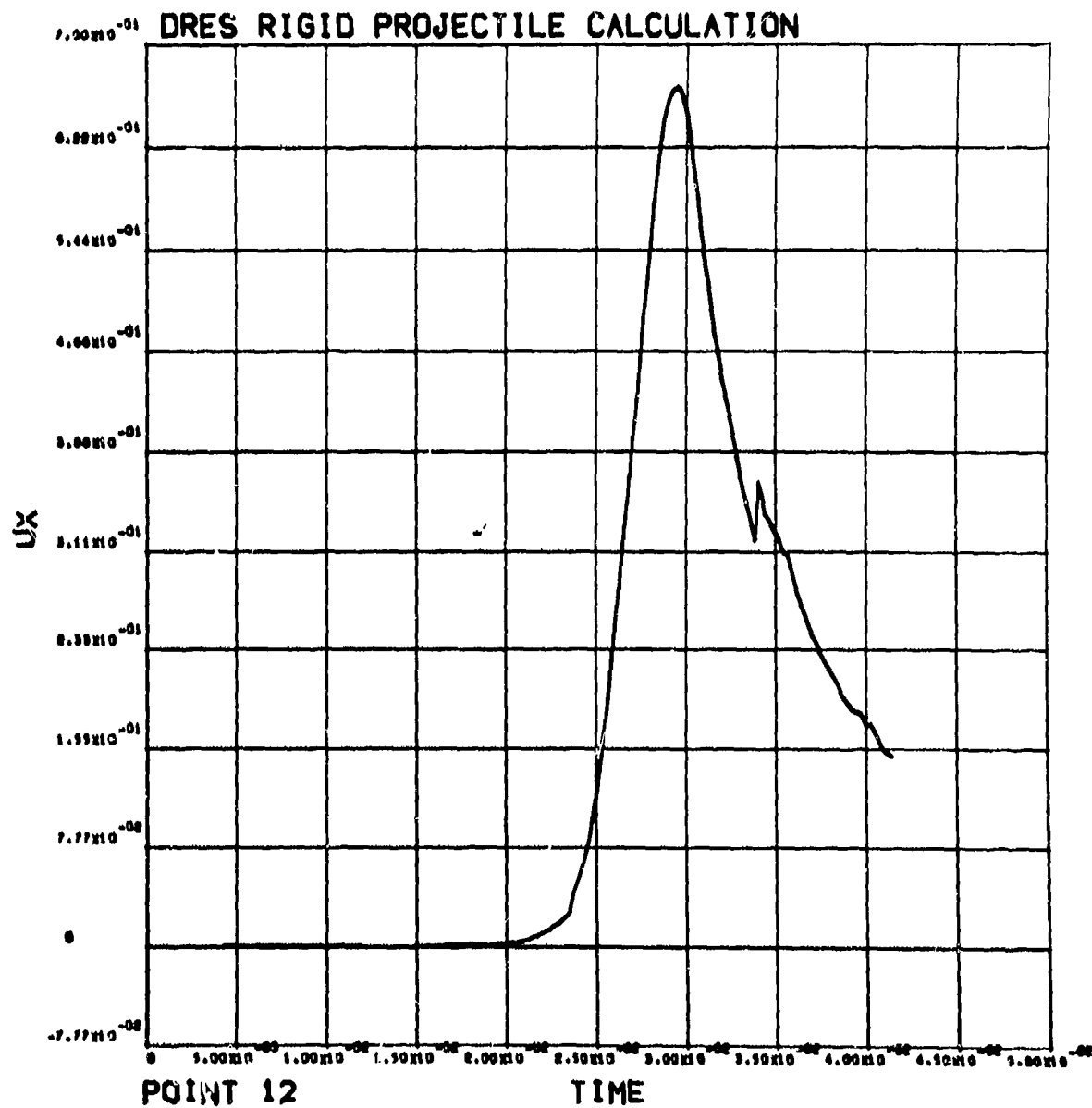
Figure A-65

Radial Velocity (m/s) versus Time (s) for Particle at Point 12, Z = 3.6 m, R = 0.9 m.
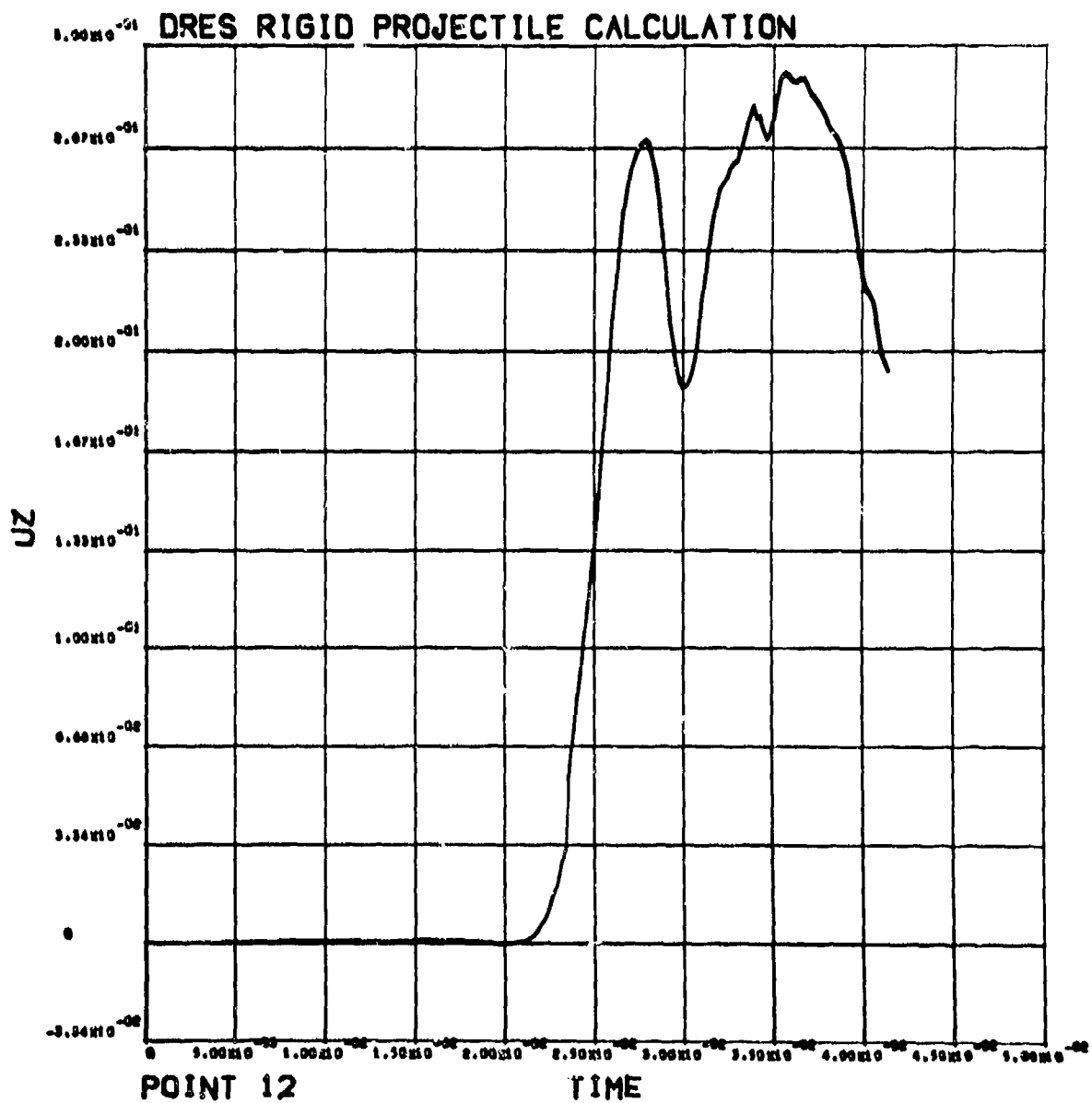
Figure A-66

Axial Velocity (m/s) versus Time (s) for Particle at Point 12, Z = 3.6 m, R = 0.9 m.

159
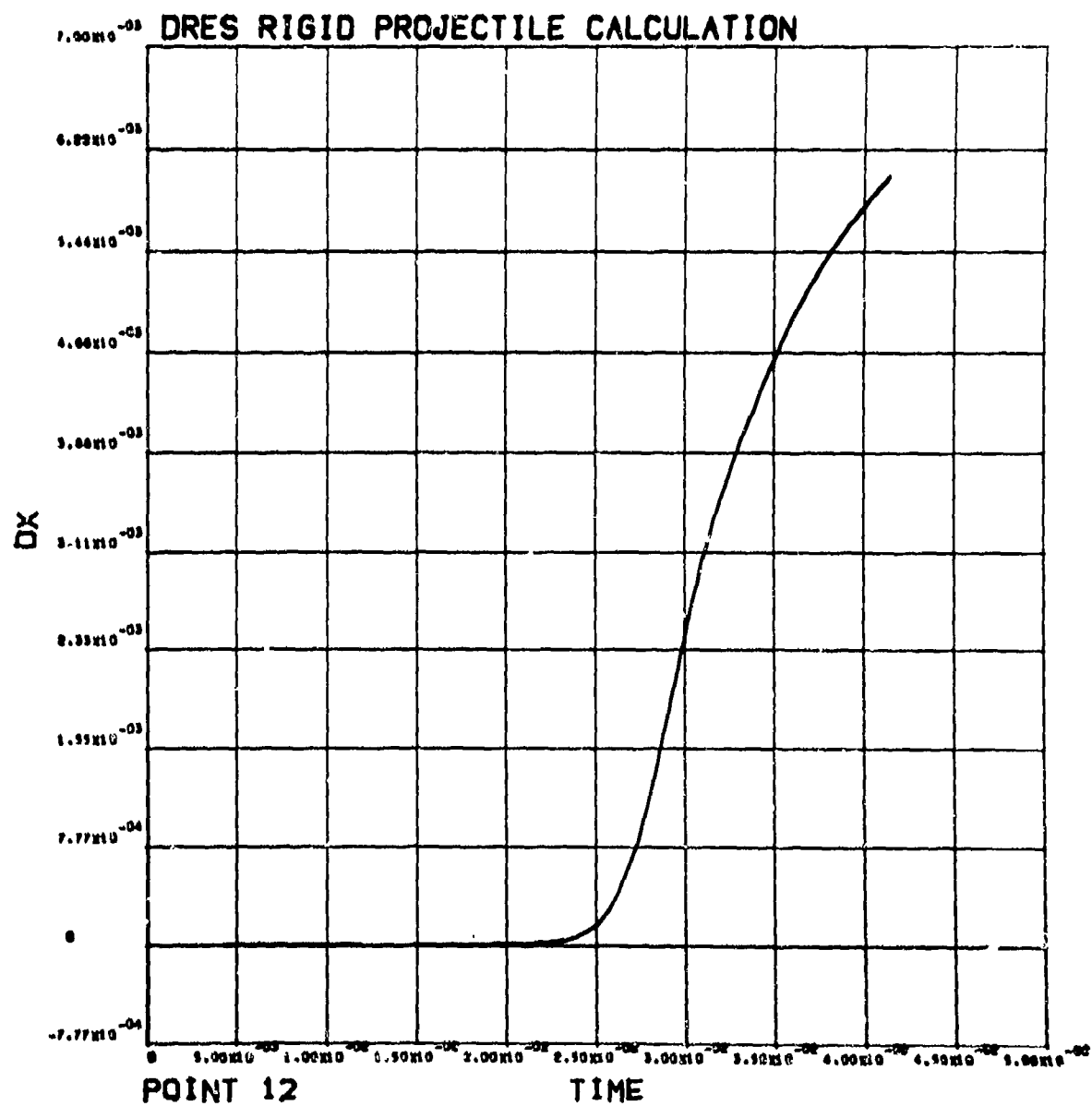
Figure A-67

Radial Displacement (m) versus Time (s) for Particle at Point 12, Z = 3.6 m, R = 0.9 m.

160
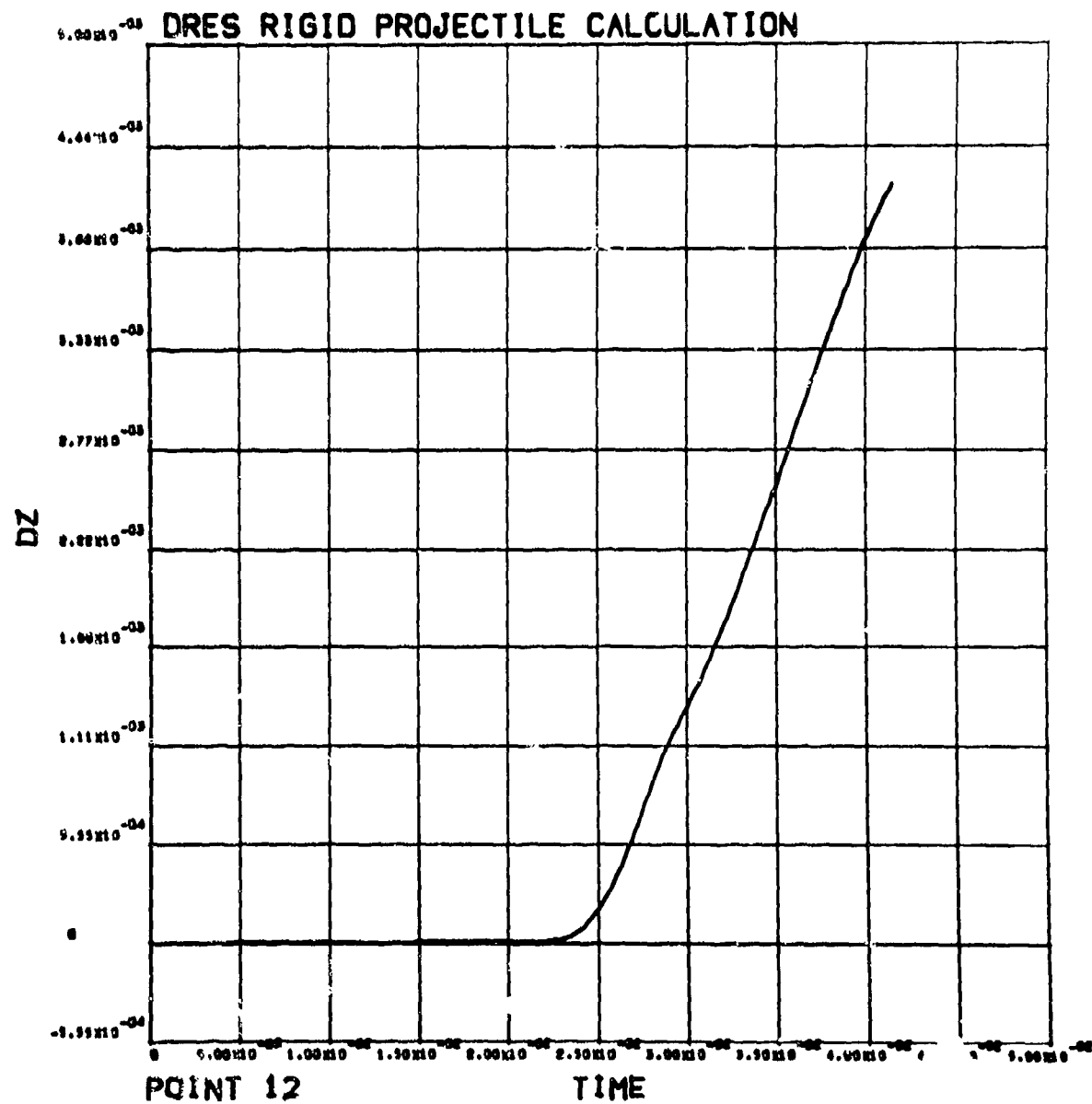
Figure A-68

Axial Displacement (m) versus Time (s) for Particle at Point 12, Z = 3.6 m, R = 0.9 m.
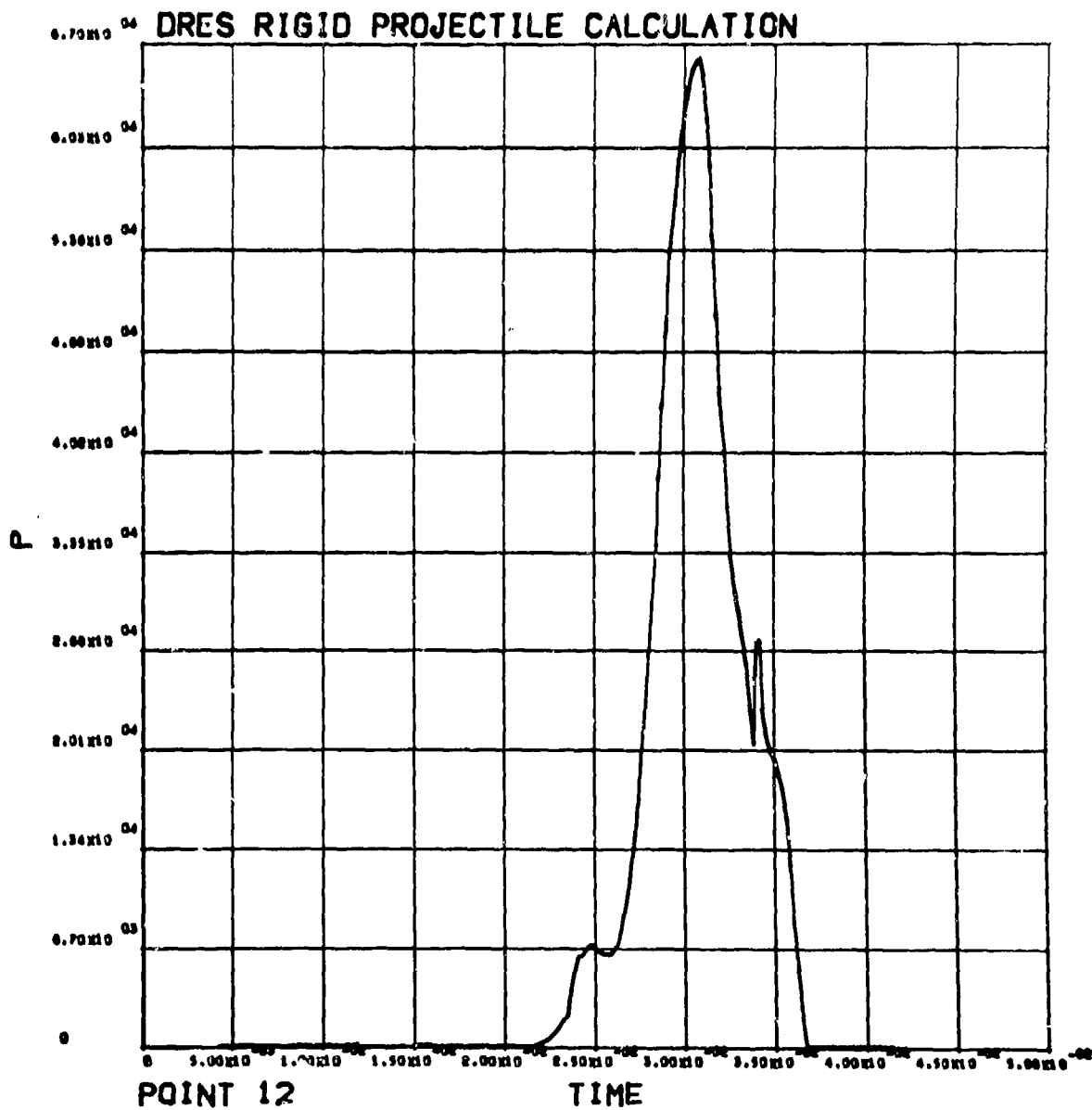
Figure A-69

Pressure (Pa) versus Time (s) for Particle at Point 12, Z = 3.6 m, R = 0.9 m.
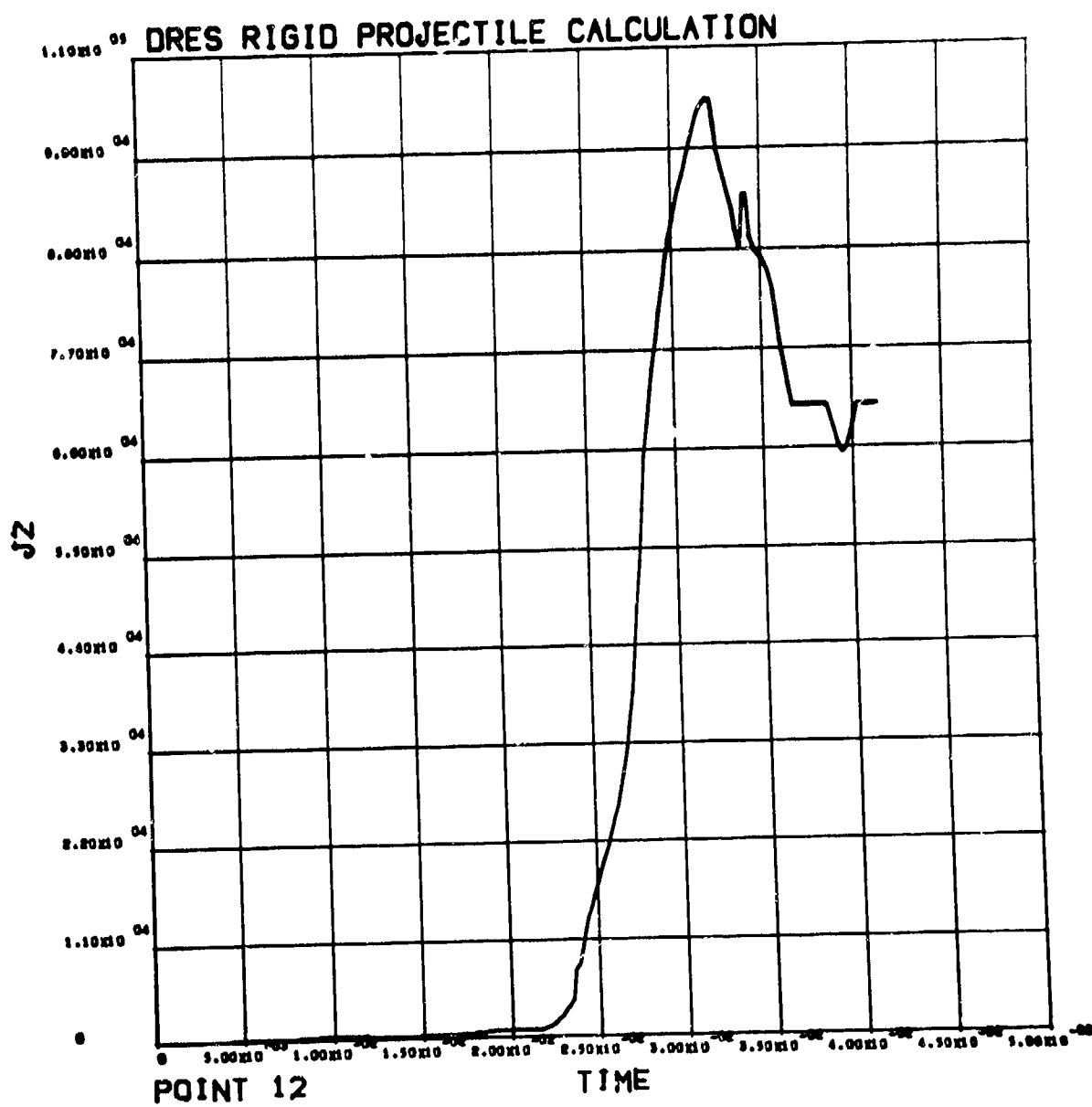
Figure A-70

Deviator Stress, J2, History (Pa) for Particle at Point 12, Z = 3.6 m, R = 0.9 m
(Octahedral Shear Stress = $\sqrt{2/3}(J2)$).

163
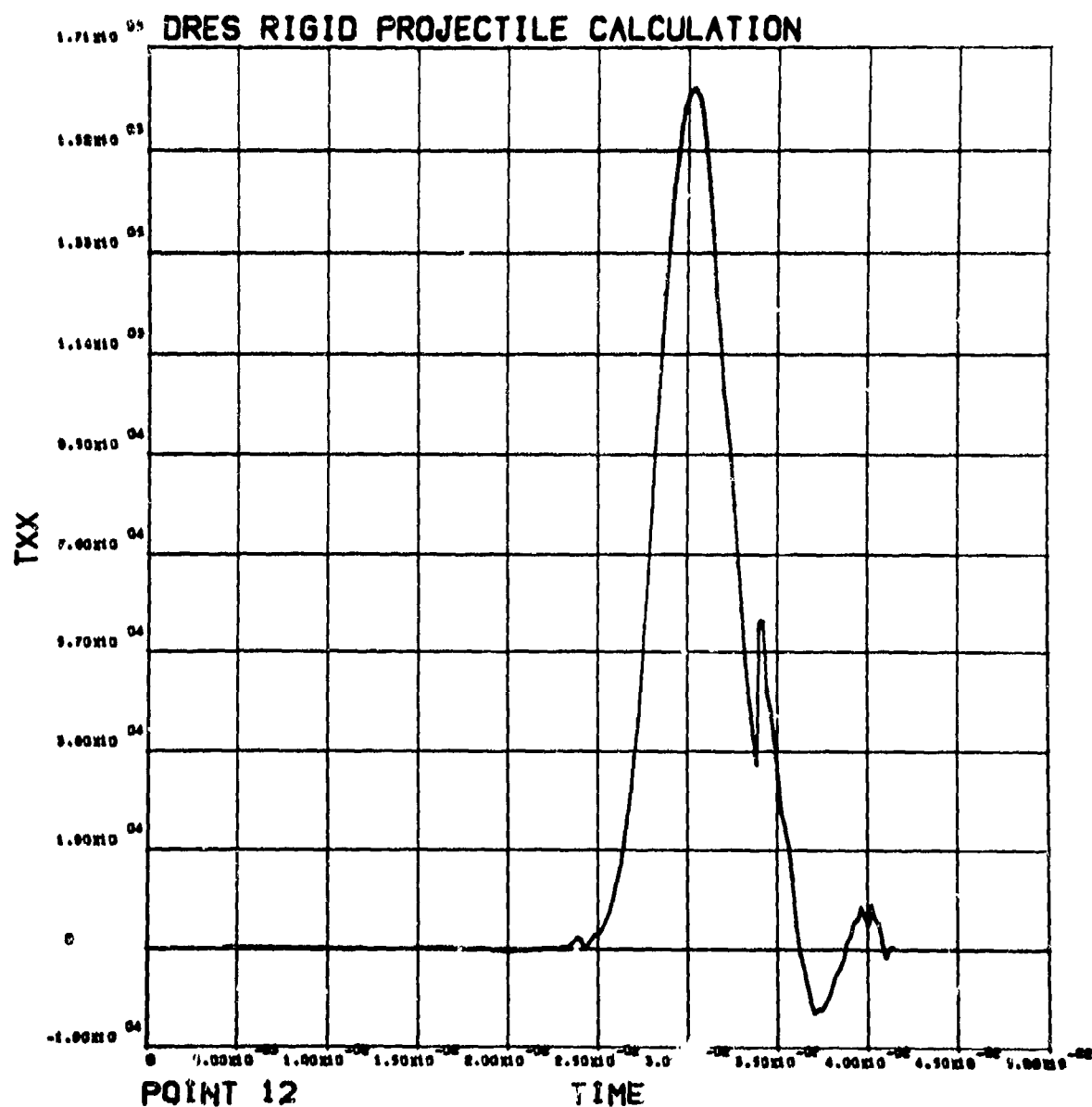
Figure A-71

Radial Stress (Pa) History for Particle at Point 12, Z = 3.6 m, R = 0.9 m.

164
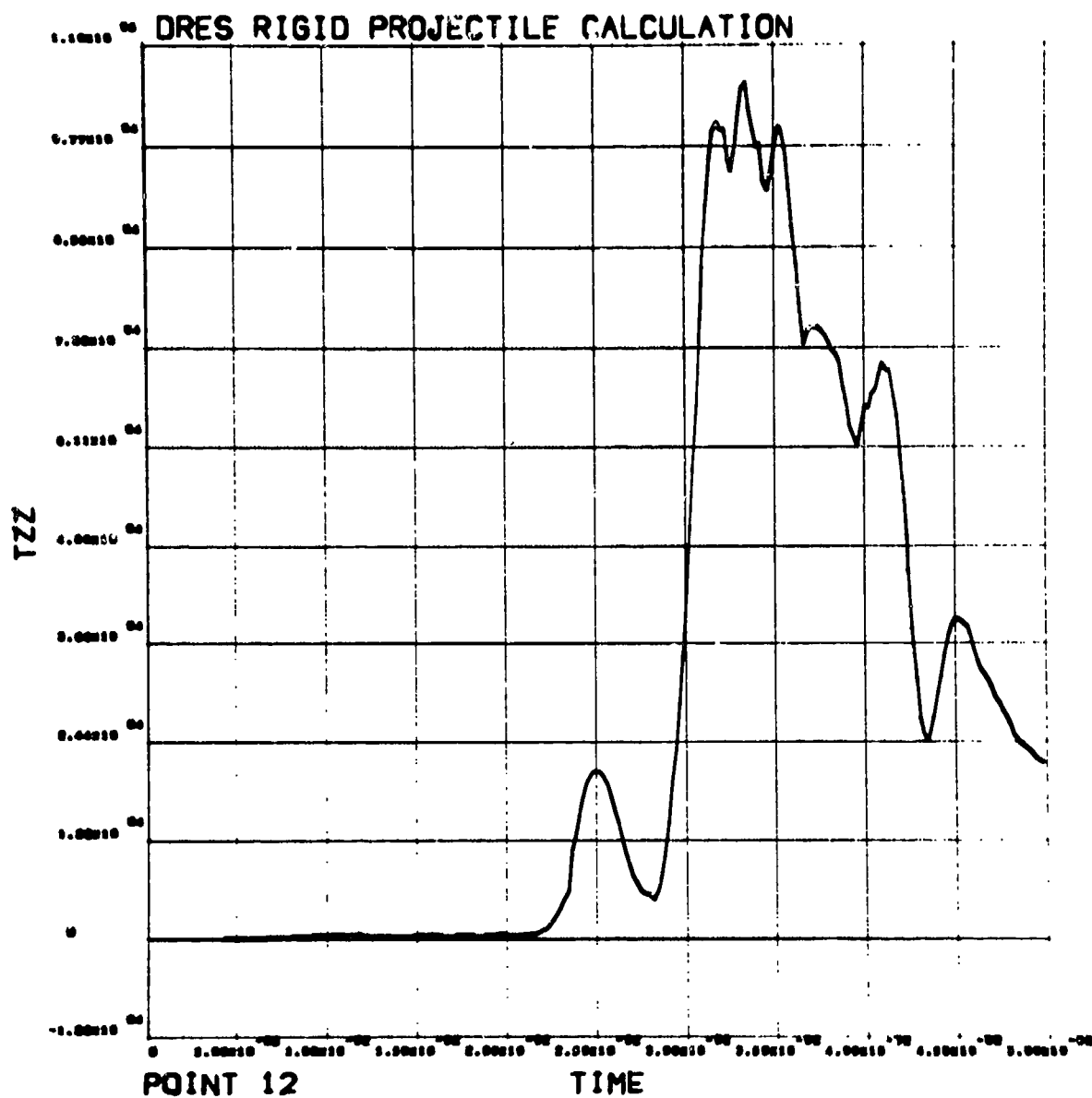
Figure A-72

Axial Stress (Pa) History for Particle at Point 12, Z = 3.6 m, R = 0.9 m.

165
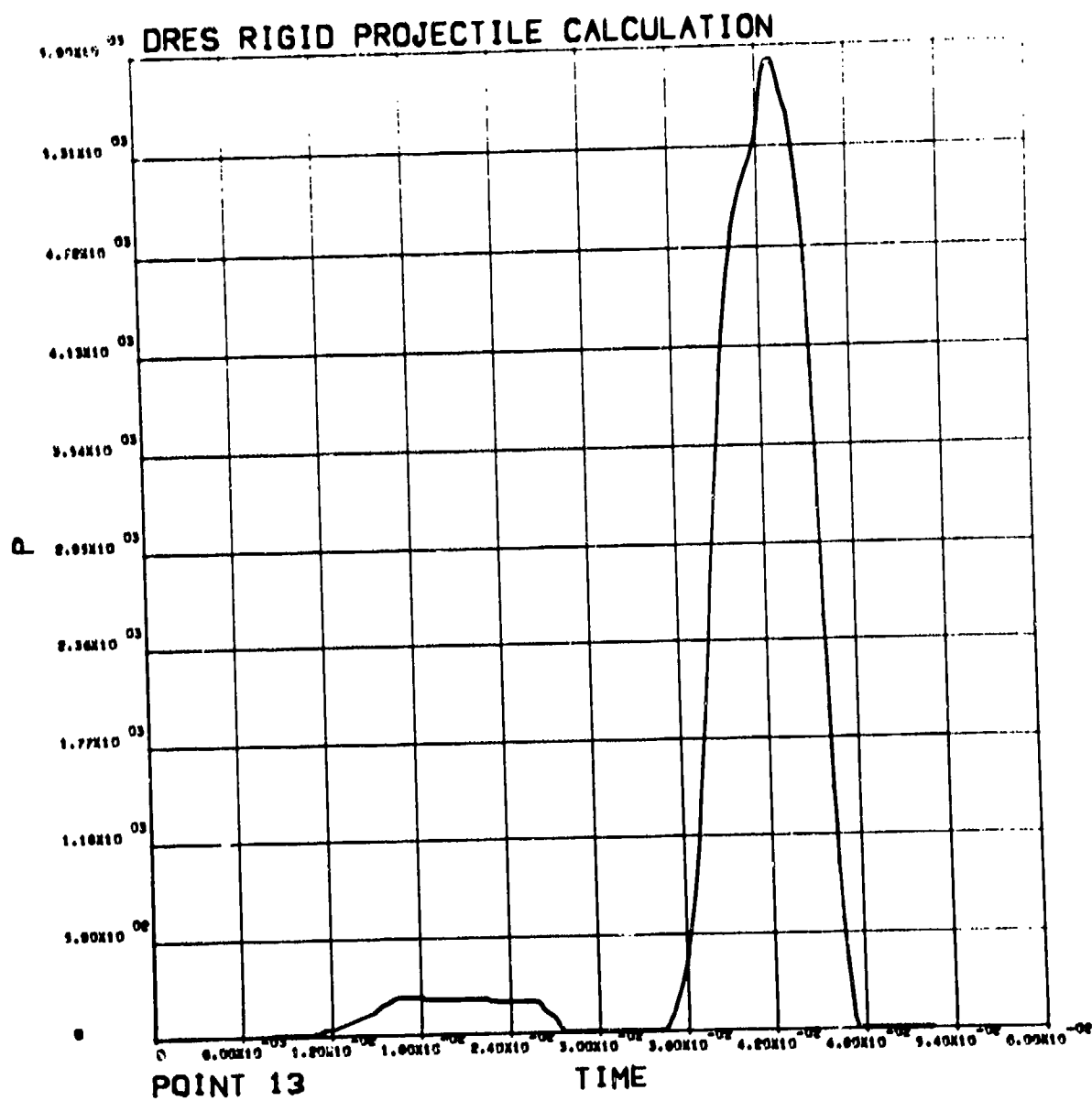
Figure A-73

Pressure (Pa) versus Time (ε) for Particle at Point 13, $Z = 5.4$ m, $R = 1.5$ m.

166
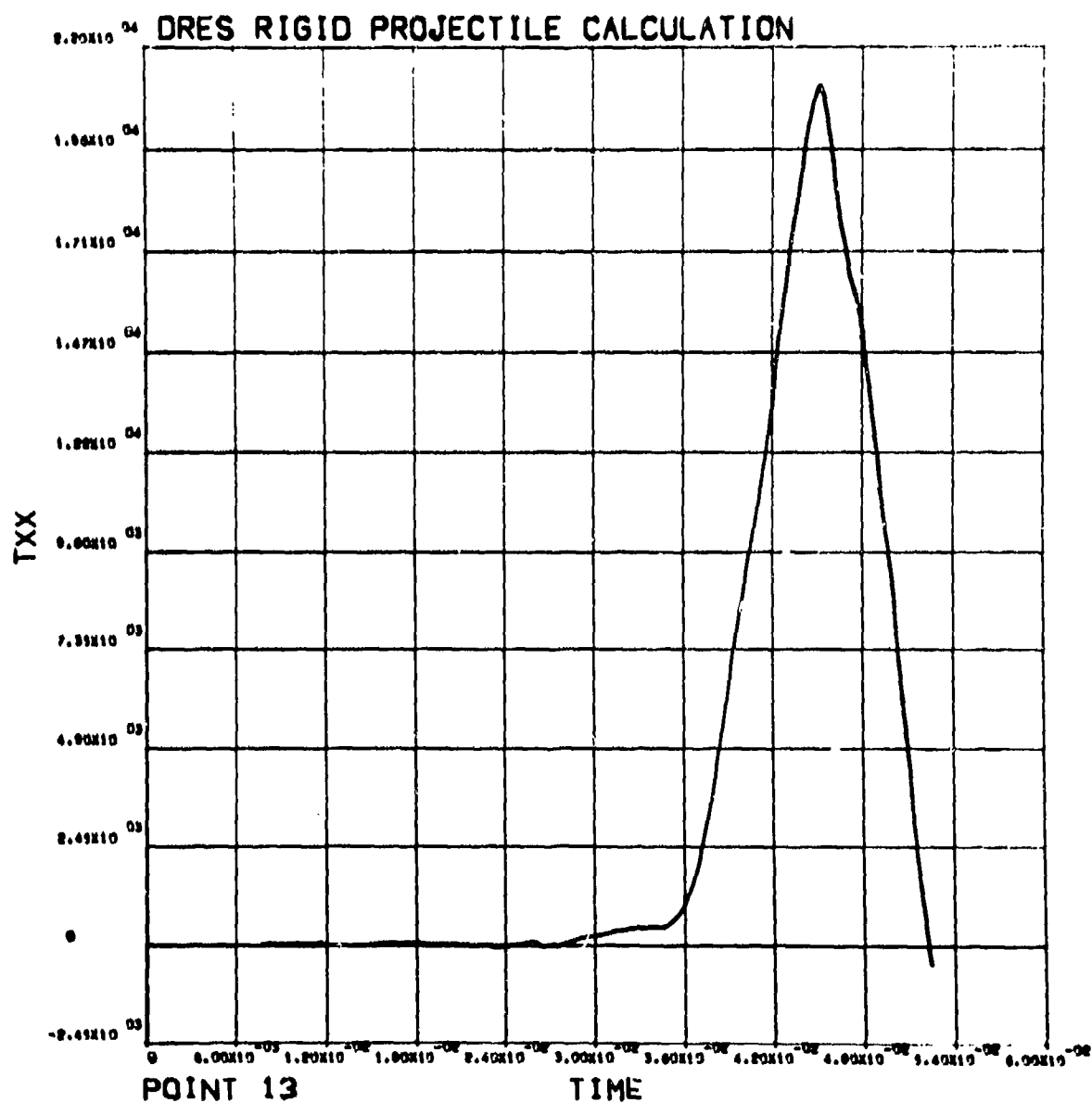
Figure A-74

Radial Stress (Pa) History for Particle at Point 13, Z = 5.4 m, R = 1.5 m.

DRES RIGID PROJECTILE CALCULATION
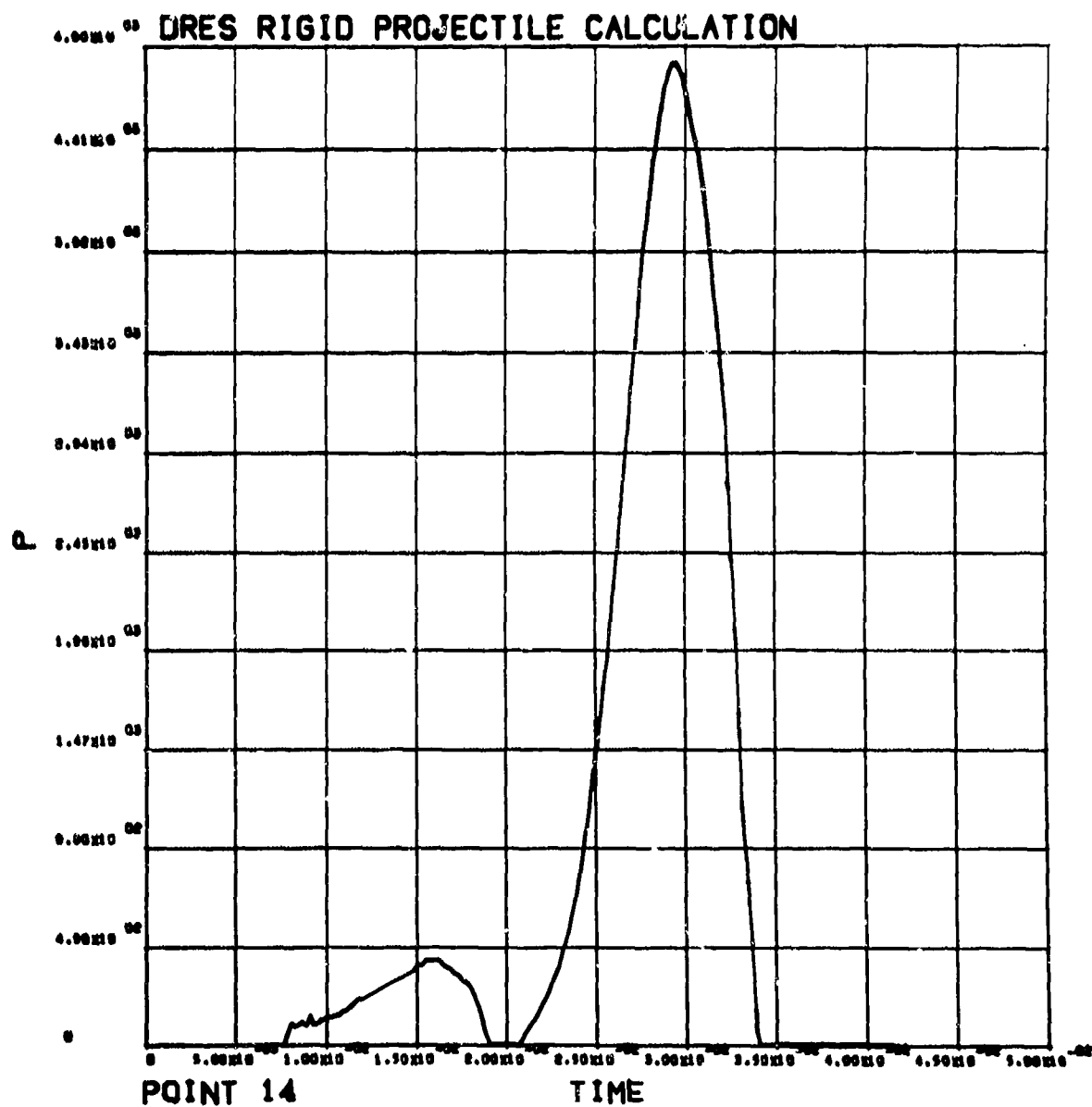
Figure A-75

Pressure (Pa) versus Time (s) for Particle at Point 14, Z = 3.6 m, R = 1.5 m.

168
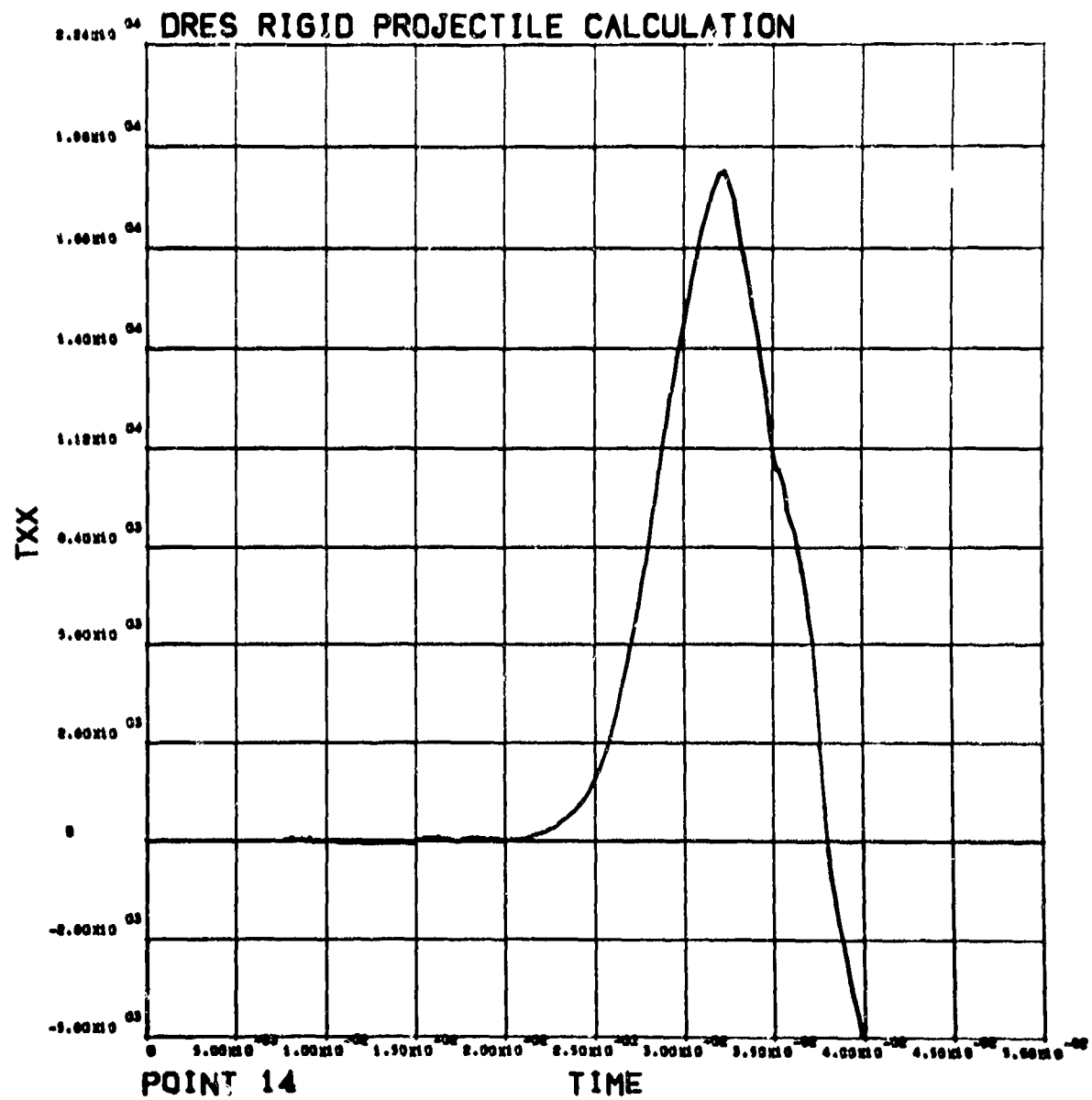
Figure A-76

Radial Stress (Pa) History for Particle at Point 14, Z = 3.6 m, R = 1.5 m.
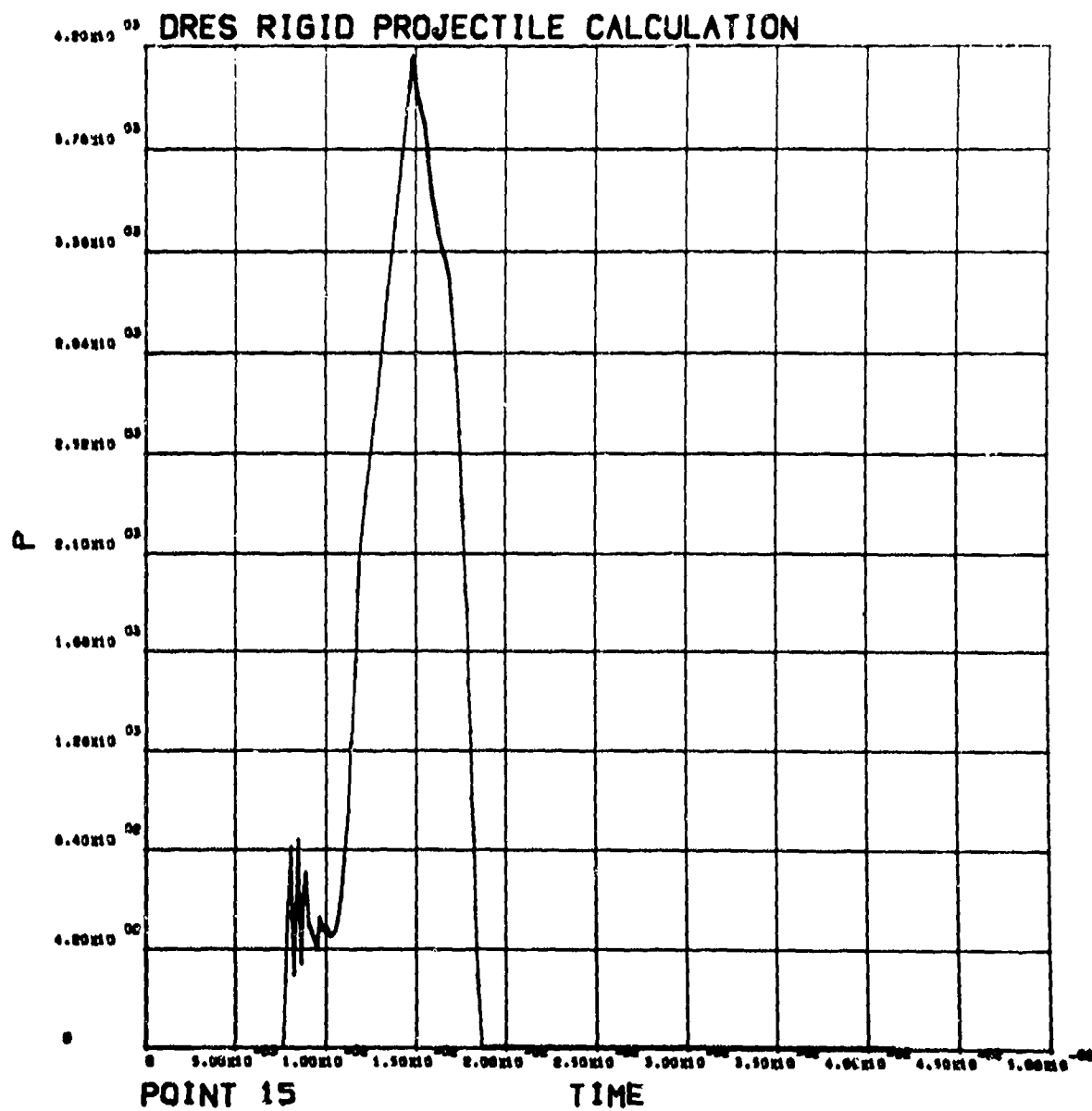
Figure A-77

Pressure (Pa) versus Time (s) for Particle at Point 15, Z = 1.8 m, R = 1.5 m.

DRES RIGID PROJECTILE CALCULATION

TXX
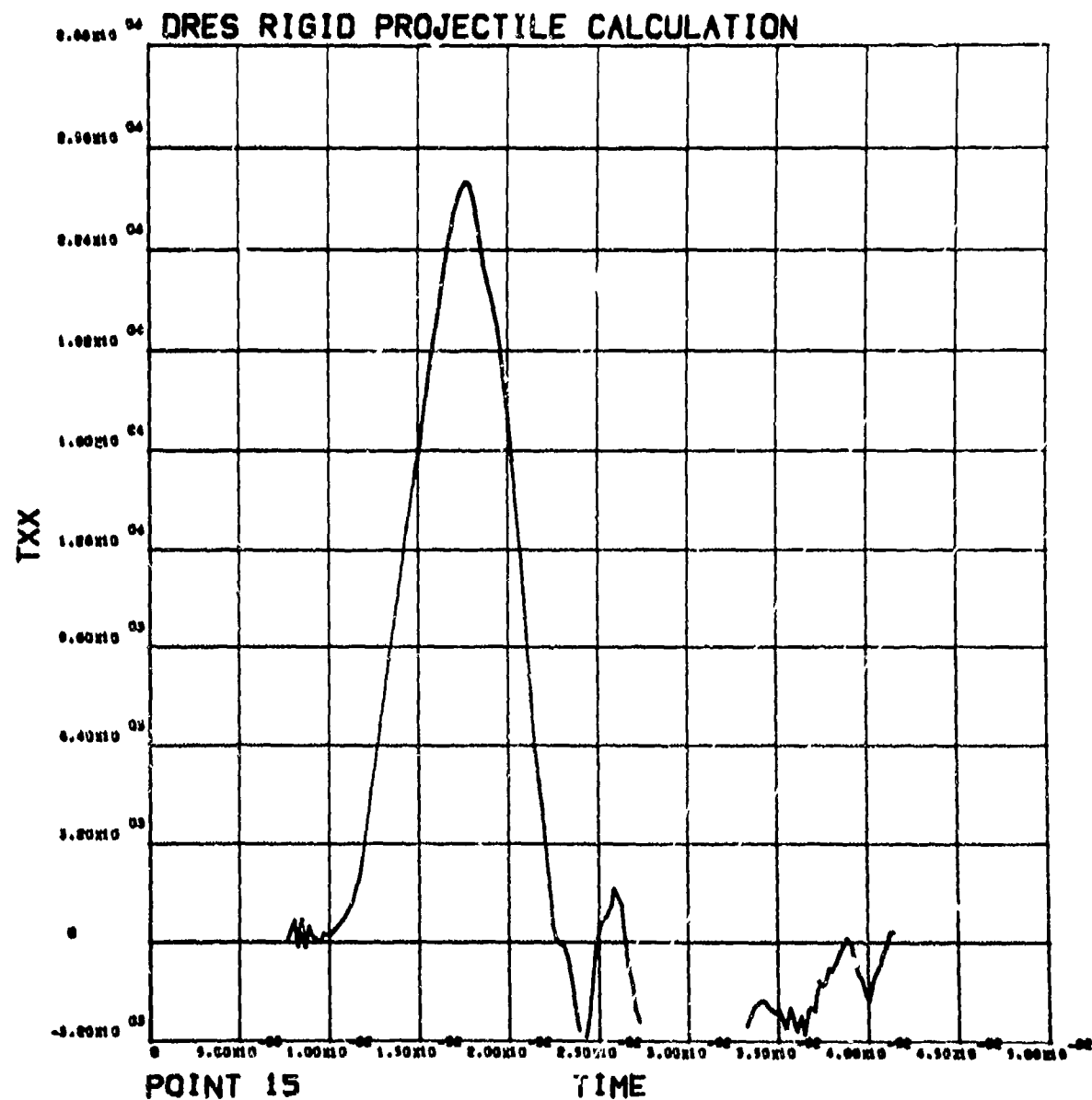
POINT 15   TIME

Figure A-78

Radial Stress (Pa) History for Particle at Point 15, Z = 1.8 m, R = 1.5 m.

171
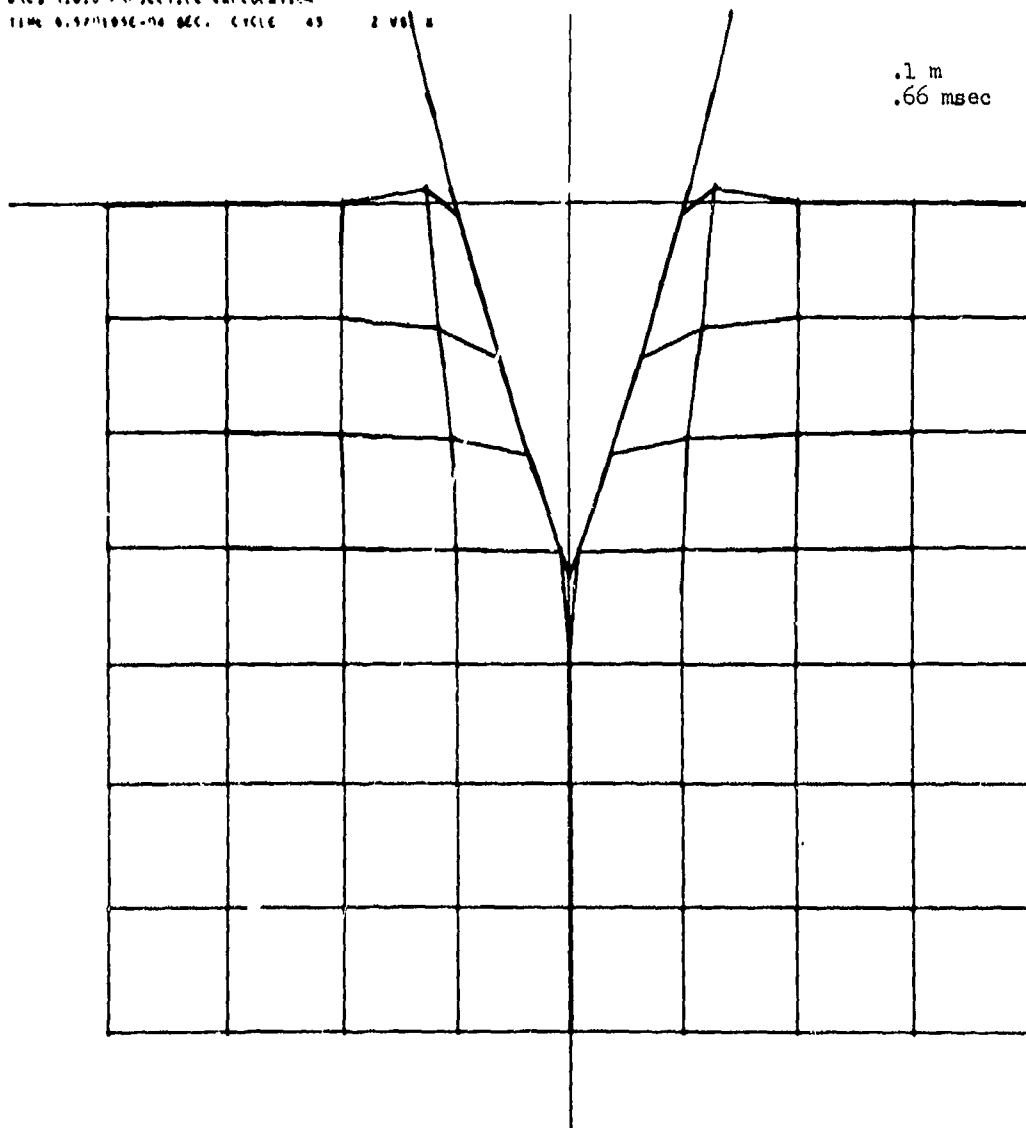
Figure A-79

Lagrangian Coordinates When Projectile Has Penetrated to Depth of 0.1 m.
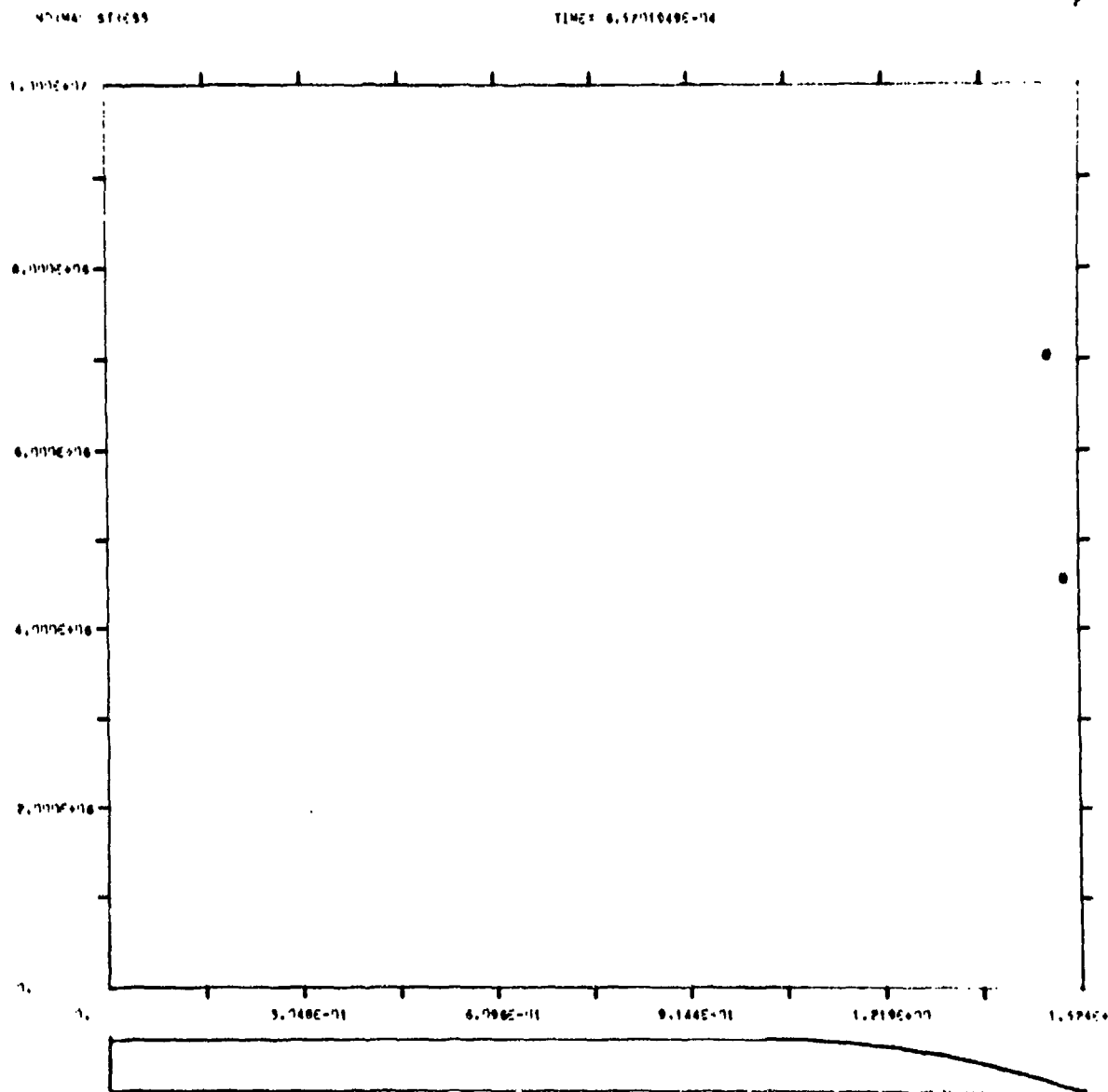
Figure A-80

Normal Stress (Pa) Along Surface of Projectile When Projectile is at 0.1 m Depth.
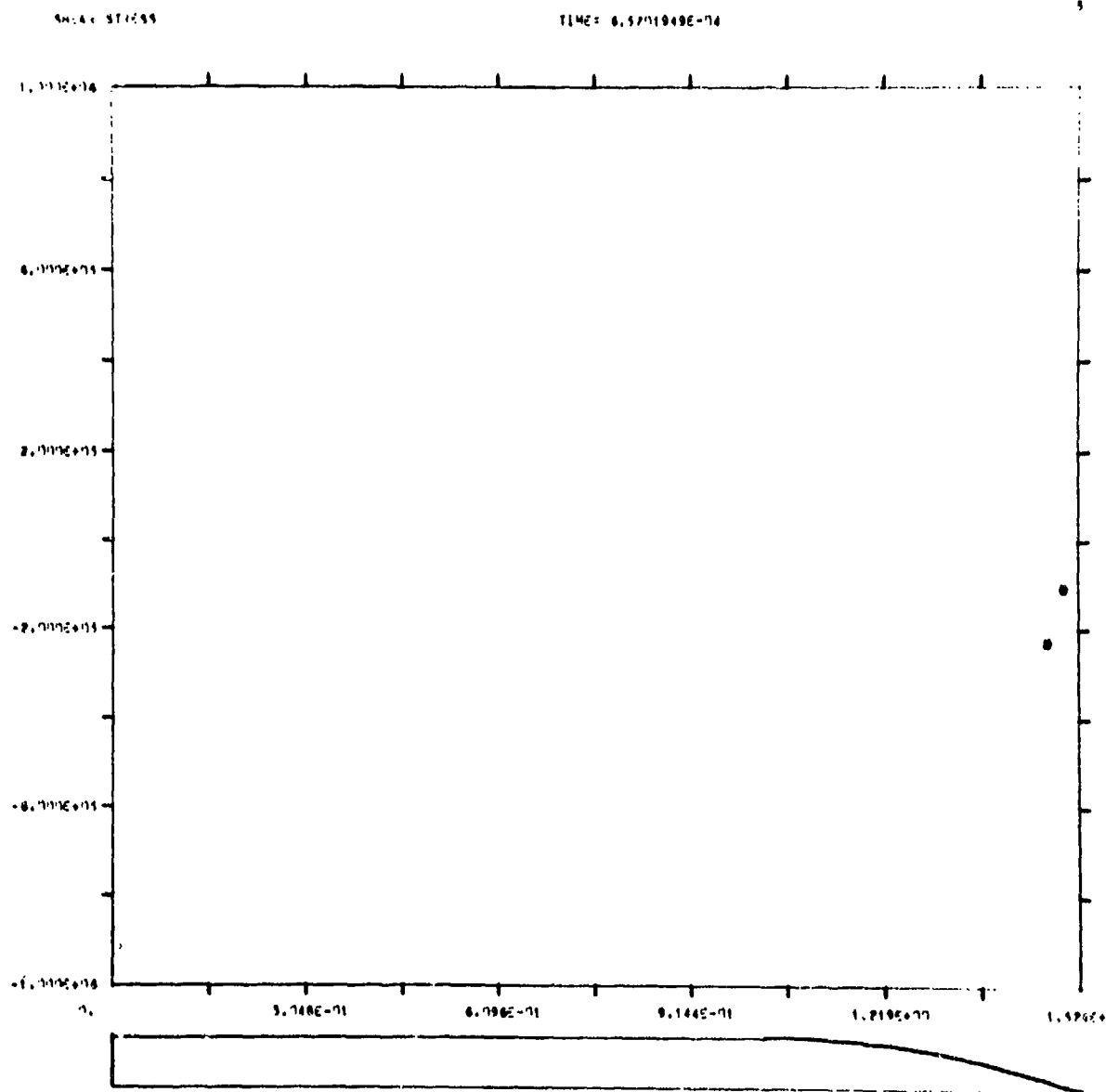
Figure A-81

Tangential Stress (Pa) Along Surface of Projectile When Projectile is at 0.1 m Depth.
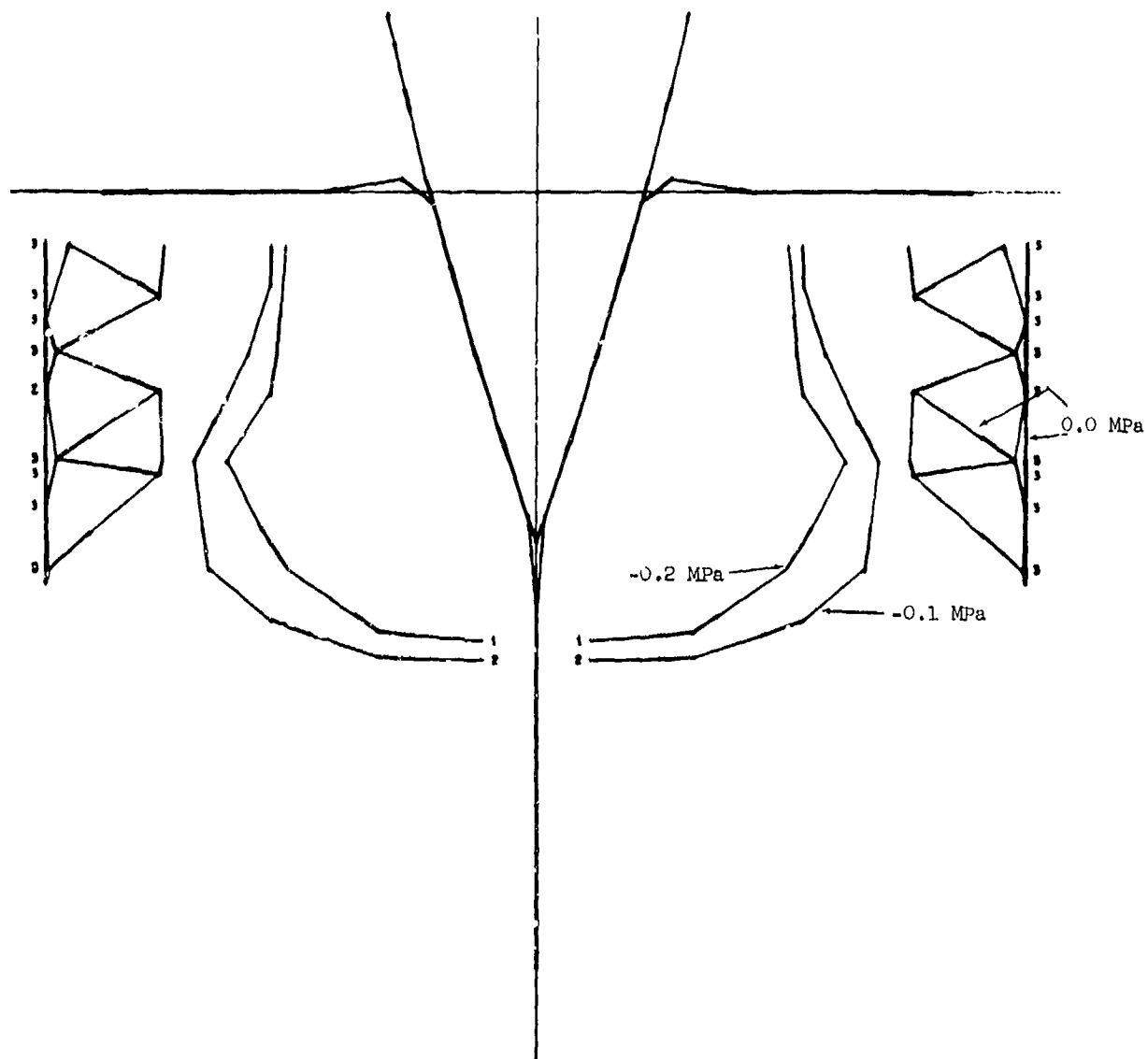
Figure A-82

Contours of Axial Stress in Target. Projectile at 0.1 m Depth.
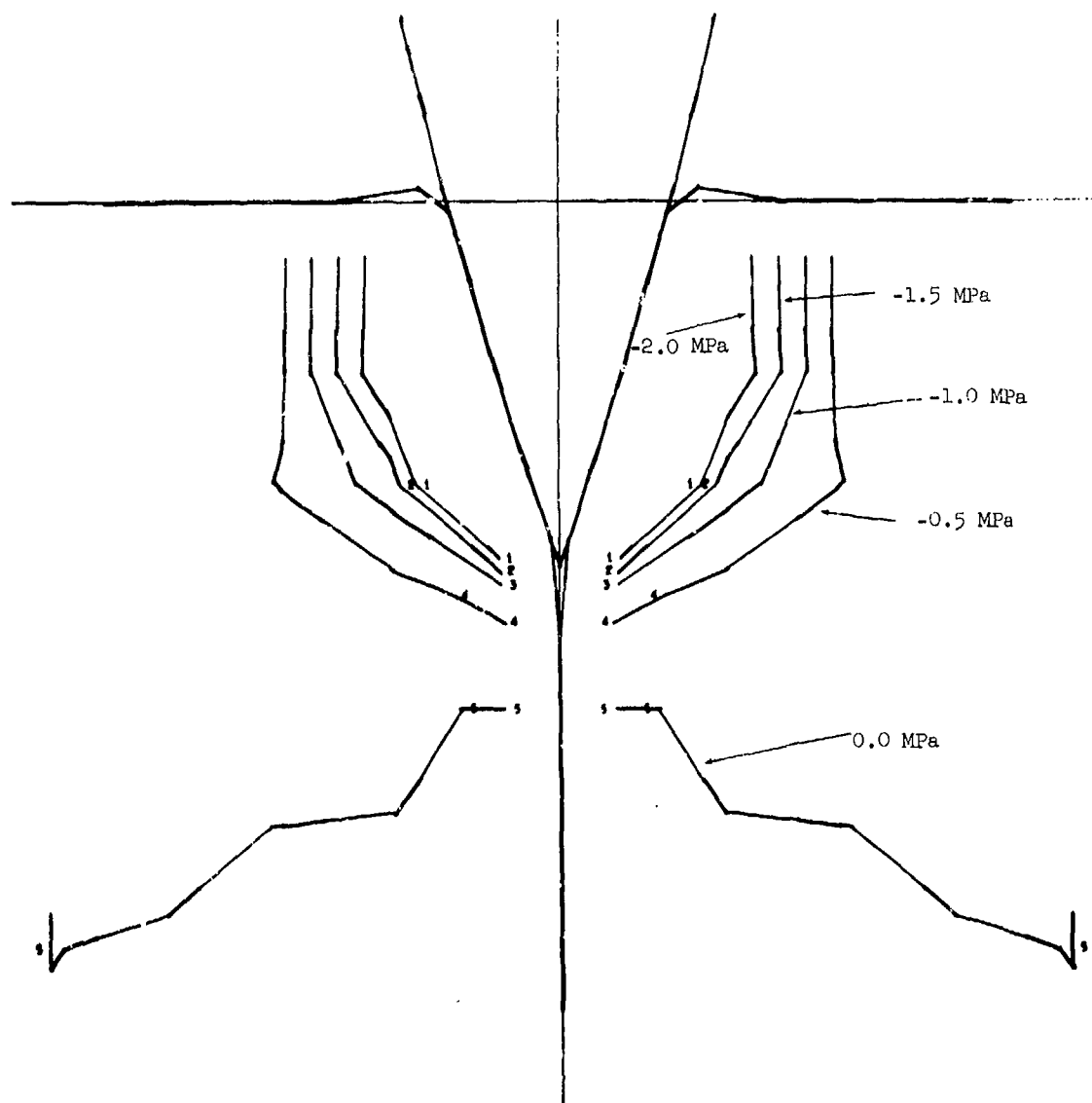
Figure A-83

Contours of Radial Stress in Target. Projectile at 0.1 m Depth.

176
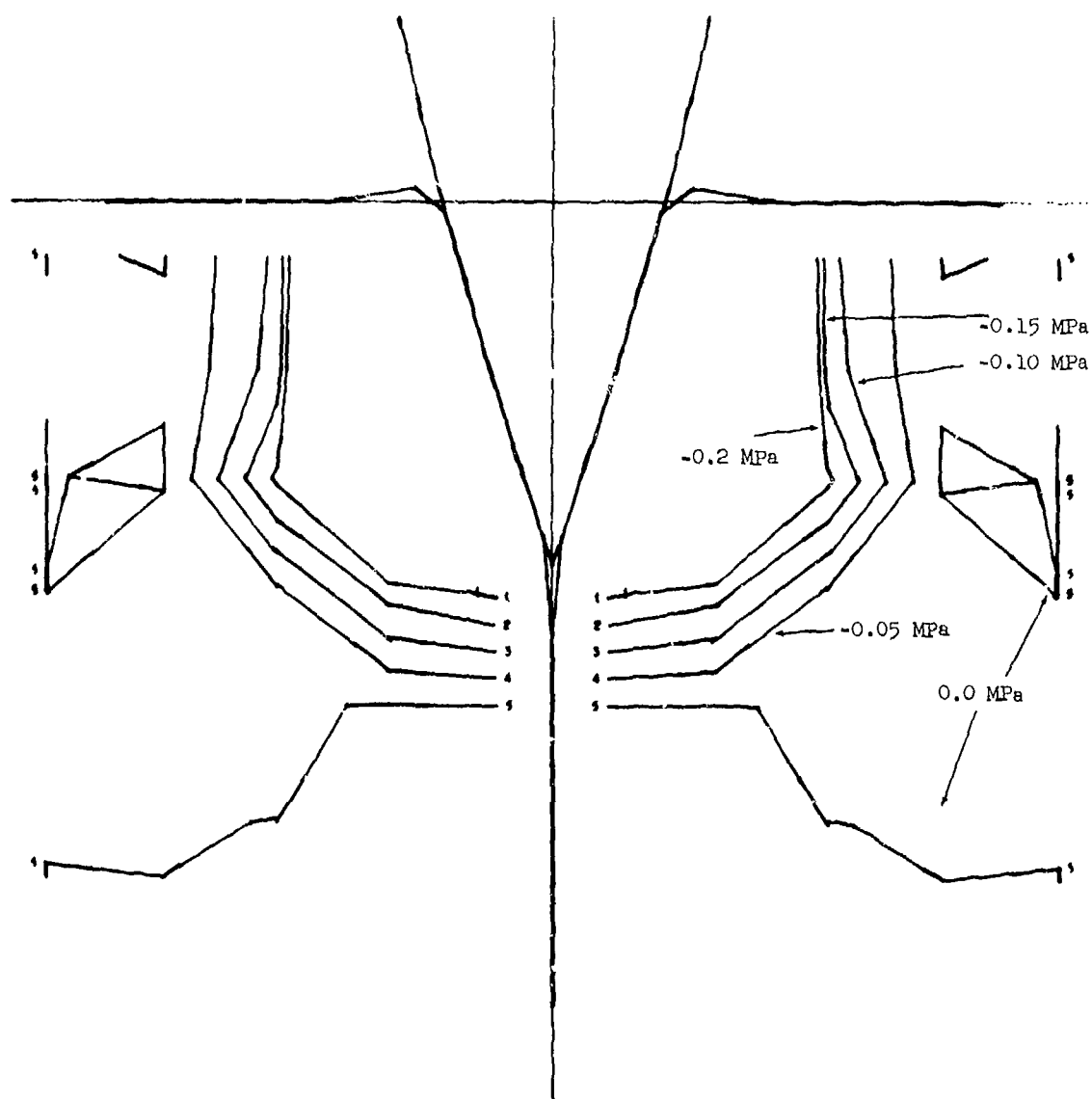
Figure A-84

Contours of Hoop Stress in Target. Projectile at 0.1 m Depth.

177
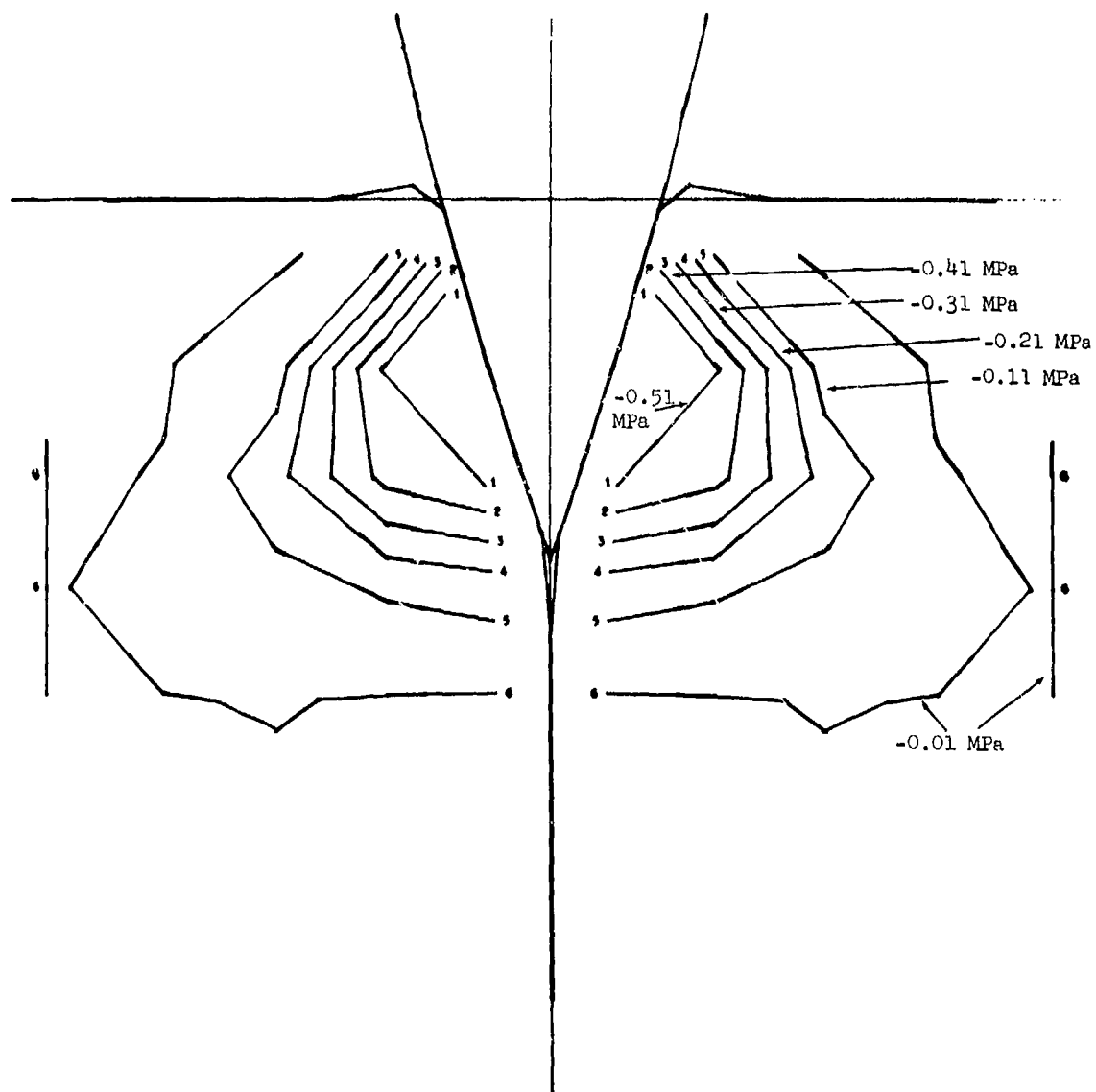
Figure A-85

Contours of Radial-Vertical Shear Stress in Target. Projectile at 0.1 m Depth.
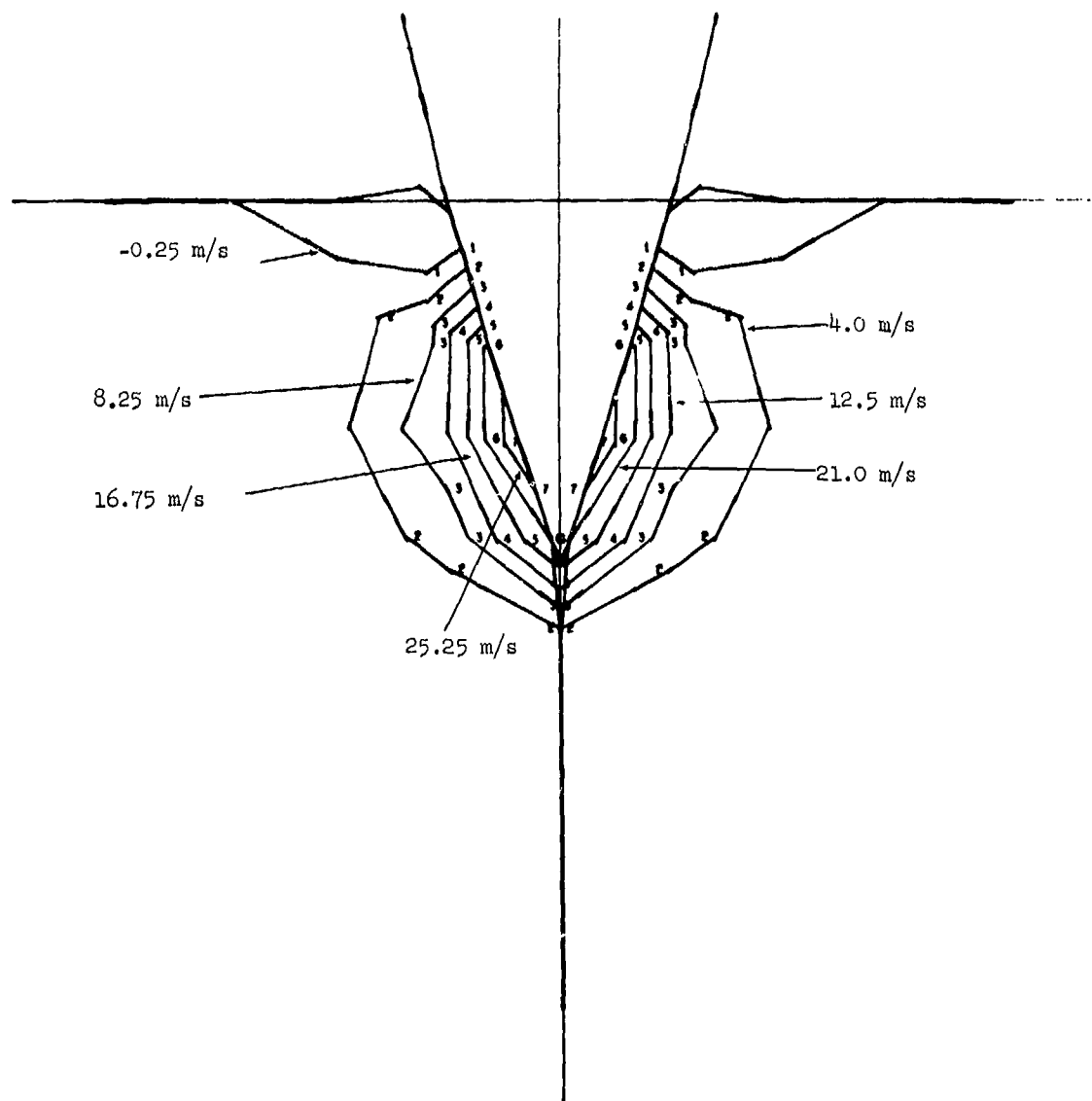
Figure A-86

Contours of Vertical Velocity in Target. Projectile at 0.1 m Depth.
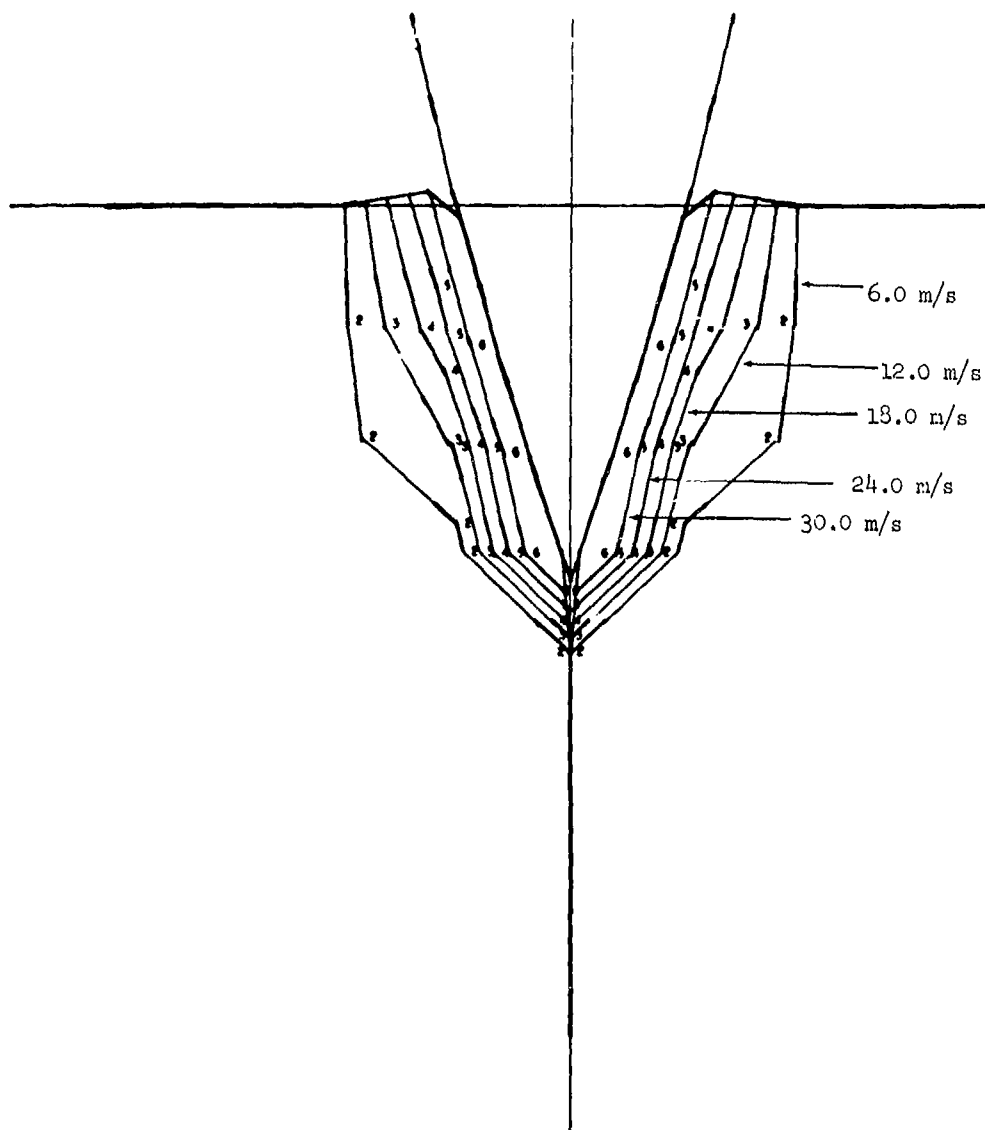
Figure A-87

Contours of Radial Velocity in Target. Projectile at 0.1 m Depth.
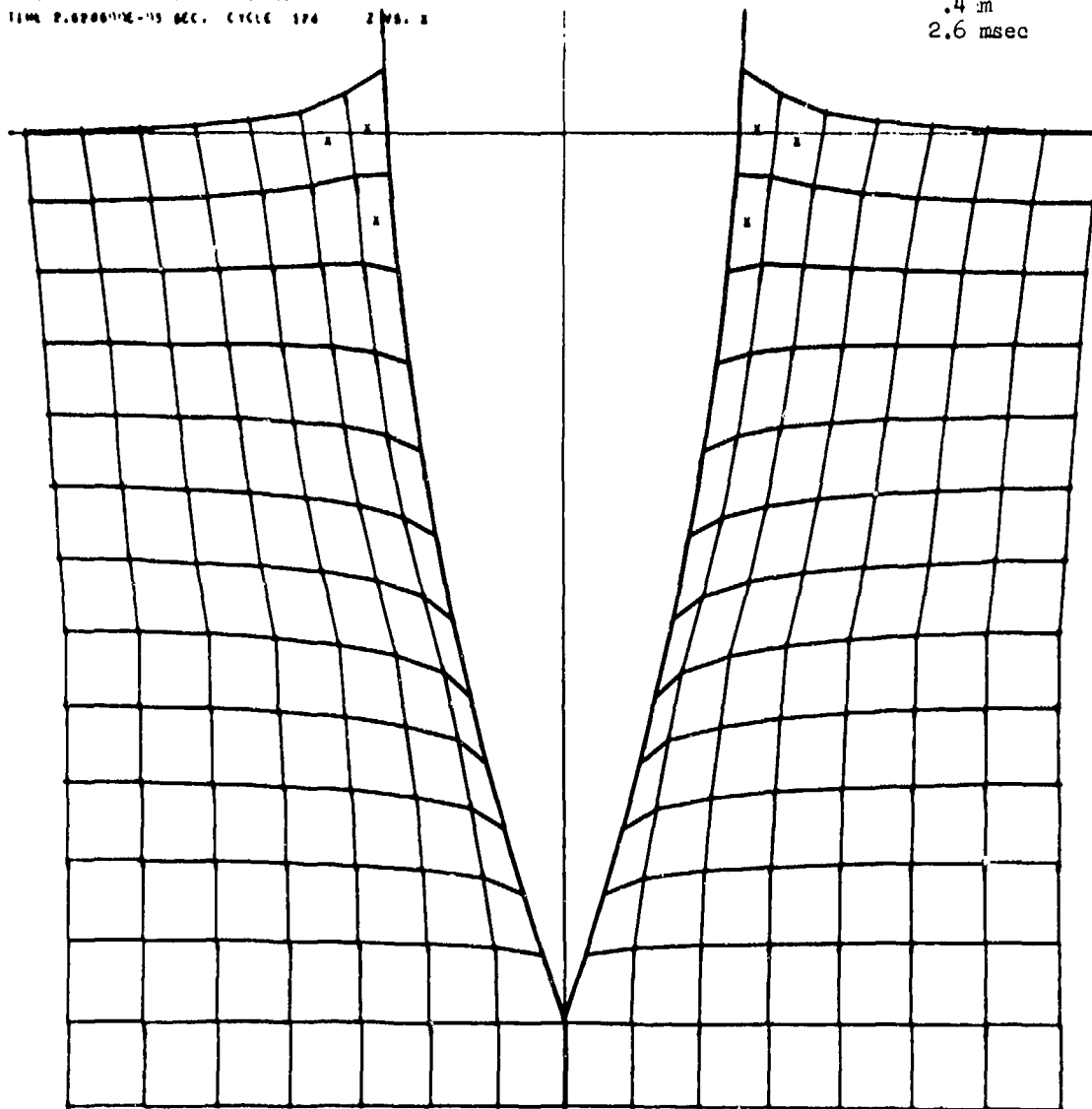
Figure A-88

Lagrangian Coordinates When Projectile has Penetrated to Depth of 0.4 m.
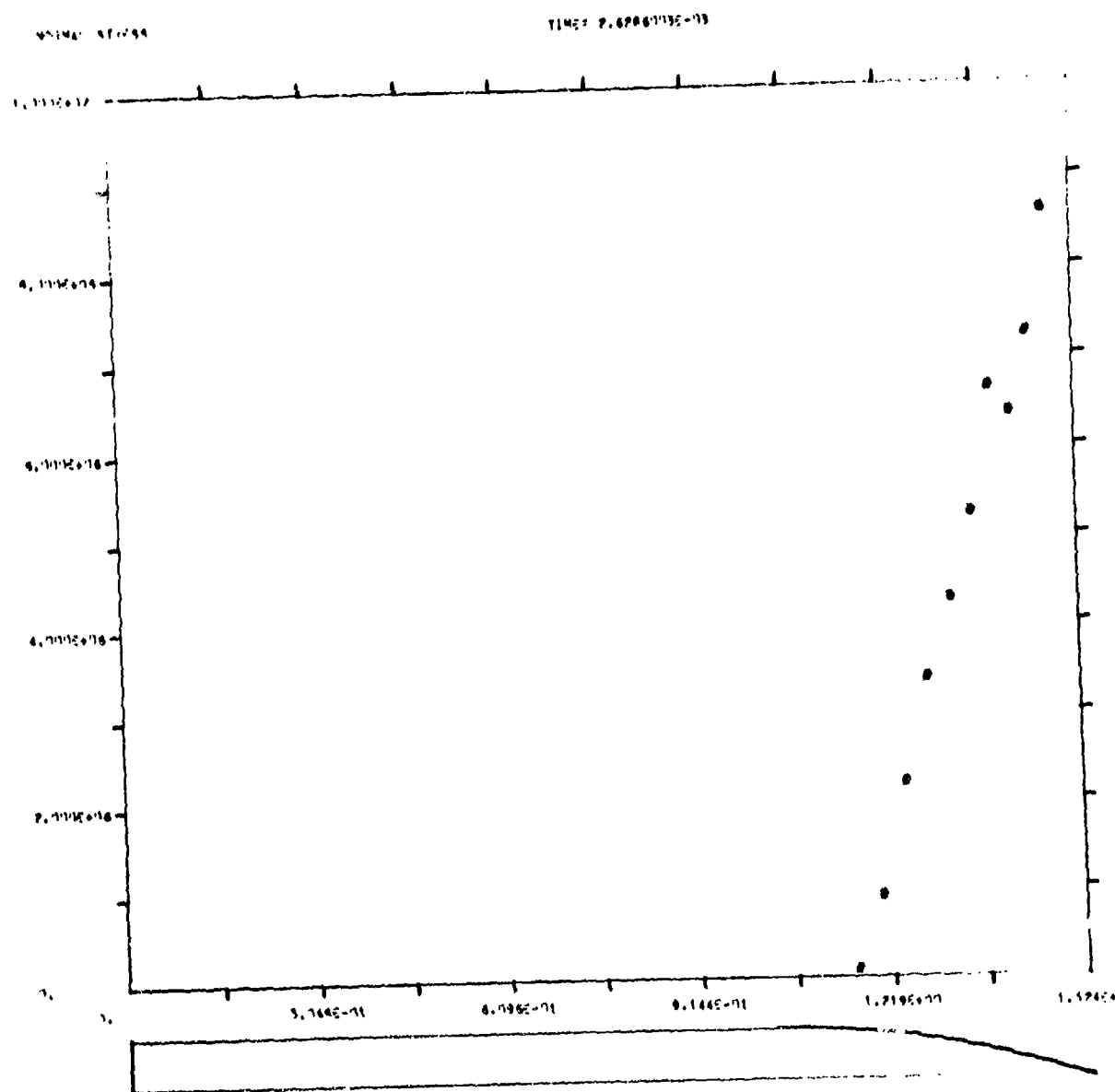
Figure A-89

Normal Stress (Pa) Along Surface of Projectile When Projectile is at 0.4 m Depth.
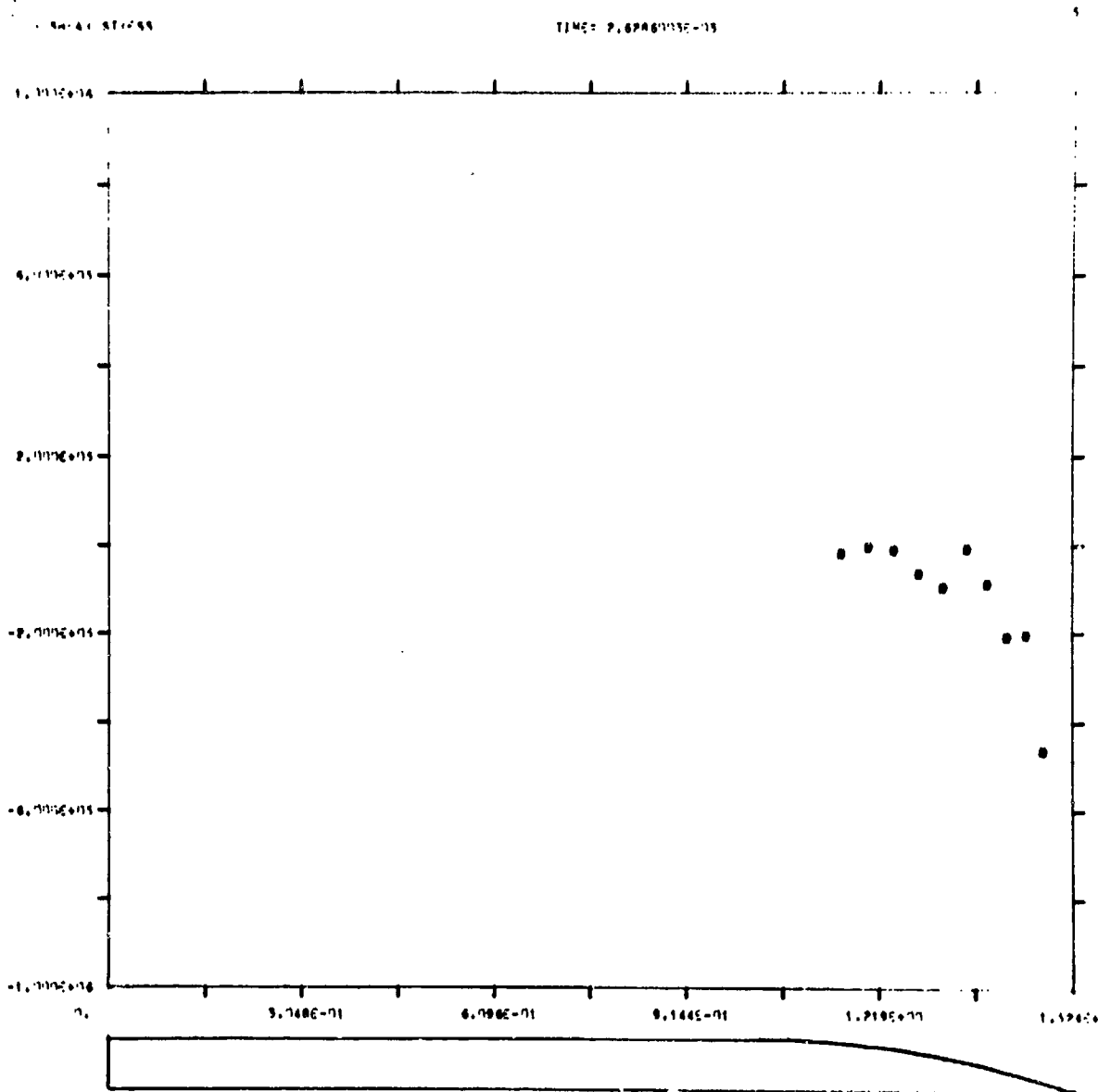
Figure A-90

Tangential Stress (Pa) Along Surface of Projectile When Projectile is at 0.4 m Depth.
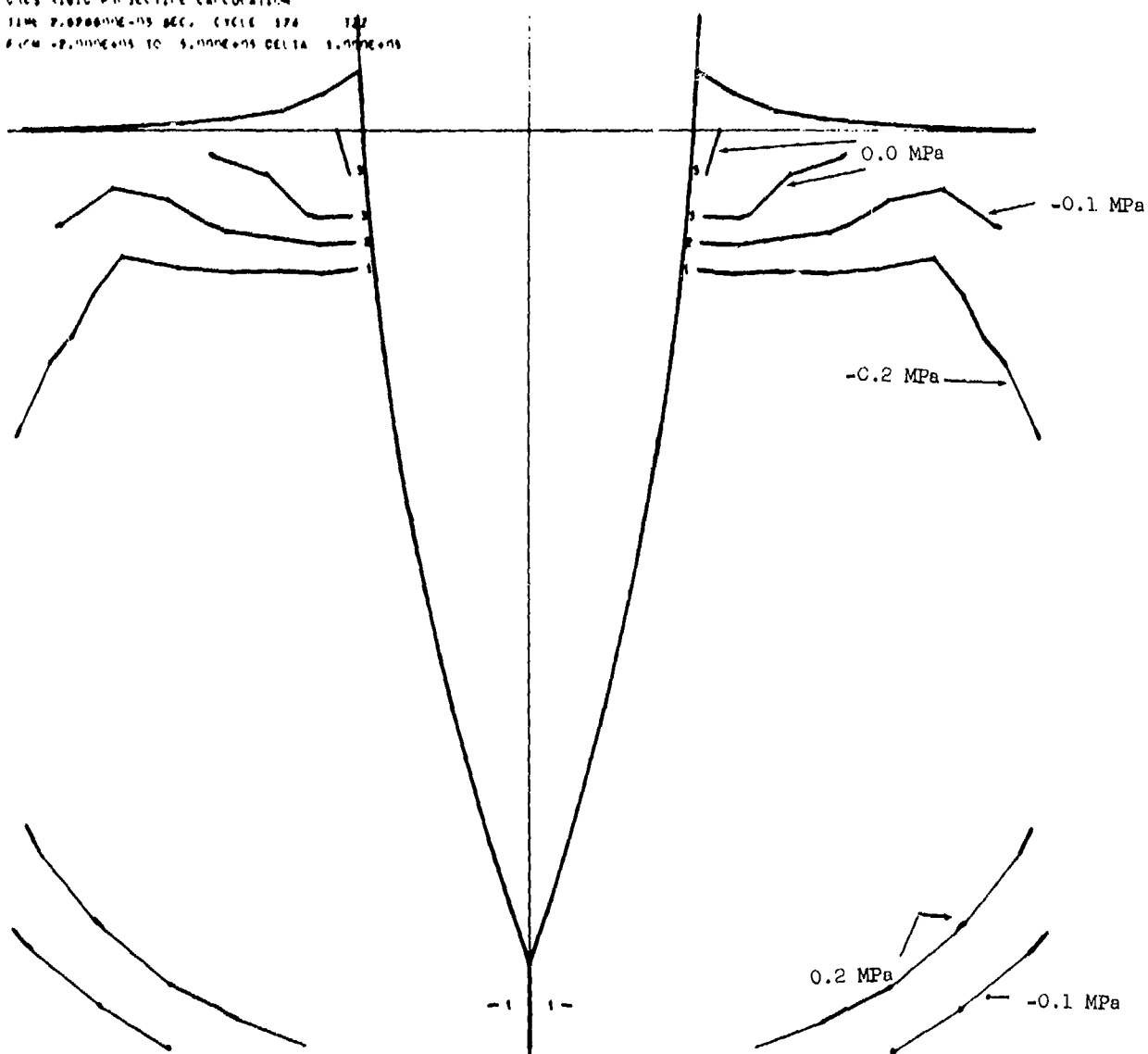
Figure A-91

Contours of Axial Stress in Target. Projectile at 0.4 m Depth.
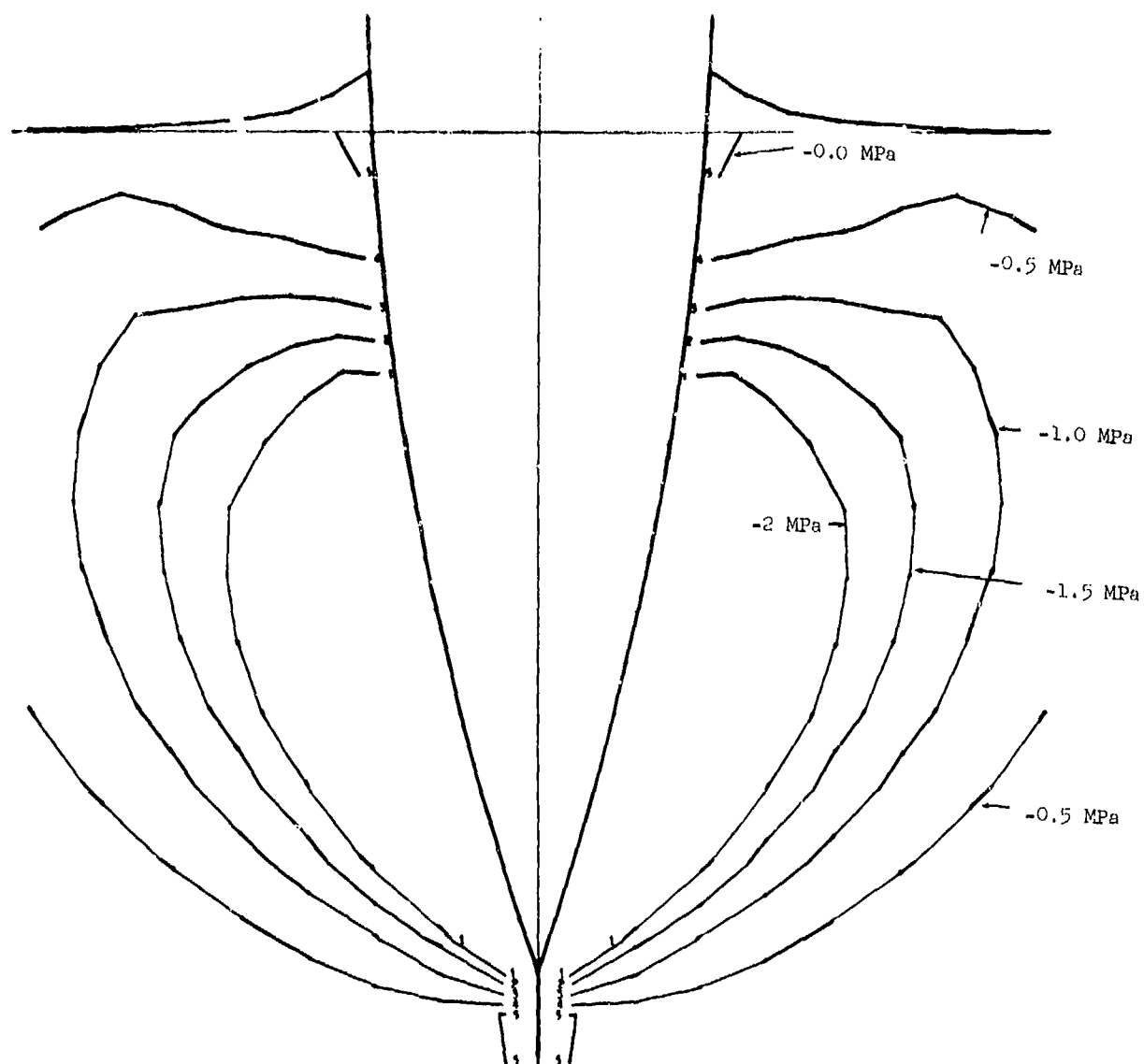
Figure A-92

Contours of Radial Stress in Target. Projectile at 0.4 m Depth.
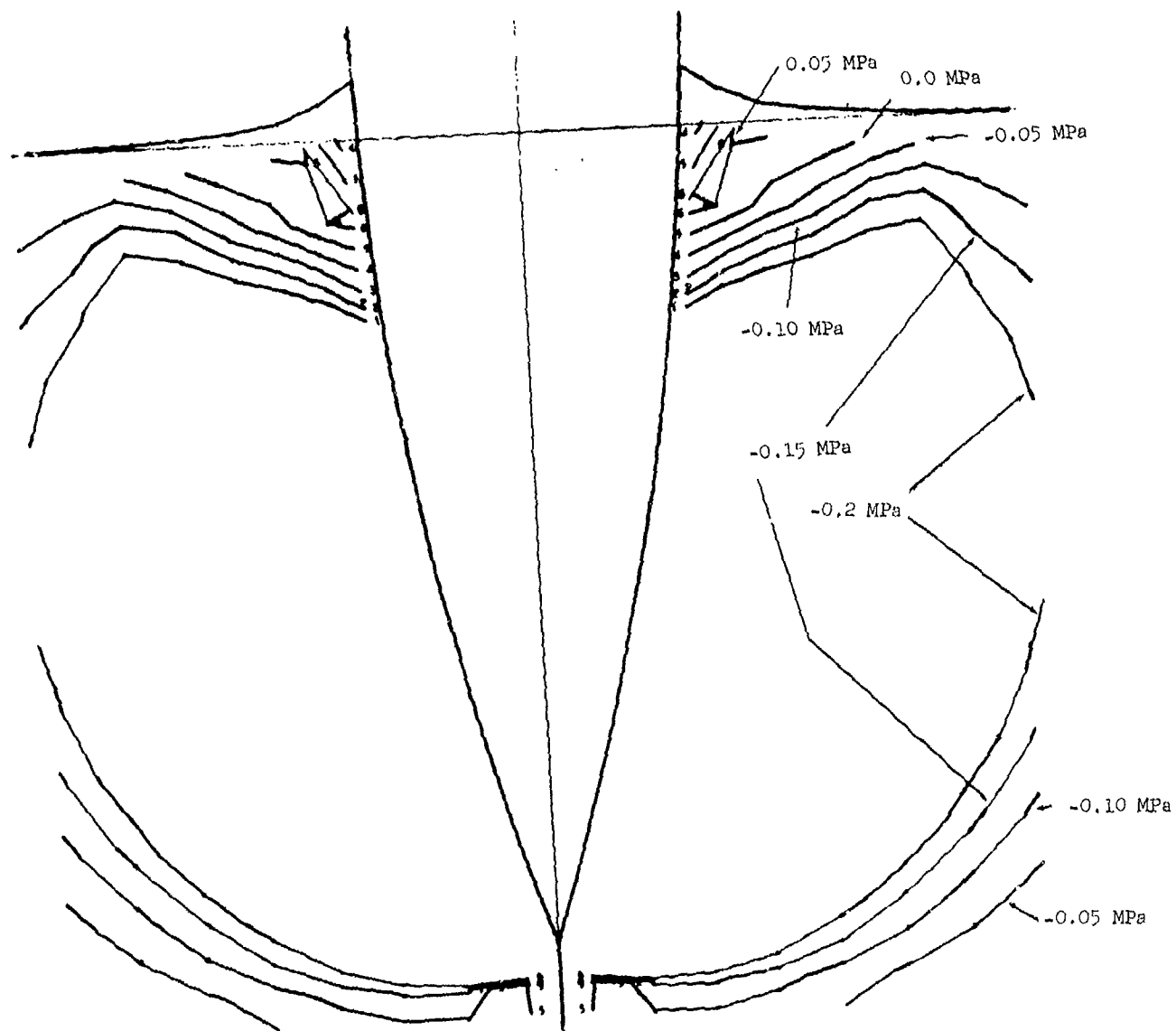
Figure A-93

Contours of Hoop Stress in Target.   Projectile at 0.4 m Depth.
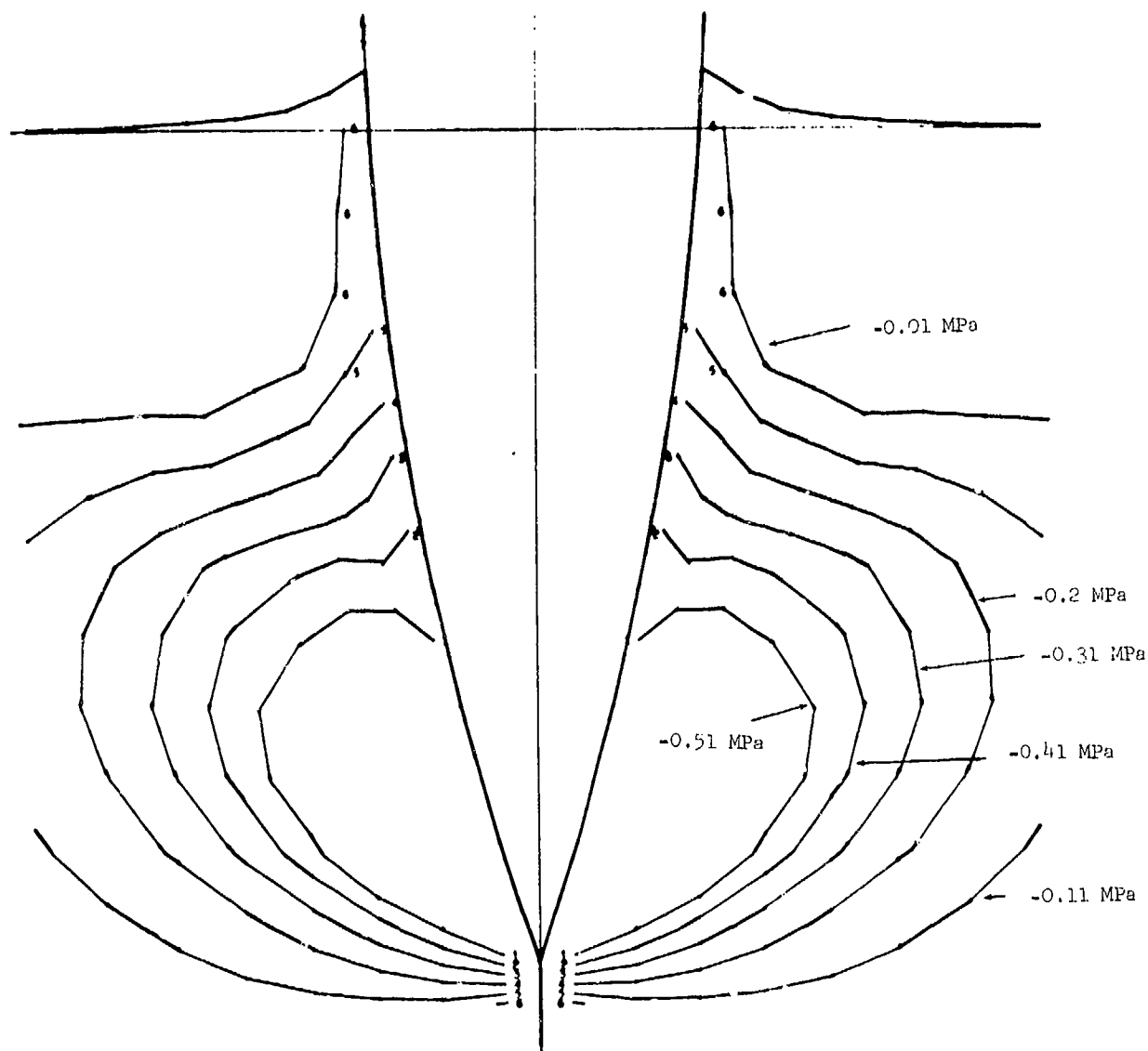
Figure A-94

Contours of Radial-Vertical Shear Stress in Target. Projectile at 0.4 m Depth.
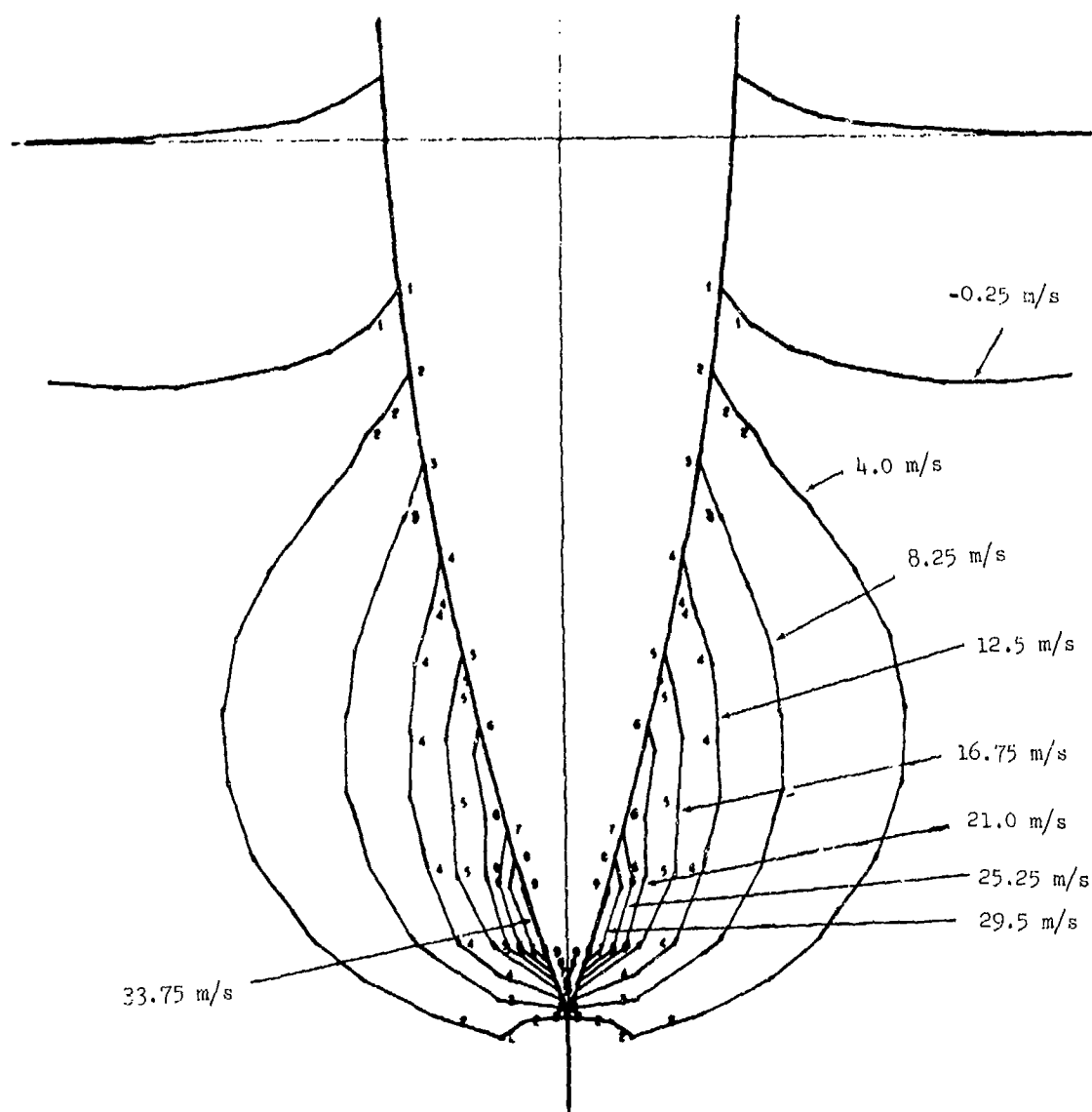
Figure A-95

Contours of Vertical Velocity in Target. Projectile at 0.4 m Depth.
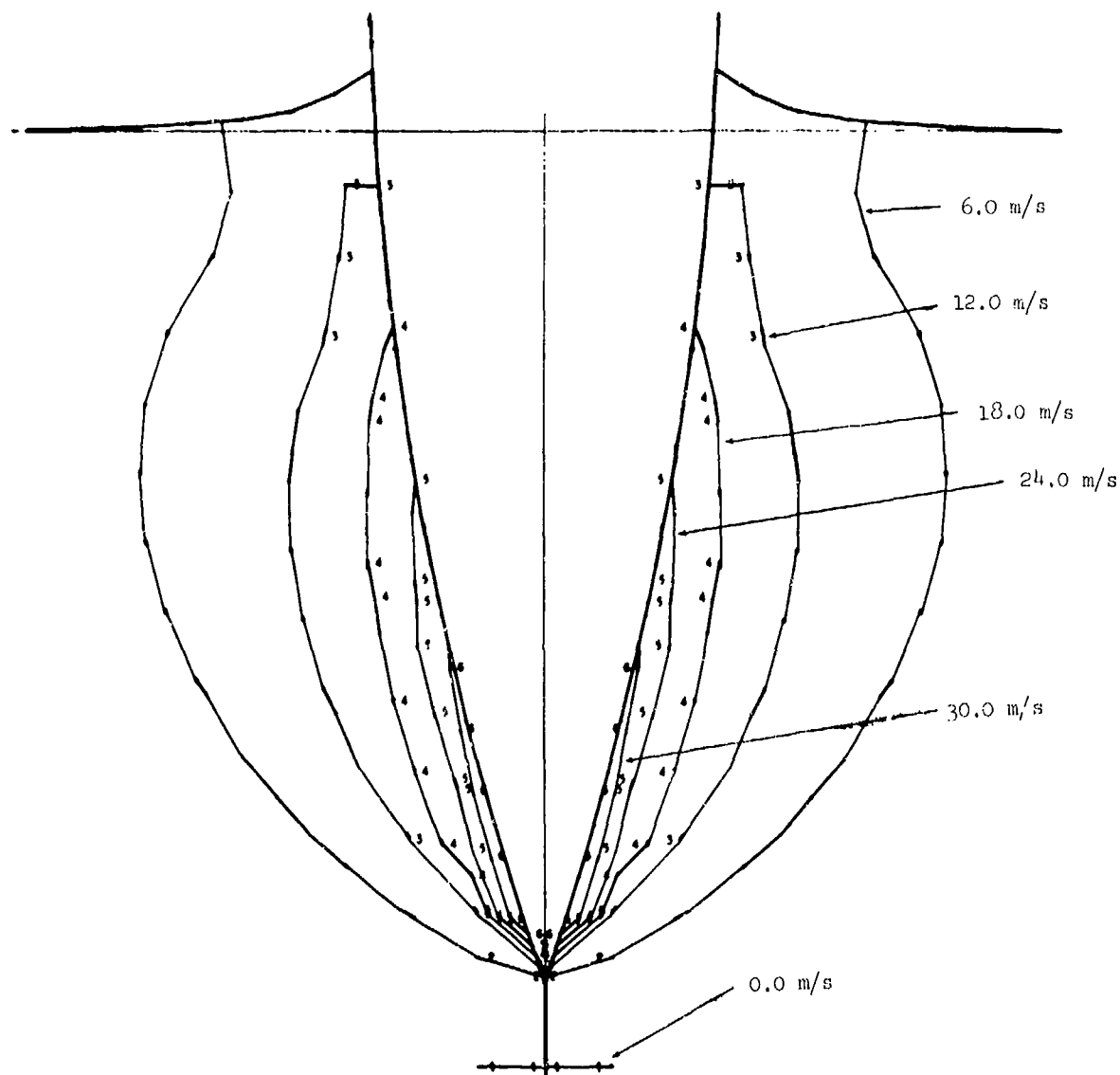
Figure A-96

Contours of Radial Velocity in Target.   Projectile at 0.4 m Depth.
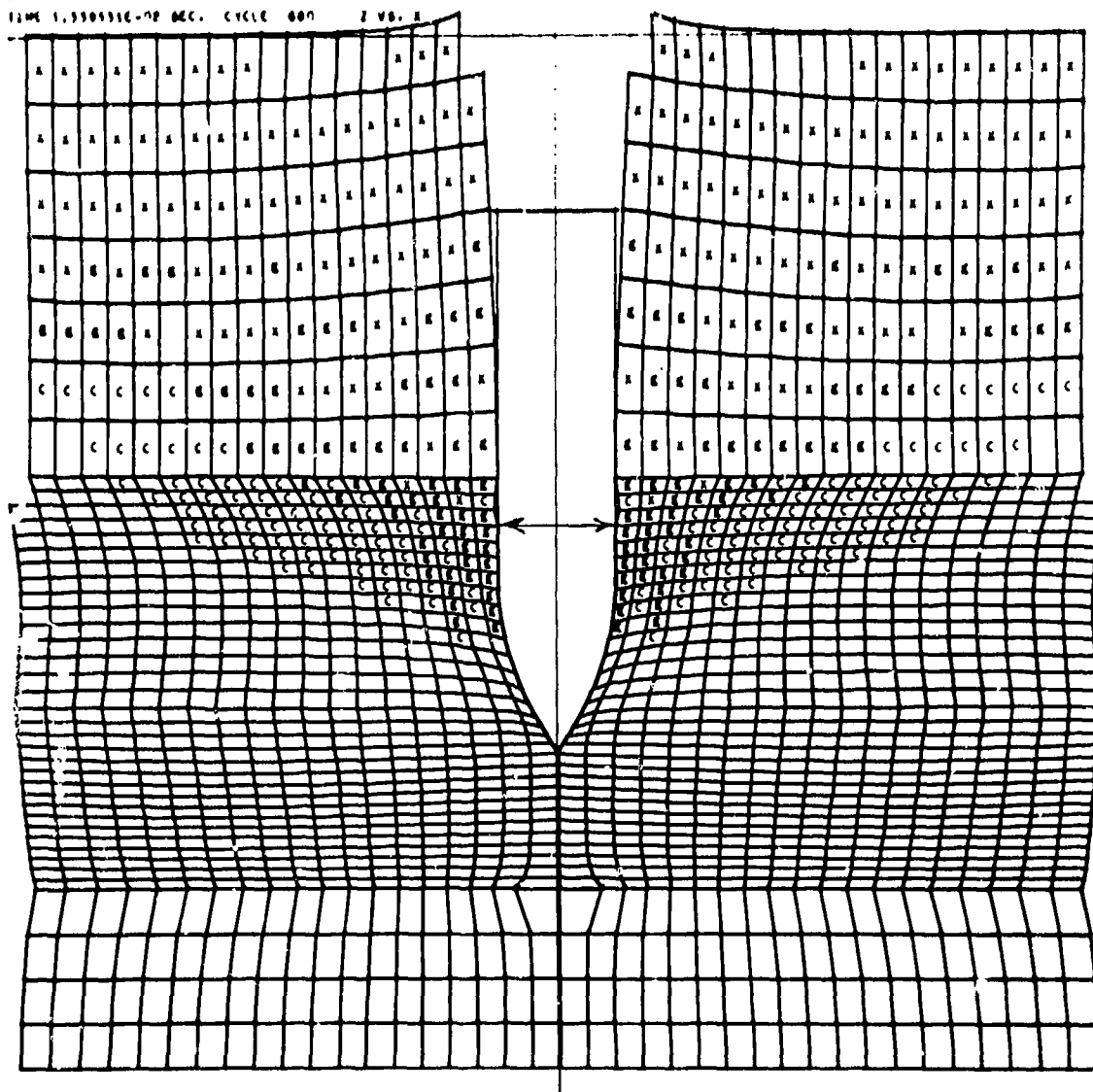
Figure A-97

Lagrangian Coordinates When Projectile has Penetrated to Depth of 2.0 m. Radial
Dimensions Doubled for Clarity.
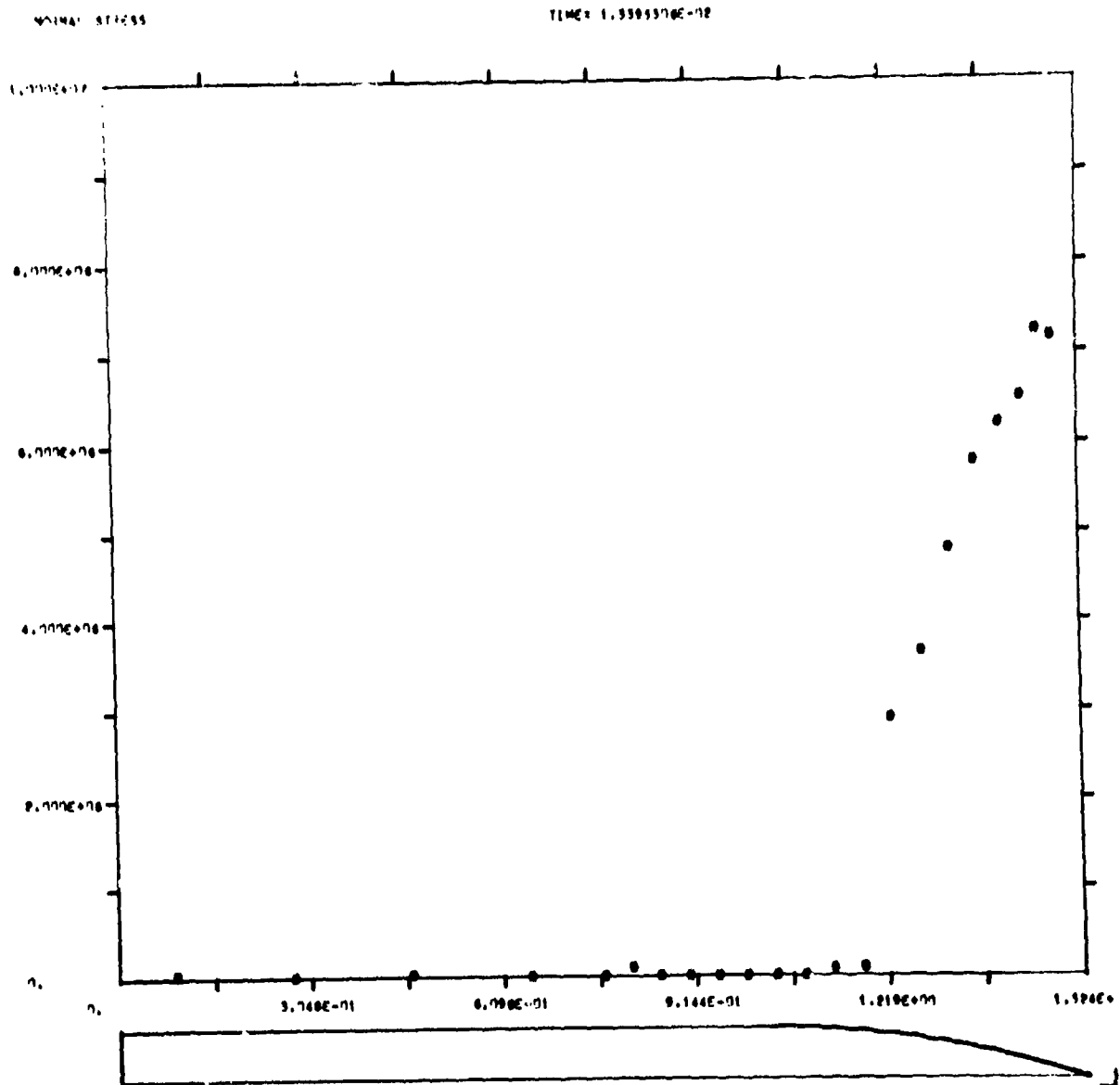
Figure A-98

Normal Stress (Pa) Along Surface of Projectile When Projectile is at 2.0 m Depth.

191

Figure A-99

Tangential Stress (Pa) Along Surface of Projectile When Projectile is at 2.0 m Depth.
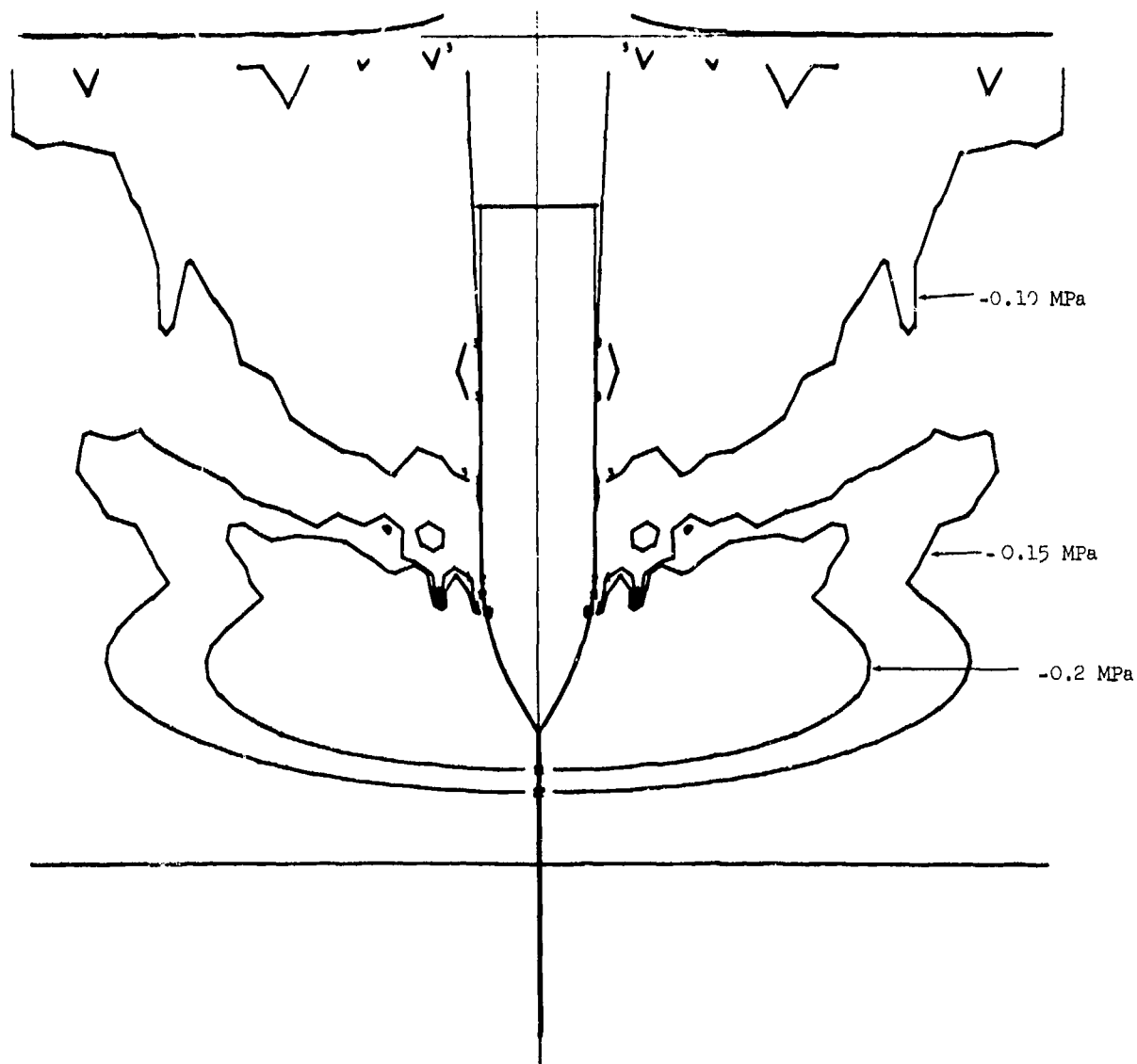
Figure A-100

Contours of Axial Stress in Target. Projectile at 2.0 m Depth.

193
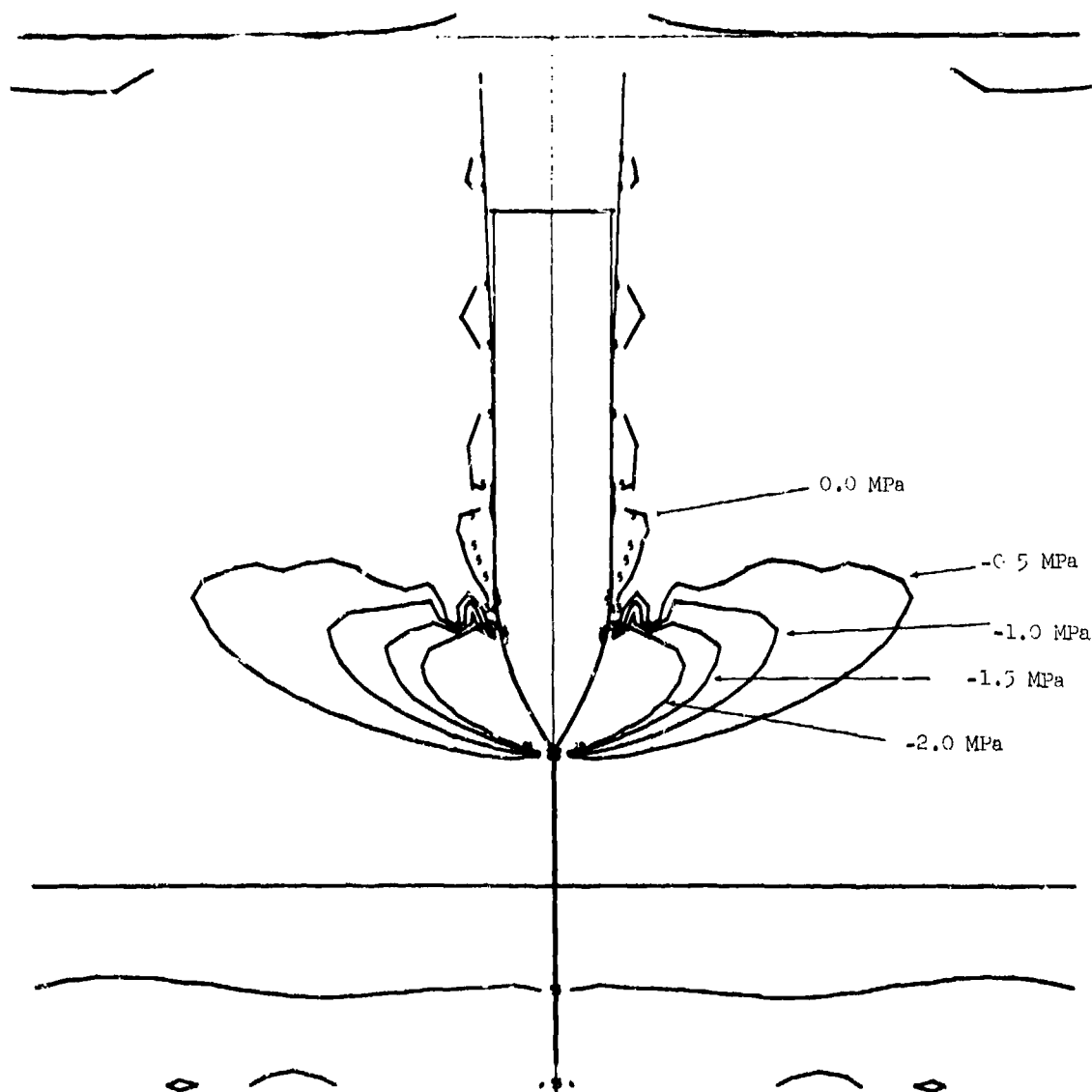
Figure A-101

Contours of Radial Stress in Target. Projectile at 2.0 m Depth.
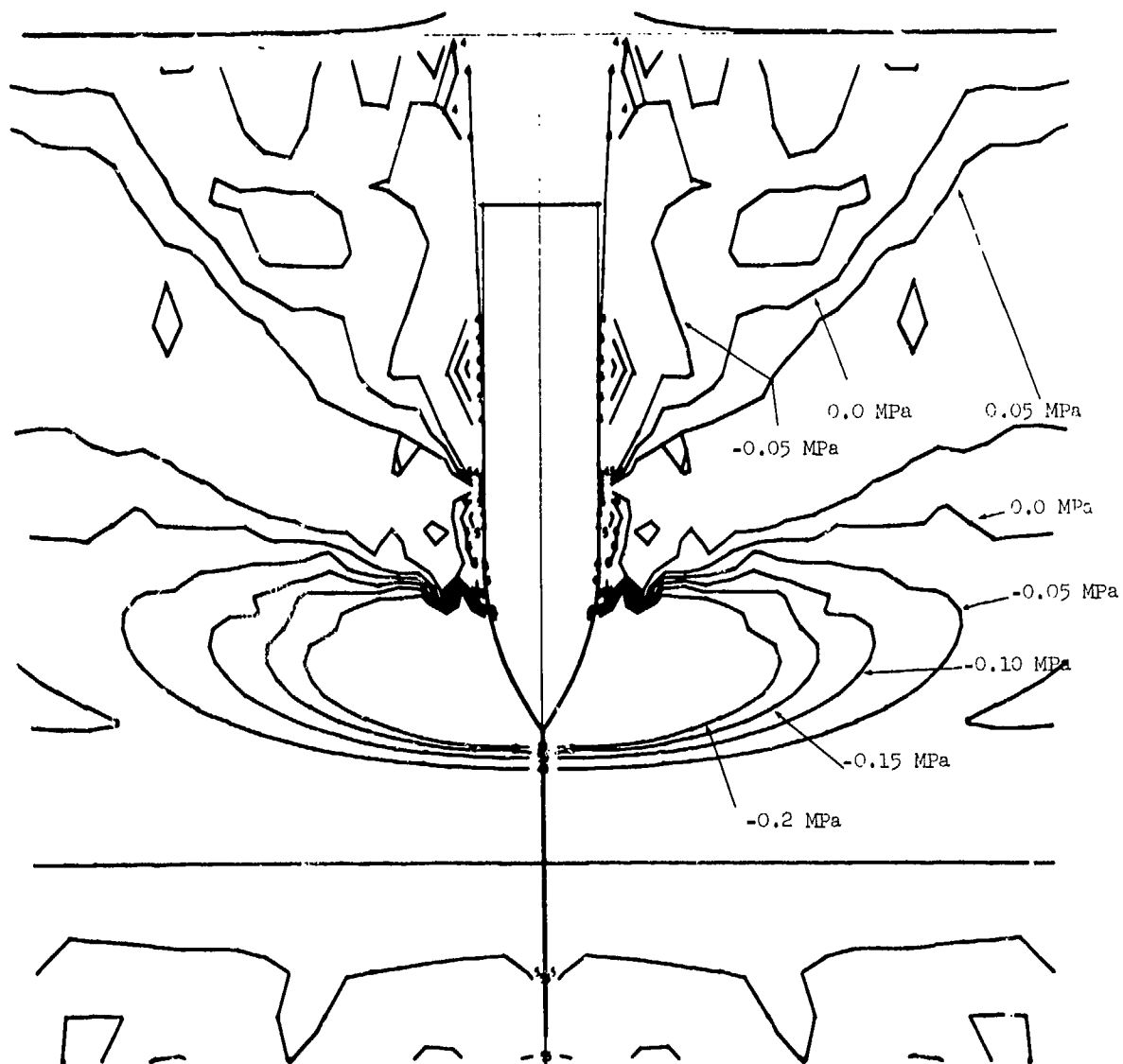
Figure A-102

Contours of Hoop Stress in Target. Projectile at 2.0 m Depth.
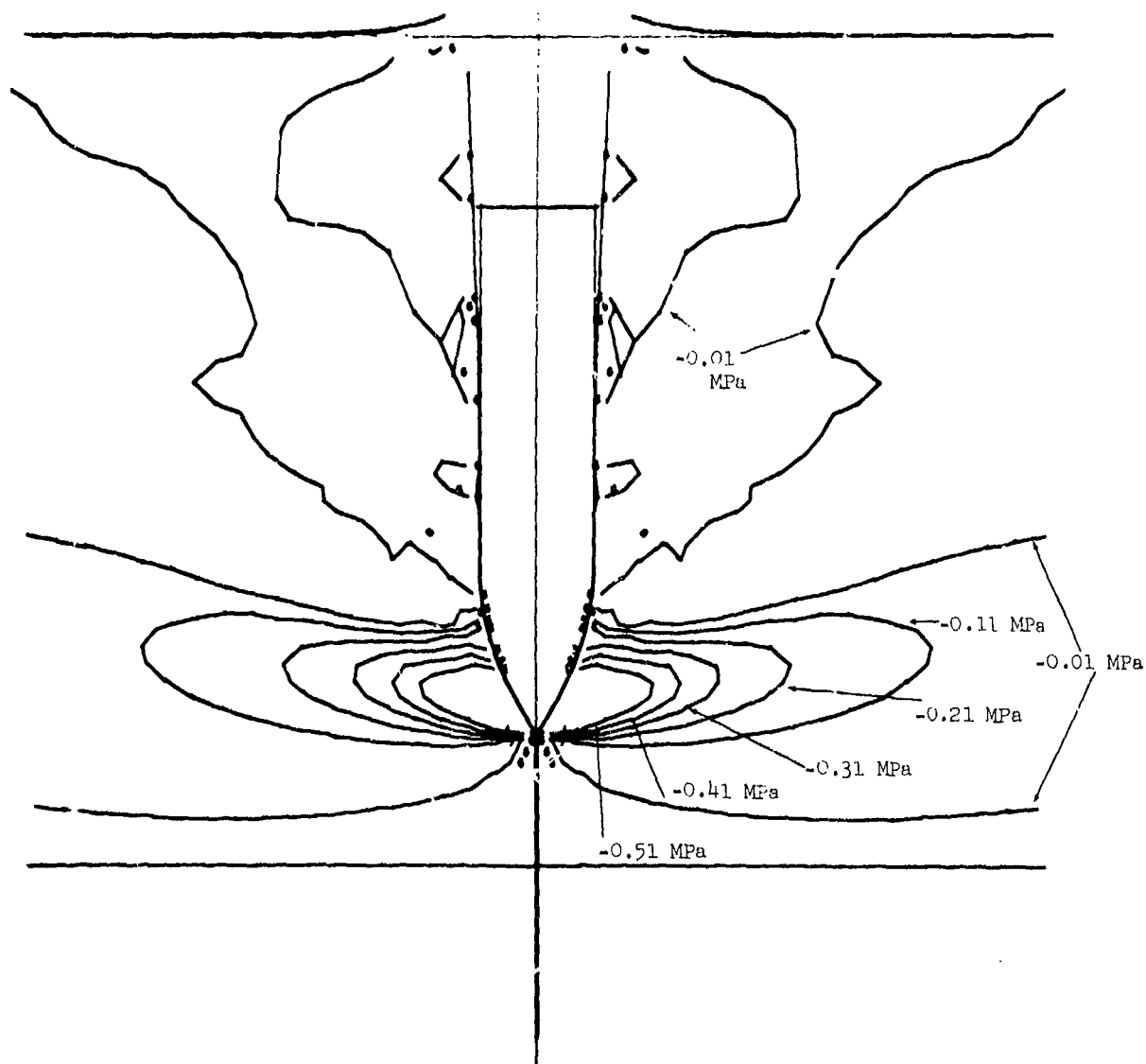
Figure A-103

Contours of Radial Vertical Shear Stress in Target. Projectile at 2.0 m Depth.
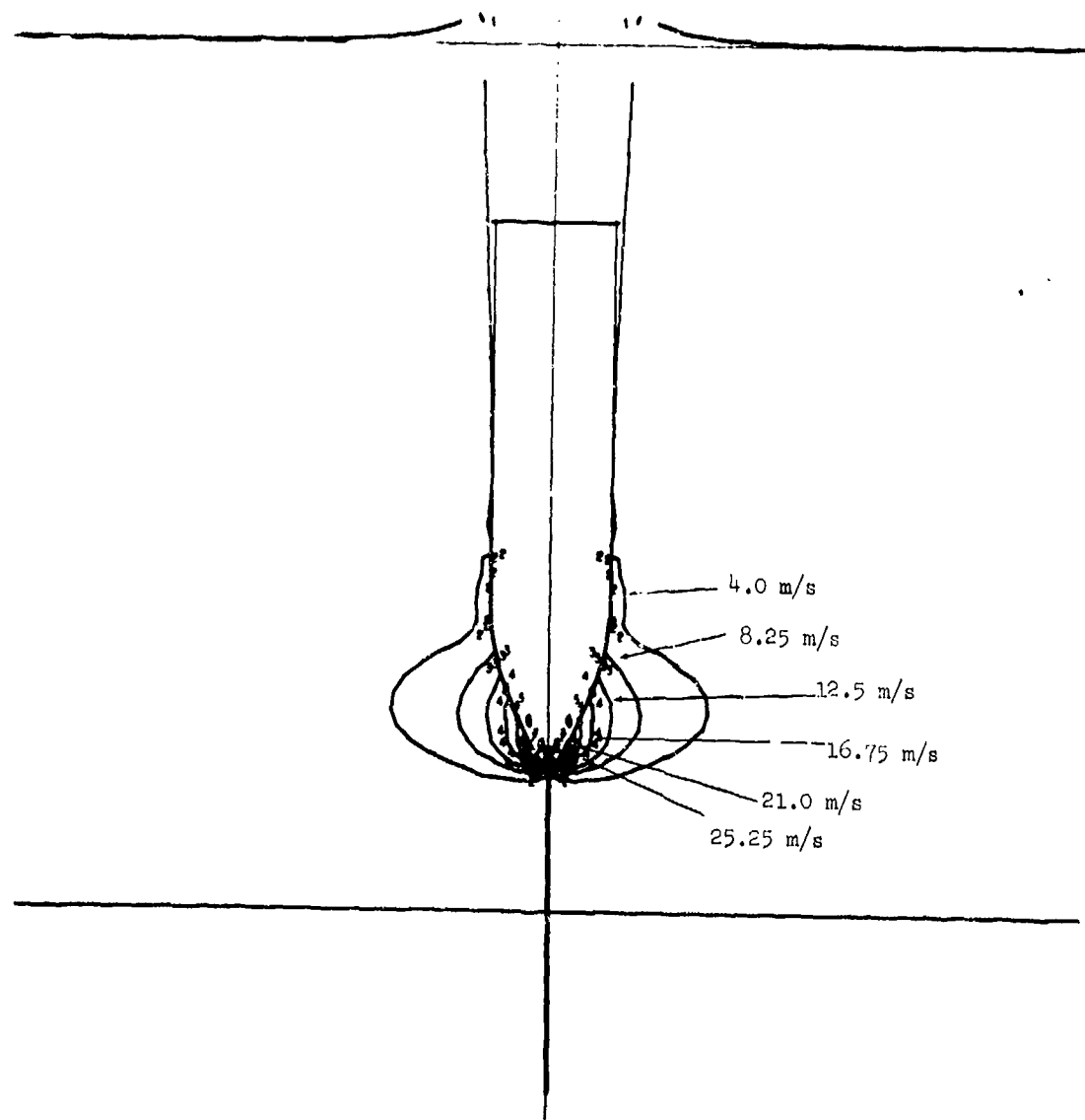
Figure A-104
Contours of Vertical Velocity in Target. Projectile at 2.0 m Depth.
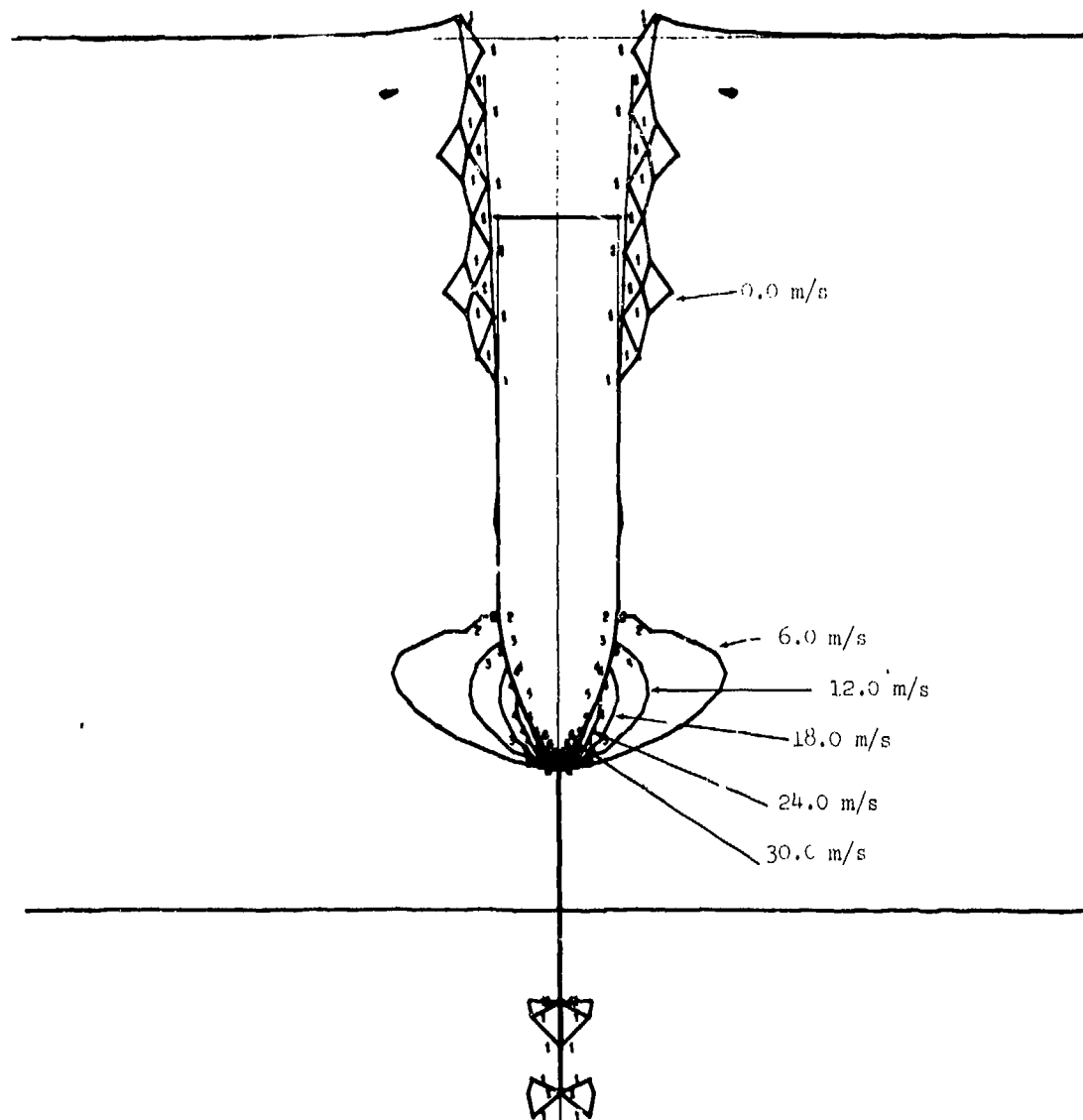
Figure A-105

Contours of Radial Velocity in Target. Projectile at 2.0 m Depth.

Figure A-106

Lagrangian Coordinates When Projectile has Penetrated to Depth of 2.8 m. Radial
Dimensions Doubled for Clarity.

Figure A-107

Normal Stress (Pa) Along Surface of Projectile When Projectile is at 2.8 m Depth.
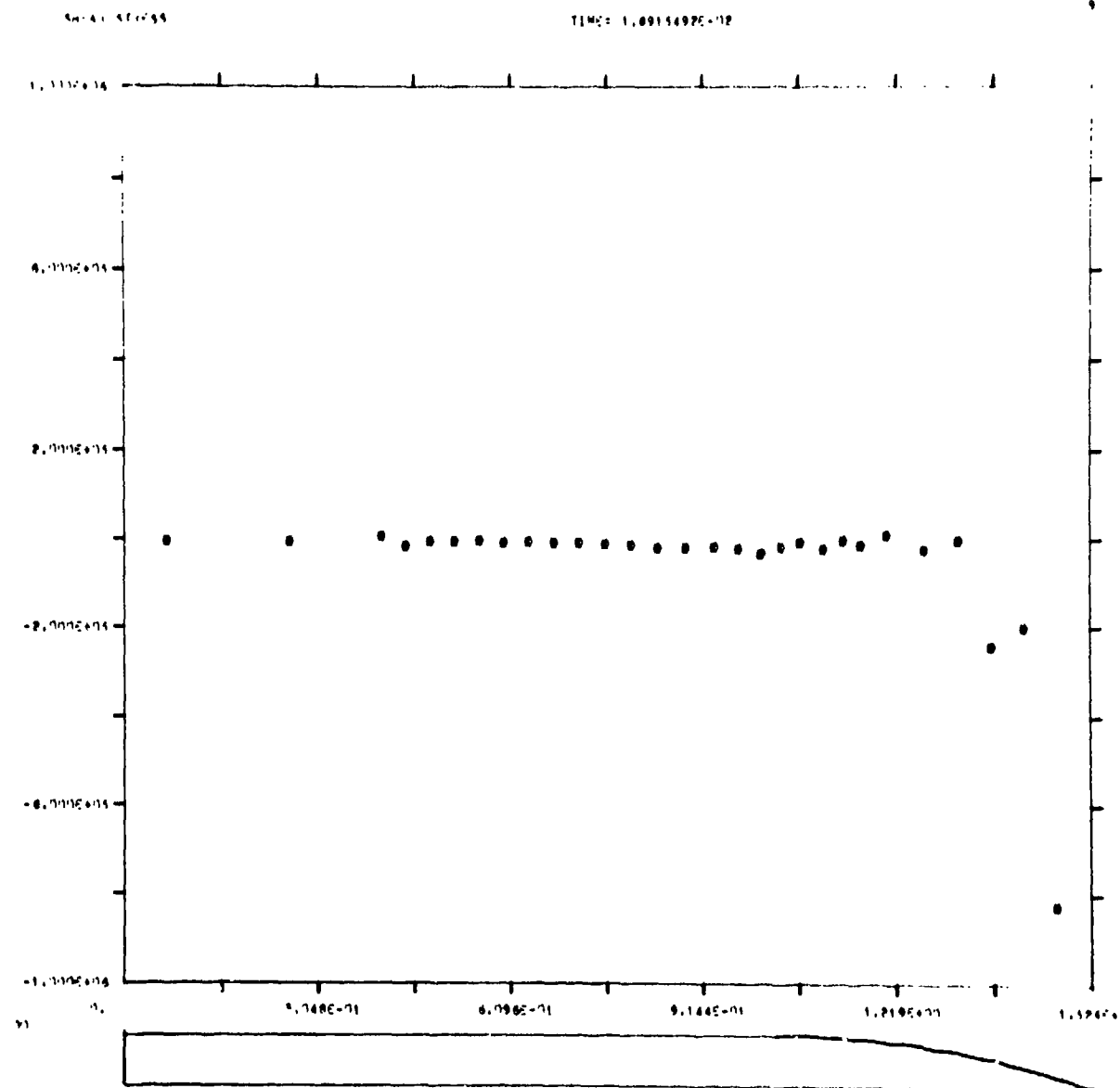
Figure A-108

Tangential Stress (Pa) Along Surface of Projectile When Projectile is at 2.8 m Depth.
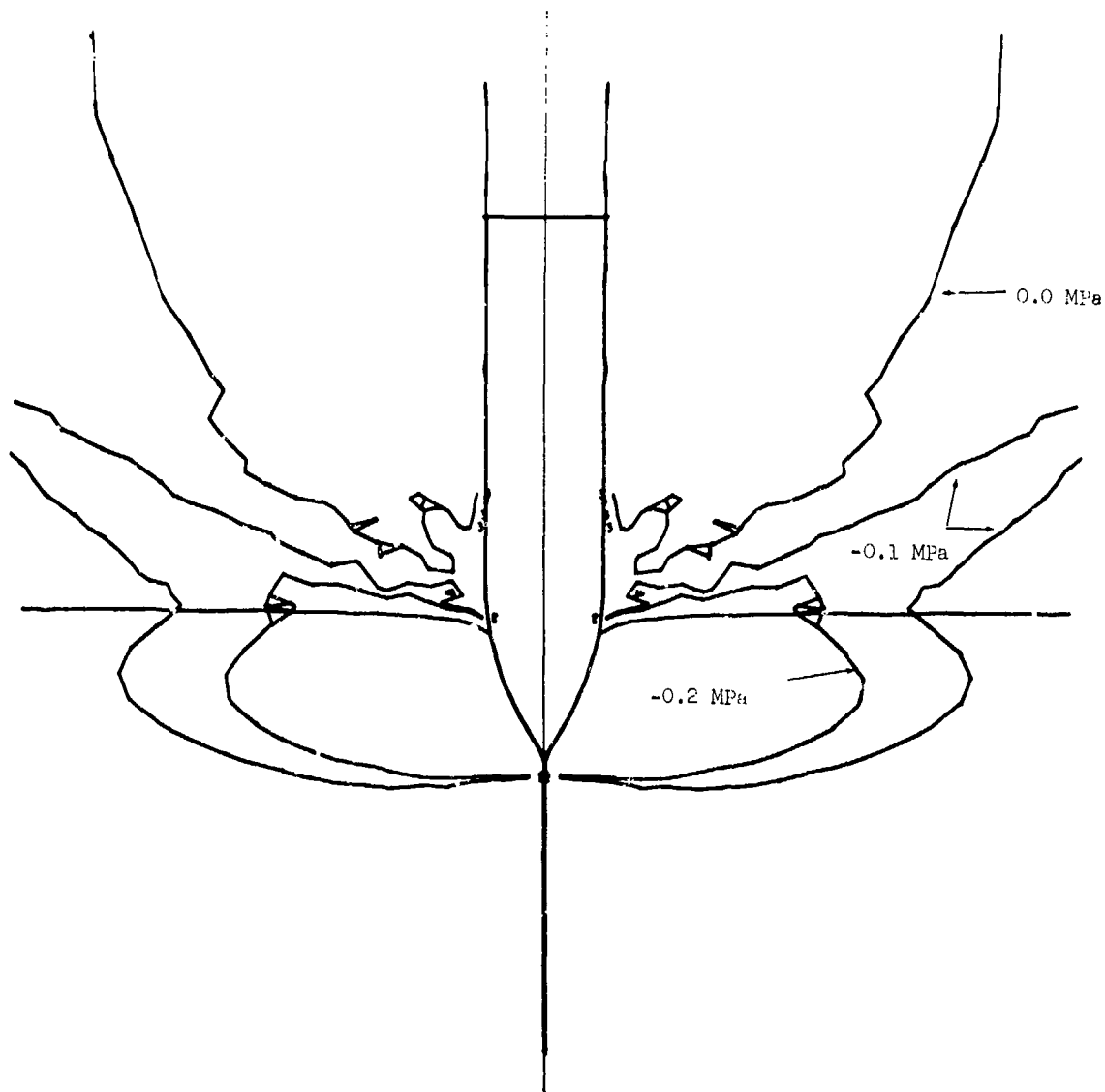
Figure A-109

Contours of Axial Stress in Target. Projectile at 2.8 m Depth.
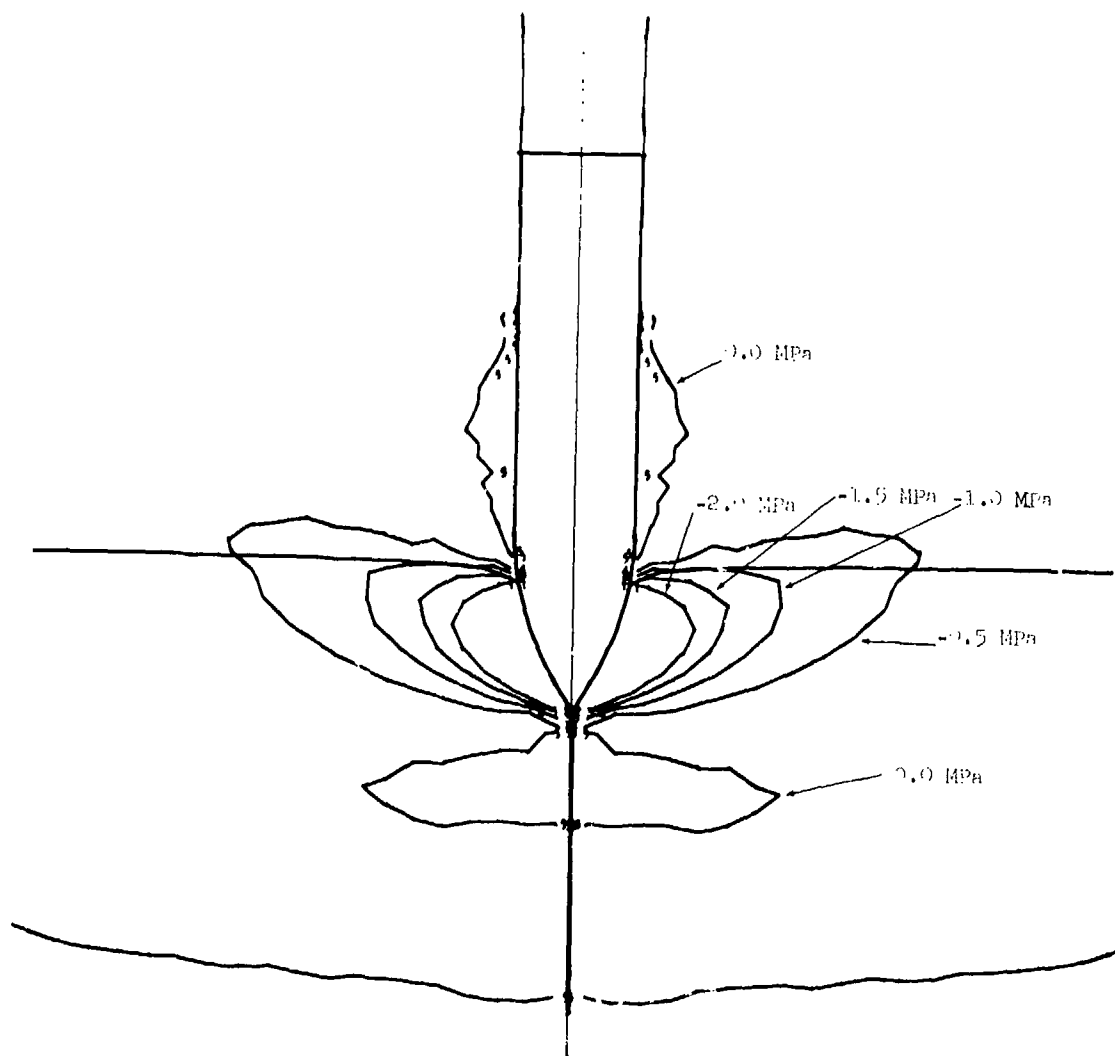
Figure A-110
Contours of Radial Stress in Target. Projectile at 2.6 m Depth.
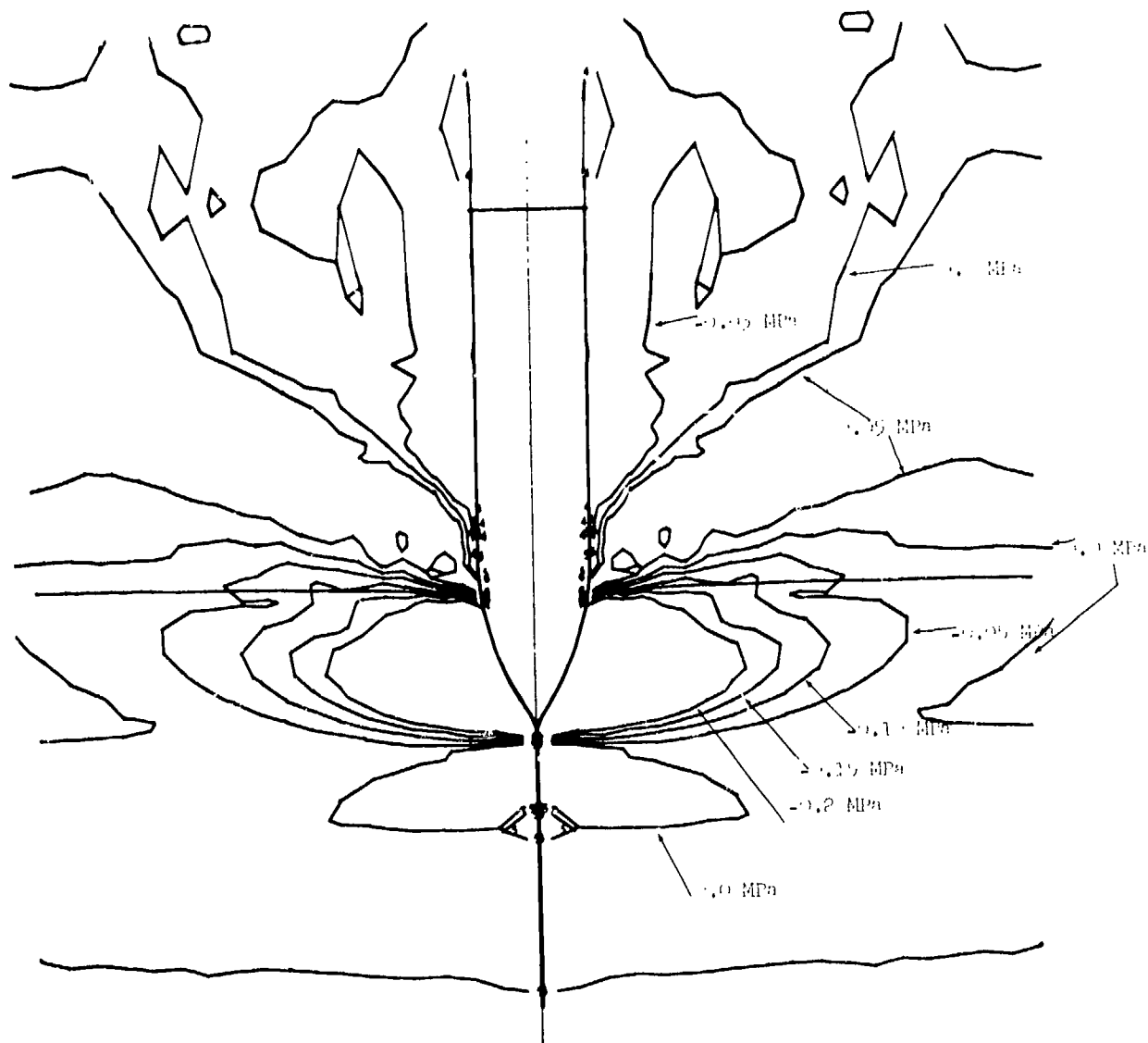
Figure A-111

Contours of Hoop Stress in Target. Projectile at 2.8 m Depth.
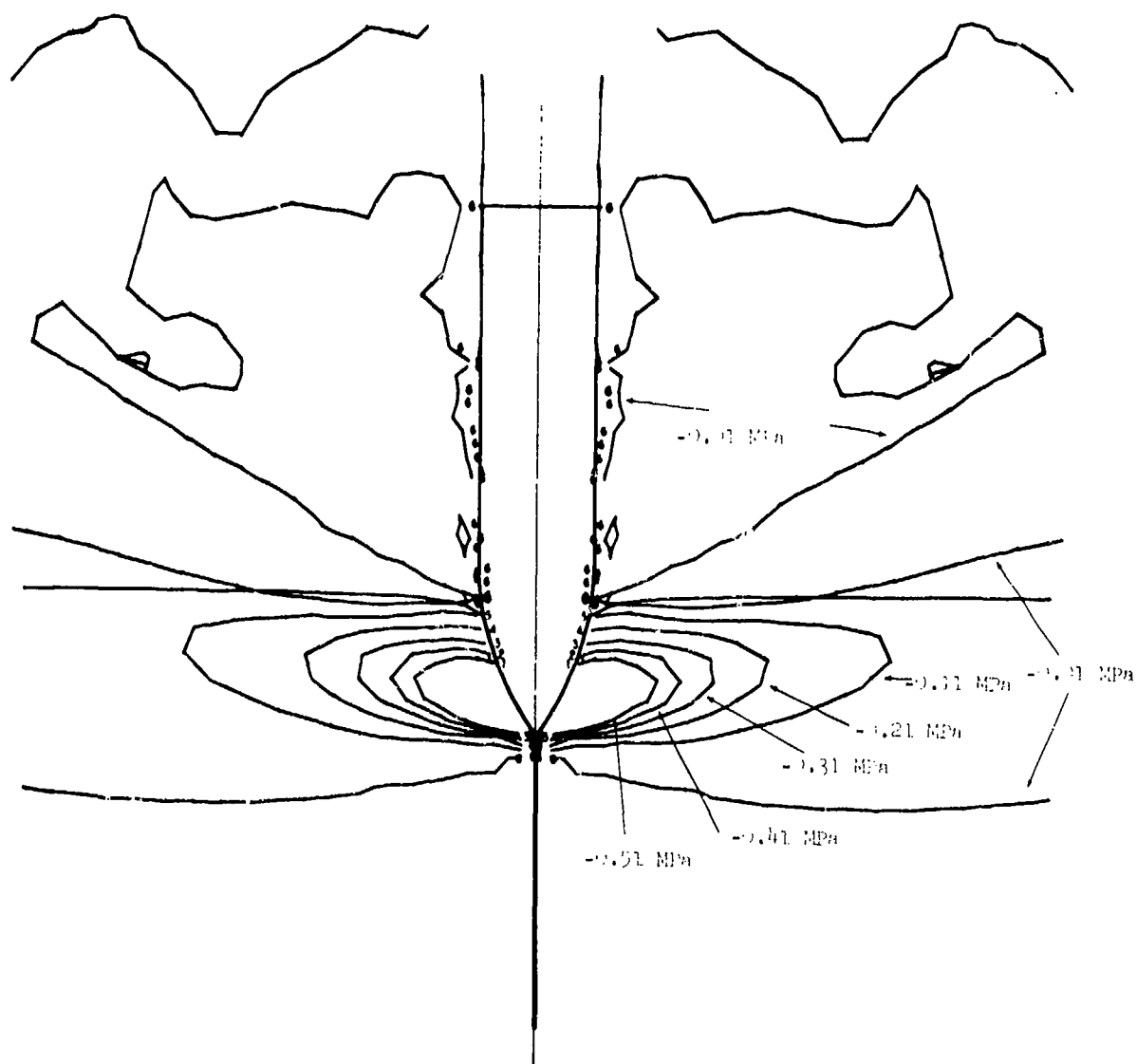
Figure A-112

Contours of Radial Vertical Shear Stress in Target. Projectile at 2.8 m Depth.
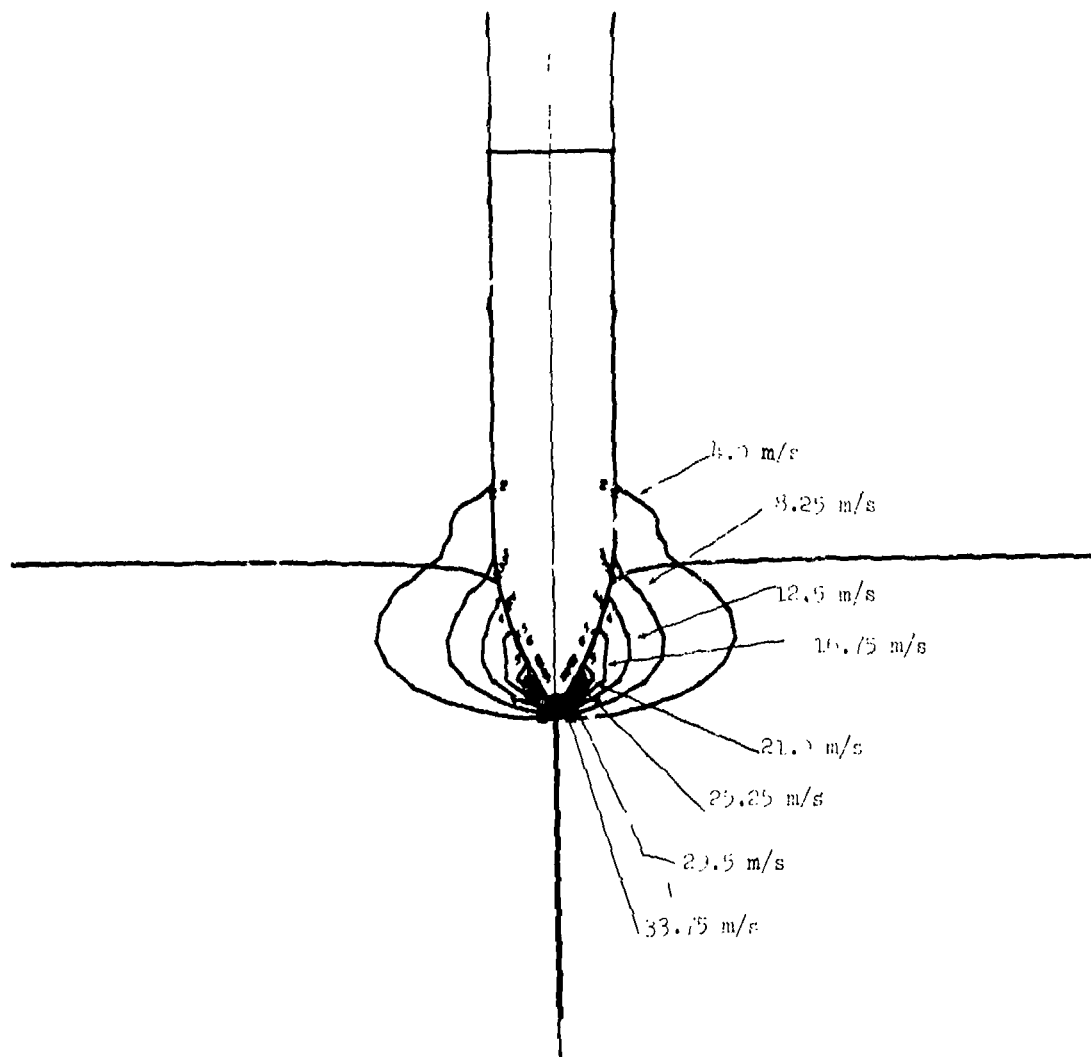
Figure A-113
Contours of Vertical Velocity in Target. Projectile at 2.8 m Depth.
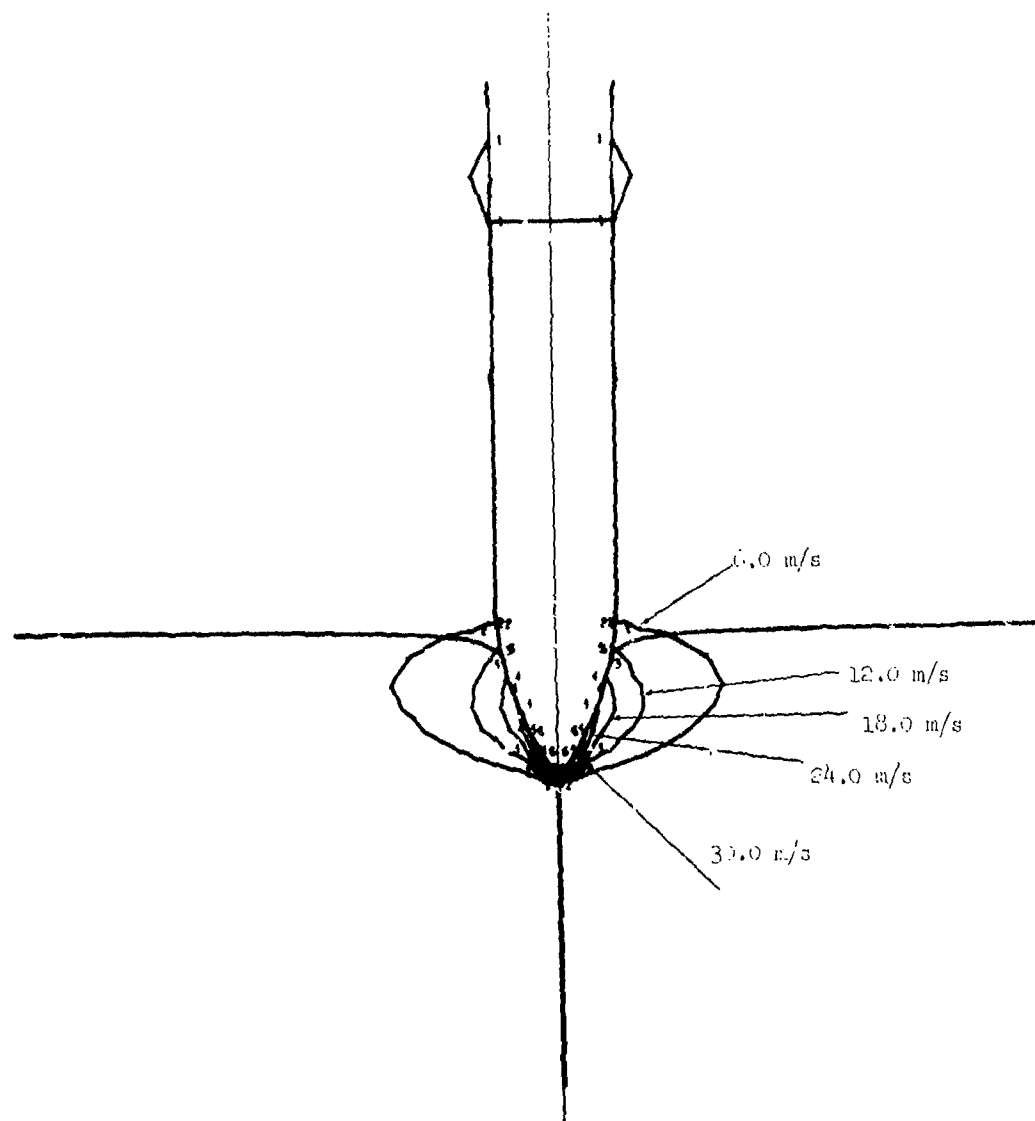
Figure A-114

Contours of Radial Velocity in Target. Projectile at 2.8 m Depth.
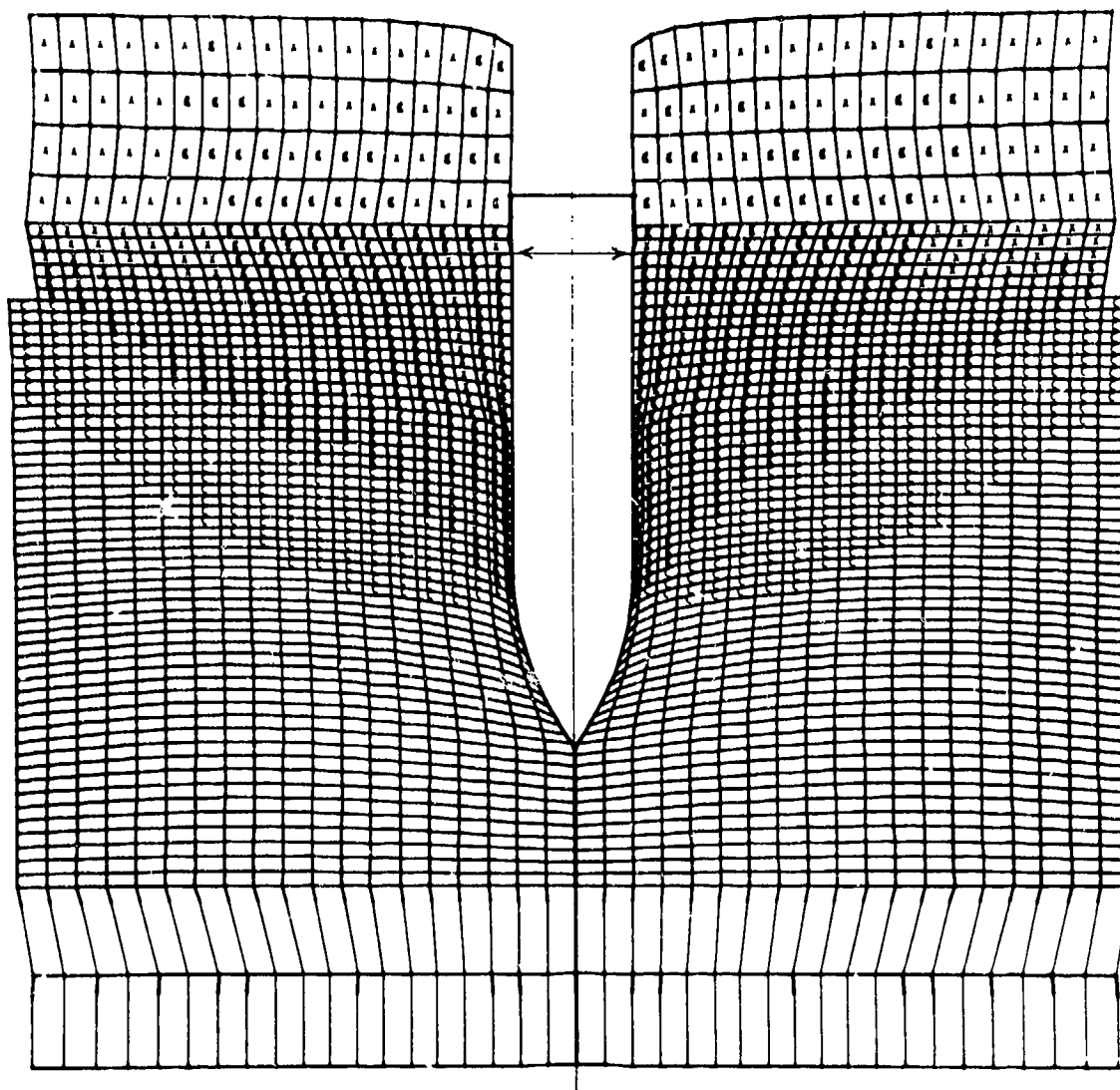
Figure A-115

Lagrangian Coordinates When Projectile has Penetrated to Depth of 4.4 m. Radial Dimensions Doubled for Clarity.
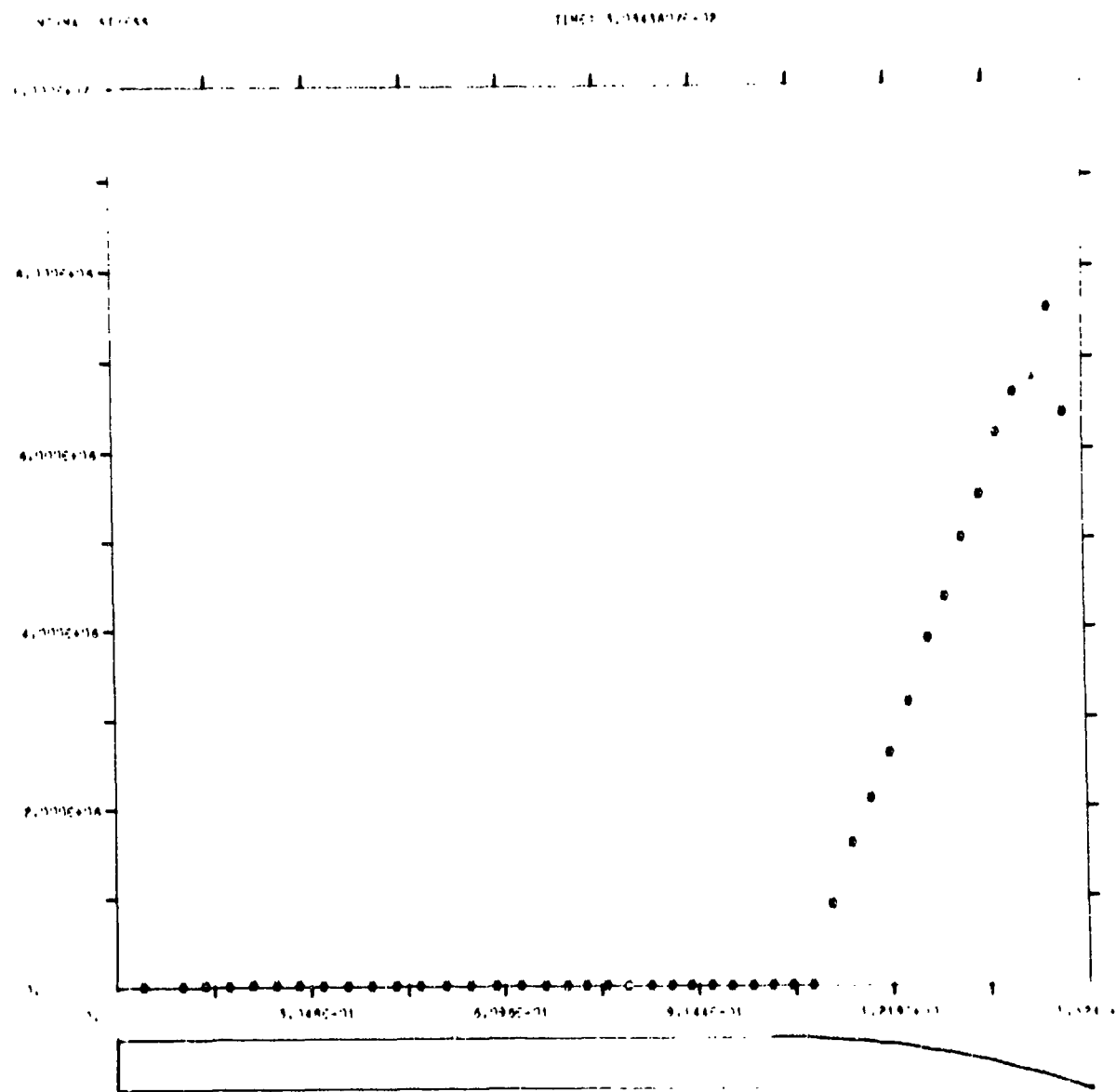
Figure A-116

Normal Stress (Pa) Along Surface of Projectile When Projectile is at 4.4 m Depth.

Figure A-117

Tangential Stress (Pa) Along Surface of Projectile When Projectile is at 4.4 m Depth.

0.0 MPa

-0.1 MPa

-0.2 MPa
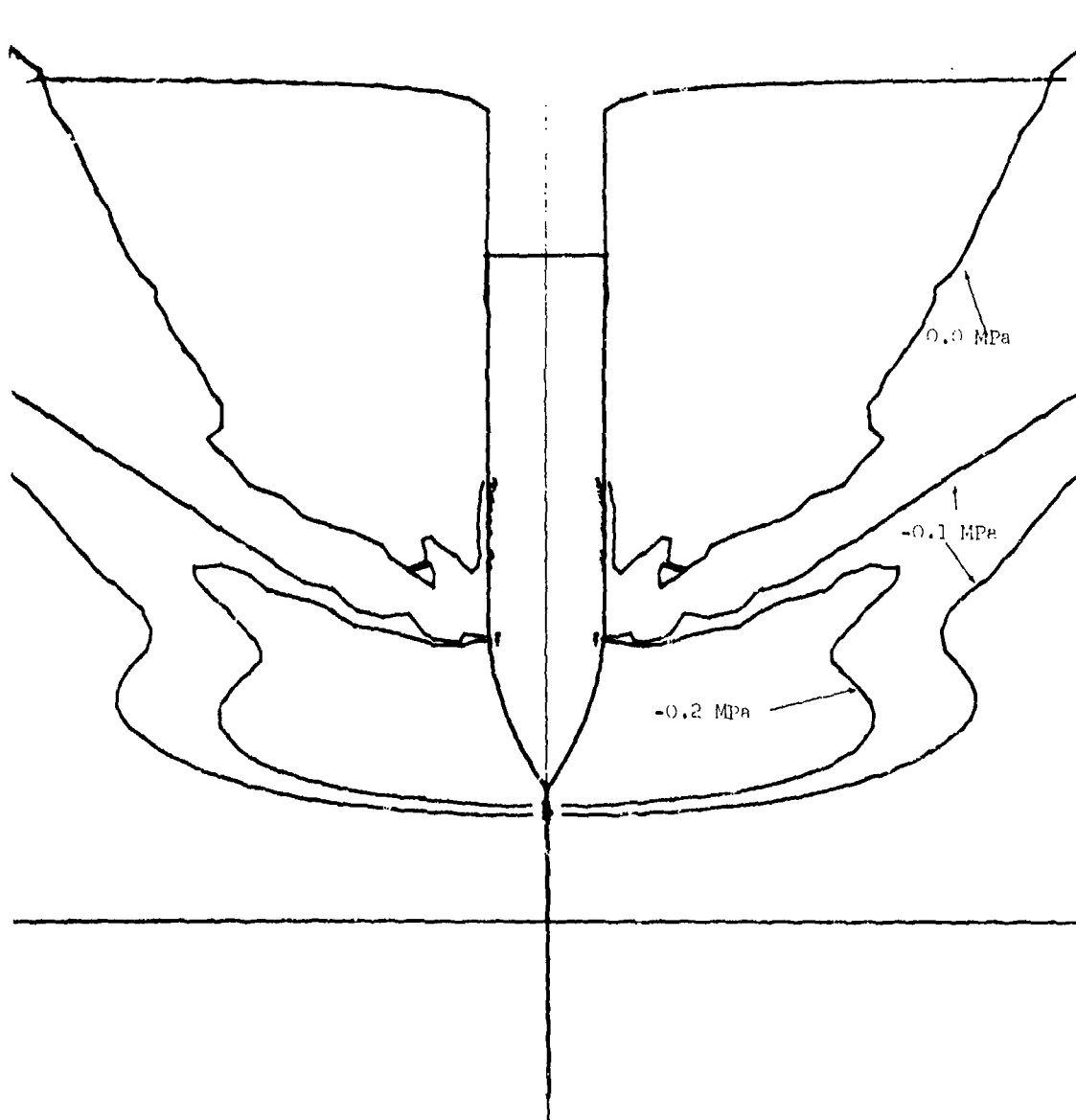
Figure A-118

Contours of Axial Stress in Target. Projectile at 4.4 m Depth.
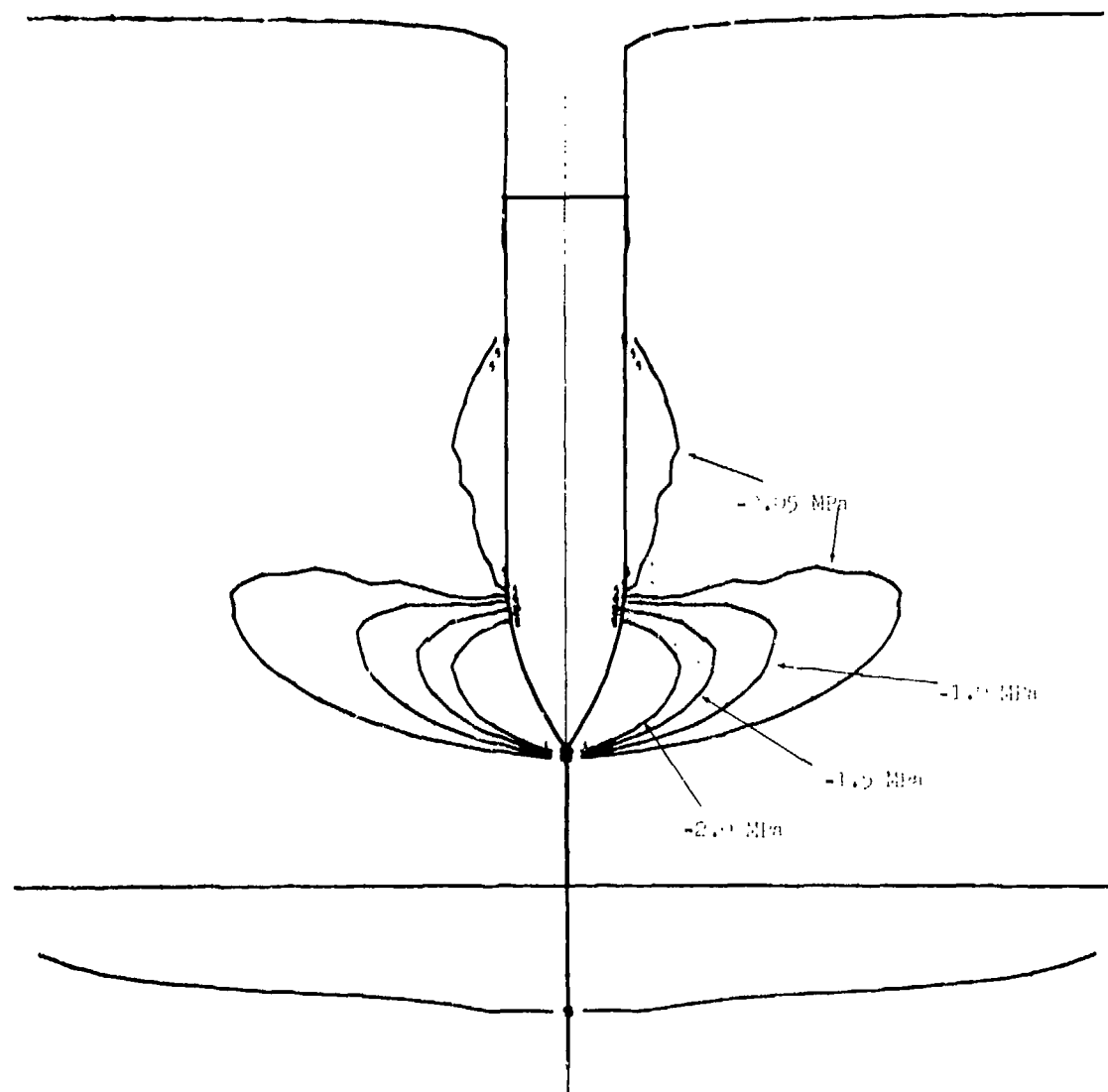
Figure A-119

Contours of Radial Stress in Target. Projectile at 4.4 m Depth.
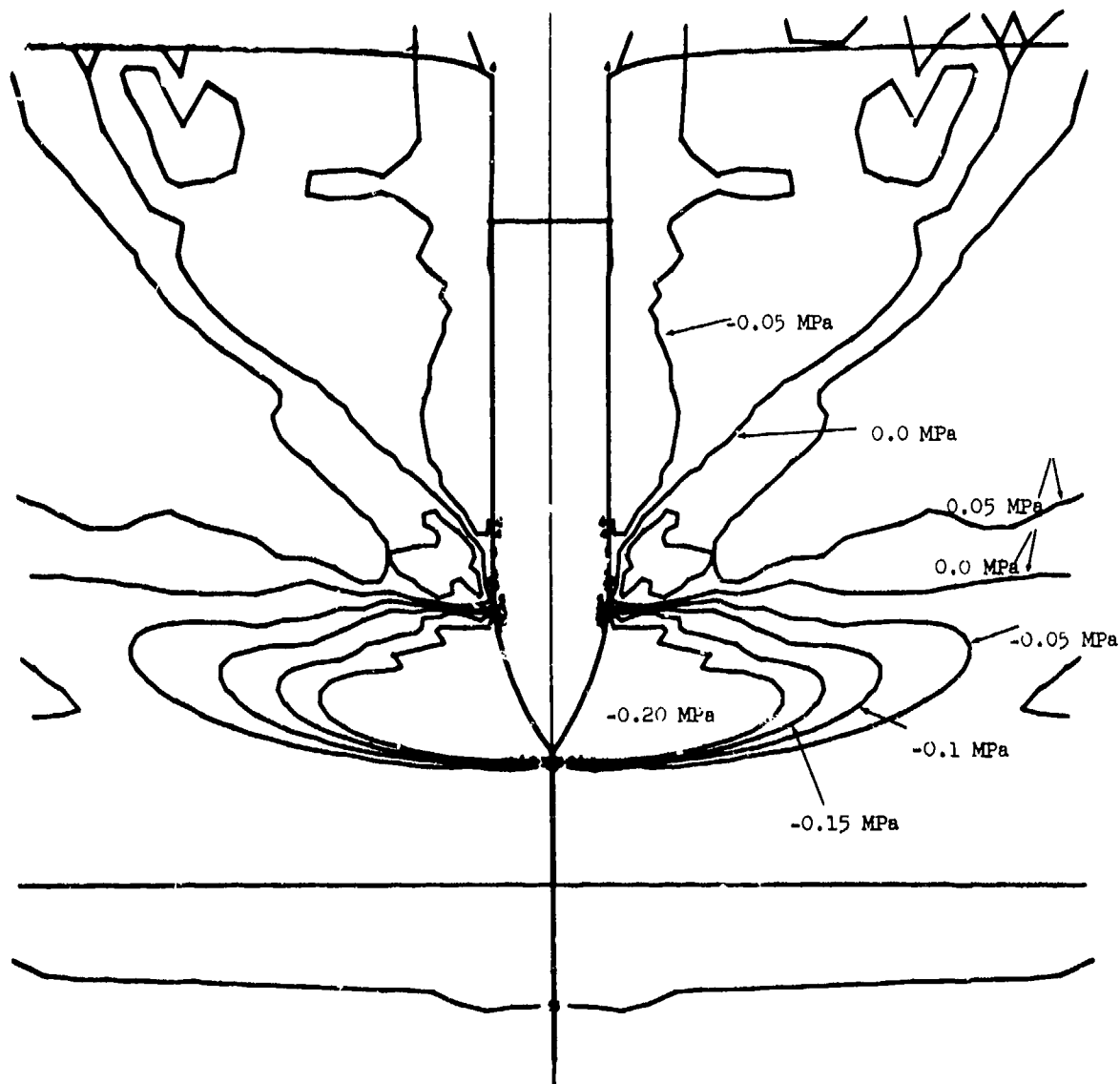
Figure A-120

Contours of Hoop Stress in Target. Projectile at 4.4 m Depth.
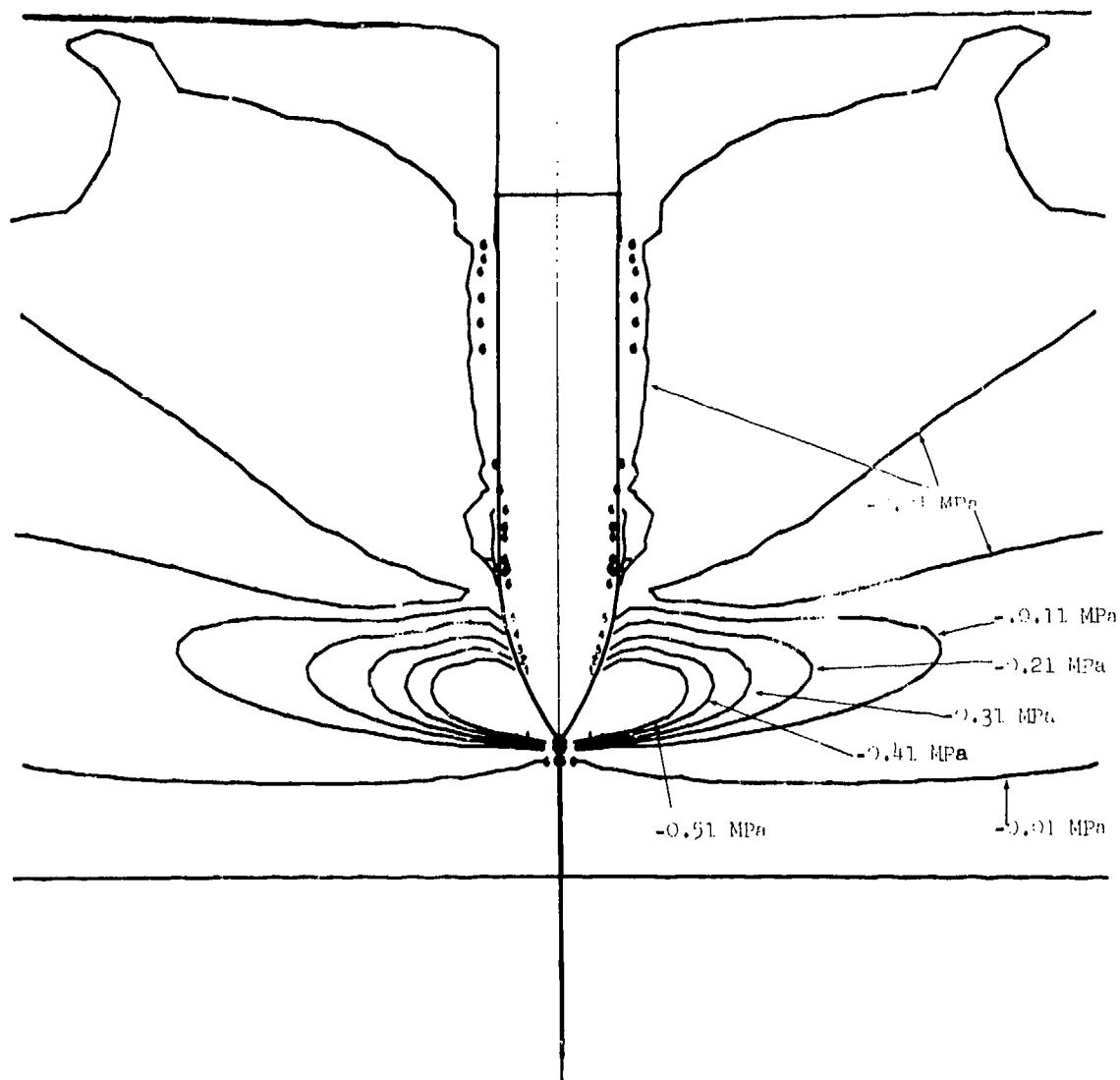
Figure A-121

Contours of Radial-Vertical Shear Stress in Target. Projectile at 4.4 m Depth.
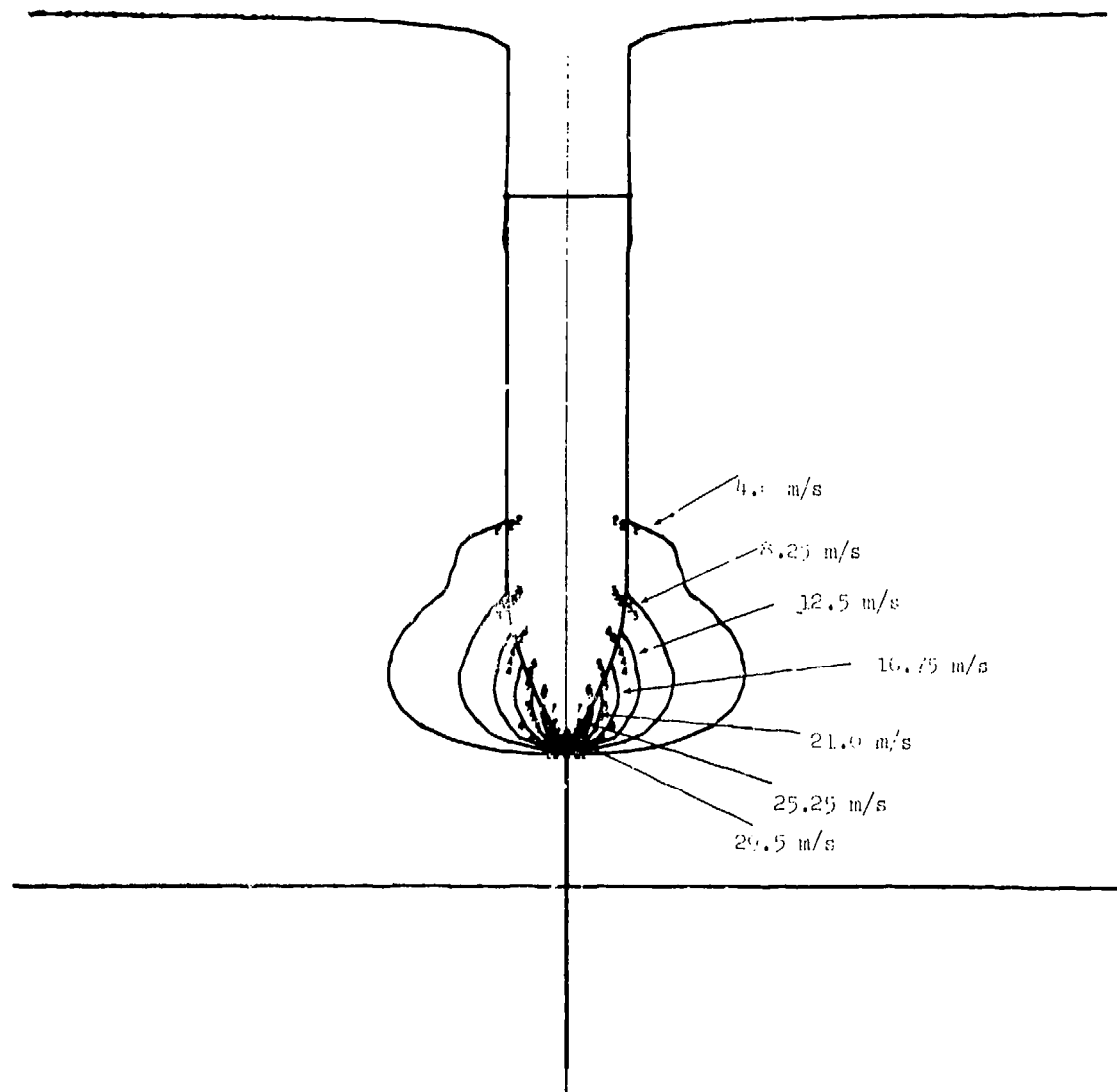
Figure A-102

Contours of Vertical Velocity in Target. Projectile at 4.4 m Depth.
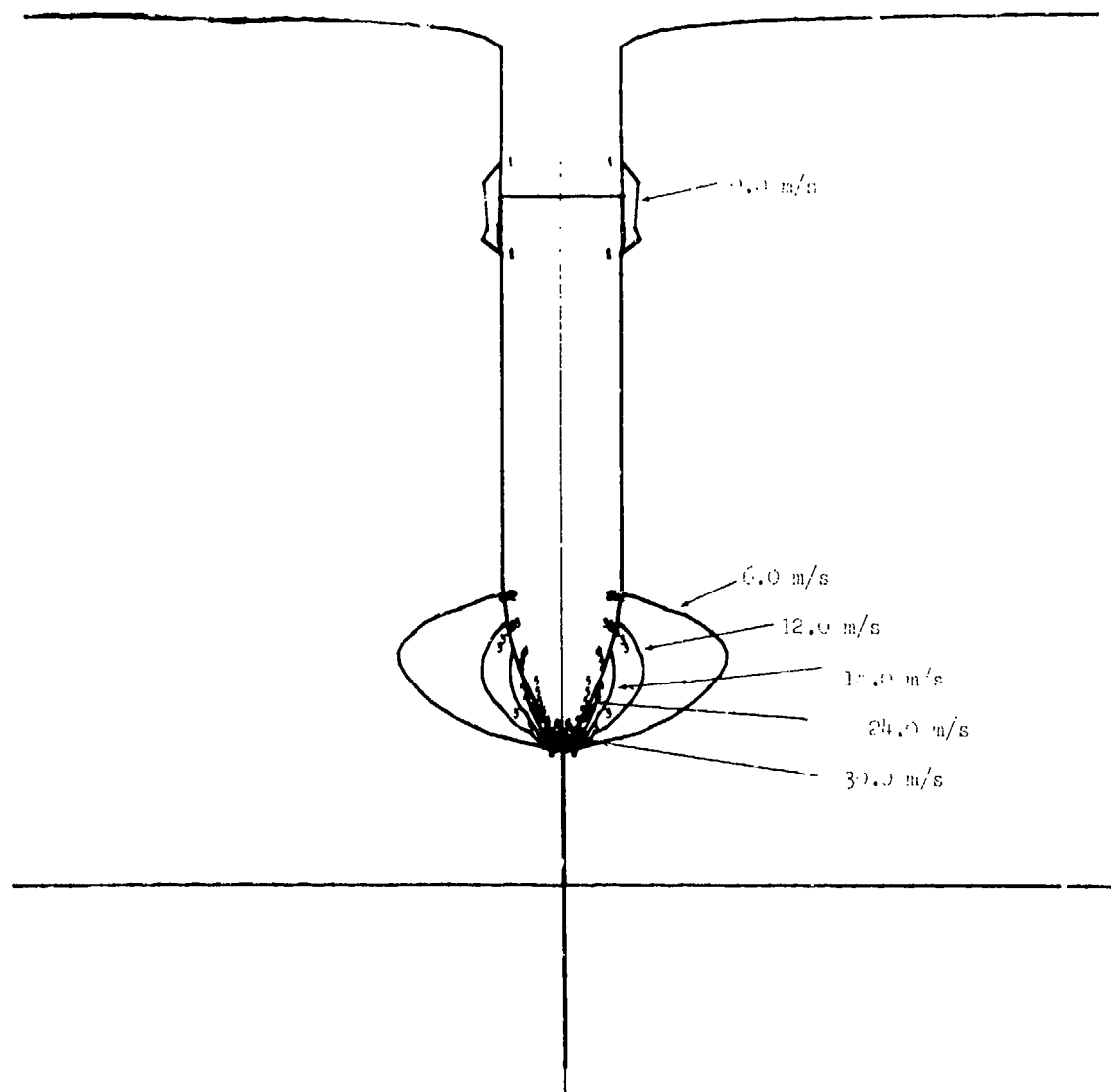
Contours of Radial Velocity in Target. Projectile at 4.4 m Depth.

Figure A-134

Lagrangian Coordinates When Projectile has Penetrated to Depth of [...] Radial
Dimensions Doubled for Clarity.
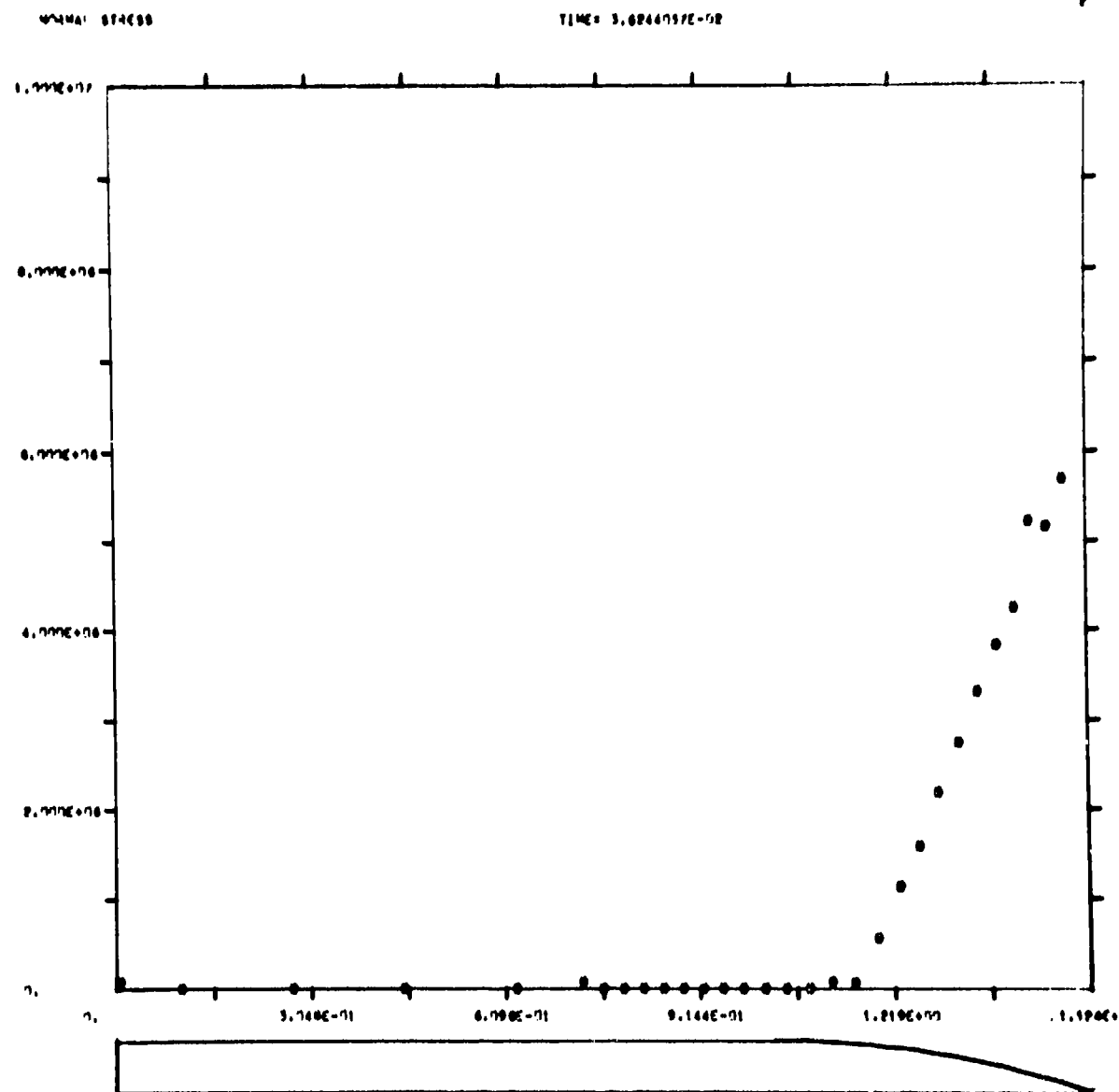
Figure A-125

Normal Stress (Pa) Along Surface of Projectile When Projectile is at 5.2 m Depth.

Figure A-126

Tangential Stress (Pa) Along Surface of Projectile When Projectile is at 5.2 m Depth.

219
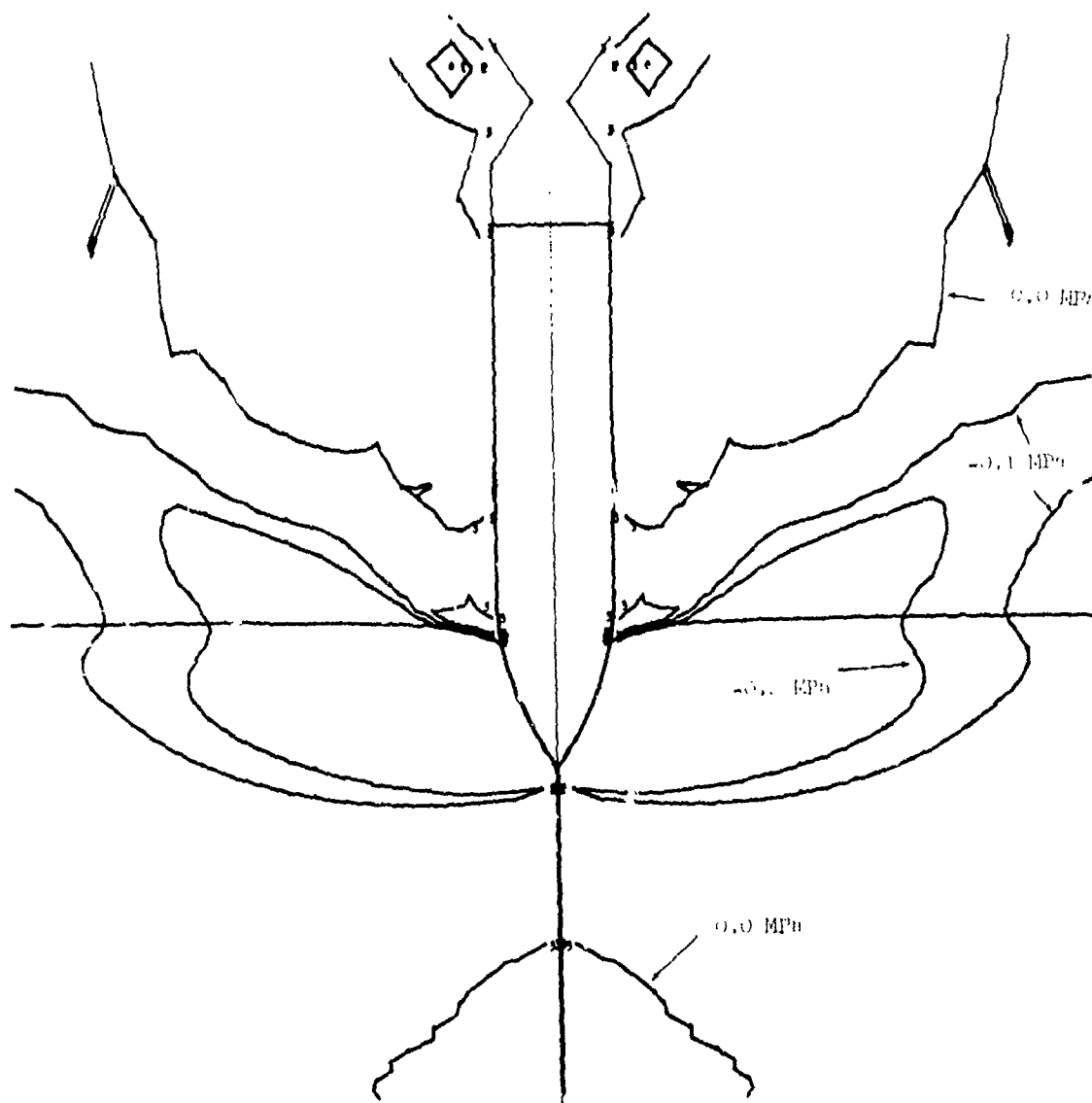
Figure A-127

Contours of Axial Stress in Target. Projectile at 5.2 m Depth.
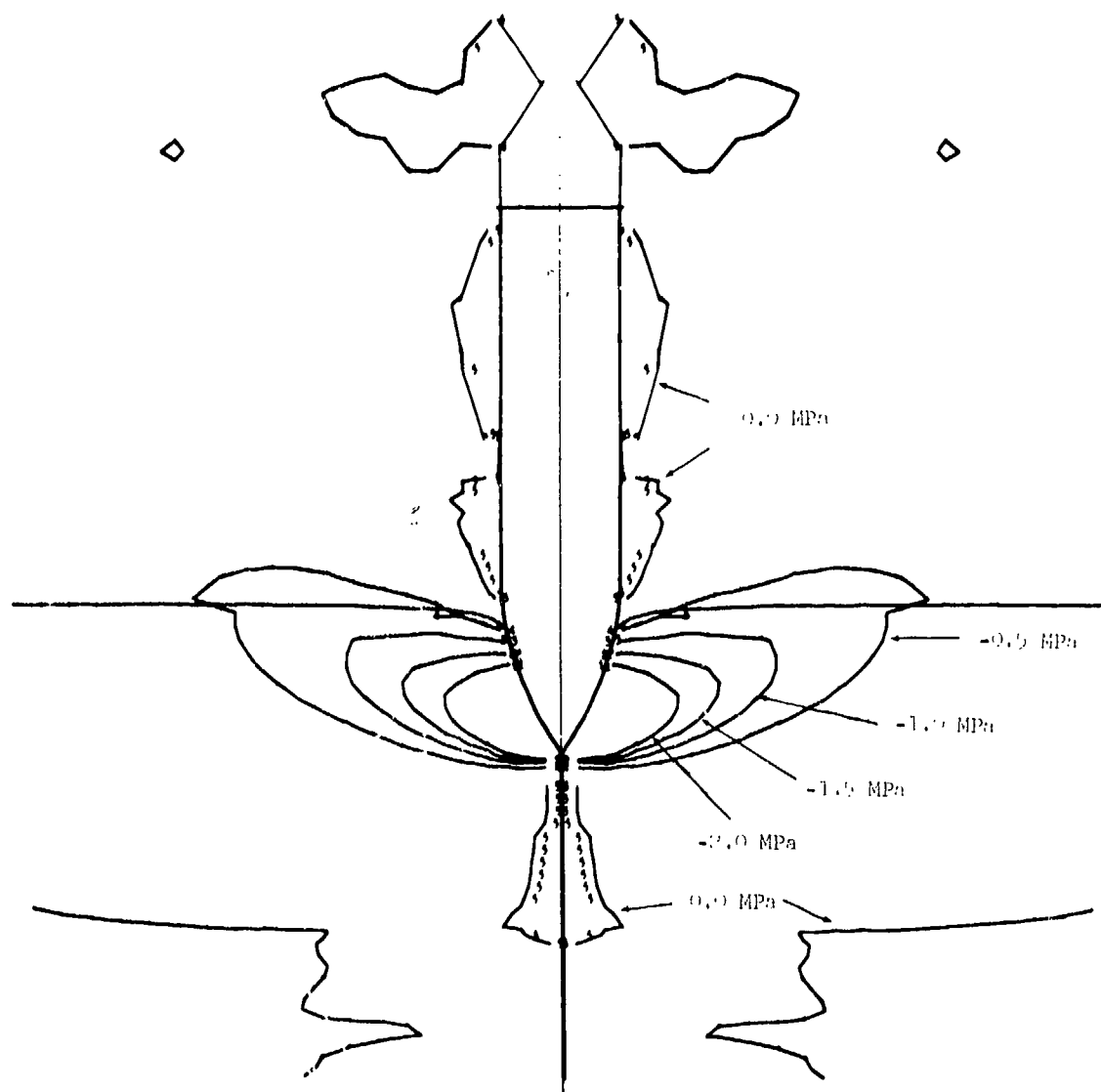
Figure A-128

Contours of Radial Stress in Target. Projectile at 5.0 m Depth.
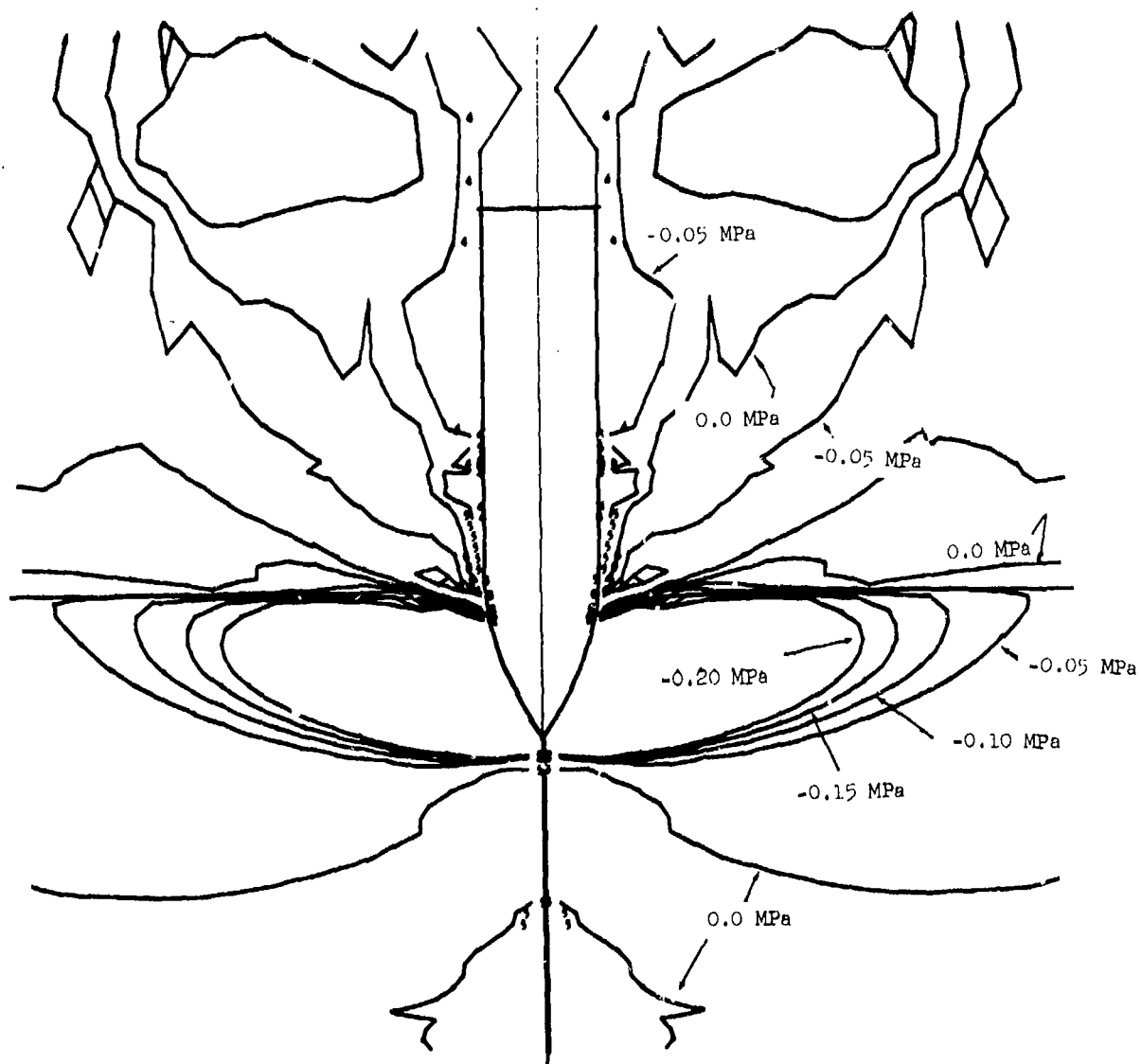
Figure A-129

Contours of Hoop Stress in Target. Projectile at 5.2 m Depth.
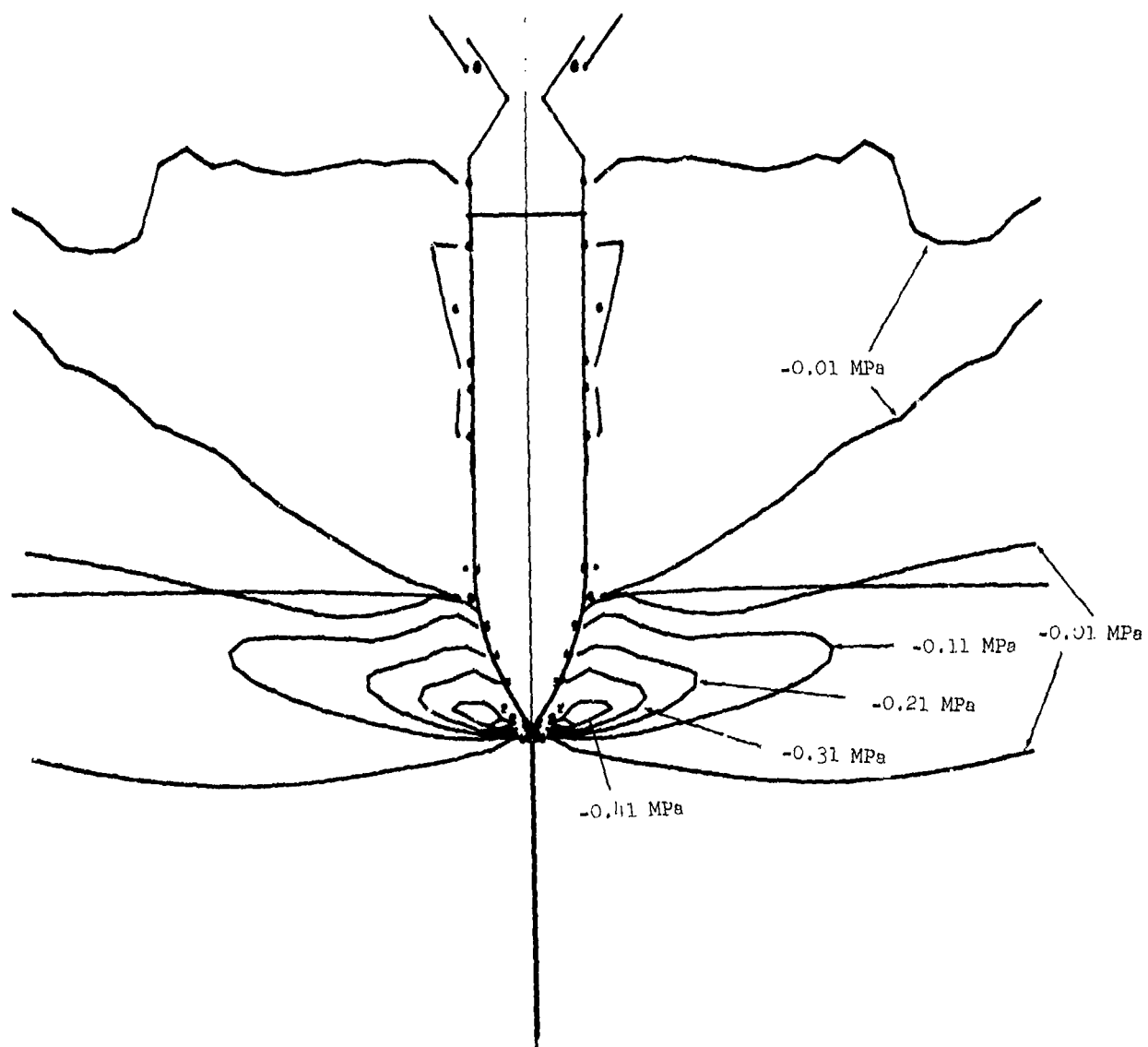
Figure A-130
Contours of Radial-Vertical Shear Stress in Target.   Projectile at 5.2 m Depth.

223
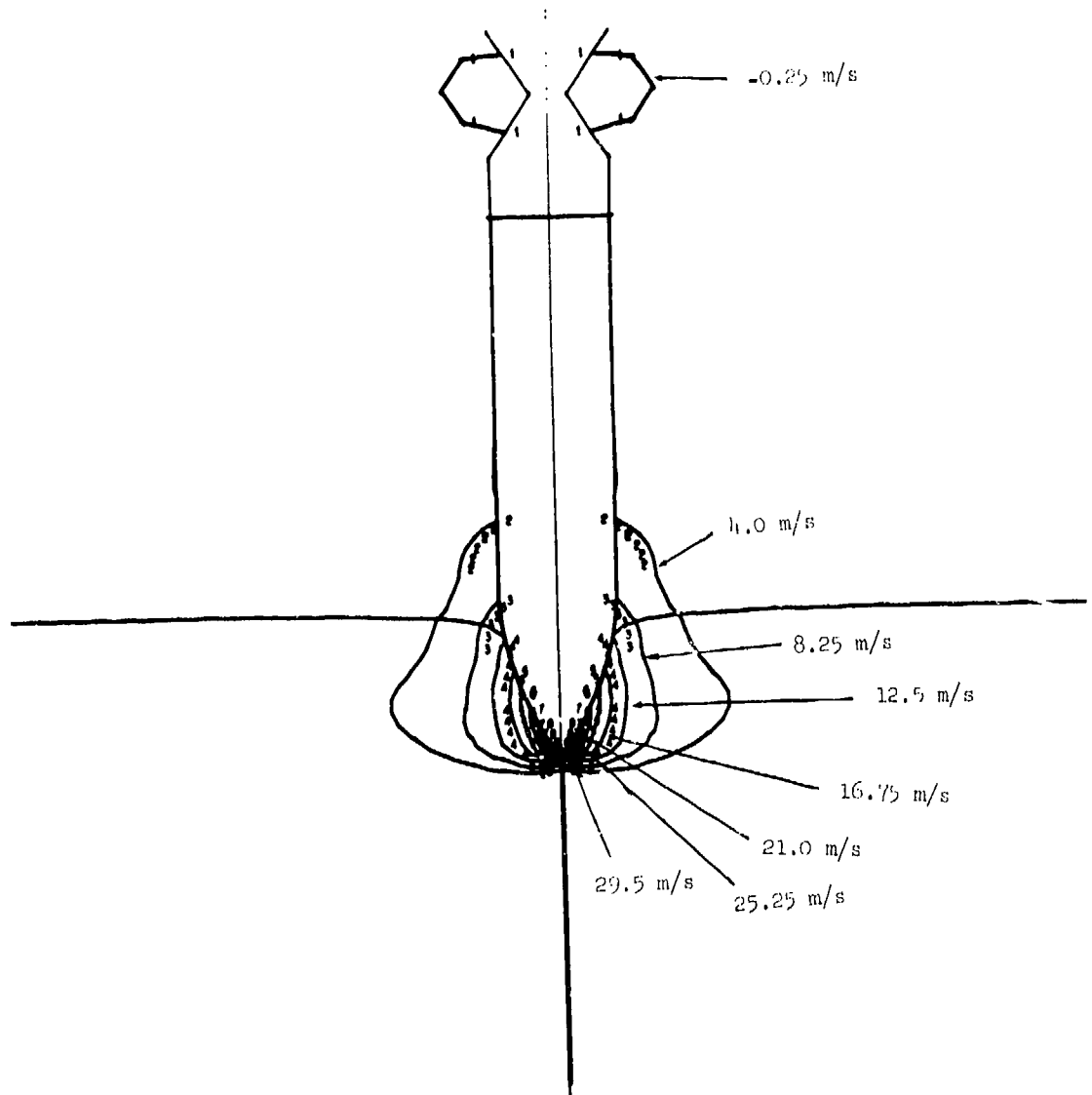
Figure A-131

Contours of Vertical Velocity in Target. Projectile at 5.2 m Depth.
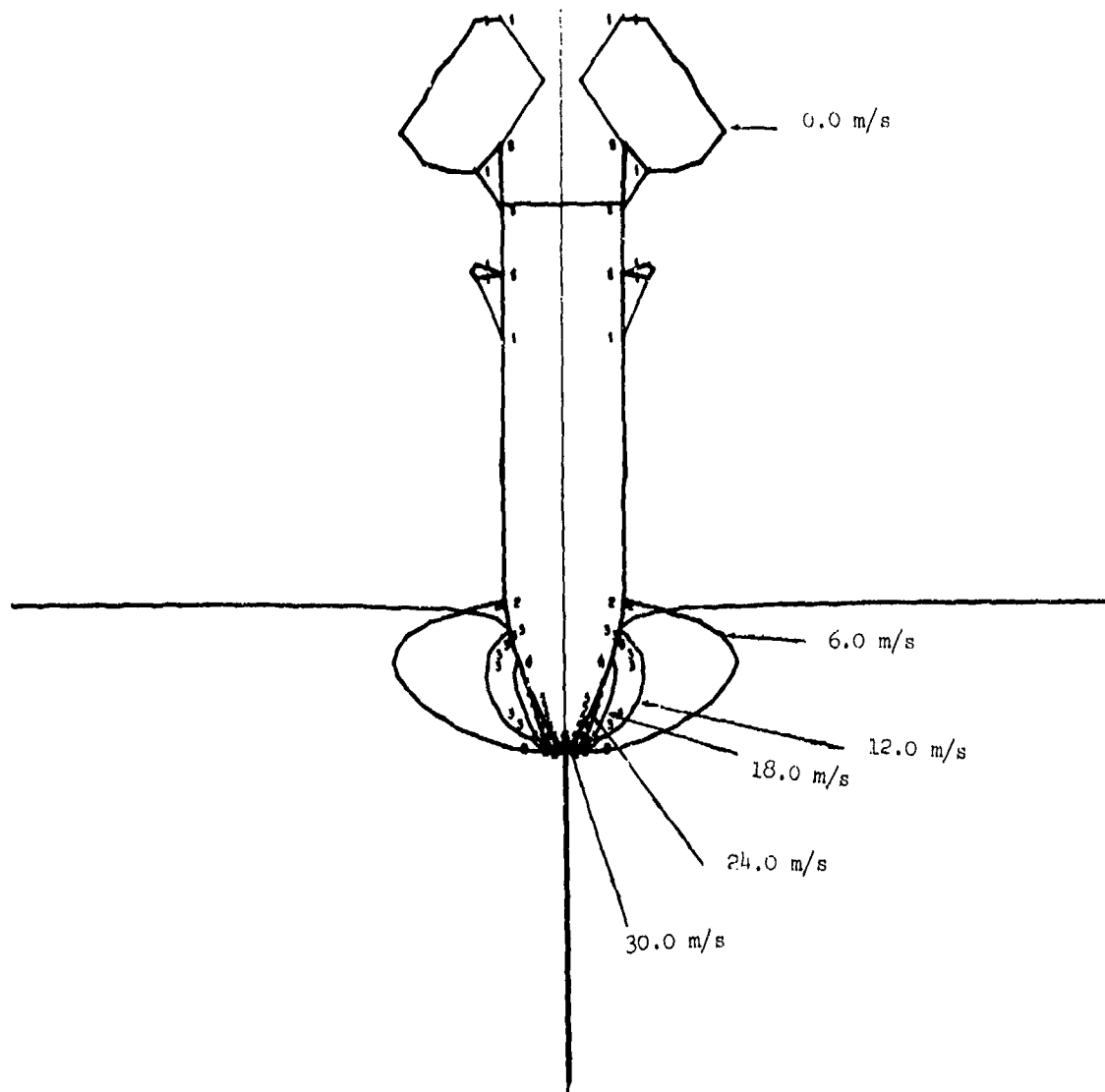
Figure A-132

Contours of Radial Velocity in Target. Projectile at 5.2 m Depth.

6.8 m
48.4 msec
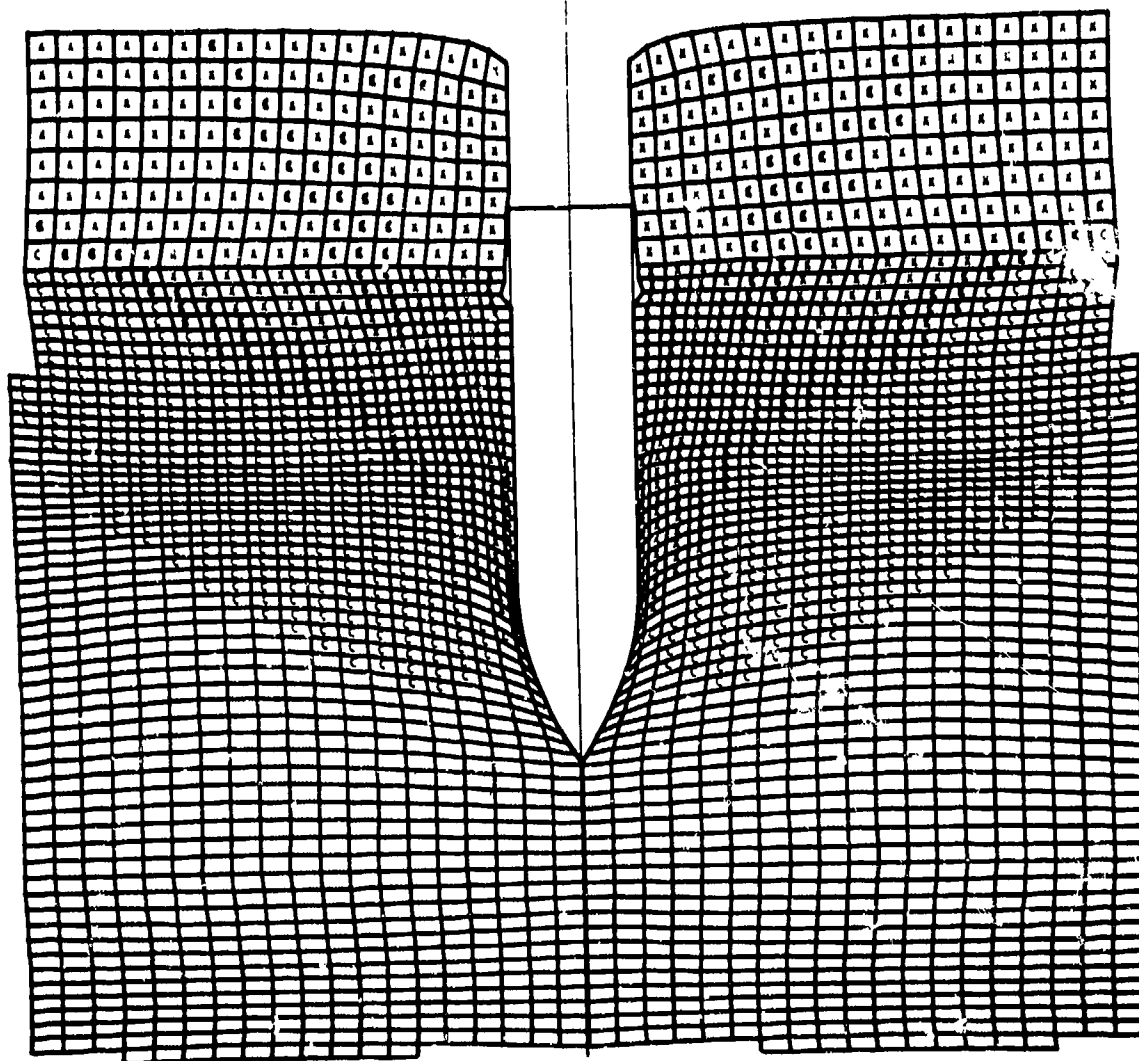
Figure A-133

Lagrangian Coordinates When Projectile has Penetrated to Depth of 6.8 m. Radial Dimensions Doubled for Clarity.
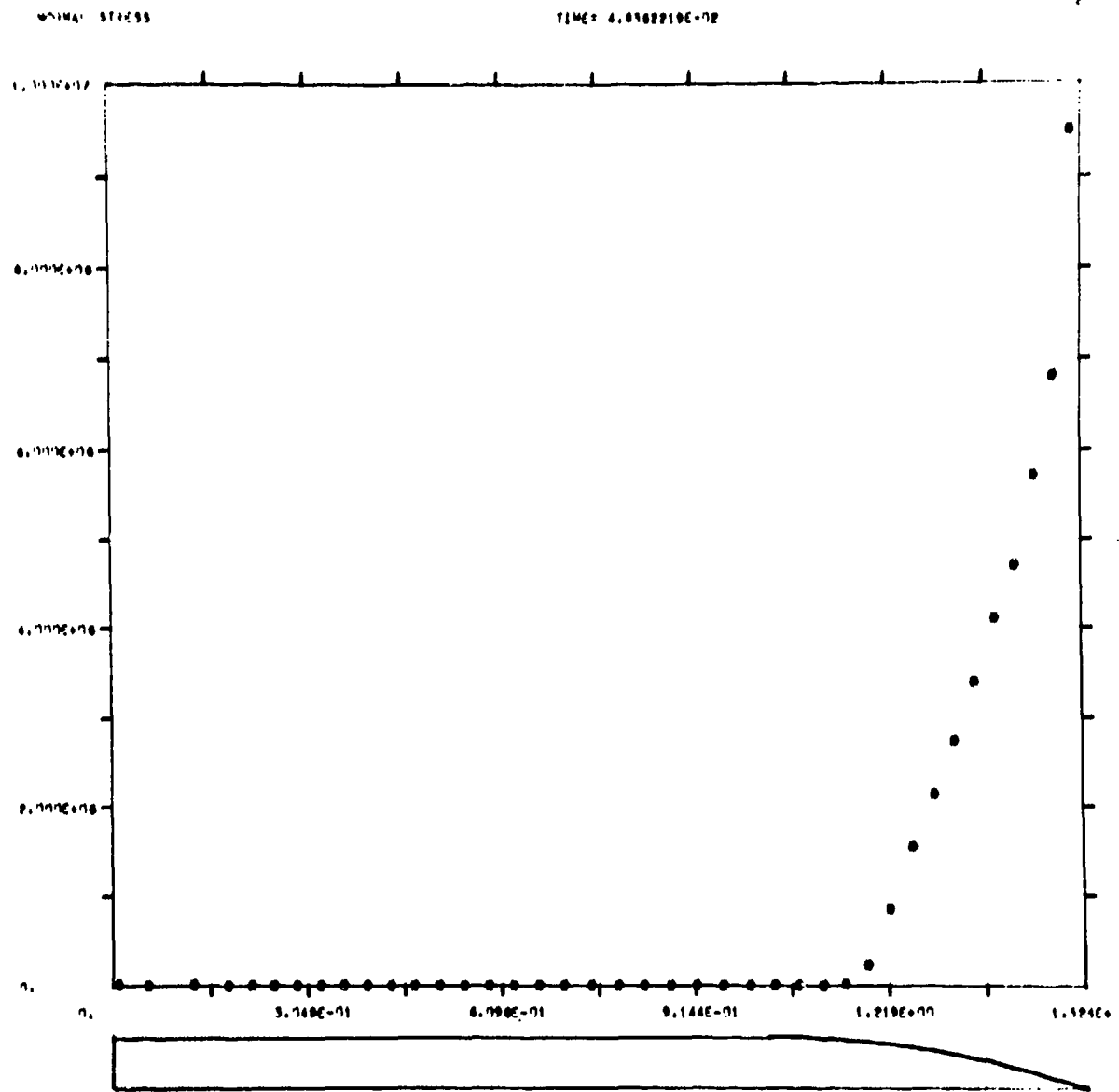
Figure A-134

Normal Stress (Pa) Along Surface of Projectile When Projectile is at 6.8 m Depth.
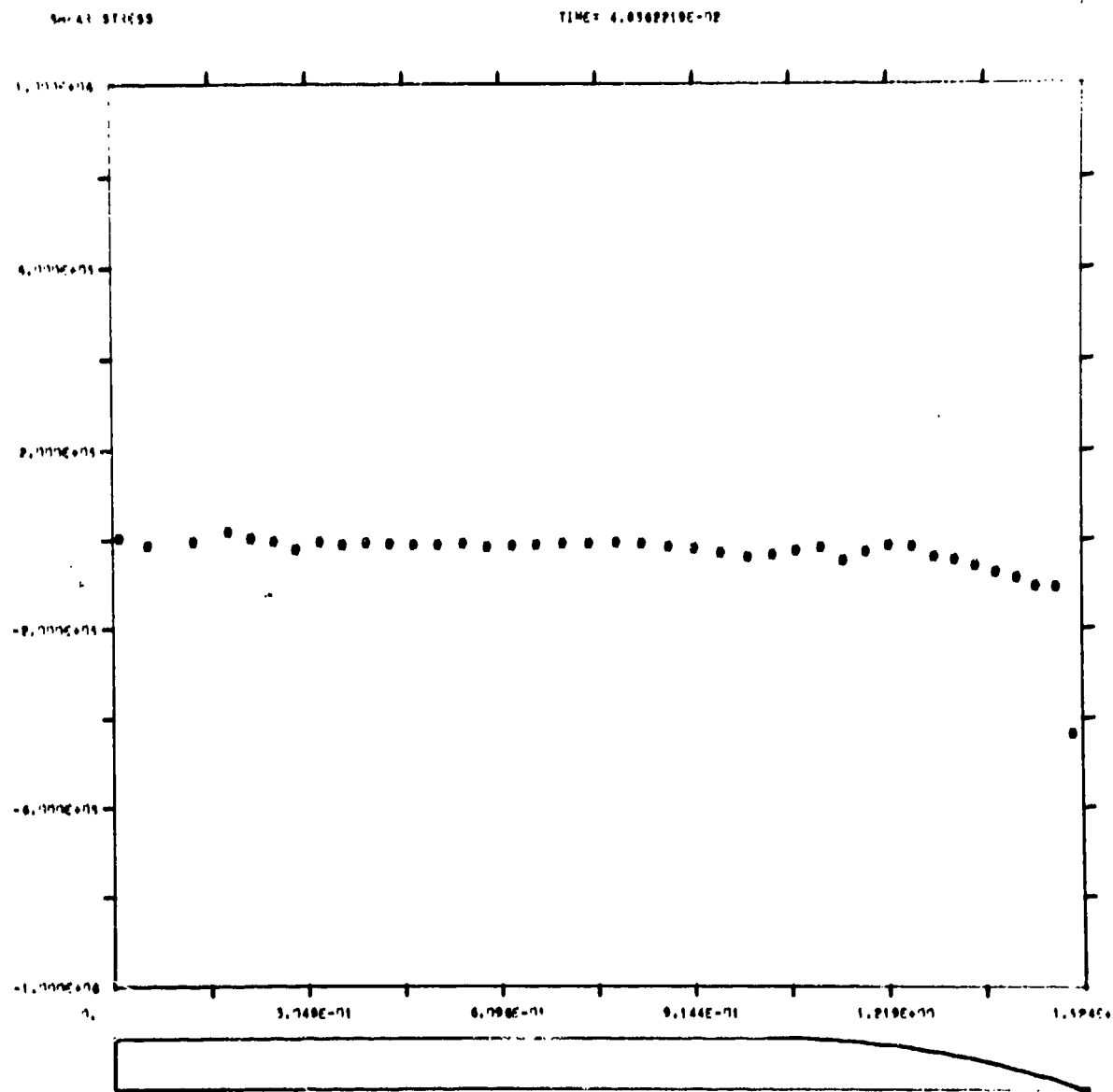
Figure A-135

Tangential Stress (Pa) Along Surface of Projectile When Projectile is at 6.8 m Depth.
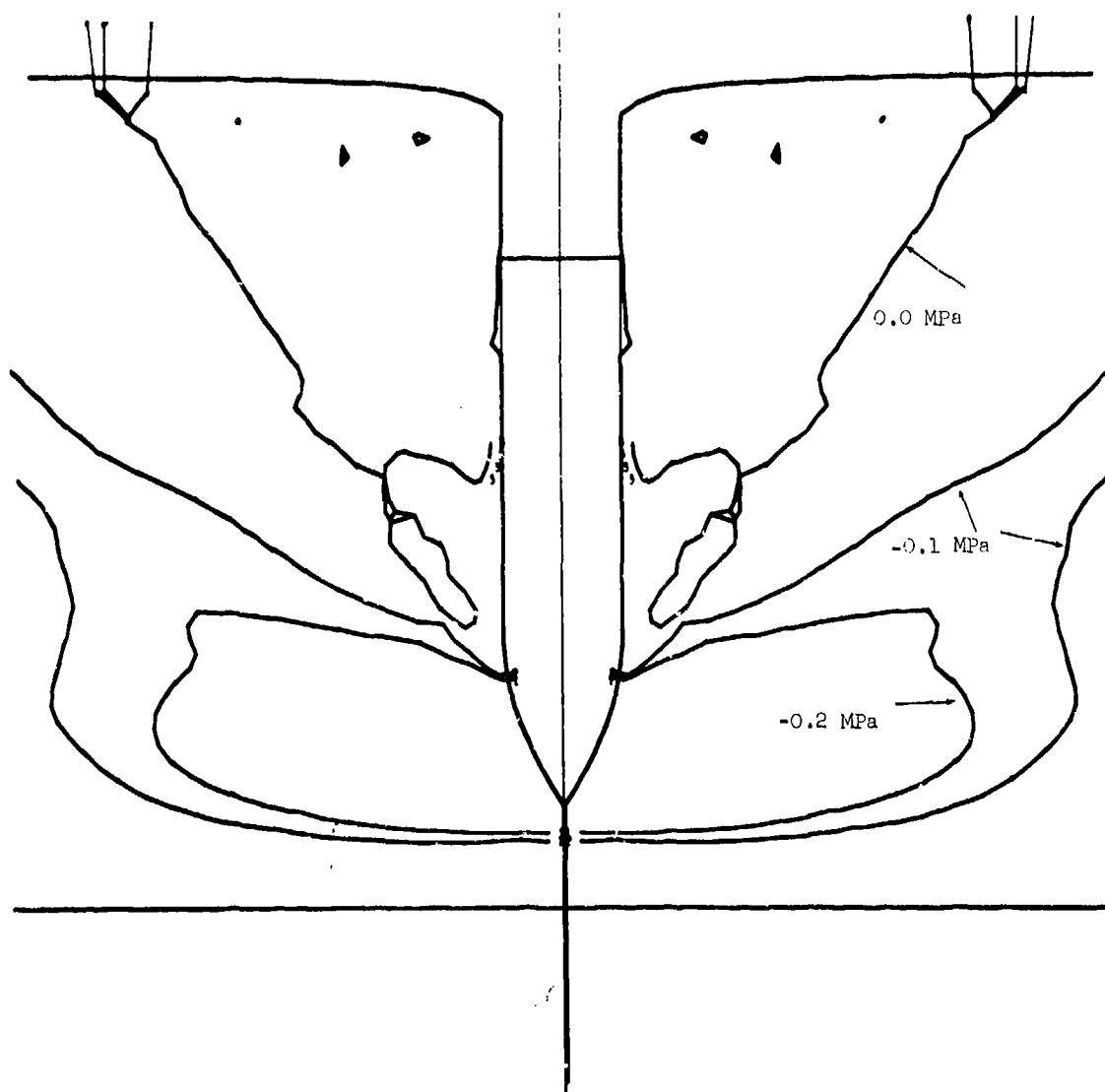
Figure A-136

Contours of Axial Stress in Target. Projectile at 6.8 m Depth.
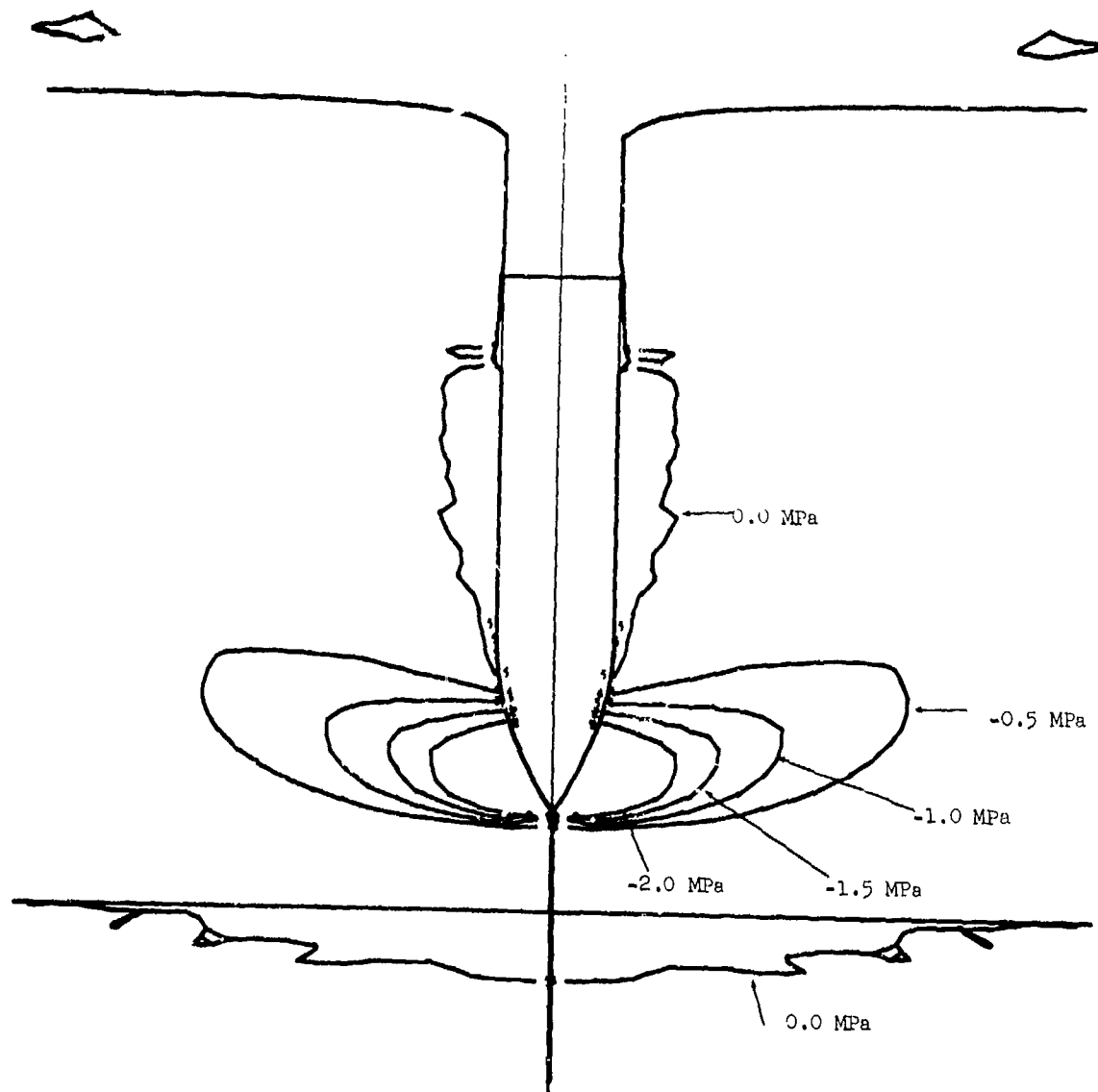
Figure A-137
Contours of Radial Stress in Target. Projectile at 6.8 m Depth.
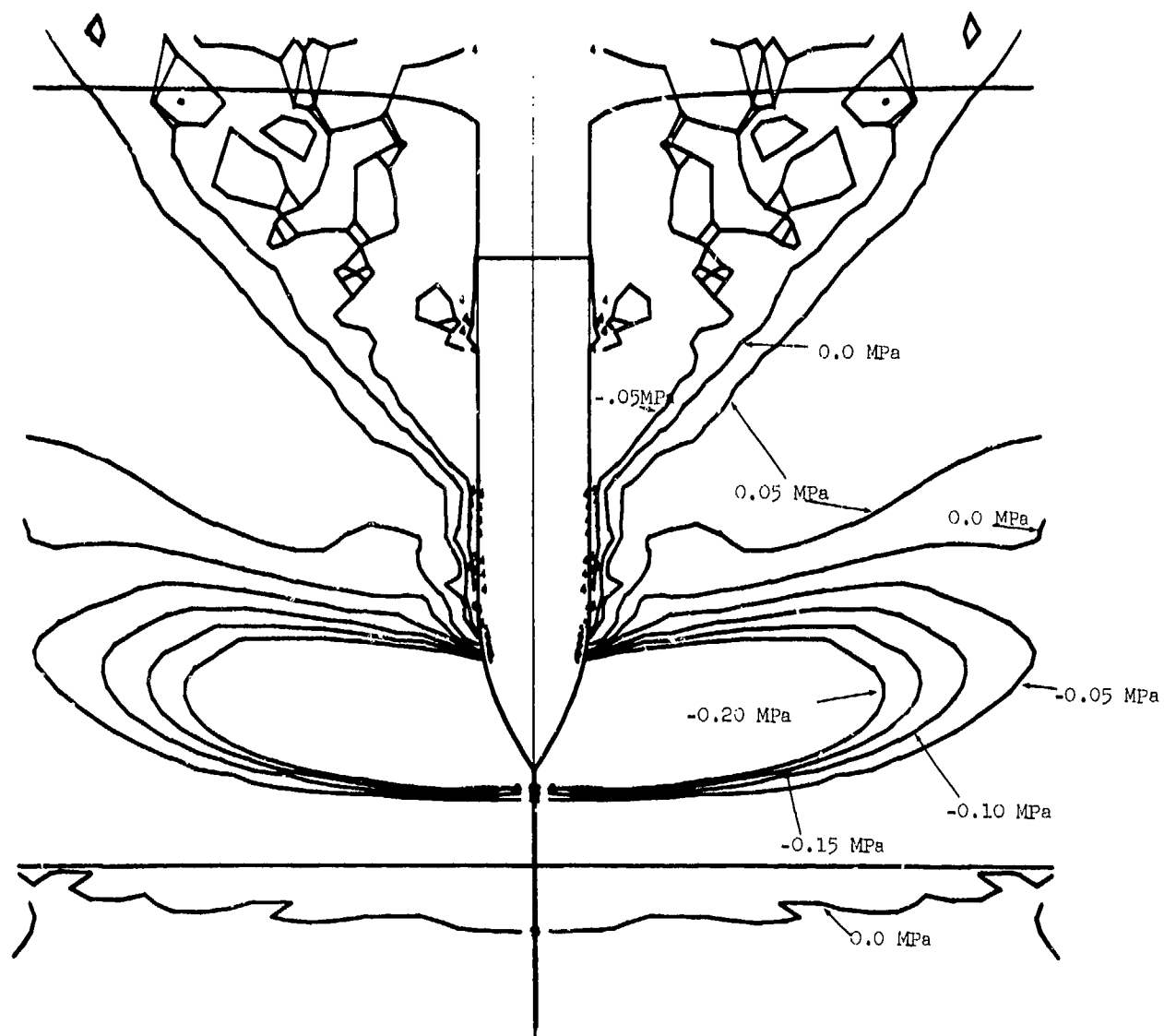
Figure A-138

Contours of Hoop Stress in Target. Projectile at 6.8 m Depth.
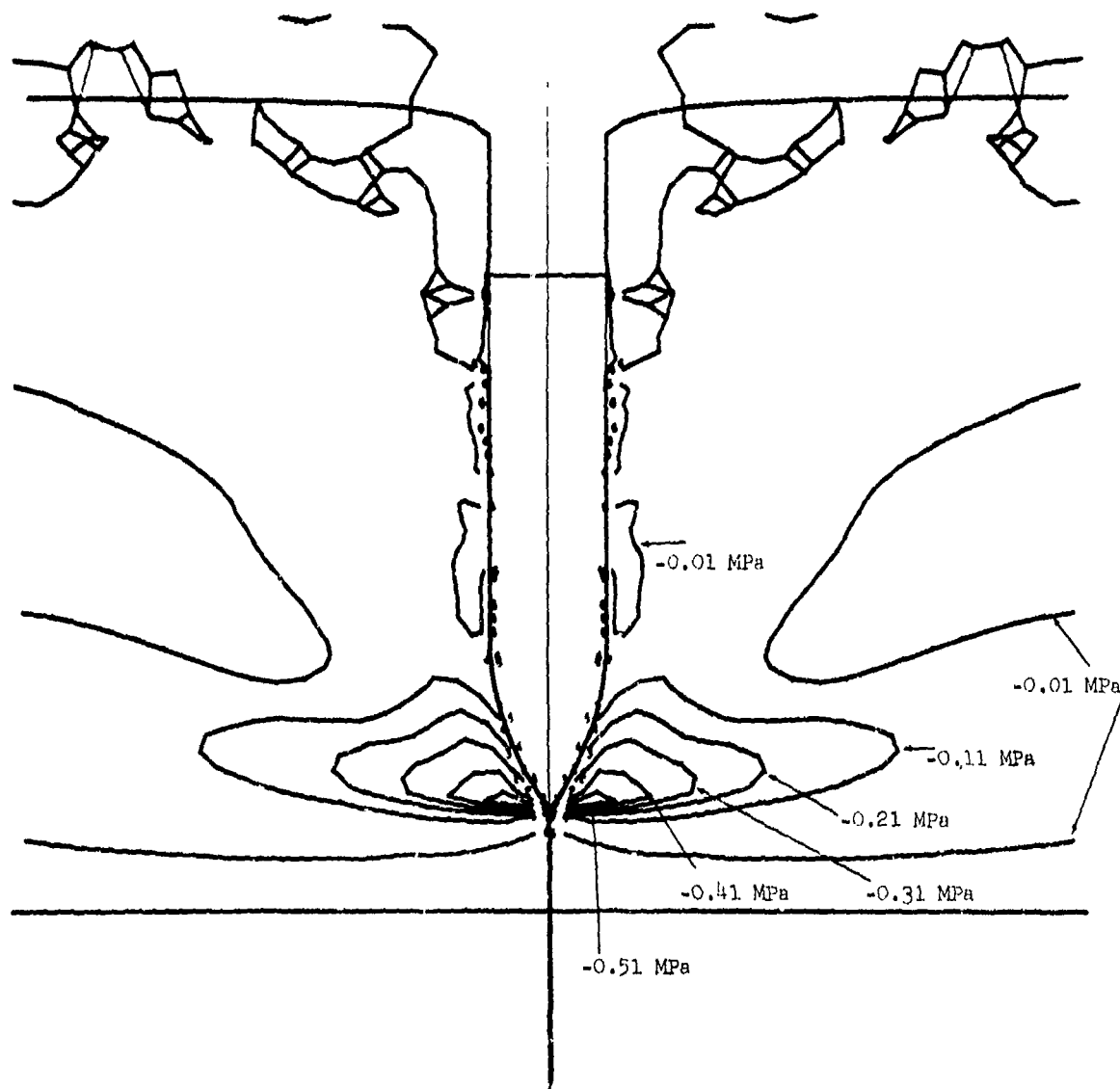
Figure A-139

Contours of Radial-Vertical Shear Stress in Target. Projectile at 6.8 m Depth.

Figure A-140
Contours of Vertical Velocity in Target. Projectile at 6.8 m Depth.

Figure A-141
Contours of Radial Velocity in Target. Projectile at 6.8 m Depth.

234

APPENDIX B

List of Illustrations Appendix B

B-58. Deviator Stress, J2, History (Pa) in Soil at Range 75 mm, Depth 0.4 m (Deformable Penetrator).

B-59. Radial Velocity History (m/s) in Soil at Range 0.14 m, Depth 0.1 m (Deformable Penetrator).

B-60. Vertical Velocity History (m/s) in Soil at Range 0.14 m, Depth 0.1 m (Deformable Penetrator).

B-61. Radial Displacement History (m) in Soil at Range 0.14 m, Depth 0.1 m (Deformable Penetrator).

B-62. Vertical Displacement History (m) in Soil at Range 0.14 m, Depth 0.1 m (Deformable Penetrator).

B-63. Pressure History (Pa) in Soil at Range 0.14 m, Depth 0.1 m (Deformable Penetrator).

B-64. Deviator Stress, J2, History (Pa) in Soil at Range 0.14 m, Depth 0.1 m (Deformable Penetrator).

B-65. Radial Velocity History (m/s) in Soil at Range 0.14 m, Depth 0.2 m (Deformable Penetrator).

B-66. Vertical Velocity History (m/s) in Soil at Range 0.14 m, Depth 0.2 m (Deformable Penetrator).

B-67. Radial Displacement History (m) in Soil at Range 0.14 m, Depth 0.2 m (Deformable Penetrator).

B-68. Vertical Displacement History (m) in Soil at Range 0.14 m, Depth 0.2 m (Deformable Penetrator).

B-69. Pressure History (Pa) in Soil at Range 0.14 m, Depth 0.2 m (Deformable Penetrator).

B-70. Deviator Stress, J2, History (Pa) in Soil at Range 0.14 m, Depth 0.2 m (Deformable Penetrator).

B-84. Vertical Velocity History (m/s) in Soil at Range 0.28 m, Depth
       0.2 m (Deformable Penetrator).

B-85. Radial Displacement History (m) in Soil at Range 0.28 m, Depth 0.2 m
       (Deformable Penetrator).

B-86. Vertical Displacement History (m) in Soil at Range 0.28 m, Depth 0.2 m
       (Deformable Penetrator).

B-87. Pressure History (Pa) in Soil at Range 0.28 m, Depth 0.2 m (Deformable
       Penetrator).

B-88. Deviator Stress, J2, History (Pa) in Soil at Range 0.28 m, Depth
       0.2 m (Deformable Penetrator).

B-89. Radial Velocity History (m/s) in Soil at Range 0.28 m, Depth 0.4 m
       (Deformable Penetrator).

B-90. Vertical Velocity History (m/s) in Soil at Range 2.28 m, Depth 0.4 m
       (Deformable Penetrator).

B-91. Radial Displacement History (m) in Soil at Range 0.28 m, Depth 0.4 m
       (Deformable Penetrator).

B-92. Vertical Displacement History (m) in Soil at Range 0.28 m, Depth 0.4 m
       (Deformable Penetrator).

B-93. Pressure History (Pa) in Soil at Range 0.28 m, Depth 0.4 m (Deformable
       Penetrator).

B-94. Deviator Stress, J2, History (Pa) in Soil at Range 0.28 m, Depth
       0.4 m (Deformable Penetrator).

B-95. Radial Velocity History (m/s) in Soil at Range 0.44 m, Depth 0.1 m
       (Deformable Penetrator).

B-96. Vertical Velocity History (m/s) in Soil at Range 0.44 m, Depth 0.1 m
       (Deformable Penetrator).

243

Figure B-1

Lagrangian coordinates at 0.4 ms (radial dimensions doubled to show deformable penetrator).
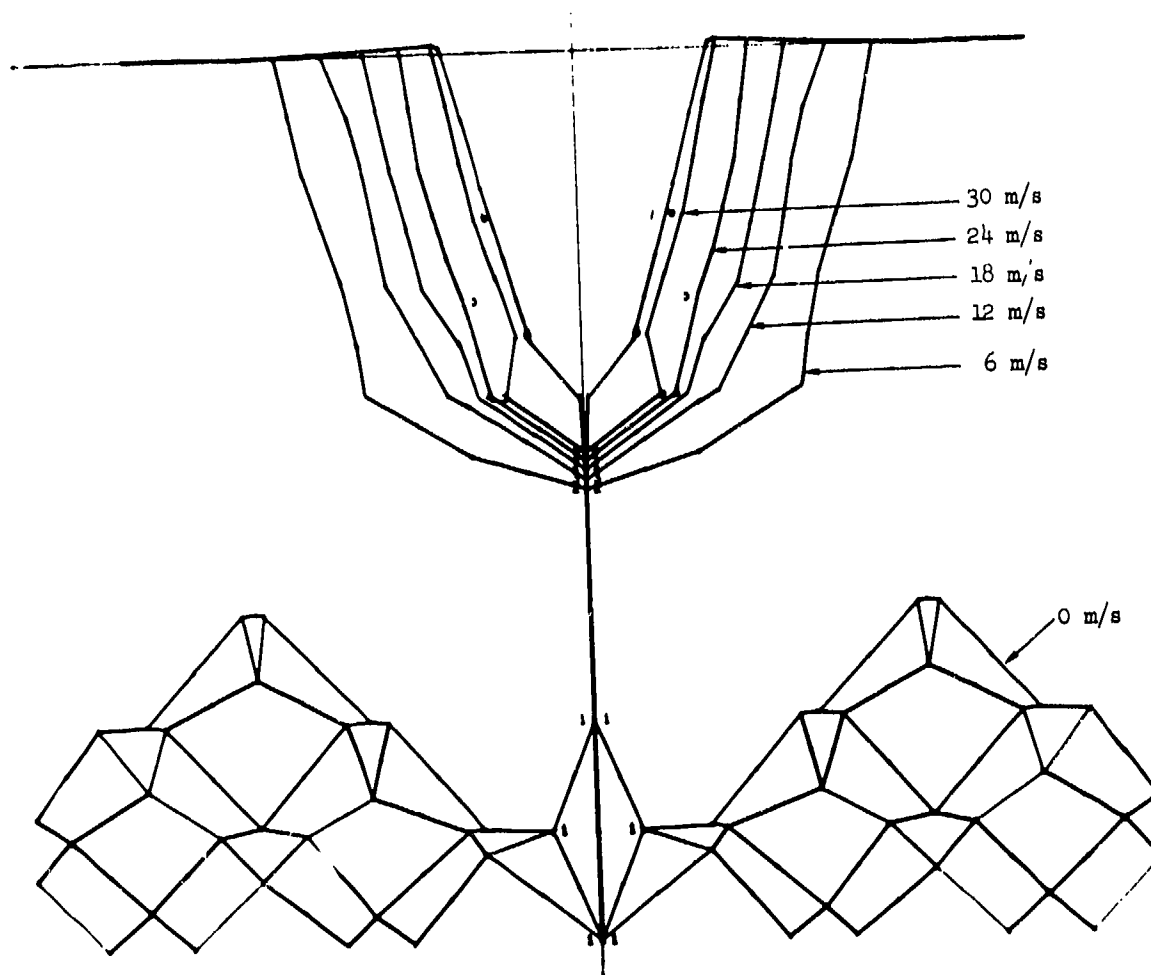
Figure B-2
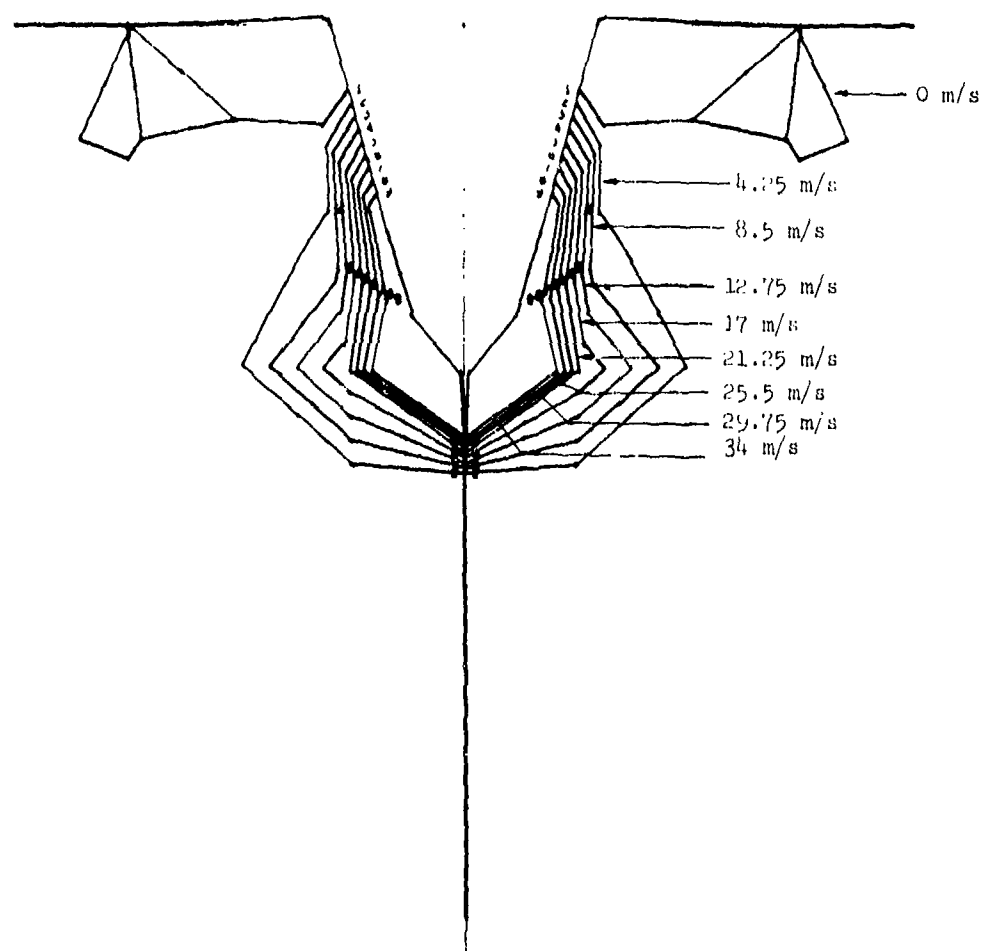Contours of radial velocity at 0.4 ms (deformable penetrator not shown).

246

Figure B-3

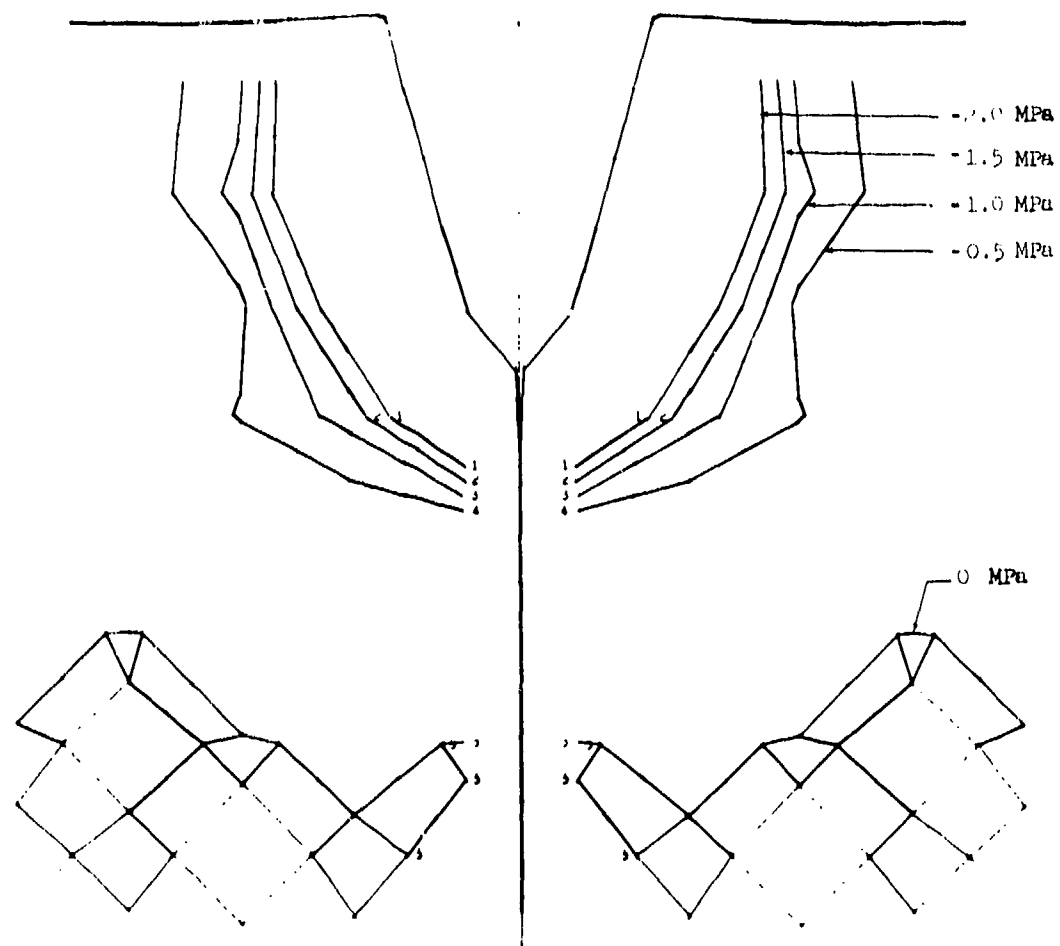Contours of vertical velocity at 0.4 ms (deformable penetrator now shown).

Figure B-4

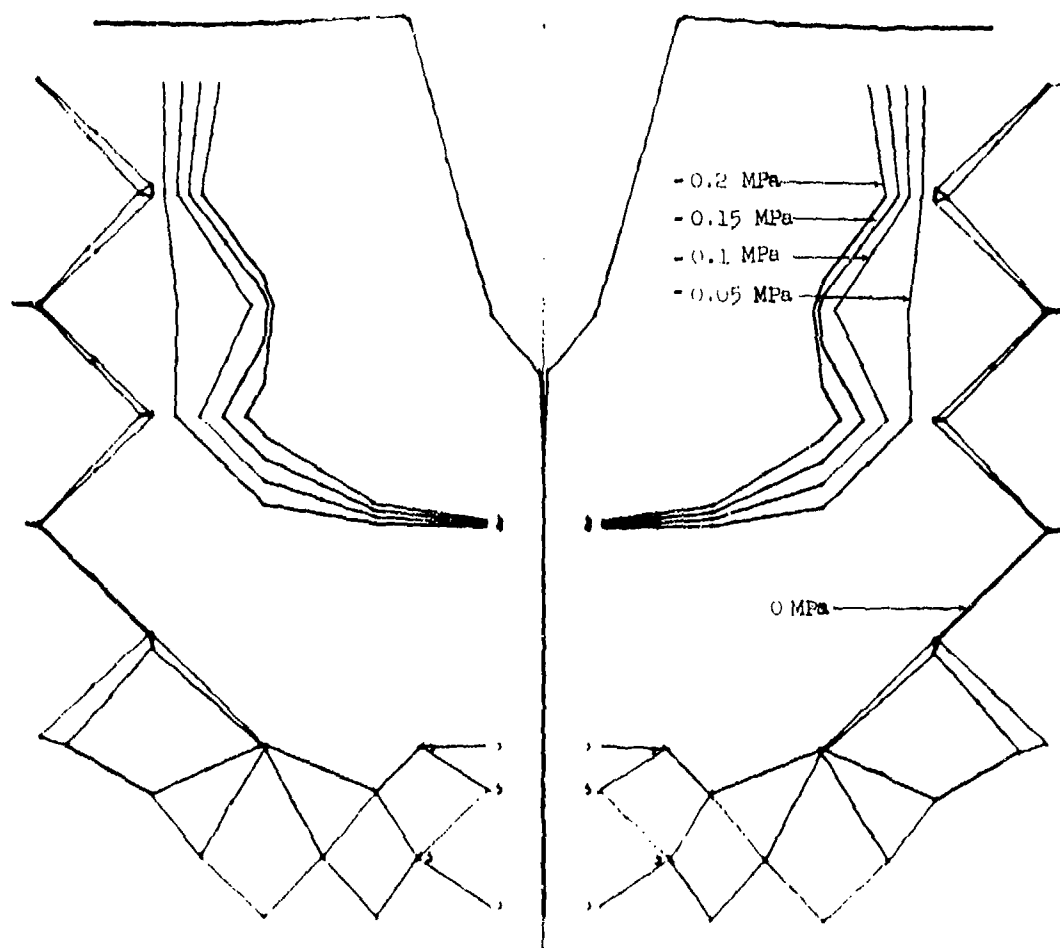Contours of radial stress at 0.4 ms (deformable penetrator not shown).

Figure B-5

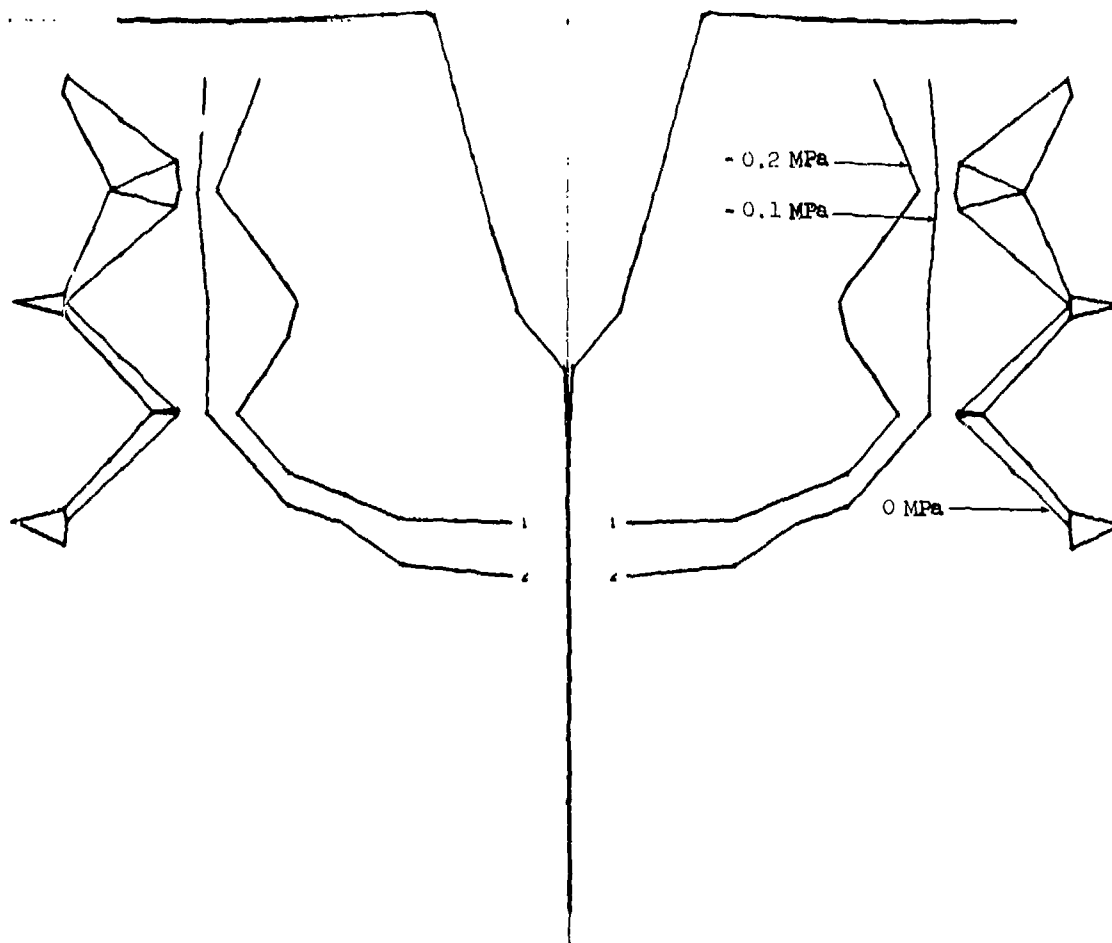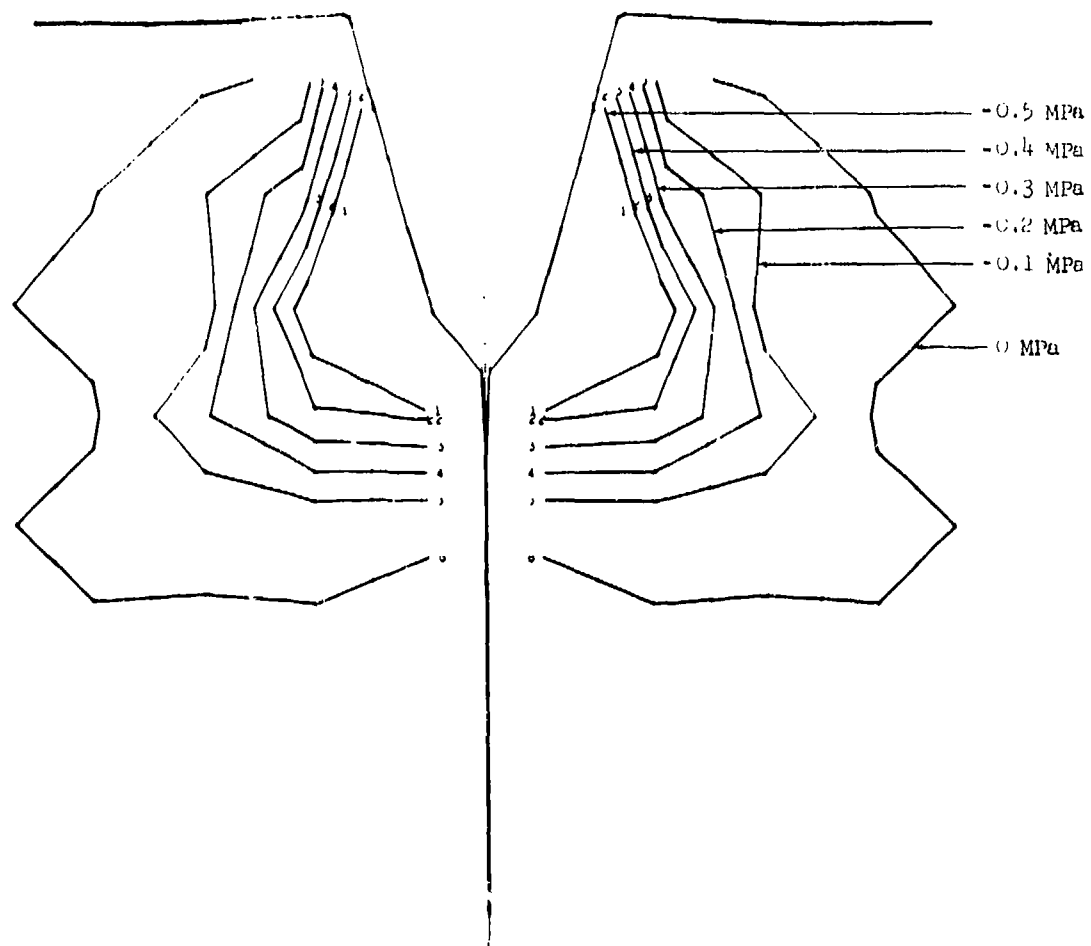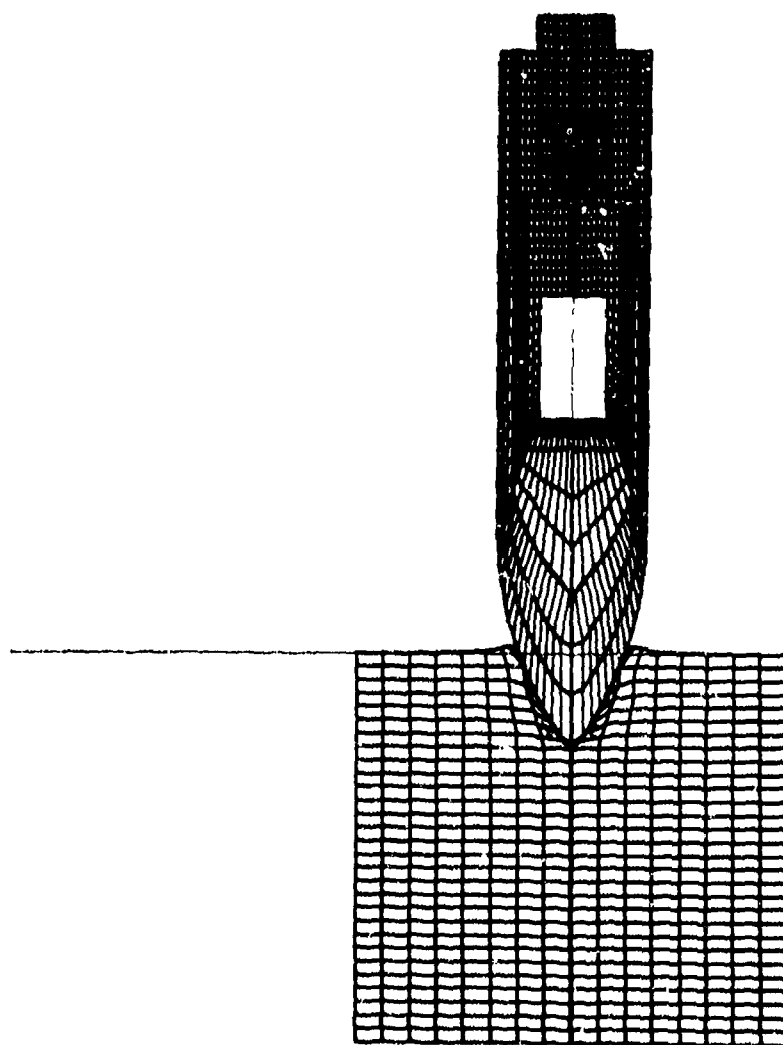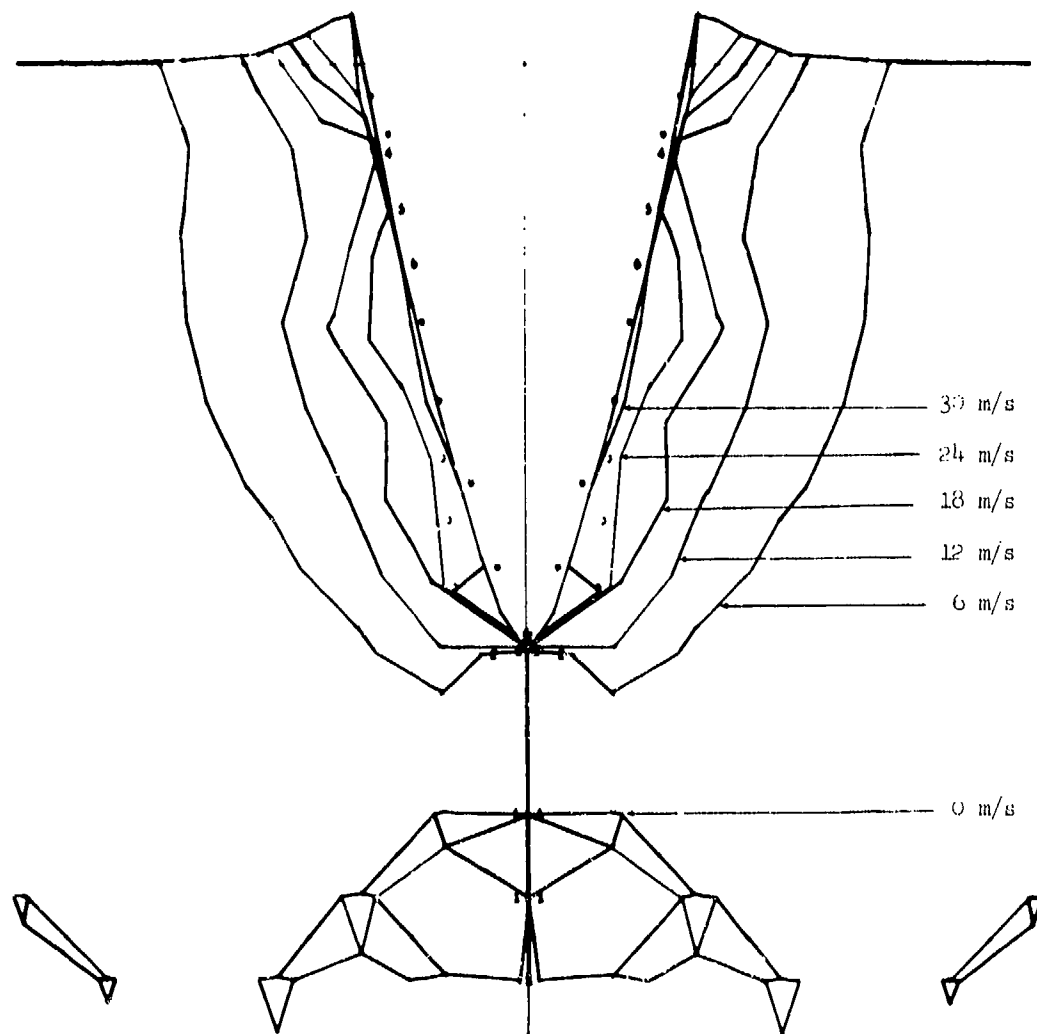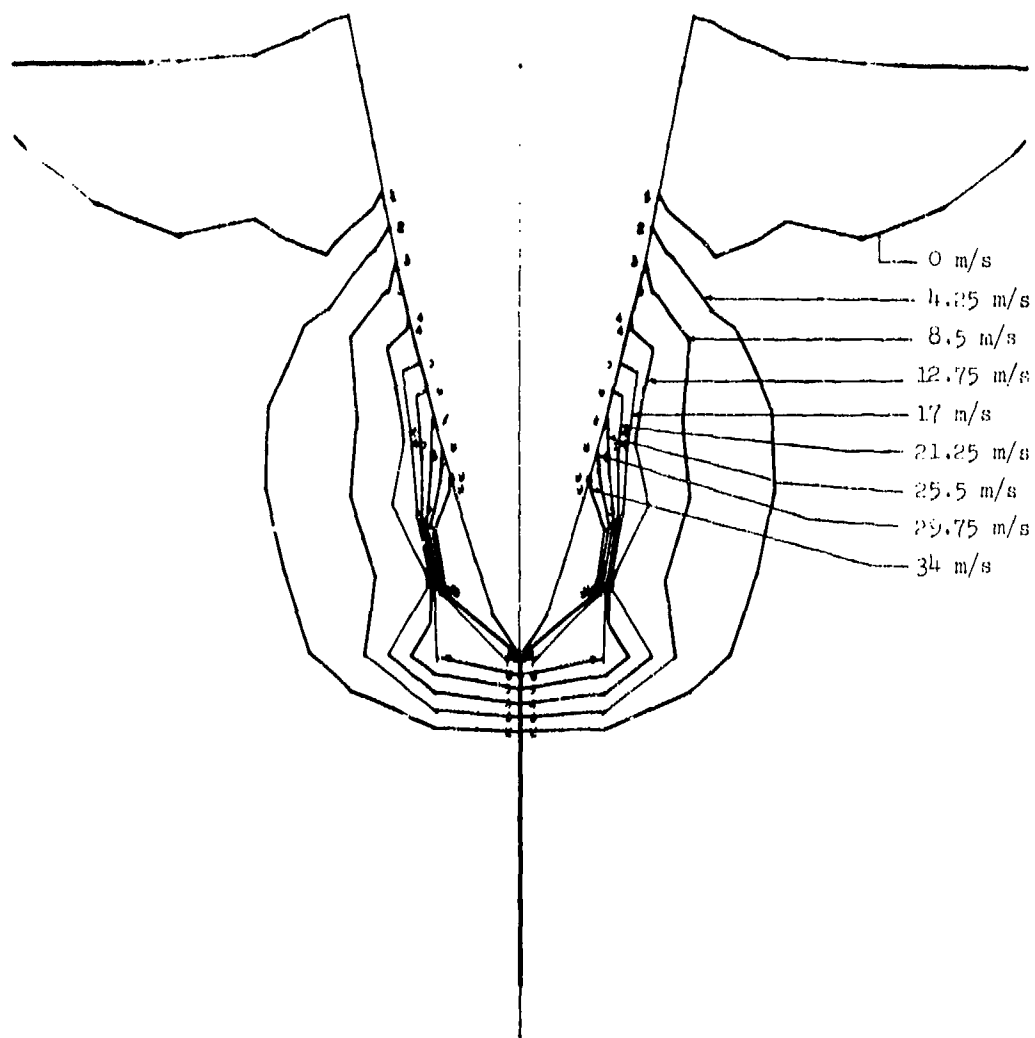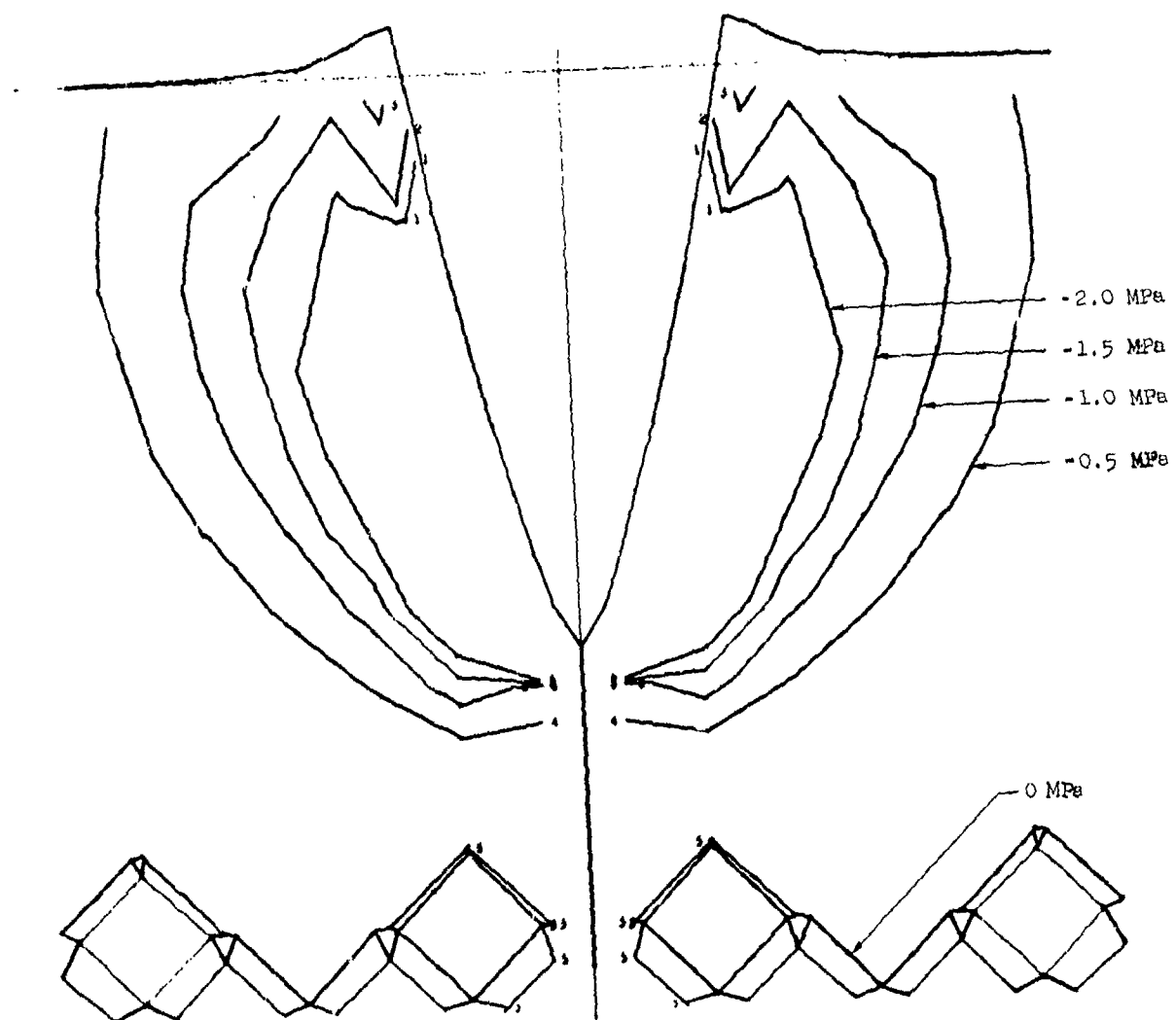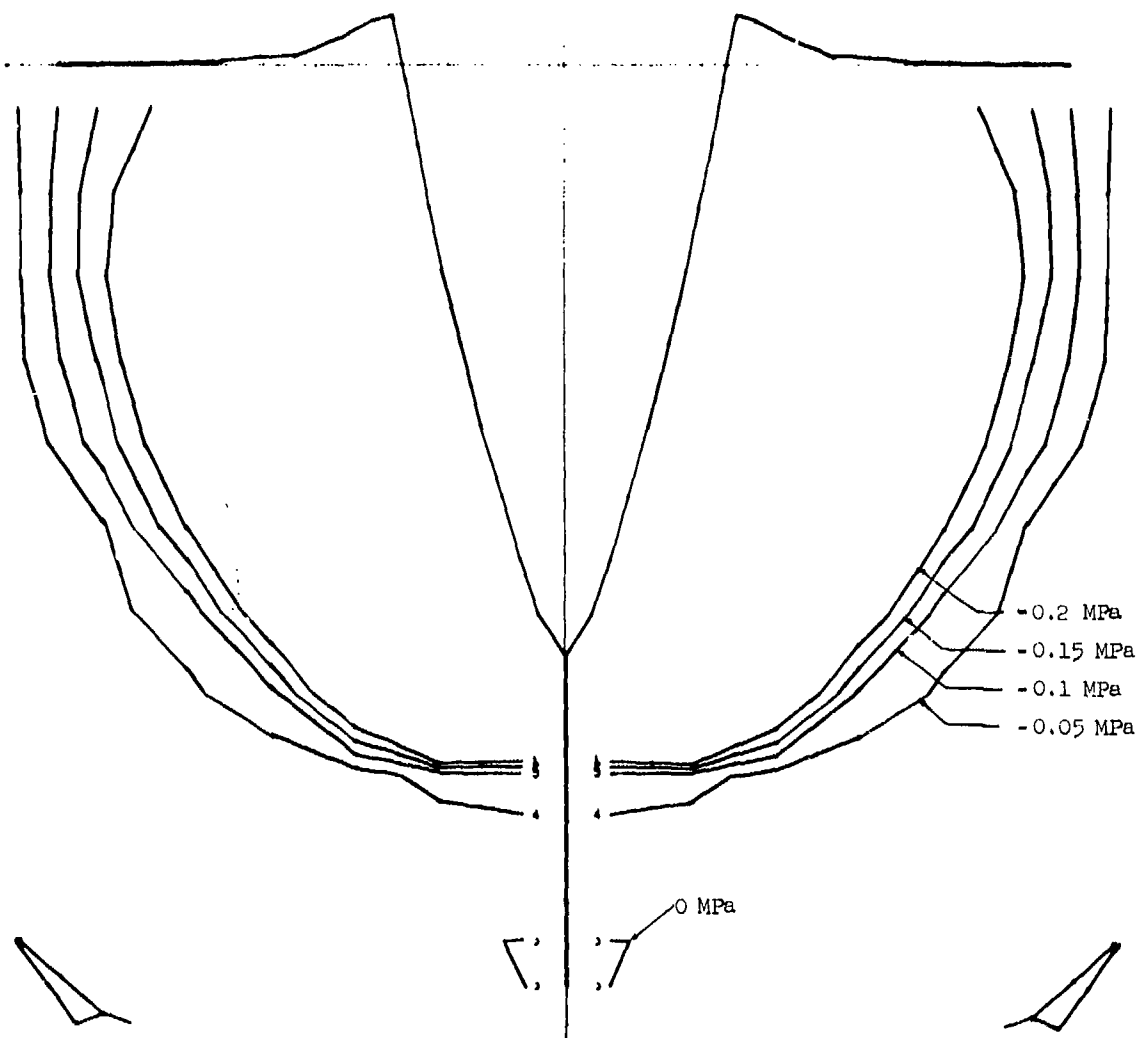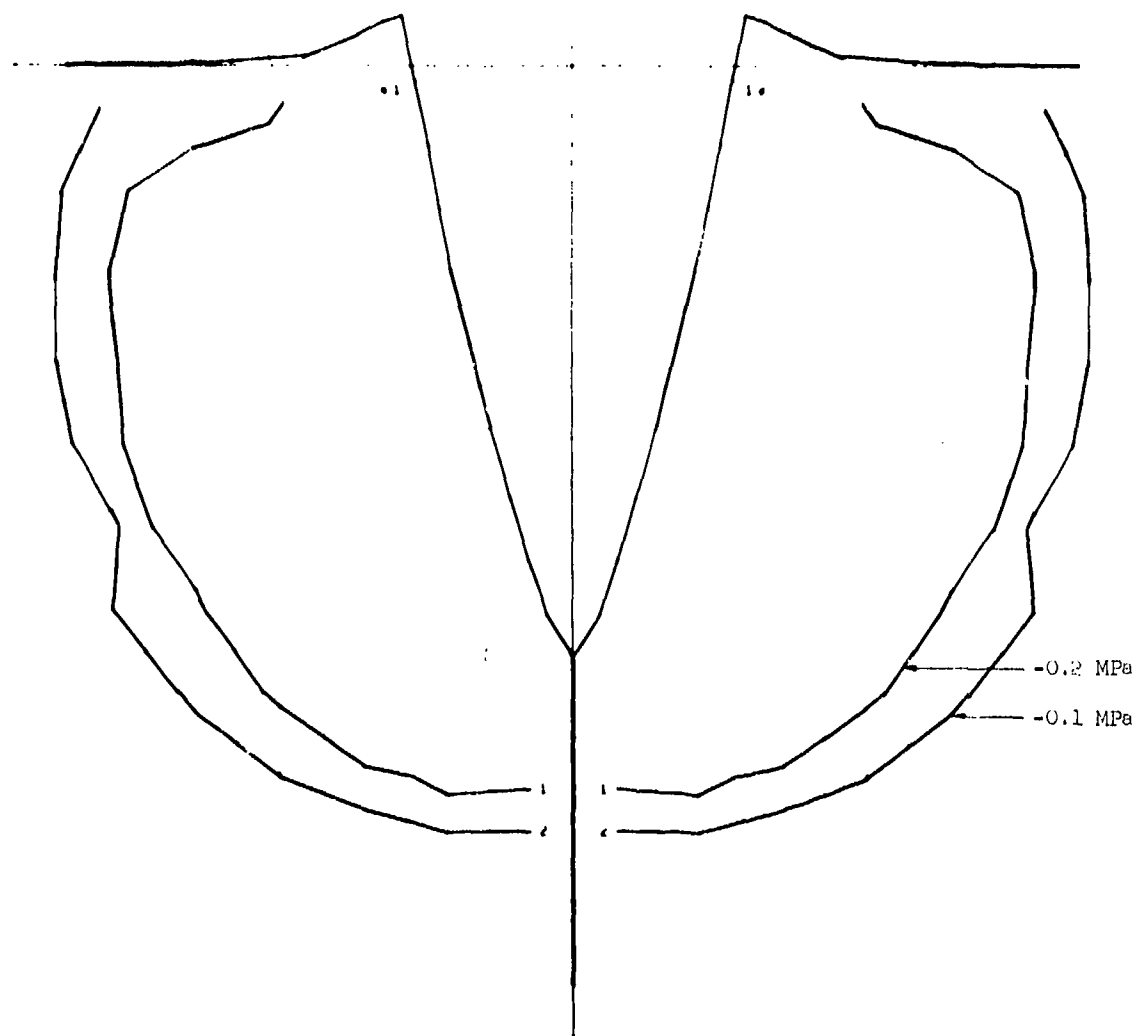Contours of hoop stress at 0.4 ms (deformable penetrator not shown).

Figure B-6

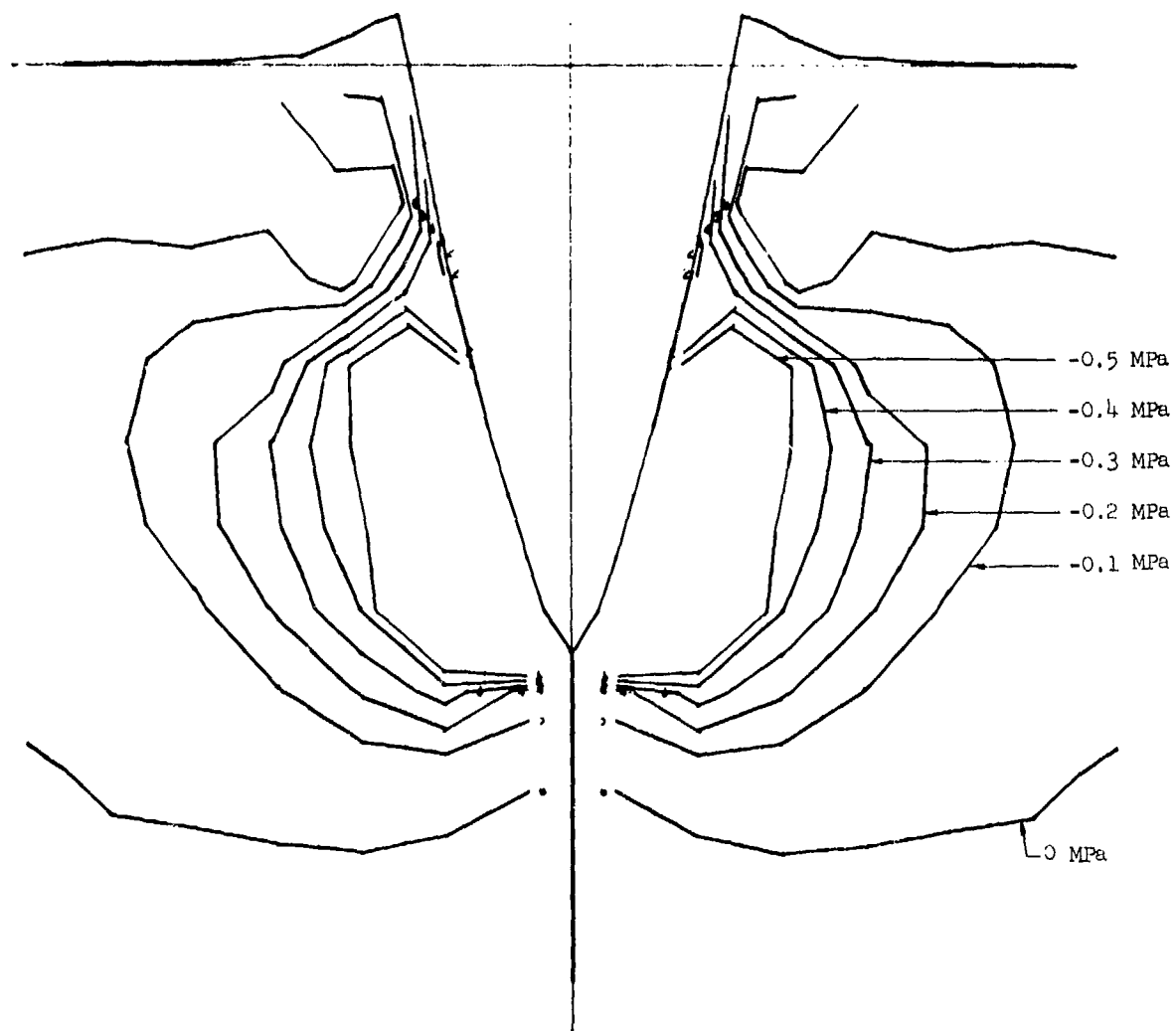Contours of vertical stress at 0.4 ms (deformable penetrator not shown).

Figure B-7

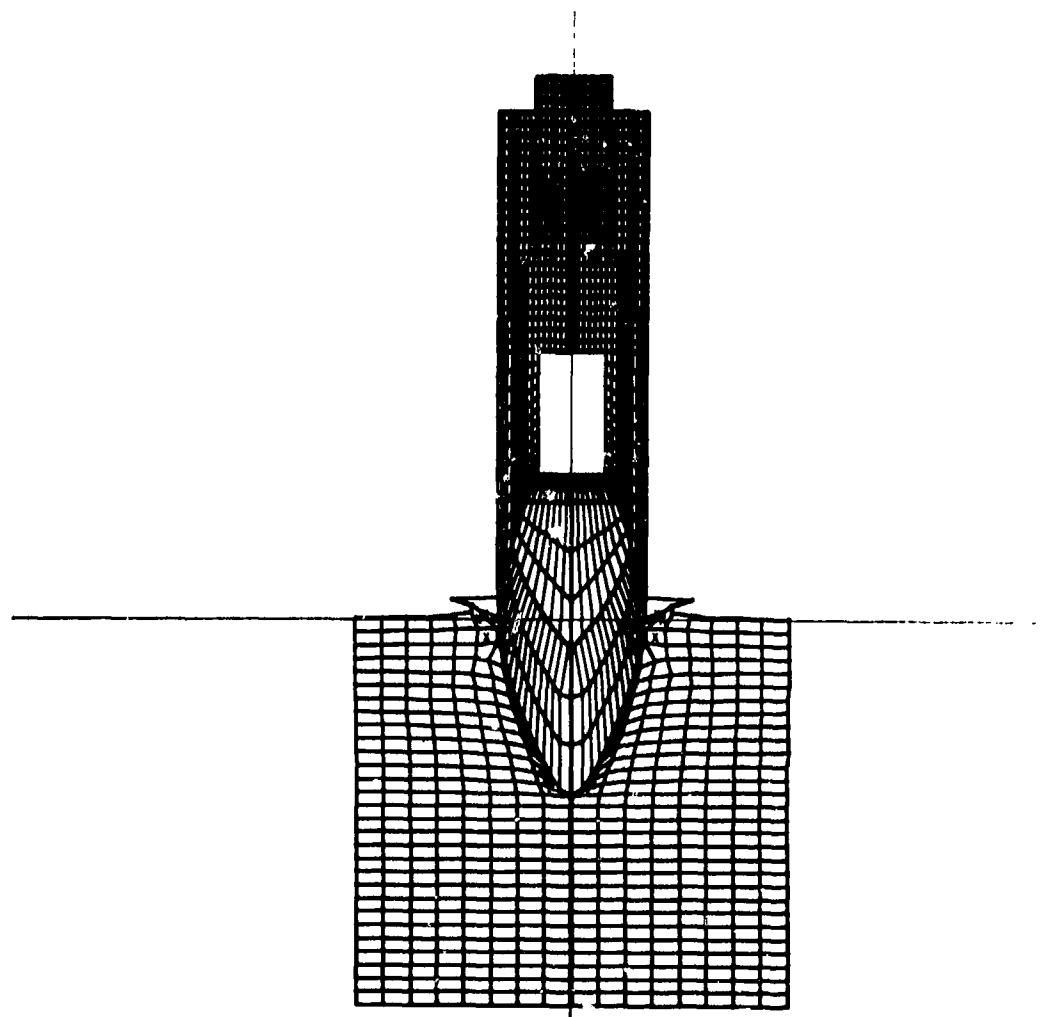Contours of radial-vertical shear stress at 0.4 ms (deformable penetrator now shown).

Figure B-8

Lagrangian coordinates at 1.1 ms (radial dimensions doubled to show deformable penetrator).

Figure B-9

Contours of radial velocity at 1.1 ms (deformable penetrator now shown).

Figure B-10
Contours of vertical velocity at 1.1 ms (deformable penetrator not shown).

-2.0 MPa
-1.5 MPa
-1.0 MPa
-0.5 MPa
0 MPa

Figure B-11

Contours of radial stress at 1.1 ms (deformable penetrator not shown).

255

Figure B-12
Contours of hoop stress at 1.1 ms (deformable penetrator not shown).

Figure B-13

Contours of vertical stress at 1.1 ms (deformable penetrator not shown).

Figure B-14

Contours of radial-vertical shear stress at 1.1 ms (deformable penetrator not shown).

Figure B-15

Lagrangian coordinates at 2.4 ms (radial dimensions doubled to show deformable penetrator).
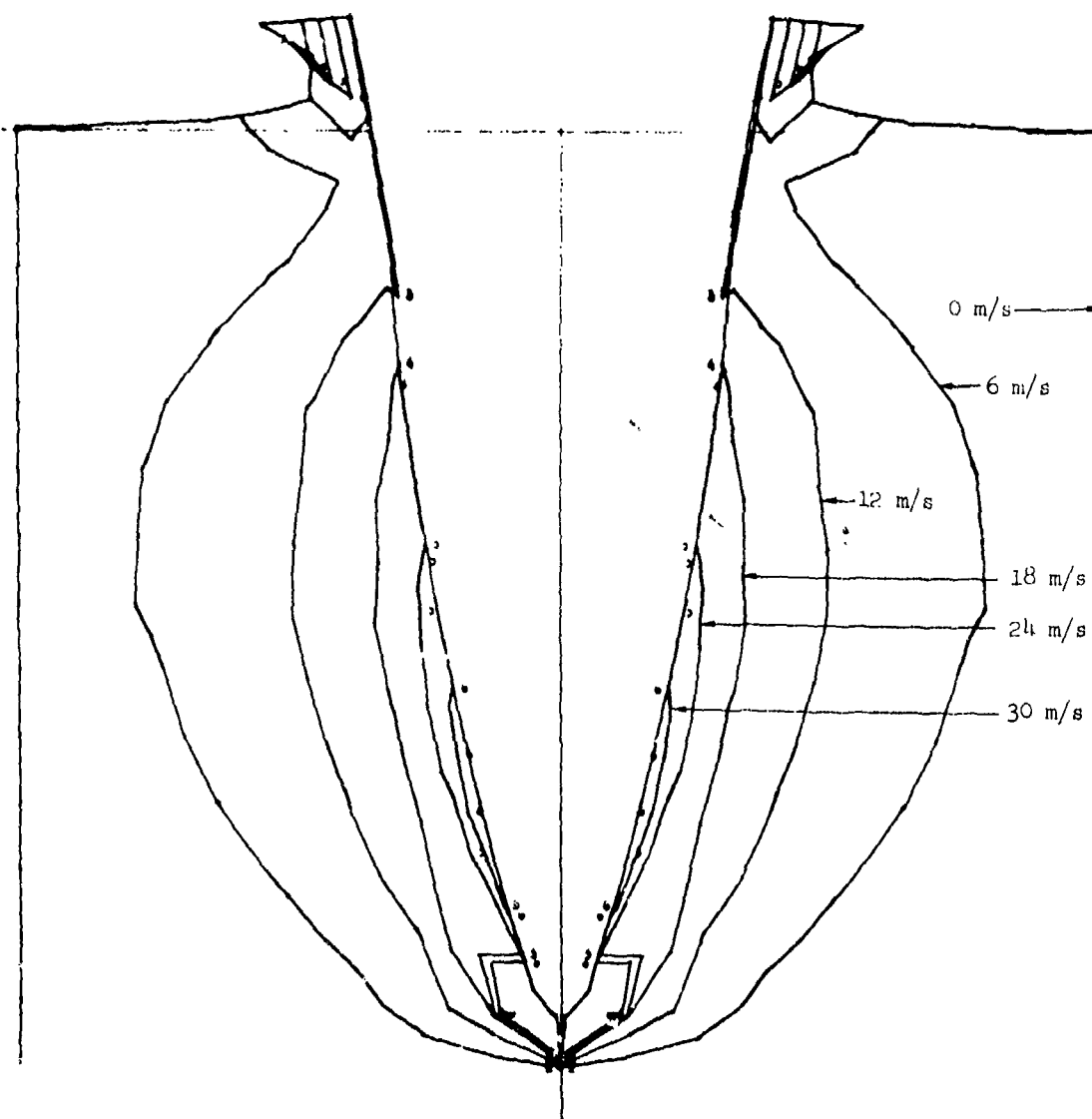
Figure B-16
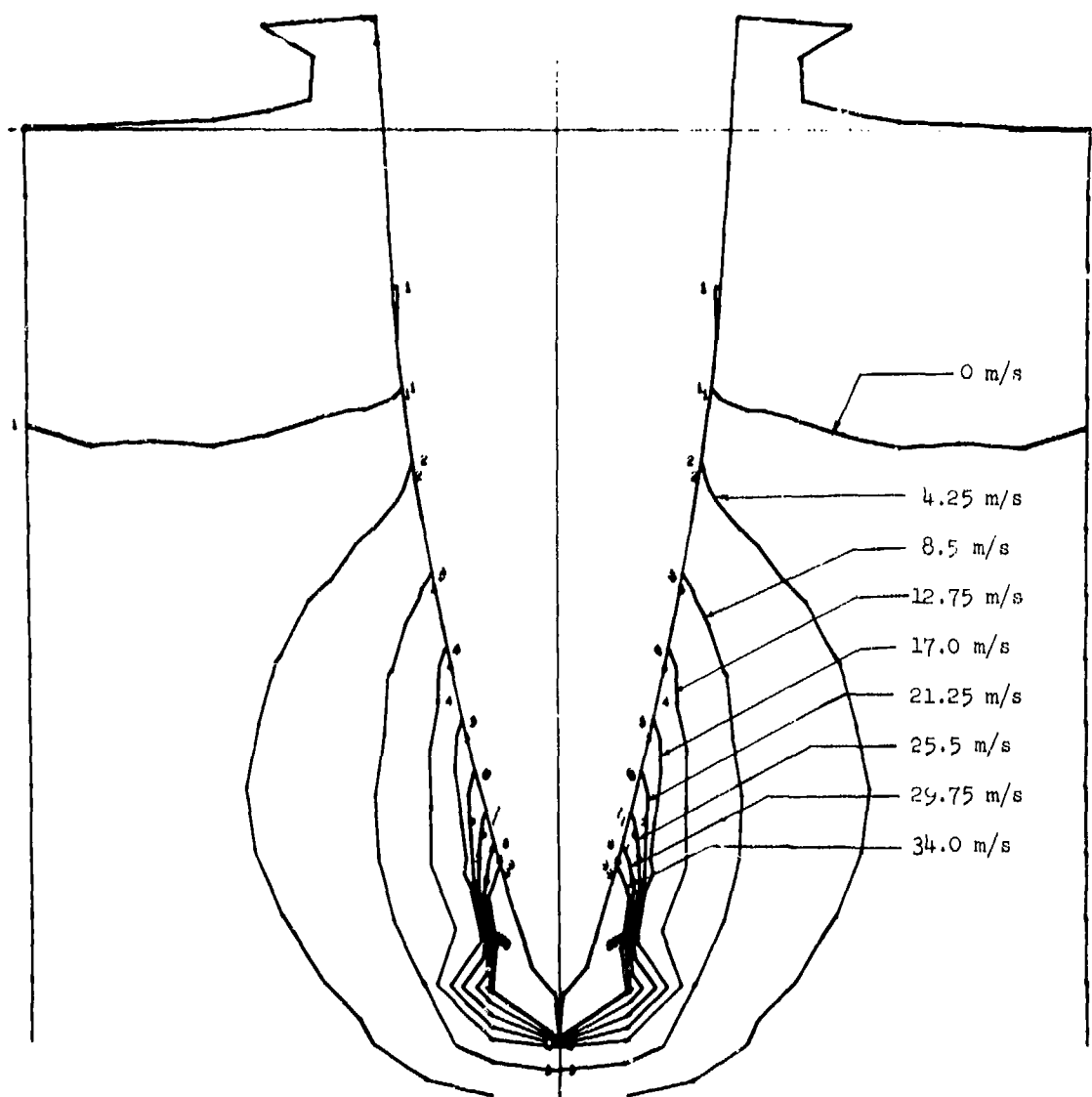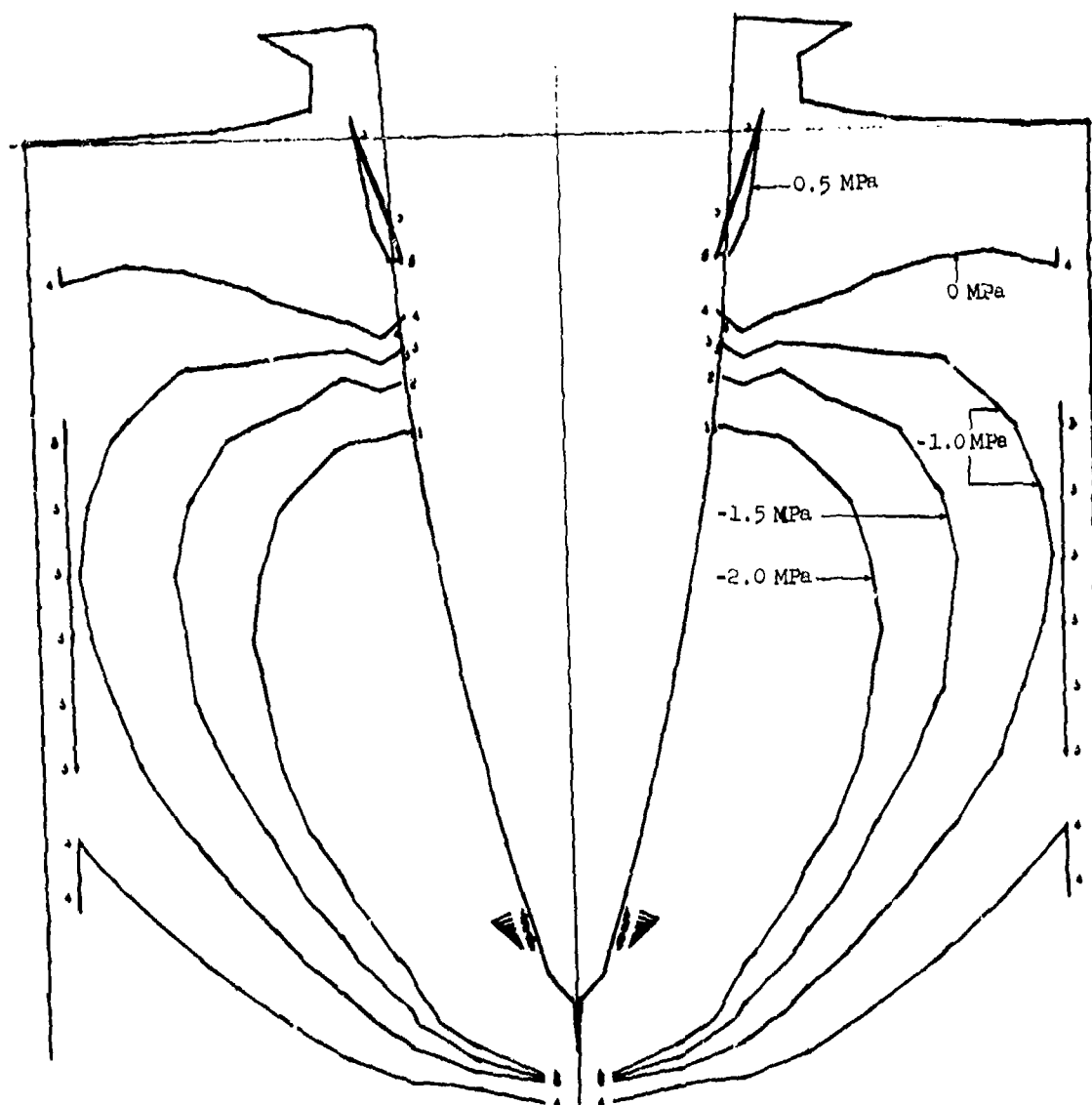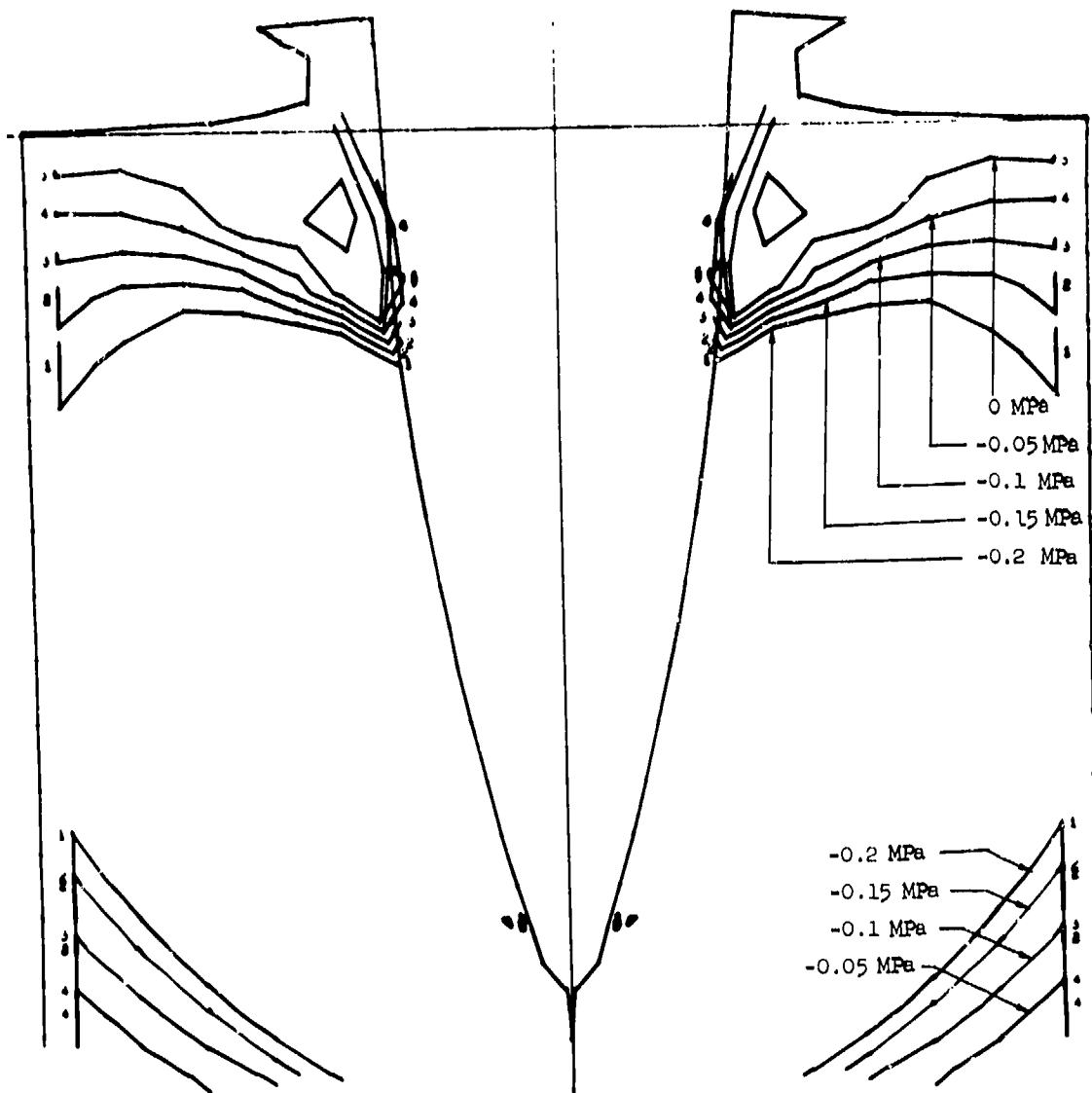Contours of radial velocity at 2.4 ms (deformable penetrator not shown).

260

Figure B-17
Contours of vertical velocity at 2.4 ms (deformable penetrator not shown).

The velocity contours are labeled:
- 0 m/s
- 4.25 m/s
- 8.5 m/s
- 12.75 m/s
- 17.0 m/s
- 21.25 m/s
- 25.5 m/s
- 29.75 m/s
- 34.0 m/s

Figure B-18

Contours of radial stress at 2.4 ms (deformable penetrator not shown).

Figure B-19

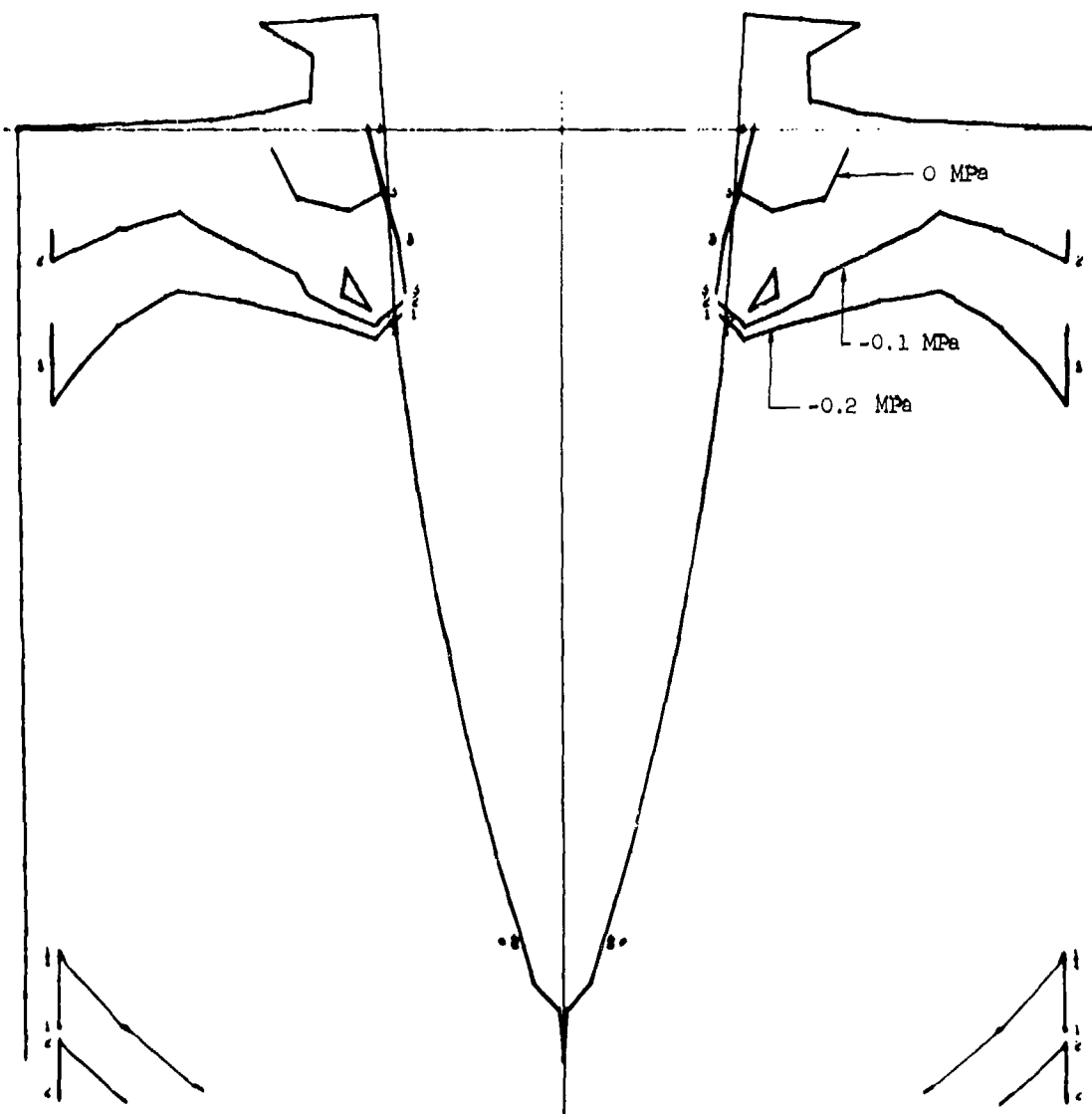Contours of hoop stress at 2.4 ms (deformable penetrator not shown).

Figure B-20

Contours of vertical stress at 2.4 ms (deformable penetrator not shown).
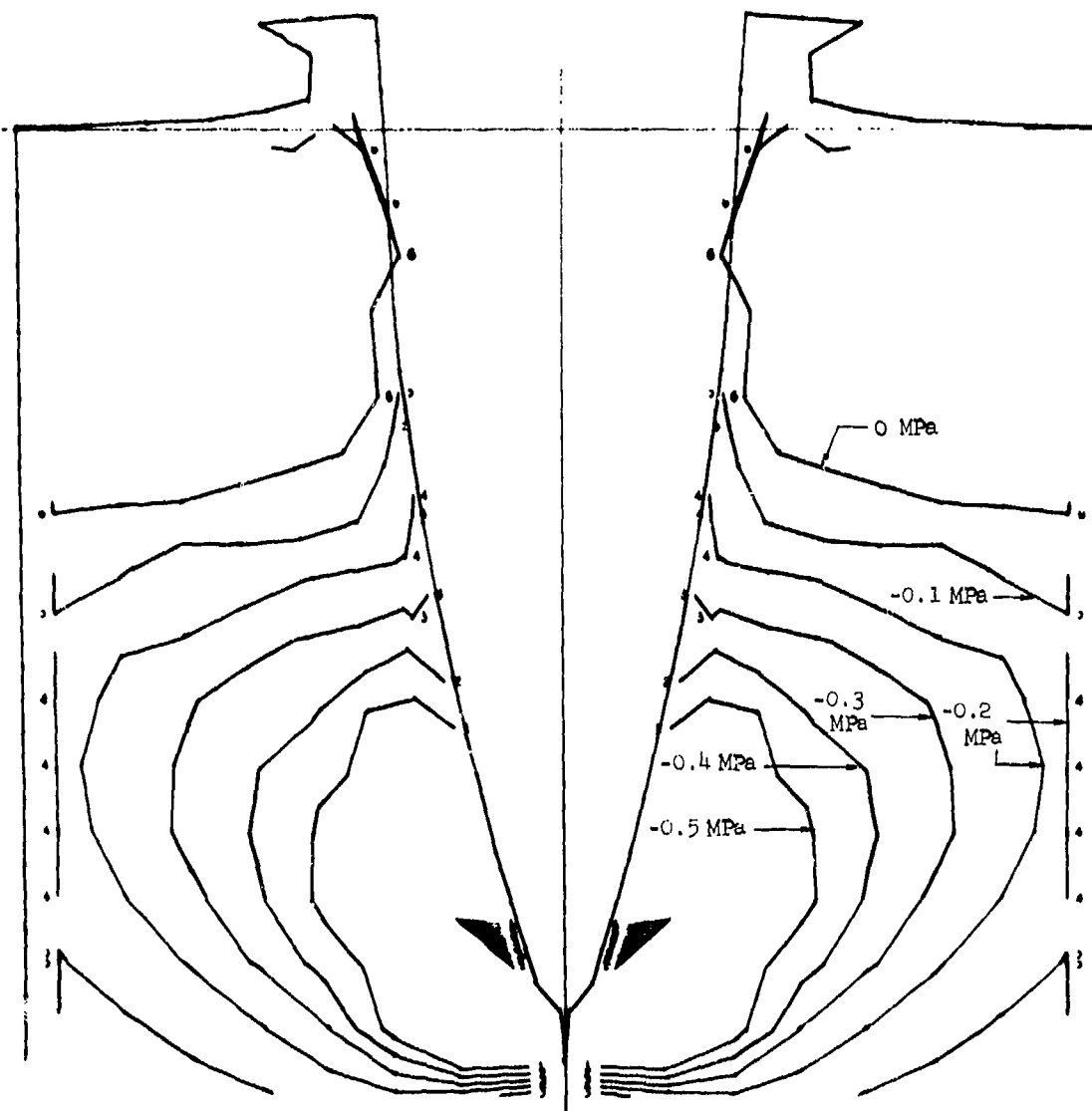
Figure B-21
Contours of radial-vertical shear stress at 2.4 ms (deformable penetrator not shown).
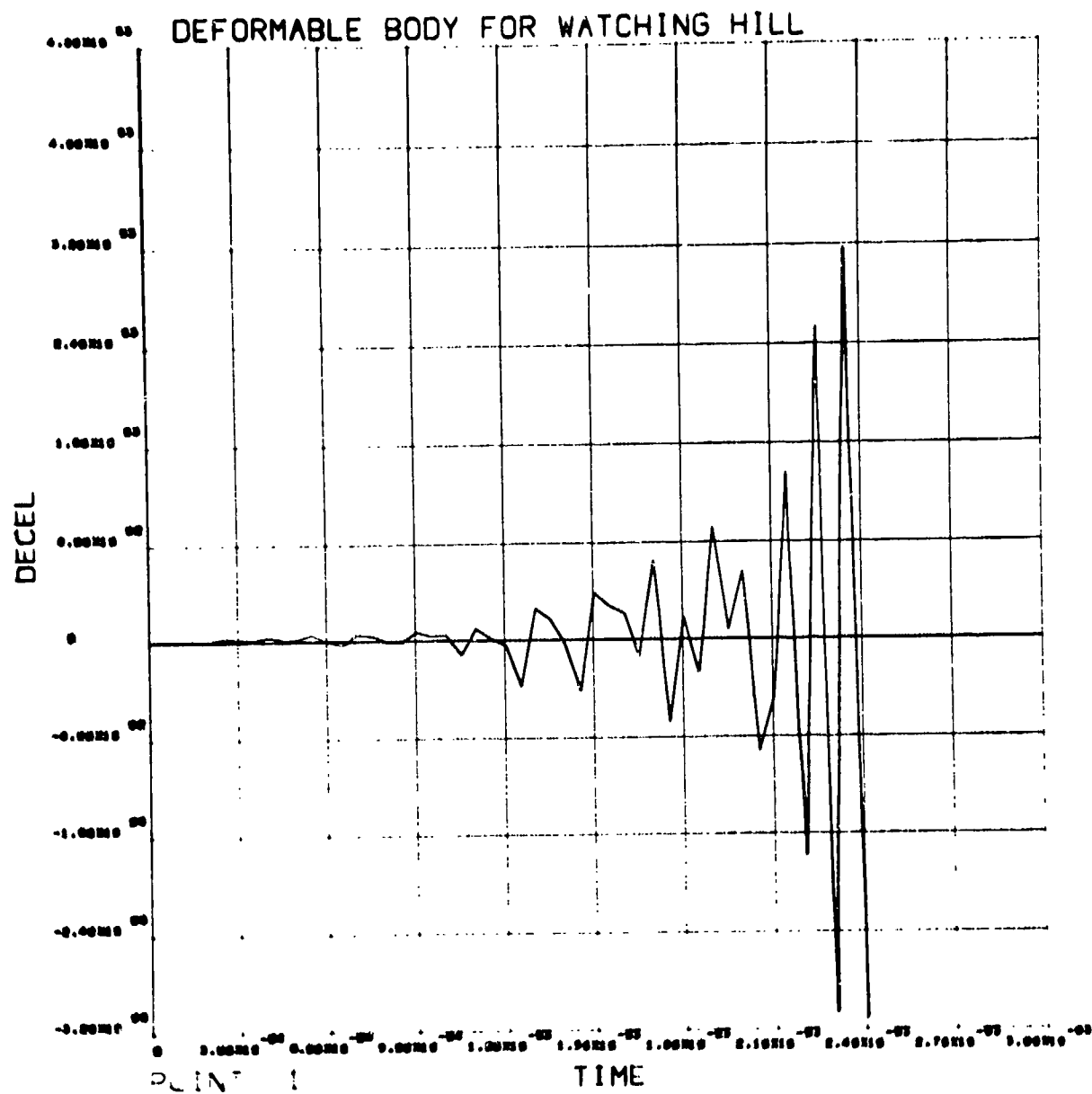
Figure B-22

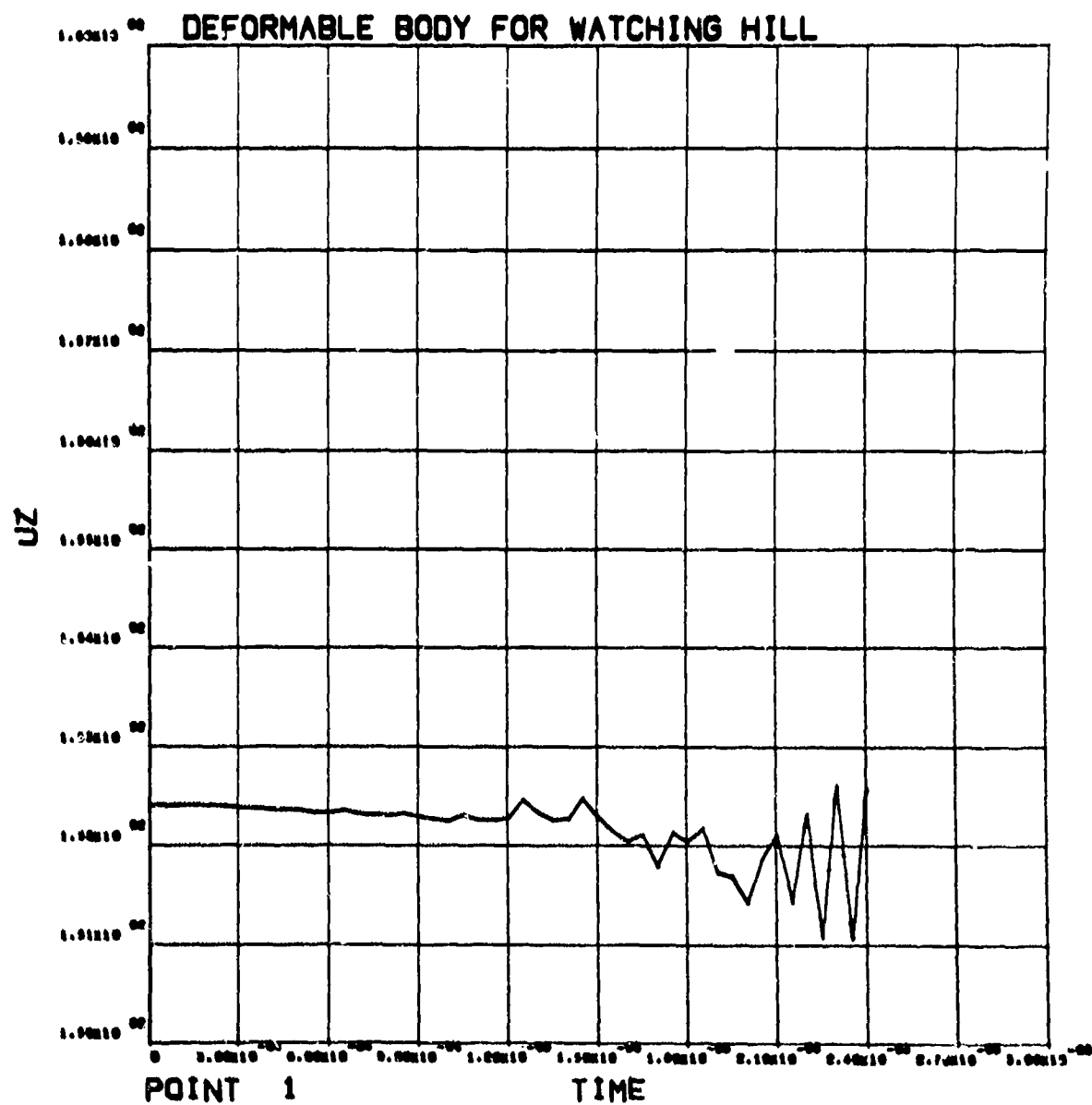Deceleration history (g) for point 1 at accelerometer (filtered above 10 kH).

Figure B-23

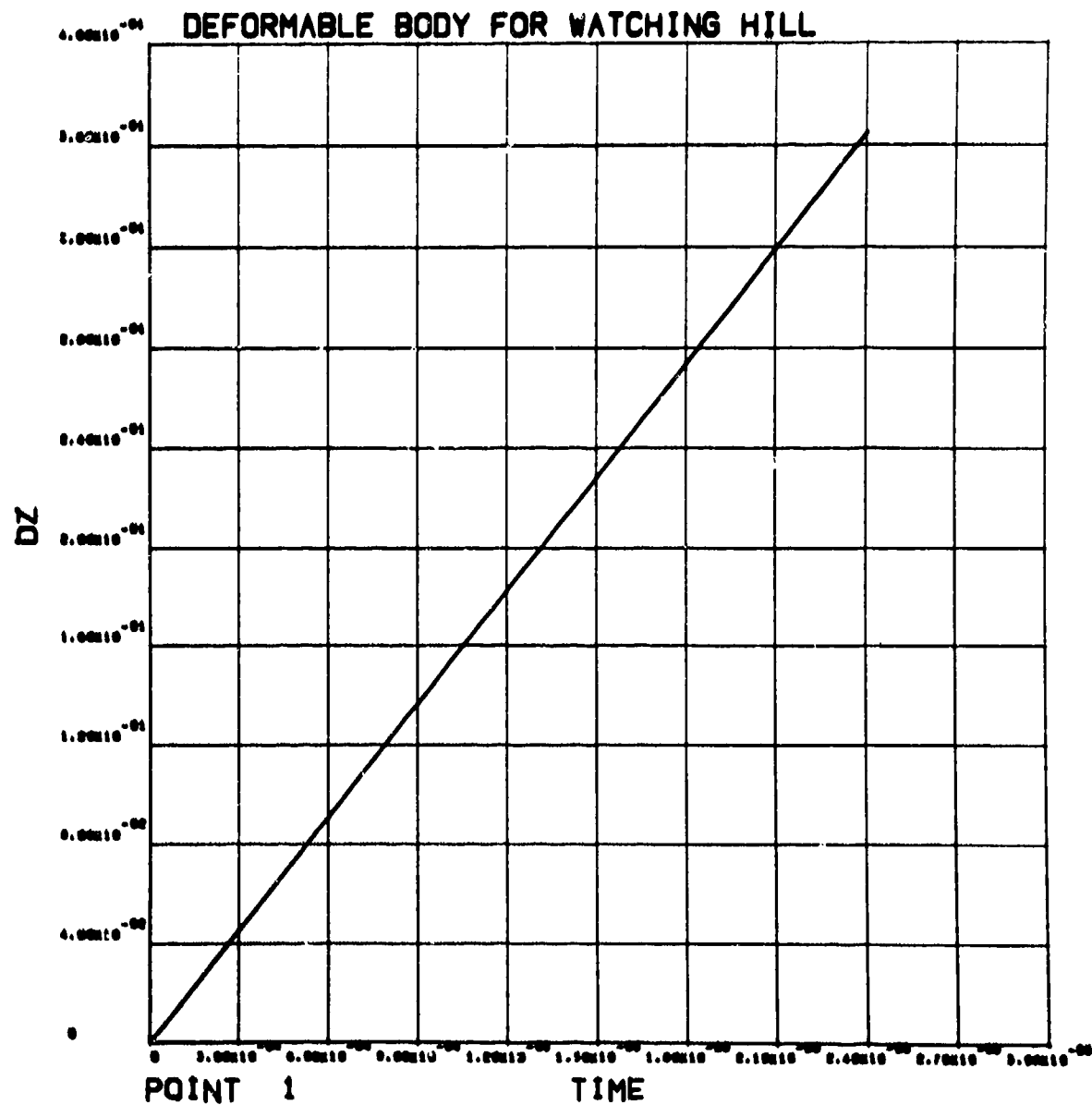Vertical velocity history (m/s) for point 1 at accelerometer.

Figure B-24

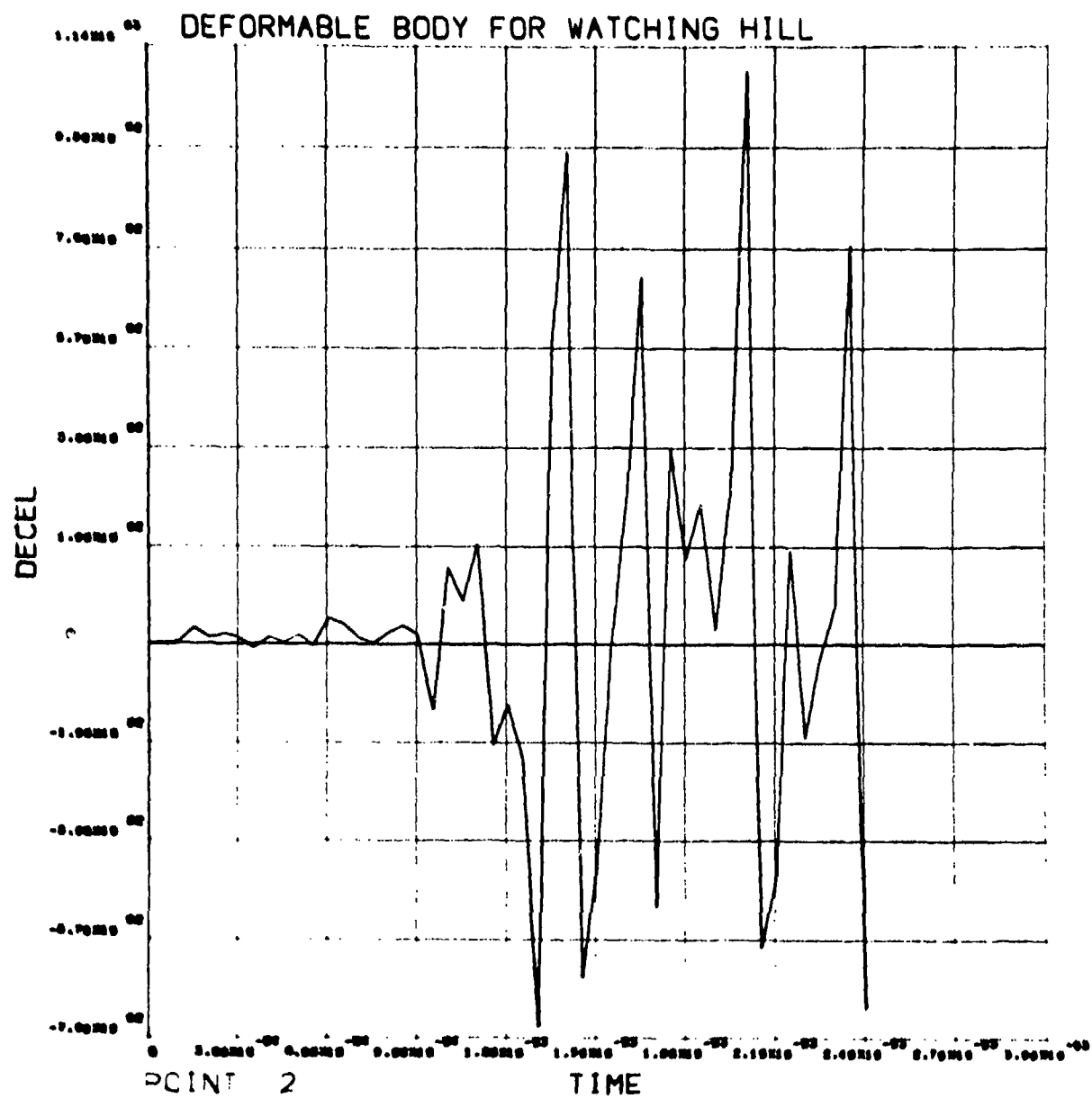Vertical displacement history (m) for point 1 at accelerometer.

Figure B-25

Deceleration history (g) for point 2, 0.58 m behind penetrator tip and 10 mm from central axis.
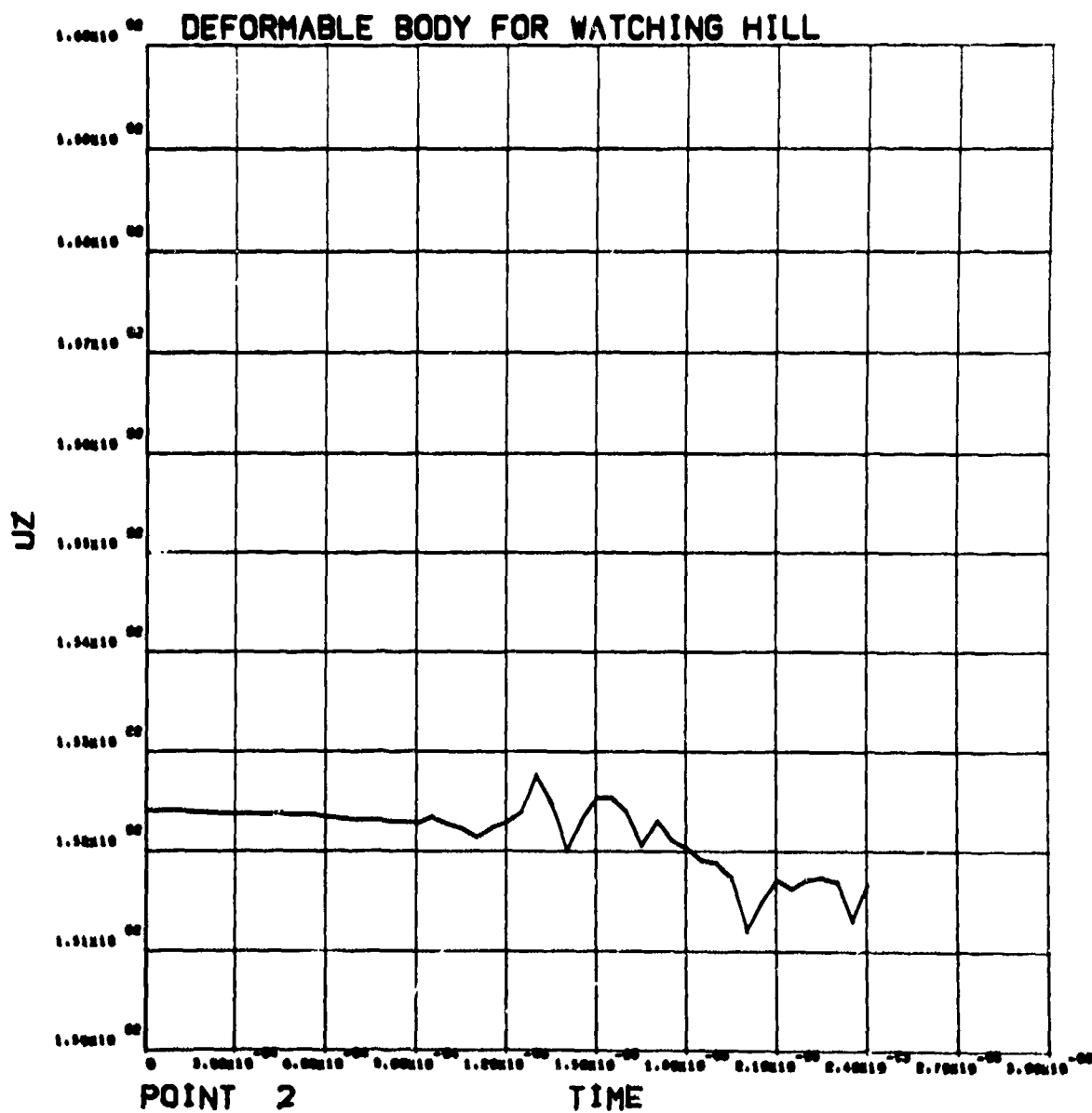
269

Figure B-26
Vertical velocity history (m/s) for point 2, 0.58 m behind penetrator tip and 10 mm from central axis.
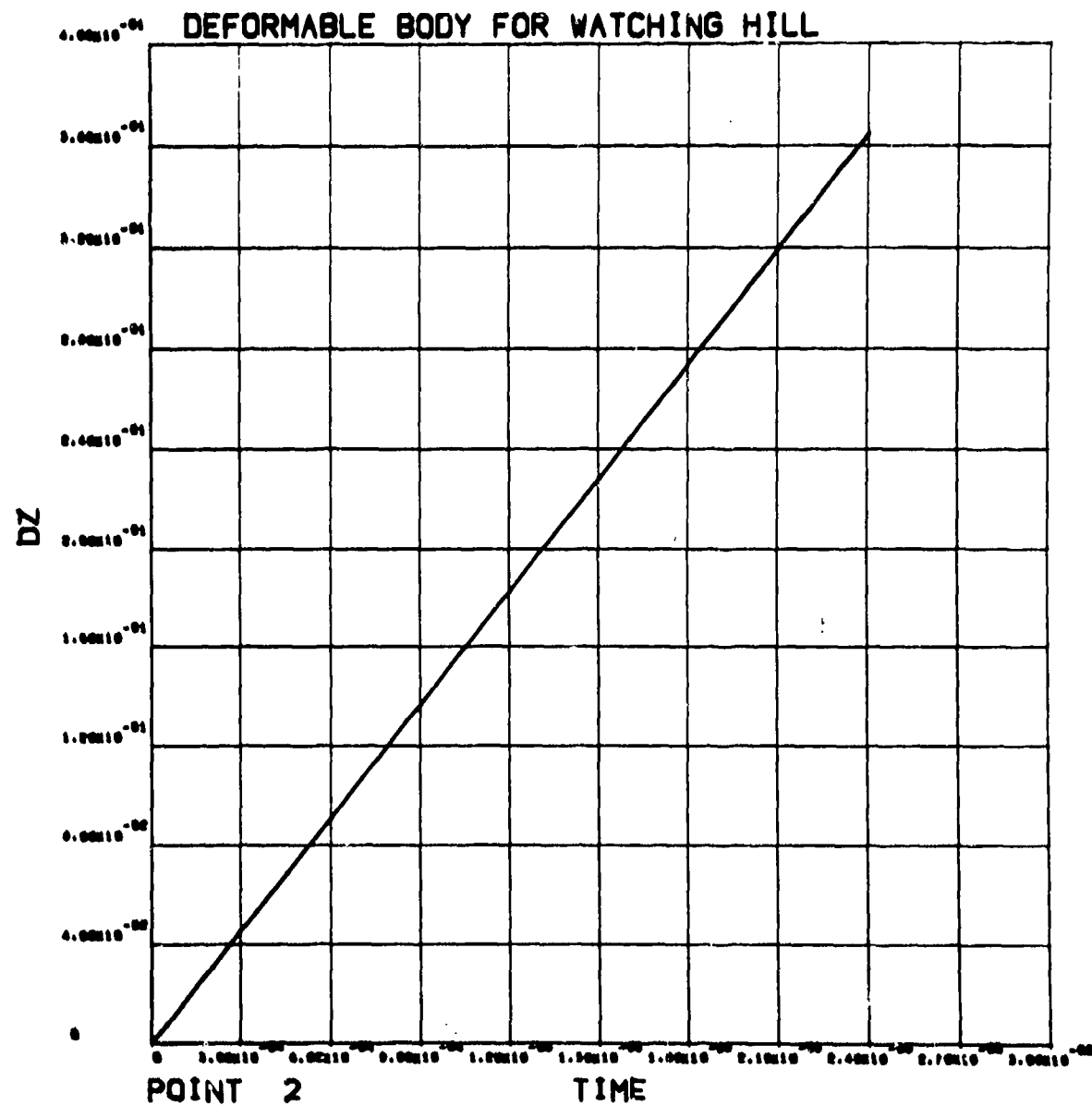
Figure B-27

Vertical displacement history (m) for point 2, 0.58 m behind penetrator tip and 10 mm from central axis.
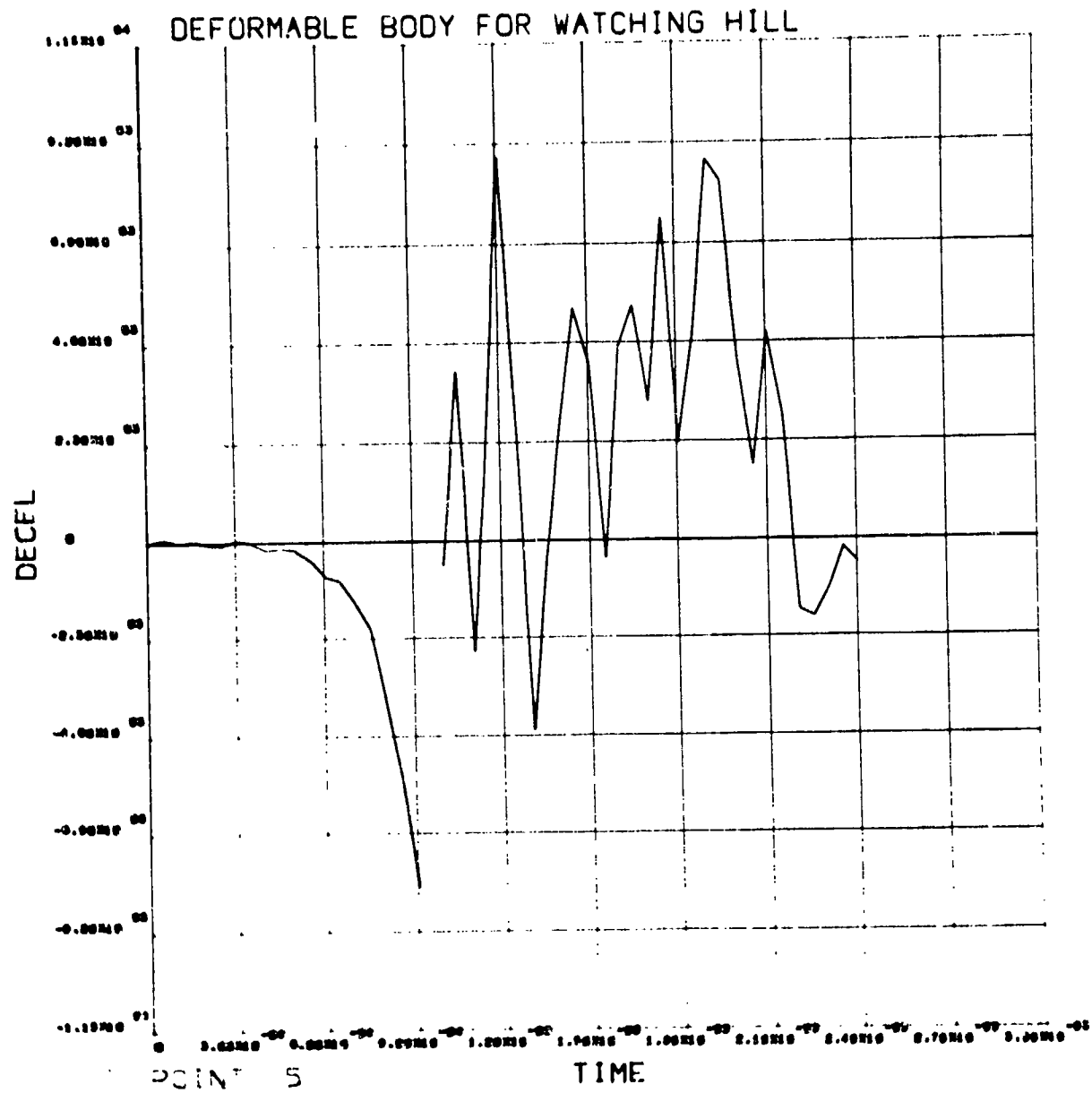
Figure B-28

Deceleration history (g) for point 5, 28 mm behind penetrator tip and 6 mm from central axis.
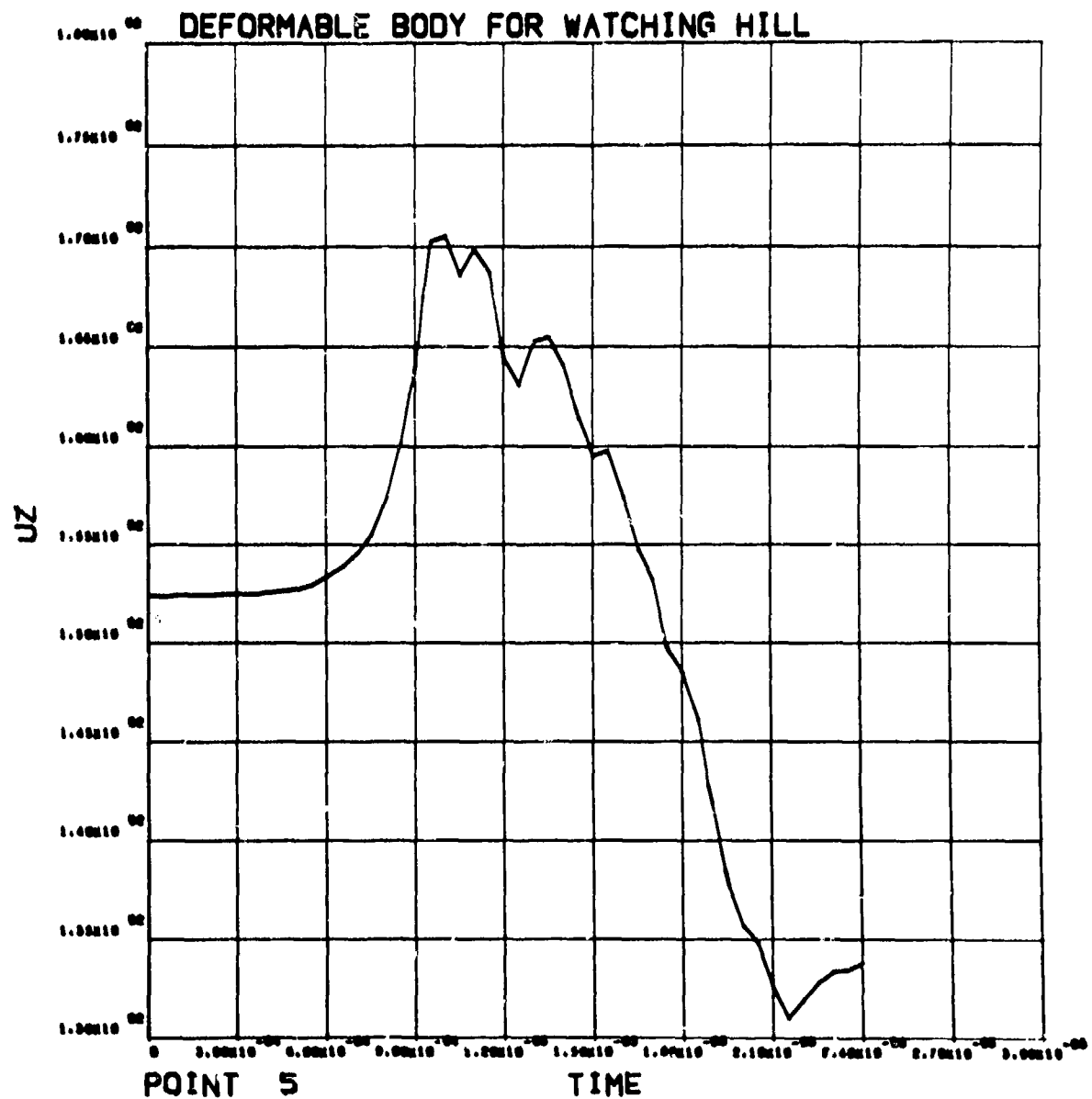
272

Figure B-29

Vertical velocity history (m/s) for point 5, 28 mm behind penetrator tip and 6 mm from central axis.
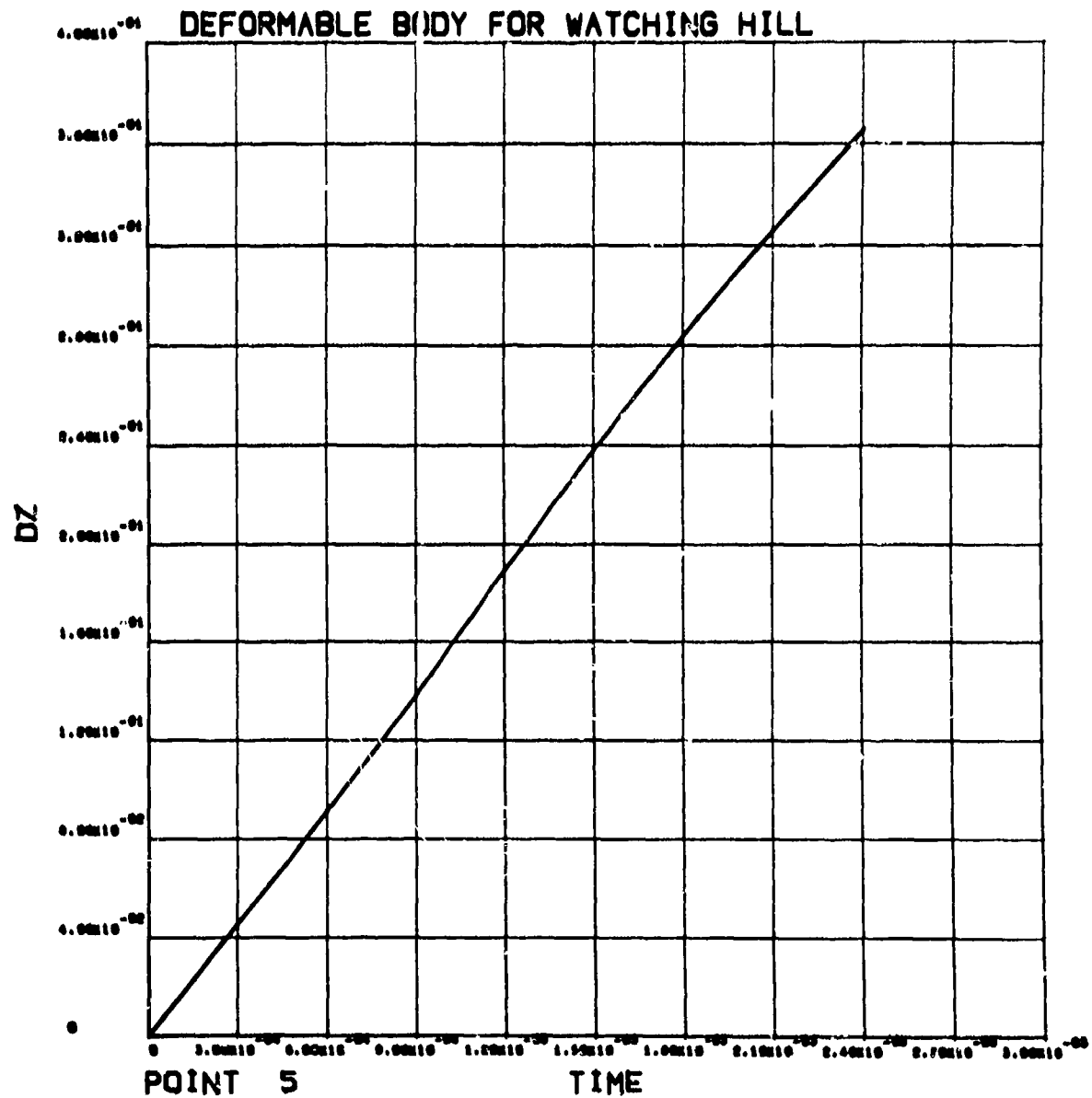
Figure B-30

Vertical displacement history (m) for point 5, 28 mm behind penetrator tip and 6 mm from central axis.
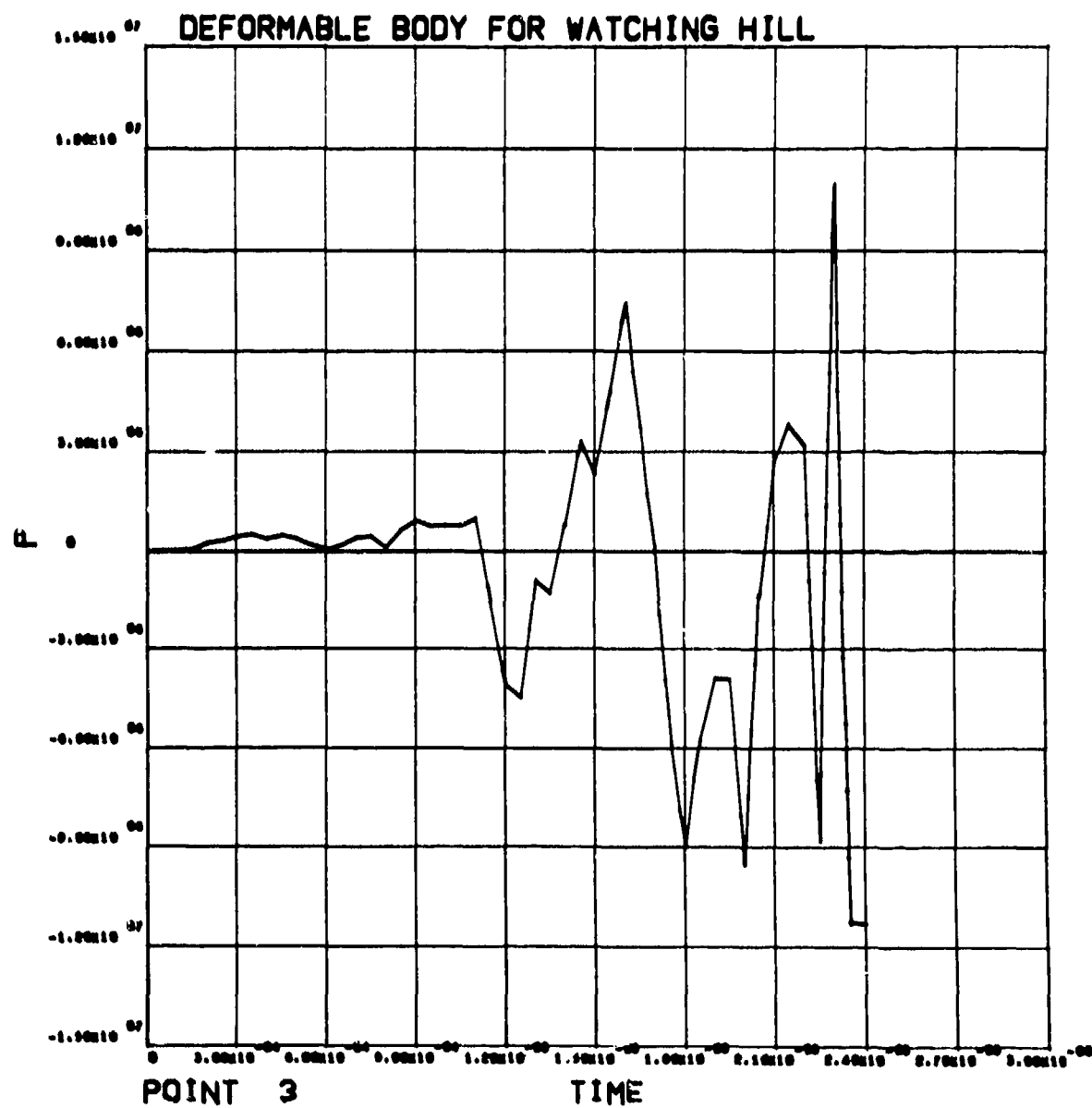
Figure B-31

Pressure history (Pa) for point 3, 0.79 m behind penetrator tip and 69 mm from central axis.

Figure B-32

Deviator stress, J2, history (Pa) for point 3, 0.79 m behind penetrator tip and 69 mm from central axis. (Octahedral shear stress = $\sqrt{2/3}$ (J2)).

Figure B-33

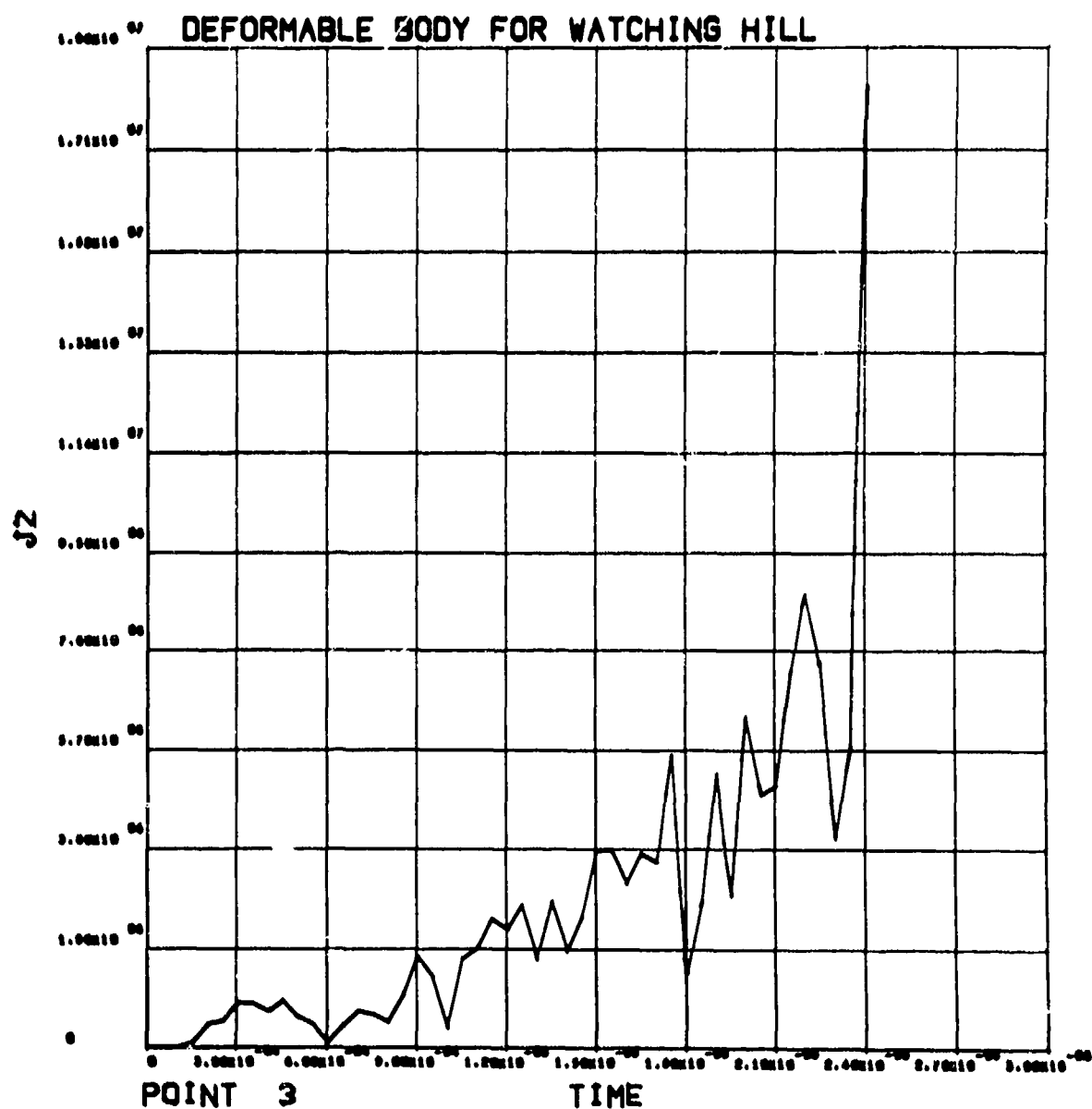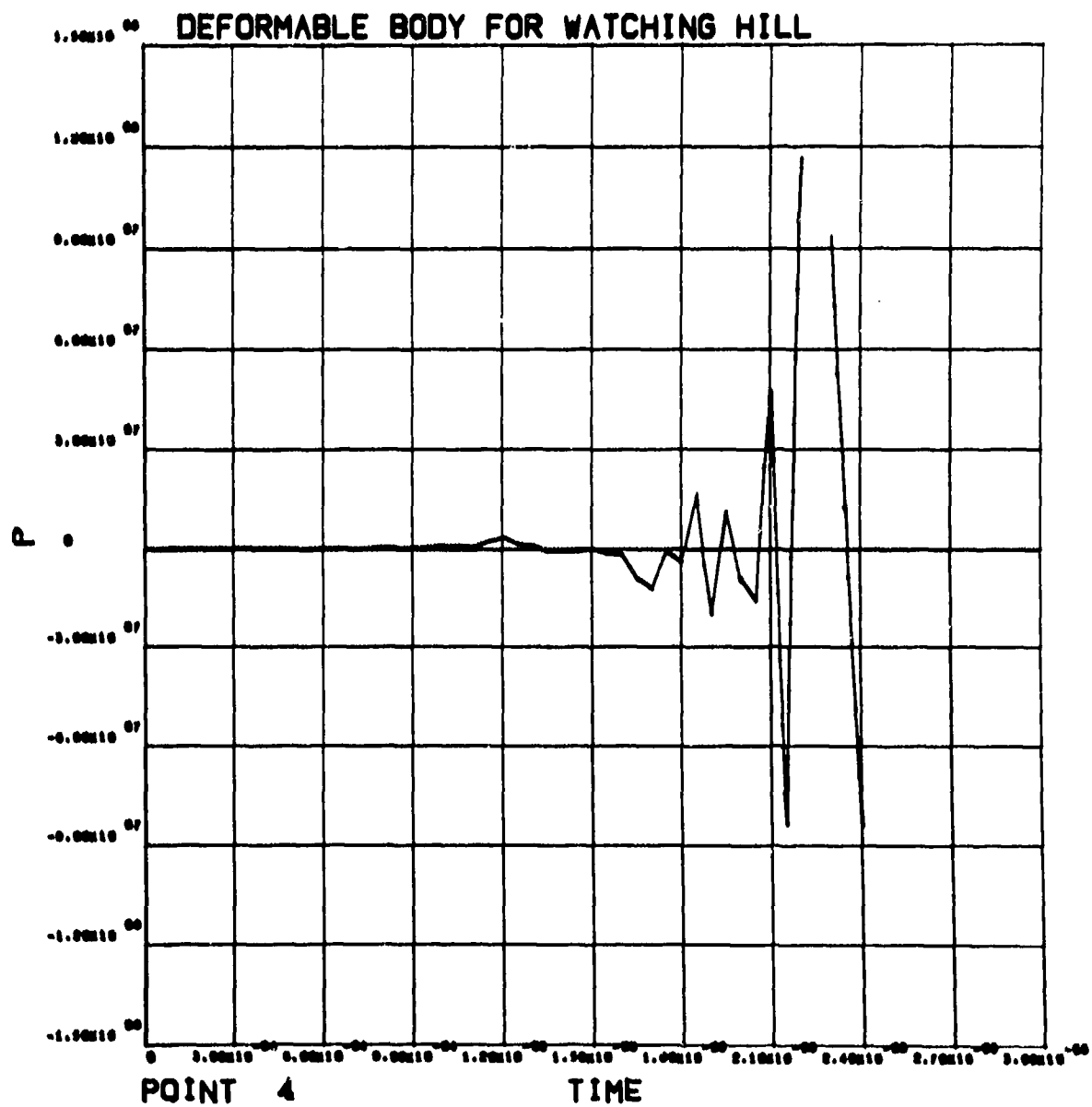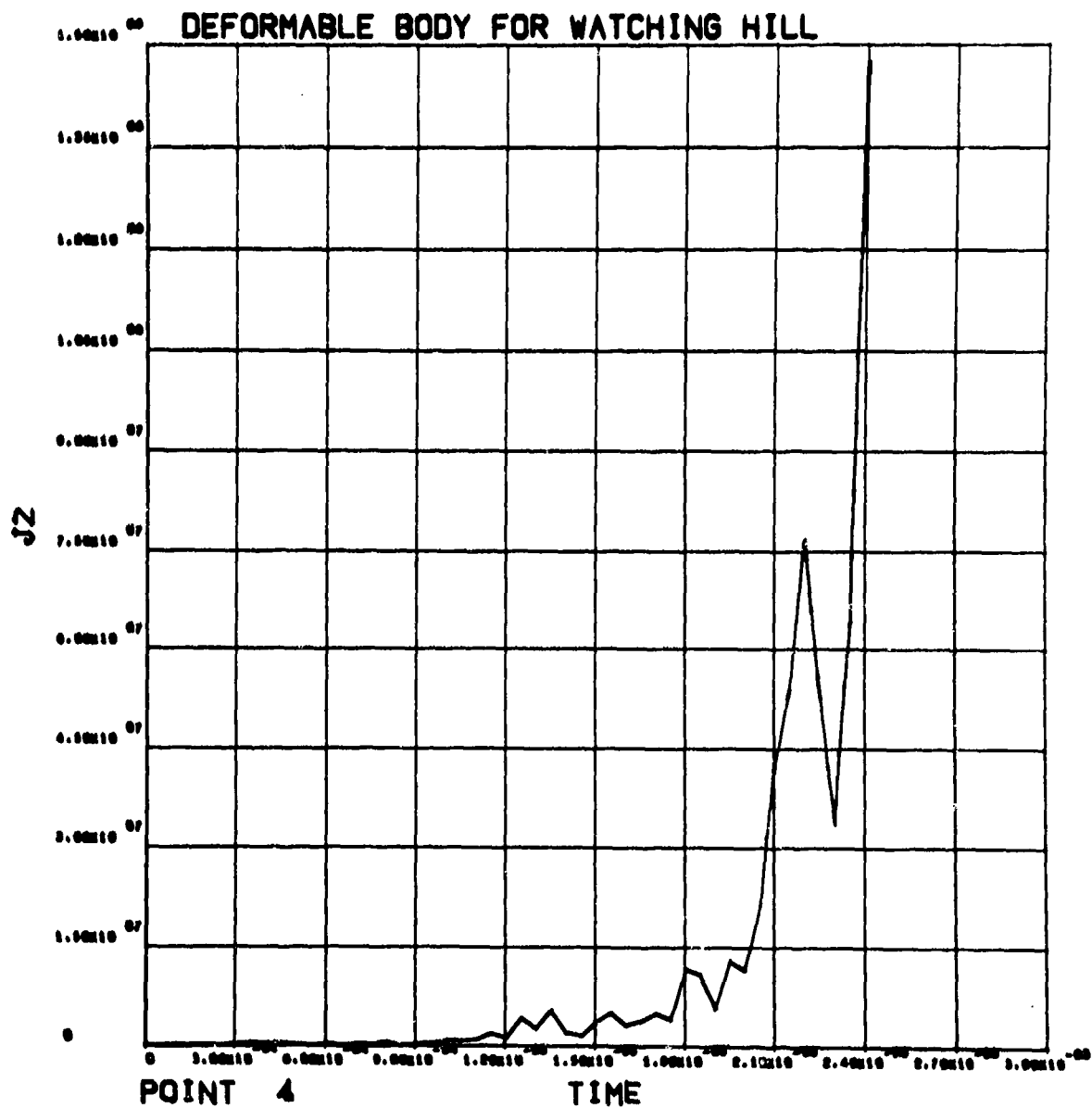Pressure history (Pa) for point 4, 1.39 m behind penetrator tip and 69 mm from central axis.

Figure B-34

Deviator stress, J2, history (Pa) for point 4. 1.39 m behind penetrator tip and 69 mm from central axis. (Octahedral shear stress = $\sqrt{2/3}$ (J2)).
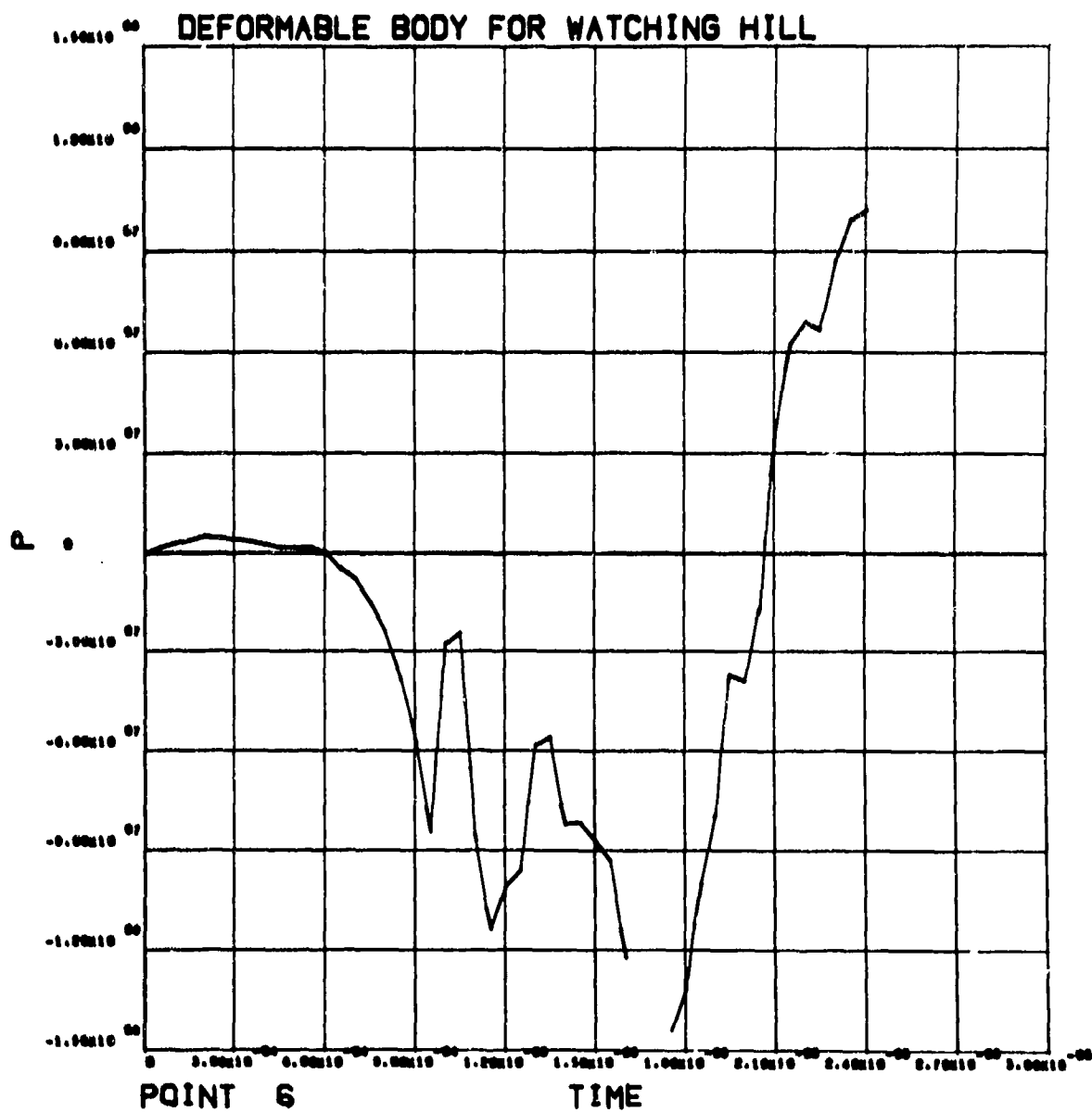
Figure B-35

Pressure history (Pa) for point 6, 48 mm behind penetrator tip and 17 mm from central axis.
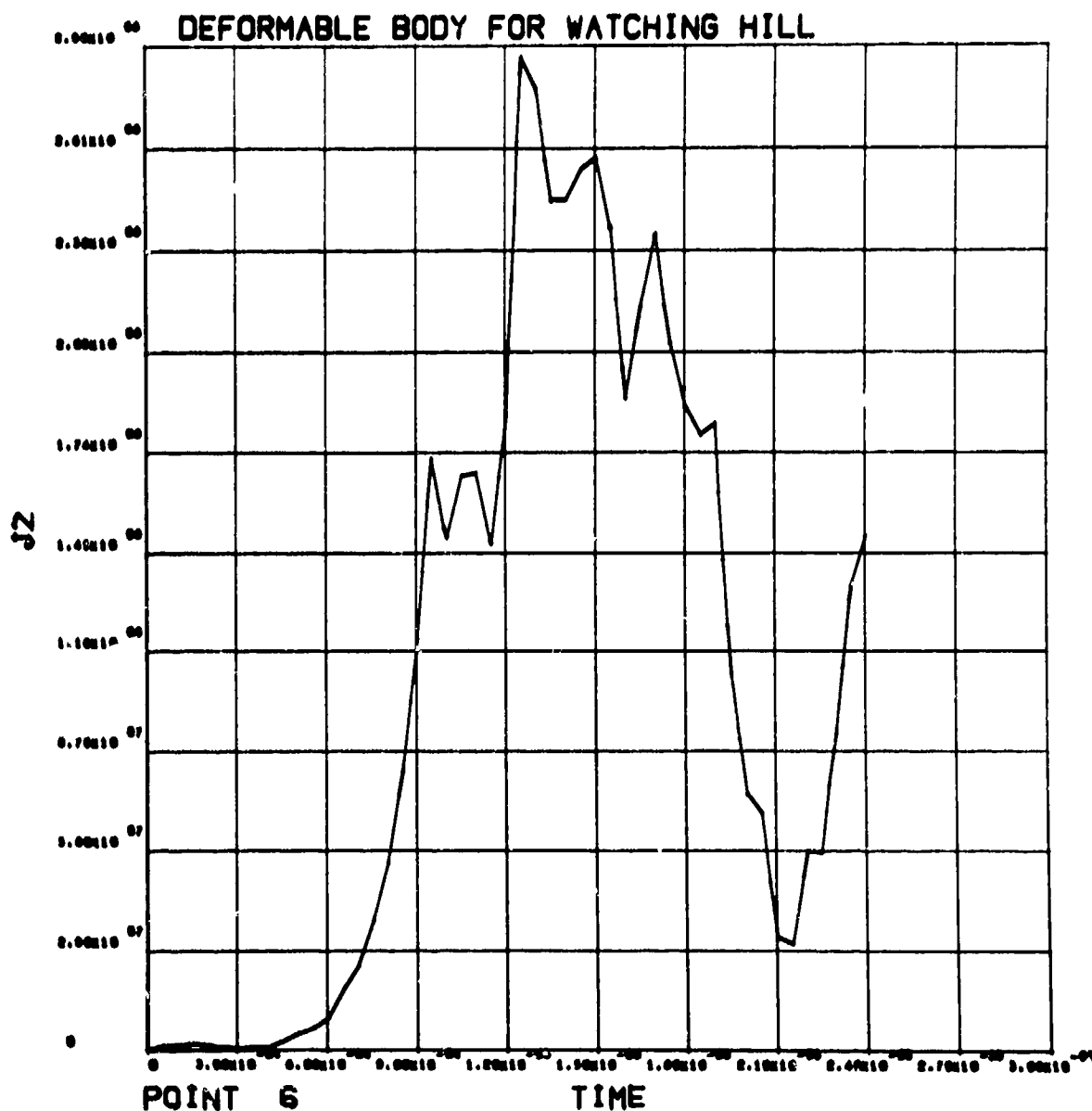
Figure B-36

Deviator stress, J2, history (Pa) for point 6.48 mm behind penetrator tip and 17 mm from central axis. (Octahedral shear stress = $\sqrt{2/3}$ (J2)).

Figure B-37

Normal stress history (Pa) for point 7, 0.14 m behind penetrator tip and 41 mm from central axis.
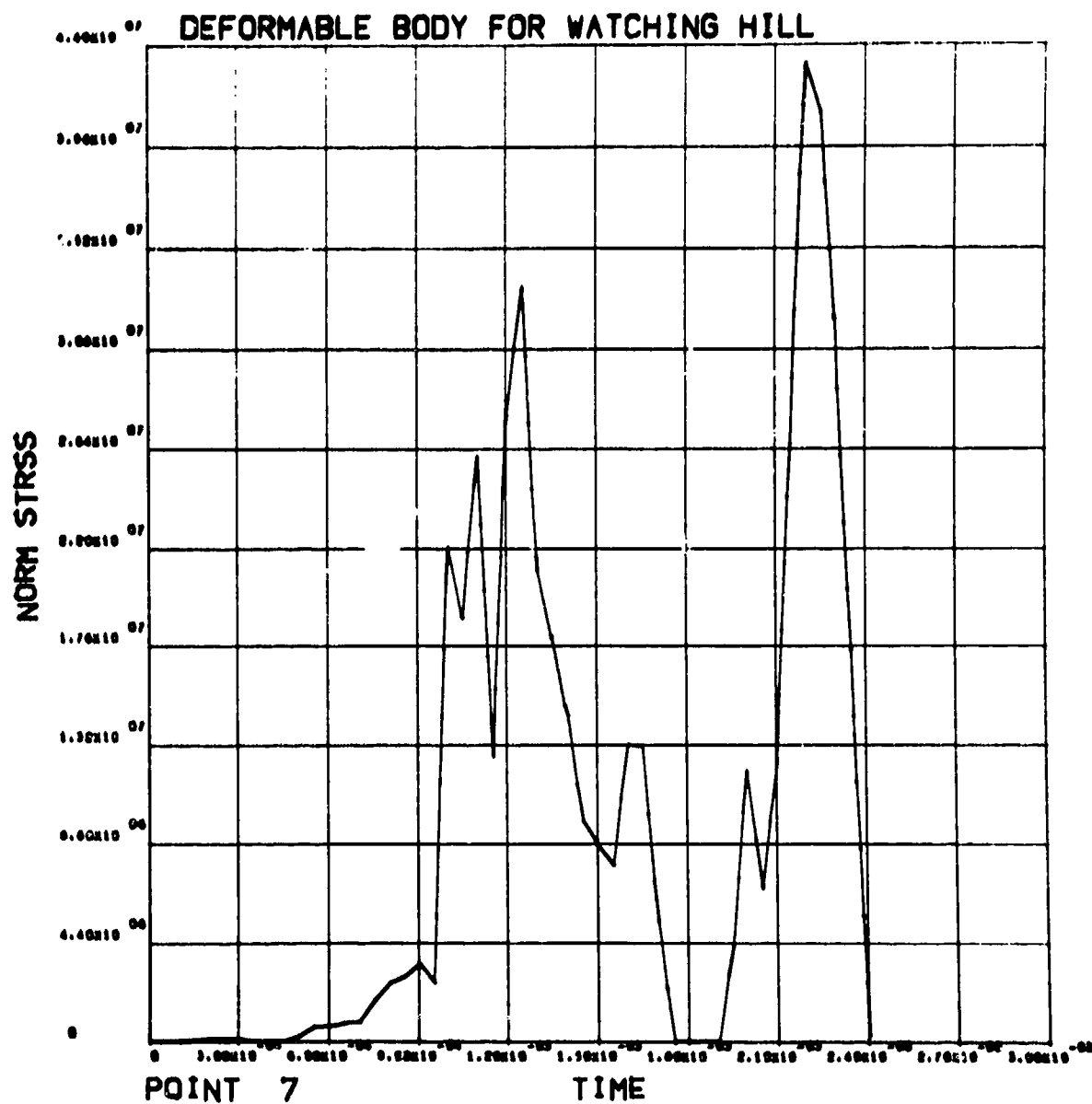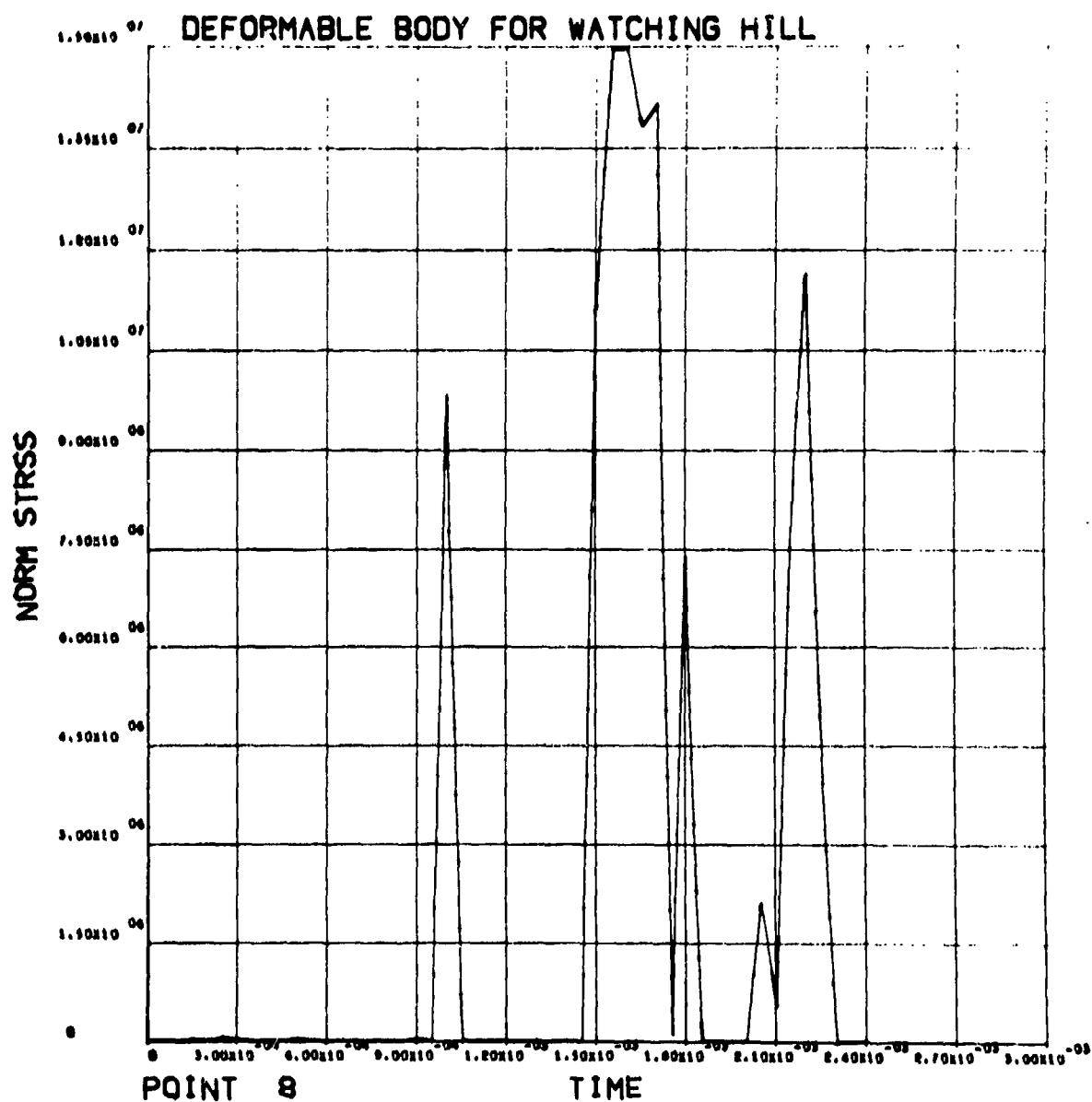
Figure B-38

Normal stress history (Pa) for point 8, 0.23 m behind penetrator tip and 60 mm from central axis.
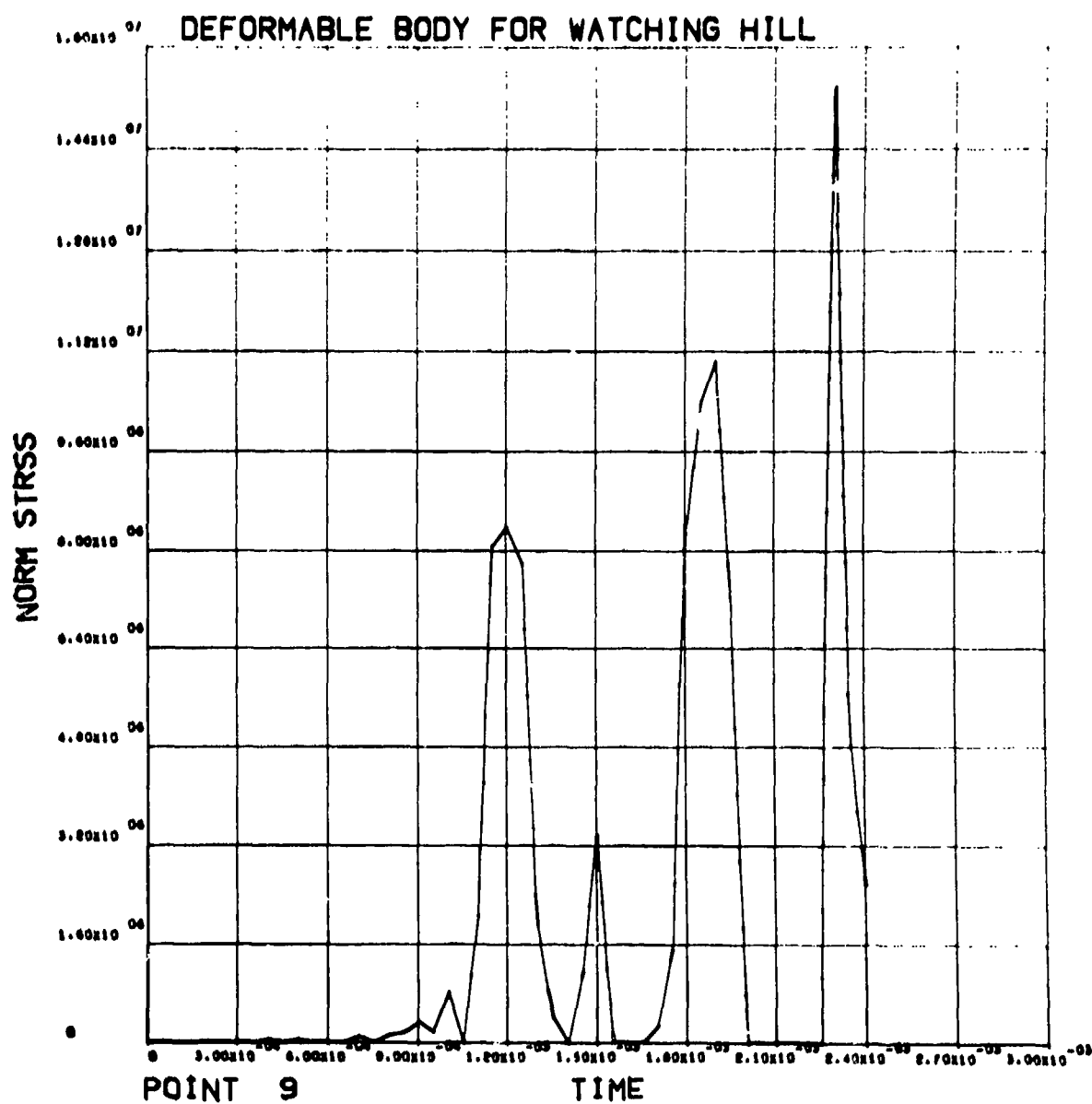
Figure B-39

Normal stress history (Pa) for point 9, 0.38 m behind penetrator tip and 77 mm from central axis.

DEFORMABLE BODY FOR WATCHING HILL
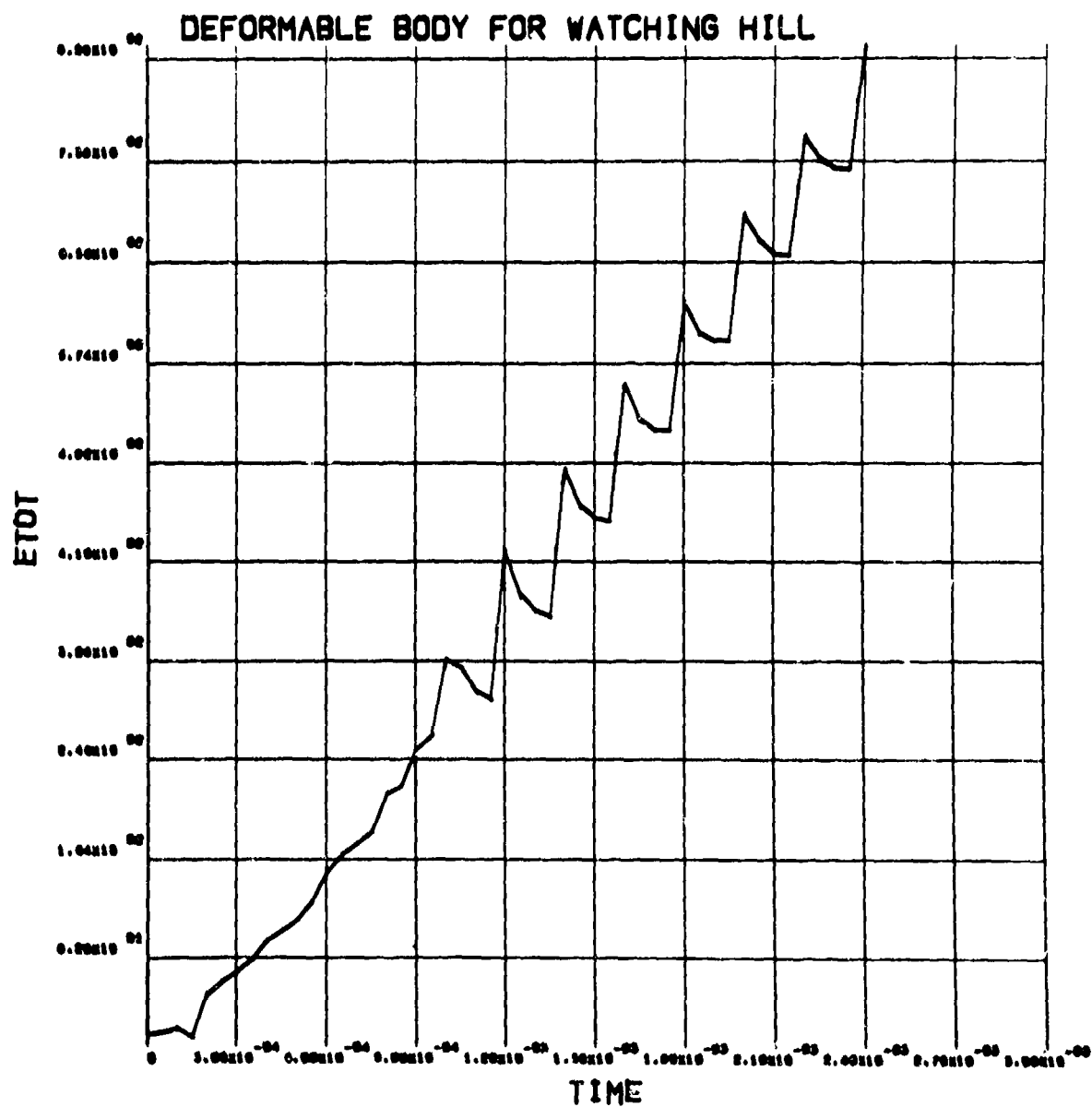
Figure B-40

Soil kinetic energy 1 radian vs time (deformable penetrator).

Figure B-41

Radial velocity history (m/s) in soil at range 75 mm, depth 0.1 m (deformable penetrator).

Figure B-42

Vertical velocity history (m/s) in soil at range 75 mm, depth 0.1 m (deformable penetrator).

286

Figure B-43

Radial displacement history (m) in soil at range 75 mm, depth 0.1 m (deformable penetrator).

Figure B-44

Vertical displacement history (m) in soil at range 75 mm, depth 0.1 m (**deformable penetrator**).

288

Figure B-45
Pressure history (Pa) in soil at range 75 mm, depth 0.1 m (deformable penetrator).

Figure B-46

Deviator stress, J2, history (Pc) in soil at range 75 mm, dep+h 0.1 m (deformable penetrator), (octahedral shear stress = $\sqrt{2/3}$ (J2)).

Figure B-47
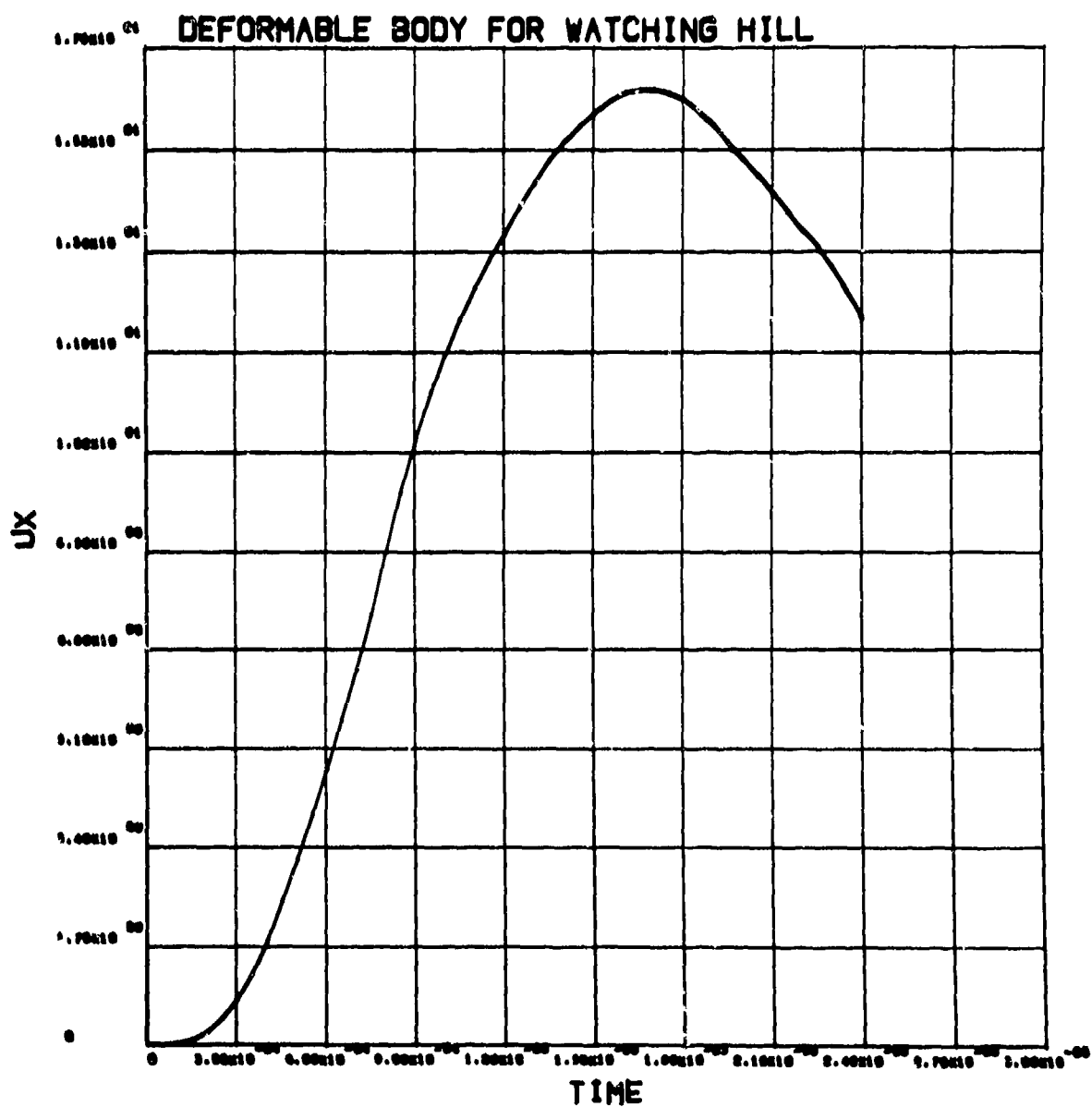Radial velocity history (m/s) in soil at range 75 mm, depth 0.2 m (deformable
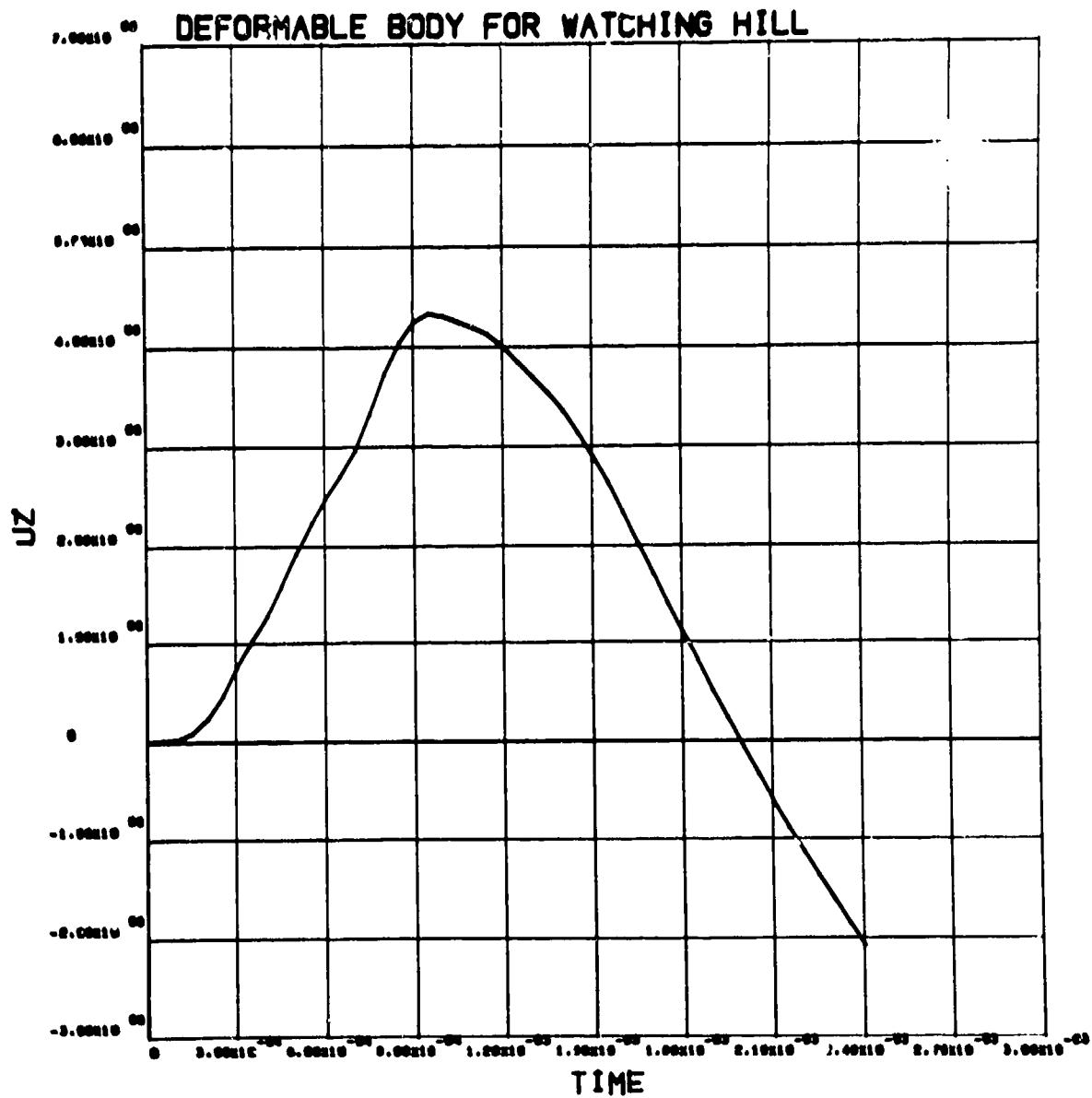penetrator).

Figure B-48
Vertical velocity history (m/s) in soil at range 75 mm, depth C.2 m (deformable penetrator).

Figure B-49
Radial displacement history (m) in soil at range 75 mm, depth 0.2 m (deformable
penetrator).

293

DEFORMABLE BODY FOR WATCHING HILL

DZ

TIME

Figure B-50

Vertical displacement history (m) in soil at range 75 mm, depth 0.2 m (deformable penetrator).

294

Figure B-51

Pressure history (Pa) in soil at range 75 mm, depth 0.2 (deformable penetrator).

295

Figure B-52

Deviator stress, J2, history (Pa) in soil at range 75 mm, depth 0.2 m (deformable penetrator).

Figure B-53

Radial velocity history (m/s) in soil at range 75 mm, depth 0.4 m (deformable penetrator).

Figure B-54

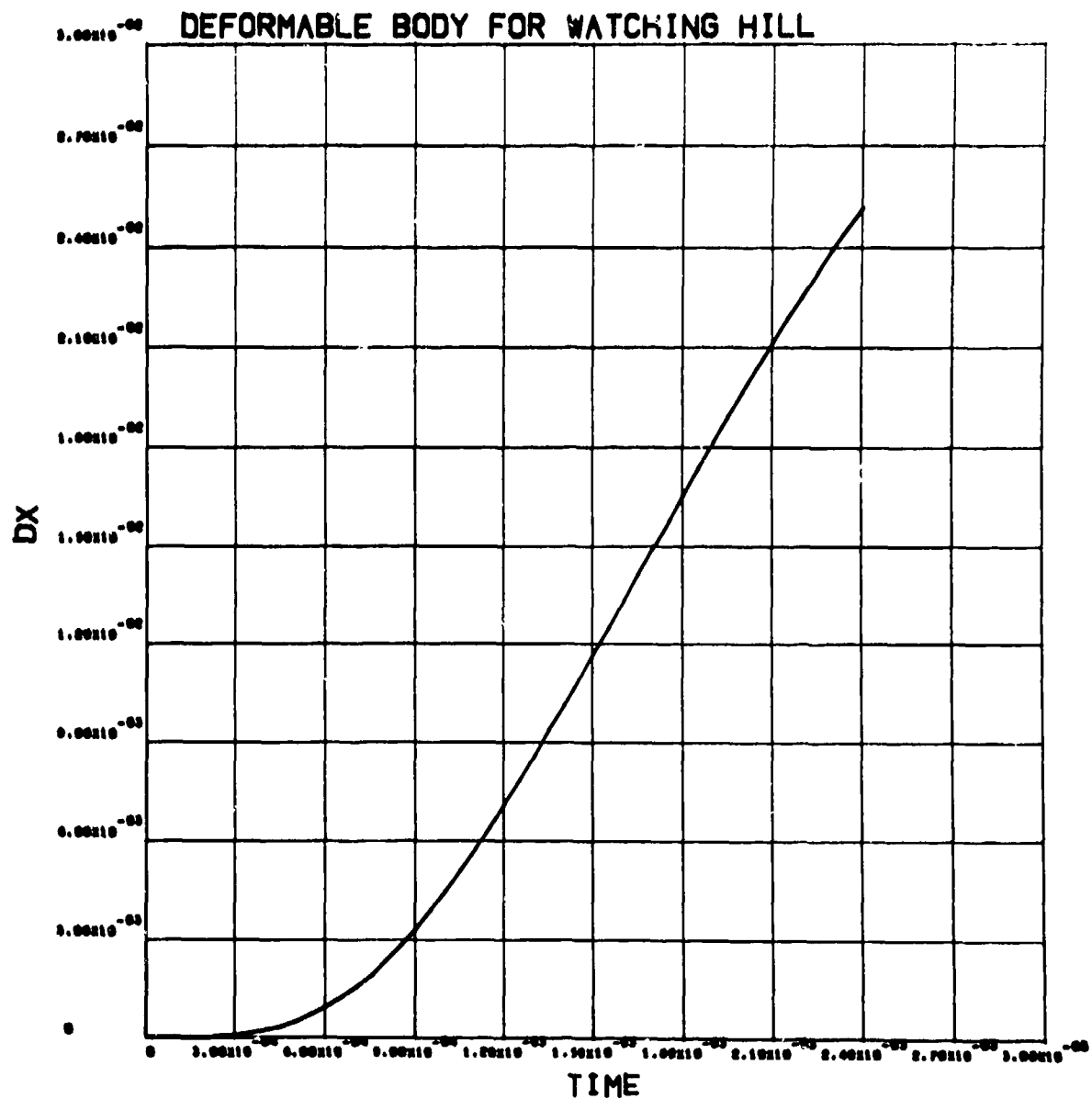Vertical velocity history (m/s) in soil at range 75 mm, depth 0.4 m (deformable penetrator).

Figure B-55

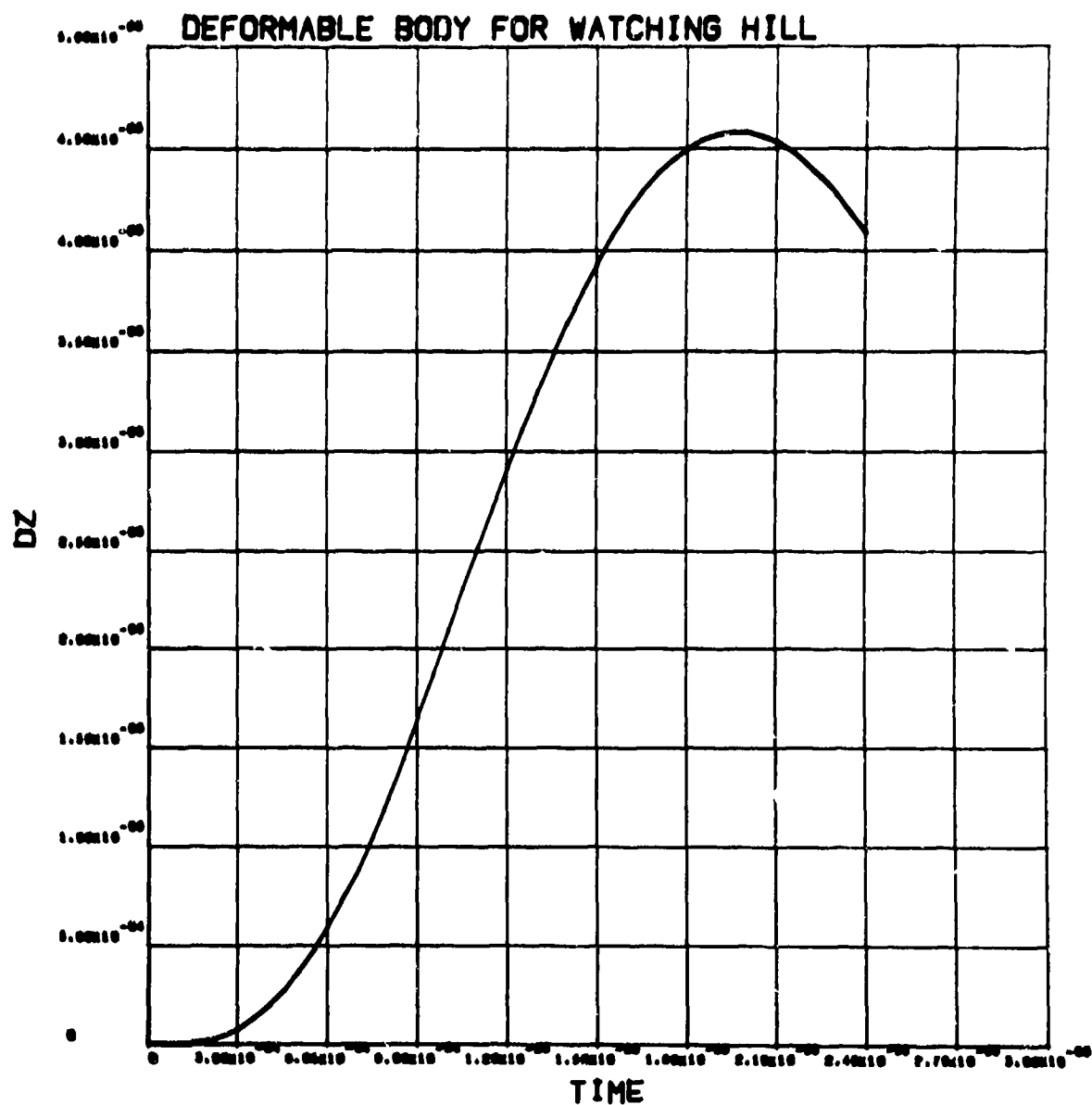Radial displacement history (m) in soil at range 75 mm, depth 0.4 m (deformable penetrator).

Figure B-56

Vertical displacement history (m) in soil at range 75 mm, depth 0.4 m (deformable penetrator).
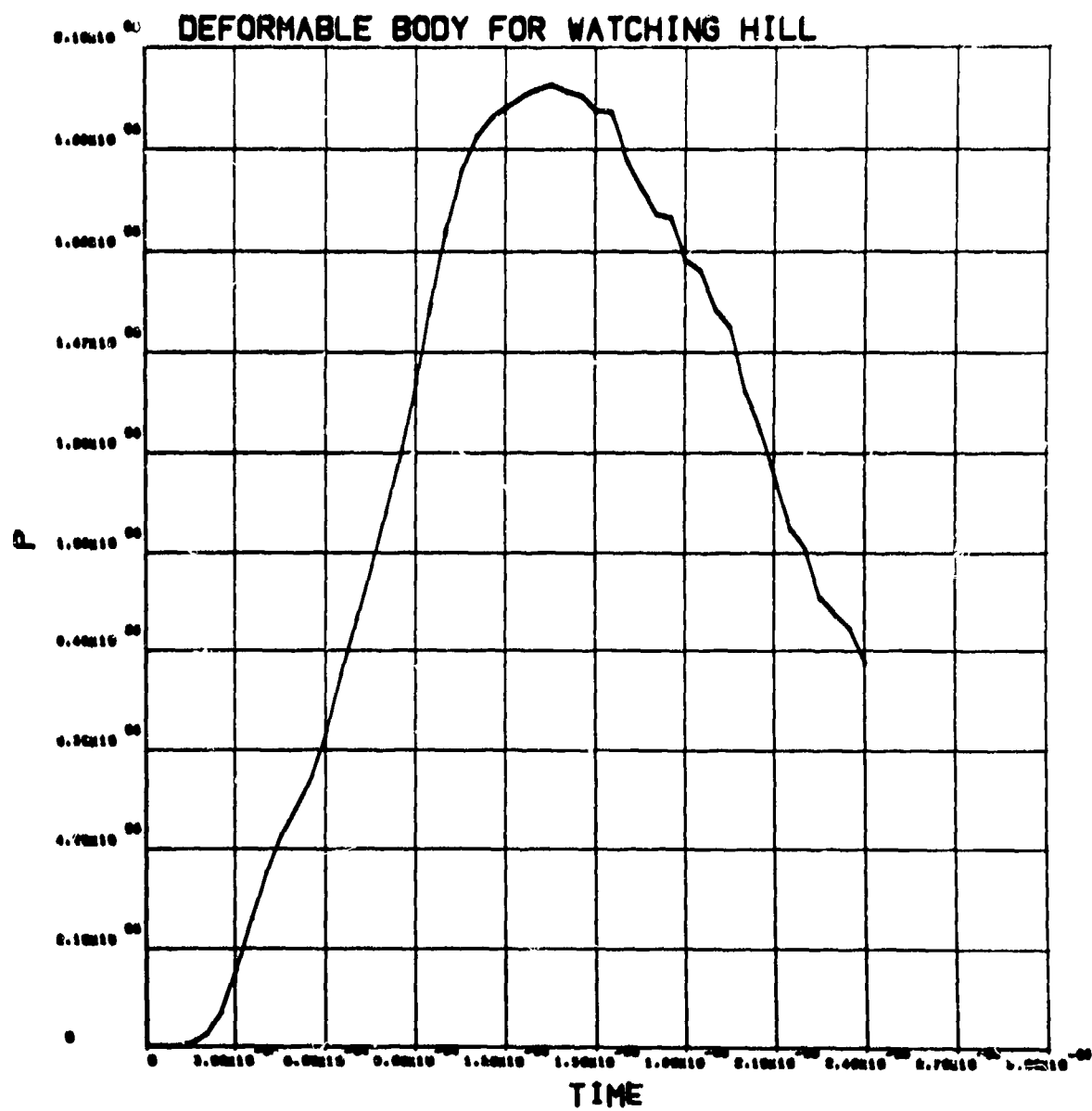
300

Figure B-57

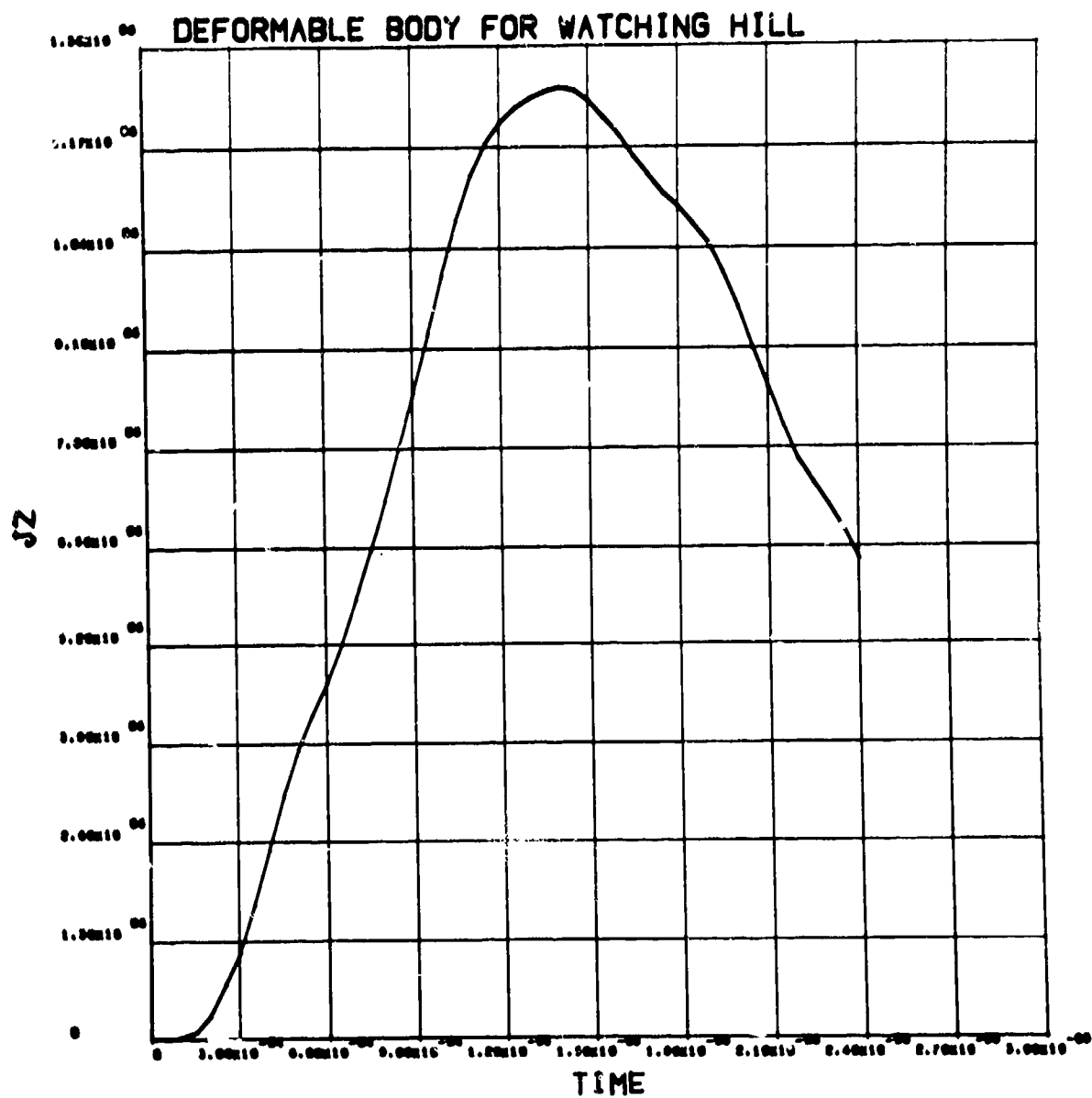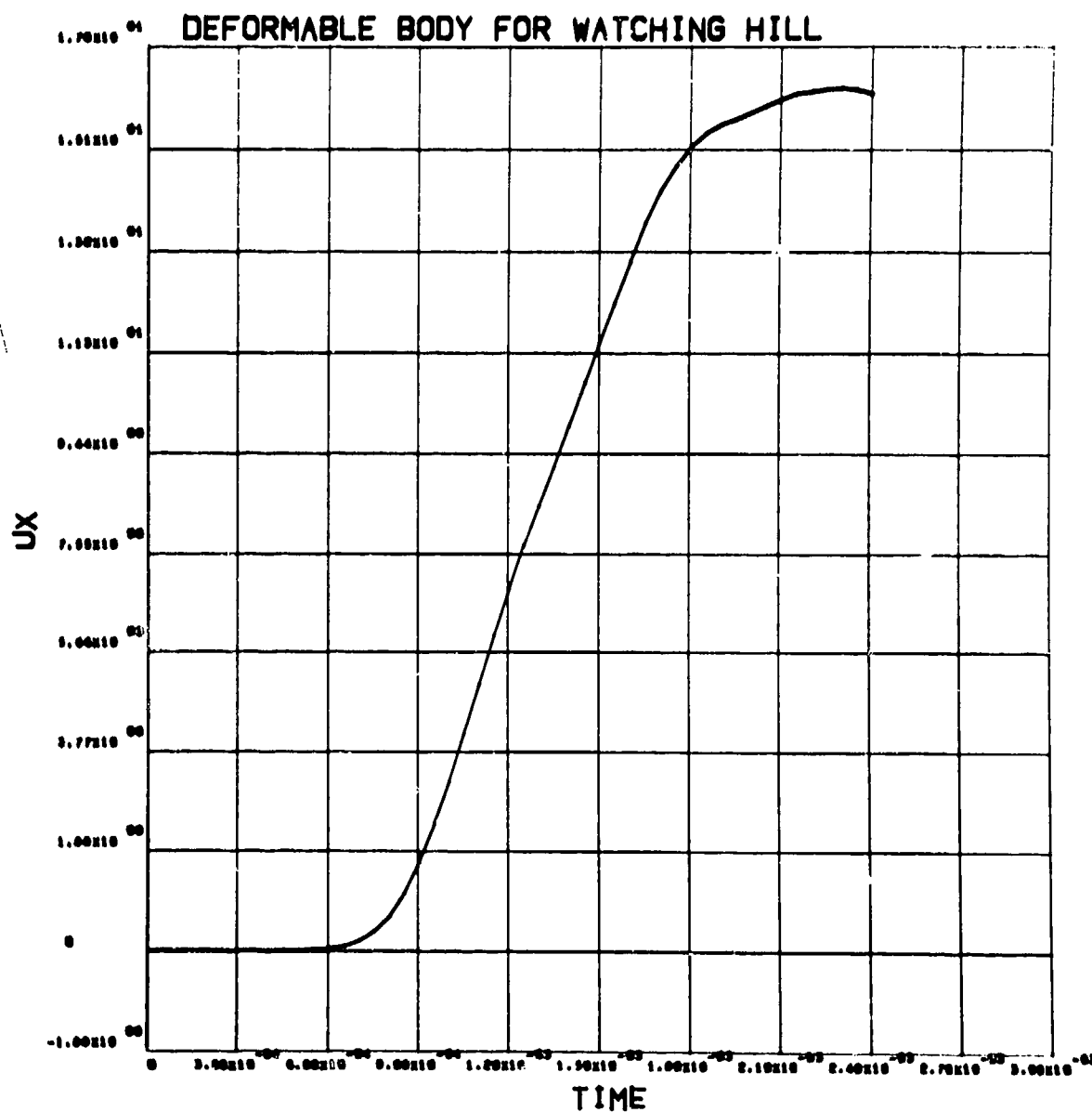Pressure history (Pa) in soil at range 75 mm, depth 0.4 m (deformable penetrator).

301

Figure B-58

Deviator stress, J2, history (Pa) in soil at range 75 mm, depth 0.4 m (deformable penetrator).

Figure B-59

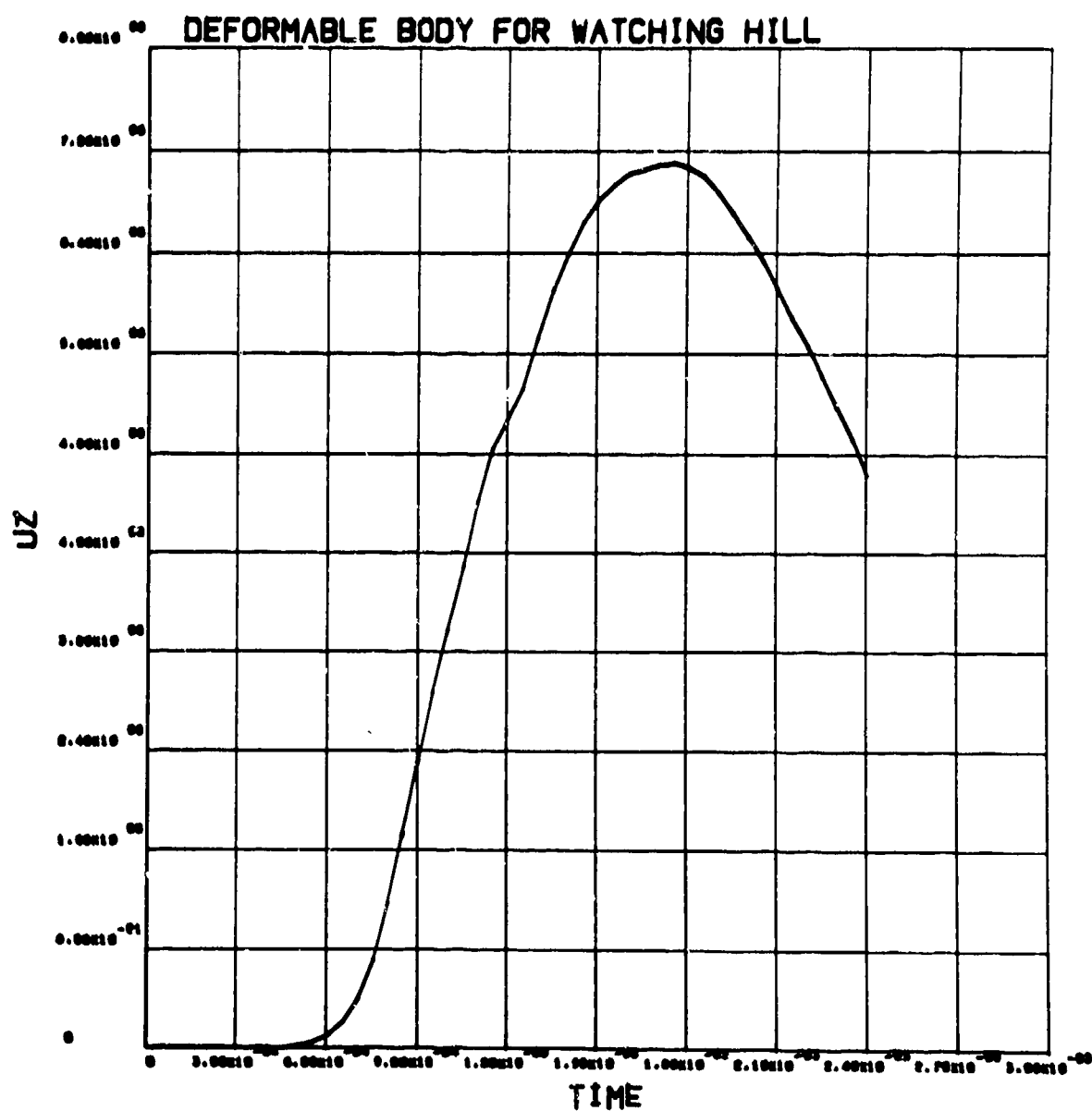Radial velocity history (m/s) in soil at range 0.14 m, depth 0.1 m (deformable penetrator).

303

Figure B-60

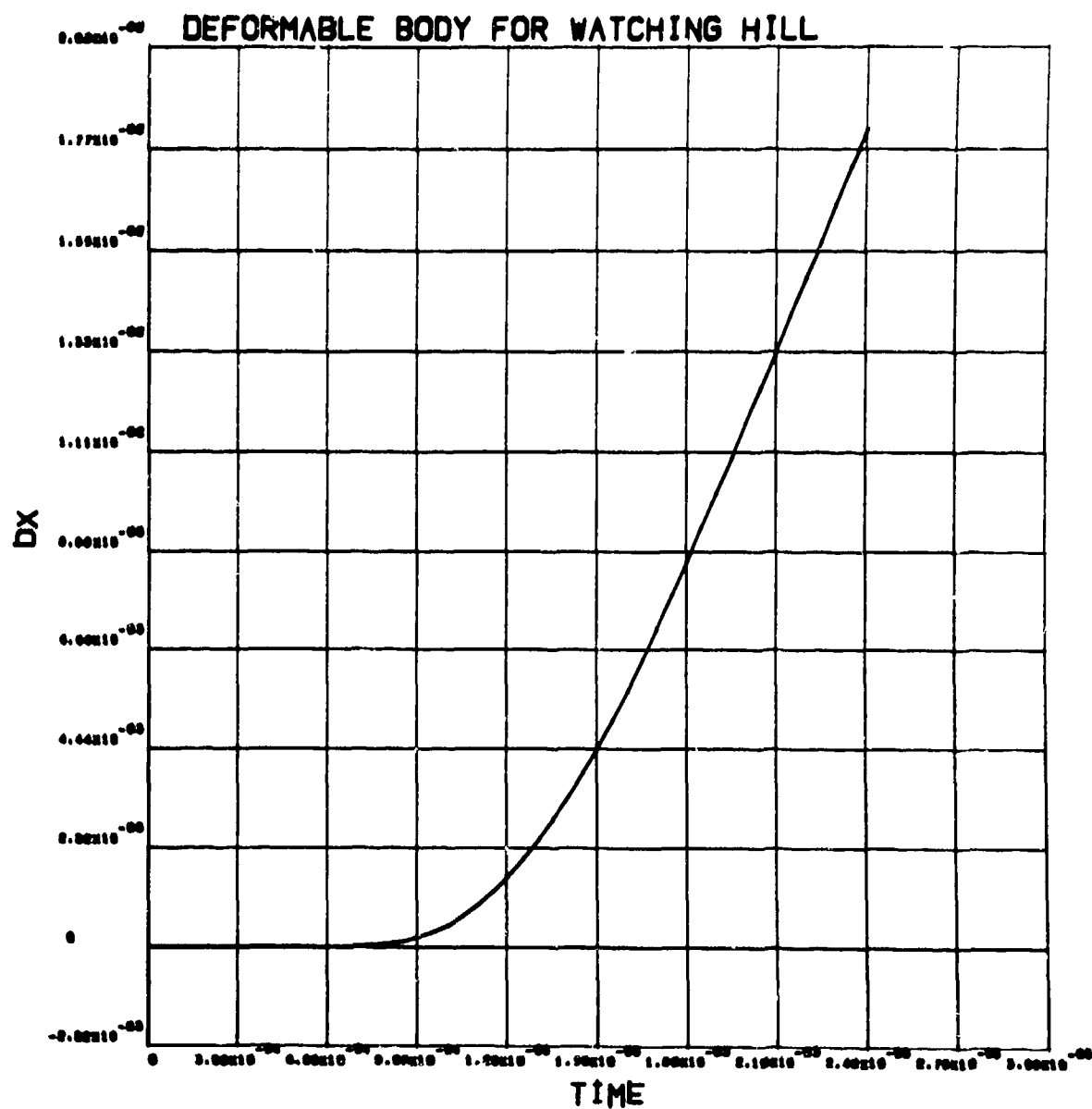Vertical velocity history (m/s) in soil at range 0.14 m, depth 0.1 m (deformable penetrator).

Figure B-61

Radial displacement history (m) in soil at range 0.14 m, depth 0.1 m (deformable penetrator).

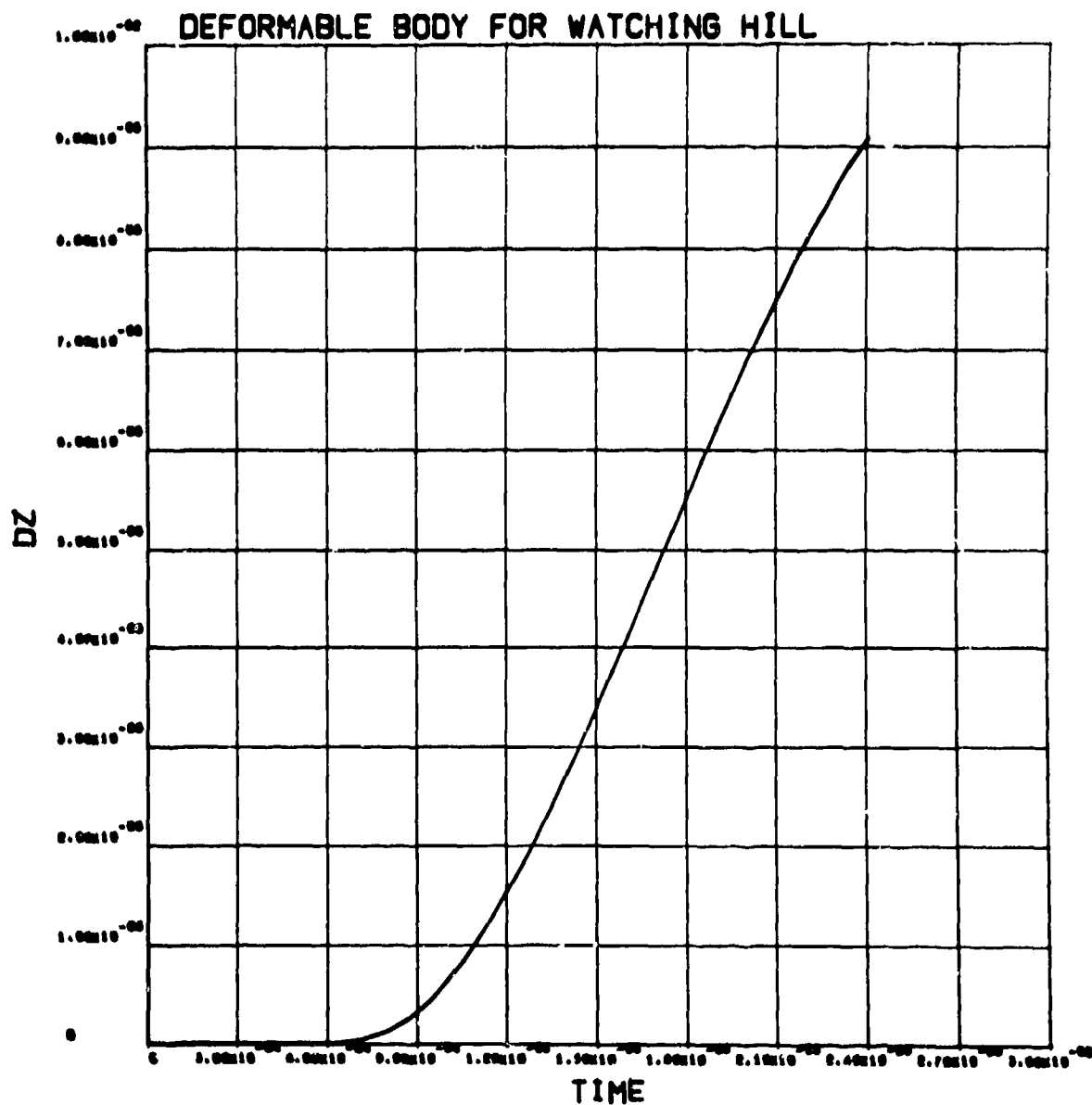Figure B-62

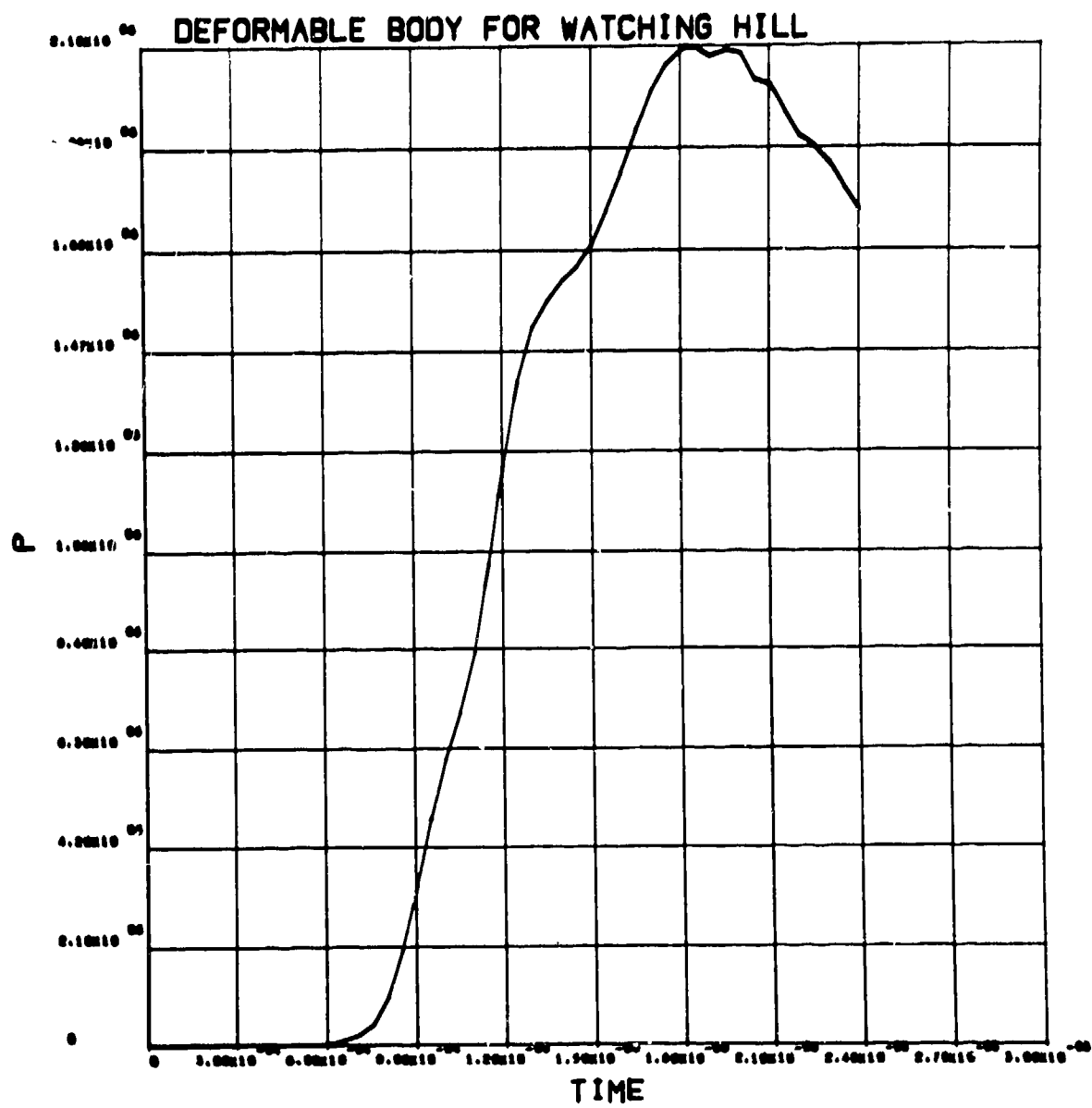Vertical displacement history (m) in soil at range 0.14 m, depth 0.1 m (deformable penetrator).

306

Figure B-63

Pressure history (Pa) in soil at range 0.14 m, depth 0.1 m (deformable penetrator).
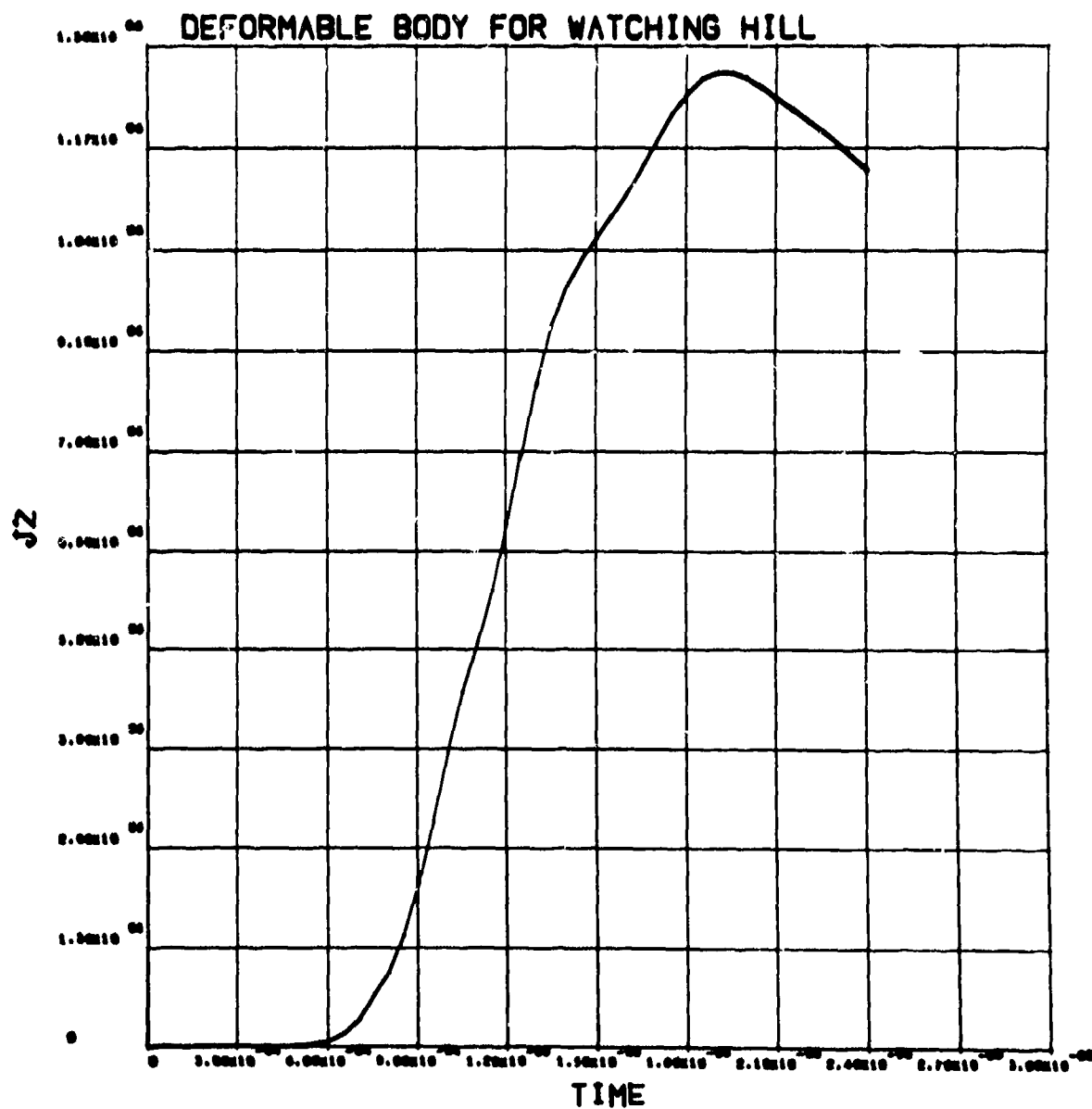
Figure B-64

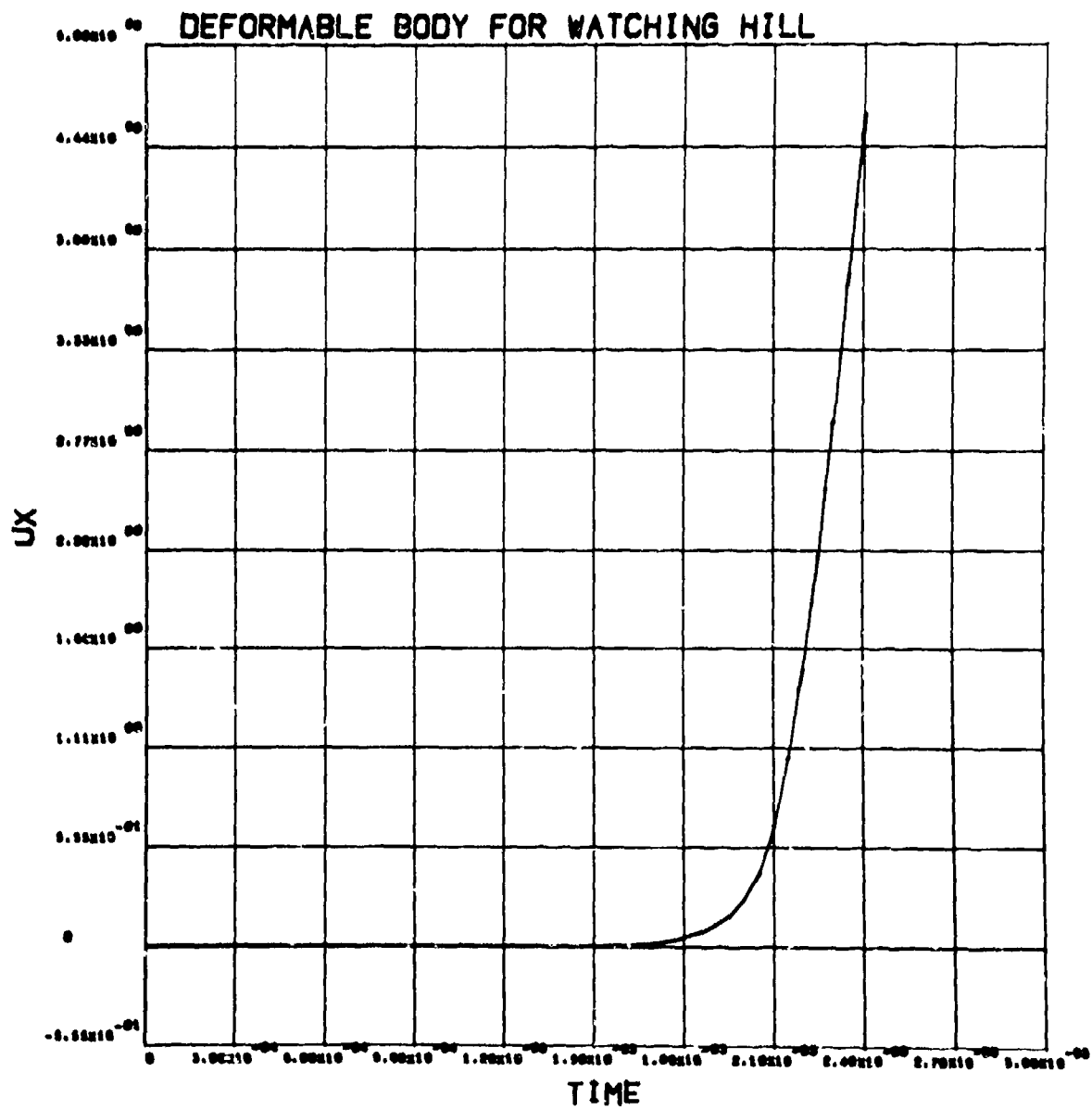Deviator stress, J2, history (Pa) in soil at range 0.14 m, depth 0.1 m (deformable penetrator).

Figure B-65

Radial velocity history (m/s) in soil at range 0.14 m, depth 0.2 m (deformable penetrator).

Figure B-66

Vertical velocity history (m/s) in soil at range 0.14 m, depth 0.2 m (deformable penetrator).

310

Figure B-67

Radial displacement history (m) in soil at range 0.14 m, depth 0.2 m (deformable penetrator).

Figure B-68

Vertical displacement history (m) in soil at range 0.14 m, depth 0.2 m (deformable penetrator).

Figure B-69
Pressure history (Pt.) in soil at range 0.14 m, depth 0.2 m (deformable penetrator).

316

Figure B-70

Deviator stress, J2, history (Pa) in soil at range 0.14 m, depth 0.2 m (deformable penetrator).

Figure B-71

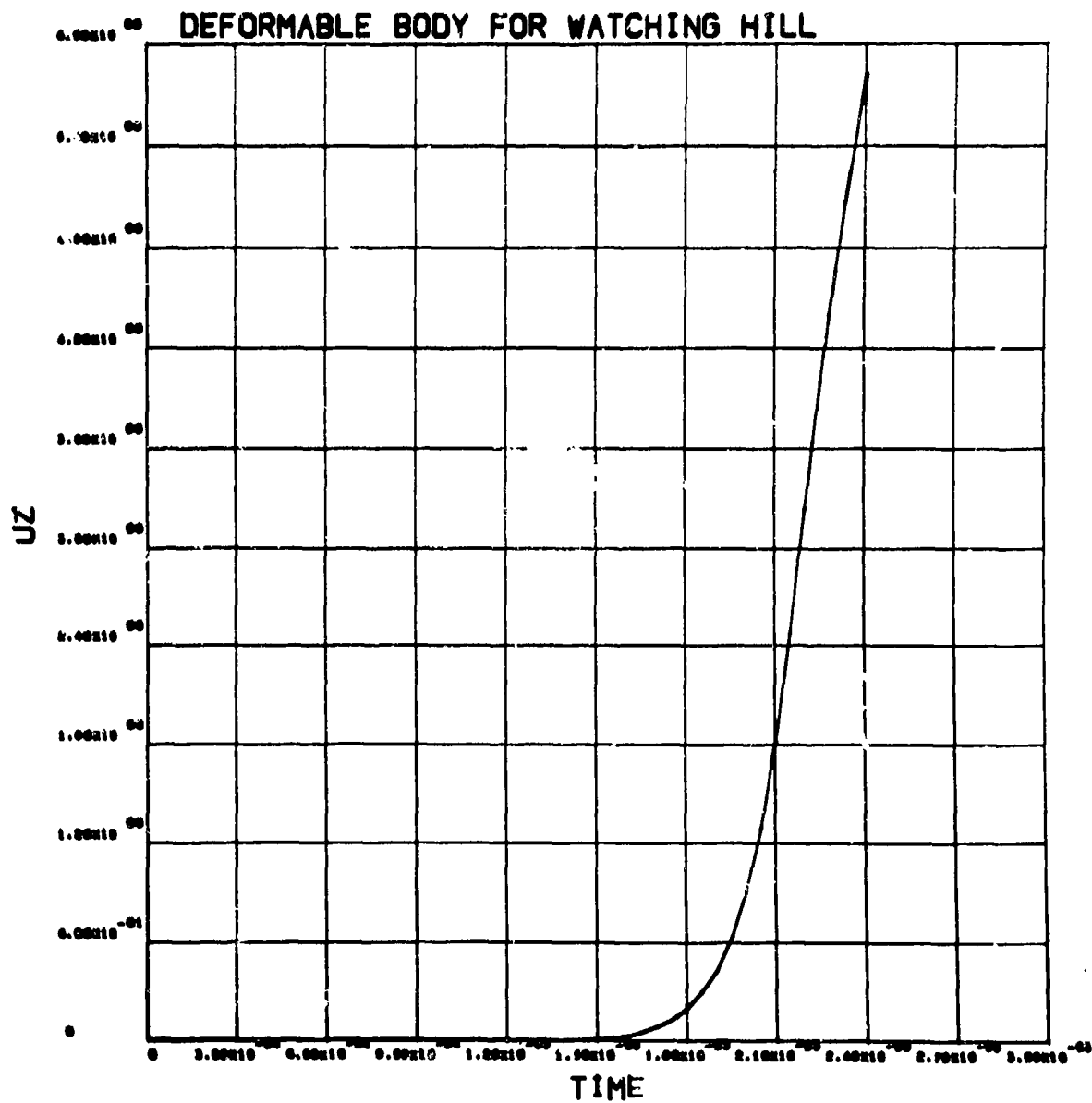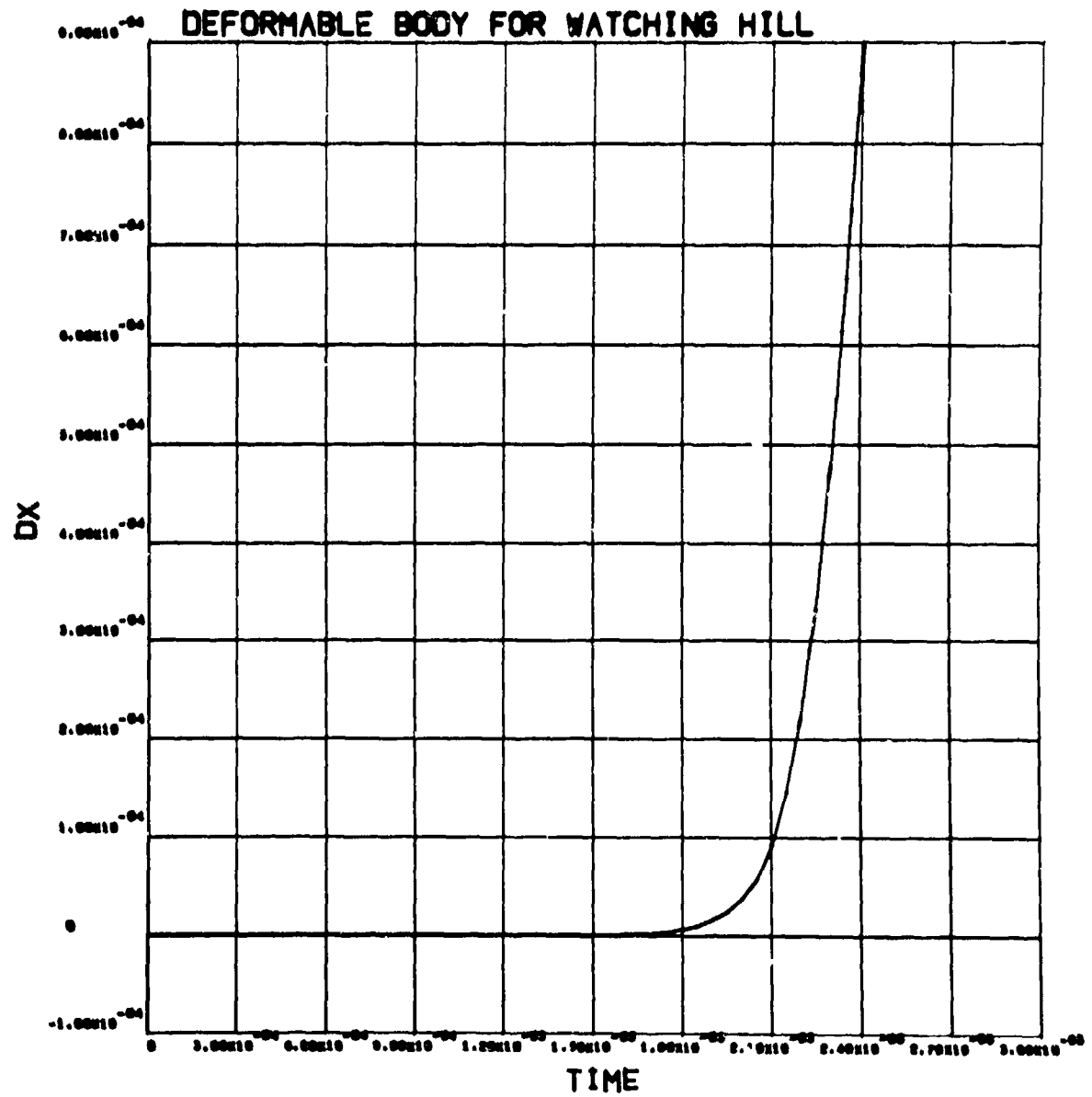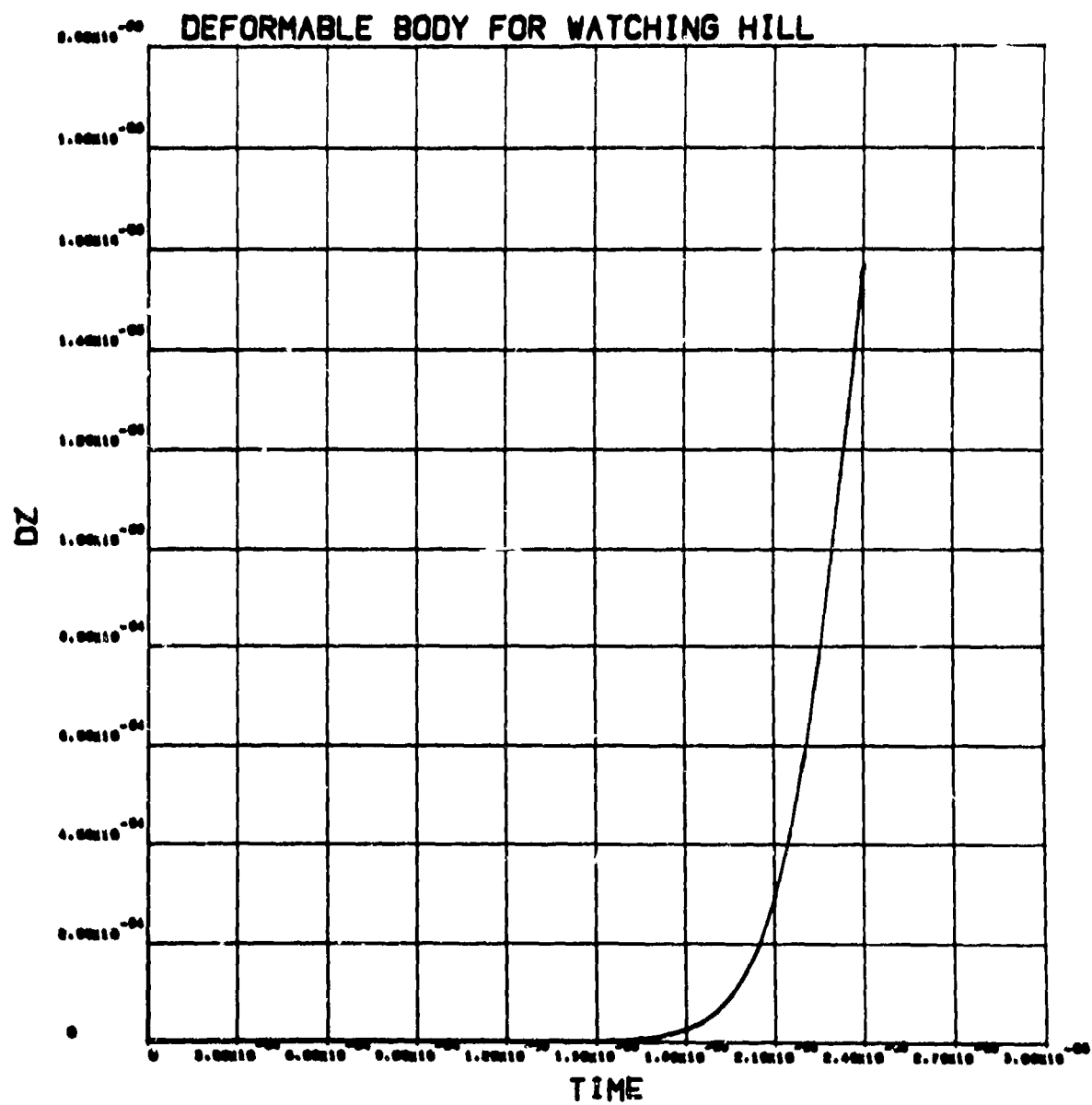Radial velocity history (m/s) in soil at range 0.14 m, depth 0.4 m (deformable penetrator).

315

Figure B-72

Vertical velocity history (m/s) in soil at range 0.14 m, depth 0.4 m (deformable penetrator).

316

Figure B-73

Radial displacement history (m) in soil at range 0.14 m, depth 0.4 m (deformable penetrator).

317

Figure B-74

Vertical displacement history (m) in soil at range 0.14 m, depth 0.4 m (deformable penetrator).
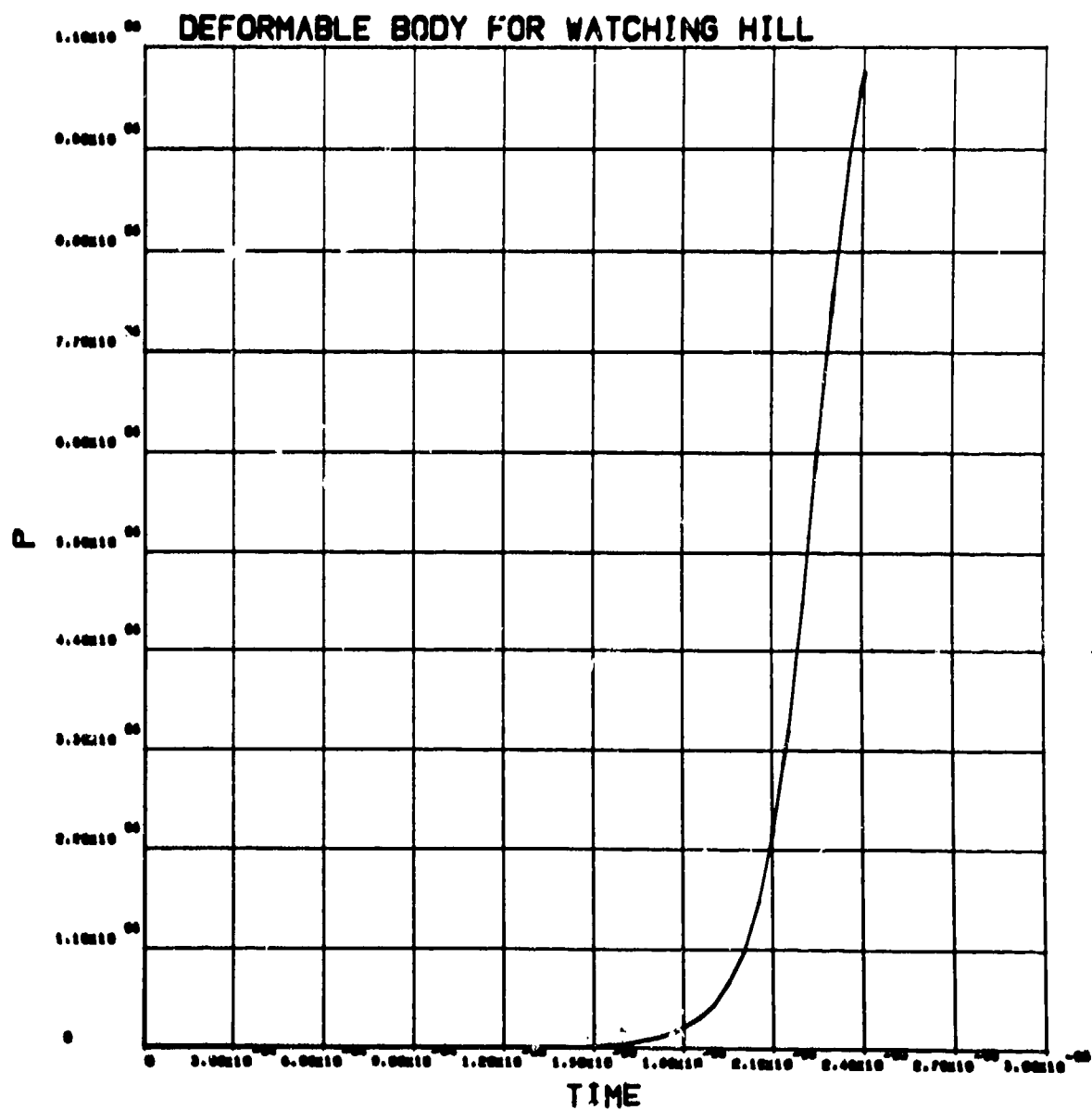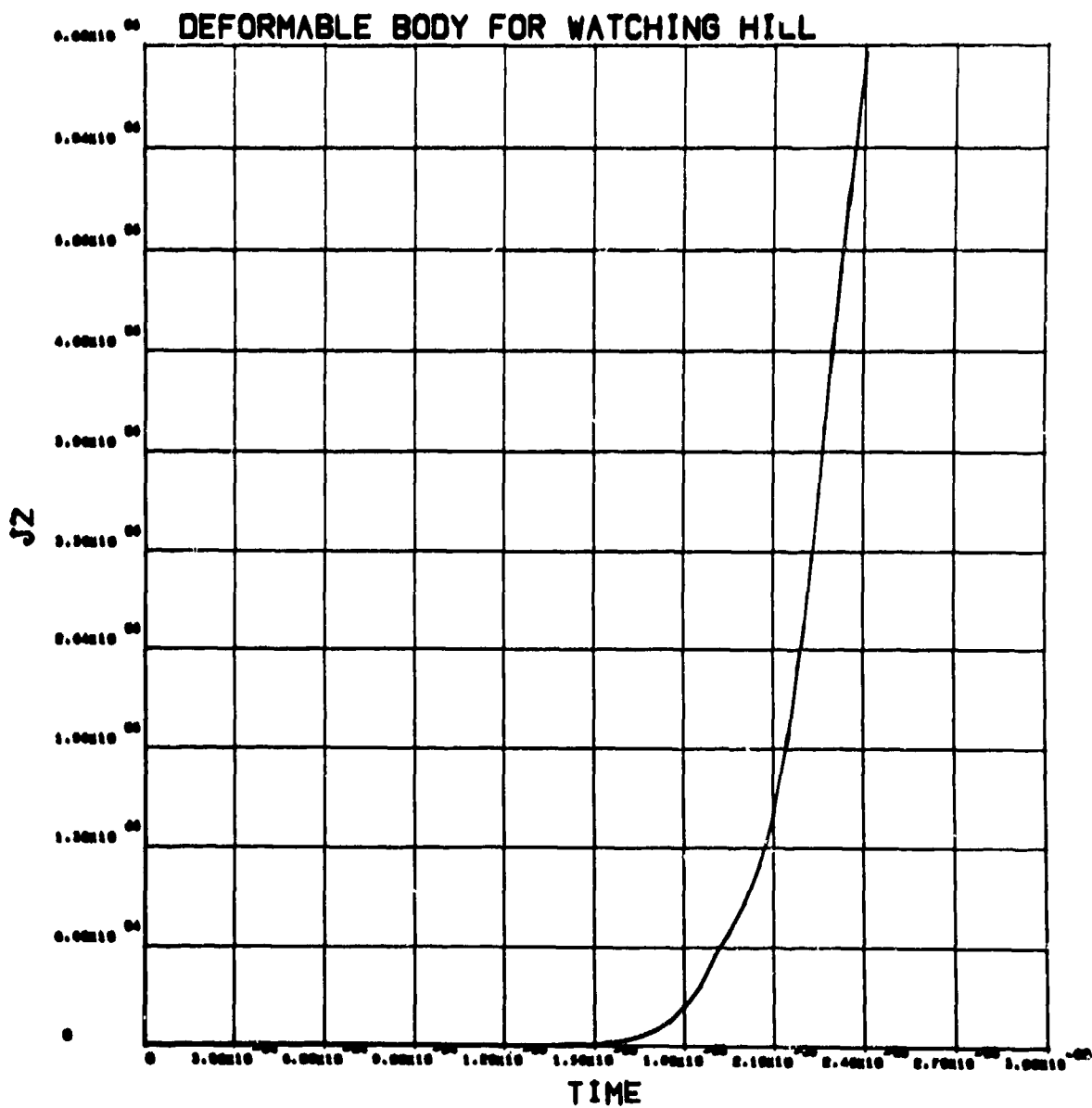
318

Figure B-75
Pressure history (Pa) in soil at range 0.14 m, depth 0.4 m (deformable penetrator).

Figure B-76

Deviator stress, J2, history (Pa) in soil at range 0.14 m, depth 0.4 m (deformable penetrator).
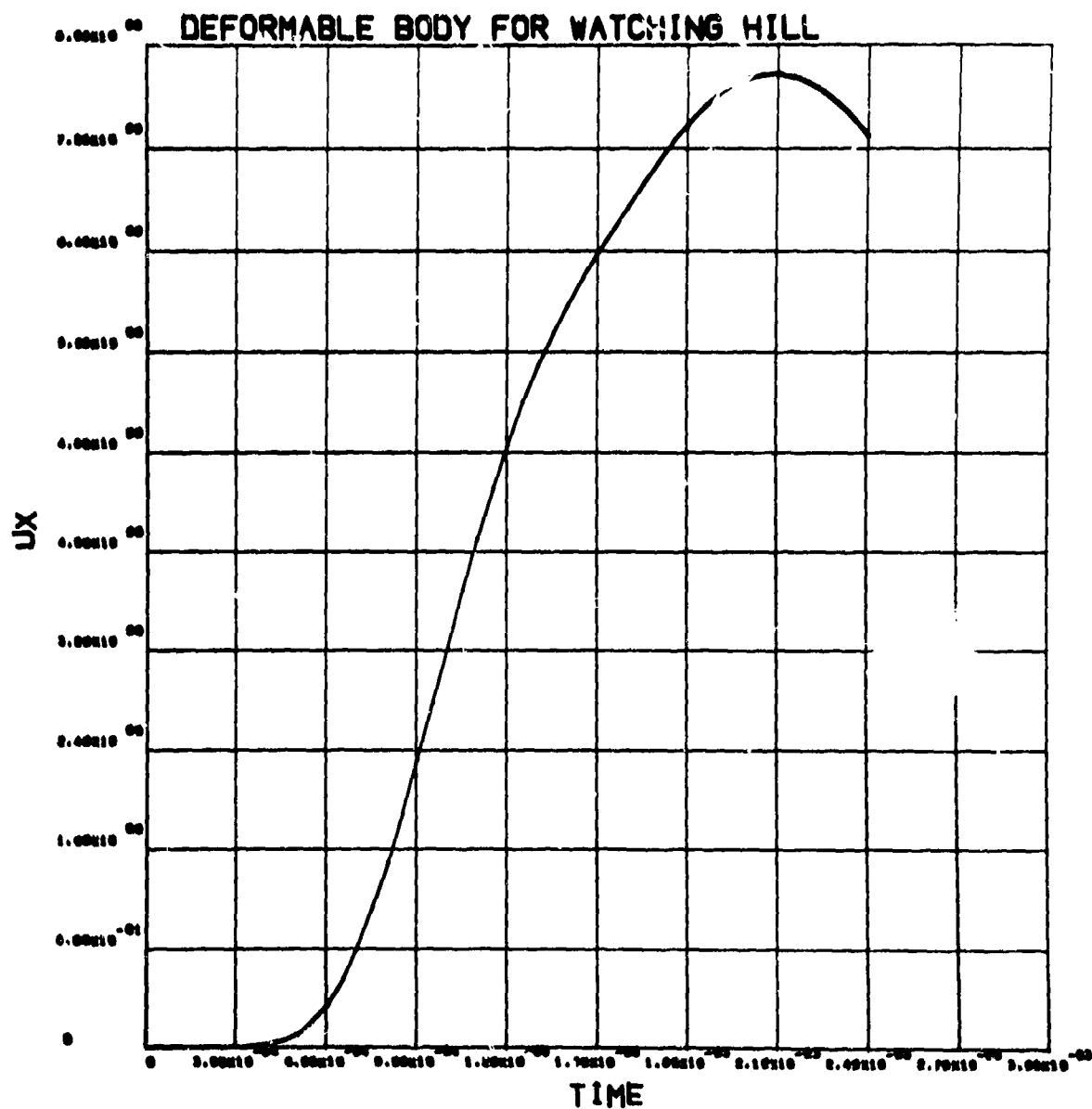
DEFORMABLE BODY FOR WATCHING HILL

Figure B-77

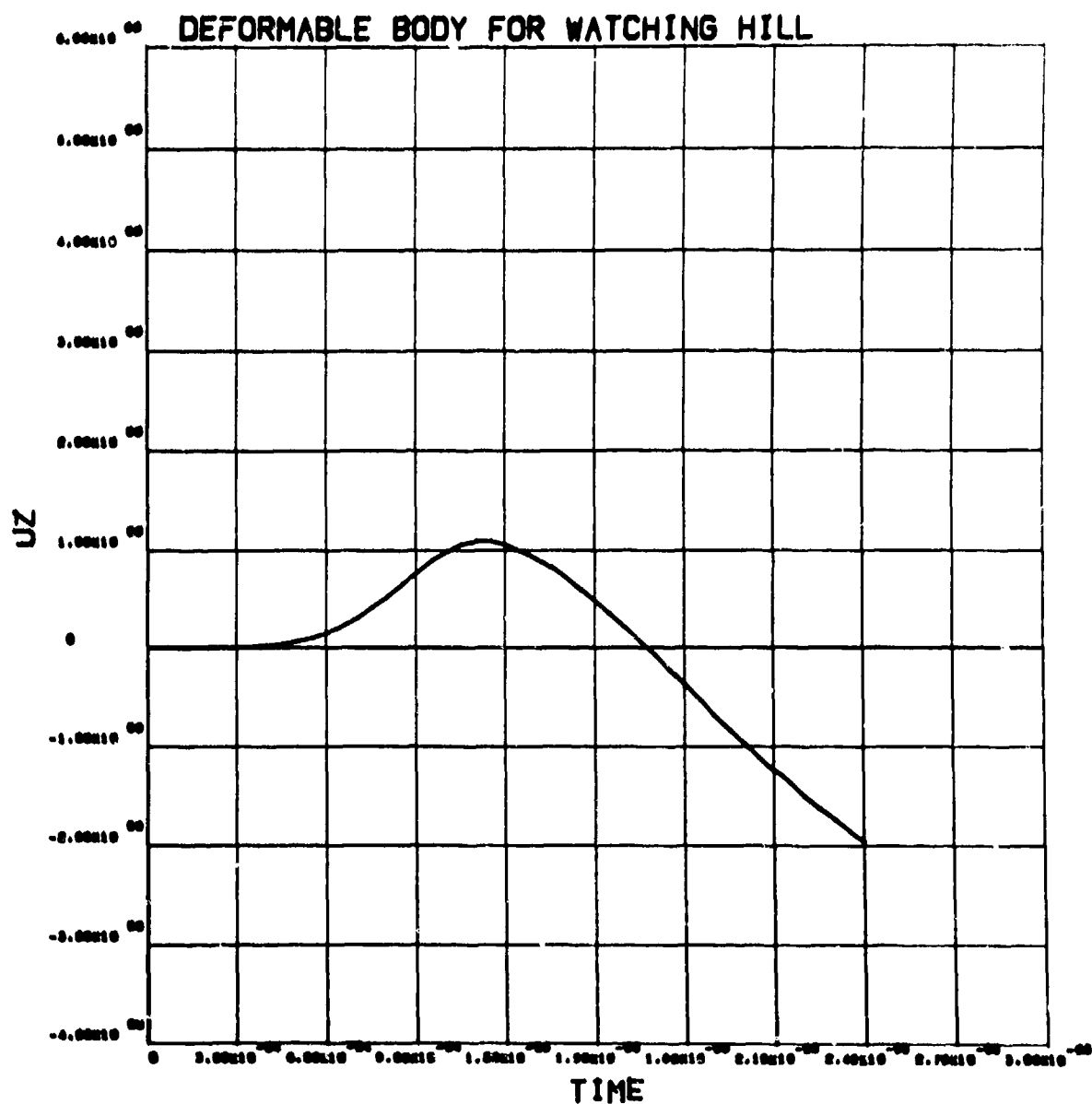Radial velocity history (m/s) in soil at range 0.28 m, depth 0.1 m (deformable penetrator).

Figure B-78
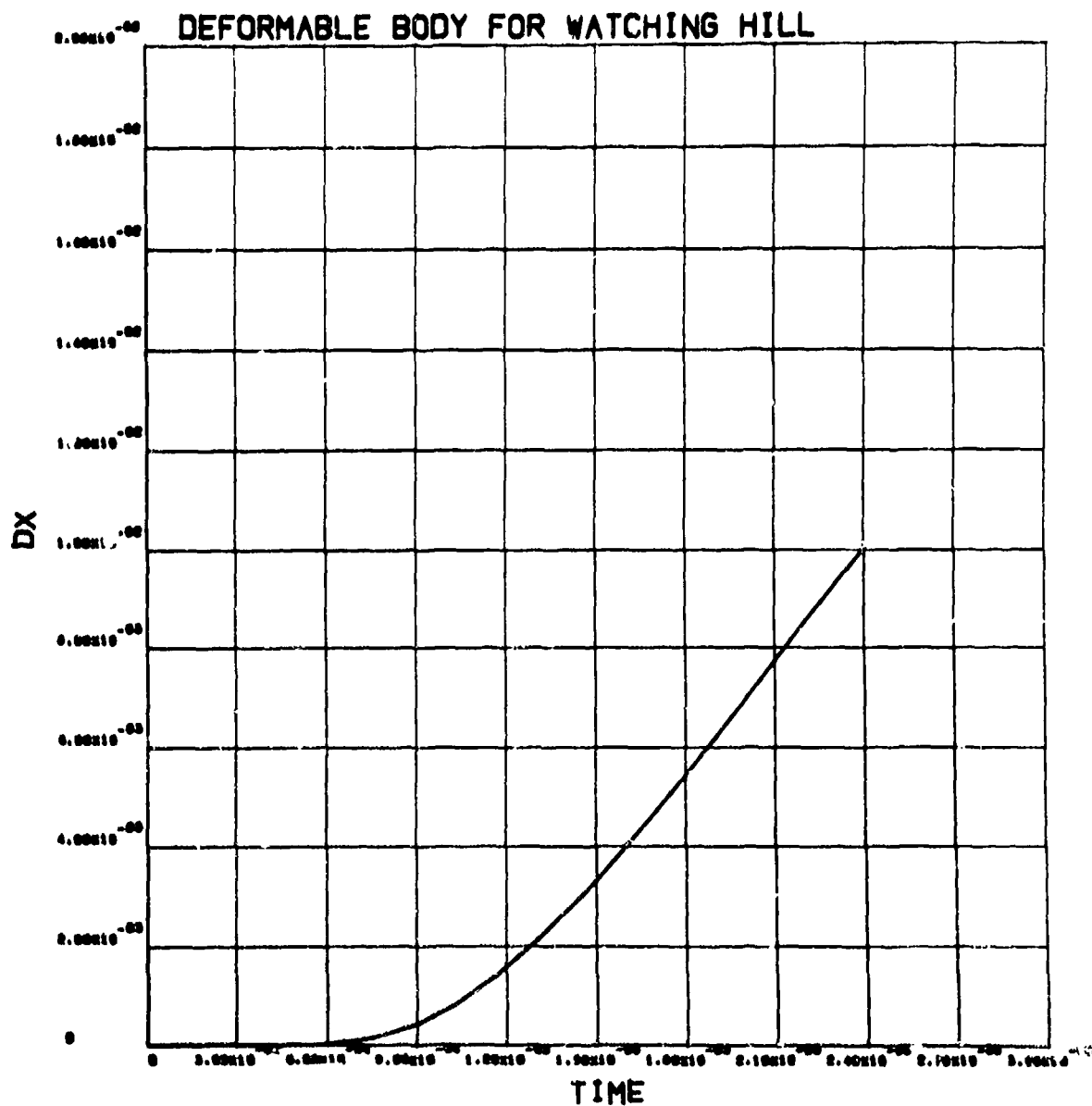Vertical velocity history (m/s) in soil at range 0.28 m, depth 0.1 m (deformable penetrator).

Figure B-79

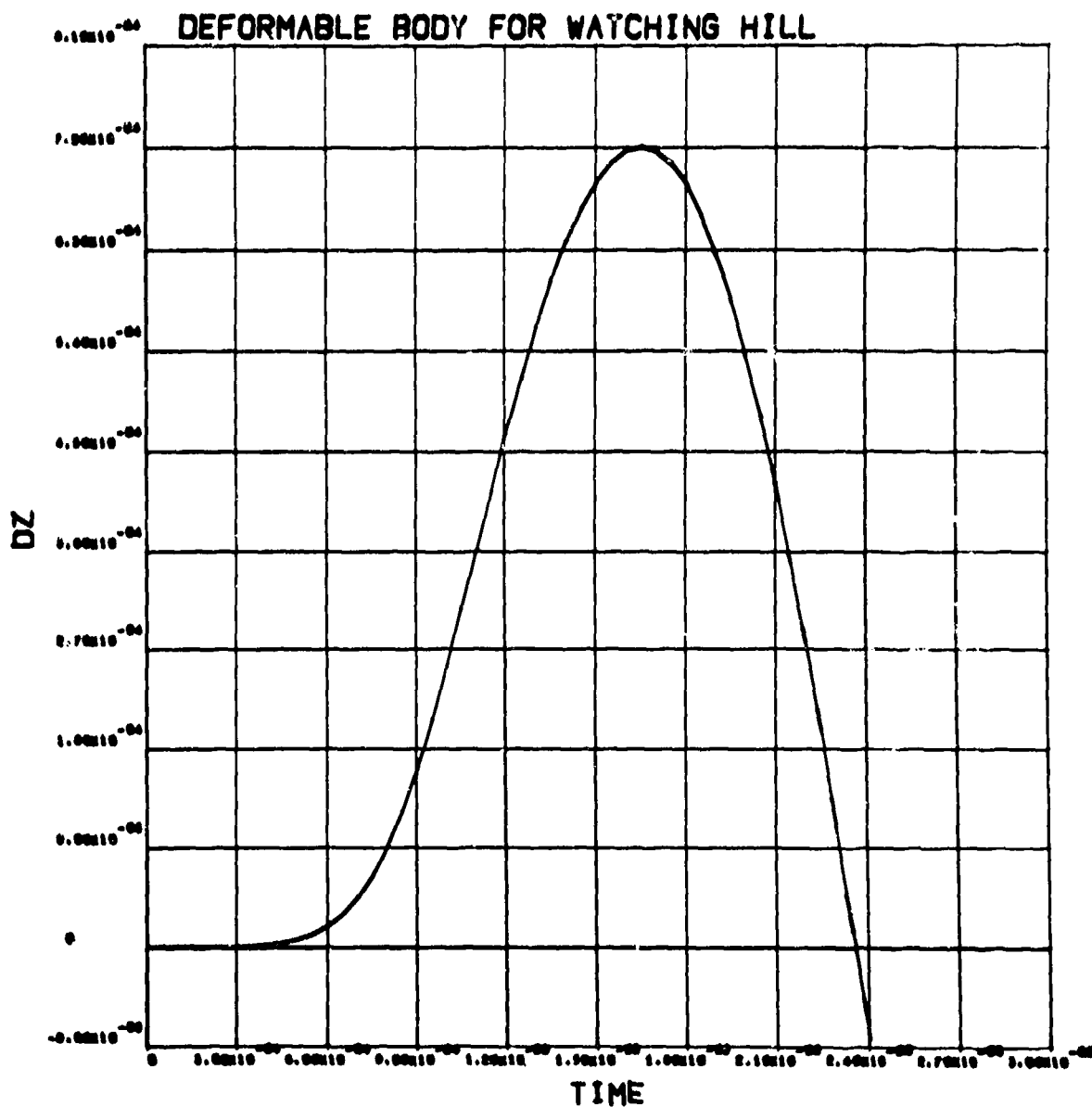Radial displacement history (m) in soil at range 0.28 m, depth 0.1 m (deformable penetrator).

Figure B-80

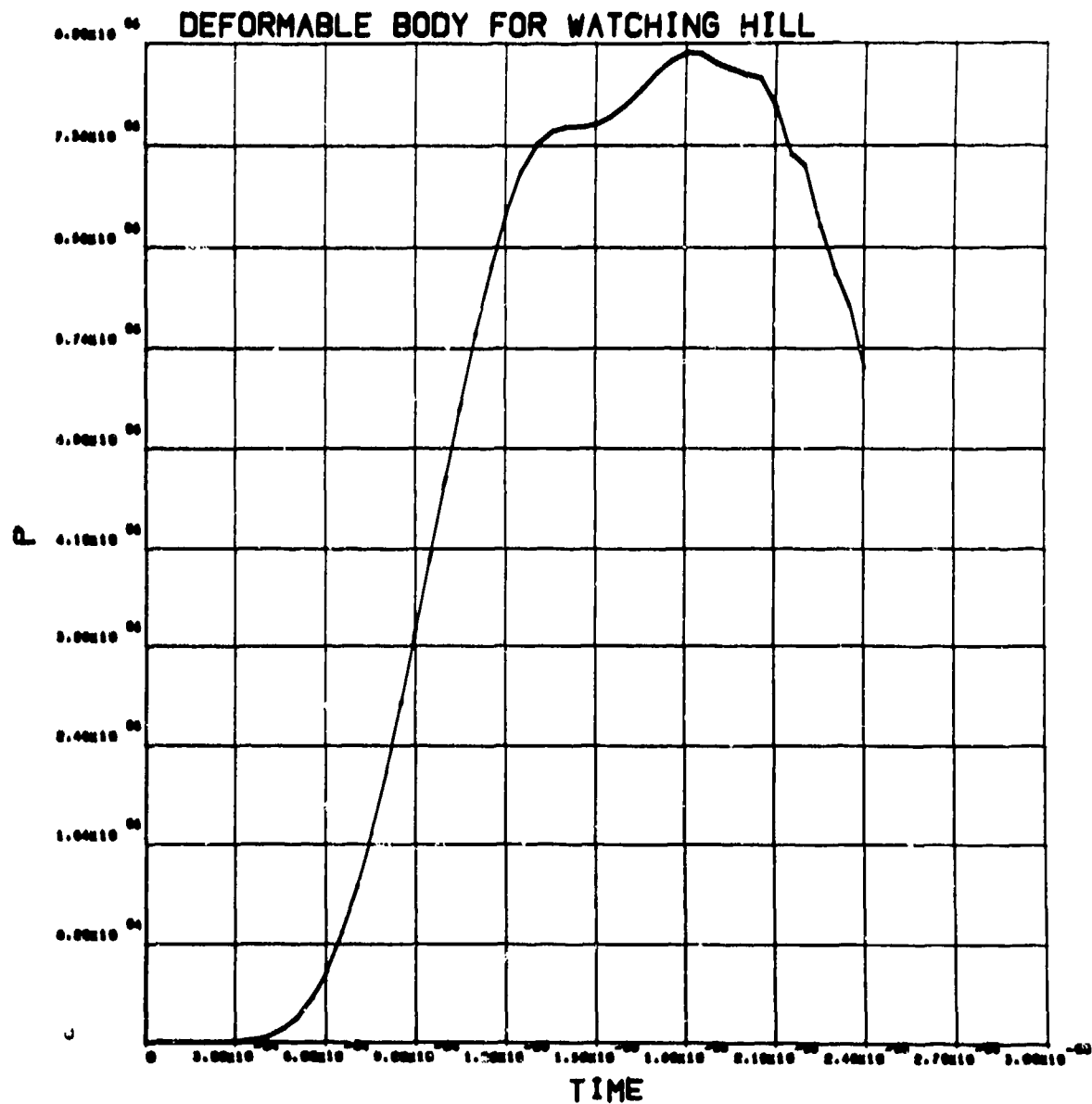Vertical displacement history (m) in soil at range 0.28 m, depth 0.1 m (deformable penetrator).

Figure B-81

Pressure history (Pa) in soil at range 0.28 m, depth 0.1 m (deformable penetrator).
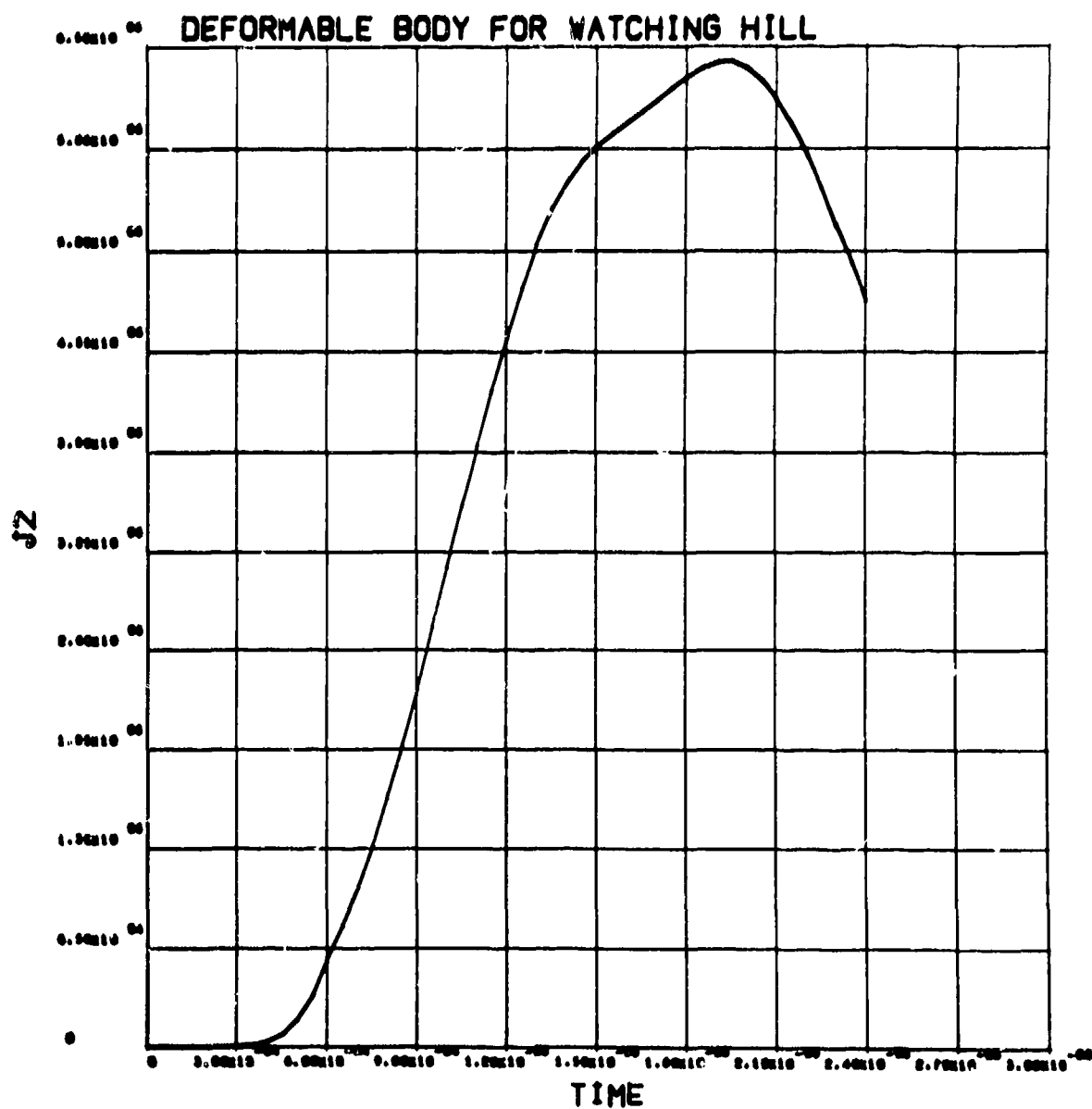
Figure B-82

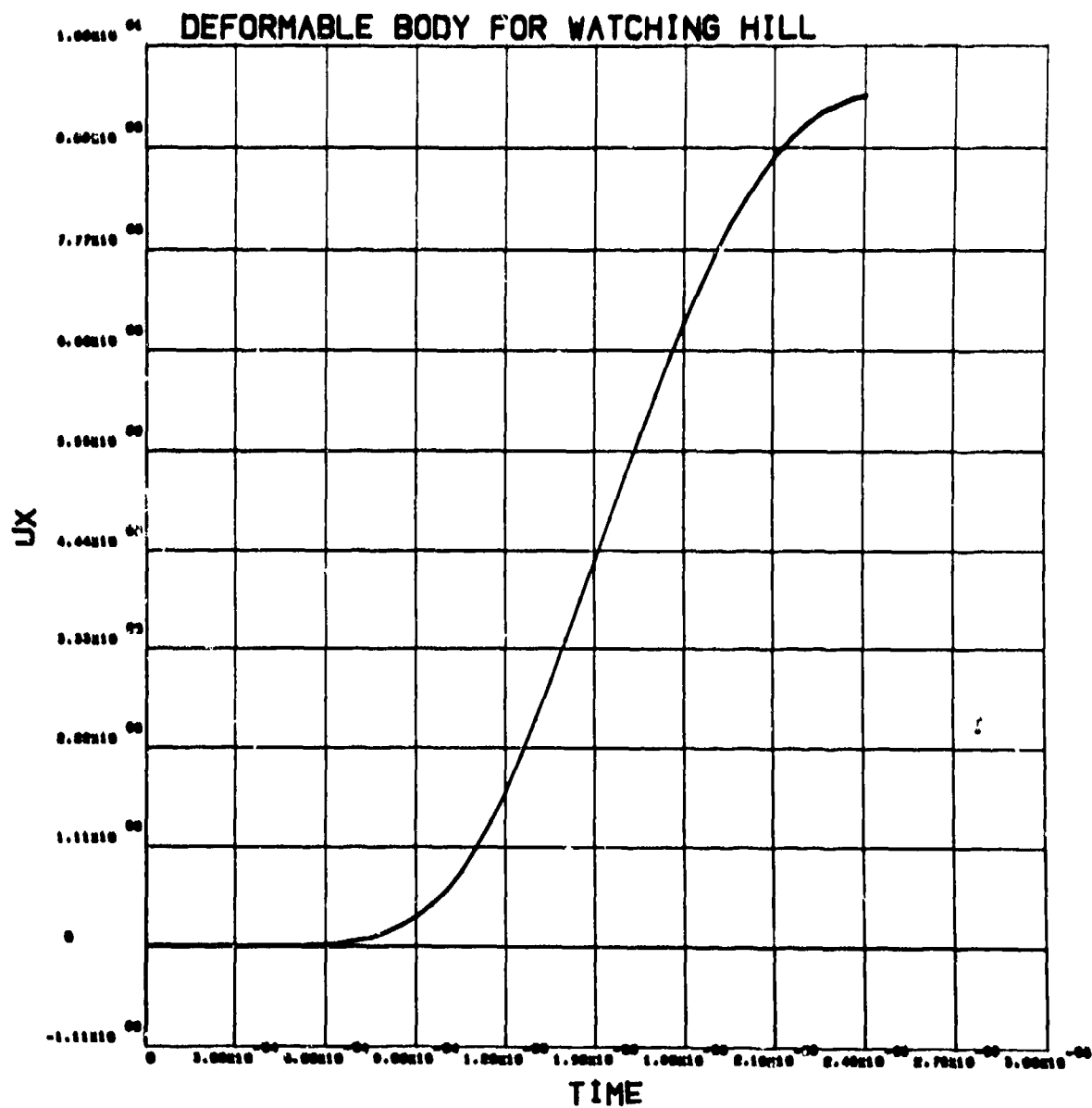Deviator stress, J2, history (Pa) in soil at range 0.28 m, depth 0.1 m (deformable penetrator).
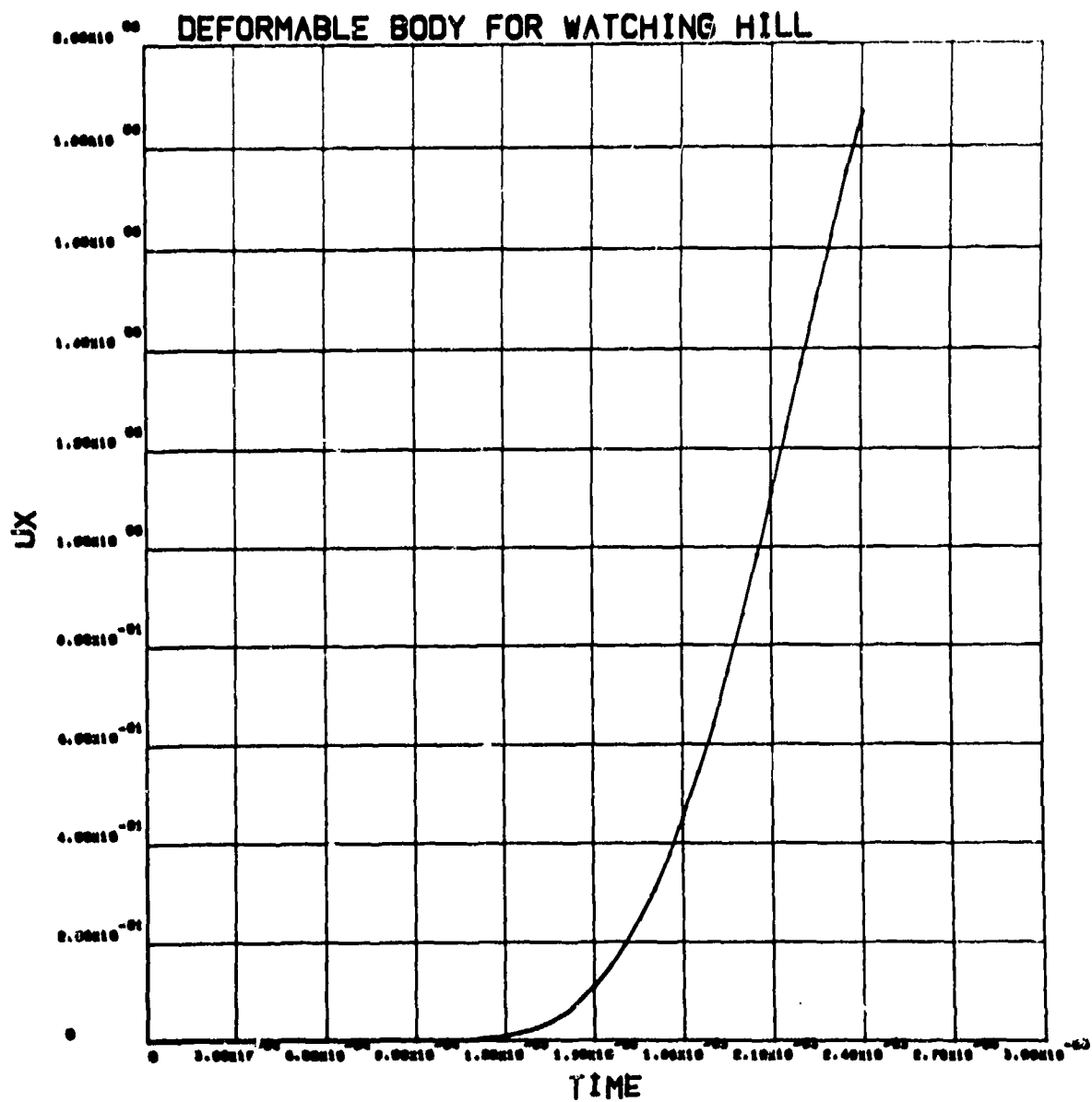
Figure B-83

Radial velocity history (m/s) in soil at range 0.28 m, depth 0.2 m (deformable penetrator).
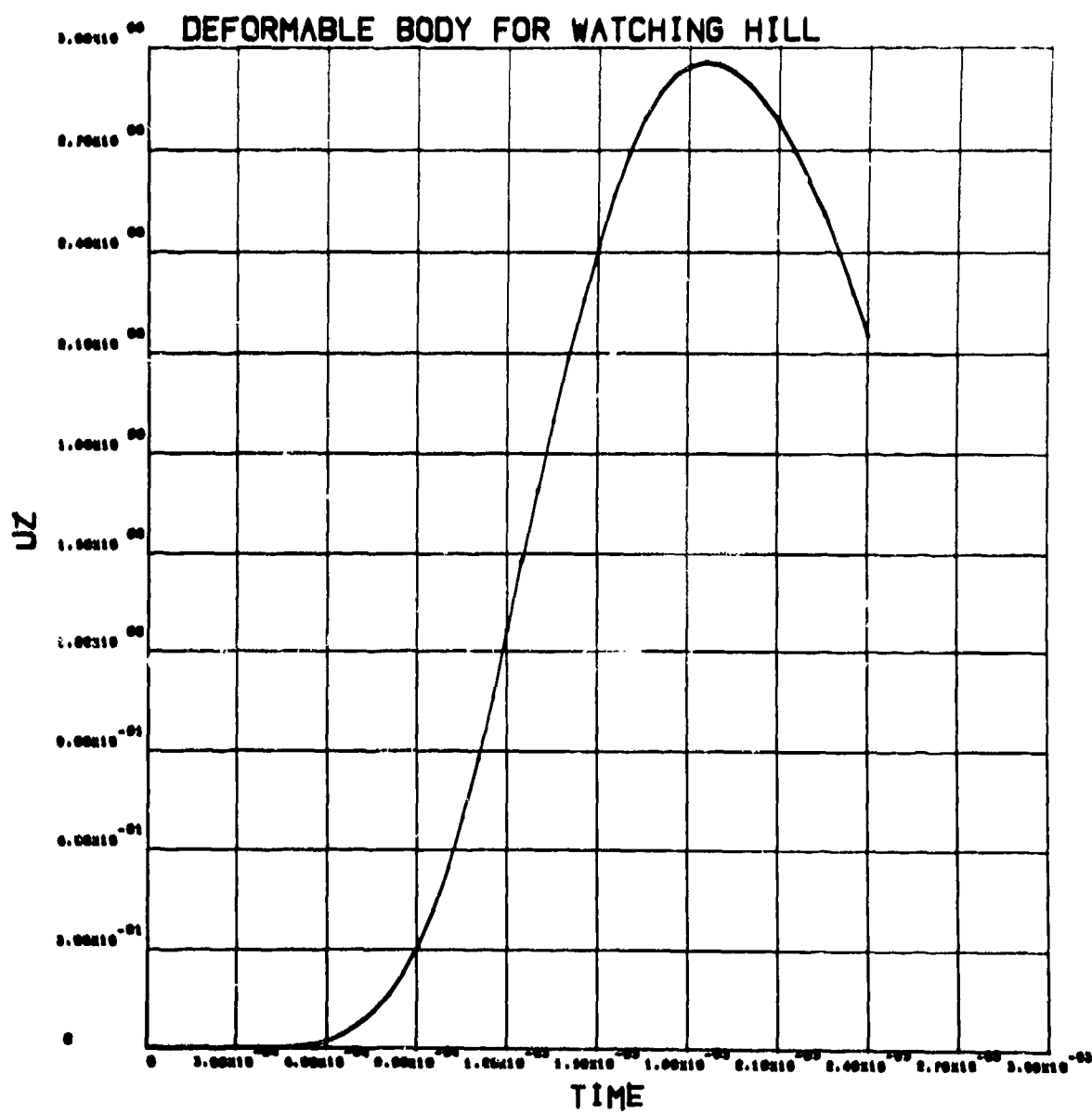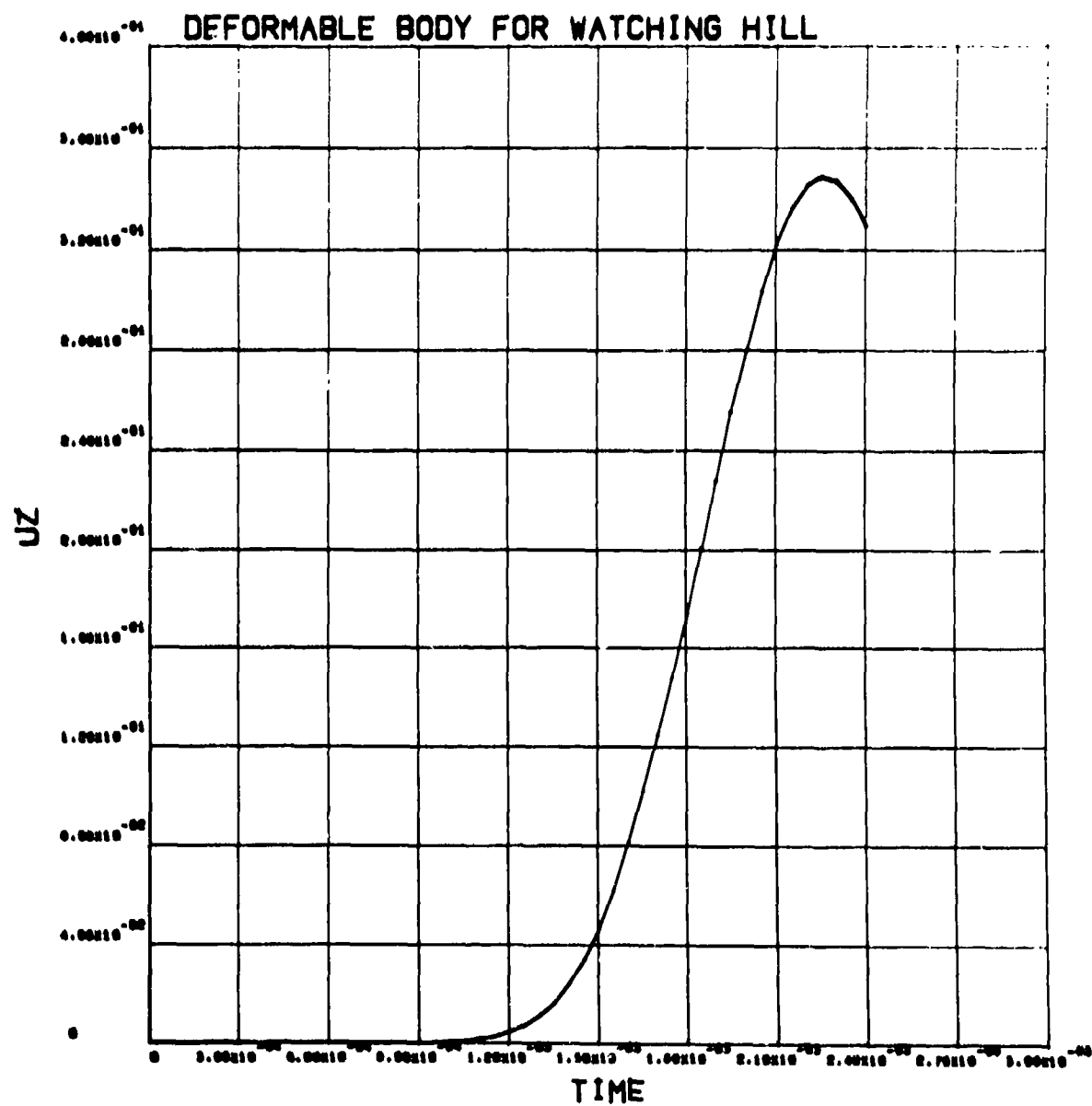
Figure B-84

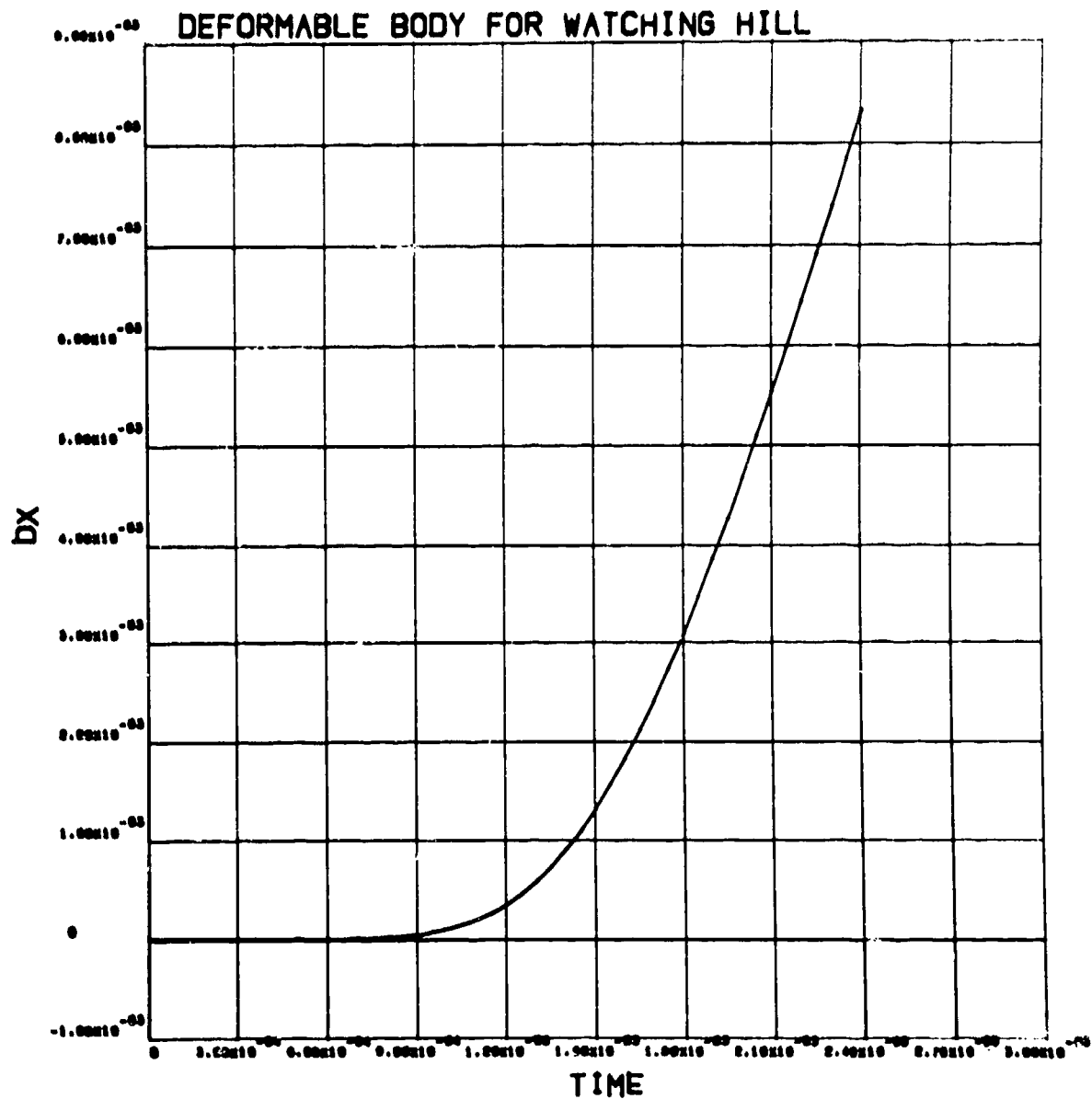Vertical velocity history (m/s) in soil at range 0.28 m, depth 0.2 m (deformable penetrator).

328
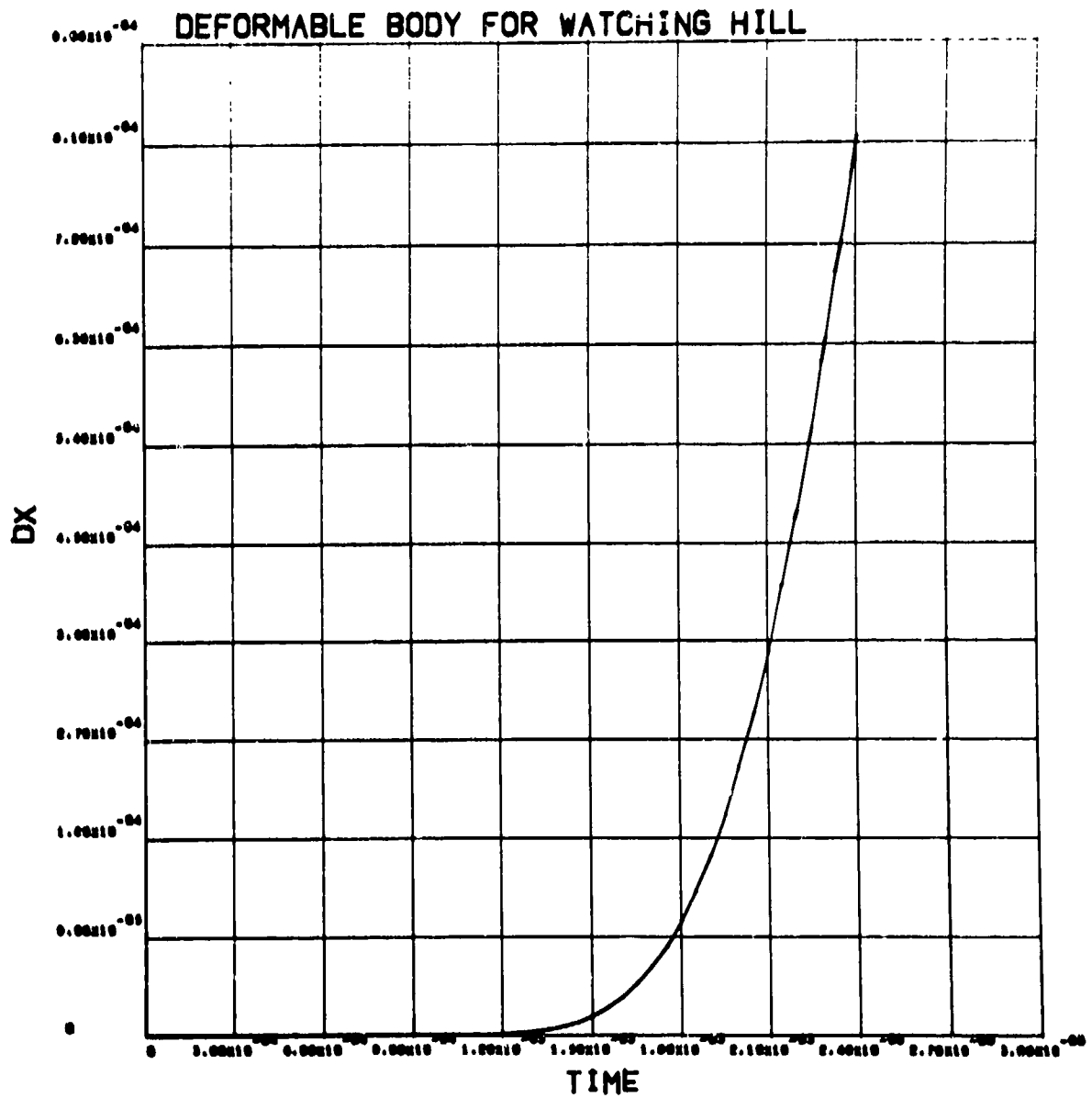
Figure B-85

Radial displacement history (m) in soil at range 0.28 m, depth 0.2 m (deformable penetrator).

Figure B-86

Vertical displacement history (m) in soil at range 0.28 m, depth 0.2 m (deformable penetrator).

330

Figure B-87

Pressure history (Pa) in soil at range 0.28 m, depth 0.? (deformable penetrator).

Figure B-88

Deviator stress, J2, history (Pa) in soil at range 0.28 m, depth 0.2 m (deformable penetrator).

332
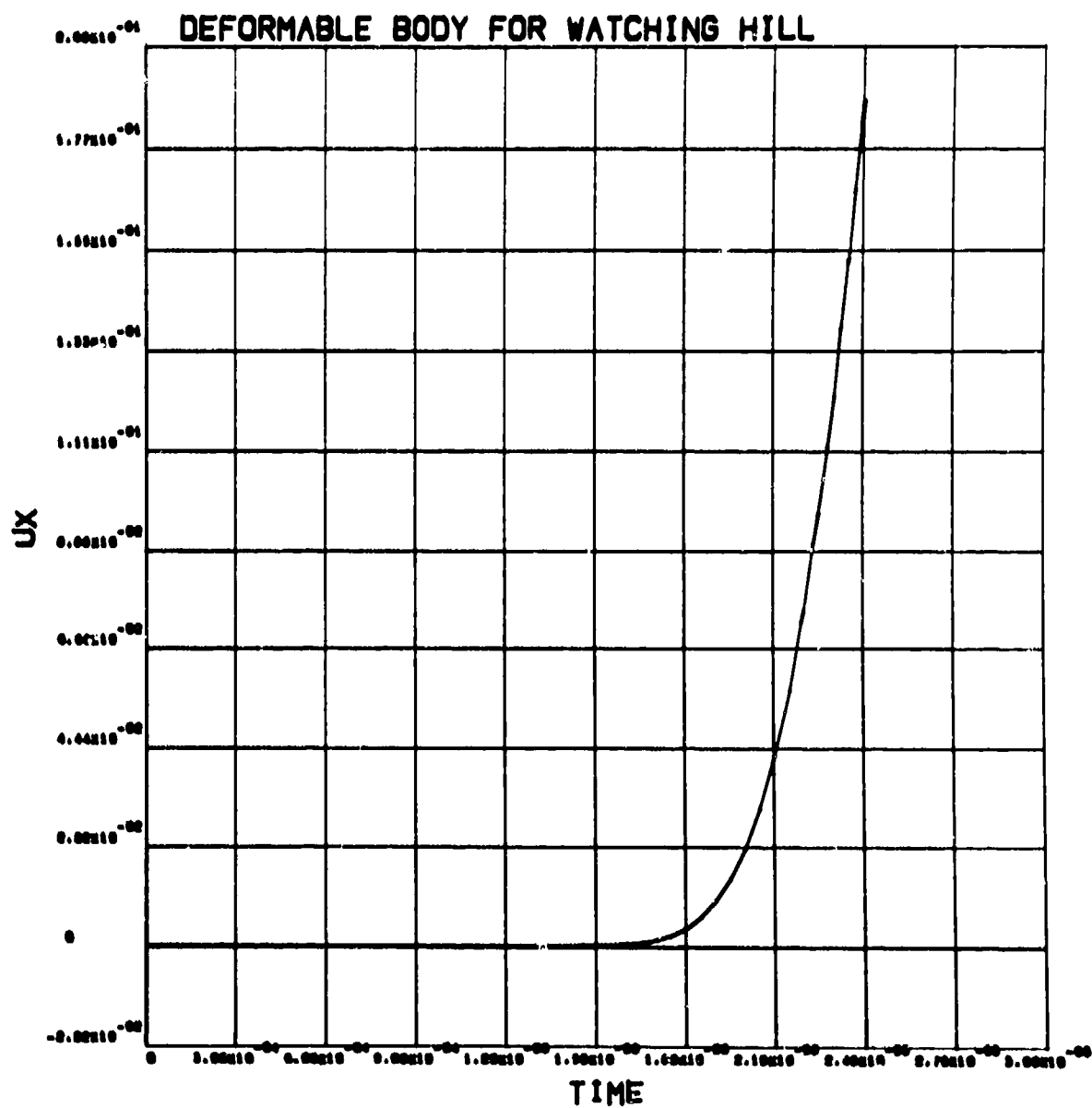
Figure B-89

Radial velocity history (m/s) in soil at range 0.28 m, depth 0.4 m (deformable penetrator).
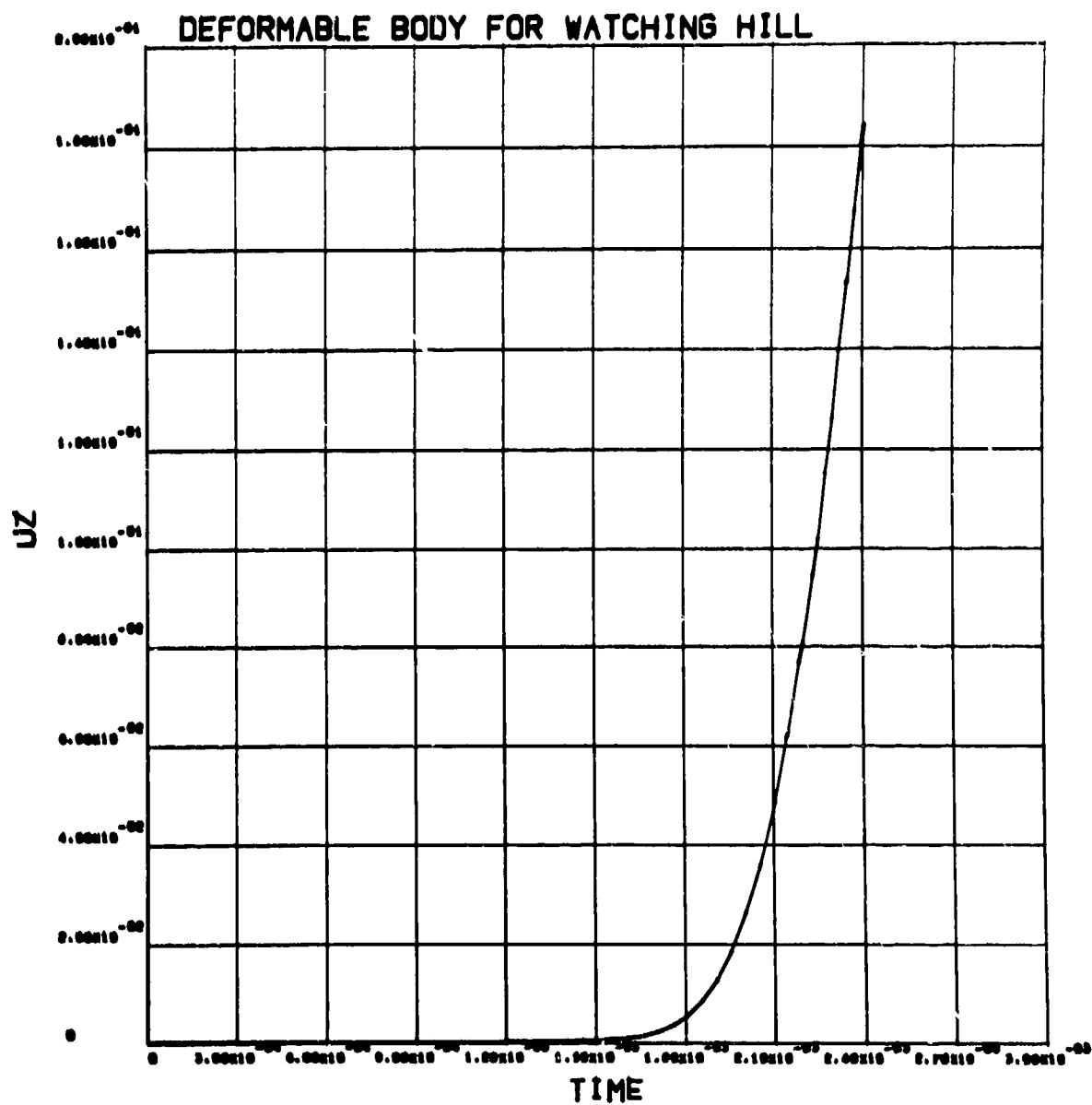
Figure B-90

Vertical velocity history (m/s) in soil at range 0.28 m, depth 0.4 m (deformable penetrator).

334
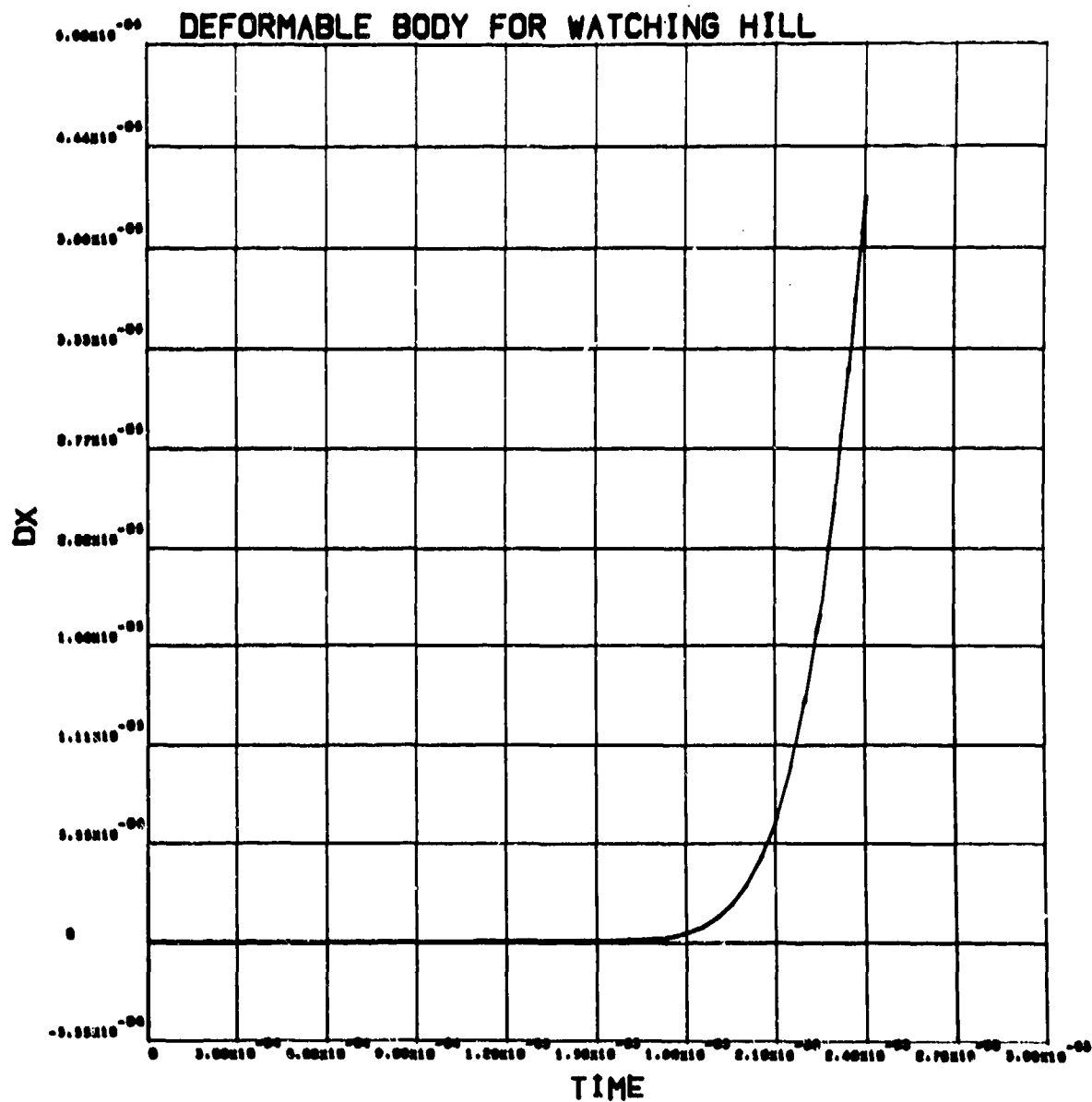
Figure B-91

Radial displacement history (m) in soil at range 0.28 m, depth 0.4 m (deformable penetrator).
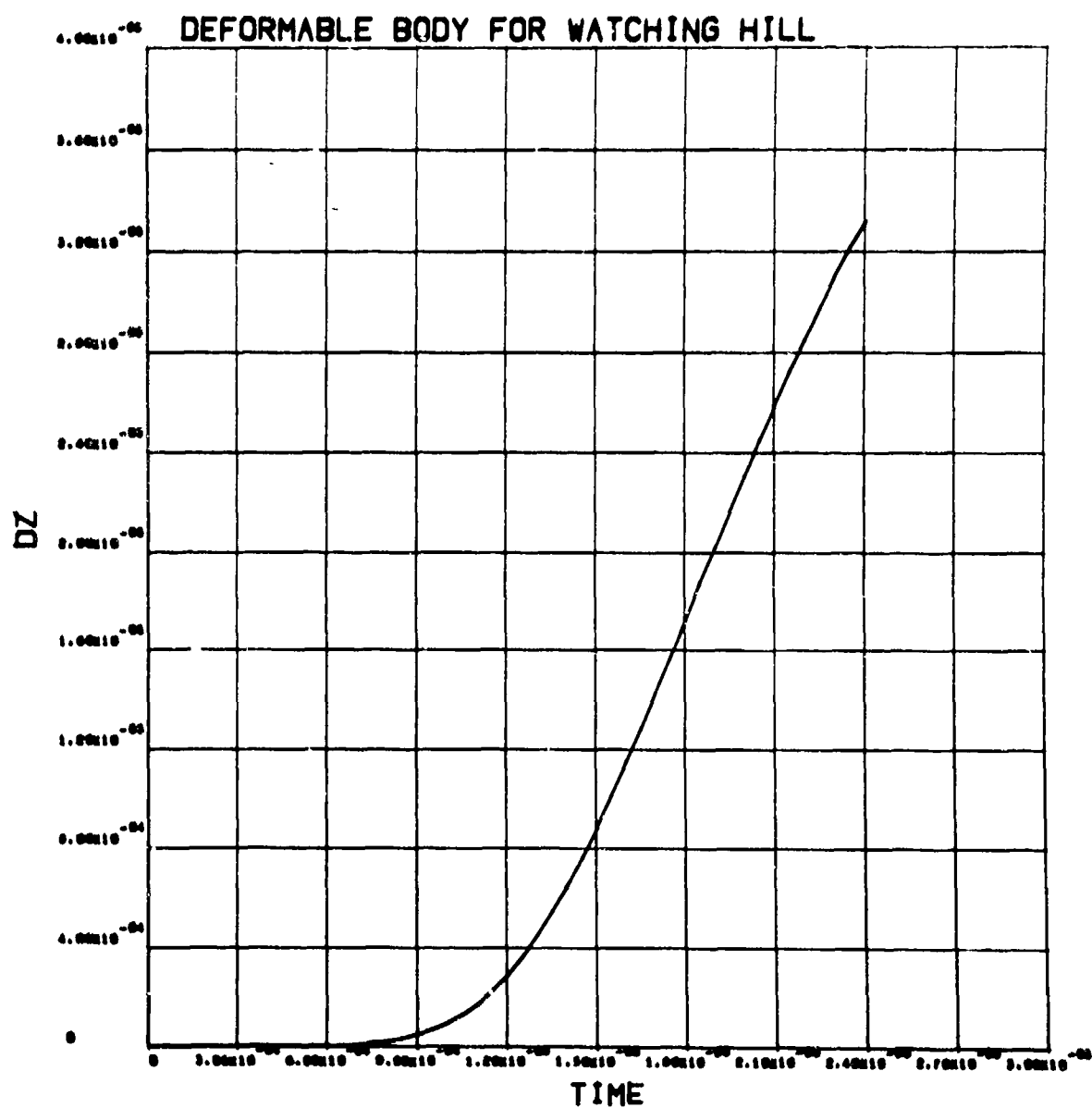
Figure B-92

Vertical displacement history (m) in soil at range 0.28 m, depth 0.4 m (deformable penetrator).
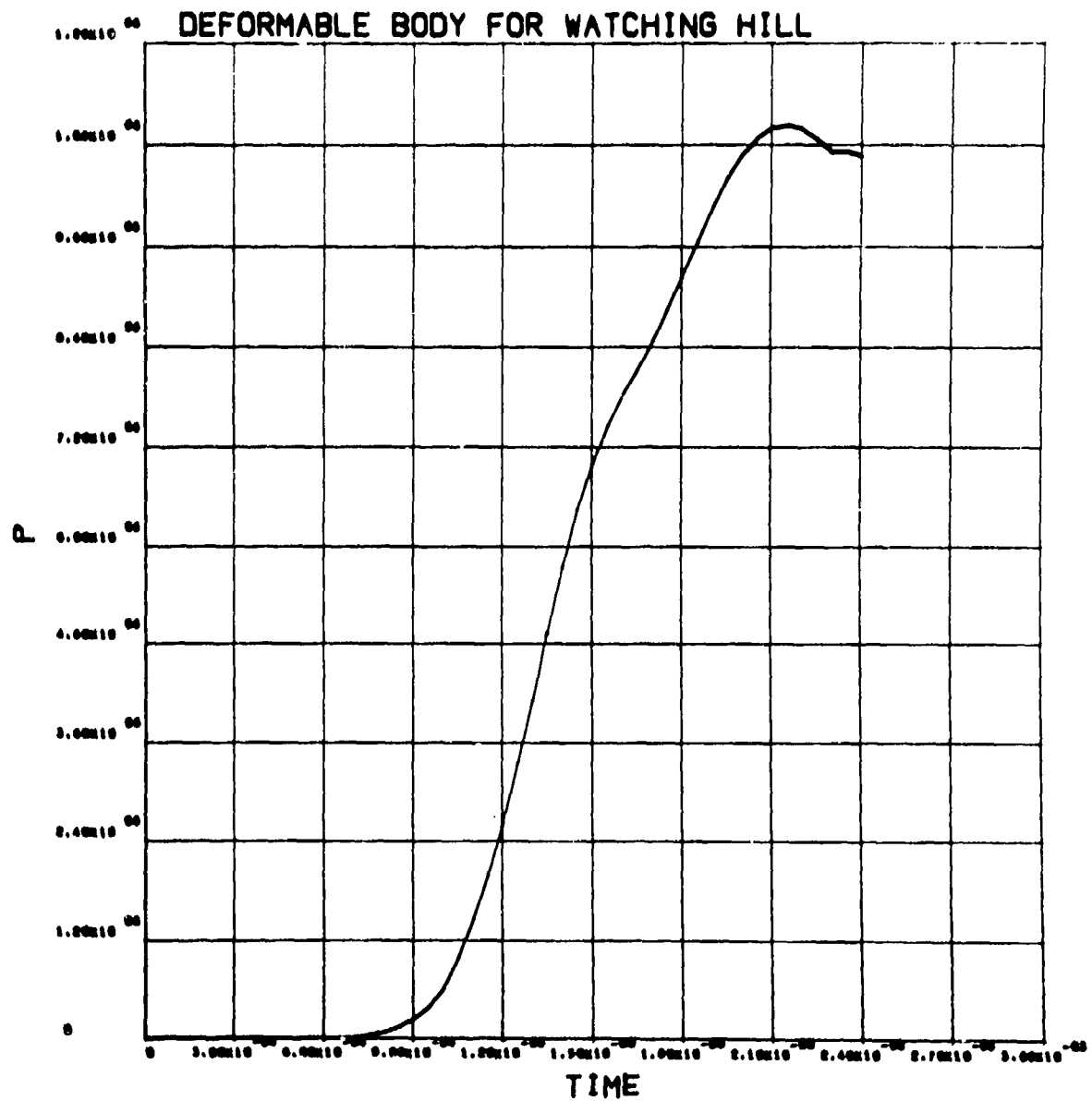
Figure B-93

Pressure history (Pa) in soil at range 0.28 m, depth 0.4 m (deformable penetrator).
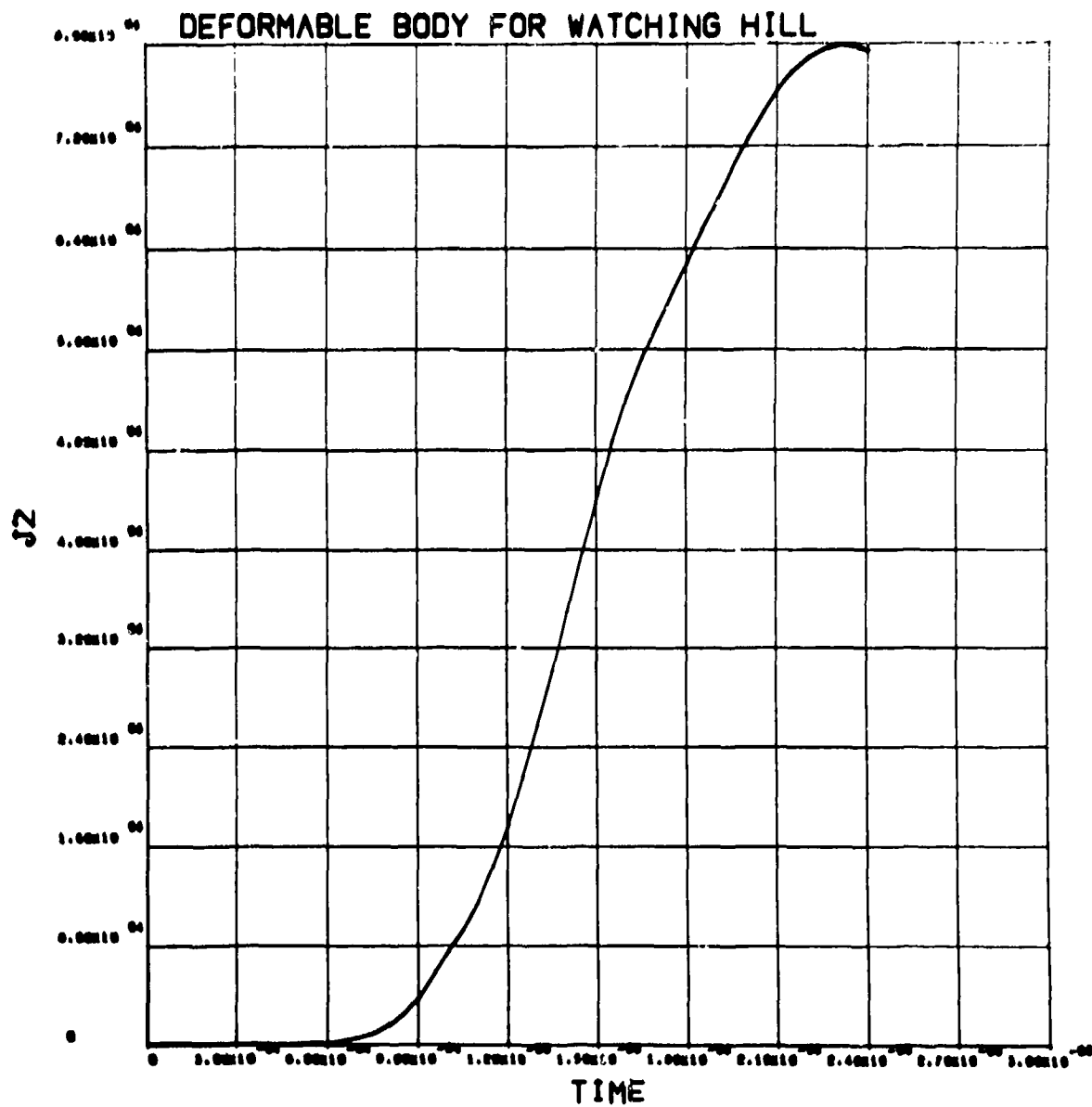
Figure B-94

Deviator stress, J2, history (Pa) in soil at range 0.28 m, depth 0.4 m (deformable penetrator).
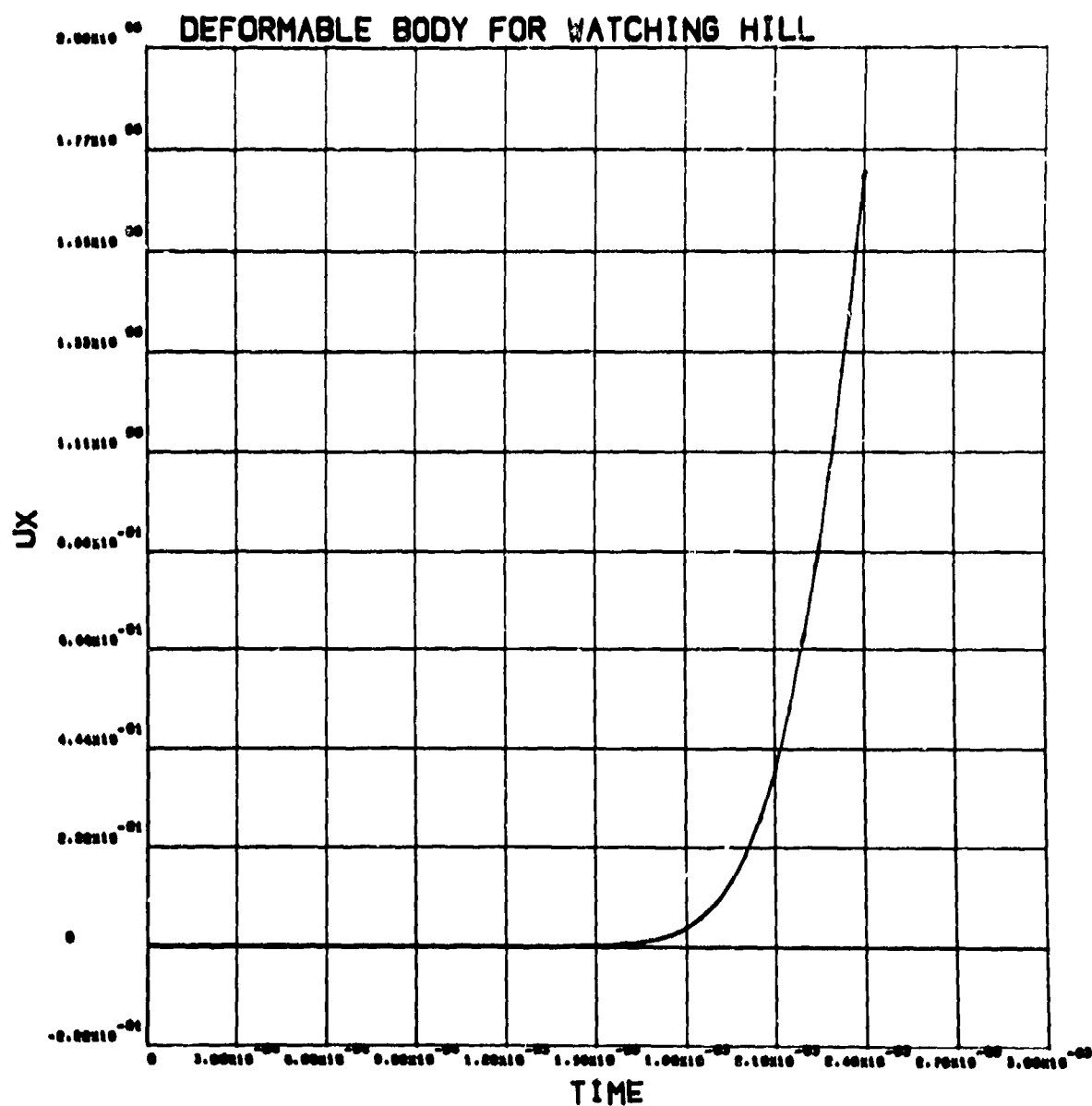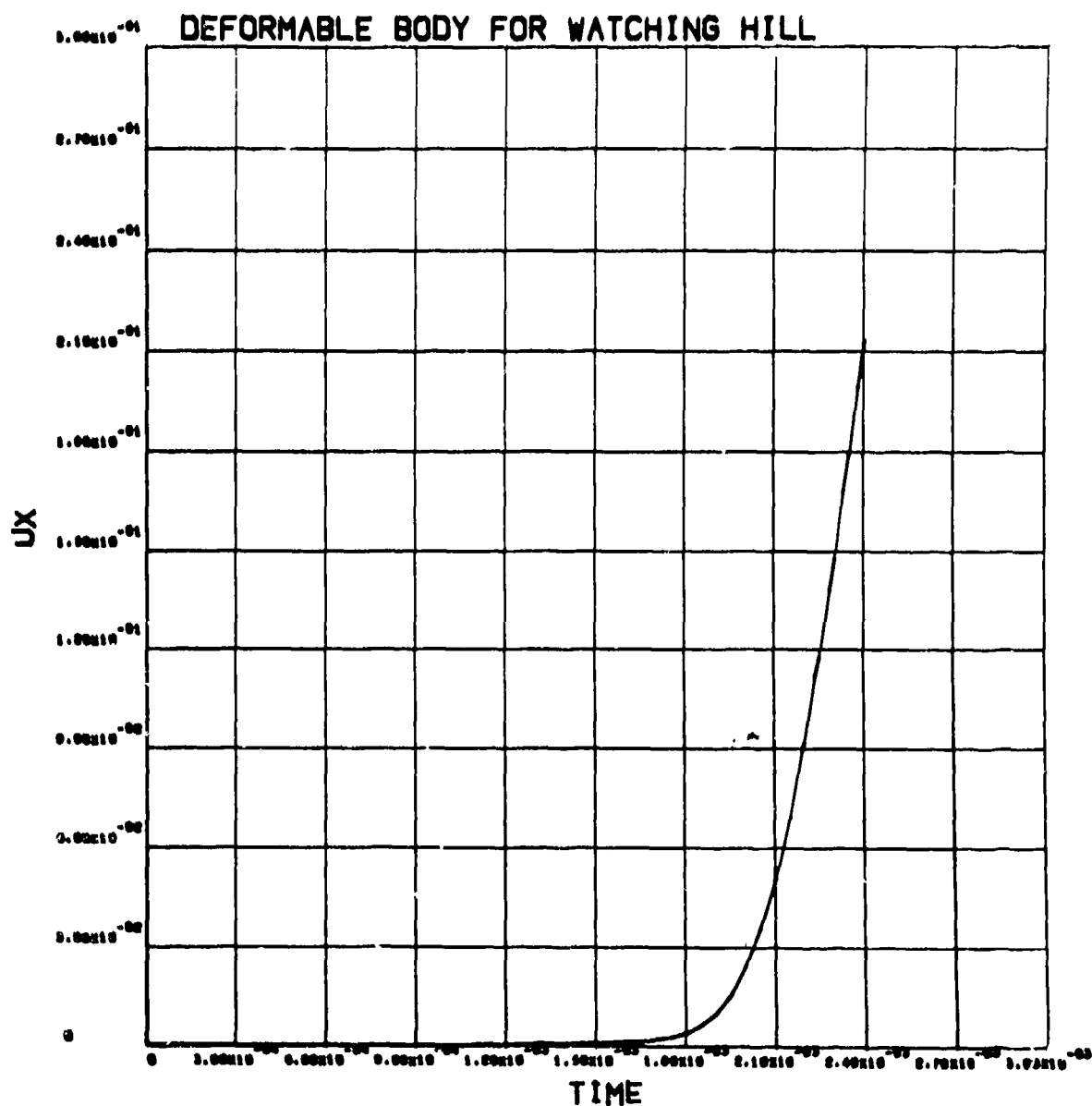
Figure B-95

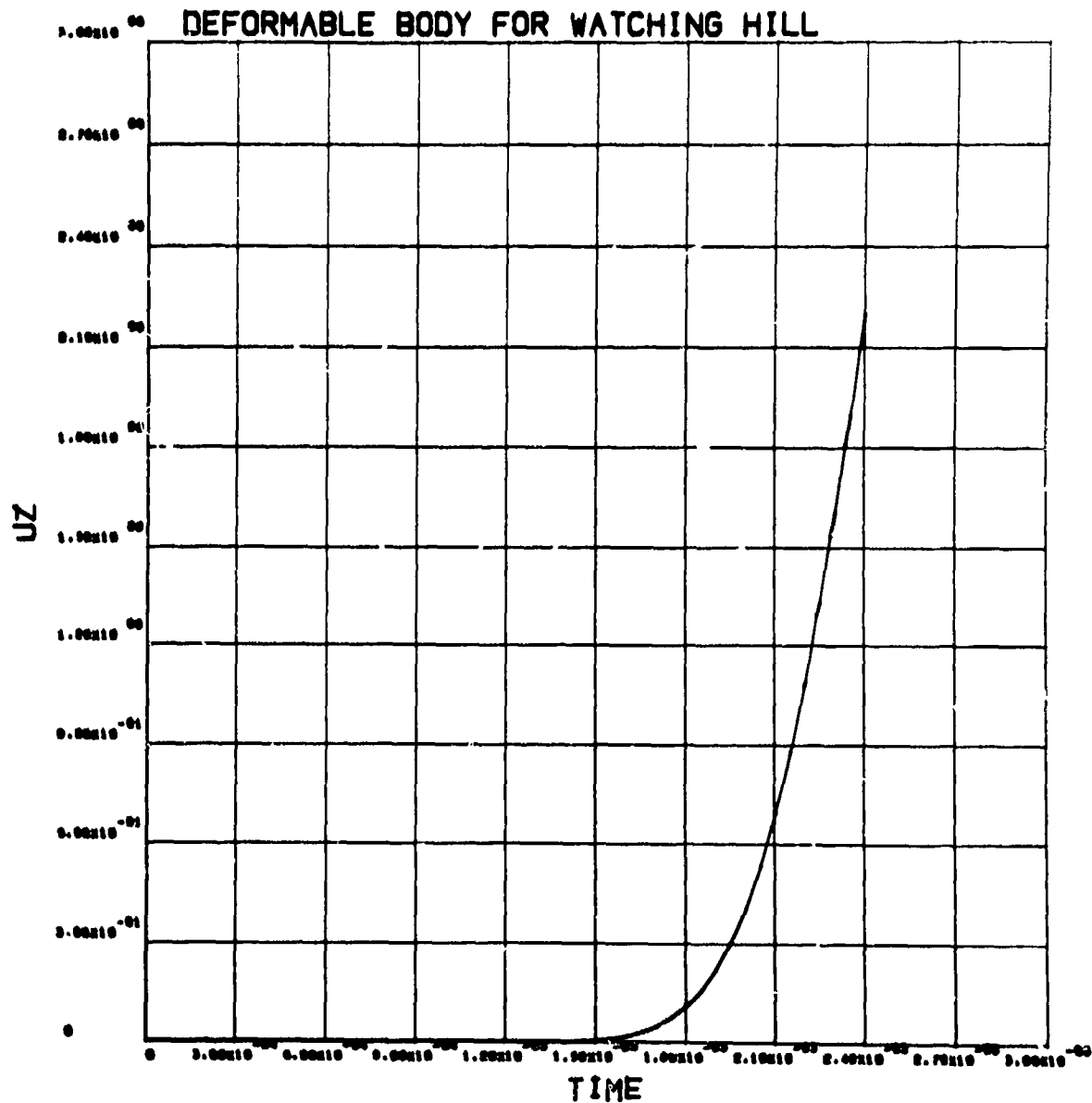Radial velocity history (m/s) in soil at range 0.44 m, depth 0.1 m (deformable penetrator).
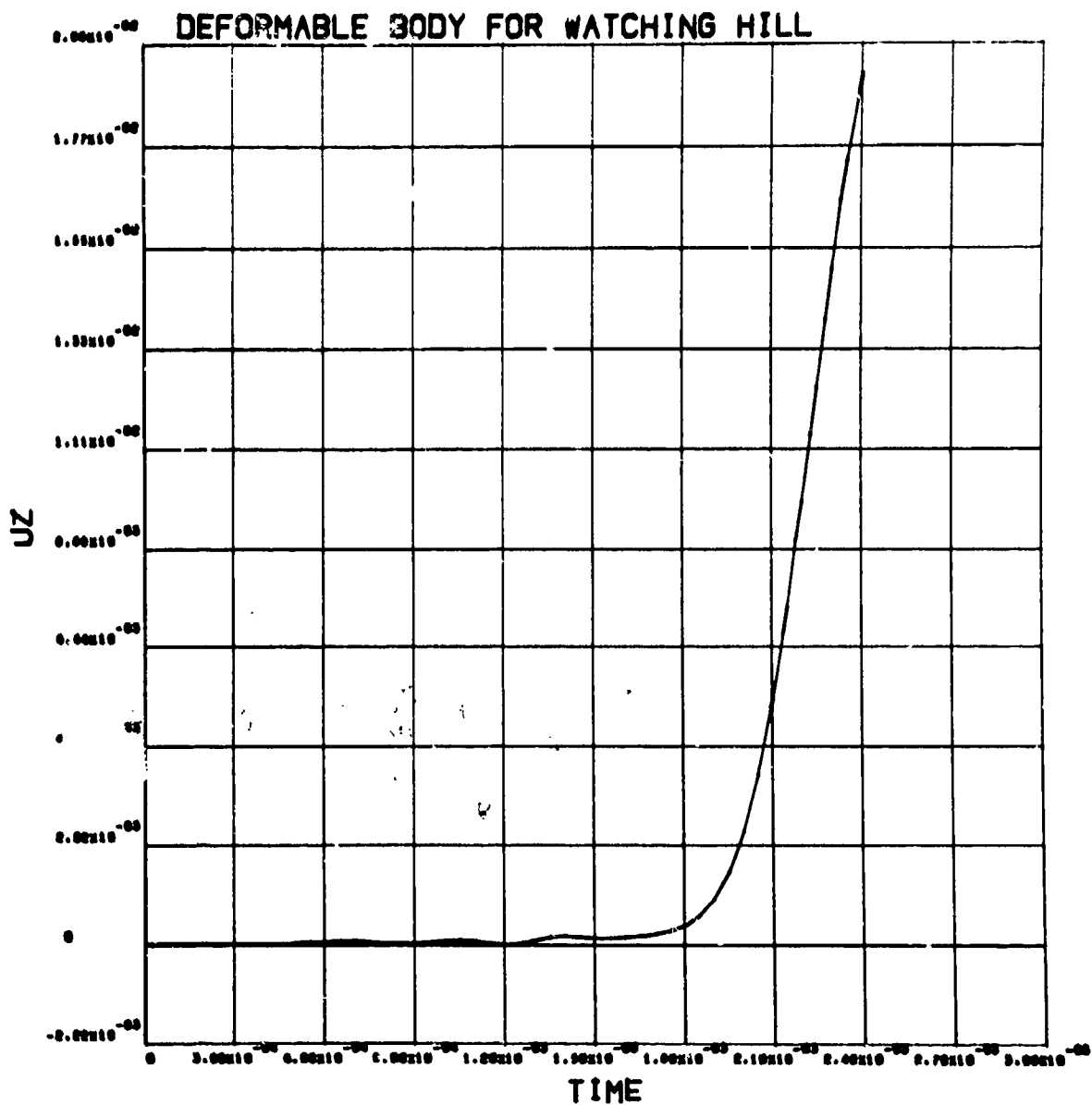
Figure B-96

Vertical velocity history (m/s) in soil at range 0.44 m, depth 0.1 m (deformable penetrator).
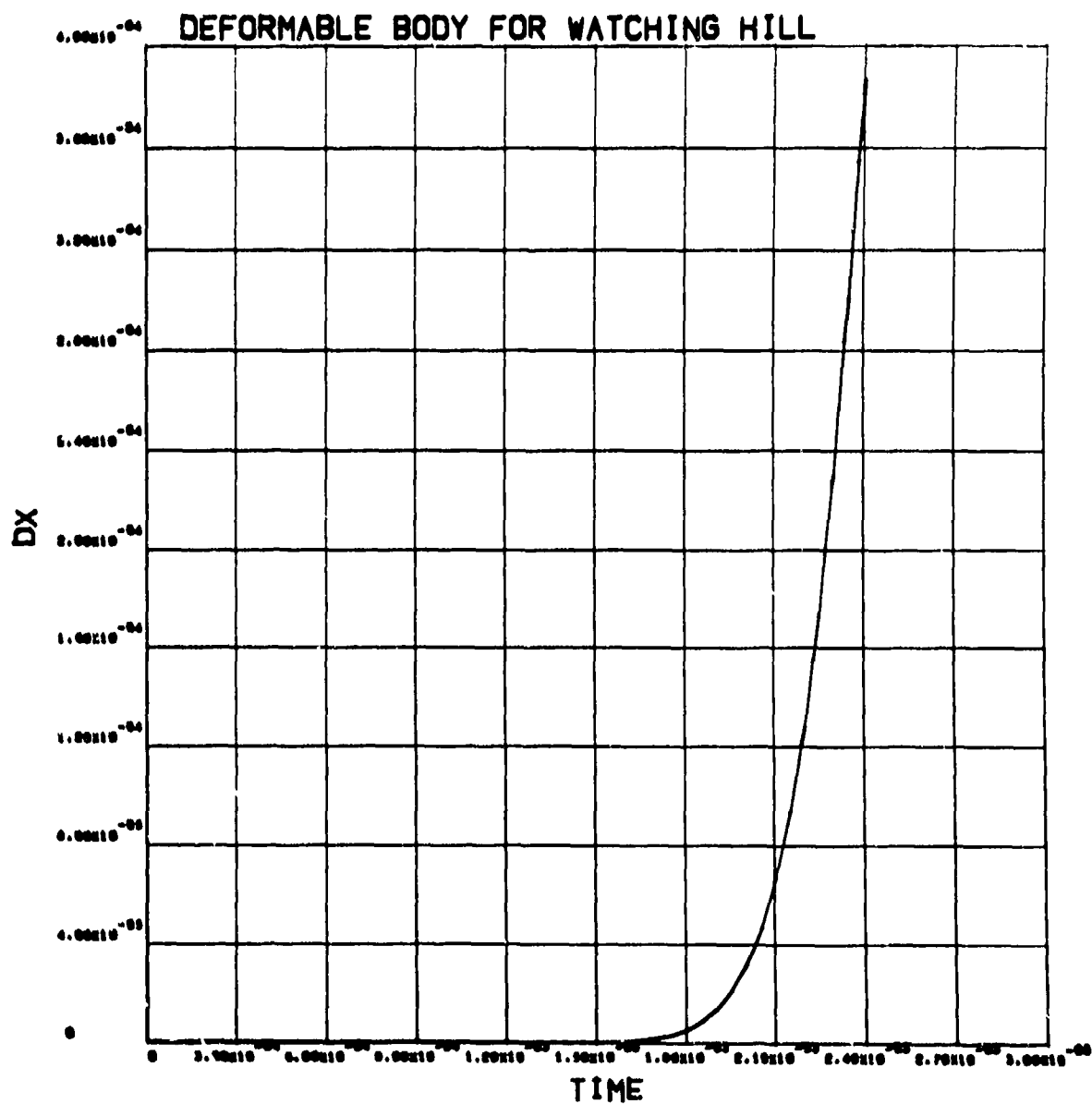
340

Figure B-97

Radial displacement history (m) in soil at range 0.44 m, depth 0.1 m (deformable penetrator).
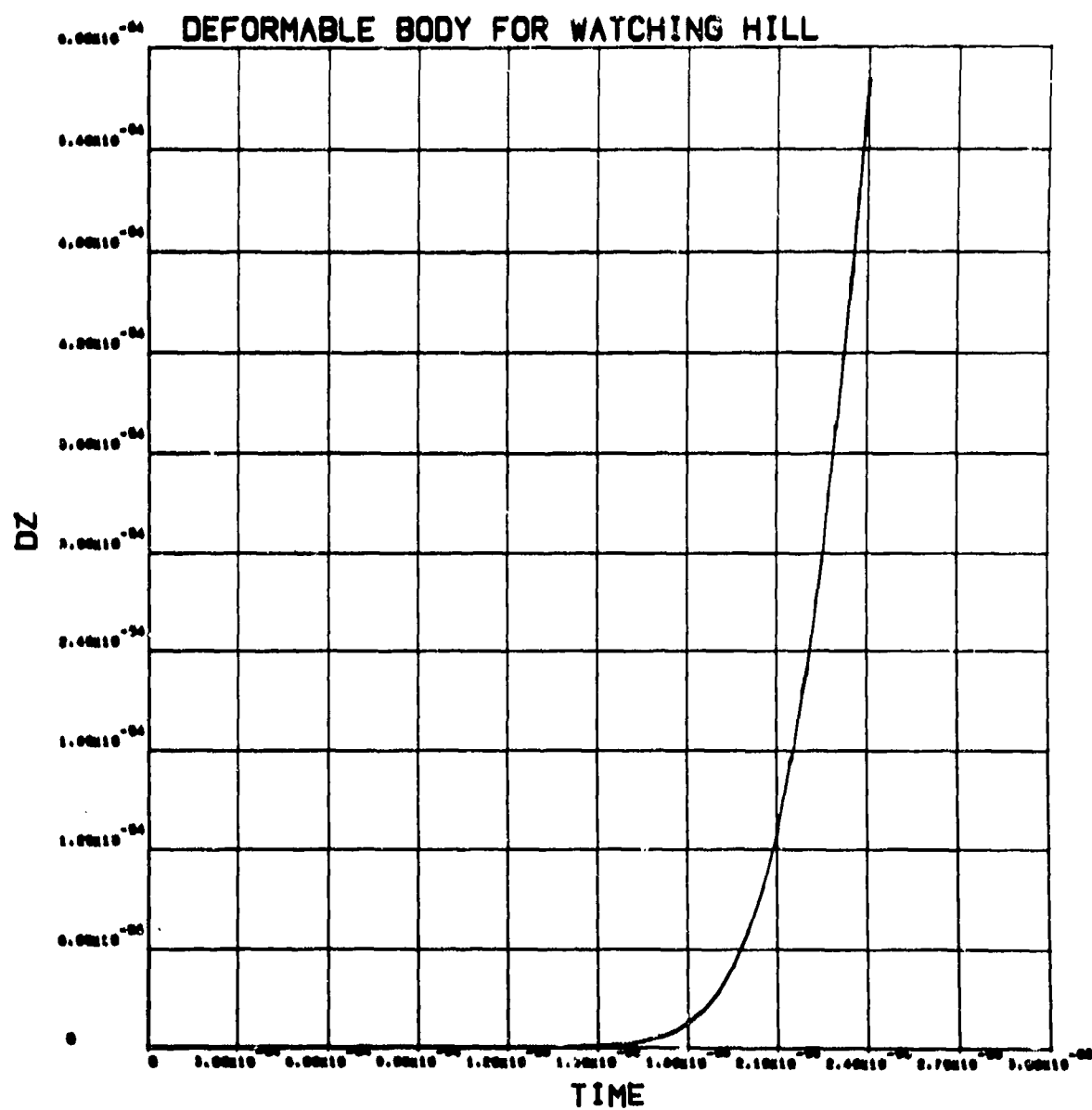
Figure B-98

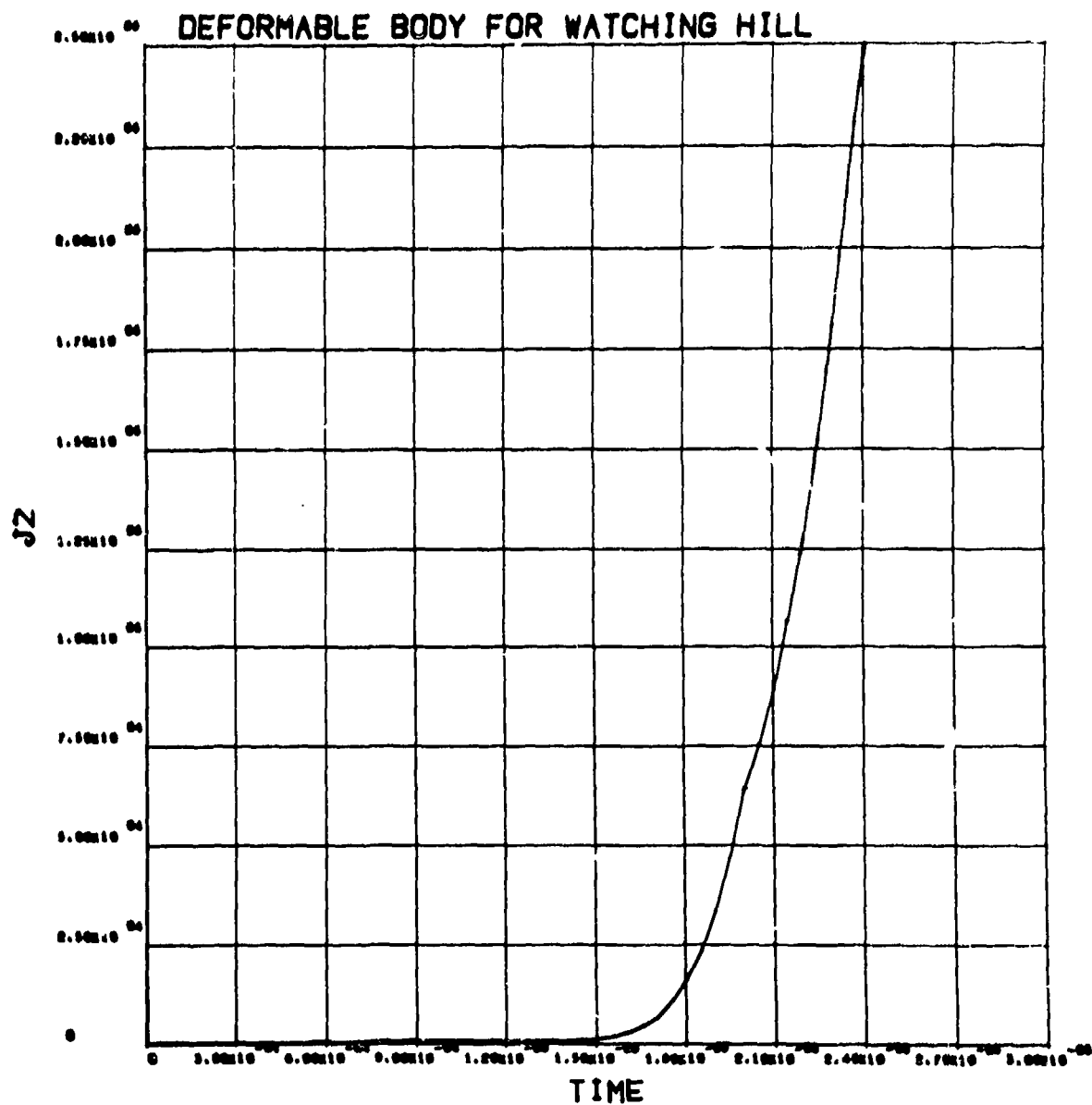Vertical displacement history (m) in soil at range 0.44 m, depth 0.1 m (deformable penetrator).
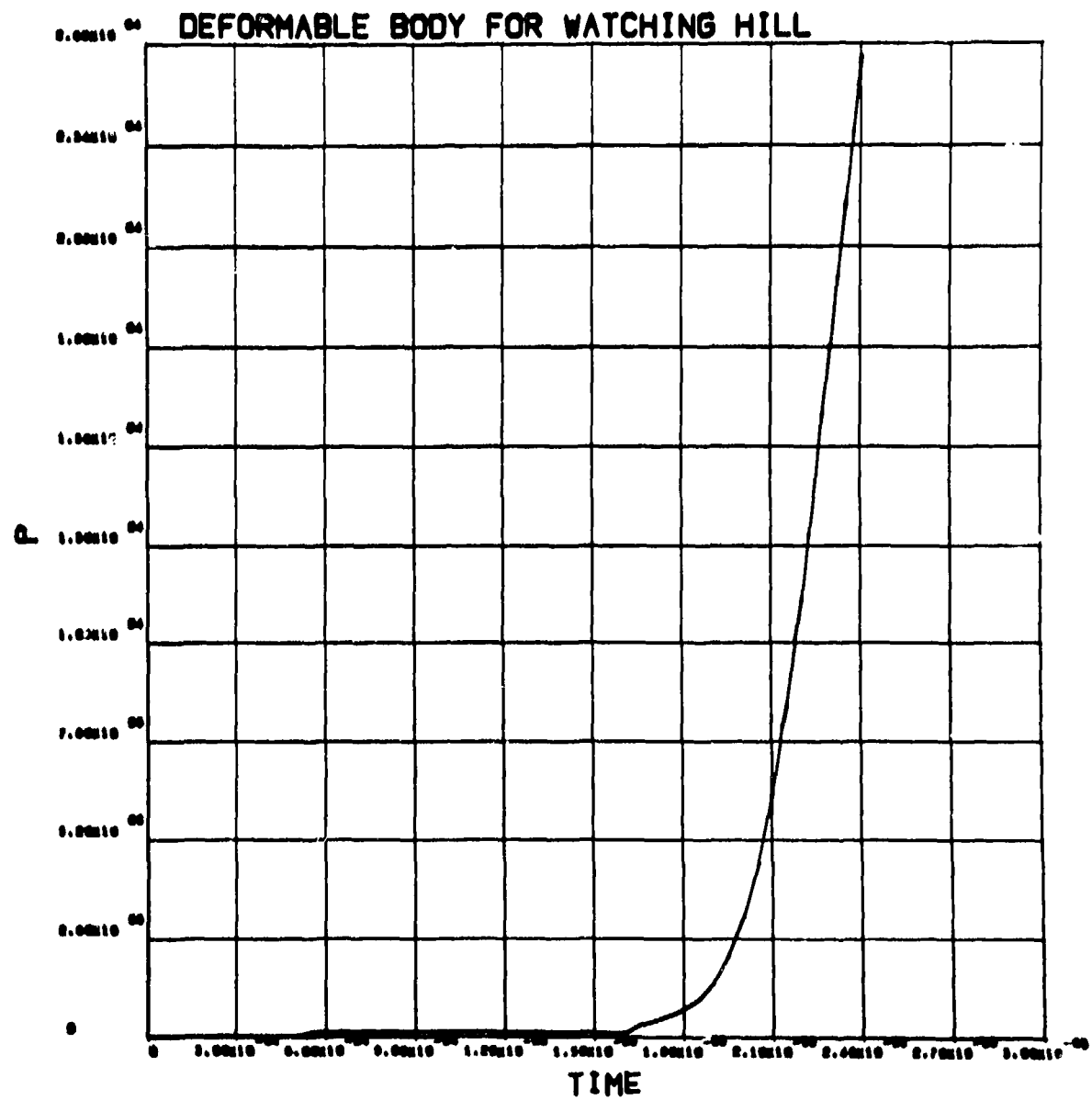
Figure B-99

Pressure history (Pa) in soil at range 0.44 m, depth 0.1 m (deformable penetrator).
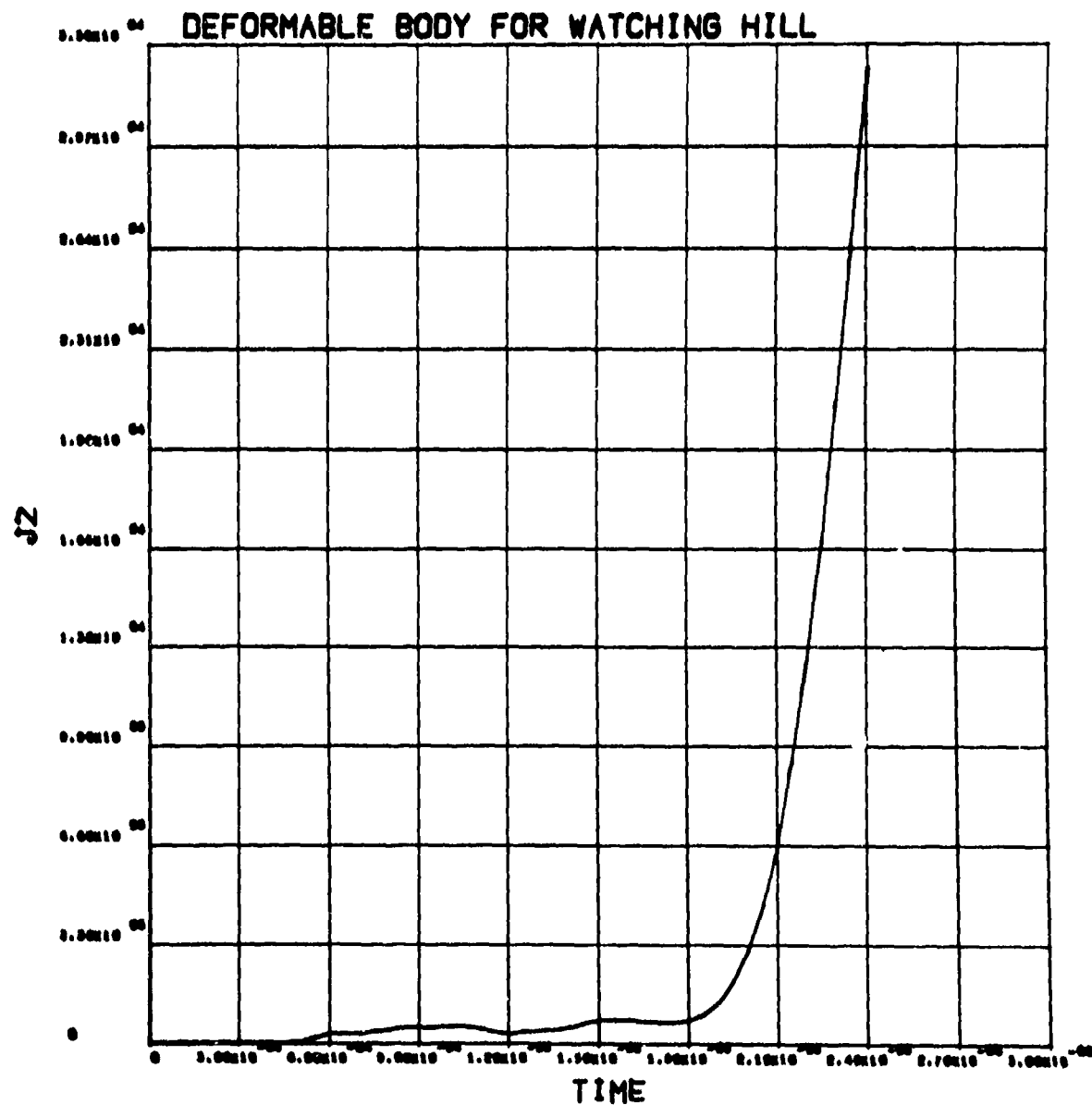
Figure B-100

Deviator stress, J2, history (Pa) in soil at range 0.44 m, depth 0.1 m (deformable penetrator).
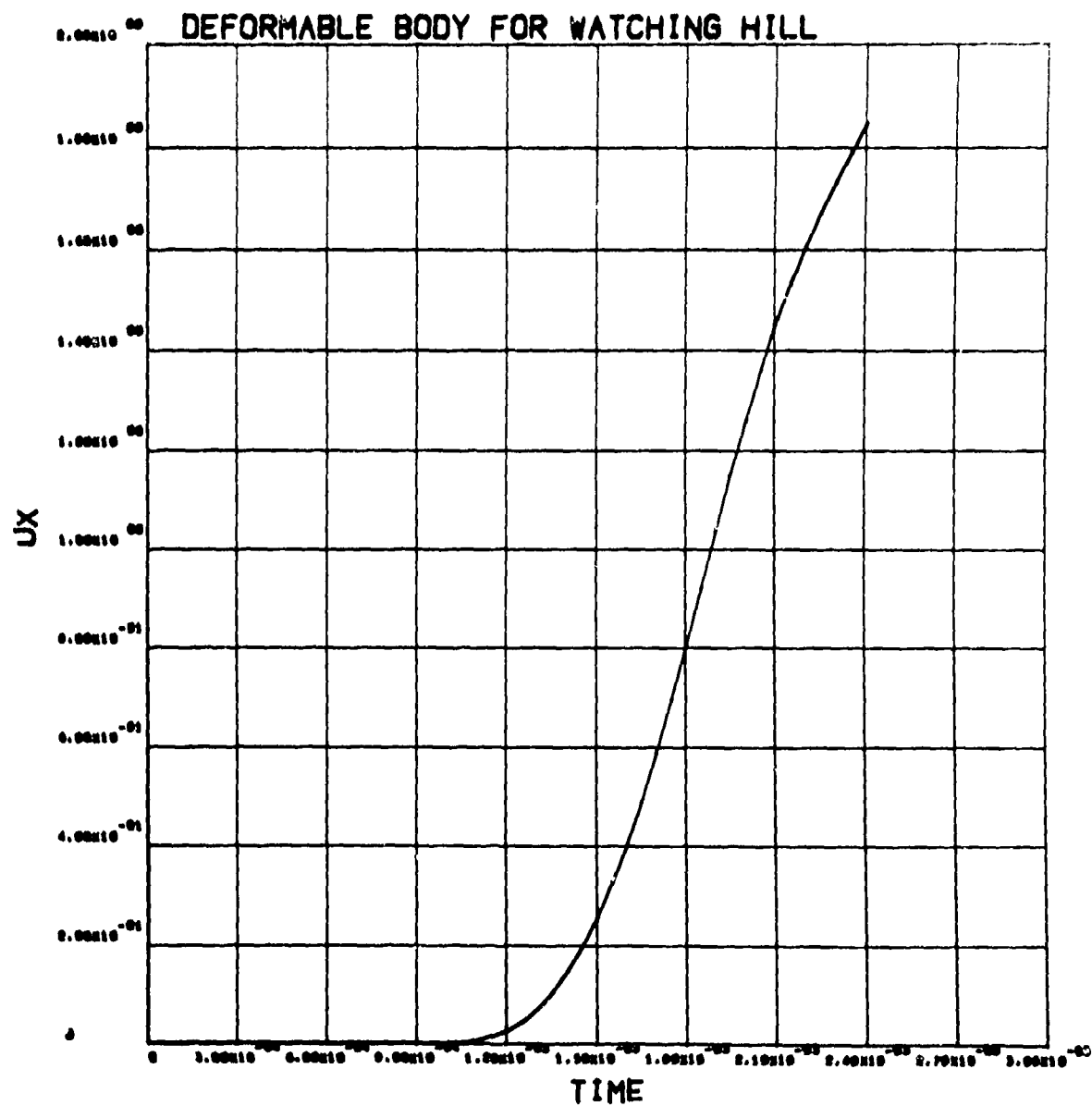
344
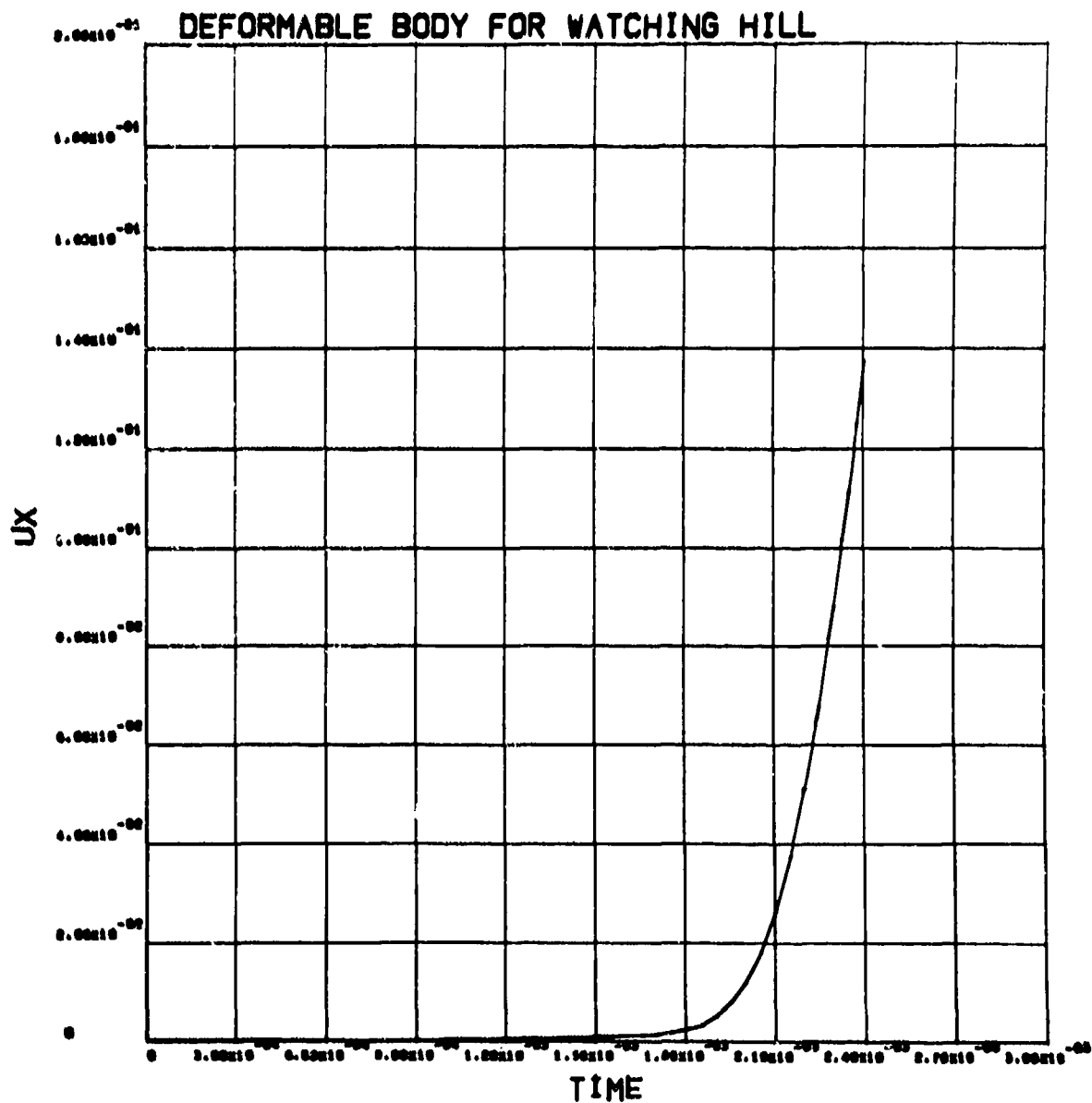
Figure B-101

Radial velocity history (m/s) in soil at range 0.44 m, depth 0.2 m (deformable penetrator).
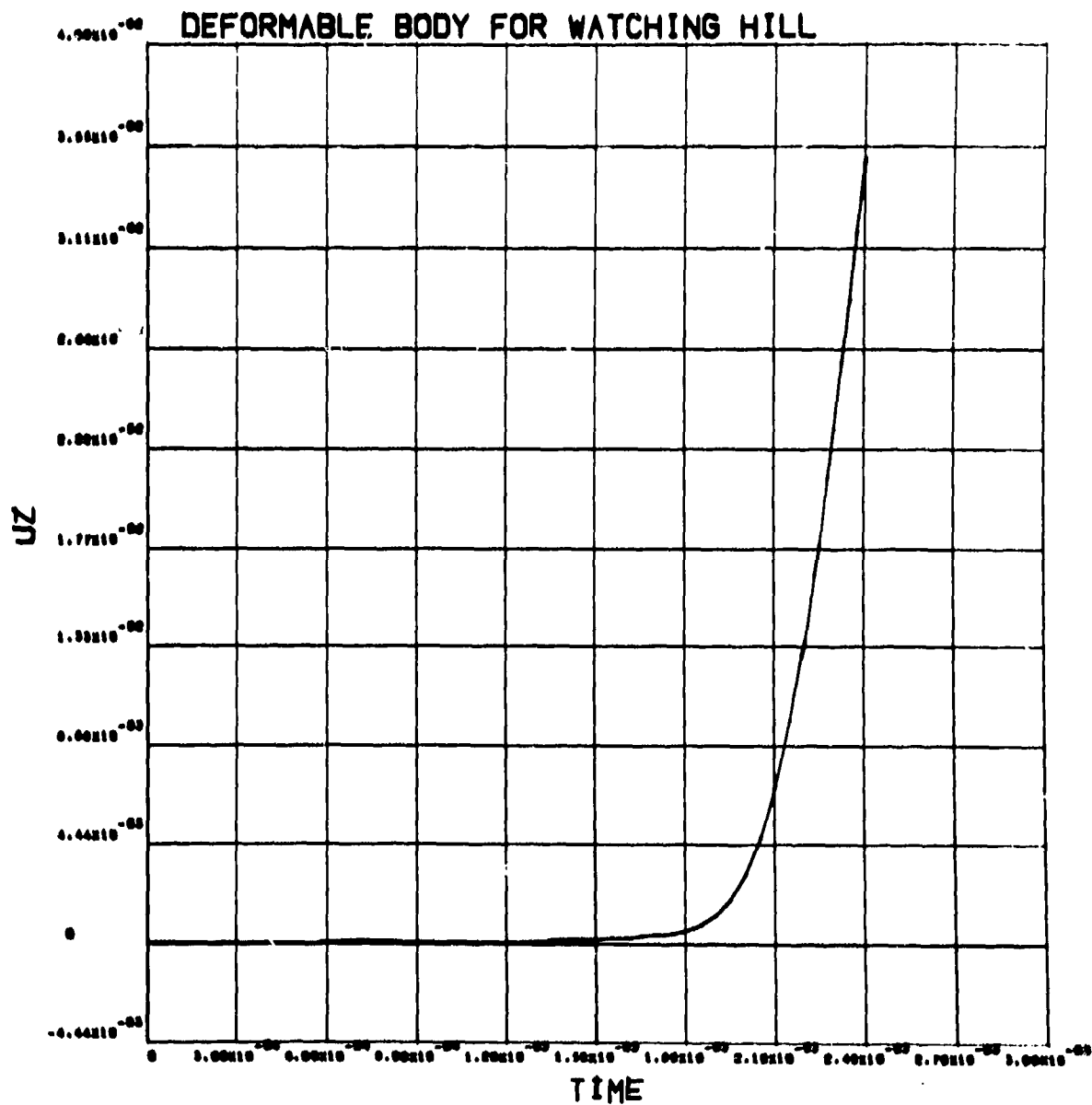
Figure B-102

Vertical velocity history (m/s) in soil at range 0.44 m, depth 0.2 m (deformable penetrator).

346
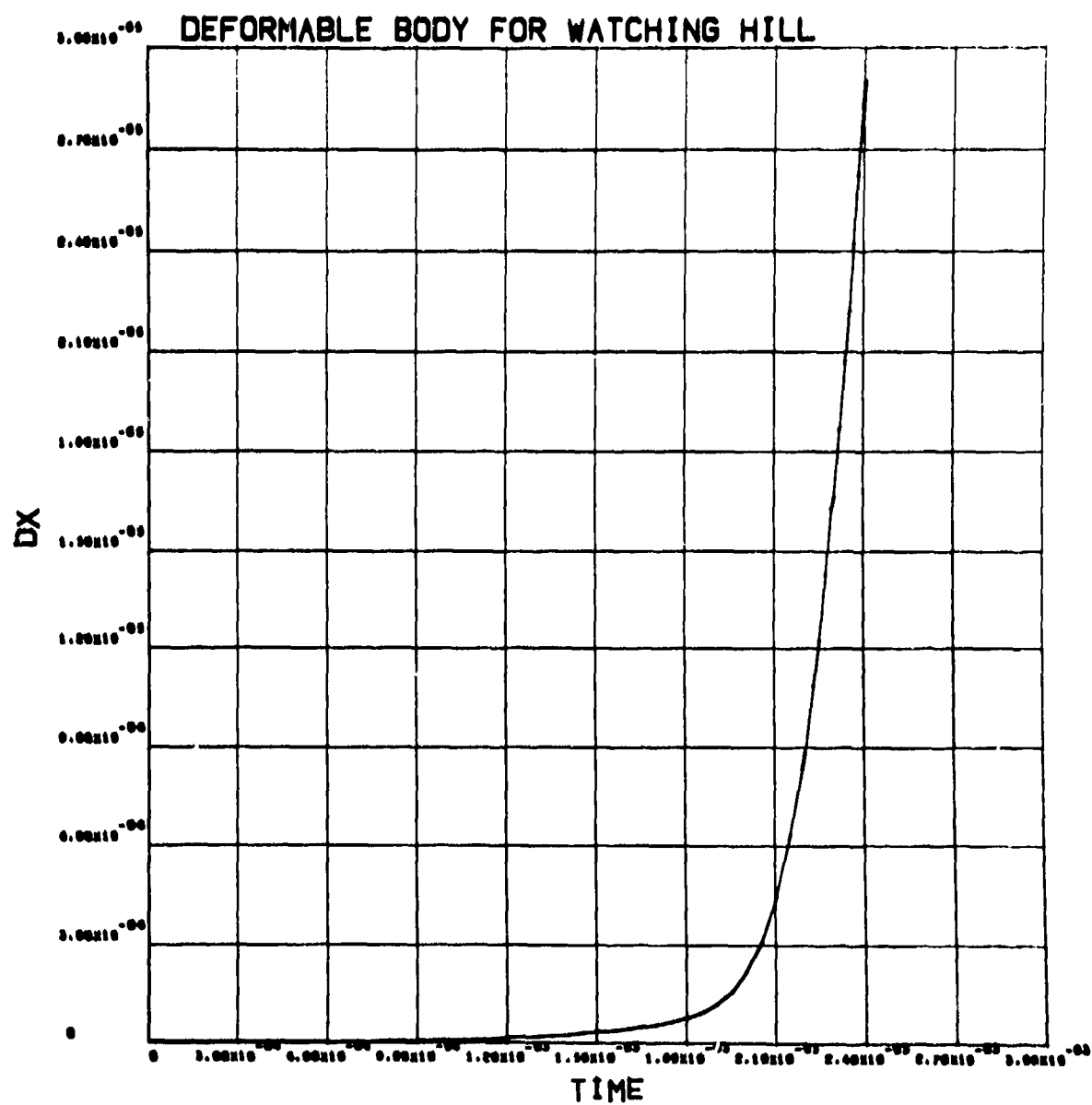
Figure B-103

Radial displacement history (m) in soil at range 0.44 m, depth 0.2 m (deformable penetrator).
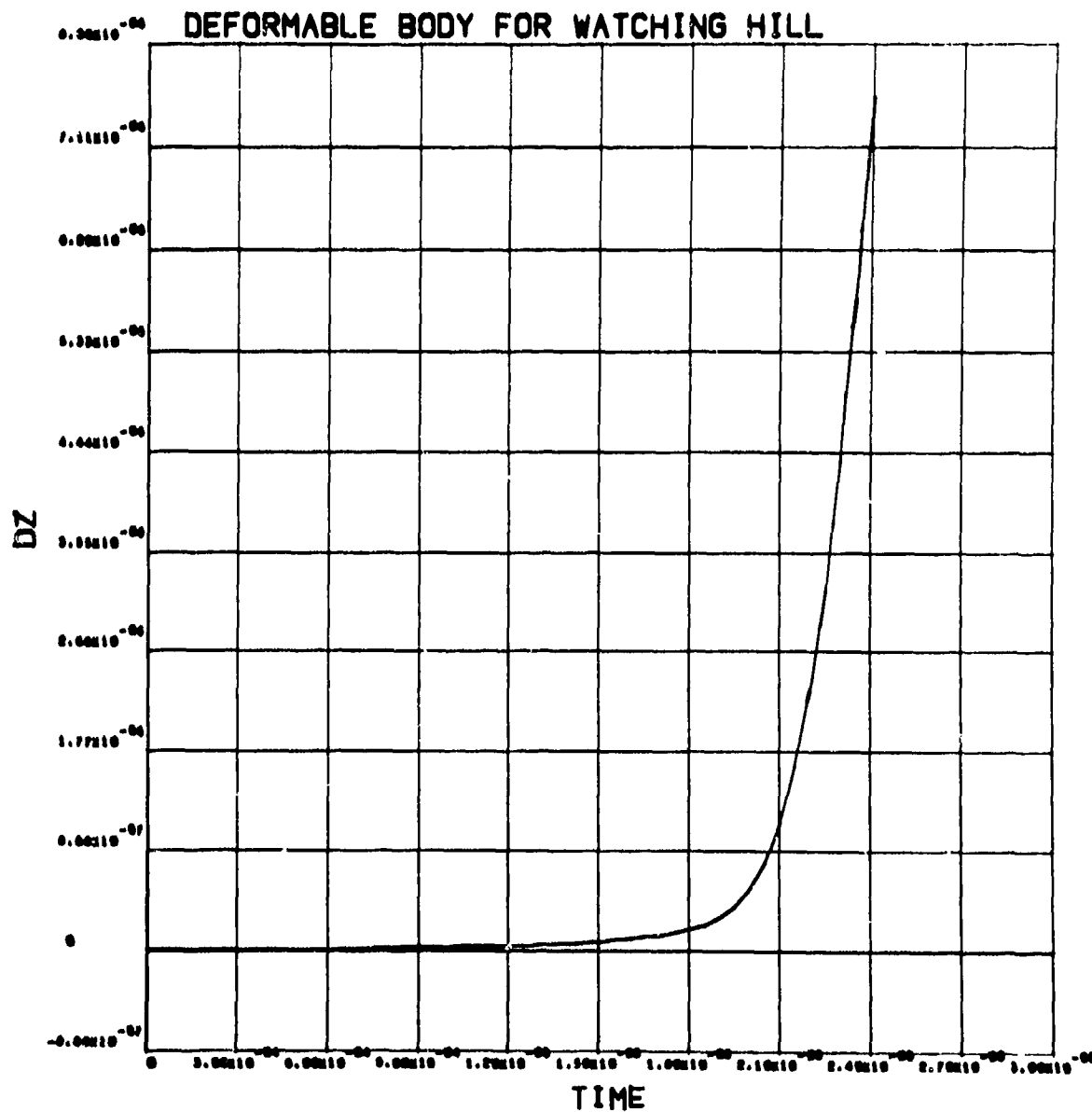
Figure B-104

Vertical displacement history (m) in soil at range 0.44 m, depth 0.2 m (deformable penetrator).
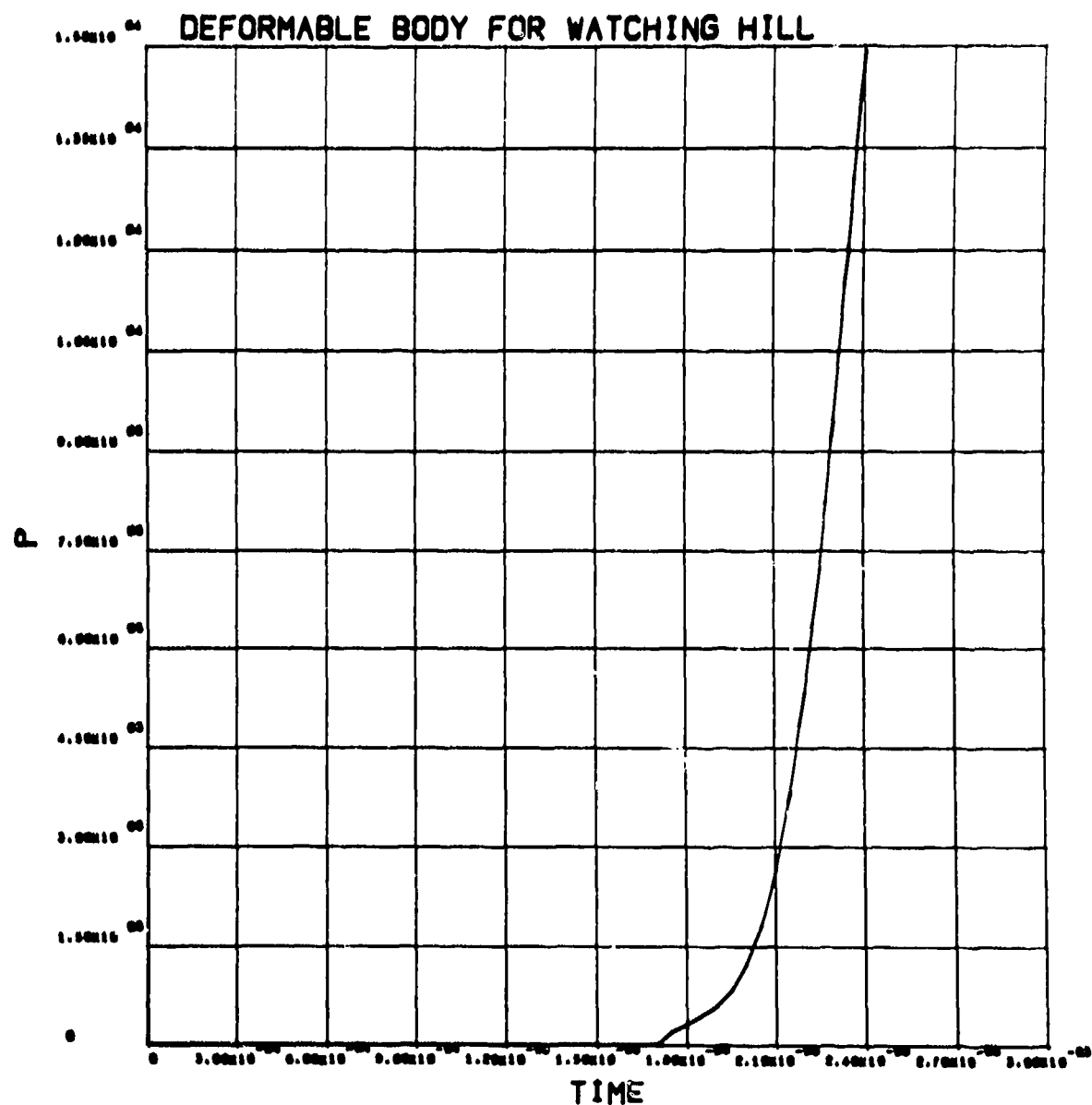
Figure B-105

Pressure history (Pa) in soil at range 0.44 m, depth 0.2 m (deformable penetrator).
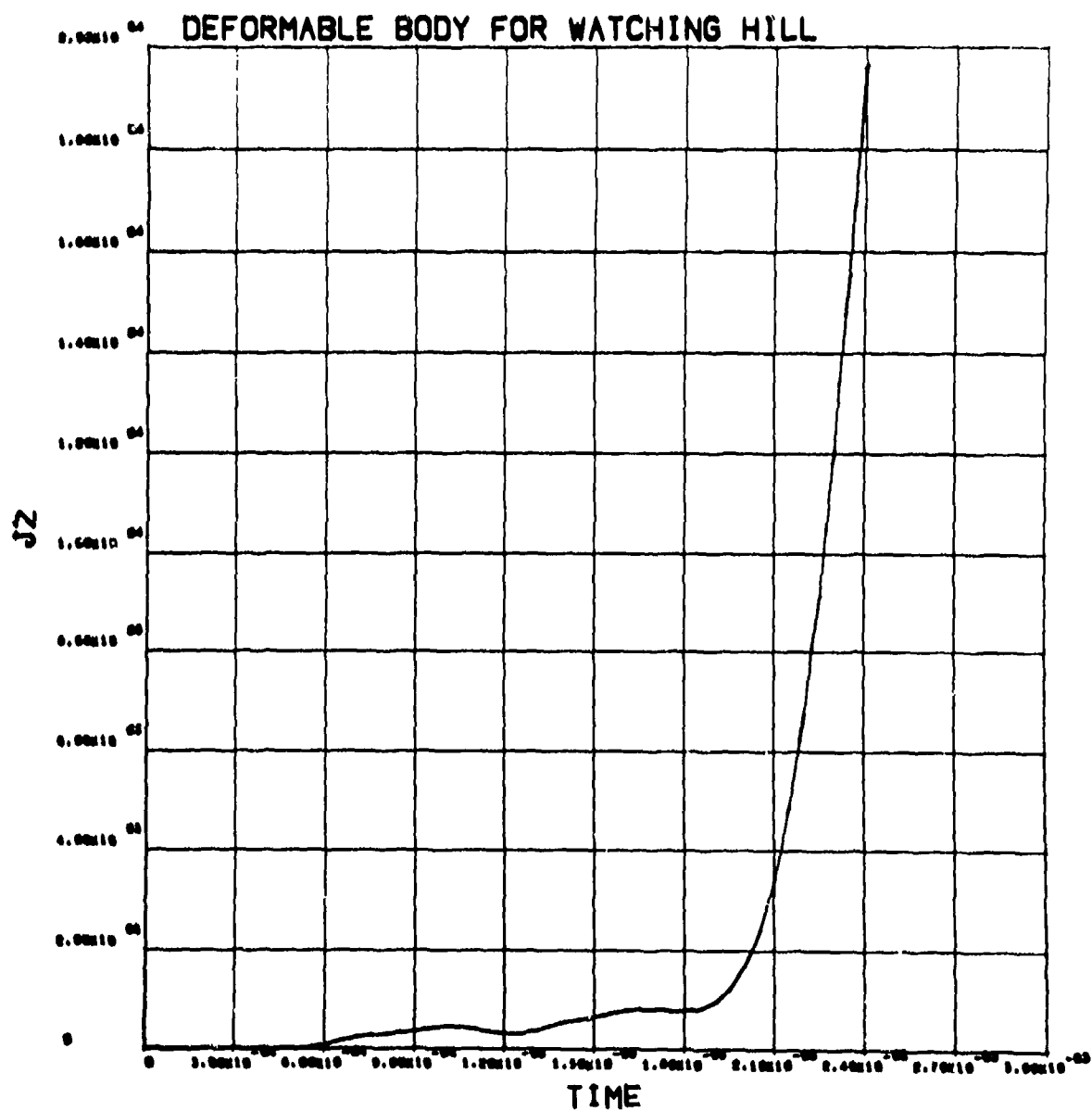
Figure B-106

Deviator stress, J2, history (Pa) in soil at range 0.44 m, depth 0.1 m (deformable penetrator).
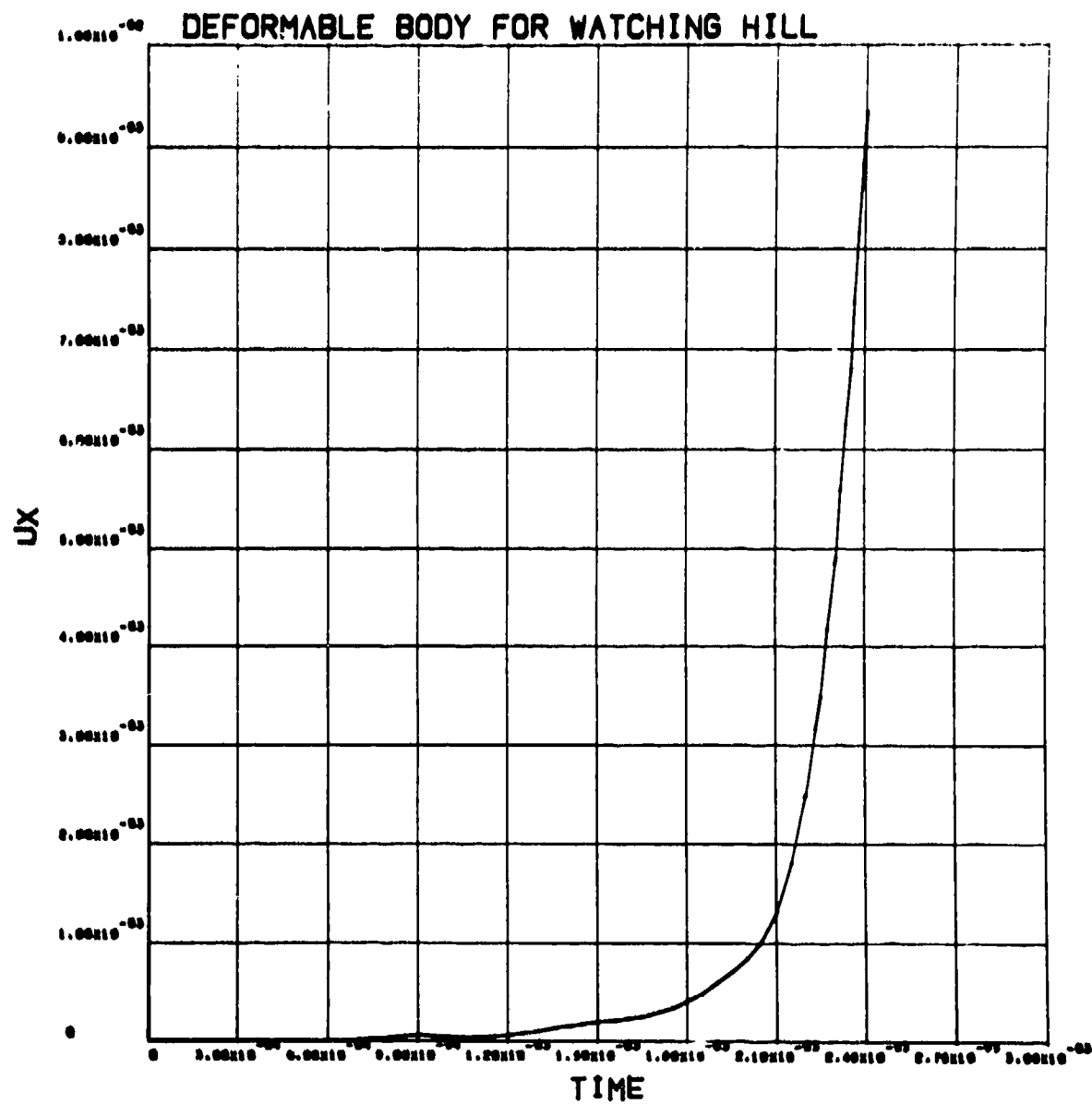
Figure B-107

Radial velocity history (m/s) in soil at range 0.44 m, depth 0.4 m (deformable penetrator).
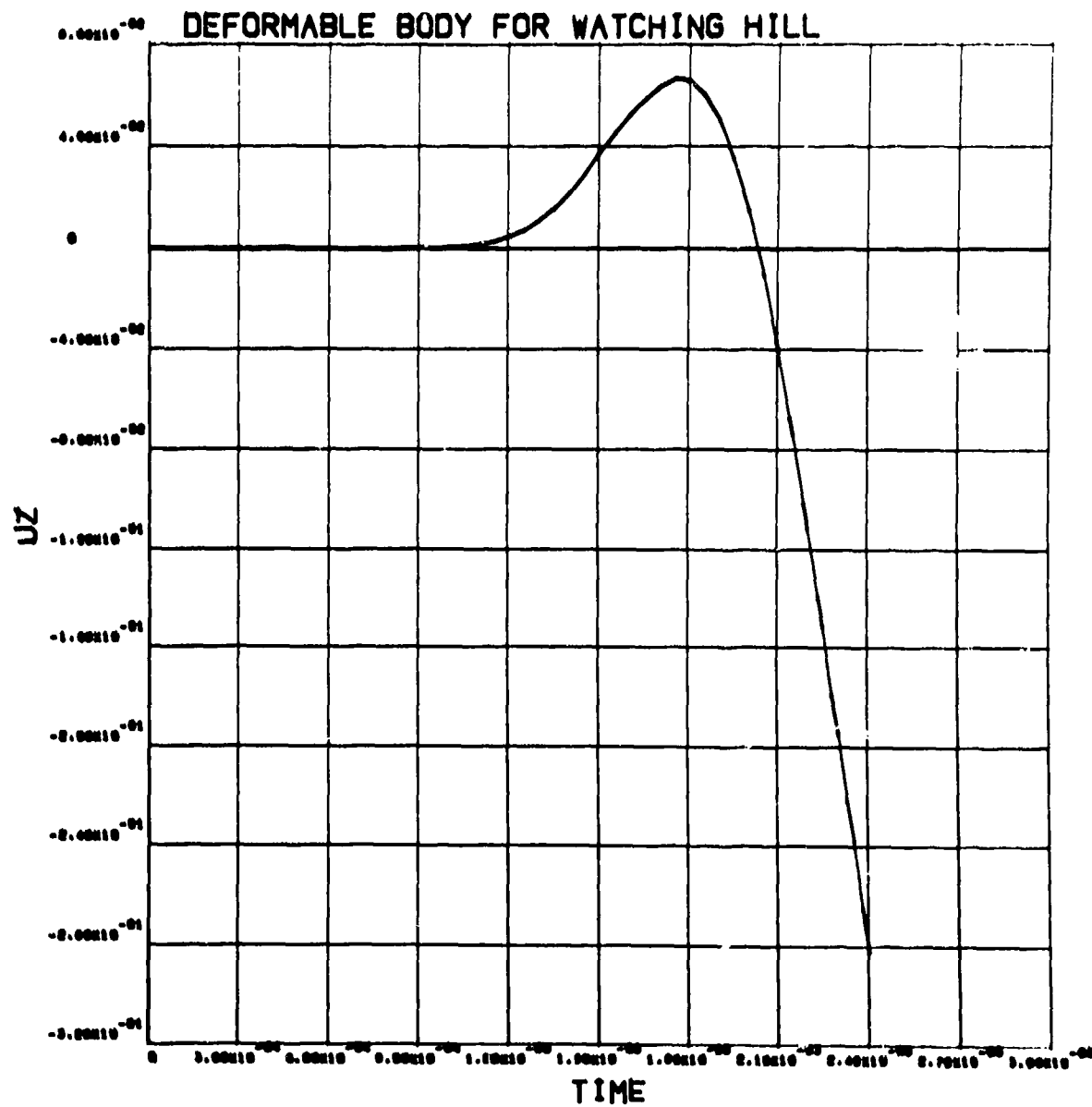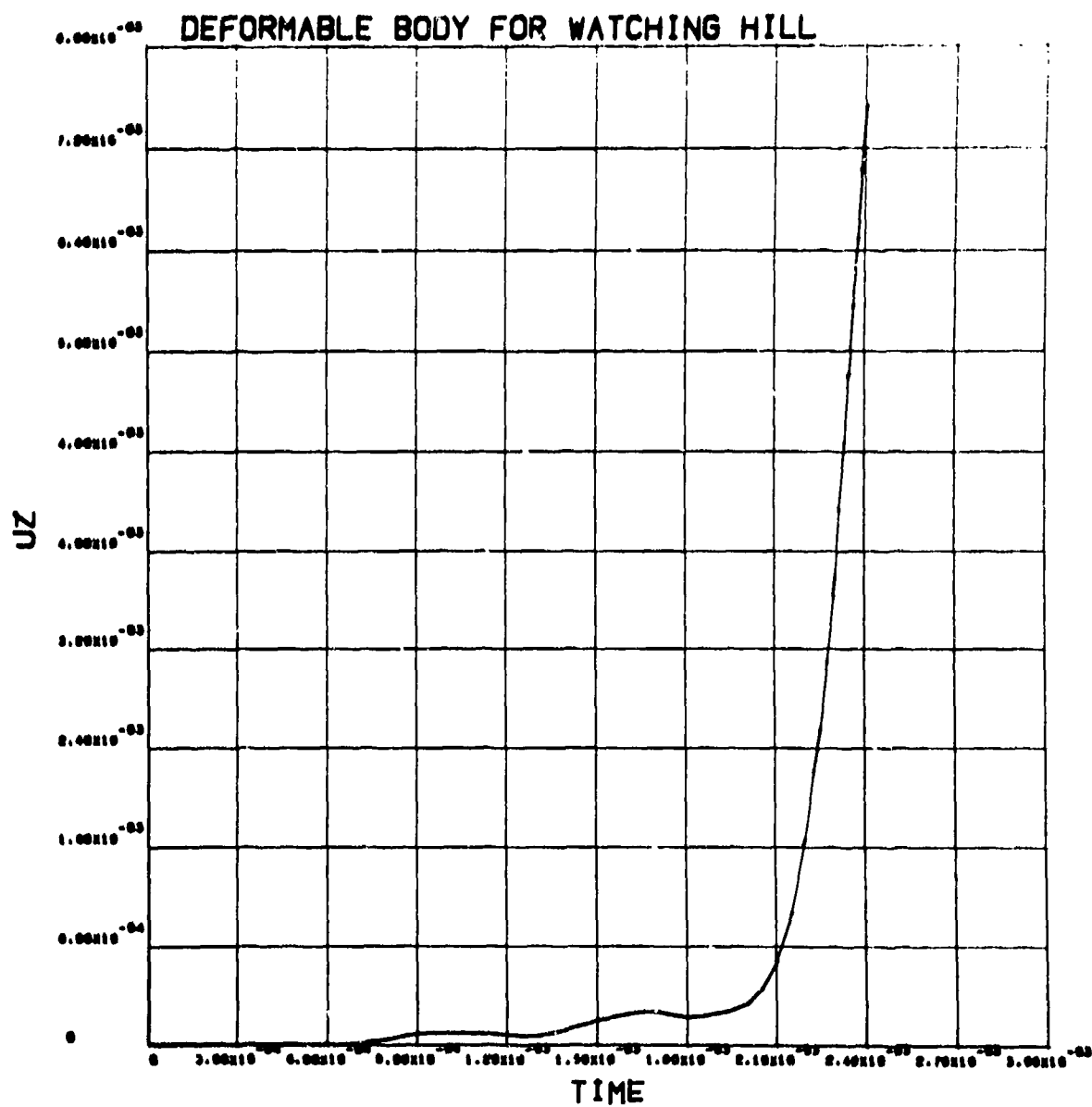
Figure B-108

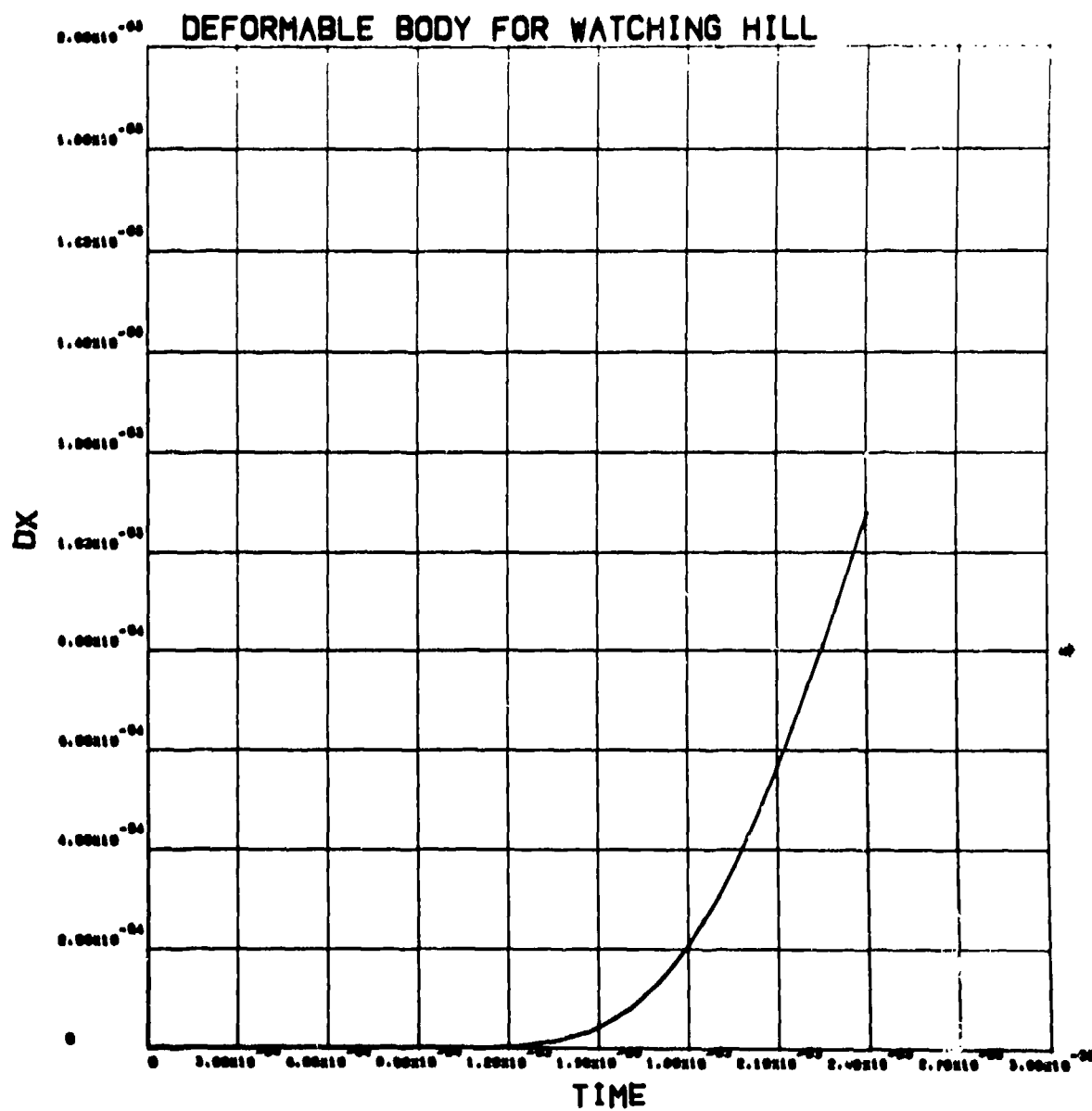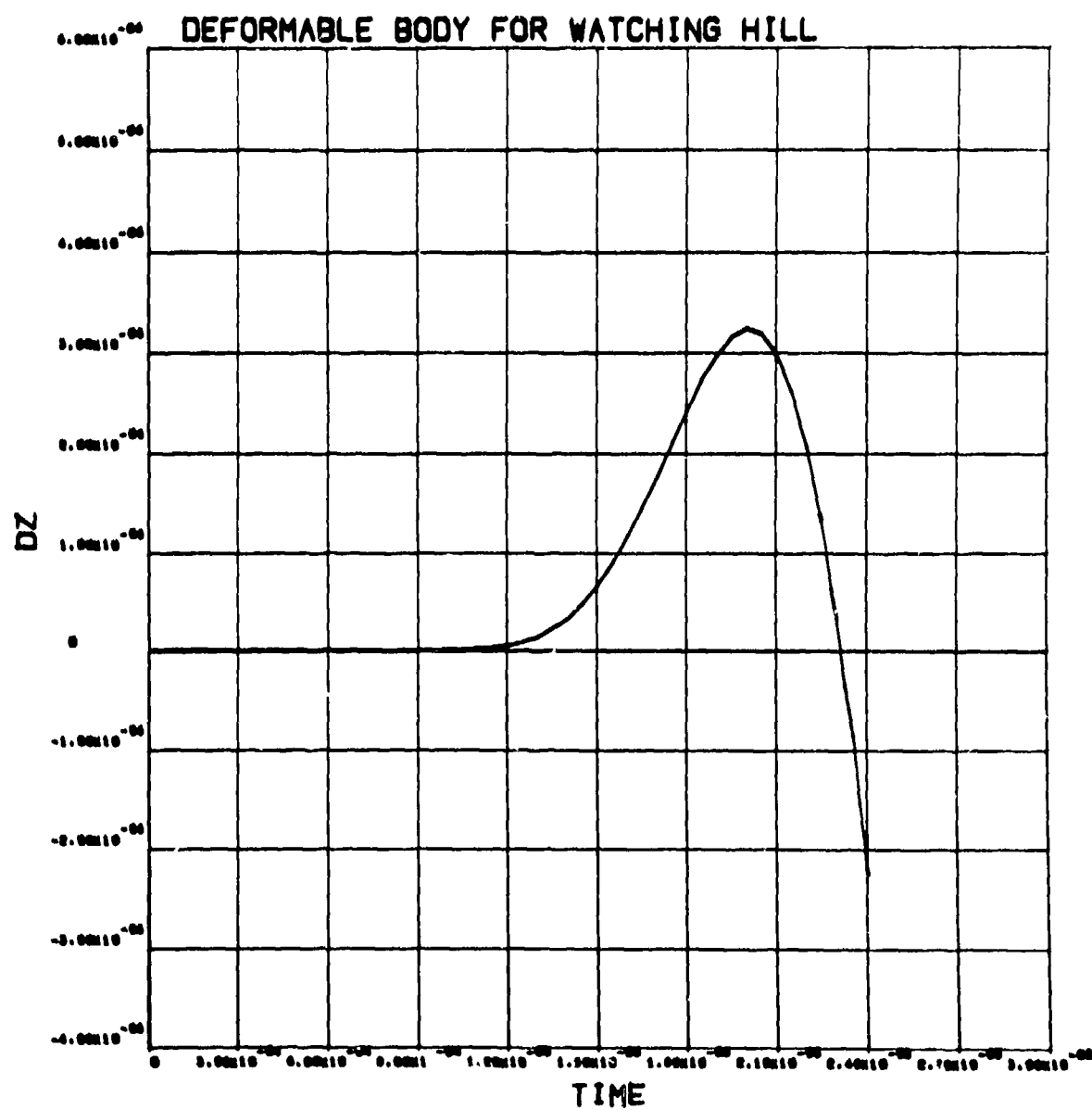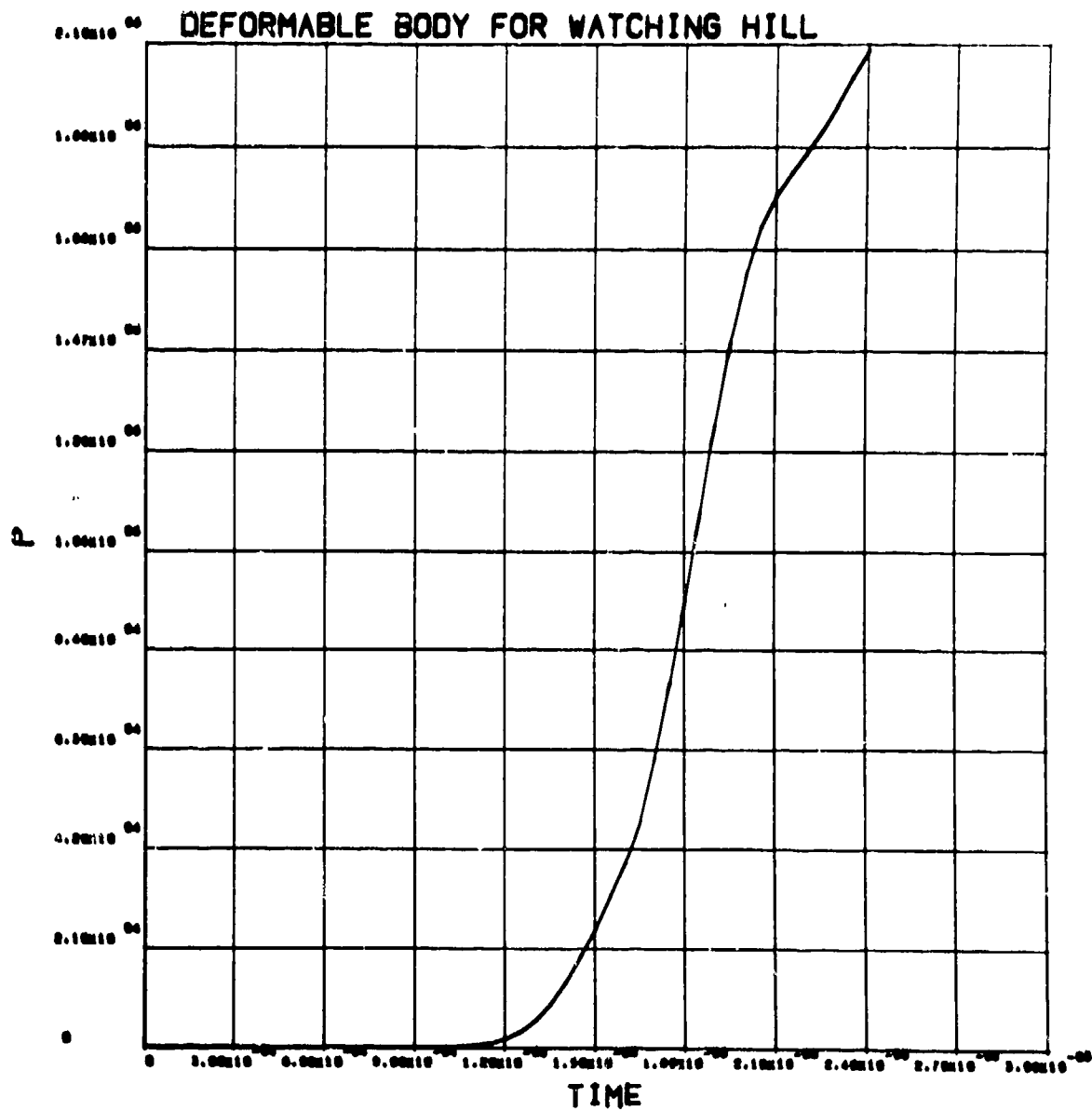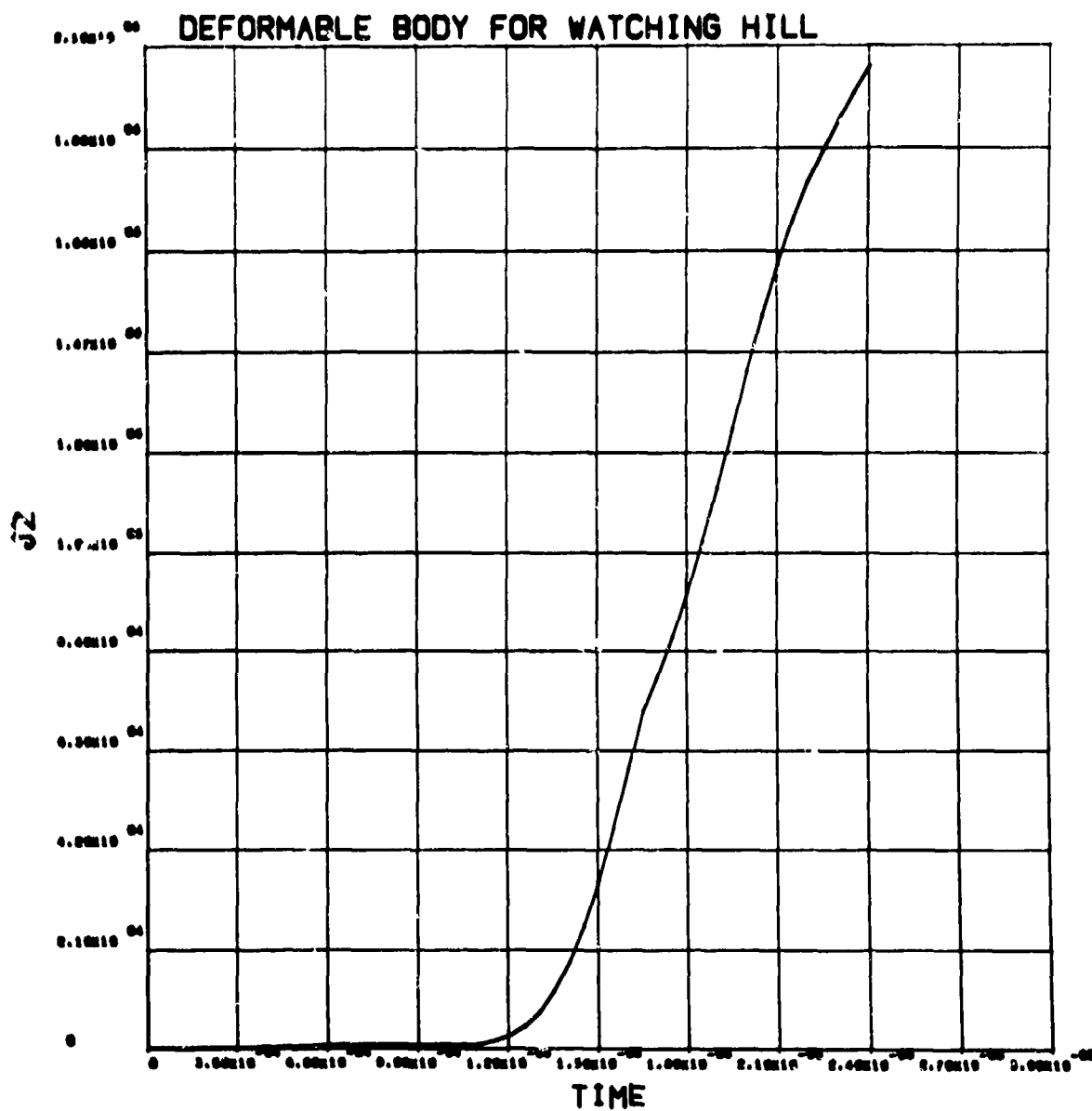Vertical velocity history (m/s) in soil at range 0.44 m, depth 0.4 m (deformable penetrator).
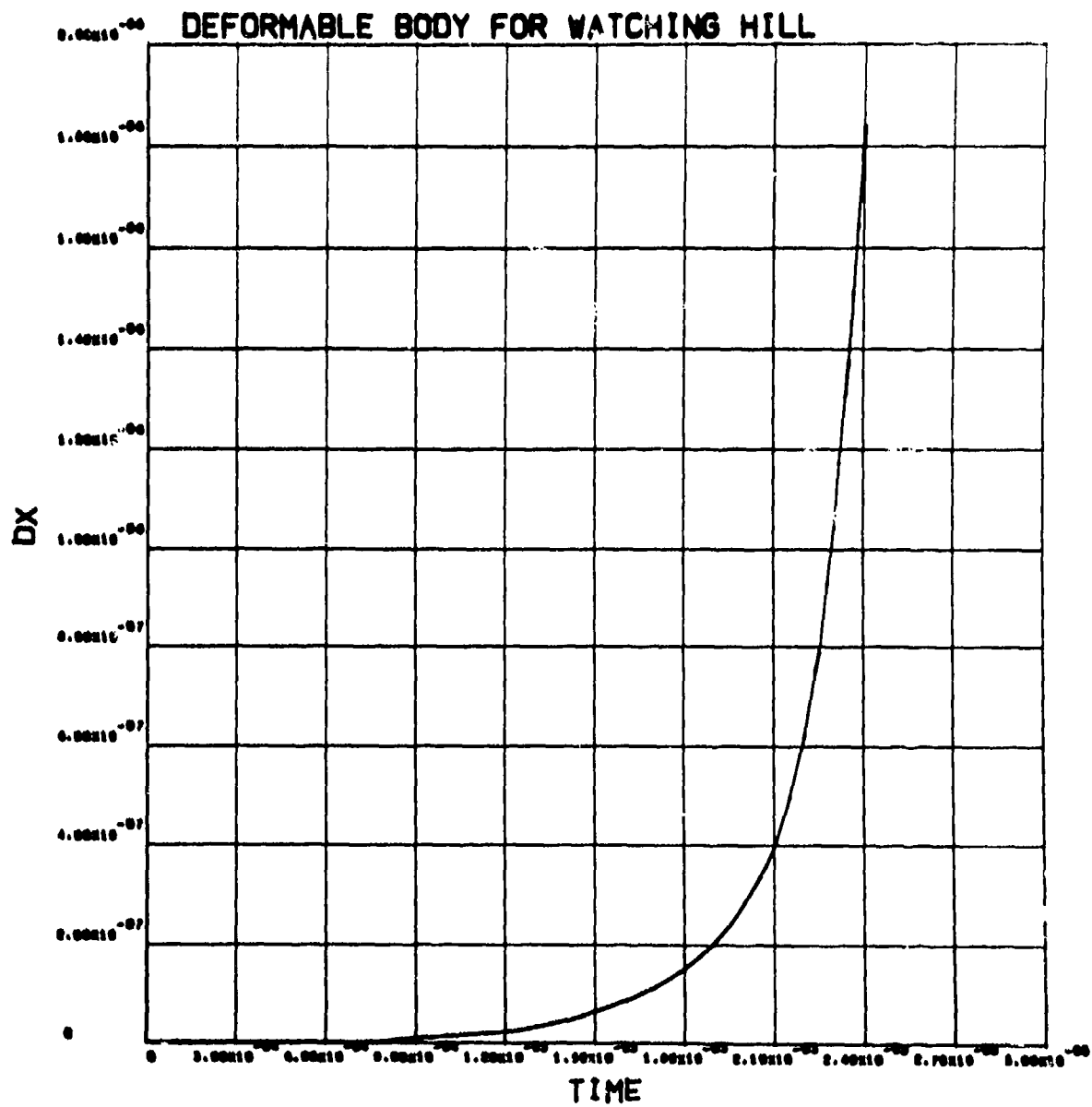
Figure B-109

Radial displacement history (m) in soil at range 0.44 m, depth 0.4 m (deformable

353
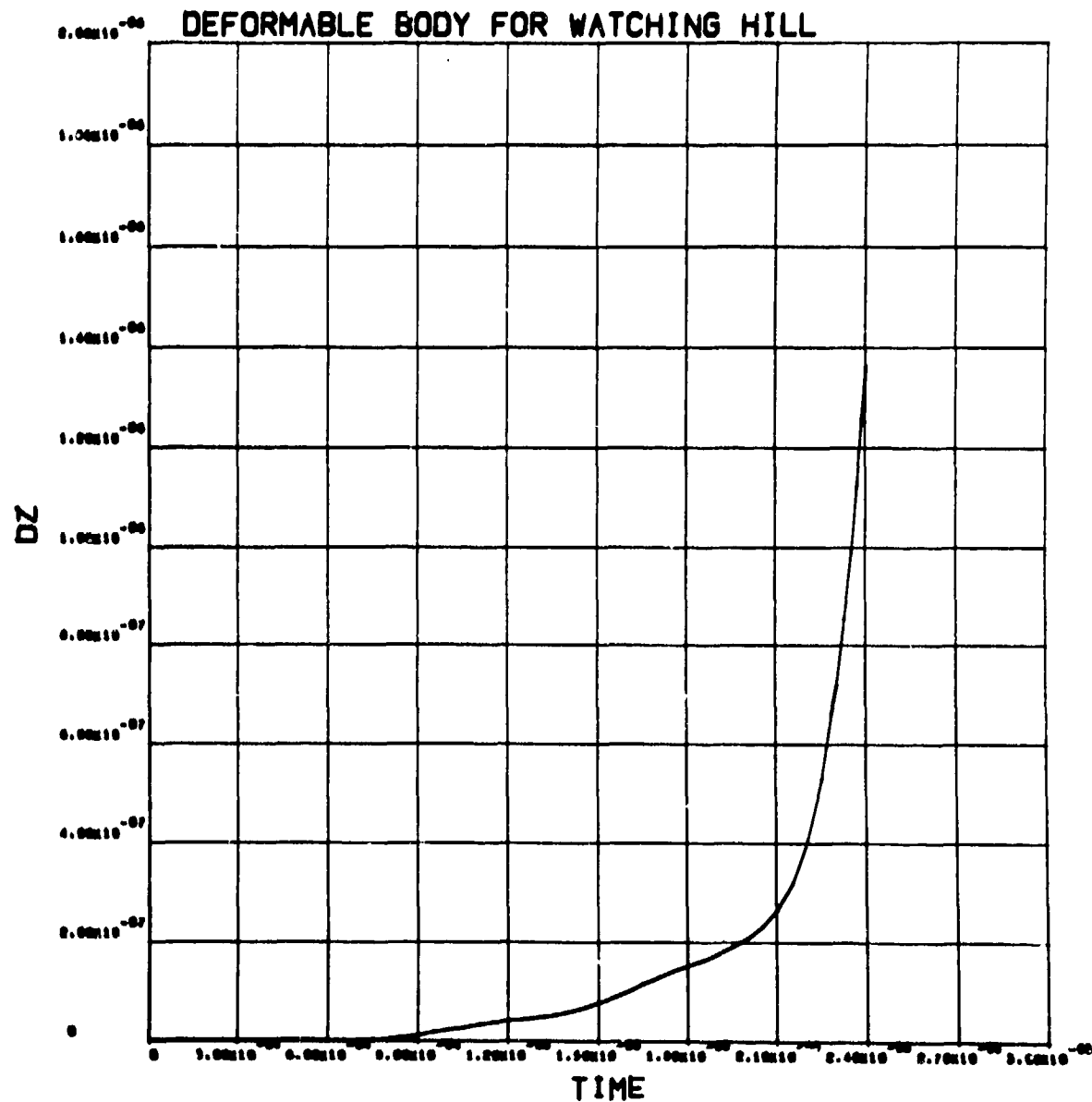
Figure B-110

Vertical displacement history (m) in soil at range 0.44 m, depth 0.4 m (deformable penetrator).

354
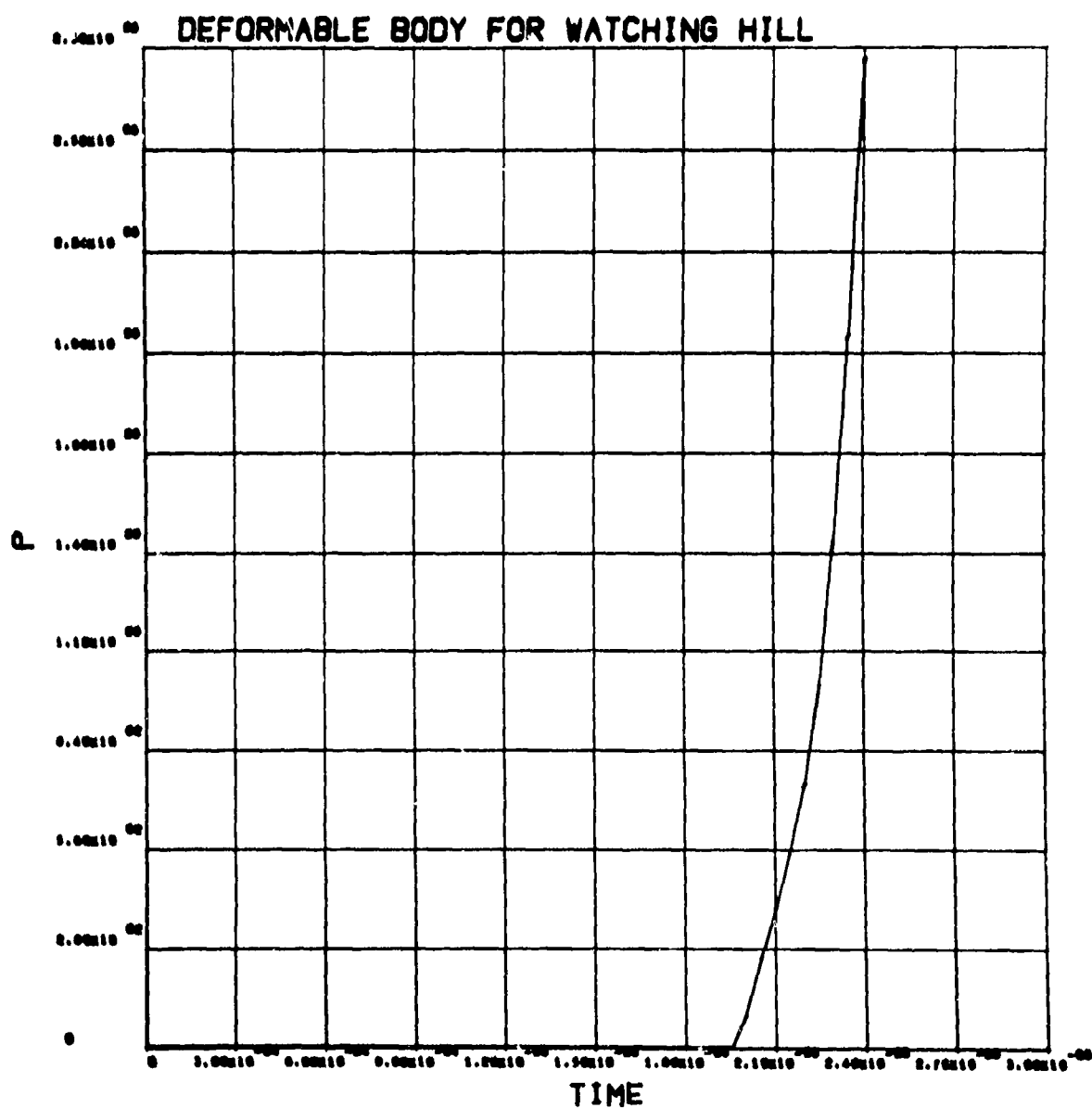
Figure B-111
Pressure history (Pa) in soil at range 0.44 m, depth 0.4 m (deformable penetrator).
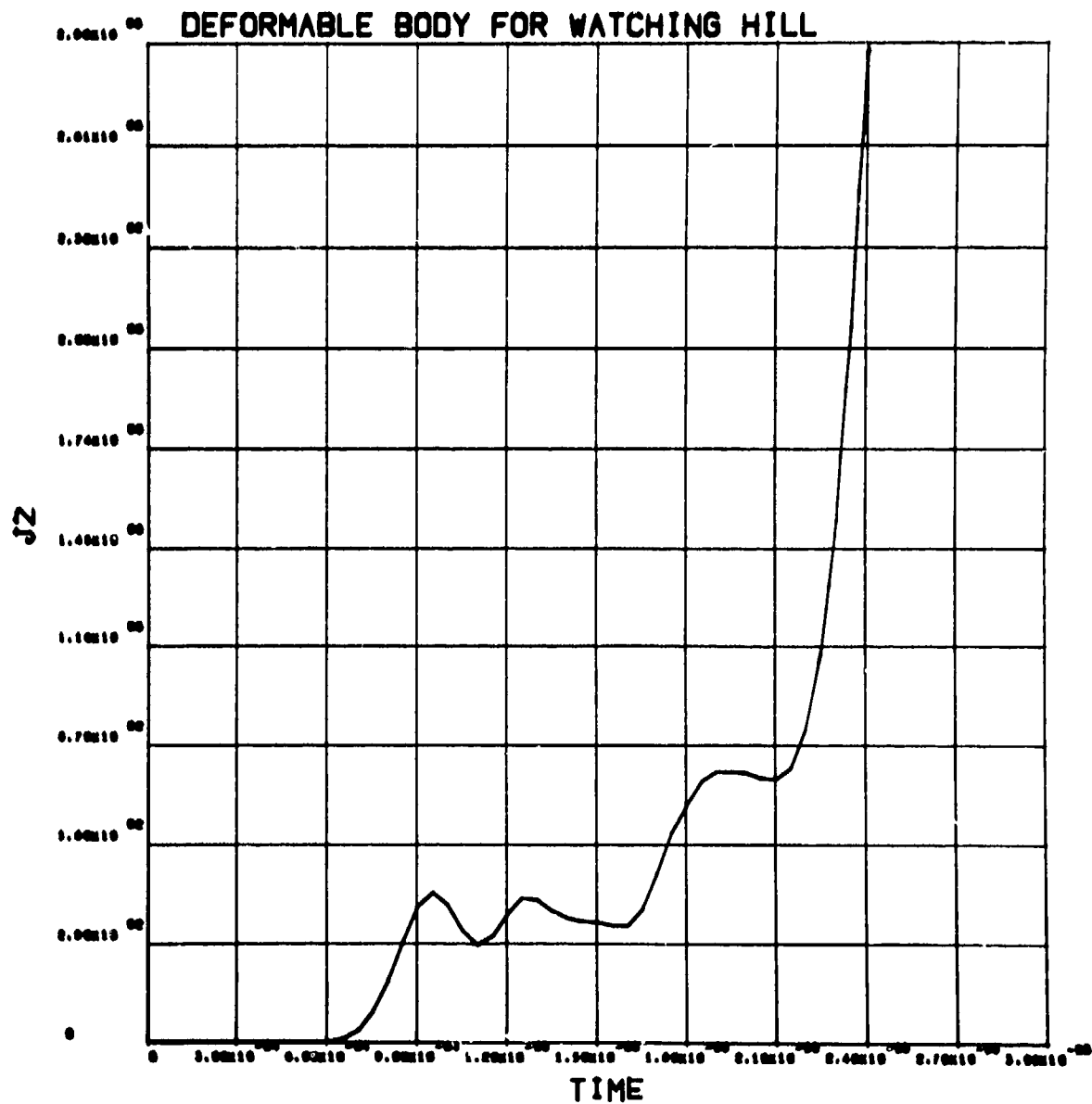
Figure B-112

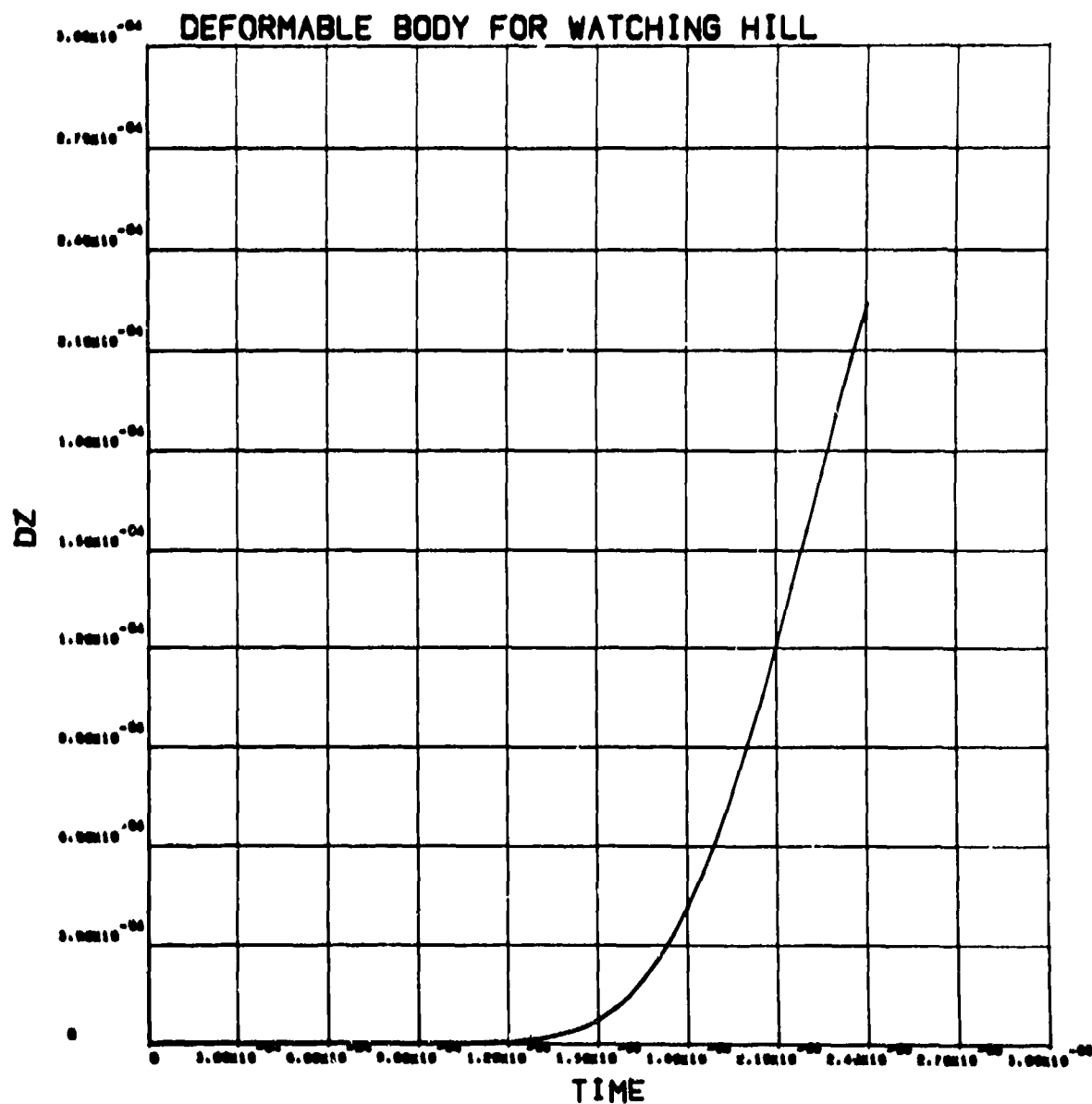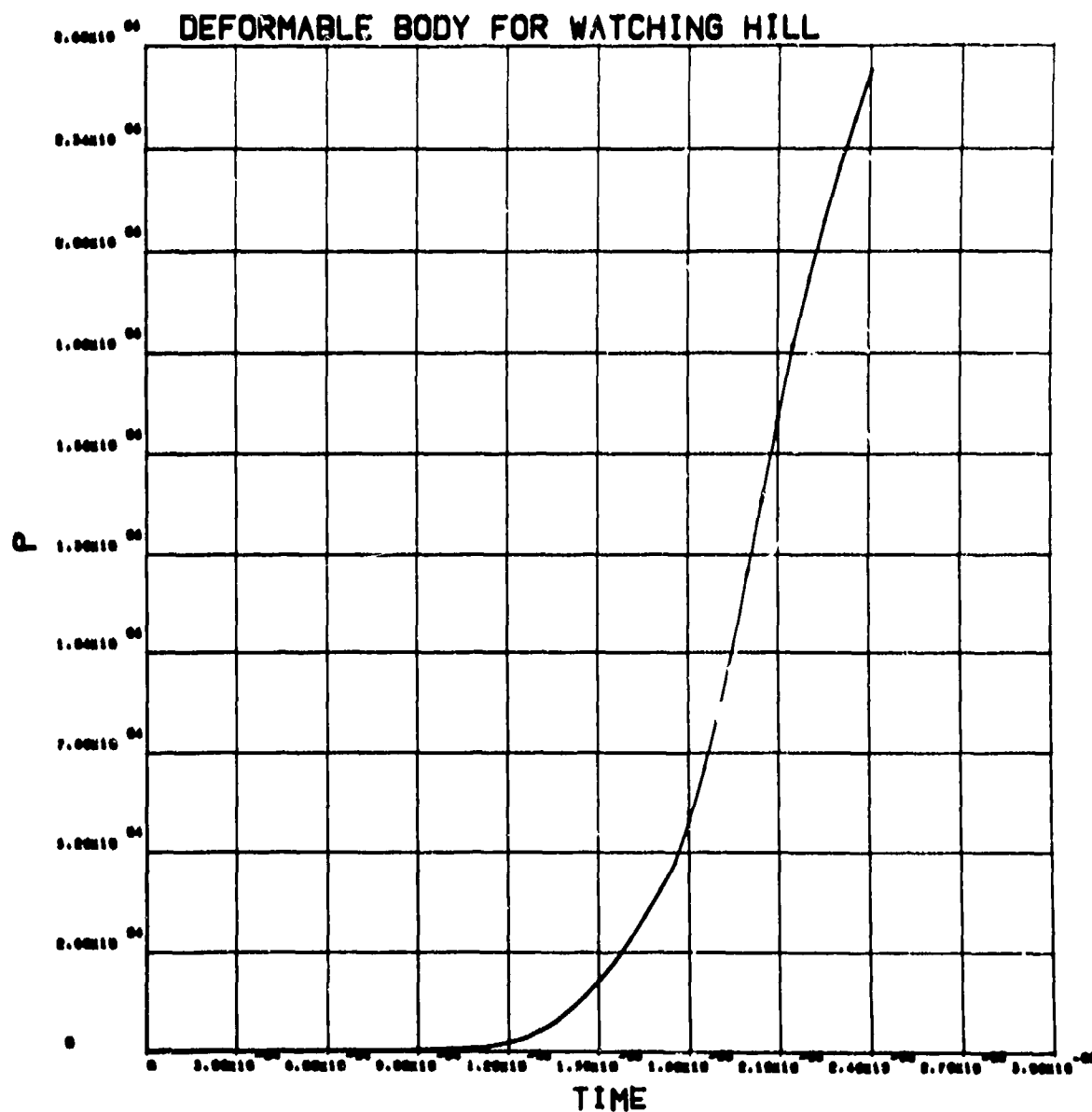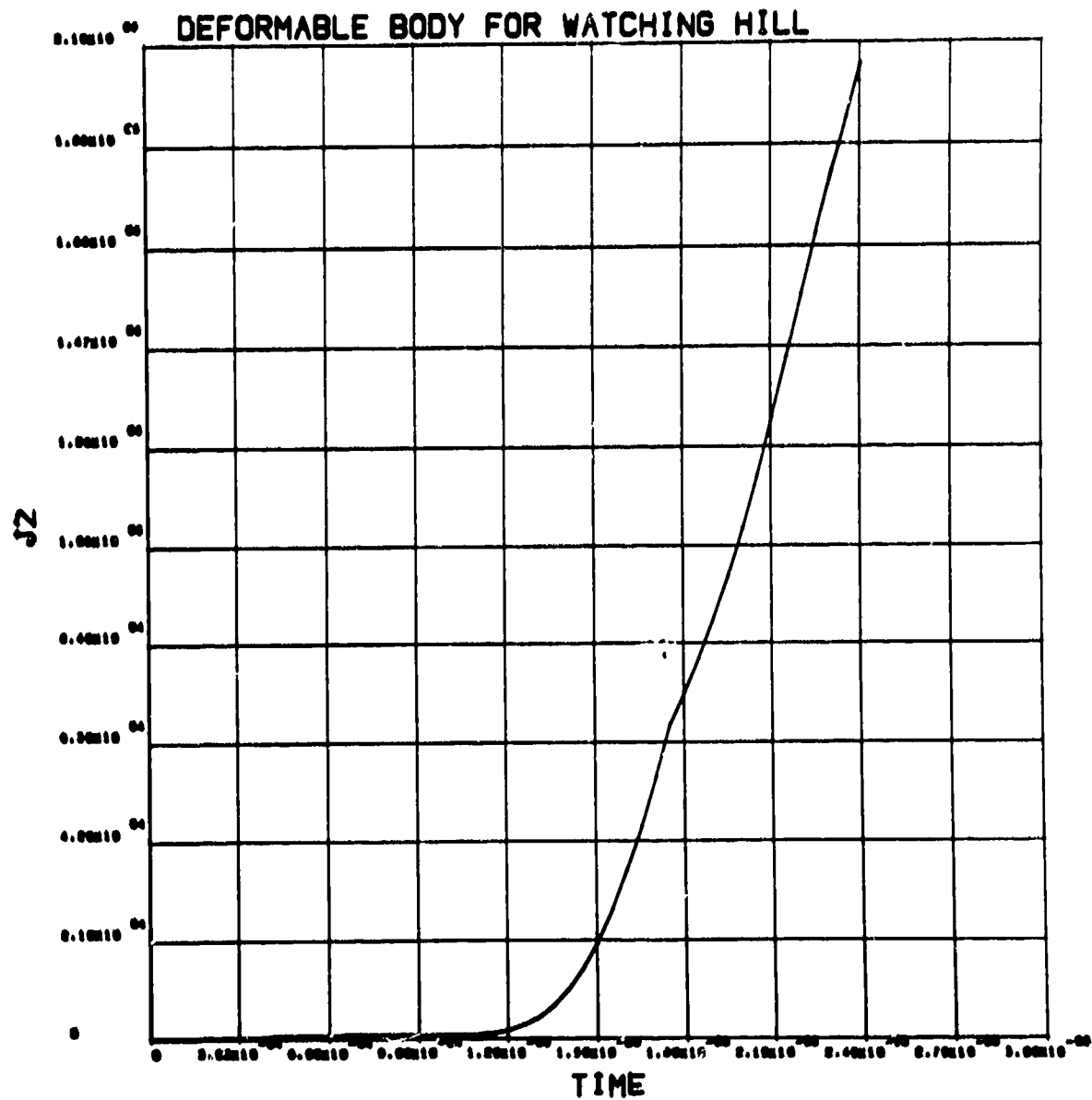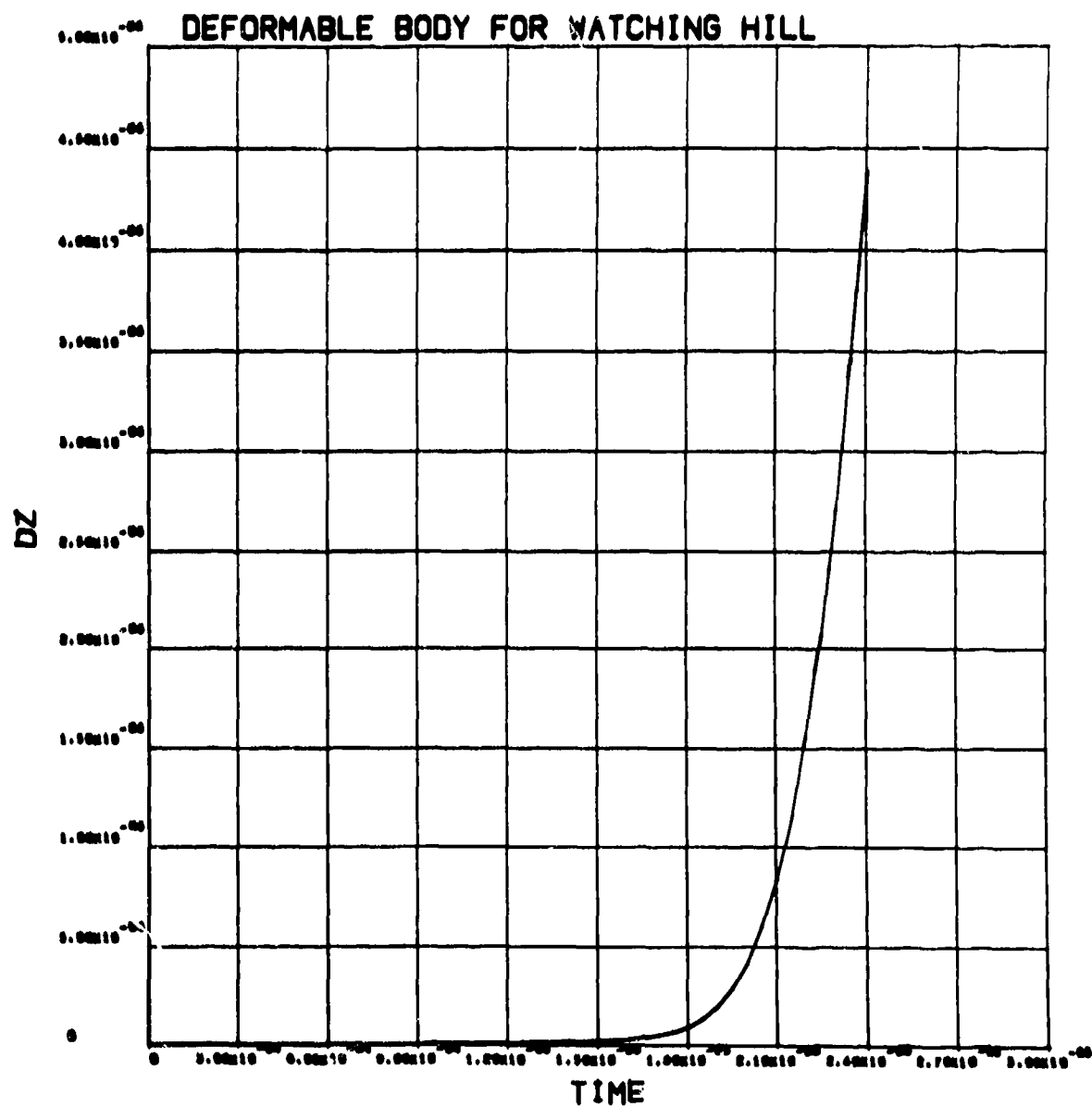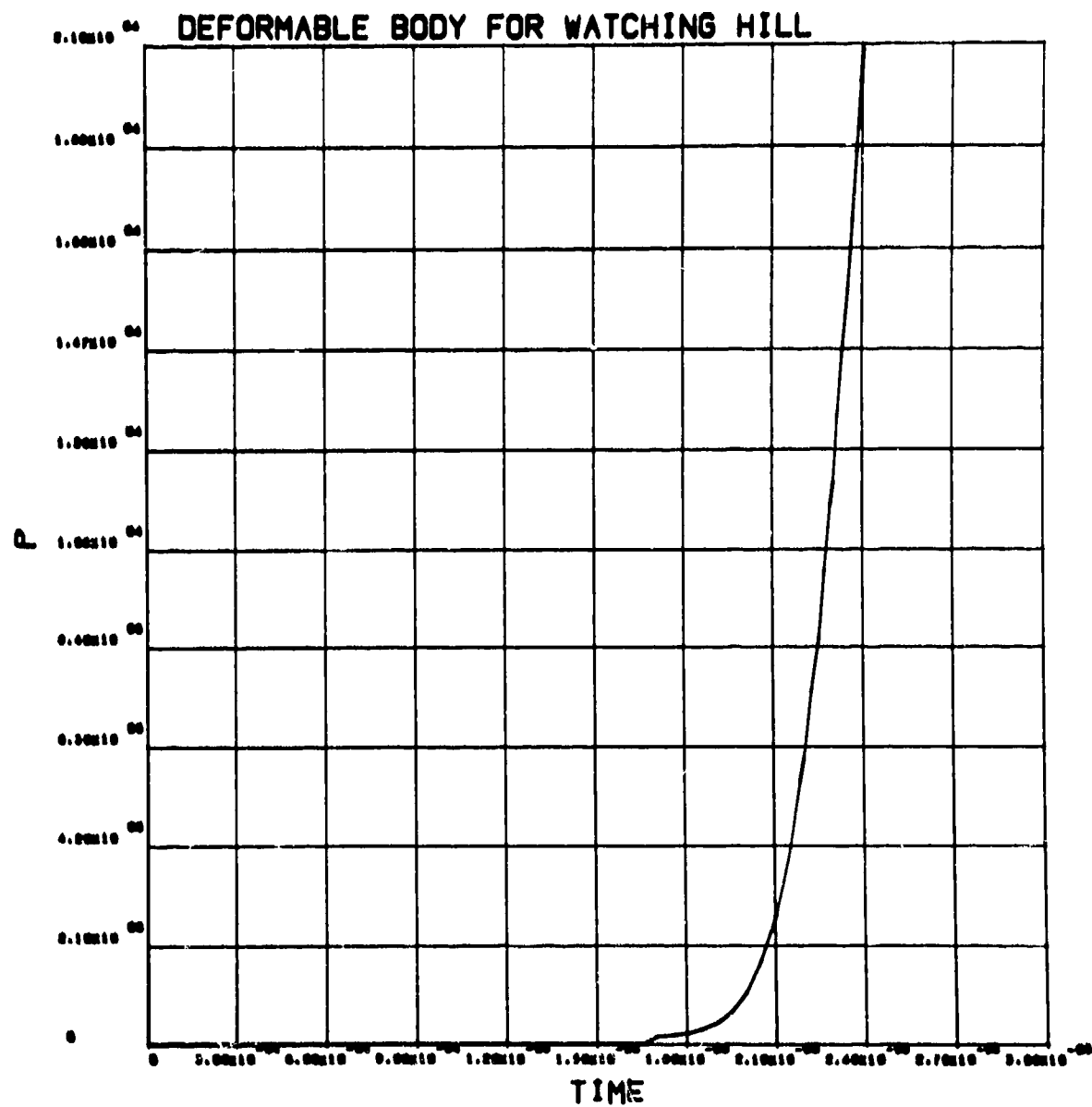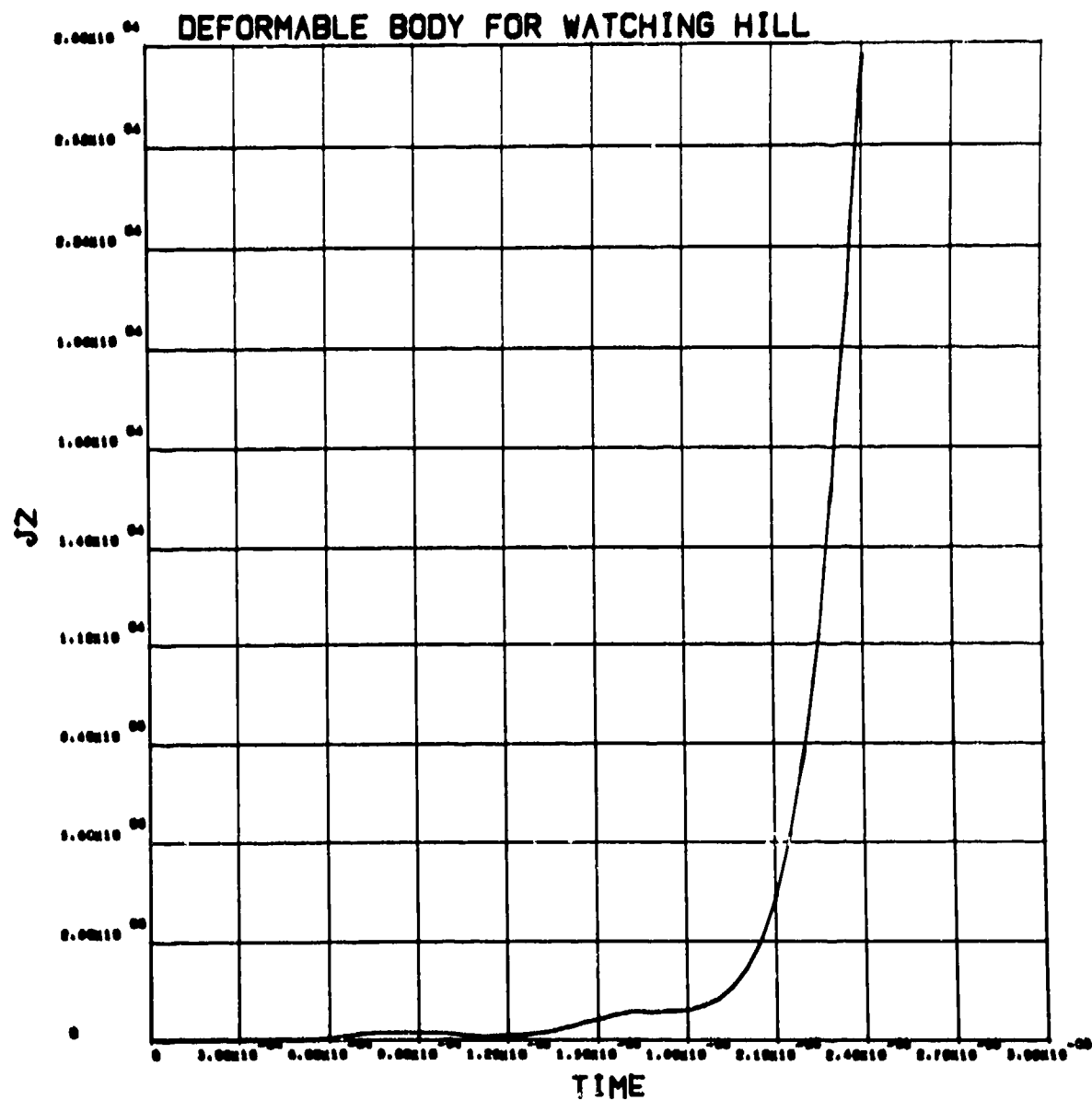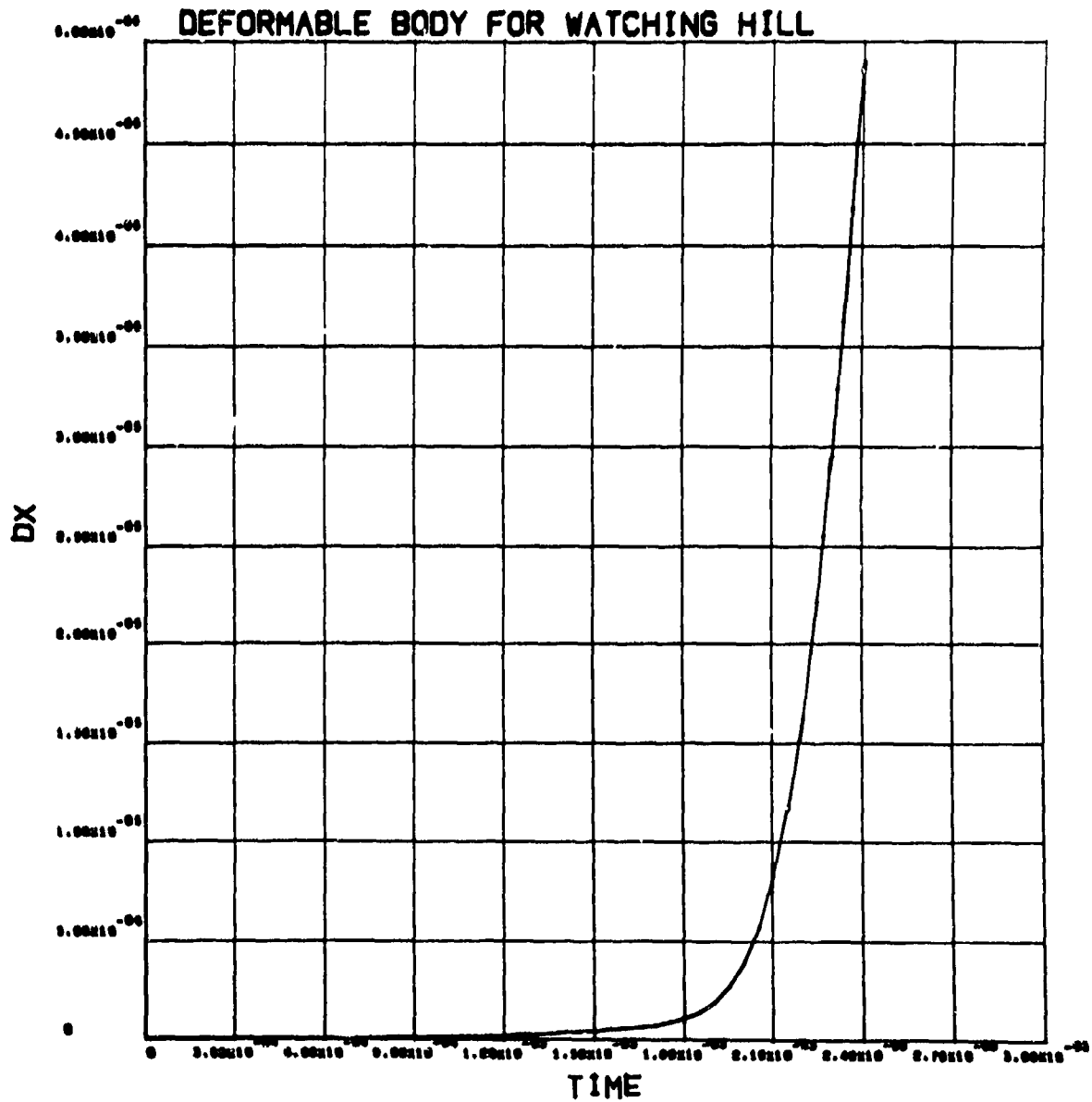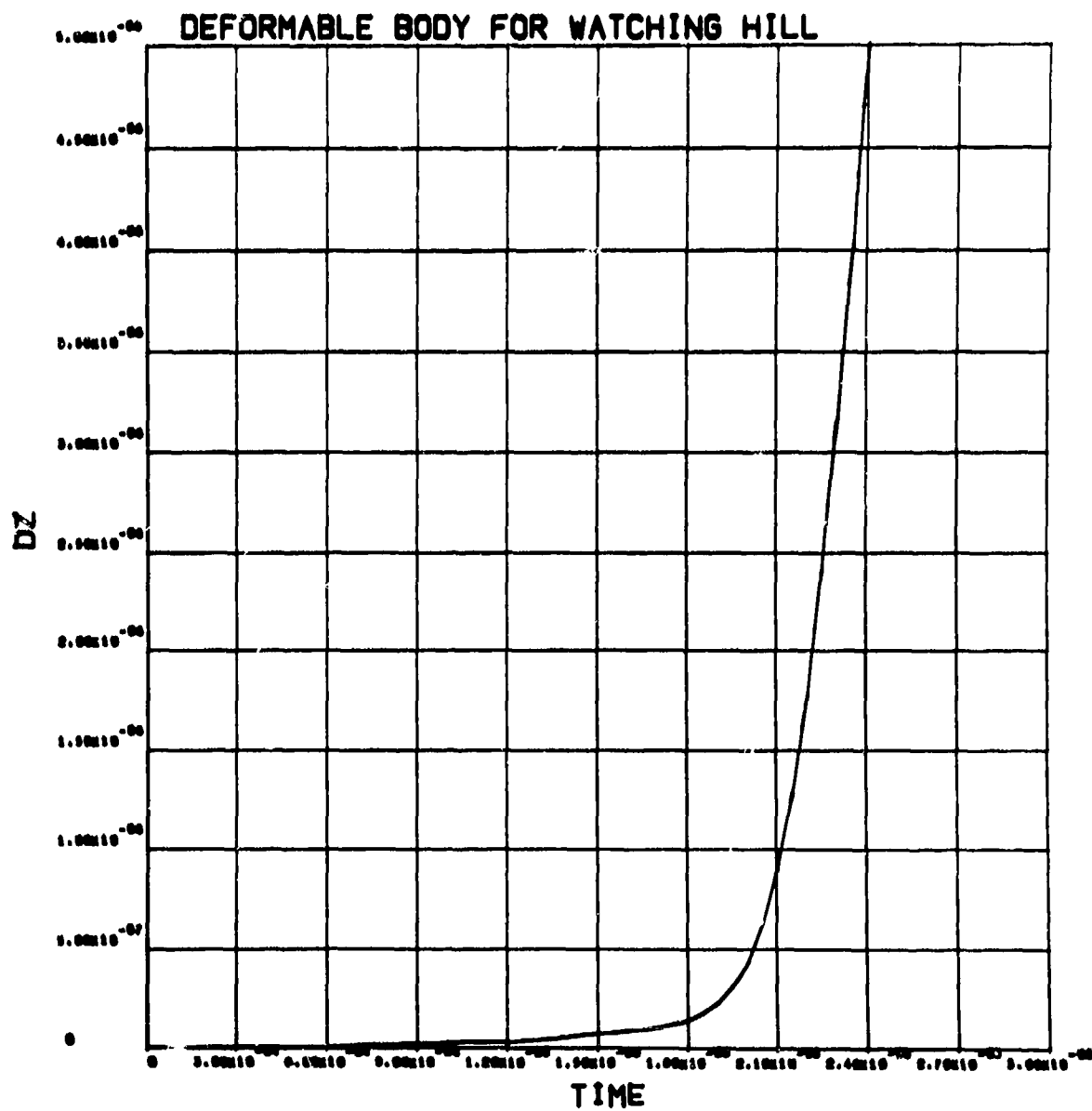Deviator stress, J2, history (Pa) in soil at range 0.44 m, depth 0.4 m (deformable penetrator), (octahedral shear stress = $\sqrt{2/3}$ (J2)).

DISTRIBUTION LIST

DEPARTMENT OF DEFENSE

Assistant to the Secretary of Defense
Atomic Energy
    ATTN: Honorable Donald R. Cotter

Director
Defense Civil Preparedness Agency
    ATTN: Technical Library

Defense Documentation Center
12 cy ATTN: TC

Director
Defense Intelligence Agency
    ATTN: Technical Library
    ATTN: DT-2, Wpns. & Sys. Div.
    ATTN: DI-7E
    ATTN: DI-7D, Edward O'Farrell

Director
Defense Mapping Agency
    ATTN: H. Lindsey

Director
Defense Nuclear Agency
    ATTN: STSI, Archives
2 cy ATTN: STTL, Tech Library
    ATTN: DDST
15 cy ATTN: SPSS

Director of Defense Research & Engineering
Department of Defense
    ATTN: R. Thorkildsen
    ATTN: Milton J. Minneman
    ATTN: DD 'TWP
    ATTN: DD 'S&SS
    ATTN: George R. Barse
    ATTN: AD 'SW
    ATTN: Craig W. Hartsell

Commander
Field Command
Defense Nuclear Agency
    ATTN: FCPR

Director
Interservice Nuclear Weapons School
    ATTN: Tech Library

Weapons Systems Evaluation Group
    ATTN: Doc Con

Chief
Livermore Division, Field Command DNA
Lawrence Livermore Laboratory
    ATTN: FCPRL

DEPARTMENT OF THE ARMY

Assistant Chief of Staff for Force Development
Department of the Army
    ATTN: Technical Library
    ATTN: Dir. of Chem. & Nuc. Ops.

Director
Ballistic Missile Defense Advanced Tech Center
Huntsville Office
    ATTN: CRDABH-S
    ATTN: CRDABH-X

Manager
Ballistic Missile Defense Program Office
    ATTN: John Shea

Headquarters
Central Army Group
    ATTN: CENEN, LTC J. L. Spruill

Department of the Army
Office Chief of Engineers
Publication Department
2 cy ATTN: DAEN-RDM
2 cy ATTN: DAEN-MCE-D

Chief of Research, Development & Acquisition
Department of the Army
    ATTN: Technical Library
    ATTN: DAMA-CSM-N, LTC E. V. Deboeser, Jr.

Commander
Frankford Arsenal
    ATTN: L. Baldini

Commander
Harry Diamond Laboratories
    ATTN: Frank J. Vraterie
    ATTN: Allen Holmes
    ATTN: AMXDO-RBH, James H. Gwaltney
    ATTN: AMXDO-NP

Commander
Picatinny Arsenal
    ATTN: Paul Harris
    ATTN: Ernie Zimpo
    ATTN: Arcadio Garcia
    ATTN: Technical Library
    ATTN: P. Angelloti
    ATTN: Jerry Pental
    ATTN: Ray Goldstein
    ATTN: Marty Margolin
    ATTN: William Meyer
    ATTN: Ray Moesner

Commander and Director
U.S. Army Cold Region Res. Engr. Lab.
    ATTN: G. Swinzow

357

DEPARTMENT OF THE ARMY

Director
U.S. Army Ballistic Research Laboratories
    ATTN: J. H. Keefer
    ATTN: G. Roecker
2 cy ATTN: Tech Library Edward Baicy
    ATTN: Norris J. Huffington, Jr.
    ATTN: B. Reiter
    ATTN: W. Taylor
    ATTN: AMXBR-TB, J. T. Frasier
    ATTN: AMXBR-X, Julius J. Meszaros
    ATTN: J. W. Apgar
    ATTN: G. Grabarek
    ATTN: D. Dunn
    ATTN: Joseph Sperazza

Commander
U.S. Army Communications Command
    ATTN: Technical Library

Command
U.S. Army Engineer Center
    ATTN: ATSEN-SY-L

Project Engineer
U.S. Army Engineer District, Huntsville
    ATTN: HNDSE-R, Michael M. Dembo

Division Engineer
U.S. Army Engineer District, Ohio River
    ATTN: Technical Library

Commandant
U.S. Army Engineer School
    ATTN: S. Grazier

Director
U.S. Army Engineer Waterways Experiment Station
    ATTN: A. Rooke
    ATTN: Leo Ingram
    ATTN: Guy Jackson
    ATTN: John N. Strange
    ATTN: P. Nadala
    ATTN: Kim Davis
    ATTN: Technical Library
    ATTN: William Flathau
    ATTN: Behzad Rohani

Commander
U.S. Army Materials & Mechanics Research Center
    ATTN: John Mescall
    ATTN: Technical Library
    ATTN: Richard Shea

Director
U.S Army Material Systems Analysis Agency
U.S. Army Aberdeen R&D Center
    ATTN: M. Reches

Commander
U.S. Army Materiel Command
    ATTN: Technical Library
2 cy ATTN: AMCRD-BN
2 cy ATTN: AMCRD-WN

Commander
U.S. Army Materiel Command
Foreign and Scientific Tech Center
    ATTN: Research & Concepts Branch

DEPARTMENT OF THE ARMY (Continued)

Commander
U.S. Army Missile Command
Redstone Arsenal
    ATTN: Technical Library
    ATTN: F. Fleming
    ATTN: W. Jann

Commander
U.S. Army Mobility Equipment R and D Center
    ATTN: Technical Library

Commander
U.S. Army Nuclear Agency
    ATTN: Tech Library
    ATTN: MAJ F. P. Weichel
    ATTN: COL Quinn

Commandant
U.S. Army War College
    ATTN: Library

Commander
U.S. Army Weapons Command
Rock Island Arsenal
    ATTN: Technical Library
    ATTN: COL C. Treat
    ATTN: Frank Black

DEPARTMENT OF THE NAVY

Chief of Naval Research
Navy Department
    ATTN: Technical Library

Officer-in-Charge
Civil Engineering Laboratory
    ATTN: R. J. Odello
    ATTN: Technical Library

Commander
Naval Electronic Systems Command
Naval Electronic Systems Command Hqs.
    ATTN: RME 117-21A

Commander
Naval Facilities Engineering Command
Headquarters
    ATTN: Technical Library

Superintendent
Naval Postgraduate School
    ATTN: Code 2124, Tech Rpts. Librarian

Director
Naval Research Laboratory
    ATTN: Code 2027, Tech Library

Commander
Naval Surface Weapons Center
    ATTN: Code 1224, Navy Nuc. Prgms. Off.
    ATTN: Code 730, Tech Library
    ATTN: G. Briggs
    ATTN: Robert D. Heidenreich
    ATTN: Jules Enig
    ATTN: Mary P. King
    ATTN: Mr. Kasdorf

DEPARTMENT OF THE NAVY (Continued)

Commander
Naval Surface Weapons Center
Dahlgren Laboratory
    ATTN: M. Weiland
    ATTN: Ted Williams
    ATTN: William Wisherd
    ATTN: Technical Library

Commander
Naval Weapons Center
    ATTN: Paul Cordle
    ATTN: Carl Austin
    ATTN: Code 533, Tech Library

Commanding Officer
Naval Weapons Evaluation Facility
    ATTN: Technical Library

Director
Strategic Systems Project Office
Navy Department
    ATTN: NSP-43, Tech Library

DEPARTMENT OF THE AIR FORCE

AF Armament Laboratory, AFSC
    ATTN: Maj Thomas Tomasetti
    ATTN: Masey Valentine
    ATTN: DLOSL-LIB
    ATTN: Dr. Kulp
    ATTN: William Cramer
    ATTN: Leonard Wilson
    ATTN: John Collins
    ATTN: Tech Library
    ATTN: Capt Larry Looney

AF Institute of Technology, AU
    ATTN: Library AFIT, Bldg. 640, Area B

AF Weapons Laboratory, AFSC
    ATTN: SUL
    ATTN: Robert Port
    ATTN: DEV, M. A. Plamondon

Headquarters
Air Force Systems Command
    ATTN: Technical Library

Commander
Armament Development & Test Center
    ATTN: Tech Library

Commander
Foreign Technology Division, AFSC
    ATTN: TD-BTA Library

HQ USAF/IN
    ATTN: INATA

HQ USAF/RD
    ATTN: RDPM, Col J. E. McCormack

Commander
Rome Air Development Center, AFSC
    ATTN: EMTLD, Doc Library

SAMSO/DE
    ATTN: DEB

ENERGY RESEARCH & DEVELOPMENT ADMINISTRATION

Division of Military Application
U. S. Energy Research & Development Administration
    ATTN: Doc Control for Test Office

University of California
Lawrence Livermore Laboratory
    ATTN: Tech Library
    ATTN: Larry W. Woodruff, L-125
    ATTN: Doc Con for W. Scanlin
    ATTN: Mark Wilkins
    ATTN: Doc Con for R. L. Walker
    ATTN: Frank Walker

Los Alamos Scientific Laboratory
    ATTN: Doc Con for G. Dials
    ATTN: Doc Con for Reports Library
    ATTN: Doc Con for Tom Dowler
    ATTN: Doc Con for C. Cremer

Sandia Laboratories
Livermore Laboratory
    ATTN: Doc Con for Tech Library
    ATTN: Doc Con for T. Gold

Sandia Laboratories
    ATTN: Doc Con for 3141 Sandia Rpt Coll
    ATTN: Doc Con for Walter Herrmann
    ATTN: Doc Con for John Colp
    ATTN: Doc Con for William Patterson
    ATTN: Doc Con for John Keizur
    ATTN: Doc Con for W. Altsmeirer
    ATTN: Doc Con for William Caudle
    ATTN: Doc Con for Luke J. Vortman
    ATTN: Doc Con for A. Narath
    ATTN: Doc Con for J. Scott
    ATTN: Doc Con for A. Chabai
    ATTN: Doc Con for R. Byers
    ATTN: Doc Con for R. Walsh

U. S. Energy Research & Development Administration
Albuquerque Operations Office
    ATTN: Doc Con for Tech Library

U. S. Energy Research & Development Administration
Division of Headquarters Services
    ATTN: Doc Con for Class. Tech. Library

U. S. Energy Research & Development Administration
Nevada Operations Office
    ATTN: Doc Con for Tech. Library

OTHER GOVERNMENT AGENCIES

Bureau of Mines
Twin Cities Research Center
    ATTN: R. E. Thill

DEPARTMENT OF DEFENSE CONTRACTORS

Aerospace Corporation
    ATTN: George Young
    ATTN: R. Strickler
    ATTN: Tech. Info. Services

Agbabian Associates
    ATTN: M. Agbabian

Applied Theory, Inc.
2 cy ATTN: John G. Trulio

DEPARTMENT OF DEFENSE CONTRACTORS (Continued)

Atomic Weapon Research Establishment
Aldermaston
ATTN: B. D. Lambourn

Avco Research & Systems Group
ATTN: David Henderson
ATTN: John Atanasoff
ATTN: Research Library A830, Rm 7201
ATTN: Frank Lasher

Bell Telephone Laboratories, Inc.
ATTN: Tech Rpt. Ctr.

Battelle Memorial Institute
ATTN: Technical Library

The BDM Corporation
ATTN: Hank Ponsford

The Boeing Company
ATTN: Reynold Atlas
ATTN: Aerospace Library

California Research & Technology, Inc.
ATTN: Ken Kreyenhagen
ATTN: Technical Library

Civil/Nuclear Systems Corp.
ATTN: Robert Crawford

EG&G, Inc.
Albuquerque Division
ATTN: Technical Library

General Dynamics Corp.
Pomona Operation
ATTN: Keith Anderson

General Electric Company
TEMPO-Center for Advanced Studies
ATTN: DASIAC

IIT Research Institute
ATTN: Technical Library

Institute for Defense Analyses
ATTN: Ida Librarian, Ruth S. Smith

J. L. Merritt
Consulting & Special Engr. Svs. Inc.
ATTN: J. L. Merritt
ATTN: Technical Library

Kaman Avidyne
Division of Kaman Sciences Corp.
ATTN: Norman P. Hobbs
ATTN: Technical Library
ATTN: E. S. Criscione

Kaman Sciences Corporation
ATTN: Library

Lockheed Missiles & Space Co., Inc.
ATTN: Technical Library
ATTN: M. Culp

Lockheed Missiles and Space Company
ATTN. Tech Info. Ctr. D'COLL

DEPARTMENT OF DEFENSE CONTRACTORS (Continued)

M. I. T.
Department of Earth & Planetary Sciences
ATTN: W. Brace

Martin Marietta Aeros., . .
Orlando Division
ATTN: N. E. Singletary
ATTN: Al Gowan
ATTN: M. Anthony

National Science Foundation
ATTN: W. Hakala

Nathan M. Newmark
Consulting Engineering Services
ATTN: Nathan M. Newmark

University of New Mexico
ATTN: G. E. Triandafalidis
ATTN: H. D. Southward

Physics International Company
ATTN: Doc Con for Dennis Orphal
ATTN: Doc Con for Robert Swift
ATTN: Doc Con for Larry A. Behrmann
ATTN: Doc Con for Fred M. Sauer
ATTN: Doc Con for Charles Godfrey
ATTN: Doc Con for Tech Library

R & D Associates
ATTN: Harold L. Brode
ATTN: Henry Cooper
ATTN: Technical Library
ATTN: Cyprus P. Knowles
ATTN: J. G. Lewis
ATTN: William B. Wright, Jr.

Science Applications, Inc.
ATTN: D. E. Maxwell
ATTN: David Bernstein

Science Applications, Inc.
ATTN: William M. Layson

Science Applications, Inc.
ATTN: C. Hudson
ATTN: Technical Library

Stanford Research Institute
ATTN: Lynn Seamans
ATTN: SRI Library, Rm G021
ATTN: George R. Abrahamson
ATTN: Carl Peterson
ATTN: Burt R. Gasten

Systems, Science and Software, Inc.
ATTN: Edward Gaffrey
ATTN: Donald R. Grine
ATTN: R. Allen
ATTN: Tech Library

Terra Tek, Inc.
ATTN: Technical Library
ATTN: Sidney Green
ATTN: A. H. Jones

Texas A & M University
ATTN: J. Handin

DEPARTMENT OF DEFENSE CONTRACTORS (Continued)

Texas A & M University System
c/o Texas A & M Research Foundation
    ATTN: Harry Coyle

The BDM Corporation
    ATTN: Technical Library

TRW Systems Group
    ATTN: Tech. Info. Center/S-1930

University of California at Los Angeles
Geology
    ATTN: O. L. Anderson

University of Utah
    ATTN: S. R. Swanson

DEPARTMENT OF DEFENSE CONTRACTORS (Continued)

University of Oklahoma
Research Institute
    ATTN: John Thompson

Washington State University
Department of Physics
    ATTN: G. Duvall

Weidlinger Associates Consulting Engineers
    ATTN: J. W. Wright
    ATTN: Melvin L. Baron

Weidlinger Associates Consulting Engineers
    ATTN: J. Isenberg